

UC Riverside

UC Riverside Electronic Theses and Dissertations

Title

Synthesis of Self-Assembled Coordination Cages for Biomimetic Catalysis

Permalink

<https://escholarship.org/uc/item/2qt5x77r>

Author

Ngai, Courtney

Publication Date

2022

Peer reviewed|Thesis/dissertation

UNIVERSITY OF CALIFORNIA
RIVERSIDE

Synthesis of Self-Assembled Coordination Cages for Biomimetic Catalysis

A Dissertation submitted in partial satisfaction
of the requirements for the degree of

Doctor of Philosophy

in

Chemistry

by

Courtney Ngai

June 2022

Dissertation Committee:

Dr. Richard J. Hooley, Chairperson

Dr. Christopher Y. Switzer

Dr. Ana Bahamonde

Copyright
Courtney Ngai
2022

The Dissertation of Courtney Ngai is approved:

Committee

Chairperson

University of California, Riverside

ACKNOWLEDGMENTS

I would like to thank my parents Jimmy and Catherine Ngai, and my siblings Nicole, Derek, Michelle, and Daren Ngai for their loving support.

To my undergraduate advisor Dr. Selina Wang and my mentor in the laboratory Xueqi (Shirley) Li at the UC Davis Olive Center: thank you for your endless patience when I first started. Under your guidance, I was able to gain confidence in myself. Everything that I learned in your laboratory has helped me build a foundation that has supported me throughout graduate school. I would also like to thank my organic chemistry professor Dr. Melekeh Nasiri and writing instructor at UC Davis Theresa Walsh. Your classes fueled my passion for both organic chemistry and teaching. I hope to become as great an educator as the both of you.

To Dr. Richard J. Hooley, thank you for guiding my professional development as a chemist at UCR. I appreciate you taking your time to help me overcome various challenges in research. I also appreciate your attention to detail and desire for me to continually push and improve myself. Thank you for your hard work in mentoring and guiding me throughout the graduate school process and providing me with the many opportunities to succeed.

To my mentors in the Hooley lab Lauren Holloway and Paul Bogie, thank you for teaching me how to synthesize cages from A to Z. It has truly enabled me to succeed in graduate school. I also would like to thank my coworkers and colleagues Adam Gill, Tabitha Miller, Briana Hickey, Colomba Sanchez-Marsetti, Bryce da Camara, Philip Dietz,

Connor Woods, Noa Bar Ziv, Jose Moreno, Ryan Wu, and Hoi-Ting Wu for their help in research these past five years. Thank you for all the fun conversations and laughs.

I also want to acknowledge my amazing friends Anh Hong and Kingsley Wu for being there for me since the first day. Anh, thank you for those long runs in the gym and running a half marathon with me.

Finally, a special thank you to Pedro Peña, for supporting me in everything that I chose to do. Thank you for all the memories, everyone, and I am looking forward to seeing what happens next!

The text of this dissertation, in part or in full, is a reprint of the material as they appear in the following publications:

Chapter 2: Bogie, P. M.; Holloway, L. R.; Ngai, C.; Miller, T. F.; Grewal, D.; Hooley, R. J. A self-assembled cage with endohedral acid groups both catalyzes substitution reactions and controls their molecularity. *Chem. Eur. J.* **2019**, *25*, 10232–10238.

Chapter 3: Ngai, C.; da Camara, B.; Woods, C. Z.; Hooley, R. J. Size and shape-selective oxocarbenium ion catalysis with a self-assembled cage host. *J. Org. Chem.* **2021**, *86*, 12862–12871.

Chapter 4: Ngai, C.; Sanchez-Marsetti, C. M.; Harman, W. H.; Hooley, R. J. Supramolecular catalysis of the oxa-Pictet–Spengler reaction with an endohedrally functionalized self-assembled cage complex. *Angew. Chem., Int. Ed.* **2020**, *59*, 23505–23509.

Chapter 5: Ngai, C.;* Bogie, P. M.;* Holloway, L. R.; Dietz, P. C.; Mueller, L. J.; Hooley, R. J. Cofactor-mediated nucleophilic substitution catalyzed by a self-assembled holoenzyme mimic. *J. Org. Chem.* **2019**, *84*, 12000-12008.

Chapter 6: Ngai, C.; Wu, HT.; da Camara B.; Williams, C. G.; Mueller, L.J.; Julian R. R.; Hooley, R. J. Moderated basicity of endohedral amine groups in an octa-cationic self-assembled cage. *Angew. Chem. Int. Ed.* **2022**, e202117011.

The co-author Richard J. Hooley listed in these publications directed and supervised the research which forms the basis for this dissertation. All other co-authors listed in these publications contributed technical expertise.

ABSTRACT OF THE DISSERTATION

Synthesis of Self-Assembled Coordination Cages for Biomimetic Catalysis

by

Courtney Ngai

Doctor of Philosophy, Graduate Program in Chemistry
University of California, Riverside, June 2022
Dr. Richard J. Hooley, Chairperson

Enzymes are catalysts found in nature that show high rate accelerations and substrate selectivity compared to synthetic catalysts. The high selectivity of enzymes derives from their active sites. These sites contain functional groups that allow enzymes to bind to substrates of specific shapes and sizes. The high efficiency and selectivity shown by enzymes has prompted chemists to mimic their behavior in a more easily analyzable system. This has led to the creation of synthetic molecules known as self-assembled metal-ligand cages. However, most cages are featureless, and lack the functional groups found in enzymes needed for binding and catalyzing reactions. My research is, therefore, geared towards overcoming the inherent problems faced when modifying these cage molecules with reactive functions.

Past studies have shown that twelve internal acid groups can be incorporated in the active site of a cage complex. My research has investigated the factors that affect the reactivity of the acid cage. The reactivity is controlled by both the nature of the nucleophile and size and orientation of the electrophile when bound. Electrophiles that have more bulk

around the basic oxygen are activated less effectively, due to being located further away from the cage's acid groups. Smaller electrophiles show minimal size-selectivity and react at a slower rate. While spherical guests are highly dependent on substitution, flat guests are unaffected by both size and shape differences in the cage. Further research has shown that the acid cage can activate complex, multistep reaction pathway. This is challenging because most reactions performed with artificial enzymes are relatively simple one or two step processes. Results from this study reveal differences in reactivity based on the size and fitting of the intermediate molecule formed inside the cage.

Enzymes can also employ "cofactors." By adding a small molecule acid to an unfunctionalized version of the acid cage, this allows size-selective, acid-catalyzed substitution reactions to occur with faster rates and variable mechanisms than simply with the acid alone. Finally, my research has formed a cage with twelve internal amine groups inside its cavity. The amine functional groups are protonated due to the water created during the assembly process. The internal amines are less basic than normal, when compared to a molecule in free solution. Similar to an enzyme's ability to control both acidity and basicity of its side-chain in its active sites, this complex can exhibit the same type of control using its internal amines and the cationic superstructure.

TABLE OF CONTENTS

Acknowledgments	iv
Abstract of the Dissertation	vii
Table of Contents	ix
List of Figures	xiii
List of Tables	ix

Chapter 1: Catalysis within Supramolecular Cages

1.1. Inspiration from Nature	1
1.2. Design and Assembly of Supramolecular Cages	2
1.3. Molecular Recognition of Unfunctionalized Coordination Complexes	6
1.4. Functionalized Complexes with Non-reactive Groups	7
1.5. Functionalized complexes with Small Endohedral Groups	9
1.6. Challenges in Catalysis	13
1.7. Cavity-directed Catalysis using Unfunctionalized Coordination Complexes	14
1.8. Encapsulating Cofactors as Guests for Supramolecular Catalysis	18
1.9. Catalysis Using Endohedral Functional Groups	21
1.10. Design and Synthesis of a Cage with Endohedral Acid Groups	24
1.11. Summary and Outlook	28
1.12. References	30

Chapter 2: Mechanistic Control of a Cage-catalyzed Nucleophilic Substitution Reaction

2.1. Introduction	41
-------------------	----

2.2. Cage-Catalyzed Nucleophilic Substitution	43
2.3. Nucleophilic Substitution Reactions with Different Electrophiles	46
2.4. Nucleophilic Substitution Reactions with Different Nucleophiles	48
2.5. Binding Studies	51
2.6. Variable Molecularity in Reaction Mechanism	53
2.7. Mechanistic Analysis	58
2.8. Catalytic Self-Destruction	61
2.9. Conclusion	63
2.10. References	65
Chapter 3: Size and Shape-selective Cage-catalyzed Oxocarbenium Ion Catalysis	
3.1. Introduction	68
3.2. Thioetherification of Vinyl Diphenylmethanol Derivatives	69
3.3. Thioetherification using THP Ether 3.4 and PrSH	74
3.4. Thioetherification using Water as the Nucleophile	77
3.5. Reactions with a Smaller Acetal Substrate	81
3.6. Thioetherification of Isochromanyl Ethers	84
3.7. Binding to Various Guest Substrates	87
3.8. Discussion of Results	89
3.9. Conclusion	93
3.10. References	94
Chapter 4: Supramolecular Cage-catalyzed oxa-Pictet Spengler Reaction	
4.1. Introduction	96

4.2. Cage-catalyzed Oxa-Pictet Spengler Reaction	97
4.3. Reaction Scope	101
4.4. Host-Guest Binding Studies	106
4.5. Mechanistic Analysis	108
4.6. Conclusion	111
4.7. References	113
Chapter 5: Biomimetic Catalysis via a CoFactor-Mediated Type Mechanism	
5.1. Introduction	117
5.2. Cofactor-mediated Catalysis	118
5.3. Binding of Various Substrates and Products	120
5.4. Varying the Size and Acidity of the Cofactor	126
5.5. Varying the Cofactor Concentration	129
5.6. Varying the Electrophile	132
5.7. Varying the Nucleophile	135
5.8. Mechanistic Analysis	137
5.9. Conclusion	140
5.10. References	141
Chapter 6: Synthesis of a Cage Complex with Endohedral Amine Groups	
6.1. Introduction	145
6.2. Synthesis of Ligand with Internal Amines	146
6.3. Assembly of the Cage Complex	149
6.4. Characterization of the Cage Complex	151

6.5. Titrations of Basic Guests into the Complex	154
6.6. Investigating Ability to Promote or Inhibit Chemical Reactions	159
6.7. Amine Detritylation Reactions	160
6.8. Conclusion	163
6.9. References	166
Chapter 7: Experimental	
7.1. General Information	170
7.2. General Binding Calculations	171
7.3. Experimental for Chapter 2	175
7.4. Experimental for Chapter 3	176
7.5. Experimental for Chapter 4	180
7.6. Experimental for Chapter 5	185
7.7. Experimental for Chapter 6	187
7.8. Selected Spectra for Chapter 2	196
7.9. Selected Spectra for Chapter 3	203
7.10. Selected Spectra for Chapter 4	239
7.11. Selected Spectra for Chapter 5	277
7.12. Selected Spectra for Chapter 6	295
7.13. References	324

LIST OF FIGURES

- Figure 1.1.** Formation of self-assembled metal-ligand cage complexes of differing stoichiometry and geometric shapes. 2
- Figure 1.2.** Comparison of linear versus V-shaped ligands for cage assembly. 4
- Figure 1.3.** The two octahedral enantiomers meridional (*mer*) and facial (*fac*) are shown here. Rotation of the *fac* centers gives rise to two enantiomers: Λ (left) and Δ (right). 5
- Figure 1.4.** a) M_4L_4 capsule shown to encapsulate a cyclohexane molecule. b) Strong molecular recognition of sucrose in water using cage **1.5**. 6
- Figure 1.5.** Synthesis of nanospheres with inert function. a) Assembly of the complex with V-shaped ligands containing 4-pyridiyl groups. b) Assembly of the complex with V-shaped ligands containing 4-ethynylpyridiyl functional group. 8
- Figure 1.6.** a) Assembly of a $Pd_{12}L_{24}$ nanosphere that is capable of encapsulating Ag^+ cations. b) Formation of smaller paddlewheel complexes capable of encapsulating two cisplatin molecules. 10
- Figure 1.7.** Selective anion templated assembly of a Ni_4L_6 tetrahedral complex. 11
- Figure 1.8.** Formation of an M_4L_6 tetrahedral complex using hydrogen-bonding groups. 12
- Figure 1.9.** a) Ga_4L_6 tetrahedral complex used its cavity alone to promote various reactions. b) An octahedral Pd_6L_4 used for the selective formation of products that are usually not observed. 15
- Figure 1.10.** Reactions catalyzed by **1.16**. a) aza-Cope rearrangement. b) Nazarov cyclization. c) Hydrolysis of orthoformates. 16
- Figure 1.11.** Reactions catalyzed by **1.17**. a) Diels-alder reaction of 9-hydroxymethylanthracene N-cyclohexylphthalimide. b) Demethylenation of cyclopropanes. c) Photoreaction of o-quinone with substituted toluene. 18
- Figure 1.12.** A Co_8L_{12} coordination cage complex using its hydroxide anions to catalyze a Kemp elimination. 20
- Figure 1.13.** $M_{12}L_{24}$ nanosphere with twenty-four endohedral guanidinium binding sites that can bind a phosphate species to co-catalyze the cyclization of acetylenic acid. 21

- Figure 1.14.** a) Formation of a $M_{12}L_{24}$ nanosphere with 24 gold-containing endohedral functional groups. b) Cage-catalyzed selective cyclization and intramolecular [4+2] cycloaddition. 22
- Figure 1.15.** a) Formation of two nanosphere complexes with endohedrally functionalized TEMPO or MacMillan-type amine catalytic groups. b) Tandem oxidation and cyclization reaction using two cage complexes. 23
- Figure 1.16.** Synthesis of an unfunctionalized cage with a medium-size cavity that possess a reactive center for adding functional groups. 25
- Figure 1.17.** Synthesis of an acid cage with 12 internal carboxylic acid groups. 26
- Figure 1.18.** a) Tandem reaction hydrolysis of acetal and cage-to-cage transformation. b) Control experiments with other catalysts for the tandem process. 27
- Figure 2.1.** a) Cage-catalyzed hydrolysis of acetal reaction. b) Cage-catalyzed nucleophilic substitution of triphenylmethanol. 42
- Figure 2.2.** Summary of all substrates and catalysts used in the S_N1 reaction. 43
- Figure 2.3.** a) Kinetic analysis of nucleophilic substitution reaction using different electrophiles and catalysts. b) Classic S_N1 mechanism and rate law. 44
- Figure 2.4.** Spectra illustrating product formation using acid cage **1.30** as the host. 45
- Figure 2.5.** 1H NMR spectra of the acid promoted substitution reaction between **1.30** and **PrSH** in the presence of: a) 30 mol % control acid **1.35** b) 30 mol % diacid **1.35** and 10 mol % suberone mesocate **2.6** (298 K, CD_3CN). 46
- Figure 2.6.** 1H NMR spectra of the acid promoted substitution reaction between **2.1** and **TolSH** in the presence of: a) 5 mol % cage **1** b) 5 mol % cage **1** under a nitrogen atmosphere in a J. Young NMR tube. Both reactions were performed at 80 °C and monitored over time (353 K, CD_3CN). 49
- Figure 2.7.** 1H NMR spectra of the acid promoted substitution reaction between **2.1** and indole **2.9** in the presence of 5 mol % cage **1.30**. The reaction was performed at 80 °C and monitored over time (353 K, CD_3CN). 51
- Figure 2.8.** Nucleophilic substitution between **2.1** and **PrSH** in the presence of 5 mol % cage **1.30**, at varying concentrations of **PrSH** a) 19.75 mM b) 39.5 mM, performed at 80 °C and monitored over time (298K, CD_3CN). 54

Figure 2.9. Initial rates with varying [PrSH] a) **2.1** with 5 % **1.30**, 333 K; b) **2.2** with 5 % **1.30**, 333 K; c) **2.1** with 5 % CF₃CO₂H, 273 K. [**2.1**] = 15.8 mM, [**1.30**] and [CF₃CO₂H] = 0.8 mM in CD₃CN; concentrations were confirmed using dioxane as standard. 55

Figure 2.10. Substrate inhibition of **2.1** with PrSH in the presence of 5 % cage **1.30** in CD₃CN. a) Averaged percent conversion over time (min); b) initial rates, using 19.75 mM PrSH (red) and 237 mM PrSH (orange). 57

Figure 2.11. Model of heterocomplex **1.30**•**2.1a**•PrSH (Hartree-Fock, SPARTAN). 58

Figure 2.12. a) Classic S_N1 reaction observed with ethyl trityl ether **2.2** as the electrophile. b) Bimolecular process observed with triphenylmethanol **2.1** as the electrophile. 60

Figure 2.13. a) Detritylation that causes a negative feedback loop. b) The product is destroyed via transimination. [**2.8**] = 15.8 mM, [PrSH] = 19.75 mM, [**1.30**] = 0.8 mM in CD₃CN, 298 K; concentrations were confirmed using dioxane as standard, rates monitored by ¹H NMR. 61

Figure 3.1. Reactions catalyzed by cage **1.30**. a) Hydrolysis of acetal. b) Nucleophilic substitution of triphenylmethanol. 69

Figure 3.2. Expanded ¹H NMR spectra of the acid promoted reaction between **3.1** and PrSH in the presence of 5 mol % cage **1.30**. 70

Figure 3.3. Expanded ¹H NMR spectra of the acid promoted reaction between **3.3** and PrSH in the presence of 5 mol % cage **1.30** or CSA **3.6**. 73

Figure 3.4. Two pathways in thioetherification of **3.4**. a) Pathway A shows carbocation formation. b) Pathway B shows oxocarbenium ion formation. 74

Figure 3.5. ¹H NMR spectra of the acid promoted reaction between **3.5** and PrSH in CD₃CN in the presence of: a) 5 mol % cage **1.30** b) 5 mol % CSA **3.6**. 75

Figure 3.6. ¹H NMR spectra of the acid promoted reaction between **3.3** and H₂O in CD₃CN in the presence of: a) 5 mol % cage **1.30** b) 5 mol % CSA **3.6**. 78

Figure 3.7. ¹H NMR spectra of the acid promoted reaction between **3.4** and H₂O in CD₃CN in the presence of: a) 5 mol % cage **1.30** b) 5 mol % CSA **3.6**. 79

Figure 3.8. Reactions with tertiary alcohol derivative **3.4** and H₂O at different temperatures. 80

Figure 3.9. ¹H NMR spectra of the acid promoted reaction between **3.10** and PrSH in CD₃CN in the presence of: a) 5 mol % cage **1.30** b) 5 mol % CSA **3.6**. 82

Figure 3.10. ¹ H NMR spectra of the acid promoted reaction between 3.10 and H₂O in CD ₃ CN in the presence of: a) 5 mol % cage 1.30 b) 5 mol % CSA 3.6 .	83
Figure 3.11. Reaction progress over time of the cage-catalyzed thioetherification of isochromanlyl ethers.	84
Figure 3.12. Reaction progress over time of the CSA-catalyzed thioetherification of isochromanlyl ethers.	85
Figure 3.13. Reaction progress over time of the 3.15 using various control catalysts.	86
Figure 3.14. Models of substrates 3.1 and 3.4 inside cage 1.30 .	90
Figure 3.15. Models of substrates 3.17 inside cage 1.30 .	92
Figure 4.1. Cage-catalyzed oxa-Pictet Spengler reaction with acid cage 1.30 .	97
Figure 4.2. Expanded ¹ H NMR spectra of the acid promoted reaction between 4.1 and 4.2 in the presence of 5 mol % cage 1.30 .	98
Figure 4.3. Control experiments with other cage hosts and acids for the oxa-Pictet Spengler reaction.	100
Figure 4.4. Reaction scheme of the oxa-Pictet Spengler reaction.	101
Figure 4.5. Indoles and acetals used in the oxa-Pictet Spengler reaction.	102
Figure 4.6. ¹ H NMR spectra of the acid promoted reaction between 4.2 and 4.16 in the presence of 5 mol % cage 1.30 .	105
Figure 4.7. Mechanistic analysis of oxa-Pictet Spengler with cage 1.30 .	108
Figure 4.8. Model of cage 1.30 binding a) nucleophile 4.2 . b) intermediate 4.4 .	109
Figure 4.9. ¹ H NMR of reaction showing disappearance of intermediate.	110
Figure 4.10. ¹ H NMR spectra of the acid promoted substitution reaction between 4.1 and 4.2 in CD ₃ CN in the presence of 5 mol % cage 1.30 and 50 mol % of NaPF ₆ .	111
Figure 5.1. Structural and graphical models of unfunctionalized cage 1.28 and acid cage 1.30 .	118

Figure 5.2. Expanded ^1H NMR spectra of the acid promoted substitution reaction between 2.1 and PrSH in the presence of 5 mol % cage 1.30 and 30 mol % acid 1.35 .	119
Figure 5.3. Comparison of initial rates to the cofactor-mediated reaction.	120
Figure 5.4. UV/Vis absorption titration of PrSH into a solution of 1.28 in CH_3CN .	123
Figure 5.5. Minimized structures of guests encapsulated in cage 5.2 .	125
Figure 5.6. Reaction progress over time for thioetherification of electrophile 2.1 and 2.2 with PrSH . a) 5% cage 1.28 /30% cofactor 1.35 , 5.1-5.4 b) 30% cofactor 1.35 , 5.1-5.4 .	127
Figure 5.7. Varying concentration of diacid 1.30 . a) Reaction progress over time with varying [1.30]; b) reaction rate vs [1.30].	130
Figure 5.8. ^1H NMR spectra of the acid promoted substitution reaction between 2.1 and PrSH in the presence of 5 mol % cage 1.28 and at varying concentrations of acid 1.30 , a) 1.58 mM, b) 3.15 mM and c) 4.73 mM.	131
Figure 5.9. Varying concentration of diacid 1.30 . a) Reaction progress over time with varying [1.30]; b) reaction rate vs [1.30].	132
Figure 5.10. Variable rate dependency on changing the electrophile in the reaction with 1.35 . a) varying [PrSH] with alcohol 2.1 b) varying [PrSH] with ether 2.2 .	133
Figure 5.11. Variable rate dependency on changing the electrophile in the reaction with 5.3 . a) varying [PrSH] with alcohol 2.1 b) varying [PrSH] with ether 2.2 .	134
Figure 5.12. ^1H NMR spectra of the acid promoted substitution reaction between 2.1 and PrSH in the presence of 5 mol % cage 1.28 and at varying concentrations of acid 5.3 a) 9.45 mM b) 18.11 mM and c) 33.08 mM.	135
Figure 5.13. ^1H NMR spectra of the acid promoted substitution reaction between 2.1 and OctSH in the presence of 5 mol % cage 1.28 and at varying concentrations of acid 1.30 , a) 11.88 mM, b) 21.26 c) 24.48 mM, and d) 62.37 mM.	136
Figure 5.14. Variable rate dependency on changing the electrophile in the reaction with 1.35 . a) varying [OctSH] with alcohol 2.1 b) varying [OctSH] with ether 2.2 .	137
Figure 5.15. Nucleophile-independent pathway in cage-catalyzed cofactor reaction.	138
Figure 5.16. Nucleophile-dependent pathway in cage-catalyzed cofactor reaction.	139

Figure 6.1. New cage complex with 12 internal alkylamine groups.	145
Figure 6.2. Synthesis of new amine ligand 6.4 .	146
Figure 6.3. Attempts at converting amides to amines using various reducing agents.	147
Figure 6.4. First attempt at forming a self-assembled complex.	149
Figure 6.5. ¹ H NMR of cage 6.1 , formed with ligand 6.4 and aldehyde 6.5 .	150
Figure 6.6. Three isomers observed in the imine region of ¹ H NMR of cage 6.1 .	151
Figure 6.7. Characterization data of cage 6.1 . a) 2D DOSY spectrum. b) 2D COSY spectrum. c) 2D ROESY spectrum.	152
Figure 6.8. UV-Vis absorption spectrum of the titration of neutral guest 3.21 into a 1.5 μM solution of cage 1 in CH ₃ CN. Neutral guest 3.21 was added in 1 μL aliquots from a 4.5 mM stock solution in CH ₃ CN.	154
Figure 6.9. Proton exchange between cage 6.1 and D ₂ O.	155
Figure 6.10. a) ¹ H NMR spectra of the titration of DABCO 6.7 into 5 mol % cage 6.1 showing cage stability b) and deuterium and hydrogen exchange. c) Dataplot of the UV absorbance changes of cage 6.1 upon titration of DABCO 6.7 in CH ₃ CN.	156
Figure 6.11. Titration of bases into cage 6.1 . a) weak base. b) strong bases.	158
Figure 6.12. ¹ H NMR spectra of the reaction between BDA and H ₂ O in the presence of 5 mol % cage 6.1 showing: a) cage stability b) product formation.	159
Figure 6.13. ¹ H NMR spectra of the reaction between benzaldehyde and malononitrile in the presence of a) 5 mol % cage 6.1 and 5% DABCO 6.7 . b) 5 % DABCO 6.7 .	160
Figure 6.14. a) Reaction progress over time monitored by ¹ H NMR with tritylated isoquinoline 6.12 (red) and N-tritylbenzylamine 6.14 (green). b) Cage 6.1 is transiminated and destroyed using N-trityl-4-bromoaniline 6.16 .	161
Figure 6.15. ¹ H NMR spectra of the reaction between 6.12 and 6.13 in the presence of 5 mol % cage 6.1 .	162
Figure 6.16. ¹ H NMR spectrum of the BF ₄ salt of cage 6.1 .	164
Figure 7.1. Dataplot of the change in chemical shift of DABCO-H ⁺ when added to cage 6.1 .	193

Figure 7.2. ^1H NMR spectra (7.80-7.20 ppm, 4.40-4.20 ppm, 2.20-1.50 ppm) of the acid promoted substitution reaction between **2.1** and adamantane thiol in the presence of 5 mol % cage **1.30**. The reaction was performed at 80 °C and monitored over time (400 MHz, 298K, CD_3CN). 196

Figure 7.3. ^1H NMR spectra (7.80-7.20 ppm, 4.40-4.20 ppm) of the acid promoted substitution reaction between **2.1** and cyclohexyl thiol in 400 μL CD_3CN in the presence of: a) 30 mol % control acid **1.35** b) 5 mol % cage **1.30**. Both reactions were performed at 80 °C and monitored over time (400 MHz, 298 K, CD_3CN). 197

Figure 7.4. ^1H NMR spectra (7.90-6.90 ppm) of the acid promoted $\text{S}_{\text{N}}1$ reaction between **2.2** and cyclohexyl thiol in the presence of: a) 30 mol % control acid **1.35** or b) 5 mol % cage **1.30**. The reaction was performed at 80 °C and monitored over time (400 MHz, 298K, CD_3CN). 198

Figure 7.5. Graphed results of the acid promoted substitution reaction between **2.1** and cyclohexyl thiol in the presence of: 5 mol % cage **1.30** (red), 30 mol % control acid **1.35** (orange). a) Averaged percent conversion values are plotted against time in minutes. b) Calculation of initial rate based on change in concentration of [product] over time in minutes. 199

Figure 7.6. ^1H NMR spectra of the acid promoted substitution reaction between **2.1** and **PrSH** in the presence of 30 mol % TFA, at varying concentrations of **PrSH** a) 9.88 mM, b) 19.75, c) 39.5 mM, and d) 59.25 mM, performed at 23 °C and monitored over time (400 MHz, 298K, CD_3CN). d) Graphed results of reaction order study represented in change in [2.5] over time in minutes. The slope of the line was taken to equal the initial rate of the reaction and the order was obtained as an average over several trials to be 0 order in nucleophile (**PrSH**). 200

Figure 7.7. UV-Vis absorption spectrum of the titration of **CySH** into a 3 μM solution of cage **1.30** in CH_3CN . **CySH** was added in 1-5 μL aliquots from a 9 mM stock solution in CD_3CN . 201

Figure 7.8. a) 1:1 binding fit model for guest **CySH** calculated via linear regression analysis using the Nelder-Mead method from the change in absorbance at two points (300 nm and 370 nm) using supramolecular.org ($K_{\text{a}} = 113.9 \pm 15.0 \times 10^3 \text{ M}^{-1}$). b) 1:2 binding fit model calculated via linear regression analysis using the Nelder-Mead method from the change in absorbance at two points (300 nm and 370 nm) using supramolecular.org¹⁻³ ($K_{11} = 156.1 \pm 11.2 \times 10^3 \text{ M}^{-1}$, $K_{12} = 4.0 \pm 0.4 \times 10^3 \text{ M}^{-1}$). 201

Figure 7.9. UV-Vis absorption spectrum of the titration of **AdSH** into a 3 μM solution of cage **1.30** in CH_3CN . **AdSH** was added in 1-5 μL aliquots from a 9 mM stock solution in CD_3CN . 202

Figure 7.10. a) 1:1 binding fit model for guest AdSH calculated via linear regression analysis using the Nelder-Mead method from the change in absorbance at two points (300 nm and 370 nm) using supramolecular.org ($K_a = 199.4 \pm 17.0 \times 10^3 \text{ M}^{-1}$). ¹⁻³ b) 1:2 binding fit model calculated for guest AdSH via linear regression analysis using the Nelder-Mead method from the change in absorbance at two points (300 nm and 370 nm) using supramolecular.org ($K_{11} = 362.7 \pm 100.1 \times 10^3 \text{ M}^{-1}$, $K_{12} = 220.8 \pm 45.3 \times 10^3 \text{ M}^{-1}$). ¹⁻³	202
Figure 7.11. ¹ H NMR spectrum of 3.3 (600 MHz, 298K, CDCl ₃).	203
Figure 7.12. ¹³ C{ ¹ H} NMR spectrum of 3.3 (151 MHz, 298K, CDCl ₃).	203
Figure 7.13. ¹ H NMR spectrum of 3.4 (600 MHz, 298K, CDCl ₃).	204
Figure 7.14. ¹³ C{ ¹ H} NMR spectrum of 3.14 (151 MHz, 298K, CDCl ₃).	204
Figure 7.15. ¹ H NMR spectrum of 3.5 (600 MHz, 298K, CD ₃ CN).	205
Figure 7.16. ¹³ C{ ¹ H} NMR spectrum of 3.5 (151 MHz, 298K, CD ₃ CN).	205
Figure 7.17. ¹ H NMR spectrum of 3.13 (400 MHz, 298K, CD ₃ CN).	206
Figure 7.18. ¹³ C{ ¹ H} NMR spectrum of 3.13 (100 MHz, 298K, CD ₃ CN)	206
Figure 7.19. ¹ H NMR spectrum of 3.20 (400 MHz, 298K, CD ₃ CN).	207
Figure 7.20. ¹³ C{ ¹ H} NMR spectrum of 3.20 (100 MHz, 298K, CD ₃ CN)	207
Figure 7.21. Full ¹ H NMR spectra of the acid promoted reaction between 3.1 and <i>n</i> -propyl thiol in the presence of 5 mol % cage 1.30 . [3.1] = 15.8 mM, [PrSH] = 19.8 mM, [1.30] = 0.8 mM, the reaction was performed at 50 °C in CD ₃ CN and monitored over time (400 MHz, CD ₃ CN).	208
Figure 7.22. Expanded ¹ H NMR spectra of the acid promoted reaction between 3.1 and <i>n</i> -propyl thiol in the presence of 5 mol % cage 1.30 showing: a) Cage stability (9.1-8.1 ppm) b) Product formation (7.6-7.0 ppm, 6.8-6.0 ppm, and 1.2-0.8 ppm). [3.1] = 15.8 mM, [PrSH] = 19.8 mM, [1.30] = 0.8 mM, the reaction was performed at 50 °C in CD ₃ CN and monitored over time (400 MHz, 323 K, CD ₃ CN).	209
Figure 7.23. ¹ H NMR spectra (7.65-7.10 ppm, 6.8-6.0 ppm, and 1.2-0.8 ppm) of the acid promoted reaction between 3.1 and <i>n</i> -propyl thiol in 400 μL CD ₃ CN in the presence of: a) 5 mol % cage 1.30 b) 5 mol % CSA 3.6 . [3.1] = 15.8 mM, [PrSH] = 19.8 mM, [1.30] = 0.8 mM, [3.6] = 0.8 mM, reactions were performed at 50 °C in CD ₃ CN and monitored over time (400 MHz, CD ₃ CN).	210

Figure 7.24. ^1H NMR spectra (7.5-7.1 ppm, 6.8-6.0 ppm, and 1.1-0.8 ppm) of the acid promoted reaction between **3.1** and *n*-propyl thiol in 400 μL CD_3CN in the presence of: a) 5 mol % pivalic acid b) 5 mol % tartaric acid c) 5 mol % trifluoroacetic acid. [**3.1**] = 15.8 mM, [**PrSH**] = 19.8 mM, [**Catalyst**] = 0.8 mM reactions were performed at 50 $^\circ\text{C}$ in CD_3CN and monitored over time (400 MHz, 323 K, CD_3CN). 211

Figure 7.25. Expanded ^1H NMR spectra of the acid promoted reaction between **3.1** and *n*-propyl thiol in the presence of 5 mol % **1.28** showing: a) Cage stability (5.85-5.55 ppm) b) Product formation (7.9-7.1 ppm, 6.8-6.0 ppm, and 1.2-0.8 ppm). [**3.1**] = 15.8 mM, [**PrSH**] = 19.8 mM, [**1.28**] = 0.8 mM, [**1.35**] = 4.7 mM, the reaction was performed at 50 $^\circ\text{C}$ in CD_3CN and monitored over time (400 MHz, 323 K, CD_3CN). 212

Figure 7.26. ^1H NMR spectra (7.65-7.10 ppm, 6.8-6.1 ppm, and 1.2-0.8 ppm) of the acid promoted reaction between **3.2** and *n*-propyl thiol in 400 μL CD_3CN in the presence of: a) 5 mol % cage **1.30** b) 5 mol % CSA **3.6**. [**3.2**] = 15.8 mM, [**PrSH**] = 19.8 mM, [**1**] = 0.8 mM, [**3.6**] = 0.8 mM, reactions were performed at 50 $^\circ\text{C}$ in CD_3CN and monitored over time (400 MHz, CD_3CN). 213

Figure 7.27. ^1H NMR spectra (7.55-7.0 ppm, 6.8-6.0 ppm, and 1.2-0.8 ppm) of the acid promoted reaction between **3.3** and *n*-propyl thiol in 400 μL CD_3CN in the presence of: a) 5 mol % cage **1.30** b) 5 mol % CSA **3.6**. [**3.3**] = 15.8 mM, [**PrSH**] = 19.8 mM, [**1.30**] = 0.8 mM, [**3.6**] = 0.8 mM, reactions were performed at 50 $^\circ\text{C}$ in CD_3CN and monitored over time (400 MHz, CD_3CN). 214

Figure 7.28. Expanded ^1H NMR spectra of the acid promoted reaction between **3.3** and *n*-propyl thiol in the presence of 5 mol % **1.28** showing: a) Cage stability (5.85-5.55 ppm) b) Product formation (7.9-7.1 ppm, 6.8-6.0 ppm, and 1.2-0.8 ppm). [**3.3**] = 15.8 mM, [**PrSH**] = 19.8 mM, [**1.28**] = 0.8 mM, [**1.35**] = 4.7 mM, the reaction was performed at 50 $^\circ\text{C}$ in CD_3CN and monitored over time (400 MHz, 323 K, CD_3CN). 215

Figure 7.29. ^1H NMR spectra (7.5-7.1 ppm, 6.8-6.0 ppm, and 1.2-0.8 ppm) of the acid promoted reaction between **3.4** and *n*-propyl thiol in 400 μL CD_3CN in the presence of: a) 5 mol % cage **1.30** b) 5 mol % CSA **3.6**. [**3.4**] = 15.8 mM, [**PrSH**] = 19.8 mM, [**1.30**] = 0.8 mM, [**3.6**] = 0.8 mM, reactions were performed at 23 $^\circ\text{C}$ in CD_3CN and monitored over time (400 MHz, CD_3CN). 216

Figure 7.30. ^1H NMR spectra (7.5-7.1 ppm, 6.8-6.0 ppm, and 1.2-0.8 ppm) of the acid promoted reaction between **3.4** and *n*-propyl thiol in 400 μL CD_3CN in the presence of: a) 5 mol % cage **1.30** b) 5 mol % CSA **3.6**. [**3.4**] = 15.8 mM, [**PrSH**] = 19.8 mM, [**1.30**] = 0.8 mM, [**3.6**] = 0.8 mM, reactions were performed at 50 $^\circ\text{C}$ in CD_3CN and monitored over time (400 MHz, CD_3CN). 217

Figure 7.31. ^1H NMR spectra (7.51-7.0 ppm and 6.8-5.8 ppm) of the acid promoted reaction between **3.4** and H_2O in 400 μL CD_3CN in the presence of: a) 5 mol % cage **1.30**

b) 5 mol % CSA **3.6**. [**3.4**] = 15.8 mM, [H₂O] = 94.5 mM, [**1.30**] = 0.8 mM, [**3.6**] = 0.8 mM, reactions were performed at 23 °C in CD₃CN and monitored over time (400 MHz, 298 K, CD₃CN). 218

Figure 7.32. ¹H NMR spectra (7.51-7.0 ppm and 6.8-5.8 ppm) of the acid promoted reaction between **3.4** and H₂O in 400 μL CD₃CN in the presence of: a) 5 mol % cage **1.30** b) 5 mol % CSA **3.6**. [**3.4**] = 15.8 mM, [H₂O] = 94.5 mM, [**1.30**] = 0.8 mM, [**3.6**] = 0.8 mM, reactions were performed at 50 °C in CD₃CN and monitored over time (400 MHz, 323 K, CD₃CN). 219

Figure 7.33. Full ¹H NMR spectra of the acid promoted reaction between **3.10** and *n*-propyl thiol in the presence of 5 mol % cage **1.30**. [**3.10**] = 15.8 mM, [**PrSH**] = 19.8 mM, [**1.30**] = 0.8 mM, the reaction was performed at 50 °C in CD₃CN and monitored over time (400 MHz, 323 K, CD₃CN). 220

Figure 7.34. Expanded ¹H NMR spectra of the acid promoted reaction between **3.10** and *n*-propyl thiol in the presence of 5 mol % cage **1.30** showing: a) Cage stability (8.7-7.3 ppm) b) Product formation (5.1 – 4.3 ppm, 4.2 -3.7 ppm, and 2.7 -2.3 ppm). [**3.10**] = 15.8 mM, [**PrSH**] = 19.8 mM, [**1.30**] = 0.8 mM, the reaction was performed at 50 °C in CD₃CN and monitored over time (400 MHz, 323 K, CD₃CN). 221

Figure 7.35. ¹H NMR spectra (4.9-4.2 ppm and 4.0-3.7 ppm) of the acid promoted reaction between **3.10** and H₂O in 400 μL CD₃CN in the presence of: a) 5 mol % cage **1.30** b) 5 mol % CSA **3.6**. [**3.10**] = 15.8 mM, [H₂O] = 94.5 mM, [**1.30**] = 0.8 mM, [**3.6**] = 0.8 mM, reactions were performed at 23 °C in CD₃CN and monitored over time (400 MHz, 296 K, CD₃CN). 222

Figure 7.36. ¹H NMR spectra (4.9-4.2 ppm and 4.0-3.7 ppm) of the acid promoted reaction between **3.10** and H₂O in 400 μL CD₃CN in the presence of: a) 5 mol % cage **1.30** b) 5 mol % CSA **3.6**. [**3.10**] = 15.8 mM, [H₂O] = 94.5 mM, [**1.30**] = 0.8 mM, [**3.6**] = 0.8 mM, reactions were performed at 50 °C in CD₃CN and monitored over time (400 MHz, 323 K, CD₃CN). 223

Figure 7.37. ¹H NMR spectra (4.9-4.2 ppm and 2.7-2.3 ppm) of the acid promoted reaction between **3.10** and **PrSH** in 400 μL CD₃CN in the presence of: a) 5 mol % cage **1.30** b) 5 mol % CSA **3.6**. [**3.10**] = 15.8 mM, [**PrSH**] = 19.8 mM, [**1.30**] = 0.8 mM, [**3.6**] = 0.8 mM, reactions were performed at 23 °C in CD₃CN and monitored over time (400 MHz, 296 K, CD₃CN). 224

Figure 7.38. ¹H NMR spectra (4.9-4.2 ppm and 2.7-2.3 ppm) of the acid promoted reaction between **3.10** and **PrSH** in 400 μL CD₃CN in the presence of: a-b) 5 mol % cage **1.30** c-d) 5 mol % CSA **3.6**. [**3.10**] = 15.8 mM, [**PrSH**] = 19.8 mM, [**1.30**] = 0.8 mM, [**3.6**] = 0.8 mM, reactions were performed at 50 °C in CD₃CN and monitored over time (400 MHz, 323 K, CD₃CN). 225

Figure 7.39. ^1H NMR spectra (5.1-4.3 ppm, 4.15-3.7 ppm, and 2.8-2.4 ppm) of the acid promoted reaction between **3.10** and *n*-octyl thiol in 400 μL CD_3CN in the presence of: a) 5 mol % cage **1.30** b) 5 mol % CSA **2**. [**3.10**] = 15.8 mM, [*n*-**C₈SH**] = 19.8 mM, [**1.30**] = 0.8 mM, [**3.6**] = 0.8 mM, reactions were performed at 23 °C in CD_3CN and monitored over time (400 MHz, CD_3CN). 226

Figure 7.40. ^1H NMR spectra (5.1-4.3 ppm, 4.15-3.7 ppm, and 2.8-2.4 ppm) of the acid promoted reaction between **3.10** and *n*-octyl thiol in 400 μL CD_3CN in the presence of: a) 5 mol % cage **1.30** b) 5 mol % CSA **3.6**. [**3.10**] = 15.8 mM, [*n*-**C₈SH**] = 19.8 mM, [**1.30**] = 0.8 mM, [**3.6**] = 0.8 mM, reactions were performed at 50 °C in CD_3CN and monitored over time (400 MHz, CD_3CN). 227

Figure 7.41. ^1H NMR spectra (5.0-4.3 ppm, 4.15-3.7 ppm, and 2.8-2.4 ppm) of the acid promoted reaction between **3.10** and *n*-dodecyl thiol in 400 μL CD_3CN in the presence of: a) 5 mol % cage **1.30** b) 5 mol % CSA **3.6**. [**3.10**] = 15.8 mM, [*n*-**C₁₂SH**] = 19.8 mM, [**1.30**] = 0.8 mM, [**3.6**] = 0.8 mM, reactions were performed at 23 °C in CD_3CN and monitored over time (400 MHz, 296 K, CD_3CN). 228

Figure 7.42. ^1H NMR spectra (5.0-4.3 ppm, 4.15-3.7 ppm, and 2.8-2.4 ppm) of the acid promoted reaction between **3.10** and *n*-dodecyl thiol in 400 μL CD_3CN in the presence of: a) 5 mol % cage **1.30** b) 5 mol % CSA **3.6**. [**3.10**] = 15.8 mM, [*n*-**C₁₂SH**] = 19.8 mM, [**1.30**] = 0.8 mM, [**3.6**] = 0.8 mM, reactions were performed at 50 °C in CD_3CN and monitored over time (400 MHz, 323 K, CD_3CN). 229

Figure 7.43. Full ^1H NMR spectra of the acid promoted reaction between **3.15** and *n*-propyl thiol in the presence of 5 mol % cage **1.30**. [**3.15**] = 15.8 mM, [**PrSH**] = 19.8 mM, [**1.35**] = 0.8 mM, the reaction was performed at 23 °C in CD_3CN and monitored over time (400 MHz, 296 K, CD_3CN). 230

Figure 7.44. Expanded ^1H NMR spectra of the acid promoted reaction between **3.15** and *n*-propyl thiol in the presence of 5 mol % cage **1.30** showing: a) Cage stability (9.1-7.4 ppm) b) Product formation (7.5-6.8 ppm, 6.4-6.0 ppm, 5.7-5.1 ppm, and 1.3-0.9 ppm). [**3.15**] = 15.8 mM, [**PrSH**] = 19.8 mM, [**1.30**] = 0.8 mM, the reaction was performed at 23 °C in CD_3CN and monitored over time (400 MHz, 296 K, CD_3CN). 231

Figure 7.45. ^1H NMR spectra (8.0-6.9 ppm, 6.4-5.3 ppm, and 1.2-0.8 ppm) of the acid promoted reaction between **3.15** and *n*-propyl thiol in 400 μL CD_3CN in the presence of 30 mol % weak acid control **1.35**. [**3.15**] = 15.8 mM, [**PrSH**] = 19.8 mM, [**1.35**] = 4.7 mM, reactions were performed at 23 °C in CD_3CN and monitored over time (400 MHz, 296 K, CD_3CN). 232

Figure 7.46. ^1H NMR spectra (7.95-6.9 ppm, 6.4-5.2 ppm, and 1.2-0.65 ppm) of the acid promoted reaction between **3.15** and *n*-propyl thiol in 400 μL CD_3CN in the presence of 5

mol % cage **1.30** and 1 equivalent of cavity-filling guest **3.21**. [**3.15**] = 15.8 mM, [**PrSH**] = 19.8 mM, [**1.30**] = 0.8 mM, [**3.21**] = 15.8 mM, reactions were performed at 23 °C in CD₃CN and monitored over time (400 MHz, 296 K, CD₃CN). 233

Figure 7.47. ¹H NMR spectra (7.4-7.0 ppm, 6.5-5.2 ppm, and 1.3-0.9 ppm) of the acid promoted reaction between **3.15** and *n*-propyl thiol in 400 μL CD₃CN in the presence of: a) 5 mol % cage **1.30** b) 5 mol % CSA **3.6**. [**3.15**] = 15.8 mM, [**PrSH**] = 19.8 mM, [**1.30**] = 0.8 mM, [**3.6**] = 0.8 mM, reactions were performed at 23 °C in CD₃CN and monitored over time (400 MHz, 296 K, CD₃CN). 234

Figure 7.48. ¹H NMR spectra (7.6-6.7 ppm, 6.5-5.3 ppm, and 1.2-0.7 ppm) of the acid promoted reaction between **3.16** and *n*-propyl thiol in 400 μL CD₃CN in the presence of: a) 5 mol % cage **1.30** b) 5 mol % CSA **3.6**. [**3.16**] = 15.8 mM, [**PrSH**] = 19.8 mM, [**1.30**] = 0.8 mM, [**3.6**] = 0.8 mM, reactions were performed at 23 °C in CD₃CN and monitored over time (400 MHz, 296 K, CD₃CN). 235

Figure 7.49. ¹H NMR spectra (7.4-6.9 ppm, 6.4-5.4 ppm, and 1.2-0.8 ppm) of the acid promoted reaction between **3.17** and *n*-propyl thiol in 400 μL CD₃CN in the presence of: a) 5 mol % cage **1.30** b) 5 mol % CSA **3.6**. [**3.17**] = 15.8 mM, [**PrSH**] = 19.8 mM, [**1.30**] = 0.8 mM, [**3.6**] = 0.8 mM, reactions were performed at 23 °C in CD₃CN and monitored over time (400 MHz, 296 K, CD₃CN). 236

Figure 7.50. ¹H NMR spectra (7.4-6.9 ppm, 6.4-5.4 ppm, and 1.2-0.8 ppm) of the acid promoted reaction between **3.18** and *n*-propyl thiol in 400 μL CD₃CN in the presence of: a) 5 mol % cage **1.30** b) 5 mol % CSA **3.6**. [**3.18**] = 15.8 mM, [**PrSH**] = 19.8 mM, [**1.30**] = 0.8 mM, [**3.6**] = 0.8 mM, reactions were performed at 23 °C in CD₃CN and monitored over time (400 MHz, 296 K, CD₃CN). 237

Figure 7.51. ¹H NMR spectra (7.4-6.9 ppm, 6.4-5.4 ppm, and 1.2-0.8 ppm) of the acid promoted reaction between **3.19** and *n*-propyl thiol in 400 μL CD₃CN in the presence of: a) 5 mol % cage **1.30** b) 5 mol % CSA **3.6**. [**3.19**] = 15.8 mM, [**PrSH**] = 19.8 mM, [**1.30**] = 0.8 mM, [**3.6**] = 0.8 mM, reactions were performed at 23 °C in CD₃CN and monitored over time (400 MHz, 296 K, CD₃CN). 238

Figure 7.52. ¹H NMR spectrum of **4.19** (600 MHz, 298K, CD₃CN). 239

Figure 7.53. ¹³C NMR spectrum of **4.19** (600 MHz, 298K, CD₃CN). 239

Figure 7.54. ¹H NMR spectrum of **4.18** (600 MHz, 298K, CD₃CN). 240

Figure 7.55. ¹³C NMR spectrum of **4.18** (600 MHz, 298K, CD₃CN). 240

Figure 7.56. ¹H NMR spectrum of **4.20** (600 MHz, 298K, CD₃CN). 241

- Figure 7.57.** ^{13}C NMR spectrum of **4.20** (600 MHz, 298K, CD_3CN). 241
- Figure 7.58.** ^1H NMR spectrum of **4.21** (600 MHz, 298K, CD_3CN). 242
- Figure 7.59.** ^{13}C NMR spectrum of **4.21** (600 MHz, 298K, CD_3CN). 242
- Figure 7.60.** ^1H NMR spectrum of **4.22** (600 MHz, 298K, CDCl_3). 243
- Figure 7.61.** ^{13}C NMR spectrum of **4.22** (600 MHz, 298K, CDCl_3). 243
- Figure 7.62.** Full ^1H NMR spectra of the acid promoted reaction between **4.1** and **4.2** in the presence of 5 mol % cage **1.30**. [**4.2**] = 15.8 mM, [**4.1**] = 19.8 mM, [**1.30**] = 0.8 mM, the reaction was performed at room temperature in CD_3CN and monitored over time (400 MHz, 298 K, CD_3CN). 244
- Figure 7.63.** Expanded ^1H NMR spectra of the acid promoted substitution reaction between **4.1** and **4.2** in the presence of 5 mol % cage **1.30** showing: a) Cage stability (5.95-5.4 ppm) b) Product formation (8.2-6.9 ppm, 6.0-5.3 ppm, 4.3-3.7 ppm). [**4.2**] = 15.8 mM, [**4.1**] = 19.8 mM, [**1.30**] = 0.8 mM, the reaction was performed at room temperature in CD_3CN and monitored over time (400 MHz, 298 K, CD_3CN). 244
- Figure 7.64.** ^1H NMR spectra (8.2-6.9 ppm, 6.0-5.3 ppm, 4.3-3.7 ppm) of the acid promoted substitution reaction between **4.1** and **4.2** in 400 μL CD_3CN in the presence of 5 mol % cage **1.30** and 50 mol % of NaPF_6 . [**4.2**] = 15.8 mM, [**4.1**] = 19.8 mM, [**1.30**] = 0.8 mM, [NaPF_6] = 7.9 mM the reaction was performed at room temperature in CD_3CN and monitored over time (600 MHz, 298 K, CD_3CN). 246
- Figure 7.65.** Expanded ^1H NMR spectra of the acid promoted substitution reaction between **4.1** and **4.2** in the presence of 5 mol % cage **1.28** showing: a) Cage stability (9.01-8.85 ppm) b) Product formation (8.2-2.4 ppm) in CD_3CN . [**4.2**] = 15.8 mM, [**4.1**] = 19.8 mM, [**1.28**] = 0.8 mM, the reaction was performed at room temperature in CD_3CN and monitored over time (600 MHz, 298 K, CD_3CN). 247
- Figure 7.66.** ^1H NMR spectra (8.05-2.35 ppm) of the acid promoted substitution reaction between **4.1** and **4.2** in 400 μL CD_3CN in the presence of 30 mol % diacid **1.35**. [**4.2**] = 15.8 mM, [**4.1**] = 19.8 mM, [**1.35**] = 4.74 mM, the reaction was performed at room temperature in CD_3CN and monitored over time (600 MHz, 298 K, CD_3CN). 248
- Figure 7.67.** ^1H NMR spectra (10.35-9.8 ppm, 7.6-6.8 ppm, 6.0-5.2 ppm, 4.3-3.68 ppm) of the acid promoted substitution reaction between **4.2** and **4.7** in 400 μL CD_3CN in the presence of 5 mol % cage **1.30**. [**4.1**] = 15.8 mM, [**4.7**] = 19.8 mM, [**1.30**] = 0.8 mM, the reaction was performed at room temperature in CD_3CN and monitored over time (600 MHz, 298 K, CD_3CN). 249

Figure 7.68. ^1H NMR spectra (10.35-9.8 ppm, 7.6-6.8 ppm, 6.0-5.2 ppm, 4.3-3.68 ppm) of the acid promoted substitution reaction between **4.2** and **4.8** in 400 μL CD_3CN in the presence of 5 mol % cage **1.30**. [**4.2**] = 15.8 mM, [**4.8**] = 19.8 mM, [**1.30**] = 0.8 mM, the reaction was performed at room temperature in CD_3CN and monitored over time (600 MHz, 298 K, CD_3CN). 250

Figure 7.69. ^1H NMR spectra (10.7-10.2 ppm, 7.35-6.9 ppm, 6.8-5.8 ppm, 4.45-3.68 ppm) of the acid promoted substitution reaction between **4.2** and **4.9** in 400 μL CD_3CN in the presence of 5 mol % cage **1.30**. [**4.2**] = 15.8 mM, [**4.9**] = 19.8 mM, [**1.30**] = 0.8 mM, the reaction was performed at room temperature in CD_3CN and monitored over time (600 MHz, 298 K, CD_3CN). 251

Figure 7.70. ^1H NMR spectra (11.6-11.3 ppm, 7.45-6.5 ppm, 4.8-3.7 ppm) of the acid promoted substitution reaction between **4.2** and **4.10** in 400 μL CD_3CN in the presence of 5 mol % cage **1.30**. [**4.2**] = 15.8 mM, [**4.10**] = 19.8 mM, [**1.30**] = 0.8 mM, the reaction was performed at room temperature in CD_3CN and monitored over time (600 MHz, 298 K, CD_3CN). 252

Figure 7.71. ^1H NMR spectra (10.25-9.8 ppm, 8.0-6.8 ppm, 6.0-5.2 ppm, 4.4-3.7 ppm) of the acid promoted substitution reaction between **4.2** and **4.11** in 400 μL CD_3CN in the presence of 5 mol % cage **1.30**. [**4.2**] = 15.8 mM, [**4.11**] = 19.8 mM, [**1.30**] = 0.8 mM, the reaction was performed at room temperature in CD_3CN and monitored over time (600 MHz, 298 K, CD_3CN). 253

Figure 7.72. ^1H NMR spectra (10.0-9.55 ppm, 7.36-6.9 ppm, 5.9-5.0 ppm, 4.35-3.3.64 ppm) of the acid promoted substitution reaction between **4.2** and **4.12** in 400 μL CD_3CN in the presence of 5 mol % cage **1.30**. [**4.2**] = 15.8 mM, [**4.12**] = 19.8 mM, [**1.30**] = 0.8 mM, the reaction was performed at room temperature in CD_3CN and monitored over time (600 MHz, CD_3CN). 254

Figure 7.73. ^1H NMR spectra (10.4-3.65 ppm) of the acid promoted substitution reaction between **4.2** and **4.13** in 400 μL CD_3CN in the presence of 5 mol % cage **1.30**. [**4.2**] = 15.8 mM, [**4.13**] = 19.8 mM, [**1.30**] = 0.8 mM, the reaction was performed at room temperature in CD_3CN and monitored over time (600 MHz, 298 K, CD_3CN). 255

Figure 7.74. ^1H NMR spectra (9.9-9.55 ppm, 7.8-6.9 ppm, 5.0-3.65 ppm) of the acid promoted substitution reaction between **4.2** and **4.14** in 400 μL CD_3CN in the presence of 5 mol % cage **1.30**. [**4.2**] = 15.8 mM, [**4.14**] = 19.8 mM, [**1.30**] = 0.8 mM, the reaction was performed at room temperature in CD_3CN and monitored over time (600 MHz, 298 K, CD_3CN). 256

Figure 7.75. ^1H NMR spectra (10.1-3.70 ppm) of the acid promoted substitution reaction between **4.2** and **4.15** in 400 μL CD_3CN in the presence of 5 mol % cage **1.30**. [**4.2**] = 15.8

mM, [4.15] = 19.8 mM, [1.30] = 0.8 mM, the reaction was performed at room temperature in CD₃CN and monitored over time (600 MHz, 298 K, CD₃CN). 257

Figure 7.76. ¹H NMR spectra (7.9 – 3.67 ppm) of the acid promoted substitution reaction between 4.2 and 4.16 in 400 μL CD₃CN in the presence of 5 mol % cage 1.30. [4.2] = 15.8 mM, [4.16] = 19.8 mM, [1.30] = 0.8 mM, the reaction was performed at room temperature in CD₃CN and monitored over time (600 MHz, 298 K, CD₃CN). 258

Figure 7.77. ¹H NMR spectra (10.25-9.8 ppm, 7.58-6.8 ppm, 6.2-5.2 ppm, 4.3-3.7 ppm) of the acid promoted substitution reaction between 4.1 and 4.5 in 400 μL CD₃CN in the presence of 5 mol % cage 1.30. [4.5] = 15.8 mM, [4.1] = 19.8 mM, [1.30] = 0.8 mM, the reaction was performed at room temperature in CD₃CN and monitored over time (600 MHz, 298 K, CD₃CN). 259

Figure 7.78. ¹H NMR spectra (10.35-3.65 ppm) of the acid promoted substitution reaction between 4.6 and 4.1 in 400 μL CD₃CN in the presence of 5 mol % cage 1.30. [4.6] = 15.8 mM, [4.1] = 19.8 mM, [1.30] = 0.8 mM, the reaction was performed at room temperature in CD₃CN and monitored over time (600 MHz, 298 K, CD₃CN). 260

Figure 7.79. UV-Vis absorption spectrum of the titration of 4.2 into a 3 μM solution of cage 1.30 in CH₃CN. 4.2 was added in 1-2 μL aliquots from a 9 mM stock solution in CD₃CN. 261

Figure 7.80. 1:1 binding fit model for guest 4.2 calculated via linear regression analysis using the Nelder-Mead method from the change in absorbance at two points (300 nm and 330 nm) using supramolecular.org.¹⁻³ ($K_a = 3.9 \pm 0.1 \times 10^3 \text{ M}^{-1}$). 261

Figure 7.81. UV-Vis absorption spectrum of the titration of 4.5 into a 3 μM solution of cage 1.30 in CH₃CN. 4.5 was added in 1 μL aliquots from a 9 mM stock solution. 262

Figure 7.82. 1:1 binding fit model for guest 4.5 calculated via linear regression analysis using the Nelder-Mead method from the change in absorbance at two points (300 nm and 330 nm) using supramolecular.org.¹⁻³ ($K_a = 4.1 \pm 0.1 \times 10^3 \text{ M}^{-1}$). 262

Figure 7.83. UV-Vis absorption spectrum of the titration of 4.6 into a 3 μM solution of cage 1.30 in CH₃CN. 4.6 was added in 1 μL aliquots from a 9 mM stock solution. 263

Figure 7.84. 1:1 binding fit model for guest 4.6 calculated via linear regression analysis using the Nelder-Mead method from the change in absorbance at two points (300 nm and 330 nm) using supramolecular.org.¹⁻³ ($K_a = 7.4 \pm 0.3 \times 10^3 \text{ M}^{-1}$). 263

Figure 7.85. UV-Vis absorption spectrum of the titration of 4.1 into a 3 μM solution of cage 1.30 in CH₃CN. 4.1 was added in 1-5 μL aliquots from a 9 mM stock solution in CD₃CN. 264

Figure 7.86. a) 1:1 binding fit model for guest **4.1** calculated via linear regression analysis using the Nelder-Mead method from the change in absorbance at two points (300 nm and 330 nm) using supramolecular.org.¹⁻³ ($K_a = 1.5 \pm .09 \times 10^3 \text{ M}^{-1}$). b) 1:2 binding fit model calculated via linear regression analysis using the Nelder-Mead method from the change in absorbance at two points (300 nm and 330 nm) using supramolecular.org.¹⁻³ ($K_1 = 8.6 \pm 0.8 \times 10^3 \text{ M}^{-1}$, $K_2 = 0.08 \pm 0.002 \times 10^3 \text{ M}^{-1}$). 264

Figure 7.87. UV-Vis absorption spectrum of the titration of **4.7** into a 3 μM solution of cage **1.30** in CH_3CN . **4.7** was added in 2 μL aliquots from a 9 mM stock solution. 265

Figure 7.88. a) 1:1 binding fit model for guest **4.7** calculated via linear regression analysis using the Nelder-Mead method from the change in absorbance at two points (300 nm and 330 nm) using supramolecular.org.¹⁻³ ($K_a = 11 \pm 0.63 \times 10^3 \text{ M}^{-1}$). b) 1:2 binding fit model calculated via linear regression analysis using the Nelder-Mead method from the change in absorbance at two points (300 nm and 330 nm) using supramolecular.org.^{[8], [9]} ($K_1 = 20.0 \pm 0.7 \times 10^3 \text{ M}^{-1}$, $K_2 = 0.03 \pm 0.001 \times 10^3 \text{ M}^{-1}$). 265

Figure 7.89. UV-Vis absorption spectrum of the titration of **4.8** into a 3 μM solution of cage **1.30** in CH_3CN . **4.8** was added in 2 μL aliquots from a 9 mM stock solution. 266

Figure 7.90. a) 1:1 binding fit model for guest **4.8** calculated via linear regression analysis using the Nelder-Mead method from the change in absorbance at two points (300 nm and 330 nm) using supramolecular.org.¹⁻³ ($K_a = 11 \pm .84 \times 10^3 \text{ M}^{-1}$). b) 1:2 binding fit model calculated via linear regression analysis using the Nelder-Mead method from the change in absorbance at two points (300 nm and 330 nm) using supramolecular.org.¹⁻³ ($K_1 = 34.0 \pm 1.3 \times 10^3 \text{ M}^{-1}$, $K_2 = 0.40 \pm 0.01 \times 10^3 \text{ M}^{-1}$). 266

Figure 7.91. UV-Vis absorption spectrum of the titration of **4.9** into a 3 μM solution of cage **1.30** in CH_3CN . **4.9** was added in 1-5 μL aliquots from a 9 mM stock solution in CD_3CN . 267

Figure 7.92. a) 1:1 binding fit model for guest **4.9** calculated via linear regression analysis using the Nelder-Mead method from the change in absorbance at two points (300 nm and 330 nm) using supramolecular.org.¹⁻³ ($K_a = 1.4 \pm 0.09 \times 10^3 \text{ M}^{-1}$). b) 1:2 binding fit model calculated via linear regression analysis using the Nelder-Mead method from the change in absorbance at two points (300 nm and 330 nm) using supramolecular.org.¹⁻³ ($K_1 = 4.7 \pm 0.4 \times 10^3 \text{ M}^{-1}$, $K_2 = 0.70 \pm 0.04 \times 10^3 \text{ M}^{-1}$). 267

Figure 7.93. UV-Vis absorption spectrum of the titration of **4.10** into a 3 μM solution of cage **1.30** in CH_3CN . **4.10** was added in 1 μL aliquots from a 9 mM stock solution in CD_3CN . 268

Figure 7.94. 1:1 binding fit model for guest **4.10** calculated via linear regression analysis using the Nelder-Mead method from the change in absorbance at two points (300 nm and 330 nm) using supramolecular.org.¹⁻³ ($K_a = 4.0 \pm 0.2 \times 10^3 \text{ M}^{-1}$). 268

Figure 7.95. UV-Vis absorption spectrum of the titration of **4.11** into a 3 μM solution of cage **1.30** in CH_3CN . **4.11** was added in 1-5 μL aliquots from a 9 mM stock solution in CD_3CN . 269

Figure 7.96. 1:1 binding fit model for guest **4.11** calculated via linear regression analysis using the Nelder-Mead method from the change in absorbance at two points (300 nm and 330 nm) using supramolecular.org.¹⁻³ ($K_a = 12.0 \pm 0.6 \times 10^3 \text{ M}^{-1}$). 269

Figure 7.97. UV-Vis absorption spectrum of the titration of **4.12** into a 3 μM solution of cage **1.30** in CH_3CN . **4.12** was added in 1 μL aliquots from a 9 mM stock solution in CD_3CN . 270

Figure 7.98. 1:1 binding fit model for guest **4.12** calculated via linear regression analysis using the Nelder-Mead method from the change in absorbance at two points (300 nm and 330 nm) using supramolecular.org.¹⁻³ ($K_a = 12.0 \pm 0.6 \times 10^3 \text{ M}^{-1}$). 270

Figure 7.99. UV-Vis absorption spectrum of the titration of **4.13** into a 3 μM solution of cage **1.30** in CH_3CN . **4.13** was added in 2 μL aliquots from a 9 mM stock solution in CD_3CN . 271

Figure 7.100. 1:1 binding fit model for guest **4.13** calculated via linear regression analysis using the Nelder-Mead method from the change in absorbance at two points (300 nm and 330 nm) using supramolecular.org.¹⁻³ ($K_a = 9.6 \pm 0.4 \times 10^3 \text{ M}^{-1}$). 271

Figure 7.101. UV-Vis absorption spectrum of the titration of **4.14** into a 3 μM solution of cage **1.30** in CH_3CN . **4.14** was added in 2 μL aliquots from a 9 mM stock solution in CD_3CN . 272

Figure 7.102. 1:1 binding fit model for guest **4.14** calculated via linear regression analysis using the Nelder-Mead method from the change in absorbance at two points (300 nm and 330 nm) using supramolecular.org.¹⁻³ ($K_a = 12.0 \pm 1.0 \times 10^3 \text{ M}^{-1}$). 272

Figure 7.103. UV-Vis absorption spectrum of the titration of **4.15** into a 3 μM solution of cage **1.30** in CH_3CN . **4.15** was added in 1 μL aliquots from a 9 mM stock solution in CD_3CN . 273

Figure 7.104. 1:1 binding fit model for guest **4.15** calculated via linear regression analysis using the Nelder-Mead method from the change in absorbance at two points (300 nm and 330 nm) using supramolecular.org.¹⁻³ ($K_a = 8.3 \pm 0.3 \times 10^3 \text{ M}^{-1}$). 273

Figure 7.105. UV-Vis absorption spectrum of the titration of **4.16** into a 3 μM solution of cage **1.30** in CH_3CN . **4.16** was added in 1-5 μL aliquots from a 9 mM stock solution in CD_3CN . 274

Figure 7.106. 1:1 binding fit model for guest **4.16** calculated via linear regression analysis using the Nelder-Mead method from the change in absorbance at two points (300 nm and 330 nm) using supramolecular.org.¹⁻³ ($K_a = 4.4 \pm 0.53 \times 10^3 \text{ M}^{-1}$). 274

Figure 7.107. UV-Vis absorption spectrum of the titration of **4.3** into a 3 μM solution of cage **1.30** in CH_3CN . **4.3** was added in 1 μL aliquots from a 9 mM stock solution 275

Figure 7.108. 1:1 binding fit model for guest **4.3** calculated via linear regression analysis using the Nelder-Mead method from the change in absorbance at two points (300 nm and 330 nm) using supramolecular.org.¹⁻³ ($K_a = 6.2 \pm 0.3 \times 10^3 \text{ M}^{-1}$). 275

Figure 7.109. UV-Vis absorption spectrum of the titration of **4.18** into a 3 μM solution of cage **1.30** in CH_3CN . **4.18** was added in 1 μL aliquots from a 9 mM stock solution in CD_3CN . 276

Figure 7.110. 1:1 binding fit model for guest **4.18** calculated via linear regression analysis using the Nelder-Mead method from the change in absorbance at two points (300 nm and 330 nm) using supramolecular.org.¹⁻³ ($K_a = 2.9 \pm 0.1 \times 10^3 \text{ M}^{-1}$). 276

Figure 7.111. ^1H NMR spectrum of **5.5** (400 MHz, 298K, CD_3CN). 277

Figure 7.112. ^{13}C NMR spectrum of **5.5** (100 MHz, 298K, CD_3CN). 277

Figure 7.113. ^1H NMR spectra (7.50-7.10 ppm, 1.10-0.70 ppm) of the acid promoted substitution reaction between **2.1** and *n*-propyl thiol in 400 μL CD_3CN in the presence of: a) 5 mol % cage **1.28** and 30 mol % acid **1.35** b) 30 mol % acid **1.35**. [**2.1**] = 15.8 mM, [**PrSH**] = 19.8 mM, [**1.28**] = 0.8 mM, [**1.35**] = 4.74 mM, reactions were performed at 80 $^\circ\text{C}$ in CD_3CN and monitored over time (400 MHz, 298 K, CD_3CN). 278

Figure 7.114. ^1H NMR spectra (7.50-7.10 ppm, 1.30-0.60 ppm) of the acid promoted substitution reaction between **2.1** and *n*-propyl thiol in 400 μL CD_3CN in the presence of: a) 5 mol % cage **1.28** and 30 mol % acid **5.3** b) 30 mol % acid **3b**. [**5.3**] = 15.8 mM, [**PrSH**] = 19.8 mM, [**1.28**] = 0.8 mM, [**5.3**] = 4.74 mM, reactions were performed at 80 $^\circ\text{C}$ in CD_3CN and monitored over time (600 MHz, 298 K, CD_3CN). 279

Figure 7.115. ^1H NMR spectra (7.5-7.10 ppm, 1.3-0.60 ppm) of the acid promoted substitution reaction between **2.1** and *n*-propyl thiol in 400 μL CD_3CN in the presence of: a) 5 mol % cage **1.28** and 30 mol % acid **5.2** b) 30 mol % acid **5.2**. [**2.1**] = 15.8 mM, [**PrSH**] = 19.8 mM, [**1.28**] = 0.8 mM, [**5.2**] = 4.74 mM, were performed at 80 $^\circ\text{C}$ in CD_3CN and monitored over time (600 MHz, 298 K, CD_3CN). 280

Figure 7.116. ^1H NMR spectra (7.5-7.10 ppm, 1.3-0.60 ppm) of the acid promoted substitution reaction between **2.1** and *n*-propyl thiol in 400 μL CD_3CN in the presence of: a) 5 mol % cage **1.28** and 30 mol % acid **5.1** b) 30 mol % acid **5.1**. [**2.1**] = 15.8 mM, [**PrSH**] = 19.8 mM, [**1.28**] = 0.8 mM, [**5.1**] = 4.74 mM, reactions were performed at 80 $^\circ\text{C}$ in CD_3CN and monitored over time (600 MHz, 298 K, CD_3CN). 281

Figure 7.117. ^1H NMR spectra (7.5-7.10 ppm, 1.30-0.70 ppm) of the acid promoted substitution reaction between **2.1** and *n*-propyl thiol in 400 μL CD_3CN in the presence of: a) 5 mol % cage **1.28** and 30 mol % acid **5.4** b) 30 mol % acid **5.4**. [**2.1**] = 15.8 mM, [**PrSH**] = 19.8 mM, [**1.28**] = 0.8 mM, [**5.4**] = 4.74 mM, reactions were performed at 80 $^\circ\text{C}$ in CD_3CN and monitored over time (600 MHz, 298 K, CD_3CN). 282

Figure 7.118. ^1H NMR spectra (7.50-7.20 ppm, 2.75-2.00 ppm, 1.10-0.70 ppm) of the acid promoted substitution reaction between **2.1** and *n*-octyl mercaptan in 400 μL CD_3CN in the presence of: a) 5 mol % cage **1.28** and 30 mol % acid **1.35** b) 30 mol % acid **1.35**. [**2.1**] = 15.8 mM, [**OctSH**] = 19.8 mM, [**1.28**] = 0.8 mM, [**1.35**] = 4.74 mM, reactions were performed at 80 $^\circ\text{C}$ in CD_3CN and monitored over time (600 MHz, 298 K, CD_3CN). 283

Figure 7.119. ^1H NMR spectra (7.55-7.10 ppm, 1.80-0.70 ppm) of the acid promoted substitution reaction between **2.2** and *n*-propyl thiol in 400 μL CD_3CN in the presence of: a) 5 mol % cage **1.28** and 30 mol % acid **1.35** b) 30 mol % acid **1.35**. [**2.2**] = 15.8 mM, [**PrSH**] = 19.8 mM, [**1.28**] = 0.8 mM, [**1.35**] = 4.74 mM, reactions were performed at 80 $^\circ\text{C}$ in CD_3CN and monitored over time (600 MHz, 298 K, CD_3CN). 284

Figure 7.120. ^1H NMR spectra (7.70-7.10 ppm, 1.90-0.70 ppm) of the acid promoted substitution reaction between **4b** and *n*-propyl thiol in 400 μL CD_3CN in the presence of: a) 5 mol % cage **1.28** and 30 mol % acid **3b** b) 30 mol % acid **3b**. [**4b**] = 15.8 mM, [**PrSH**] = 19.8 mM, [**1**] = 0.8 mM, [**3b**] = 4.74 mM, reactions were performed at 80 $^\circ\text{C}$ in CD_3CN and monitored over time (600 MHz, 298 K, CD_3CN). 285

Figure 7.121. ^1H NMR spectra (7.50-7.20 ppm, 2.75-2.00 ppm, 1.14-0.70 ppm) of the acid promoted substitution reaction between **2.2** and *n*-octyl mercaptan in 400 μL CD_3CN in the presence of: a) 5 mol % cage **1.28** and 30 mol % acid **1.35** b) 30 mol % acid **1.35**. [**2.2**] = 15.8 mM, [**OctSH**] = 19.8 mM, [**1.28**] = 0.8 mM; [**1.35**] = 4.74 mM, reactions were performed at 80 $^\circ\text{C}$ in CD_3CN and monitored over time (600 MHz, 298 K, CD_3CN). 286

Figure 7.122. ^1H NMR spectra of the acid promoted substitution reaction between **2.1** and *n*-propyl thiol in the presence of 5 mol % cage **1.28** and 30 mol % acid **1.35**, at varying concentrations of **PrSH** a) 19.75 mM b) 37.3 mM c) 59.25 mM and d) 76.07 mM. [**2.1**] = 15.8 mM, [**1.28**] = 0.8 mM; [**1.35**] = 4.74 mM, reactions were performed at 80 $^\circ\text{C}$ in CD_3CN and monitored over time (400 MHz, 298K, CD_3CN). 287

Figure 7.123. ^1H NMR spectra of the acid promoted substitution reaction between **2.1** and *n*-propyl thiol in the presence of 5 mol % cage **1.28** and at varying concentrations of acid

1.35, a) 1.58 mM, b) 3.15 mM and c) 4.73 mM. [2.1] = 15.8 mM, [PrSH] = 19.8 mM, [1.28] = 0.8 mM, reactions were performed at 80 °C in CD₃CN and monitored over time (600 MHz, CD₃CN). 288

Figure 7.124. ¹H NMR spectra of the acid promoted substitution reaction between **2.1** and *n*-propyl thiol in the presence of 5 mol % cage **1.28** and 30 mol % acid **5.3**, at varying concentrations of **PrSH** a) 9.45 mM b) 18.11 mM and c) 33.08 mM. [2.1] = 15.8 mM, [1.28] = 0.8 mM, [5.3] = 4.74 mM, reactions were performed at 80 °C in CD₃CN and monitored over time (400 MHz, 298K, CD₃CN). 289

Figure 7.125. ¹H NMR spectra of the acid promoted substitution reaction between **2.1** and *n*-propyl thiol in the presence of 5 mol % cage **1.28** and at varying concentrations of acid **5.3**, a) 0.79 mM, b) 1.58 mM, c) 3.15 mM and d) 4.73 mM. [2.1] = 15.8 mM, [PrSH] = 19.8 mM, [1.28] = 0.8 mM, reactions were performed at 80 °C in CD₃CN and monitored over time (600 MHz, 298K, CD₃CN). 290

Figure 7.126. ¹H NMR spectra of the acid promoted substitution reaction between **2.1** and *n*-octyl mercaptan in the presence of 5 mol % cage **1.28** and 30 mol % acid **1.35**, at varying concentrations of **OctSH** a) 11.88 mM, b) 21.26 c) 24.48 mM, and d) 62.37 mM. [2.1] = 15.8 mM, [1.28] = 0.8 mM, [1.35] = 4.74 mM, reactions were performed at 80 °C in CD₃CN and monitored over time (600 MHz, 298K, CD₃CN). 291

Figure 7.127. ¹H NMR spectra of the acid promoted substitution reaction between **2.2** and *n*-propyl thiol in the presence of 5 mol % cage **1.28** and 30 mol % acid **1.35**, at varying concentrations of **PrSH** a) 14.96 mM, b) 23.63, c) 39.5 mM, and d) 54.96 mM. [2.2] = 15.8 mM, [1.28] = 0.8 mM, [1.35] = 4.74 mM, reactions were performed at 80 °C in CD₃CN and monitored over time (400 MHz, 298K, CD₃CN). 292

Figure 7.128. ¹H NMR spectra of the acid promoted substitution reaction between **2.2** and *n*-propyl thiol in the presence of 5 mol % cage **1.28** and 30 mol % acid **5.3**, at varying concentrations of **PrSH** a) 10.08 mM, b) 18.11, and c) 56.3 mM. [2.2] = 15.8 mM, [1.28] = 0.8 mM, [5.3] = 4.74 mM, reactions were performed at 80 °C in CD₃CN and monitored over time (400 MHz, 298K, CD₃CN). 293

Figure 7.129. ¹H NMR spectra of the acid promoted substitution reaction between **2.2** and *n*-octyl mercaptan in the presence of 5 mol % cage **1.28** and 30 mol % acid **1.35**, at varying concentrations of **OctSH** a) 12.28 mM, b) 20.94 mM, c) 39.37 mM, and d) 57.65 mM. [2.2] = 15.8 mM, [1.28] = 0.8 mM, [1.35] = 4.74 mM, reactions were performed at 80 °C in CD₃CN and monitored over time (600 MHz, 298K, CD₃CN). 294

Figure 7.130. ¹H NMR spectrum of **6.2** (CD₃CN, 400 MHz, 298 K). 295

Figure 7.131. ¹³C{¹H} NMR spectrum of **6.2** (CDCl₃, 100 MHz, 298 K). 295

Figure 7.132. ^1H NMR spectrum of 6.3 (CD_3CN , 400 MHz, 298 K).	296
Figure 7.133. $^{13}\text{C}\{^1\text{H}\}$ NMR spectrum of 6.3 (CDCl_3 , 100 MHz, 298 K).	296
Figure 7.134. ^1H NMR spectrum of 6.4 ($\text{DMSO}-d_6$, 400 MHz, 298 K).	297
Figure 7.135. $^{13}\text{C}\{^1\text{H}\}$ NMR spectrum of 6.4 ($\text{DMSO}-d_6$, 100 MHz, 298 K).	297
Figure 7.136. ^1H NMR spectrum of cage 6.1 (CD_3CN , 400 MHz, 298 K).	298
Figure 7.137. Expansions of the ^1H NMR spectrum of cage 6.1 (CD_3CN , 400 MHz, 298 K): a) imine region (H^e); b) aniline region (H^f), indicating isomer distribution.	298
Figure 7.138. $^{13}\text{C}\{^1\text{H}\}$ NMR spectrum of cage 6.1 (CD_3CN , 100 MHz, 298 K).	298
Figure 7.139. 2D-DOSY NMR spectrum of cage 6.1 (CD_3CN , 600 MHz, 298 K, $D(\mathbf{6.1}) = 4.04 \times 10^{-10} \text{ m}^2/\text{s}^2$).	299
Figure 7.140. gCOSY NMR spectrum of cage 6.1 (CD_3CN , 400 MHz, 298 K).	299
Figure 7.141. TOCSY NMR spectrum of cage 6.1 (CD_3CN , 600 MHz, 298 K, mixing time = 80 ms).	300
Figure 7.142. Expansion of the aromatic region of the TOCSY NMR spectrum of cage 6.1 (CD_3CN , 600 MHz, 298 K, mixing time = 80 ms).	300
Figure 7.143. DEPT-HSQC NMR spectrum of cage 6.1 (CD_3CN , 400 MHz, 298 K).	301
Figure 7.144. Expansion of the aliphatic region of the DEPT-HSQC NMR spectrum of cage 6.1 indicating the CH_2 (blue) and NMe_2 groups (red) in the spectrum (CD_3CN , 400 MHz, 298 K).	301
Figure 7.145. HMBC NMR spectrum of cage 6.1 (CD_3CN , 400 MHz, 298 K).	302
Figure 7.146. gNOESY NMR spectrum of cage 6.1 (CD_3CN , 600 MHz, 298 K, mixing time = 300 ms).	303
Figure 7.147. Expansions of the gNOESY NMR spectrum of cage 6.1 (CD_3CN , 600 MHz, 298 K, mixing time = 300 ms).	303
Figure 7.148. gROESY NMR spectrum of cage 6.1 (CD_3CN , 600 MHz, 298 K, mixing time = 300 ms).	304

- Figure 7.149.** Expansions of the gROESY NMR spectrum of cage **6.1** (CD₃CN, 600 MHz, 298 K, mixing time = 300 ms). 304
- Figure 7.150.** ¹H NMR spectrum of **6.12** (CD₃CN, 400 MHz, 298 K). 305
- Figure 7.151.** ¹³C{¹H} NMR spectrum of **6.12** (CDCl₃, 100 MHz, 298 K). 305
- Figure 7.152.** Expanded region from 567-633 m/z of ESI-mass spectrum of cage **6.1** in 100 % CH₃CN. 306
- Figure 7.153.** ¹H NMR spectra of the titration of D₂O into 5 mol % cage **6.1** showing: a) Cage stability (9.1 – 7.2 ppm, 6.2 – 5.5 ppm, and 3.2 – 2.3 ppm) b) Deuterium and hydrogen exchange (4.0 – 1.7 ppm). [**6.1**] = 0.8 – 0.63 mM, the reaction was performed at 23 °C in CD₃CN and monitored over time (400 MHz, 296 K, CD₃CN). 307
- Figure 7.154.** ¹H NMR spectra of the titration of DABCO **6.7** into 5 mol % cage **6.1** showing: a) Cage stability (9.2 – 6.8 ppm and 6.2 – 5.2 ppm) b) Formation of ammonium salt (3.3 – 2.5 ppm). [DABCO **6.7**] = 1.5 – 15.75 mM, [**6.1**] = 0.8 – 0.39 mM, the reaction was performed at 23 °C in CD₃CN and monitored over time (400 MHz, 296 K). 308
- Figure 7.155.** ¹H NMR spectra of the titration of DMA **6.9** into 5 mol % cage **6.1** showing: a) Cage stability (9.15 – 7.55 ppm and 6.2 – 5.45 ppm) b) Formation of ammonium salt (7.35 – 7.40 ppm and 3.3 – 2.85 ppm). [DMA **6.9**] = 1.5 – 23.6 mM, [**6.1**] = 0.8 – 0.2 mM, the reaction was performed at 23 °C in CD₃CN and monitored over time (400 MHz, 296 K, CD₃CN). 309
- Figure 7.156.** ¹H NMR spectra of the titration of DBU into 5 mol % cage **6.1** showing: a) Cage stability (9.2 – 6.8 ppm and 6.4 – 5.1 ppm) b) Formation of ammonium salt (3.8 – 1.45 ppm). [DBU] = 1.5 – 10.5 mM, [**6.1**] = 0.8 – 0.53 mM, the reaction was performed at 23 °C in CD₃CN and monitored over time (400 MHz, 296 K, CD₃CN). 310
- Figure 7.157.** ¹H NMR spectra of the titration of KO^tBu into 5 mol % cage **6.1** showing: a) Cage stability (9.2 – 6.8 ppm and 6.2 – 5.1 ppm) b) Formation of ammonium salt (3.2 – 1.0 ppm). [KO^tBu] = 0.77–10.5 mM, [**6.1**] = 0.8 – 0.53 mM, the reaction was performed at 23 °C in CD₃CN and monitored over time (400 MHz, 296 K, CD₃CN). 311
- Figure 7.158.** ¹H NMR spectra of the reaction between benzaldehyde dimethyl acetal (BDA) and H₂O in the presence of 5 mol % cage **6.1** showing: a) Cage stability (8.99 – 8.89 ppm) b) Product formation (10.3 – 9.8 ppm, 8.2 – 7.0 ppm, and 5.8 – 5.2 ppm). [BDA] = 15.75 mM [H₂O] = 94.5 mM, [**6.1**] = 0.8 mM, reaction was performed at 50 °C in CD₃CN and monitored over time (400 MHz, 323 K, CD₃CN). 312
- Figure 7.159.** ¹H NMR spectra of the reaction between benzaldehyde and malononitrile in the presence of 5 mol % cage **1** and 5 mol % DABCO showing: a) Cage stability (8.99 –

8.82 ppm) b) No product formation (10.1 – 3.5). [Benzaldehyde] = 15.75 mM [Malononitrile] = 19.6 mM, [1] = 0.8 mM, [DABCO] = 0.8 mM, reaction was performed at 23 °C in CD₃CN and monitored over time (400 MHz, 296 K, CD₃CN). 313

Figure 7.160. ¹H NMR spectra of the reaction between benzaldehyde and malononitrile in the presence of 5 mol % DABCO **6.7** showing product formation (10.1 – 3.5). [Benzaldehyde] = 15.75 mM [Malononitrile] = 19.6 mM, [DABCO **6.7**] = 0.8 mM, reaction was performed at 23 °C in CD₃CN and monitored over time (400 MHz, 296 K, CD₃CN). 314

Figure 7.161. Full ¹H NMR spectra of the reaction of **6.12** in the presence of 5 mol % cage **6.1**. [6.12] = 15 mM, [6.1] = 1.25 mM, the reaction was performed at 23 °C in CD₃CN and monitored over time (400 MHz, 296 K, CD₃CN). 315

Figure 7.162. Expanded ¹H NMR spectra of the reaction of **6.12** in the presence of 5 mol % cage **6.1** showing: a) Cage stability (6.9 – 5.5 ppm) b) Product formation (4.4 – 2.9). [6.12] = 15 mM, [6.1] = 1.25 mM, the reaction was performed at 23 °C in CD₃CN and monitored over time (400 MHz, 296 K, CD₃CN). 316

Figure 7.163. Full ¹H NMR spectra of the reaction of N-tritylbenzylamine **6.14** in the presence of 8 mol % cage **6.1**. [6.14] = 15 mM, [6.1] = 1.25 mM, the reaction was performed at 23 °C in CD₃CN and monitored over time (400 MHz, 296 K, CD₃CN). 317

Figure 7.164. Expanded ¹H NMR spectra of the reaction of N-tritylbenzylamine **6.14** in the presence of 8 mol % cage **6.1** showing: a) Cage stability (7.1 – 5.4 ppm) b) Product formation (4.4 – 3.2). [6.14] = 15 mM, [6.1] = 1.25 mM, the reaction was performed at 23 °C in CD₃CN and monitored over time (400 MHz, 296 K, CD₃CN). 318

Figure 7.165. Expanded ¹H NMR spectra of the reaction of N-tritylbenzylamine **6.14** in the presence of 32 mol % cage **6.1** showing: a) Cage stability (7.1 – 5.4 ppm) b) Product formation (4.5 – 3.1). [6.14] = 15 mM, [6.1] = 5 mM, the reaction was performed at 23 °C in CD₃CN and monitored over time (400 MHz, 296 K, CD₃CN). 319

Figure 7.166. Full ¹H NMR spectra of the reaction of N-trityl-4-bromoaniline in the presence of 8 mol % cage **6.1**. [2.8] = 15 mM, [6.1] = 1.25 mM, the reaction was performed at 23 °C in CD₃CN and monitored over time (400 MHz, 296 K, CD₃CN). 320

Figure 7.167. Expanded ¹H NMR spectra of the reaction of N-trityl-4-bromoaniline **2.8** in the presence of 32 mol % cage **6.1** showing: a) Cage stability (7.1 – 5.4 ppm) b) Product formation (4.5 – 3.1). [2.8] = 15 mM, [6.1] = 5 mM, the reaction was performed at 23 °C in CD₃CN and monitored over time (400 MHz, 296 K, CD₃CN). 321

Figure 7.168. UV-Vis absorption spectrum of the titration of DABCO **6.7** into a 1.5 μM solution of cage **6.1** in CH_3CN . DABCO **6.7** was added in 1 μL aliquots from a 4.5 mM stock solution in CH_3CN . 322

Figure 7.169. UV-Vis absorption spectrum of DBU **6.10** into a 1.5 μM solution of cage **6.1** in CH_3CN . DBU **6.10** was added in 1 μL aliquots from a 4.5 mM stock solution in CH_3CN . 322

Figure 7.170. UV-Vis absorption spectrum of DMA **6.9** into a 1.5 μM solution of cage **1** in CH_3CN . DMA **6.9** was added in 2-5 μL aliquots from a 4.5 mM stock solution in CH_3CN . 323

Figure 7.171. UV-Vis absorption spectrum of the titration of neutral guest **3.21** into a 1.5 μM solution of cage **6.1** in CH_3CN . **3.21** was added in 1 μL aliquots from a 4.5 mM stock solution in CH_3CN . 323

LIST OF TABLES

Table 2.1. Initial rates using various substrates and catalysts.	48
Table 2.2. Binding affinities of electrophiles, nucleophiles, and products.	52
Table 3.1. Thioetherification of vinyl diphenylmethanol derivatives with acid catalysts.	71
Table 3.2. Initial Rates and % conversion of thioetherification reaction using various controls.	72
Table 3.3. Oxocarbenium ion vs carbocation selectivity of acetal 4d .	76
Table 3.4. Thioether/ether exchange with the small THP ether 3.10 .	75
Table 3.5. Binding of various substrates and products in cage 1.30 .	82
Table 4.1. Yields for cyclization reaction promoted by cage 1.30 and CSA 3.6 .	96
Table 4.2. Binding affinities of various substrates and products.	99
Table 5.1. Binding affinities to various substrates and products.	121
Table 5.2. Initial rates of thioetherification of electrophile 2.1 and 2.2 with PrSH .	128
Table 6.1. Assigned ions for experimentally observed peaks.	153
Table 7.1. Assigned ions for experimentally observed peaks.	306

Chapter 1 – Catalysis within Supramolecular Cages

1.1. Inspiration from Nature

The main difference between enzymes and small molecule synthetic catalysts is that enzymes have a wide scope of selectivity and catalytic performance.¹ They derive this from their active sites, something that small molecule catalysts do not have. These active sites contain functional groups that allow enzymes to bind to substrates of specific shapes and sizes. In doing so, enzymes can catalyze reactions with high degrees of selectivity.² Despite their increasing use in chemical reactions, enzymes also have some limitations. First, their structures are large and complex, making atomic-level understanding of their function challenging.³ They are also not tolerant to harsh conditions, which limits their efficacy in some situations.⁴ In addition, their selectivity limits their scope, as most enzymes act only on a single target.⁵ In light of this, they are limited in terms of the reactions they can catalyze when compared to small molecules. Nevertheless, enzymes are conceptually the “ideal” catalyst, with rates that are a million or more times faster than what would be attainable in their absence.⁶⁻⁷

The high efficiency and selectivity shown by enzymes has attracted considerable attention in synthetic chemistry and has prompted chemists to mimic their behavior in a more easily analyzable system. Significant efforts have been dedicated to both designing and synthesizing catalysts that possess these enzyme-like functions.⁸⁻¹³ In fact, supramolecular chemists have designed small macrocycles with defined, hydrophobic cavities that can mimic the active site of enzymes.¹⁴⁻¹⁸ Early hosts with these cavities include small cyclic oligomers¹⁹ and multicyclic covalent assemblies.²⁰ However, these

supramolecular catalysts possess small cavities, which means that multiple substrates cannot be encapsulated for catalysis. Guests that fit too tightly within the host cavity have their movement within the complex inhibited. To enable more favorable binding, the synthesis of more elaborate and larger hosts is essential. Smaller cavities cannot bind larger guests, so larger cavities are needed.²¹ However, synthesizing covalent macrocycles with large cavities can be difficult. New strategies to create supramolecular hosts need to be explored.

1.2. Design and Assembly of Supramolecular Cages

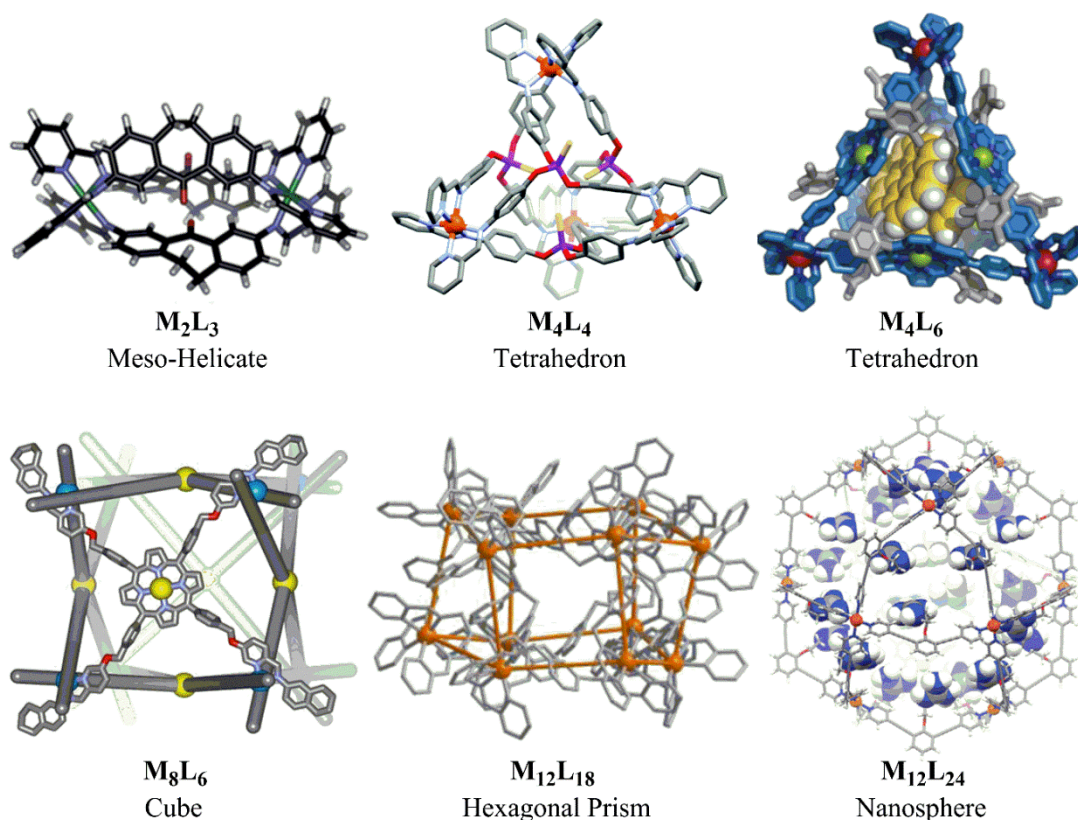


Figure 1.1. Formation of self-assembled metal-ligand cage complexes of differing stoichiometry and geometric shapes.³⁹⁻⁴⁴

The self-assembly of hosts using coordination bonds between metals and donor ligands is a powerful method for the synthesis of larger assemblies.²²⁻²⁴ These hosts, known as self-assembled coordination cages, have drawn substantial attention as “artificial enzymes” and biomimetic catalysts.²⁵⁻³⁰ These cage complexes are held together by reversible dative bonds. They are formed through the coordination of the organic ligand molecules with two or more metal cations.³¹ Some commonly used metals in these complexes are Fe²⁺, Pd²⁺, and Pt²⁺.³² Other metals, such as Co²⁺, Ni²⁺, and the rare earth lanthanides and actinide elements can also be used for assembly.³³ While the coordinating group may vary, those most commonly used are monodentate pyridyl coordination³⁴ or bidentate coordination with bipyridyl,³⁵ iminopyridine,³⁶ pyridyl pyrazole,³⁷ or catechol³⁸ functional groups. Through this coordination, metal-ligand complexes of differing stoichiometry and geometric shapes are formed. They range from small M₂L₃ meso-helicates³⁹ to M₄L₆ tetrahedra⁴¹, to even larger M₂₄L₂₈ nanospheres⁴⁴ (Figure 1.1). A successful reaction results in the most stable thermodynamic cage product, excluding structures with unfavorable geometry or stoichiometry.⁴⁵

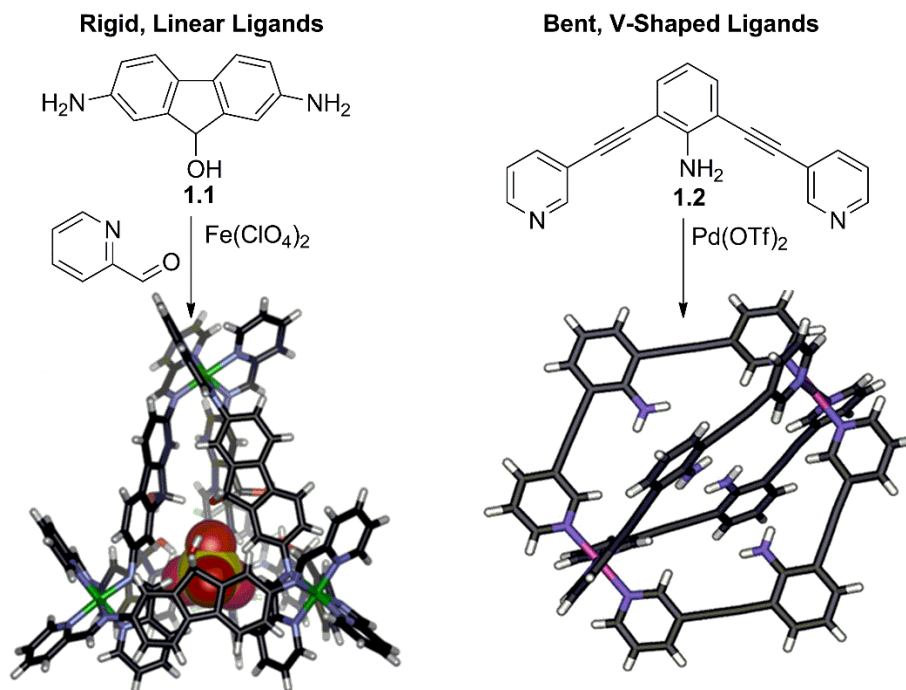


Figure 1.2. Comparison of linear versus V-shaped ligands for cage assembly.⁴⁵⁻⁴⁶

It is worth noting that factors such as the rigidity, angle, and distance between the cording groups in the ligand's structure can affect the formation of a self-assembled cage. If the ligand is too flexible, the structural integrity can be affected. If it is too rigid, it can prevent assembly from occurring altogether.⁴⁵ However, rigid ligands (Figure 1.2) tend to be more amenable to assembly than those that can bend more, allowing the formation of products that are (comparatively) highly symmetrical. The coordination angle also impacts this process. Ligands (Figure 1.2) that are more bent and V-shaped create smaller M_2L_3 helicates,⁴⁷ whereas the more linear ones favor the M_4L_6 tetrahedral complex (Figure 1.2).⁴⁸

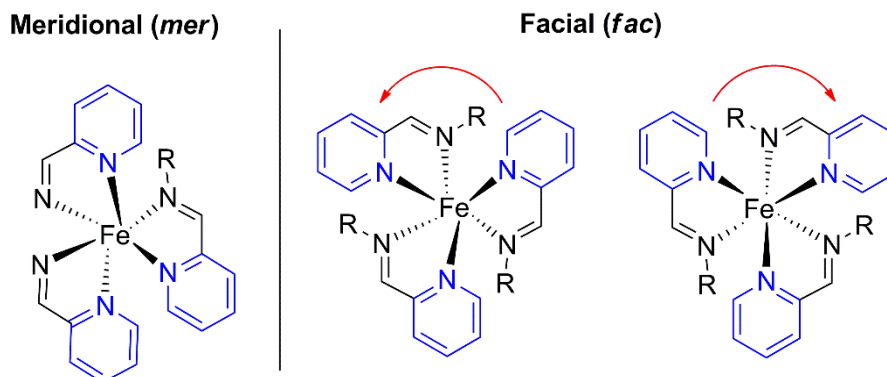


Figure 1.3. The two octahedral enantiomers meridional (*mer*) and facial (*fac*) are shown here. Rotation of the *fac* centers gives rise to two enantiomers: Λ (left) and Δ (right).

Exerting control over stereochemistry can be a potential problem in assembly. As an example, the use of octahedral metals can lead to metal-based stereoisomerism. In octahedral metal salts, multiple isomeric possibilities exist when handled with bidentate chelators.⁴⁹⁻⁵² These chelators exist in either the facial (*fac*) or meridional (*mer*) configurations. In the smaller M_2L_3 , the *mer*-geometry is not observed due to a significant strain in its structure. However, in larger M_4L_6 complexes, more rotational freedom is allowed. This enables the incorporation of *mer*-metal centers, thereby increasing the potential number of isomers being formed.⁵³ *Fac*-centers are rather common, while *mer*-centers are more rare.^{48,54} There are three isomers that can exist within the all-*fac* tetrahedral complex, with two potential enantiomers, Λ (left) or Δ (right), that derive from the rotation of the *fac*-centers (Figure 1.3).⁵³ One of these isomers has T symmetry (*fac*- $\Lambda\Lambda\Lambda\Lambda$ or *fac*- $\Delta\Delta\Delta\Delta$). The geometries are completely matched and is more symmetrical. By changing the rotation of one metal center, isomers with both a C_3 (*fac*- $\Delta\Lambda\Lambda\Lambda$ or *fac*- $\Lambda\Delta\Delta\Delta$) and S_4 (*fac*- $\Lambda\Lambda\Delta\Delta$) symmetry can be formed.⁴⁹

1.3. Molecular Recognition of Unfunctionalized Coordination Complexes

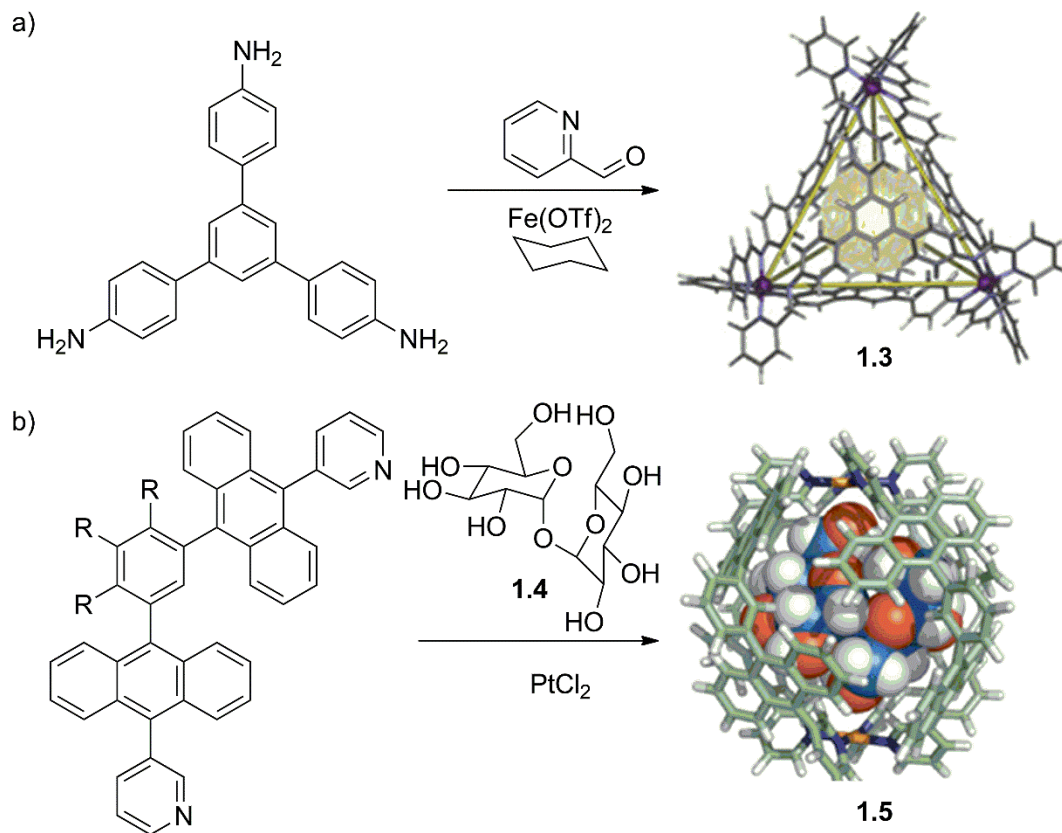


Figure 1.4. a) M₄L₄ capsule shown to encapsulate a cyclohexane molecule.⁵⁶ b) Strong molecular recognition of sucrose in water using cage **1.5**.⁵⁸

Cage complexes are usually constructed using flat aromatic panels. Aromatic walls are commonly used because they can block large gaps that exist between the individual ligands.⁵⁵ This results in a more enclosed cavity for molecular recognition. Moreover, guest encapsulation can be controlled by aromatic panels. For example, Nitschke and colleagues showed high binding affinity to a variety of hydrocarbons inside an M₄L₄ capsule **1.3** (Figure 1.4a).⁵⁶ However, little selectivity was observed between guests of different sizes.

From this, it was understood that the proper size and shape matching of the guest inside the host will provide more selective binding.⁵⁷

Yoshizawa and coworkers demonstrated the inner walls of an anthracene paneled paddlewheel **1.5** show strong molecular recognition for sucrose **1.4** in water using because of the CH- π interactions (Figure 1.4b). Cage **1.4** exhibited rare selectivity for sucrose over other carbohydrates. This complex does not interact with monosaccharides such as glucose and fructose and other common disaccharides such as lactose, maltose and trehalose. Furthermore, cage **1.4** competitively bound sucrose with 100% selectivity when in a mixture of two disaccharides with the same molecular formula. The only difference between these disaccharides is the configuration, yet cage **1.4** was still able to recognize subtle differences and exclusively encapsulate sucrose.⁵⁸

These cages are essentially featureless and function only as the host. To create hosts with more versatile functions, other strategies and properties should be used to incorporate the functional groups necessary to mimic enzymes.

1.4. Functionalized Complexes with Non-reactive Groups

Various scaffolds have been used to incorporate functional groups into cage complexes. The most versatile scaffolds are those prepared by Fujita. Their ligand frameworks are V-shaped and possess either a 4-pyridiyl or 4-ethynylpyridiyl functional group at the 2 and 6 position of the aromatic ring (Figure 1.5a-b).⁵⁹⁻⁶⁴ V-shaped ligands direct and position functional groups into the interior of the cavity instead of its exterior upon assembly. These ligands can be used to assemble large $M_{12}L_{24}$ nanospheres. These nanospheres are stable,

highly cationic, soluble in water, and have large enough cavities to incorporate functional groups inside of them.

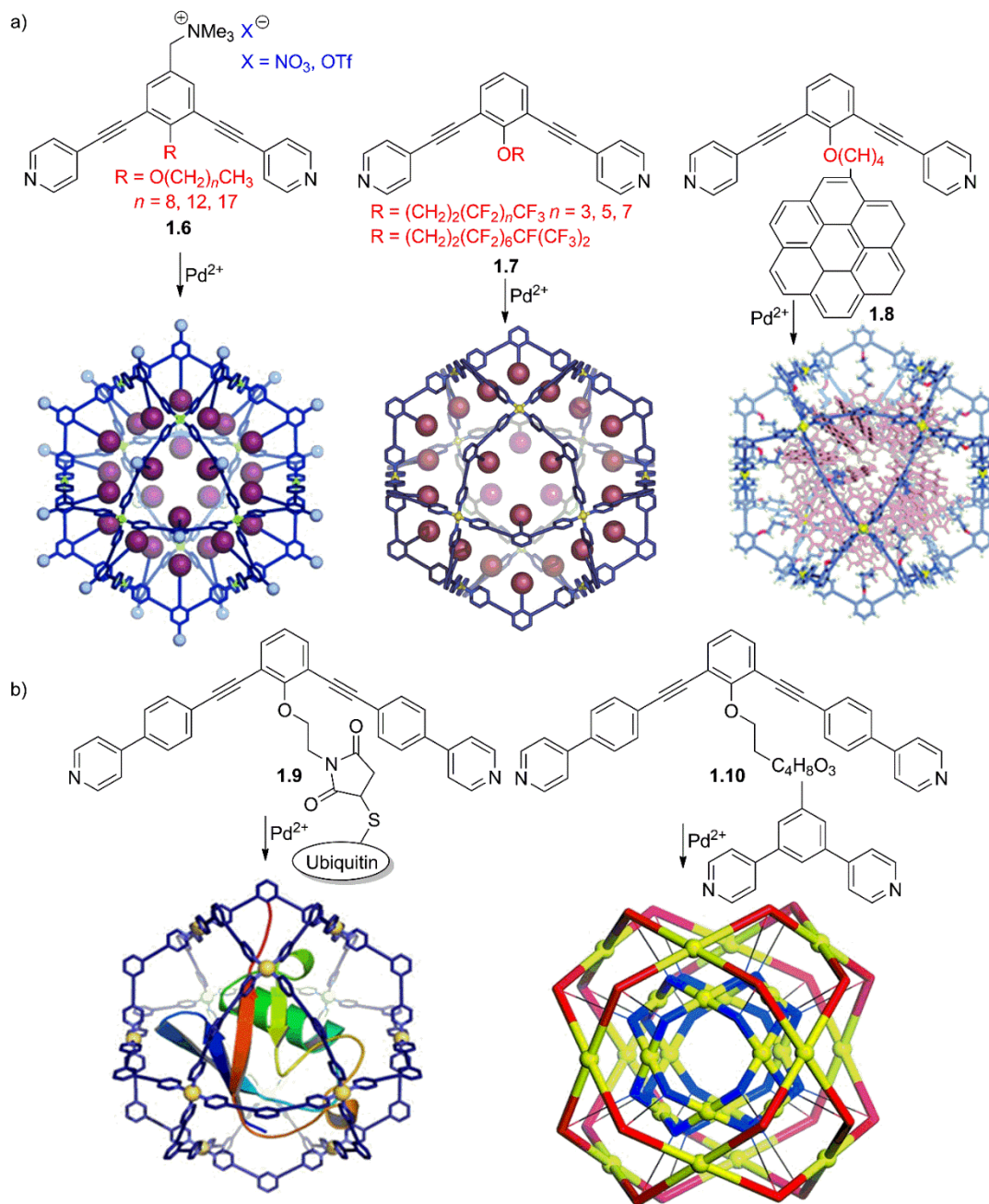


Figure 1.5. Synthesis of nanospheres with inert function. a) Assembly of the complex with V-shaped ligands containing 4-pyridiyl groups.⁵⁹⁻⁶² b) Assembly of the complex with V-shaped ligands containing 4-ethynylpyridiyl functional group.^{63,64}

In these nanospheres, simple and unreactive functional groups were incorporated. These groups consist of long alkyl groups inside the cavity of the cage as seen in ligand **1.6**.⁶⁰ This creates a hydrophobic environment that can encapsulate lipophilic molecules such as Nile red. Likewise, the derivatizations at these positions can help add perfluoroalkyl groups, as shown in ligand **1.7**, and can also be used to produce various fluorinated nanodroplets.⁶¹ Moreover, by internally adding a coronene group, such as in ligand **1.8**, a highly aromatic environment can be created that enables the complex to bind molecules such as C₆₀ and naphthalenediimide in water (Figure 1.5a).⁶² The large and robust framework of the nanosphere can help incorporate various groups into the cage complex such as the protein complex found inside ligand **1.9**.⁶³ Adding functional groups into the ligand can lead to an even more complex cage molecule. By attaching a short bis-pyridine group into the interior of a large bis-pyridyl one in ligand **1.10**, a “Matryoshka Doll” can be assembled (Figure 1.5b).⁶⁴ These nanospheres have shown remarkable properties and large cavity volumes. However, due to their size, it is difficult to selectively bind smaller molecules when compared to enzymes. Overall, these complexes are inert and provide separate nanophases for the reaction to occur. To mimic the active site of an enzyme, complexes with smaller cavities will be needed to increase the selectivity for specific substrates.

1.5. Functionalized complexes with Small Endohedral Groups

In the discussion above, Fujita and coworkers have shown that large functional groups in large nanospheres are effective in encapsulating hydrophobic and aromatic molecules. The incorporation of smaller functional groups can enhance the functionality as well.

Smaller cavities are, therefore, required to accommodate these smaller functional groups. Even simple functional groups whose only contribution is a lone pair, or a hydrogen-bonding group can introduce novel properties into the complex. Seemingly featureless cages can also find some function, such as the selective capture of ions.

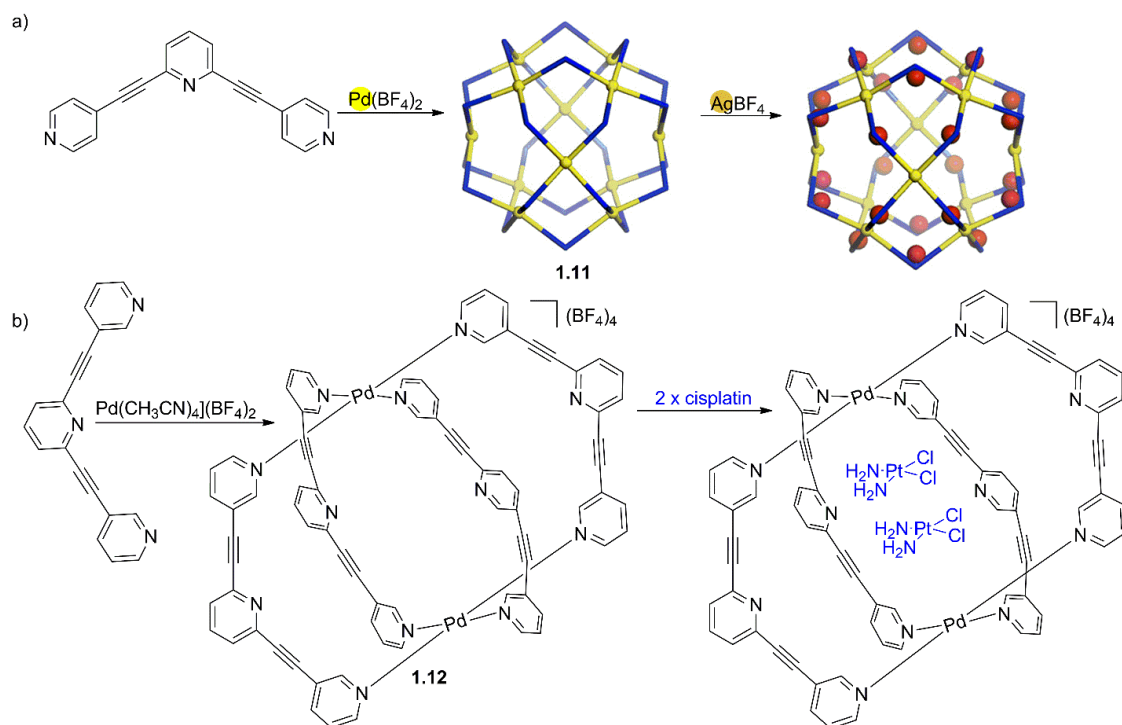


Figure 1.6. a) Assembly of a $\text{Pd}_{12}\text{L}_{24}$ nanosphere that is capable of encapsulating Ag^+ cations.⁶⁵ b) Formation of smaller paddlewheel complexes capable of encapsulating two cisplatin molecules.⁶⁶

The encapsulation of positively charged cations as guests is seldom observed in cage structures that are featureless. This is because most cage assemblies are highly cationic in nature. For instance, Fujita's $\text{Pd}_{12}\text{L}_{24}$ nanosphere **1.11** with pyridyl nitrogen displays a 24^+ charge and can encapsulate Ag^+ cations within the cage's interior (Figure 1.6a). However, the pyridyl rings for the most part can be regarded as independent in capturing the guest due to the complex's large structure.⁶⁵ Smaller paddlewheel complexes **1.12** have been

made by changing the pyridyl orientation from 4, 4' to 3, 3' (Figure 1.6b). This alteration was shown to effectively direct groups towards the inner cavity. With this change in pyridyl group orientation, the complex is effective in encapsulating cationic guests. Through the hydrogen bonding between the guest and its lone pairs, the cage is capable of encapsulating two cis-platin molecules. The encapsulation is shown to be dependent on the hydrogen bonding since no affinity to cis-platin was observed in water.⁶⁶

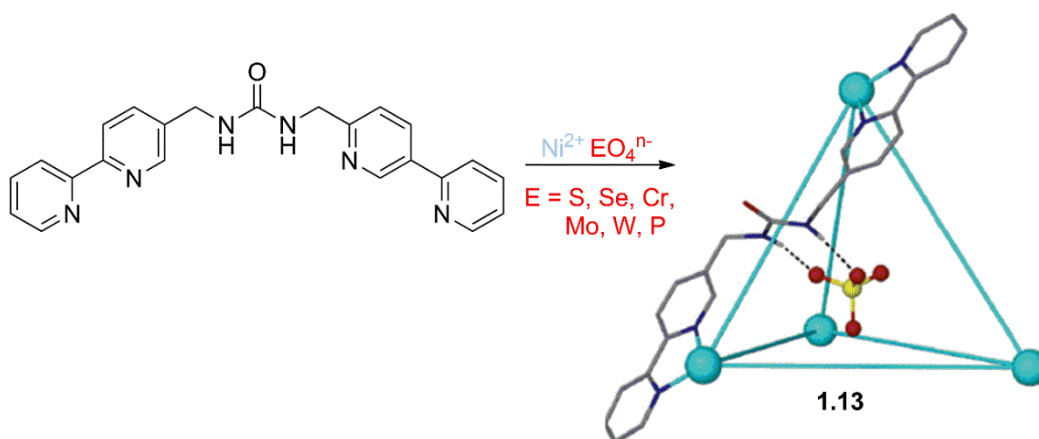


Figure 1.7. Selective anion templated assembly of a Ni_4L_6 tetrahedral complex.⁶⁷

It is far more difficult to bind anionic molecules in cages than cationic species. Hydrogen bonding interactions between the ligand and anion forms the template of the cage complex. Custelcean et. al. have demonstrated this fact by assembling a complex using an anion as a template, given its ability to enable the formation of a tetrahedral complex with urea groups. The Ni_4L_6 tetrahedral complex **1.13** utilizes its urea groups to selectively bind a sulfate anion through a hydrogen bond interaction (Figure 1.7). The affinity for the anion observed ($K_a = 6 \times 10^6 \text{ M}^{-1}$) is similar to that of a sulfate-binding protein. Further experimentation shows a trend in the selectivity for the following anions

in the assembly of other complexes: $\text{PO}_4^{3-} \gg \text{CrO}_4^{2-} > \text{SO}_4^{2-} > \text{SeO}_4^{2-} > \text{SeO}_4^{2-} > \text{SeO}_4^{2-} > \text{MoO}_4^{2-} > \text{WO}_4^{2-}$.⁶⁷

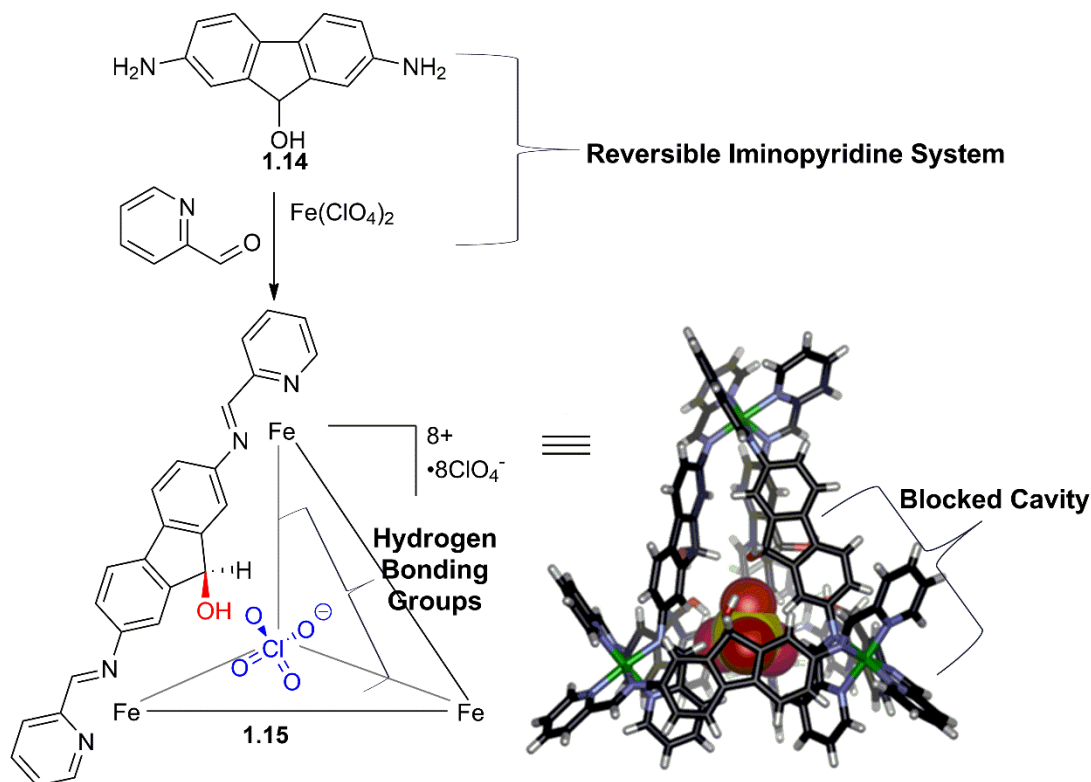


Figure 1.8. Formation of an M_4L_6 tetrahedral complex using hydrogen-bonding groups.⁴⁸

Alcohols are another form of hydrogen-bond donors found in complexes that have been shown to influence its ability in recognizing anions. Moreover, a cage complex's assembly can also be templated and controlled using these anions. The previous work in the Hooley lab has demonstrated that the stereoselective formation of tetrahedral Fe-iminopyridine cage complexes can be enabled using hydrogen-bonding groups. These complexes were created through an imine condensation reaction between a diamine and pyridyl aldehyde whereby the metal facilitated the condensation within one step. With 2,7-dibromo-9H-fluoren-9-ol **1.14**, 2-formylpyridine, and $\text{Fe}(\text{ClO}_4)_2$, a $\text{mer}_3:\text{fac}$ M_4L_6 tetrahedral cage **1.15** was assembled. This was unexpected as these complexes usually exhibit the features of an

all-*fac* tetrahedral complex. Since there are four metal centers, three possible isomers can exist. Moreover, the internal alcohol group becomes chiral after the complex is assembled. This chirality increases the number of isomers formed. In total, over 100 isomeric possibilities can exist.

These fluorene cores exhibit the correct angle to orient ligands to selectively form one discrete product with the ClO_4^- ion. Templating the formation of the cage, the hydrogen bonding interactions between the alcohol in the ligand and the oxygens in the ClO_4^- anion (Figure 1.8) begins the assembly. Other ions, such as BF_4^- , can also be used to form the cage complex. Fe^{2+} salts, such as OTf^- and SO_4^{2-} , are not effective templates as non-discrete coordination polymers are formed when using OTf^- as the counterion. The reversible nature of the assembly can convert these polymers into a cage complex through an anion exchange using ClO_4^- anions. The size of the anion significantly impacts the formation of the cage. Anions that are too large show trouble fitting inside the cavity, while the smaller ones will show problems in orienting the internal hydrogen-bond groups to form the complex. The ClO_4^- anion controls the formation of the cage complex, but the ClO_4^- anion also blocks the resulting cavity.⁴⁸ This results in a cavity too small to incorporate functional groups that are reactive, inhibiting the addition of groups essential for biomimetic catalysis.

1.6. Challenges in Catalysis

The cages discussed so far possess functional groups that are non-reactive. The most attractive feature of self-assembled hosts is their ability to catalyze biologically relevant reactions. As previously shown, the internal cavities of cages are ideal for molecular recognition of a wide variety of guests. However, to perform more specific recognition

necessary for catalysis, several challenges present themselves. First, the ability for cages to properly differentiate between multiple different guests inside their cavities is still underdeveloped, which can produce problems in turnover through both product and substrate inhibition.^{68,69} Furthermore, the metal-ligand contacts that keep the cage together are sensitive to nucleophiles and could be damaged through the reaction, especially subjected to harsh conditions. As such, the reaction conditions must be selected carefully to prevent destruction of the cage.⁶⁸ To successfully catalyze a reaction within the cavity of a self-assembled complex, the following must be taken into consideration: recognition and encapsulation of substrate, promotion of reaction by reducing enthalpy, and product release to permit turnover.⁷⁰ Up to now, over hundreds of self-assembled complexes have been reported. However, not all of them can perform supramolecular catalysis.

1.7. Cavity-directed Catalysis using Unfunctionalized Coordination Complexes

For some cage complexes, the cavity serves as an active site for catalyzing a variety of reactions. These complexes act like “empty boxes” in which the cavity alone controls the reaction. With regard to this, Raymond and coworkers have synthesized a water-soluble Ga₄L₆ tetrahedral complex and explored its ability to catalyze various reactions for over 20 years (Figure 1.4b).⁷¹ A notable design of cage **1.16** is the naphthalene panels which provide a hydrophobic cavity for the structure. The cage uses its cation- π and CH- π interactions to encapsulate the guests in the solution. Like enzymes, a precise structural control of the active site is attained through noncovalent interactions. Due to these CH- π interactions, the complex can promote a variety of reactions such as an aza-Cope rearrangement (Figure 1.10a). The rearrangement was accelerated when the substrates were

encapsulated by cage **1.16** due to a decrease in the entropy of activation. Mechanistically, the cavity of the complex binds the allylenammonium substrates in a closely packed, preorganized configuration, closely resembling the conformation of a chair-like transition state.^{24, 71-74}

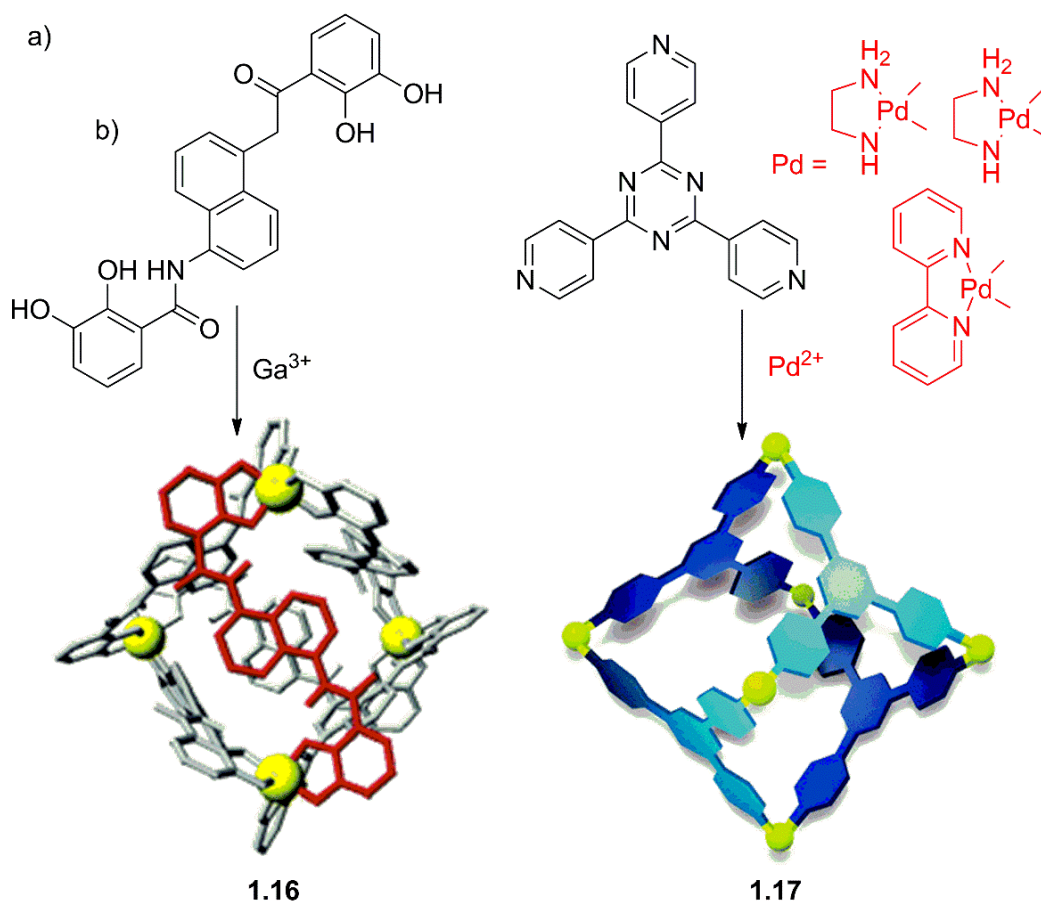


Figure 1.9. a) Ga_4L_6 tetrahedral complex used its cavity alone to promote various reactions.^{24, 71-79} b) An octahedral Pd_6L_4 used for the selective formation of products that are usually not observed.⁸⁰⁻⁸⁹

Cage **1.16** can also catalyze a Nazarov cyclization of 1,4-pentadien-3-ol to form a cyclopentadiene (Figure 1.10b). The reaction proceeds via a diallylic carbocation intermediate that undergoes a conrotatory electrocyclic ring closure. Initially, the conversion of the reaction was low due to inhibition of the reaction rate by the product. To

overcome product inhibition, the product was converted to a poor guest by introducing maleimide into the reaction as a trapping agent to produce the Diels-Alder adduct of the diene product. By doing this, rate accelerations of up to 2.1 million relative to the background reactivity were observed due to the increased basicity of the alcohol functional group upon encapsulation, pre-organization of the bound substrate, and stabilization of the transition state.^{75,76}

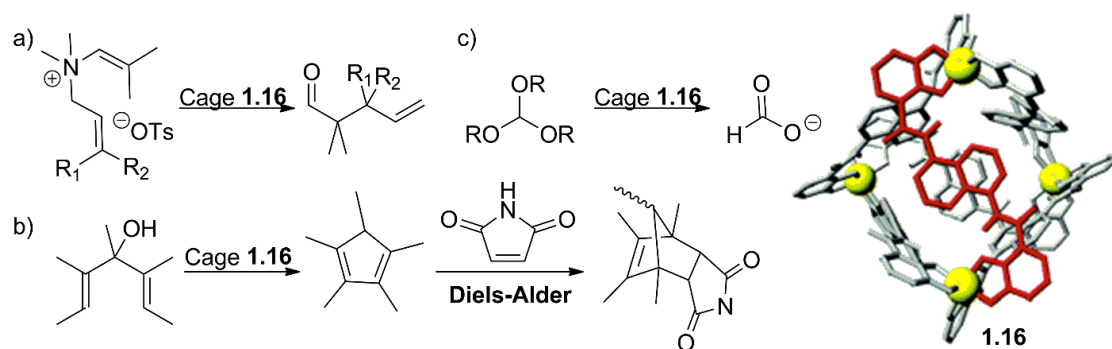


Figure 1.10. Reactions catalyzed by **1.16**. a) aza-Cope rearrangement.⁷¹⁻⁷⁴ b) Nazarov cyclization.^{75,76} c) Hydrolysis of orthoformates.⁷⁷⁻⁷⁹

Cage **1.16** can also be used to shift the pK_a of guest molecules to catalyze acidic reactions such as the hydrolysis of orthoformates in basic solutions (Figure 1.10c). Initial studies found that the cage, with its highly charged cavity, can encapsulate amines and phosphines in their protonated form even at high pH. Also as noteworthy, the basicity of the protonated amines is increased by up to 4.5 pK_a units upon encapsulation. Orthoformates are usually highly stable in basic or neutral solutions. However, in the presence of cage **1.16**, triethyl orthoformate was hydrolyzed. Once the neutral substrate enters the cage, the molecule becomes protonated by water and undergoes two consecutive hydrolysis reactions within the cavity to form the protonated formate ester.⁷⁷⁻⁷⁹

In addition to Raymond, Fujita and coworkers have also used the cavity to control the formation of unusual products under thermal, photochemical, and radical conditions with his octahedral Pd₆L₄ **1.17**. The cage is assembled by coordinating triazine-core tridentate ligands with Pd²⁺ or Pt²⁺ metals (Figure 1.4c).⁸⁰ These features allow the cage complex to bind substrates in fixed positions. This particular cage is capable of performing numerous reactions on the interior, including Diels Alder reactions,⁸¹⁻⁸⁶ photo-directed 1,4 radical addition,⁸⁷ Knoevenagel condensation,⁸⁸ and demethylenation of cyclopropanes.⁸⁹ When using this cage as a host, selectivity was obtained for the product that is typically not observed when using a small molecule catalyst. In the Diels-alder reaction of 9-hydroxymethylanthracene and N-cyclohexylphthalimide, the syn 1,4-Diels-Alder adduct was formed over the typically observed 9,10-Diels-Alder adduct (Figure 1.11a).⁸¹ Another example of selectivity includes the photoreaction of o-quinone with substituted toluene. Using cage **1.17** as the catalyst, the complex was observed to be selective toward the formation of unusual 1,4-adduct (Figure 1.11c).⁸⁷ Recent studies have shown the complex being able to remove a methylene group from cyclopropane while in its cavity via a guest-to-host electron transfer. This reaction was shown to only occur when a phenyl ring or alkene group was added to the cyclopropane rings (Figure 1.11b).⁸⁹

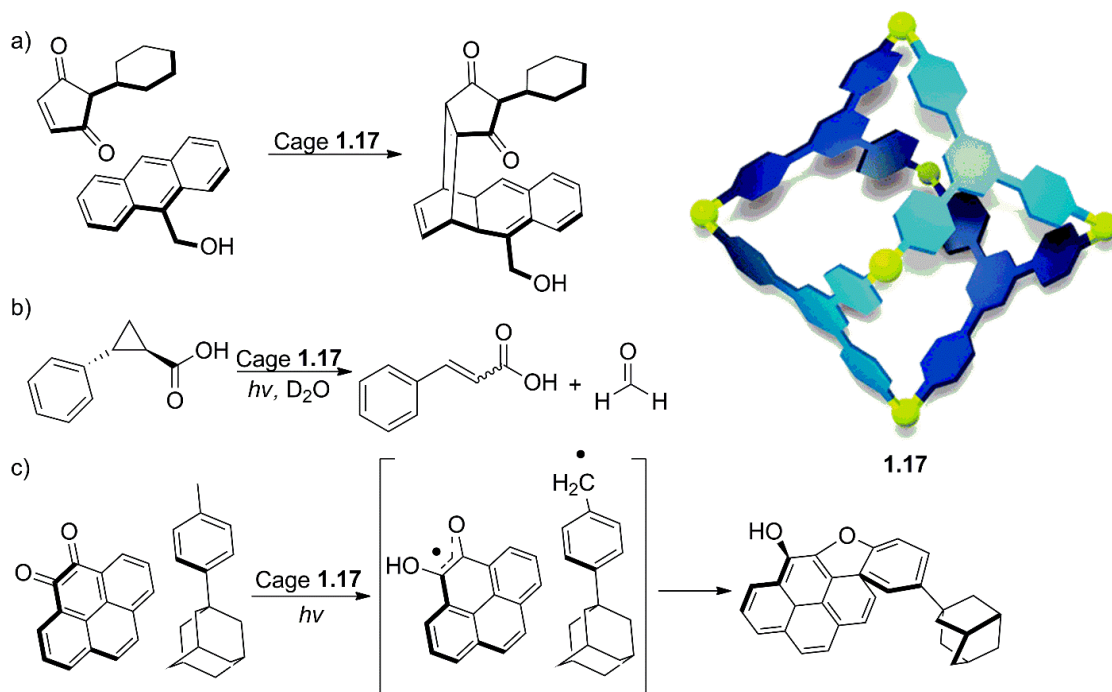


Figure 1.11. Reactions catalyzed by **1.17**. a) Diels-alder reaction of 9-hydroxymethylanthracene N-cyclohexylphthalimide.⁸¹ b) Demethylenation of cyclopropanes.⁸⁹ c) Photoreaction of o-quinone with substituted toluene.⁸⁷

For the reactions catalyzed by complexes **1.6** and **1.7** to occur, their cavities must preorganize the bound substrate(s) with an appropriate reactive conformation for catalysis. To truly mimic enzymes, reactive functional groups must be incorporated. Other strategies must be investigated to create functionalized catalytic systems.

1.8. Encapsulating Cofactors as Guests for Supramolecular Catalysis

Enzymes in no small part owe their high catalytic activity to their cofactors. Integrating cofactors into our cages is thus an effective strategy to improve supramolecular catalysis. Enzymes use cofactors to assist in performing certain, biologically necessary reactions that they would otherwise be unable to catalyze. By binding tightly to an apoenzyme (an inactive enzyme), an active holoenzyme complex can be formed.⁹⁰ The host can then activate and facilitate a reaction with the bound cofactor. Currently, there are few examples

of cofactor-mediated catalysis with self-assembled cage hosts. Binding and activating a diverse set of guests within the cage structure followed by turnover into binary, ternary, or quaternary complexes can be a difficult process. As more guests are bound within the cage, larger entropic penalties are experienced by the host.⁸⁸⁻⁹³ The ability to encapsulate two or more guests to form homoternary⁹⁴⁻⁹⁷ complexes is relatively common, but formation of heteroternary⁹⁸⁻¹⁰¹ complexes is less frequent. Furthermore, smaller cavities (and by extension cages) can be advantageous in promoting the selectivity for different reactants. Despite their smaller cavity and subsequent increase in selectivity, their use can result in product inhibition and poor turnover numbers.¹⁰² This has resulted in most hosts having nanosized cavities to overcome the limitations experienced by smaller cavities, largely the issues with turnover and product inhibition.^{91,92}

While cages with nanosized cavities outperform smaller complexes, their ability to bind numerous guests can incur large energetic penalties. One solution used to overcome entropic difficulties from binding multiple guests in solution is to use small cofactor-like ions.¹⁰³⁻¹⁰⁷ Ward and colleagues have synthesized a cationic Co_8L_{12} coordination cage **1.18** that attracts hydroxide anions from solution (Figure 1.12). Cage **1.18** showed strong affinity for neutral guests and a weak affinity for anionic compounds, which indicated its ability to capture and release guest can be controlled by pH. Cage **1.18** was shown to catalyze a Kemp elimination with benzisoxazole and hydroxide to form 2-cyanophenolate. Since benzisoxazole is neutral, the complex binds the guest strongly with an affinity of $4 \times 10^3 \text{ M}^{-1}$. By bringing the guest near the surface hydroxide ions, higher rates are observed for the elimination reaction when compared to an uncatalyzed reaction. The hydroxide

anions on the surface of the complex can be replaced by competing anions such as chlorine. The reaction rate decreases with increased concentration of the competitive chlorine ions. When the reaction is inhibited, the product begins to act as a base and displaces the chlorine ions on the surface of the cage. The autocatalytic route only occurs in the absence of a base.^{109,110}

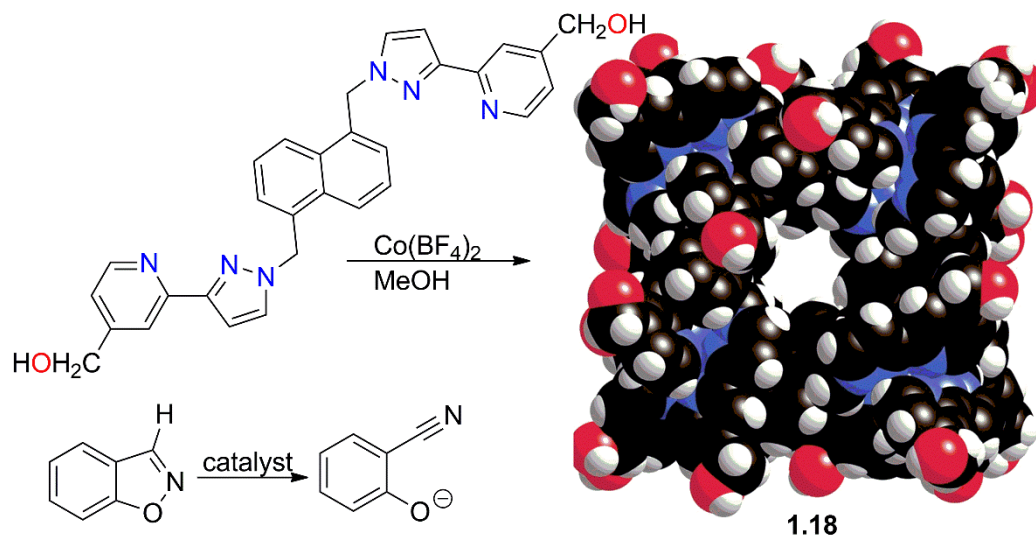


Figure 1.12. A Co_8L_{12} coordination cage complex using its hydroxide anions to catalyze a Kemp elimination.^{109,110}

In contrast to small cofactors, the addition of larger cofactors requires complexes that are bigger in size such as nanospheres. These hosts have cavities large enough to fit multiple guests. Reek and colleagues derivatized Fujita's nanosphere **1.19** with 24 endohedral guanidinium binding sites that are capable of binding sulfonates and carboxylates inside the cavity of the complex (Figure 1.13). Sulfonate guests are bound stronger than carboxylates due to cooperative binding from the multiple guanidinium binding sites present. The binding sites were used to firmly fix a sulfonated gold-based catalyst, while the remaining binding sites are used to organize the carboxylate groups that

are to be converted into product. The local high concentration of the sulfonated gold-based catalyst combined with the pre-organization of the substrate resulted in enhanced reaction rates in comparison to systems where the catalyst and reactants are not pre-organized.⁴⁴ By incorporating cofactors as a source of reactive function in the active sites, these nanosized cages can be used as biomimetic catalytic systems.

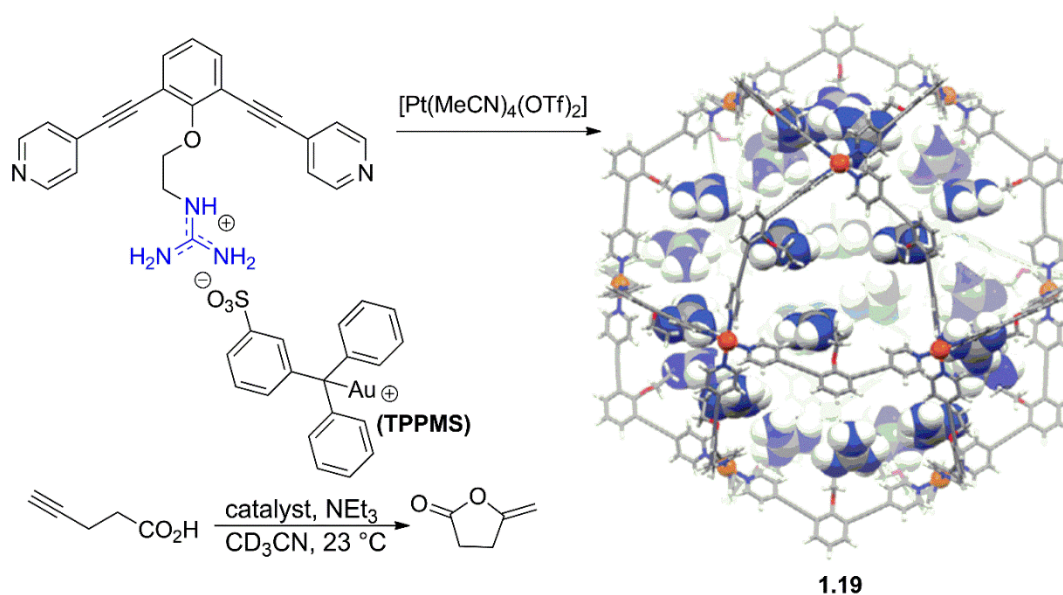


Figure 1.13. $M_{12}L_{24}$ nanosphere with twenty-four endohedral guanidinium binding sites that can bind a phosphate species to co-catalyze the cyclization of acetylenic acid.⁴⁴

1.9. Catalysis Using Endohedral Functional Groups

The size of the cavity is an important factor in enabling the internal reactivity, namely endohedral functionality, inside the cage. It must be large enough to incorporate these reactive functional groups as well as the substrates themselves. As a result, the most prominent endohedral functionalized cage reactions are carried out using large $M_{12}L_{24}$ nanospheres. In this regard, Fujita's bent bispyridinyl scaffold seen above is ideal for internal functionalization. Weakly coordinating groups, such as phosphines, were found to

not disrupt the Pd-ligand bond and overall assembly of the cage complex. By incorporating a phosphine gold (I) chloride group, 24 gold species were observed inside nanosphere **1.20** (Figure 1.14a).^{105,106}

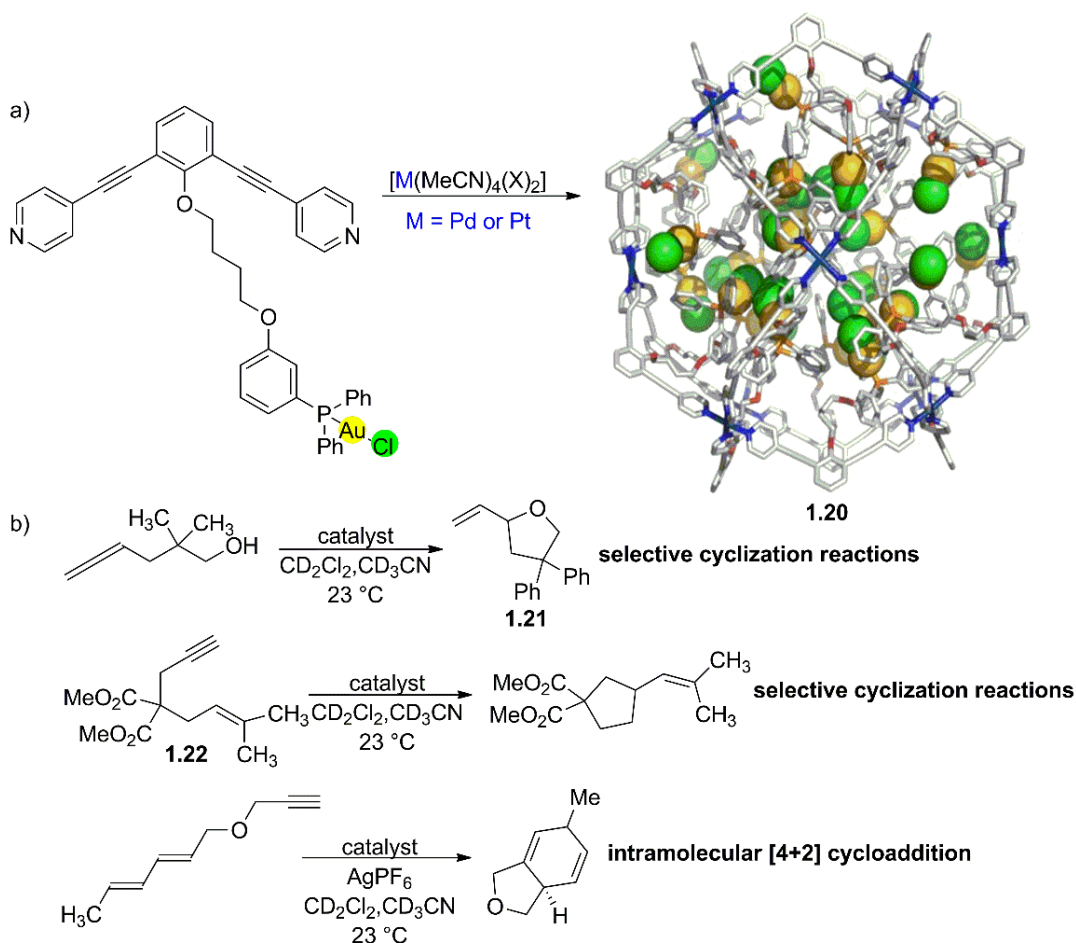


Figure 1.14. a) Formation of a $M_{12}L_{24}$ nanosphere with 24 gold-containing endohedral functional groups. b) Cage-catalyzed selective cyclization and intramolecular [4+2] cycloaddition.^{105,106}

The internalized Au(I) phosphine catalyst can effectively catalyze the hydroalkoxylation of γ -allenol, resulting in an 88% yield. This is because the increased local concentration of Au(I) inside the cavity of the cage activates the neutral gold species. The cage-catalyzed reaction is also capable of selectively forming the five-membered

cyclization product **1.21**. The same formation was also observed in the less reactive 1,6-enyne substrate **1.22**. A more robust and stable assembly can be made when the Pd^{2+} vertices are replaced with Pt^{2+} . This $\text{Pt}_{12}\text{L}_{24}$ cage **1.20** not only performs these cyclization reactions but can also ensure higher conversions in an intramolecular [4+2] cycloaddition (Figure 1.14b).^{105,106}

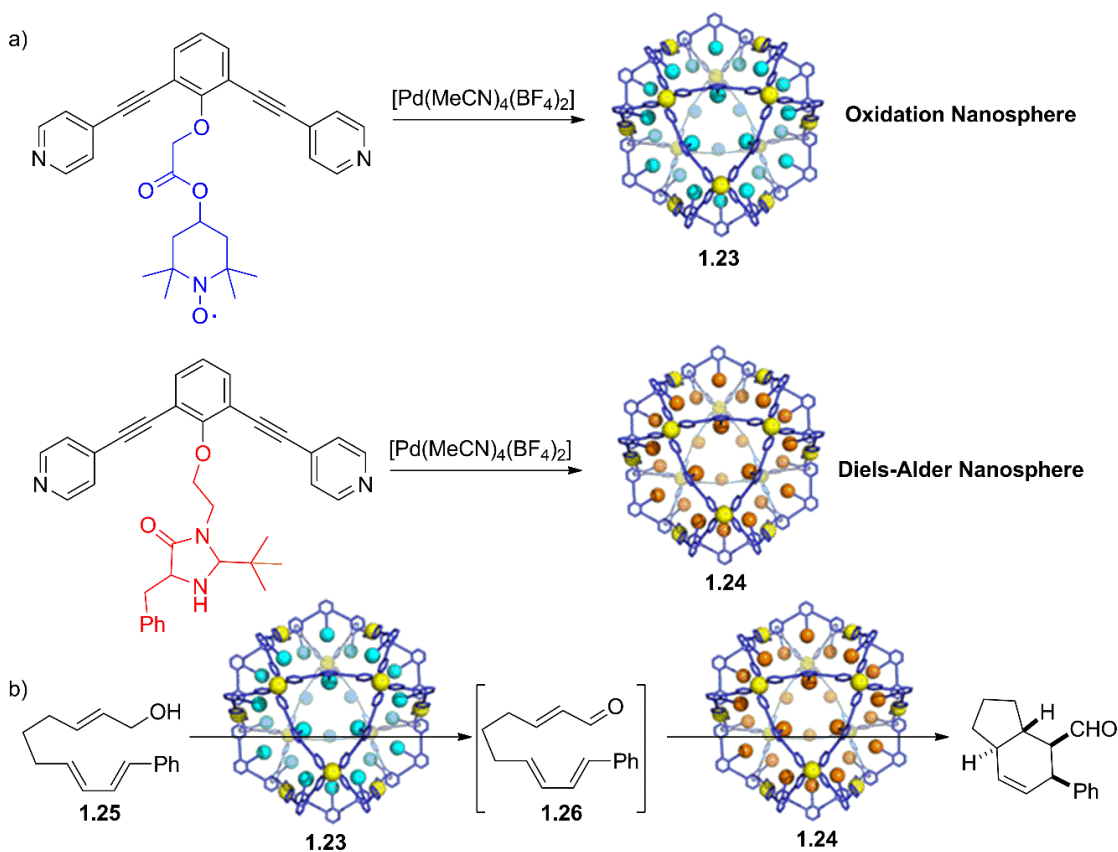


Figure 1.15. a) Formation of two nanosphere complexes with endohedrally functionalized TEMPO or MacMillan-type amine catalytic groups. b) Tandem oxidation and cyclization reaction using two cage complexes.¹⁰⁷

There are many advantages to using internally functionalized nanospheres over a small molecule catalyst. One such advantage is the ability to perform one-pot chemical cascade reactions. The researchers have also designed a two-cage system that could catalyze an

allylic oxidation followed by a Diels-Alder cycloaddition. The cascade process can be performed separately using (2,2,6,6-Tetramethylpiperidin-1-yl)oxyl (TEMPO) to oxidize the alcohol and a MacMillan's catalyst to catalyze the cyclization reaction. However, if using both the catalysts together, the MacMillan's catalyst would be oxidized by TEMPO instead of the alcohol. By incorporating these catalysts into two different self-assembled nanospheres **1.23** and **1.24**, it was able to prevent the deactivation of both catalysts in the reaction (Figure 1.15a). In the cascade reaction, the substrate **1.25** was first oxidized into the aldehyde **1.26** by cage **1.23**. Through an intramolecular Diels-Alder cycloaddition, the aldehyde was then cyclized by cage **1.24** (Figure 1.15b). Not only did the product have four stereogenic centers, but high enantio- and diastereoselectivity was also observed in the process. Control experiments show neither complex can perform the tandem reaction alone. Only by combining the two nanospheres can you observe the reaction occur in tandem.¹⁰⁷

1.10. Design and Synthesis of a Cage with Endohedral Acid Groups

While many advances have been made in mimicking enzymes using supramolecular cages as biomimetic catalysts, the cavities in these hosts are extremely large and the selectivity for the guests are limited. Greater selectivity can be obtained in endohedral functionalized complexes with medium-size cavities. To accomplish this goal, Hooley and colleagues focused on incorporating functionality into the smaller M_4L_6 tetrahedral complexes. These structures are not only smaller than nanospheres but retain cavities large enough to incorporate these functional groups. However, it is worth remembering that several factors affect the formation of a tetrahedron in the first place. Namely, the ligand must also possess the correct coordination angle. In this regard, the Hooley group had

previously shown the formation of a M_4L_6 tetrahedral complex **1.15** using 2,7-dibromo-9H-fluoren-9-ol **1.14** as the ligand.⁴⁶ The resulting cavity was too small to incorporate functional groups, but the coordination angle of the ligand was ideal. By increasing the length of the 2,7-diaminofluorene **1.27** scaffold with the addition of aromatic rings through a Suzuki coupling, a self-assembled coordination cage **1.28** with an expanded cavity was formed. Even though the complex was unfunctionalized, it possessed doubly reactive benzylic CH_2 groups in the ligand (Figure 1.16).¹⁰⁸

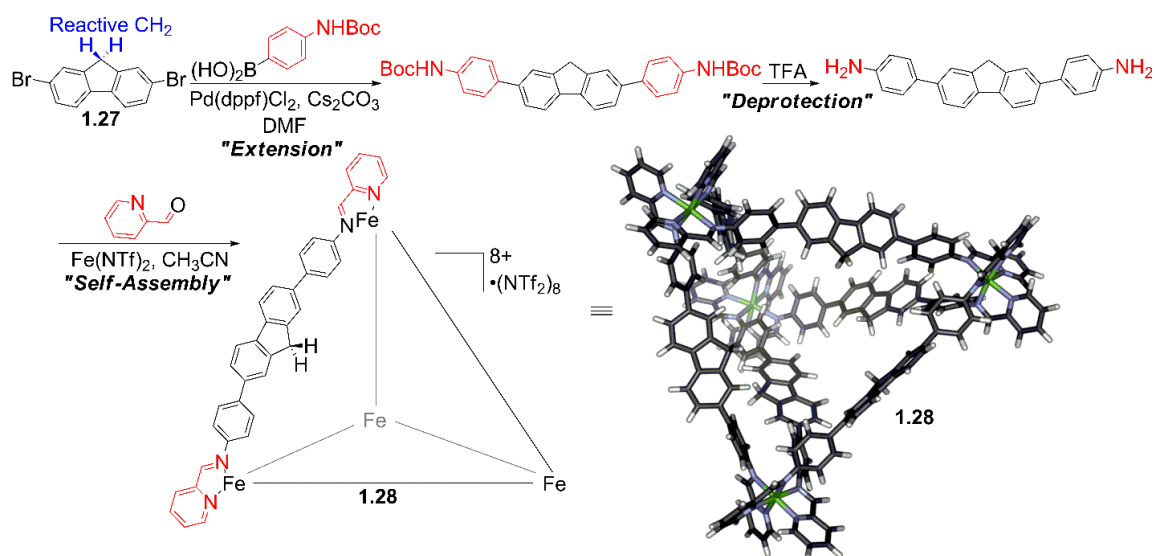


Figure 1.16. Synthesis of an unfunctionalized cage with a medium-size cavity that possess a reactive center for adding functional groups.¹⁰⁸

Benzylic CH_2 groups provide an effective scaffold for the incorporating carboxylic acid functional groups. To synthesize such a complex, a nucleophilic substitution reaction must be performed which incorporates two diester groups. Using the same extension technique for the unfunctionalized version of the cage, the length of the diester ligand was increased with aromatic rings using a Suzuki coupling. The tert-butoxycarbonyl protecting groups (BOC groups) were then deprotected using neat trifluoroacetic acid (TFA) to obtain a

diamine. After deprotection, the diester group was reduced to two carboxylic acid groups. With ligand **1.29** in hand, a cage **1.30** with 12 internal carboxylic acid groups was assembled (Figure 1.17).¹⁰⁸

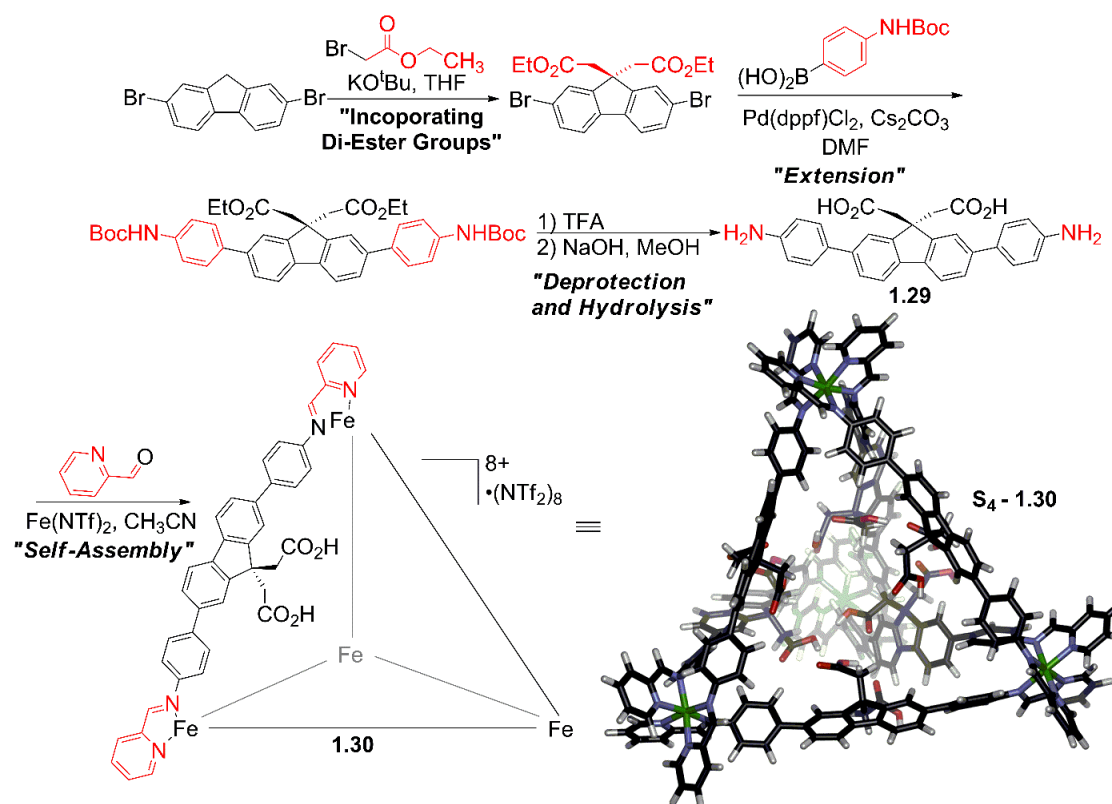


Figure 1.17. Synthesis of an acid cage with 12 internal carboxylic acid functional groups.¹⁰⁸

Assembly of a cage featuring 12 internal carboxylic acid functional groups is challenging. This is due to the existence of varied protonation states of ligand **1.29** during the hydrolysis step. The two most commonly observed states are the protonated (carboxylic acid) and deprotonated (carboxylate) forms. When using the deprotonated ligand, the carboxylates can coordinate with iron during self-assembly, causing the ^1H NMR spectrum of the cage to broaden greatly. In addition, the concentration is very important in this

process. If the reaction is too dilute, the assembly process can remain incomplete. However, if the reaction is too concentrated, intermediate complexes can form.¹¹⁴

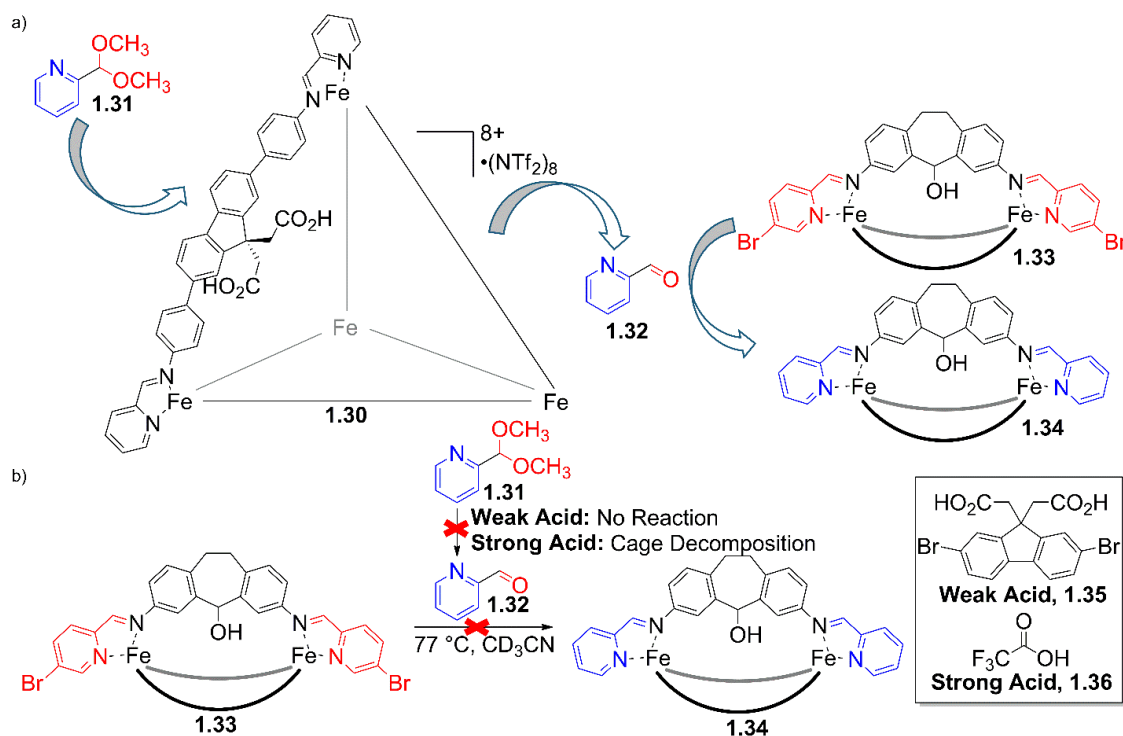


Figure 1.18. a) Tandem reaction hydrolysis of acetal and cage-to-cage transformation. b) Control experiments with other catalysts for the tandem process.¹⁰⁸

As a biomimetic catalyst, this “acid cage” **1.30** has been shown to exhibit enzyme-mimicking behavior by accelerating a cascade reaction by 1000-fold, while showing size selectivity in the process (Figure 1.18a). The cascade process involves two separate reactions that would ordinarily be incompatible, but as the cage is size-selective, it allows the reactions to proceed in a single step. This tandem process consists of hydrolyzing 2-formylpyridine dimethylacetal **1.31** creating aldehyde **1.32** used to cause cage **1.33** to cage **1.34** conversion. However, this tandem process cannot be performed using either a weak diacid **1.35** or strong acid **1.36**. This is because a weak acid cannot hydrolyze the acetal, while a strong acid causes the cage structures to decompose in the process (Figure 1.18b).

Overall, the acid cage is capable of functioning as a biomimetic catalyst, mimicking enzymes' ability to achieve both high rates and selectivity.¹¹³

1.11. Summary and Outlook

Self-assembled cages possess an internal cavity for the encapsulation of a range of substrates. This feature gives them the ability to mimic the catalytic ability of natural enzymes. Supramolecular cages can use their confined spaces, encapsulated cofactors, and active ligand sites for molecular recognition and catalysis. Although these self-assembled cages have progressed notably over several decades, many challenges still exist in the creation and application of these supramolecular structures.

One challenge is the type of supramolecular cages used in biomimetic catalysis is very limited. Due to this, new synthesis methods must be developed. In addition to this, the stability and solubility of these complexes in reactions should be improved. When synthesizing these endohedral functionalized supramolecular cages, a proper orientation of functional groups must be ensured, as the structure of these complexes has shown to be quite sensitive to the presence of active groups. To synthesize more rigid and stable cage complexes that can retain their structure, the reaction conditions must be controlled. Lastly, the current reactions catalyzed by these supramolecular cages are relatively simple. New methods to discover and catalyze more complex, multistep reactions must be considered.

Despite recent and promising developments, being able to truly mimic enzymes has yet to be accomplished. The cavities of enzymes are small, yet highly defined, and contain multiple functional groups that can selectively confine, stabilize, and activate a chiral substrate. The creation of a supramolecular complex that functions in the same respect with

high specificity and selectivity is still being investigated. In this dissertation, an in-depth investigation will be conducted to explore the reactive abilities of acid cage **1.30**, create new catalytic systems using cofactors, and overcome the challenges to synthesize various functionalized self-assembled cage complexes. By analyzing the behavior behind the molecular recognition of these supramolecular cage hosts, my aim is to create highly selective catalytic systems that can closely mimic enzymatic behavior and show properties not seen by “normal” small molecule catalysts.

1.12. References

1. Knowles, R. R.; Jacobsen, E. N. Attractive noncovalent interactions in asymmetric catalysis: Links between enzymes and small molecule catalysts. *Proc. Natl. Acad. Sci. U. S.A.* **2010**, *107*, 20678–20685.
2. Kirby, A. J. Enzyme mechanisms, models, and mimics. *Angew. Chem., Int. Ed.* **1996**, *35*, 707–724.
3. Copeland, R. A. *Enzymes: a practical introduction to structure, mechanism, and data analysis*. John Wiley & Sons. **2000**.
4. Daniel, R. M.; Danson, M. J. A new understanding of how temperature affects the catalytic activity of enzymes. *Trends Biochem. Sci.* **2010**, *35*, 584–591.
5. Reetz, M. T. What are the limitations of enzymes in synthetic organic chemistry? *Chem. Rec.* **2016**, *16*, 2449–2459.
6. Dalby, P. A. Optimising enzyme function by directed evolution. *Curr. Opin. Struct. Biol.* **2003**, *13*, 500–505.
7. Patel, A. K.; Singhanian, R. R.; Pandey, A. Production, purification, and application of microbial enzymes. In *Biotechnology of Microbial Enzymes* (pp. 13-41). Academic Press. **2017**.
8. Wiester, M. J.; Ulmann, P. A.; Mirkin, C. A. Enzyme mimics based upon supramolecular coordination chemistry. *Angew. Chem., Int. Ed.* **2011**, *50*, 114–137.
9. Raynal, M.; Ballester, P.; Vidal-Ferran, A.; Van Leeuwen, P. W. Supramolecular catalysis. Part 1: non-covalent interactions as a tool for building and modifying homogeneous catalysts. *Chem. Soc. Rev.* **2014**, *43*, 1660–1733.
10. Raynal, M.; Ballester, P.; Vidal-Ferran, A.; Van Leeuwen, P. W. Supramolecular catalysis. Part 2: artificial enzyme mimics. *Chem. Soc. Rev.* **2014**, *43*, 1734–1787.
11. Koblenz, T. S.; Wassenaar, J.; Reek, J. N. Reactivity within a confined self-assembled nanospace. *Chem. Soc. Rev.* **2008**, *37*, 247–262.

12. Yoshizawa, M.; Klosterman, J. K.; Fujita, M. Functional molecular flasks: new properties and reactions within discrete, self-assembled hosts. *Angew. Chem., Int. Ed.* **2009**, *48*, 3418–3438.
13. Vriezema, D. M.; Comellas Aragonès, M.; Elemans, J. A.; Cornelissen, J. J.; Rowan, A. E.; Nolte, R. J. Self-assembled nanoreactors. *Chem. Rev.* **2005**, *105*, 1445–1490.
14. Freeman, W. A.; Mock, W. L.; Shih, N. Y. J. Cucurbituril. *J. Am. Chem. Soc.* **1981**, *103*, 7367–7368.
15. Day, A.; Arnold, A. P.; Blanch, R. J.; Snushall, B. Controlling factors in the synthesis of cucurbituril and its homologues. *J. Org. Chem.* **2001**, *66*, 8094–8100.
16. Isaacs, L.; Park, S. K.; Liu, S.; Ko, Y. H.; Selvapalam, N.; Kim, Y.; Kim, K. The inverted cucurbit [n] uril family. *J. Am. Chem. Soc.*, **2005**, *127*, 18000–18001.
17. M. L. Bender und M. Komiyama: *Cyclodextrin Chemistry*. New York, **1978**.
18. Gerbeleu, N. V.; Arion, V. B.; Burgess, J. P. *Template synthesis of macrocyclic compounds*. John Wiley & Sons. **2008**.
19. Komiyama, M. Cyclic oligomers as highly selective catalysts. *Prog. Polym.* **1993**, *18*, 871–898.
20. Ercolani, G. Thermodynamics of metal-mediated assemblies of porphyrins. In *Non-Covalent Multi-Porphyrin Assemblies* (pp. 167–215). Springer, Berlin, Heidelberg. **2006**.
21. Rizzuto, F. J.; von Krbek, L. K.; Nitschke, J. R. Strategies for binding multiple guests in metal–organic cages. *Nat. Rev. Chem.* **2019**, *3*, 204–222.
22. Northrop, B. H.; Yang, H. B.; Stang, P. J. Coordination-driven self-assembly of functionalized supramolecular metallacycles. *Chem. Com.* **2008**, *45*, 5896–5908.
23. Bogie, P. M.; Miller, T. F.; Hooley, R. J. Synthesis and applications of endohedrally functionalized metal-ligand cage complexes. *Isr. J. Chem.* **2019**, *59*, 130–139.

24. Smulders, M. M. J.; Riddell, I. A.; Browne, C.; Nitschke, J. R. Building on architectural principles for three-dimensional metallosupramolecular construction. *Chem. Soc. Rev.* **2013**, *42*, 1728–1754.
25. Hong, C. M.; Bergman, R. G.; Raymond, K. N.; Toste, F. D. Self-assembled tetrahedral hosts as supramolecular catalysts. *Acc. Chem. Res.* **2018**, *51*, 2447–2455.
26. Otte, M. Size-selective molecular flasks. *ACS. Catal.* **2016**, *6*, 6491–6510.
27. Catti, L.; Zhang, Q.; Tiefenbacher, K. Advantages of catalysis in self-assembled molecular capsules. *Chem. Eur. J.* **2016**, *22*, 9060–9066.
28. Tan, C.; Chu, D.; Tang, X.; Liu, Y.; Xuan, W.; Cui, Y. Supramolecular coordination cages for asymmetric catalysis. *Chem. Eur. J.* **2019**, *25*, 662–672.
29. Li, X.; Wu, J.; He, C.; Meng, Q.; Duan, C. Asymmetric catalysis within the chiral confined space of metal–organic architectures. *Small.* **2019**, *15*, 1804770.
30. Jongkind, L. J.; Caumes, X.; Hartendorp, A. P.; Reek, J. N. Ligand template strategies for catalyst encapsulation. *Acc. Chem. Res.* **2018**, *51*, 2115–2128.
31. Caulder, D. L.; Raymond, K. N. The rational design of high symmetry coordination clusters. *J. Chem. Soc., Dalton Trans.* **1999**, *8*, 1185–1200.
32. Ronson, T. K.; Giri, C.; Beyeh, N. K.; Minkkinen, A.; Topić, F.; Holstein, J. J.; Rissanen, K.; Nitschke, J. R. Size-selective encapsulation of hydrophobic guests by self-assembled M₄L₆ cobalt and nickel cages.” *Chem. Eur. J.* **2013**, *19*, 3374–3382.
33. Johnson, A. M.; Young, M. C.; Zhang, X.; Julian, R. R.; Hooley, R. J. Cooperative thermodynamic control of selectivity in the self-assembly of rare earth metal-ligand helices. *J. Am. Chem. Soc.* **2013**, *135*, 17723–17726.
34. Fujita, M.; Tominaga, M.; Hori, A.; Therrien, B. Coordination assemblies from a Pd(II)-cornered square complex.” *Acc. Chem. Res.* **2005**, *38*, 369–378.
35. Hall, B. R.; Manck, L. E.; Tidmarsh, I. S.; Stephenson, A.; Taylor, B. F.; Blaikie, E. J.; Vander Griend, D. A.; Ward, M. D. Structures, host–guest chemistry and mechanism

- of stepwise self-assembly of M₄L₆ tetrahedral cage complexes. *Dalton Trans.* **2011**, 40, 12132–12145.
36. Mal, P.; Schultz, D.; Beyeh, K.; Rissanen, K.; Nitschke, J. R. An unlockable-relockable iron cage by subcomponent self-assembly. *Angew. Chem., Int. Ed.* **2008**, 47, 8297–8301.
37. Tidmarsh I. S; Faust, T. B.; Adams, H.; Harding, L. P.; Russo, L.; Clegg, W.; Ward, M. D. Octanuclear cubic coordination cages. *J. Am. Chem. Soc.* **2008**, 130, 15167–15175.
38. Kersting, B.; Meyer, M.; Powers, R. E.; Raymond, K. N. Dinuclear catecholate helicates: their inversion mechanism. *J. Am. Chem. Soc.* **1996**, 118, 7221–7222.
39. Holloway, L. R.; McGarraugh, H. H.; Young, M. C.; Sontising, W.; Beran, G. J.; Hooley, R. Structural switching in self-assembled metal–ligand helicate complexes via ligand-centered reactions. *Chem. Sci.* **2016**, 7, 4423–4427.
40. Butler, P. W.; Kruger, P. E.; Ward, J. S. Self-assembly of M₄L₄ tetrahedral cages incorporating pendant P [double bond, length as m-dash] S and P [double bond, length as m-dash] Se functionalised ligands. *Chem. Commun.* **2019**, 55, 10304–10307.
41. Yamashina, M.; Tanaka, Y.; Lavendomme, R.; Ronson, T. K.; Pittelkow, M.; Nitschke, J. R. An antiaromatic-walled nanospace. *Nature* **2019**, 574, 511–515.
42. Mosquera, J.; Szyszko, B.; Ho, S. K.; Nitschke, J. R. Sequence-selective encapsulation and protection of long peptides by a self-assembled FeII₈L₆ cubic cage. *Nat. Commun.* **2017**, 8, 1–6.
43. Lai, Y. L.; Wang, X. Z.; Zhou, X. C.; Dai, R. R.; Zhou, X. P.; Li, D. Self-assembly of a mixed valence copper triangular prism and transformation to cage triggered by an external stimulus. *Inorg. Chem.* **2020**, 59, 17374–17378.
44. Wang, Q. Q.; Gonell, S.; Leenders, S. H.; Dürr, M.; Ivanović-Burmazović, I.; Reek, J. N. Self-assembled nanospheres with multiple endohedral binding sites pre-organize catalysts and substrates for highly efficient reactions. *Nat. Chem.* **2016**, 8, 225–230.

45. Nash, T. The role of entropy in molecular self-assembly. *J. Nanomed. Res.* **2017**, *5*, 00126.
46. T. R. Cook, Y.-R. Zheng, P. J. Stang, Metal-organic frameworks and self-assembled supramolecular coordination complexes: comparing and contrasting the design, synthesis, and functionality of metal-organic materials. *Chem. Rev.* **2013**, *113*, 734–777.
47. Johnson, A.M.; Moshe, O.; Gamboa, A.S.; Langloss, B.W.; Limtiaco, J.F.K.; Larive, C.K.; Hooley, R.J. *Inorg. Chem.* **2011**, *50*, 9430.
48. Young, M. C.; Holloway, L. R.; Johnson, A. M.; Hooley, R. J. A supramolecular sorting hat: Stereocontrol in metal–ligand self-assembly by complementary hydrogen bonding. *Angew. Chem., Int. Ed.* **2014**, *126*, 9990–9994.
49. Meng, W.; Clegg, J. K.; Thoburn, J. D.; Nitschke, J. R. Controlling the transmission of stereochemical information through space in terphenyl-edged Fe₄L₆ cages. *J. Amer. Chem. Soc.* **2011**, *133*, 13652–13660.
50. Xu, J.; Parac, T. N.; Raymond, K. N. meso Myths: What drives assembly of helical versus meso-[M₂L₃] clusters? *Angew. Chem., Int. Ed.* **1999**, *38*, 2878–2882.
51. Metherell, A. J.; Cullen, W.; Stephenson, A; Hunter, C. A.; Ward, M. D. Fac and mer isomers of Ru (II) tris (pyrazolyl-pyridine) complexes as models for the vertices of coordination cages: structural characterisation and hydrogen-bonding characteristics. *Dalton Trans.* **2014**, *43*, 71–84.
52. Kieffer, M.; Pilgrim, B. S.; Ronson, T. K.; Roberts, D. A.; Aleksanyan, M.; Nitschke, J. R. Perfluorinated ligands induce meridional metal stereochemistry to generate M₈L₁₂, M₁₀L₁₅, and M₁₂L₁₈ prisms. *J. Am. Chem. Soc.* **2016**, *138*, 6813–6821.
53. Meng, W.; Ronson, T. K.; Nitschke, J. R. Symmetry breaking in self-assembled M₄L₆ cage complexes. *Proc. Natl. Acad. Sci.* **2013**, *110*, 10531–10535.
54. Bogie, P. M.; Holloway, L. R.; Lyon, Y.; Onishi, N. C.; Beran, G. J.; Julian, R. R.; Hooley, R. J. A springloaded metal-ligand mesocate allows access to trapped intermediates of self-assembly. *Inorg. Chem.* **2018**, *57*, 4155–4163.

55. Fujita, M.; Umemoto, K.; Yoshizawa, M.; Fujita, N.; Kusukawa, T.; Biradha, K. Molecular paneling *via* coordination. *Chem. Commun.* **2001**, 509–518.
56. Bilbeisi, R. A.; Clegg, J. K.; Elgrishi, N.; de Hatten, X.; Devillard, M.; Breiner, B.; Mal, P.; Nitschke, J. R. Subcomponent self-assembly and guest-binding properties of face-capped $\text{Fe}_4\text{L}_4^{8+}$ capsules. *J. Am. Chem. Soc.* **2012**, *134*, 5110–5119.
57. Mecozi, S.; Rebek, Jr, J. The 55% solution: a formula for molecular recognition in the liquid state. *Chem. Eur. J.* **1998**, *4*, 1016–1022.
58. Yamashina, M.; Akita, M.; Hasegawa, T.; Hayashi, S.; Yoshizawa, M. A polyaromatic nanocapsule as a sucrose receptor in water. *Sci. Adv.* **2017**, e1701126.
59. Fujita, D.; Takahashi, A.; Sato, S.; Fujita, M. Self-assembly of Pt(II) spherical complexes via temporary labilization of the metal–ligand association in 2,2,2-trifluoroethanol. *J. Am. Chem. Soc.* **2011**, *133*, 13317–13319.
60. Suzuki, K.; Iida, J.; Sato, S.; Kawano, M.; Fujita, M. Discrete and well-defined hydrophobic phases confined in self-assembled spherical complexes. *Angew. Chem., Int. Ed.* **2008**, *47*, 5780–5782.
61. Sato, S.; Iida, J.; Suzuki, K.; Kawano, M.; Ozeki, T.; Fujita, M. Fluorous nanodroplets structurally confined in an organopalladium sphere. *Science*. **2006**, *313*, 1273–1276.
62. Suzuki, K.; Takao, K.; Sato, S.; Fujita, M. Coronene nanophase within coordination spheres: increased solubility of C_{60} . *J. Am. Chem. Soc.* **2010**, *132*, 2544–2545
63. Fujita, D.; Suzuki, K.; Sato, S.; Yagi-Utsumi, M.; Yamaguchi, Y.; Mizuno, N.; Kumasaka, T.; Takata, M.; Noda, M.; Uchiyama, S.; Kato, K.; Fujita, M. Protein encapsulation within synthetic molecular hosts. *Nat. Comm.* **2012**, *3*, 1093–1099.
64. Sun, Q.-F.; Murase, T.; Sato, S.; Fujita, M. A Sphere-in-Sphere Complex by Orthogonal Self-Assembly. *Angew. Chem., Int. Ed.* **2011**, *50*, 10318–10321.
65. Harris, K.; Sun, Q.-F.; Sato, S.; Fujita, M. $\text{M}_{12}\text{L}_{24}$ spheres with endo and exo coordination sites: scaffolds for non-covalent functionalization. *J. Am. Chem. Soc.* **2013**, *135*, 12497–12499.

66. Lewis, J. E. M.; Gavey, E. L.; Cameron, S. A.; Crowley, J. D. Stimuli-responsive Pd₂L₄ metallosupramolecular cages: towards targeted cisplatin drug delivery. *Chem. Sci.* **2012**, *3*, 778–784.
67. Custelcean, R.; Bonnesen, P. V.; Duncan, N. C.; Zhang, X.; Watson, L. A.; Van Berkel, G.; Parson, W. B.; Hay, B. P. Urea-functionalized M₄L₆ cage receptors: Anion-templated self-assembly and selective guest exchange in aqueous solutions. *J. Am. Chem. Soc.* **2012**, *134*, 8525–8534.
68. Hooley, R. J. No, not that way, the other way: Creating active sites in self-assembled host molecule. *Synlett.* **2020**, *31*, 1448–1463.
69. Hooley, R. J. Taking on the turnover challenge. *Nat. Chem.* **2016**, *8*, 202–204.
70. Fang, Y.; Powell, J. A.; Li, E.; Wang, Q.; Perry, Z.; Kirchon, A.; Zhou, H. C. Catalytic reactions within the cavity of coordination cages. *Chem. Soc. Rev.* **2019**, *48*, 4707–4730.
71. Fiedler, D.; Bergman, R. G.; Raymond, K. N. Supramolecular catalysis of a unimolecular transformation: Aza-Cope rearrangement within a self-assembled host. *Angew. Chem., Int. Ed.* **2004**, *116*, 6916–6919.
72. Fiedler, D.; van Halbeek, H.; Bergman, R. G.; Raymond, K. N. Supramolecular catalysis of unimolecular rearrangements: Substrate scope and mechanistic insights. *J. Am. Chem. Soc.* **2006**, *128*, 10240–10252.
73. Hastings, C. J.; Fiedler, D.; Bergman, R. G.; Raymond, K. N. Aza cope rearrangement of propargyl enammonium cations catalyzed by a self-assembled “nanozyme.” *J. Am. Chem. Soc.* **2008**, *130*, 10977–10983.
74. Brown, C. J.; Bergman, R. G.; Raymond, K. N. Enantioselective catalysis of the aza-cope rearrangement by a chiral supramolecular assembly. *J. Am. Chem. Soc.* **2009**, *131*, 17530–17531.
75. Hastings, C. J.; Pluth, M. D.; Bergman, R. G.; Raymond, K. N. Enzyme-like catalysis of the Nazarov cyclization by supramolecular encapsulation. *J. Am. Chem. Soc.* **2010**, *132*, 6938–6940.

76. Hastings, C. J.; Backlund, M. P.; Bergman, R. G.; Raymond, K. N. Enzyme-like control of carbocation deprotonation regioselectivity in supramolecular catalysis of the Nazarov cyclization. *Angew. Chem., Int. Ed.* **2011**, *123*, 10758–10761.
77. Hart-Cooper, W. M.; Clary, K. N.; Toste, F. D.; Bergman, R. G.; Raymond, K. N. Selective monoterpene-like cyclization reactions achieved by water exclusion from reactive intermediates in a supramolecular catalyst. *J. Am. Chem. Soc.* **2012**, *134*, 17873–17876.
78. Pluth, M. D.; Bergman, R. G.; Raymond, K. N. Acid catalysis in basic solution: a supramolecular host promotes orthoformate hydrolysis. *Science*. **2007**, *316*, 85–88.
79. Pluth, M. D.; Bergman, R. G.; Raymond, K. N. Supramolecular catalysis of orthoformate hydrolysis in basic solution: An enzyme-like mechanism. *J. Am. Chem. Soc.* **2008**, *130*, 11423–11429.
80. Fujita, M.; Tominaga, M.; Hori, A.; Therrien, B. Coordination assemblies from a Pd (II)-cornered square complex. *Acc. Chem. Res.* **2005**, *38*, 369–378.
81. Yoshizawa, M.; Tamura, M.; Fujita, M. Diels-Alder in aqueous molecular hosts: unusual regioselectivity and efficient catalysis. *Science*. **2006**, *312*, 251–254.
82. Nishioka, Y.; Yamaguchi, T.; Yoshizawa, M.; Fujita, M. Unusual [2+4] and [2+2] cycloadditions of arenes in the confined cavity of self-assembled cages. *J. Am. Chem. Soc.* **2007**, *129*, 7000–7001.
83. Murase, T.; Horiuchi, S.; Fujita, M. Naphthalene Diels–Alder in a self-assembled molecular flask. *J. Am. Chem. Soc.* **2010**, *132*, 2866–2867.
84. Horiuchi, S.; Nishioka, Y.; Murase, T.; Fujita, M. Both [2+2] and [2+4] additions of inert aromatics via identical ternary host–guest complexes. *Chem. Commun.* **2010**, *46*, 3460–3462.
85. Horiuchi, S.; Murase, T.; Fujita, M. Diels-Alder reactions of inert aromatic compounds within a self-assembled coordination cage. *Chem. Asian J.* **2011**, *6*, 1839–1847.

86. Fang, Y.; Murase, T.; Fujita, M. Cavity-promoted Diels-Alder reactions of unsubstituted naphthalene: Fine reactivity tuning by cavity shrinkage. *Chem. Lett.* **2015**, *44*, 1095–1097.
87. Yamaguchi, T.; Fujita, M. Highly selective photomediated 1, 4-radical addition to o-Quinones controlled by a self-assembled cage. *Angew. Chem., Int. Ed.* **2008**, *120*, 2097–2099.
88. Murase, T.; Nishijima, Y.; Fujita, M. Cage-catalyzed Knoevenagel condensation under neutral conditions in water. *J. Am. Chem. Soc.* **2012**, *134*, 162–164.
89. Cullen, W.; Takezawa, H.; Fujita, M. Demethylenation of cyclopropanes via photoinduced guest-to-host electron transfer in an M₆L₄ cage. *Angew. Chem., Int. Ed.* **2019**, *131*, 9269–9271.
90. Berg, J. M.; Tymoczko, J. L.; Stryer, L. Enzymes: basic concept and kinetics. *Biochemistry*. 5th edition. **2002**, 301–307.
91. Rizzuto, F. J.; von Krbek, L. K. S.; Nitschke, J. R. Strategies for binding multiple guests in metal-organic cages. *Nat. Rev. Chem.* **2019**, *3*, 204–222.
92. Hof, F.; Craig, S. L.; Nuckolls, C.; Rebek, J., Jr. Molecular encapsulation. *Angew. Chem., Int. Ed.* **2002**, *41*, 1488–1508.
93. Brown, C. J.; Toste, F. D.; Bergman, R. G.; Raymond, K. N. Supramolecular catalysis in metal-ligand cluster hosts. *Chem. Rev.* **2015**, *115*, 3012–3035.
94. Kang, J.M.; Rebek, J., Jr. Entropically driven binding in a self-assembling molecular capsule. *Nature*. **1996**, *382*, 239–241.
95. Yamauchi, Y.; Yoshizawa, M.; Akita, M.; Fujita, M. Engineering double to quintuple stacks of a polarized aromatic in confined cavities. *J. Am. Chem. Soc.* **2010**, *132*, 960–966.
96. Yoshizawa, M.; Tamura, M.; Fujita, M. AND/OR bimolecular recognition. *J. Am. Chem. Soc.* **2004**, *126*, 6846–6847.

97. Samanta, D.; Gemen, J.; Chu, Z.; DiskinPosner, Y.; Shimon, L. J. W.; Klajn, R. Reversible photoswitching of encapsulated azobenzenes in water. *Proc. Natl. Acad. Sci. U. S. A.* **2018**, *115*, 9379–9384.
98. Kang, J. M.; Rebek, J., Jr. Acceleration of a Diels-Alder reaction by a self-assembled molecular capsule. *Nature.* **1997**, *385*, 50–52.
99. Chen, J.; Rebek, J., Jr. Selectivity in an encapsulated cycloaddition reaction. *Org. Lett.* **2002**, *4*, 327–329.
100. Sawada, T.; Fujita, M. A single Watson-Crick G•C base pair in water: Aqueous hydrogen bonds in hydrophobic cavities. *J. Am. Chem. Soc.* **2010**, *132*, 7194–7201.
101. Mahata, K.; Frischmann, P. D.; Würthner, F. Giant electroactive M4L6 tetrahedral host self-assembled with Fe(II) vertices and perylene bisimide dye edges. *J. Am. Chem. Soc.* **2013**, *135*, 15656–15661.
102. Hooley, R. J.; Biroš, S. M.; Rebek, J., Jr. A deep, water-soluble cavitand acts as a phase-transfer catalyst for hydrophobic species. *Angew. Chem., Int. Ed.* **2006**, *45*, 3517–3519.
103. Zhang, Q.; Catti, L.; Tiefenbacher, K. Catalysis inside the hexameric resorcinarene capsule. *Acc. Chem. Res.* **2018**, *51*, 2107–2114.
104. Zhang, Q.; Tiefenbacher, K. Terpene cyclization catalyzed inside a self-assembled cavity. *Nat. Chem.* **2015**, *7*, 197–202.
105. Zhang, Q.; Catti, L.; Pleiss, J.; Tiefenbacher, K. Terpene cyclizations inside a supramolecular catalyst: Leaving-group-controlled product selectivity and mechanistic studies. *J. Am. Chem. Soc.* **2017**, *139*, 11482–1149.
106. Brauer, T. M.; Zhang, Q.; Tiefenbacher, K. Iminium catalysis inside a self-assembled supramolecular capsule: Modulation of enantiomeric excess. *Angew. Chem., Int. Ed.* **2016**, *55*, 7698–7701.
107. Catti, L.; Tiefenbacher, K. Brønsted acid-catalyzed carbonyl-olefin metathesis inside a self-assembled supramolecular host. *Angew. Chem., Int. Ed.* **2018**, *57*, 14589–14592.

108. Cullen, W.; Misuraca, M. C.; Hunter, C. A.; Williams, N. H.; Ward, M. D. Highly efficient catalysis of the Kemp elimination in the cavity of a cubic coordination cage. *Nat. Chem.* **2016**, *8*, 231–236.
109. Cullen, W.; Metherell, A. J.; Wragg, A. B.; Taylor, C. G. P.; Williams, N. H.; Ward, M. D. Catalysis in a cationic coordination cage using a cavity-bound guest and surface-bound anions: inhibition, activation, and autocatalysis. *J. Am. Chem. Soc.* **2018**, *140*, 2821–2828.
110. Gramage-Doria, R.; Hessels, J.; Leenders, S. H. A. M.; Tröppner, O.; Dürr, M.; Ivanović-Burmazović, I.; Reek, J. N. H. Gold(I) catalysis at extreme concentrations inside self-assembled nanospheres. *Angew. Chem., Int. Ed.* **2014**, *53*, 13380–13384.
111. Leenders, S. H. A. M.; Dürr, M.; Ivanović-Burmazović, I.; Reek, J. N. H. Gold functionalized platinum M₁₂L₂₄-nanospheres and their application in cyclization reactions. *Adv. Synth. Catal.* **2016**, *358*, 1509–1518.
112. Ueda, Y.; Ito, H.; Fujita, D.; Fujita, M. Permeable self-assembled molecular containers for catalyst isolation enabling two-step cascade reactions.” *J. Am. Chem. Soc.* **2017**, *139*, 6090–6093.
113. Holloway, L. R.; Bogie, P. M.; Lyon, Y.; Ngai, C.; Miller, T. F.; Julian, R. R.; Hooley, R.J. Tandem reactivity of a self-assembled cage catalyst with endohedral acid groups. *J. Am. Chem. Soc.* **2018**, *140*, 8078–8081.
114. Bogie, P. M. Designing functional cages: From luminescent sensors to artificial enzymes. **2019**. (Doctoral dissertation, UC Riverside).

Chapter 2 – Mechanistic Control of a Cage-catalyzed Nucleophilic Substitution Reaction

2.1. Introduction

The internally functionalized acid cage **1.30** is an effective catalyst for hydrolyzing acetals (as described in chapter 1), exhibiting high rate accelerations of over 1000-fold with respect to ligand control diacid **1.35** (Figure 2.1a).¹ This reactivity is supported by an increased effective concentration of carboxylic acids in the internal cavity of **1.30** and strong binding affinities to the acetal substrate **1.33** ($K_a = 1.3 \times 10^4 \text{ M}^{-1}$).¹ This “enzyme-like” activity suggested that the complex could be used to promote other acid-catalyzed reactions. Since cage **1.30** has a large cavity capable of binding multiple guests, the next set of experiments focused on catalyzing reactions that involve multiple components. As most self-assembled complexes (and especially those with Fe-iminopyridine vertices) are quite fragile,² the reaction chosen must be mild enough to limit the decomposition of **1.30**. After testing out various reactions, Dr. Lauren Holloway found that the complex can catalyze a simple S_N1 nucleophilic substitution reaction, involving two different guests, triphenylmethanol **2.1** and *n*-propanethiol (**PrSH**) (Figure 2.1b).³

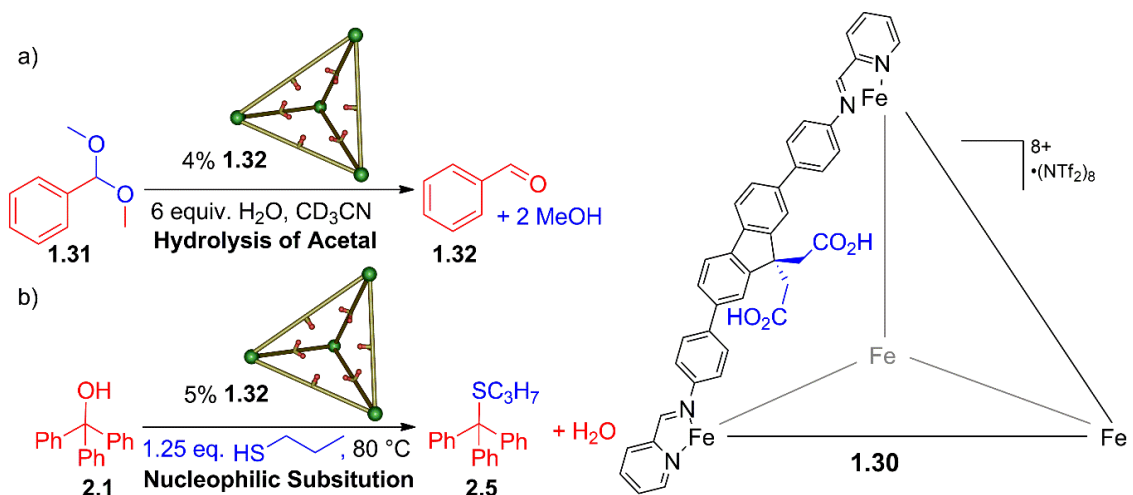


Figure 2.1. a) Cage-catalyzed hydrolysis of acetal reaction. b) Cage-catalyzed nucleophilic substitution of triphenylmethanol.^{1,3}

The ability of **1.30** to catalyze this reaction is both interesting and surprising. One limitation in supramolecular catalysis is the ability to catalyze polar reactions, especially nucleophilic substitution reactions due to their sensitivity to even weak nucleophiles.⁴ There are a few instances where these assemblies can promote these polar reactions,⁵⁻⁹ even so, their use in these assemblies is still quite limited. Other limitations include binding neutral molecules due to the cationic nature of these cage hosts and binding small molecule guests that can easily go in and out of the cavity.¹¹⁻¹³ In the following discussion, cage **1.30** not only catalyzes a substitution reaction, but the molecularity of the reaction also varied depending on the substrate used.

2.2. Cage-Catalyzed Nucleophilic Substitution

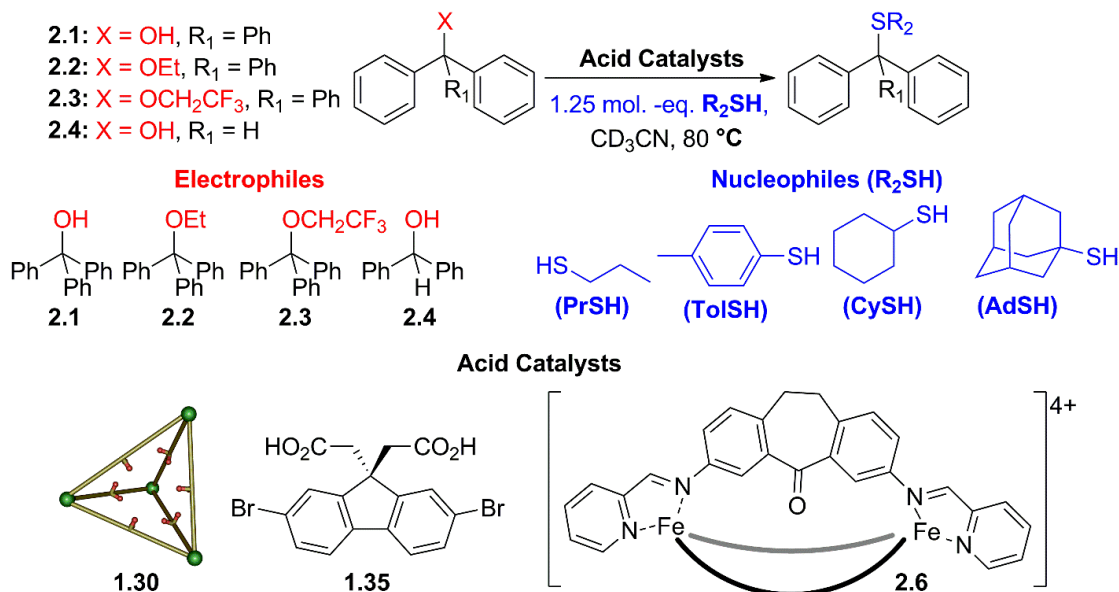


Figure 2.2. Summary of all substrates and catalysts used in the S_N1 reaction.³

Initially, the following four electrophiles were chosen as substrates: triphenylmethanol **2.1**, ethyl trityl ether **2.2**, trifluoroethyl ether **2.3**, and benzhydrol **2.4** (Figure 2.2). Trityl- and diphenylmethyl electrophiles are well-known S_N1 reactants due to their highly stabilized cationic intermediates.¹¹ An important feature of these electrophiles is their leaving groups. Once activated, these electrophiles form either a water or alcohol byproduct. Cage **1.30** is tolerant to these byproducts, and therefore, does not decompose in the process. To help prevent cage decomposition, mild neutral thiol nucleophiles were used. The nucleophile was carefully chosen as the cage is sensitive to other, ostensibly mild, nucleophiles such as chloride.¹⁴ By combining these tri- or diphenylmethyl electrophiles with thiols, thioethers are formed by means of an acid-catalyzed dissociative substitution mechanism.¹⁵⁻¹⁶

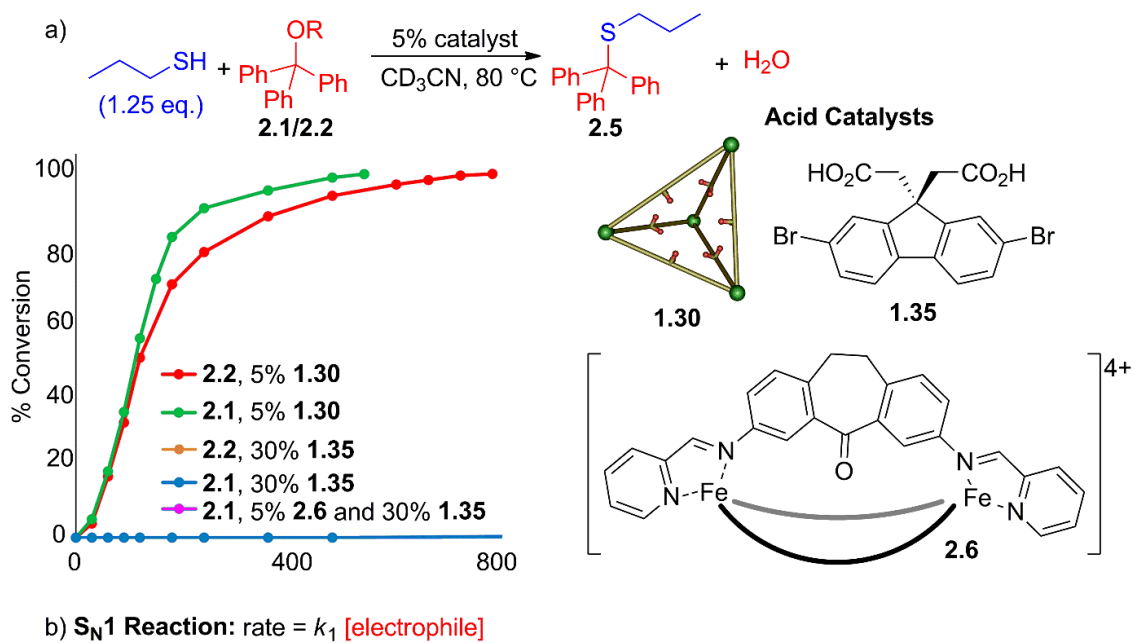


Figure 2.3. a) Kinetic analysis of nucleophilic substitution reaction using different electrophiles and catalysts. b) Classic S_N1 mechanism and rate law.³

The four different electrophiles were reacted with *n*-propanethiol (**PrSH**) using either acid cage **1.30** or diacid **1.35** as the catalyst (Figure 2.3a). The progress of the reaction was monitored by ^1H NMR, and the relative rates were calculated. Acid cage **1.30** was shown to be a highly effective catalyst for this nucleophilic substitution. When only 5% of the complex was used, 100% conversion was obtained within 8 h using either triphenylmethanol **2.1** or trityl ethyl ether **2.2** as the electrophile. The reaction was selective, as only **1.30**, the reactants, and product **2.5** were observed in the ^1H NMR spectrum. No evidence of product inhibition or side products were detected. More importantly, the cage was intact during the reaction process and was tolerant to the thiol

nucleophiles. The ^1H NMR shows that the imine CH signals of the C₃ and S₄ isomers at δ 8.9-9.1 are unaffected by the reaction (Figure 2.4).¹

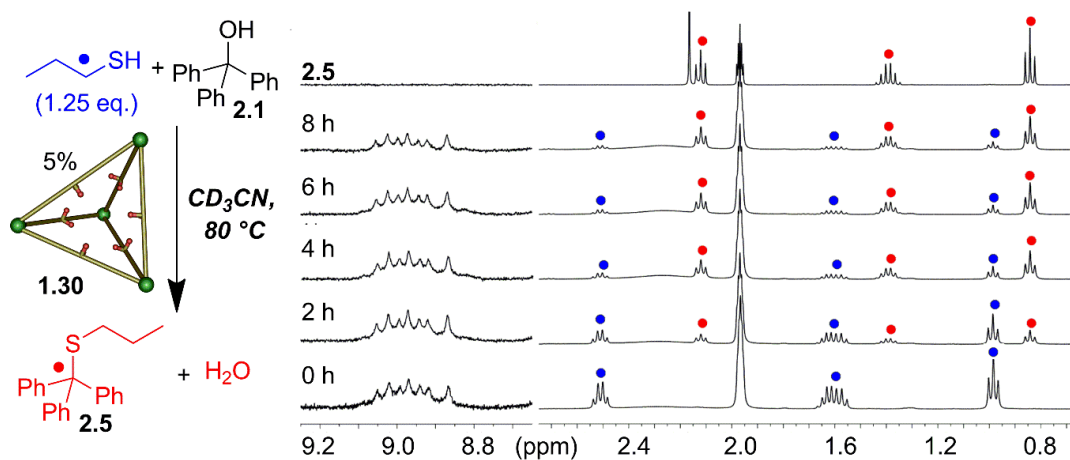


Figure 2.4. Spectra illustrating product formation using acid cage **1.30** as the host.³

To determine the mechanism, and reasons for the effectiveness of reaction using cage **1.30** as the catalyst, the nucleophilic substitution of **2.1** and **2.2** was replicated using 30% diacid **1.35**, which is equivalent to the concentration of the acid in the solution. This control showed that the reaction catalyzed by diacid **1.35** was slow, and no conversion to sulfide product **2.5** was observed even after 10 h at 80 °C for either electrophile. After 24 h, the product could be detected, but only a 1% conversion was obtained. Another possibility for the rapid reaction in the presence of **1.30** could be that the acid-catalyzed process was promoted by small amounts of Fe^{2+} ions leached into the solution. To eliminate this possibility, the reaction was repeated with 10% *meso*-helicite **2.6**¹⁷ and 30% diacid **1.35**. *Meso*-helicite **2.6** in theory should not be able to catalyze the Lewis acid reaction, since it does not possess a defined cavity or acid functional groups. Under the same conditions used above, no reaction was observed even after 48 h at 80 °C (Figure 2.5).

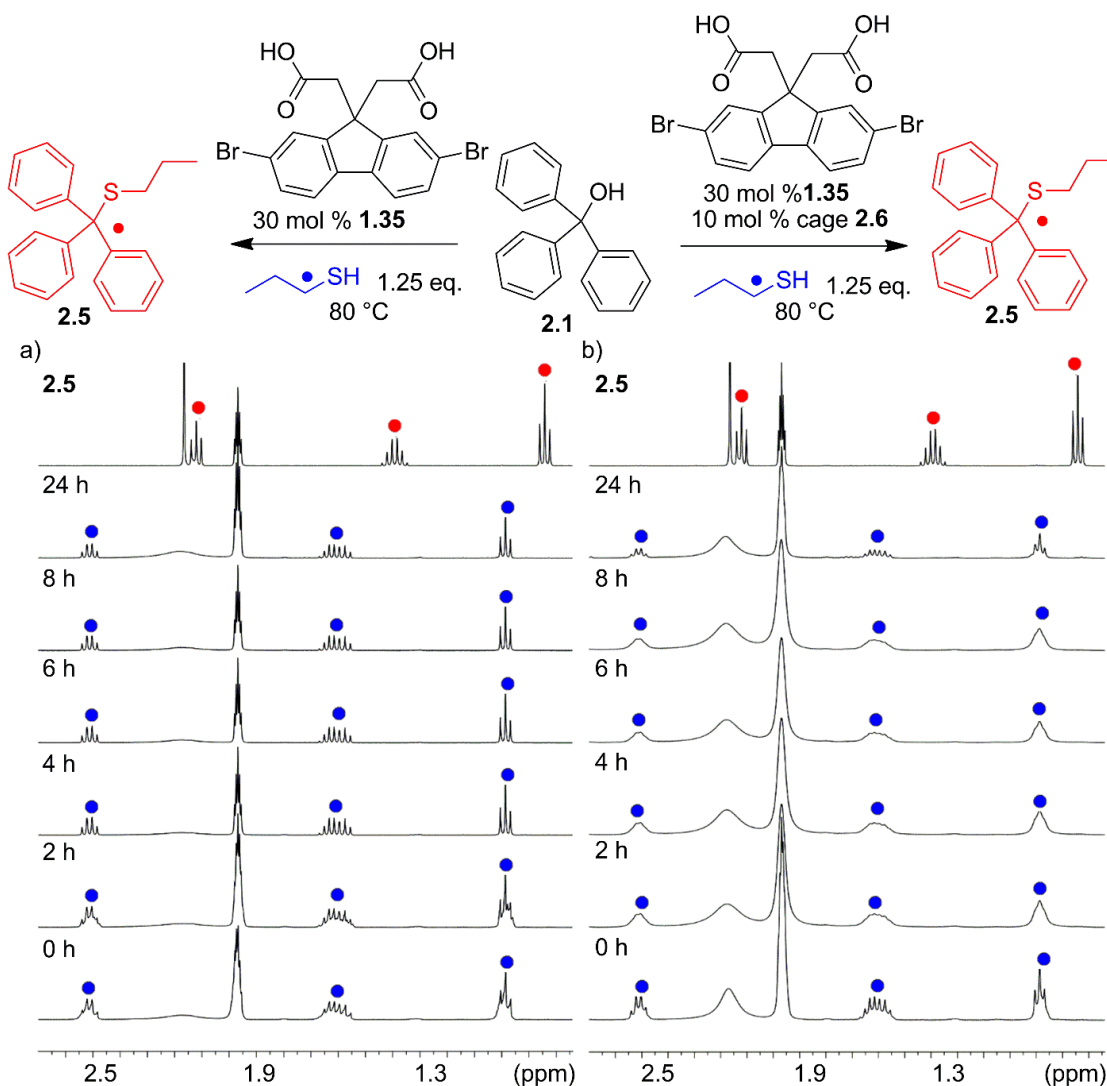


Figure 2.5. ^1H NMR spectra of the acid promoted substitution reaction between **1.30** and **PrSH** in the presence of: a) 30 mol % control acid **1.35** b) 30 mol % diacid **1.35** and 10 mol % suberone mesocate **2.6** (298 K, CD_3CN).³

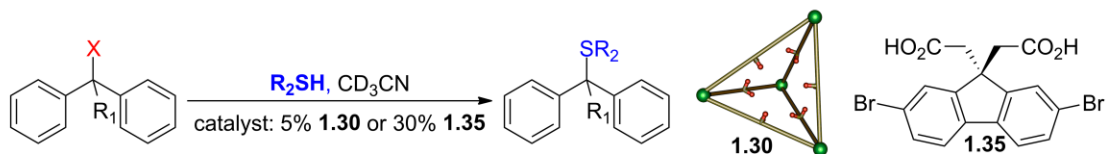
2.3. Nucleophilic Substitution Reactions with Different Electrophiles

Varying electrophiles were used to determine the effect cage **1.30** has on the reaction. The following experiments and results using different electrophiles were obtained by Dr. Paul Bogie. A summary of the average initial rate and relative rate accelerations of the thioetherification process are shown in Table **2.1**. When using cage **1.30** as the catalyst,

rate accelerations of up to 1023-fold with respect to diacid **1.35** were observed, even though the two catalysts possess carboxylic acid groups comparable levels of acidity. The reactivity shows little dependence on the basicity of the electrophile. For instance, electrophile **2.1** (pK_a of conjugate acid: ~ 3.5) and **2.2** (pK_a of conjugate acid: ~ 2)³ vary significantly in basicity. However, the relative rates of substitution and ~1000-fold rate accelerations are practically identical. The reactivity could be altered with large changes in basicity in the electrophile. When trifluoroethyl ether **2.3** was used as the electrophile, no product formation was observed even after prolonged reaction times, despite it having the same the cationic intermediate as electrophiles **2.1/2.2**.

Reactivity is influenced by the stability of the cation formed in the reaction. When benzhydrol **2.4** was used as the electrophile, the less stable 2° cation was formed in the process, decreasing the overall reactivity and resulting in a slower reaction in comparison to **2.1** and cage **1.30**. After 72h, only 58 % conversion was observed. Significant rate acceleration was still present in this instance, however. When 30% diacid **1.35** was used, no reactivity was observed with **2.4**.

Table 2.1. Initial rates using various substrates and catalysts.



Electrophile	Nucleophile	Initial Rate V(1.30) (x 10 ⁻⁴ mM/min)	Initial Rate V(1.35) (x 10 ⁻⁴ mM/min)	Acceleration
4.1	PrSH	778	0.76	1023
4.1	CySH	541	1.4	386
4.1	ToISH	211	0.81	260
4.1	AdSH	no reaction	no reaction	N/A
4.1	EtOH	77	no reaction	N/A
4.1	PrSH	723	0.65	1112
4.1	ToISH	156	1.1	107
4.1	CySH	156	2.9	47
4.1	PrSH	no reaction	no reaction	N/A
4.1	PrSH	39	no reaction	N/A

R₂SH

HS-CH₂-CH₂-CH₂-CH₃
(PrSH)

HO-C₆H₄-SH
(ToISH)

C₆H₁₁-SH
(CySH)

Ad-SH
(AdSH)

Reaction was performed at 353 K in CD₃CN; [**2.1-2.4**] = 15.8 mM, [**R₂SH**] = 19.8 mM, [**1.30**] = 0.8 mM; [**1.35**] = 4.74 mM; concentrations were confirmed using dioxane as standard (7.9 mM).³

2.4. Nucleophilic Substitution Reactions with Different Nucleophiles

In addition to varying the electrophile, nucleophiles of similar and different sizes were also varied. In concert with Dr. Paul Bogie, we showed that cage **1.30** is tolerant to the following nucleophiles: 1-cyclohexane thiol (**CySH**), *p*-tolyl disulfide (**ToISH**), and 1-adamantanethiol (**AdSH**). When the nucleophilic substitution was performed with the more hindered **CySH**, the initial rate with both electrophiles **2.1** and **2.2** was found to be slightly slower than the rate observed with **PrSH** in the cage-catalyzed reaction. Clean conversion to the sulfide product was observed in both instances, despite the reduction in reactivity.

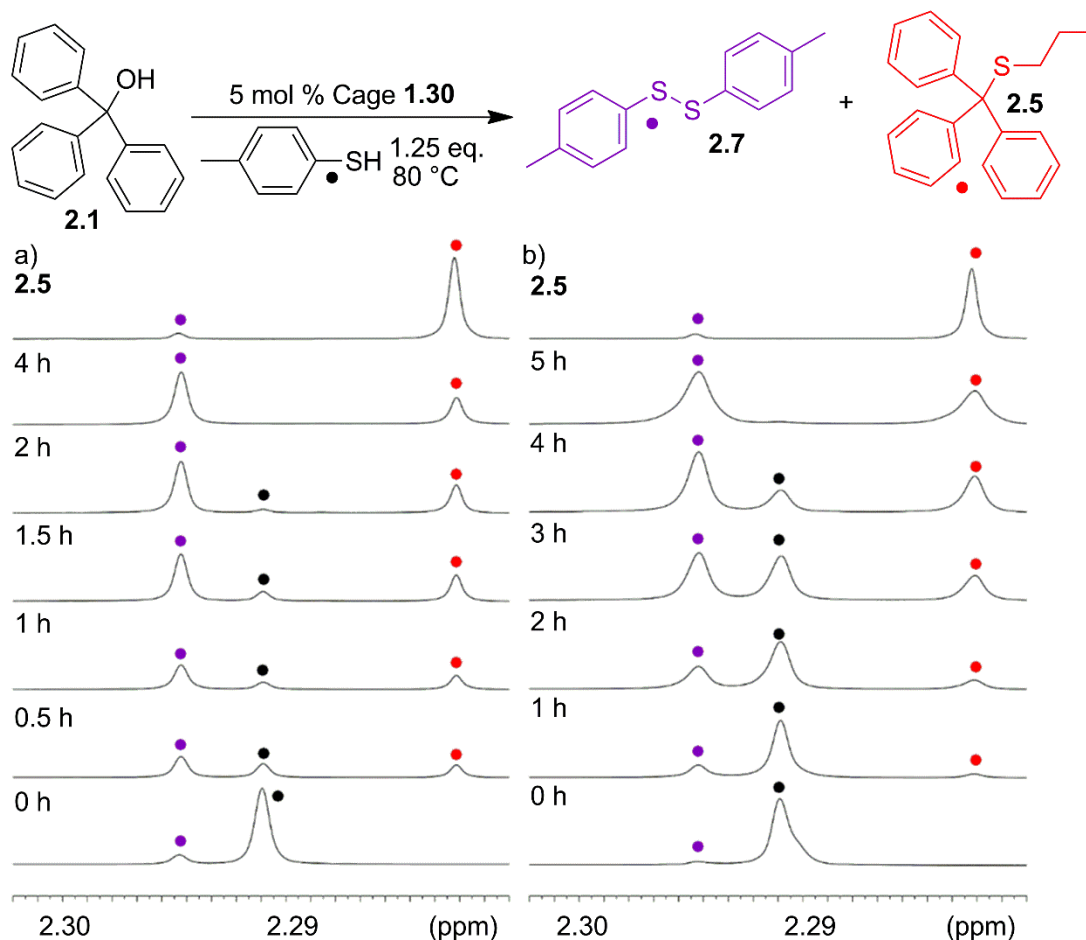


Figure 2.6. ¹H NMR spectra of the acid promoted substitution reaction between **2.1** and **TolSH** in the presence of: a) 5 mol % cage **1.30** b) 5 mol % cage **1.30** under a nitrogen atmosphere in a J. Young NMR tube. Both reactions were performed at 80 °C and monitored over time (353 K, CD₃CN).³

Clean conversion was not obtained when the comparably sized **TolSH** was used as the nucleophile. Even though similar rate accelerations to that of **CySH** were observed, the reaction formed the competitive disulfide oxidation product **2.7**. It is known that disulfides can be catalyzed by Fe²⁺ and oxygen. To limit the formation of the side product, the reaction was performed again under N₂ in a J. Young tube. By reacting in inert conditions, the amount of disulfide **2.7** formed was decreased, but **2.7** was still found to be the major product observed in the reaction (Figure 2.6). Despite all other reactions being performed

in air, only **TolSH** was oxidized and subjected to disulfide formation. Control experiments with diacid **1.35** showed minimal oxidation during the reaction process, indicating that the oxidation reaction is catalyzed solely by the cage.

Weaker nucleophiles such as **EtOH** were also tested, which were successful, albeit at a slower rate. While using **CySH** and **TolSH** as the nucleophiles showed modest reductions in initial rate, no reaction was observed when using the bulkier **AdSH**, even after 24 h. Moreover, longer reaction times caused cage **1.35** to decompose in the process. Overall, mild thiol and alcohol nucleophiles are found to be well tolerated inside the cavity of the cage. However, more reactive carbon-based nucleophiles pose threats to the stability of the cage. When dimedone **2.8** or indole **2.9** was used as the nucleophile, some conversions were observed during the process; however, the cage rapidly decomposed. In less than 2 h, a complete destruction of cage **1.30** was observed with **2.9** (Figure 2.7).

The reactivity for the different thiols inside the internal cavity of cage **1.30** provides insight into the host-mediated nature of the catalysis. Substitution using trityl electrophiles occurs through a classic S_N1 mechanism in which the rate-determining step in the reaction is the slow formation of the trityl cation (Figure 2.3b).¹¹ Once the cation is formed, the addition of the nucleophile occurs rapidly. The rate shows no dependence on the nucleophile in the rate equation. The only factor involved in the rate equation is the concentration of electrophile (Figure 2.2). Therefore, identical initial rates should be observed regardless of the nucleophile used. However, this “classical” mechanism was not observed when the substitution was catalyzed by cage **1.30**. Large variations in the rate were observed during the cage-catalyzed process between the different nucleophiles and

electrophiles **2.1** and **2.2**. The unusual reactivity is interesting and shows that molecular recognition between **1.30** and reagents must be involved during the catalyzed reaction.

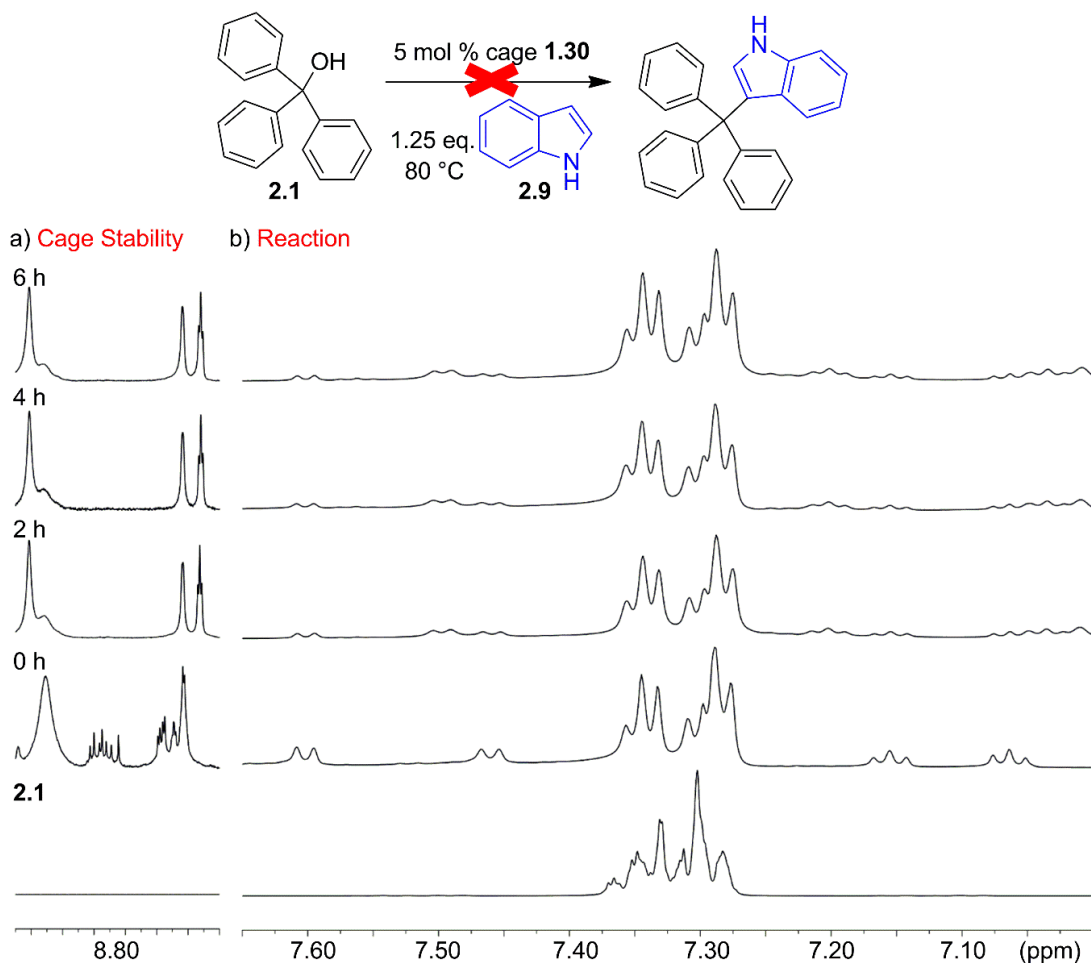


Figure 2.7. ¹H NMR spectra of the acid promoted substitution reaction between **2.1** and indole **2.9** in the presence of 5 mol % cage **1.30**. The reaction was performed at 80 °C and monitored over time (353 K, CD₃CN).³

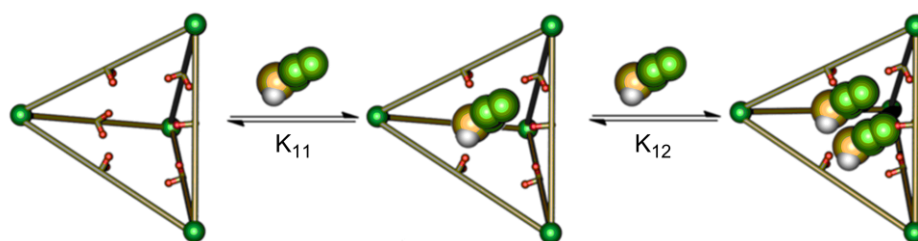
2.5. Binding Studies

To understand why large variations in the rate may occur, binding affinities were obtained to analyze the cage's effect on each guest. NMR was not a viable method for quantifying affinity because all guests exhibited rapid in/out kinetics, preventing the formation of long-lived Michaelis complexes. Other methods such as UV-Vis titrations

served as a viable method for measuring the binding affinities of these guests inside the cage host. Together, Dr. Paul Bogie and I titrated various substrates and products that were involved in the reaction process into the cage. The affinities were calculated in Bindfit via linear regression analysis. The Nelder-Mead method was used to fit each guest to either a 1:1 or 1:2 binding model at two points (300/330 nm and 370 nm) where the change in absorbance is greatest.^{18,19}

Large electrophiles **2.1-2.4** fit best in the 1:1 binding model. However, the fit for other guests was more unclear, especially the binding of the thiol nucleophiles. The smallest thiols **PrSH** and **CySH** best fit the 1:2 binding model, whereas the bulky **AdSH** best bound to the host in a 1:1 manner. Higher levels of error were present in the affinity of **ToISH** in comparison to the other thiol nucleophiles. Due to these errors, it was difficult to tell whether the nucleophile was bound in a 1:1 or 1:2 manner (Table 2.2).

Table 2.2. Binding affinities of electrophiles, nucleophiles, and products.



Guest	$K_{11} (1.30) \times 10^3 \text{ M}^{-1}$	Guest	$K_{11} (1.30) \times 10^3 \text{ M}^{-1}$	$K_{12}(1.30) \times 10^3 \text{ M}^{-1}$
2.1	15.8 ± 0.3	PrSH	114 ± 15	$0.75 \pm .008$
2.2	20.1 ± 1.2	ToISH	80.6 ± 9.7	N/A
2.3	3.2 ± 1.3	CySH	116 ± 10	4.0 ± 0.4
2.4	6.9 ± 0.4	AdSH	199 ± 17	N/A
2.5	6.5 ± 1.3			

Reaction was performed in CD_3CN ; $[\mathbf{1.30}] = 3 \mu\text{M}$, absorbance changes measured at 300/330 nm and 370 nm.^{3,18-19}

High binding affinities were observed for all substrates inside cage **1.30** with affinities ranging from 3200 M⁻¹ (trifluoroethyl ether **4.5c**) to 199,000 M⁻¹ (**AdSH**). It is not entirely apparent why cage **1.30** exhibits such high affinities to these substrates. One possible explanation for the high affinities of each guest is the presence of hydrogen bond donor and acceptor groups. This is supported by the high affinities (80,000 M⁻¹ to 199,000 M⁻¹) obtained when titrating the various thiols into the host complex. To further support this hypothesis, a simple hydrocarbon adamantane was added. No affinity was observed for this guest, further reinforcing this theory. Further studies demonstrate that the shape of the electrophile does not seem to significantly affect the affinity. The electrophiles were still strongly bound into the cavity with affinities up to 20,100 M⁻¹. Notably, thioether product **2.5** exhibited a significantly lower binding affinity of 6500 M⁻¹, demonstrating that the binding affinity is also affected by polar interactions with acid groups, as well as CH- π or π - π interactions with the aromatic cage: all are important factors in obtaining such high affinities.

2.6. Variable Molecularity in Reaction Mechanism

Strong affinities between the host cage and various guests can guide the outcome of the reaction. In terms of the cage-catalyzed substitution, results show that the process does not follow the simple S_N1 mechanism but follows more of a bimolecular process. To support these findings, the substitution reaction of **2.1** and **2.2** with 5% cage was repeated by Dr. Paul Bogie with varying concentrations of nucleophile. The small change in the leaving group from -OH to -OEt displays a large effect on the dependence on the nucleophile in the reaction. In the cage-catalyzed process with triphenylmethanol **2.1**, the rate increases

with increasing **[PrSH]**, showing a strong dependence on the concentration of nucleophile in the rate equation (Figure 2.8). The order of the reaction was measured to ~ 1.2 with respect to **[PrSH]** (Figure 2.9a). In contrast, the reaction of the larger, more basic ether **2.2**, showed no rate increase with increasing **[PrSH]** (Figure 2.9b). Zero dependence on the concentration of nucleophile was observed in the equation, despite having nearly identical binding affinities and initial rates.

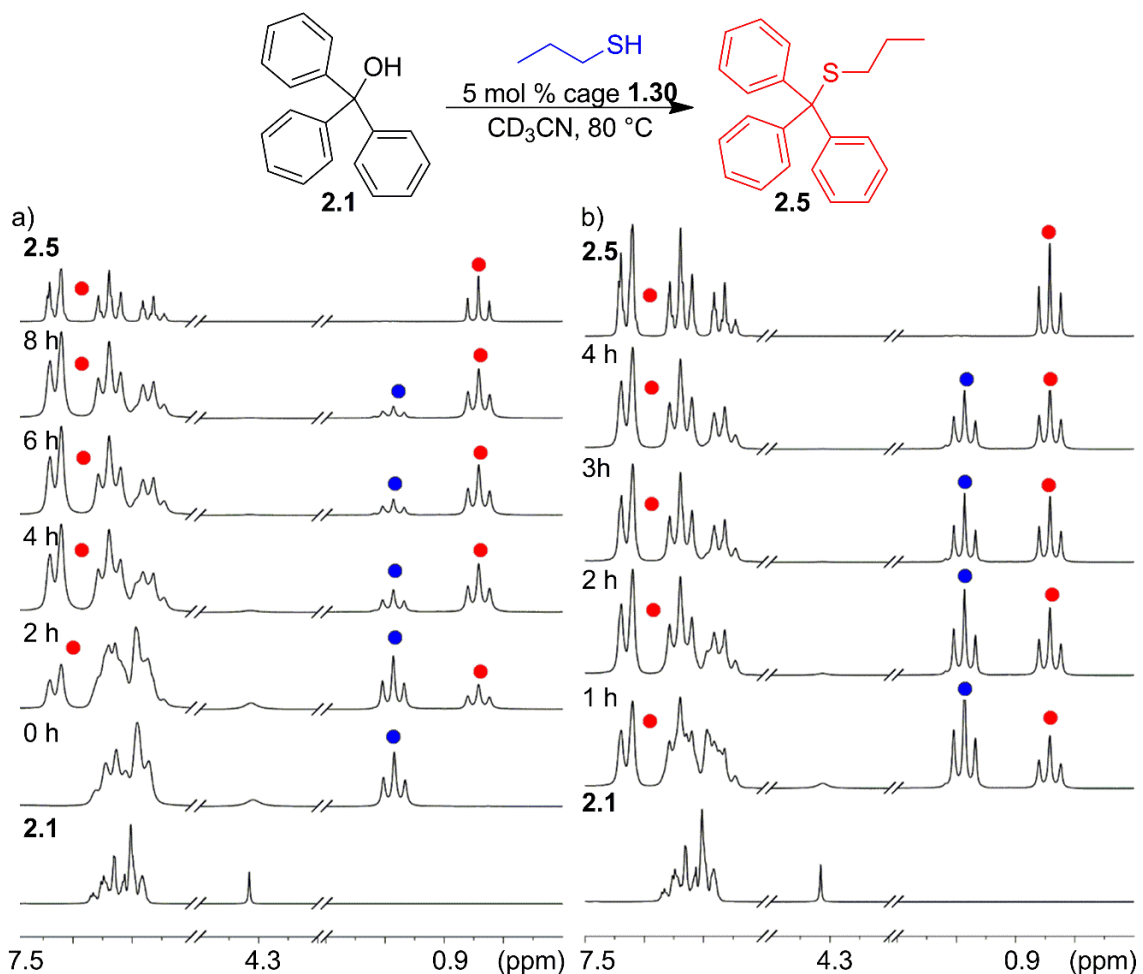


Figure 2.8. Nucleophilic substitution between **2.1** and **PrSH** in the presence of 5 mol % cage **1.30**, at varying concentrations of **PrSH** a) 19.75 mM b) 39.5 mM, performed at 80 °C and monitored over time (298K, CD₃CN).³

To verify that the acid-catalyzed thioetherification indeed follows a classic S_N1 mechanism, control experiments were carried out. When the reaction was performed with diacid **1.35**, the process was far too slow for accurate measurement, requiring over four days for minimal conversion. The reaction was performed using 5% CF_3CO_2H at ambient temperature and was monitored for several hours. As expected, no rate increase was observed with increasing $[PrSH]$ (Figure 2.9c), confirming the fact that the rate for a simple acid should be independent of nucleophile concentration. Therefore, molecular recognition effects play a significant part in varying the molecularity of the reaction.

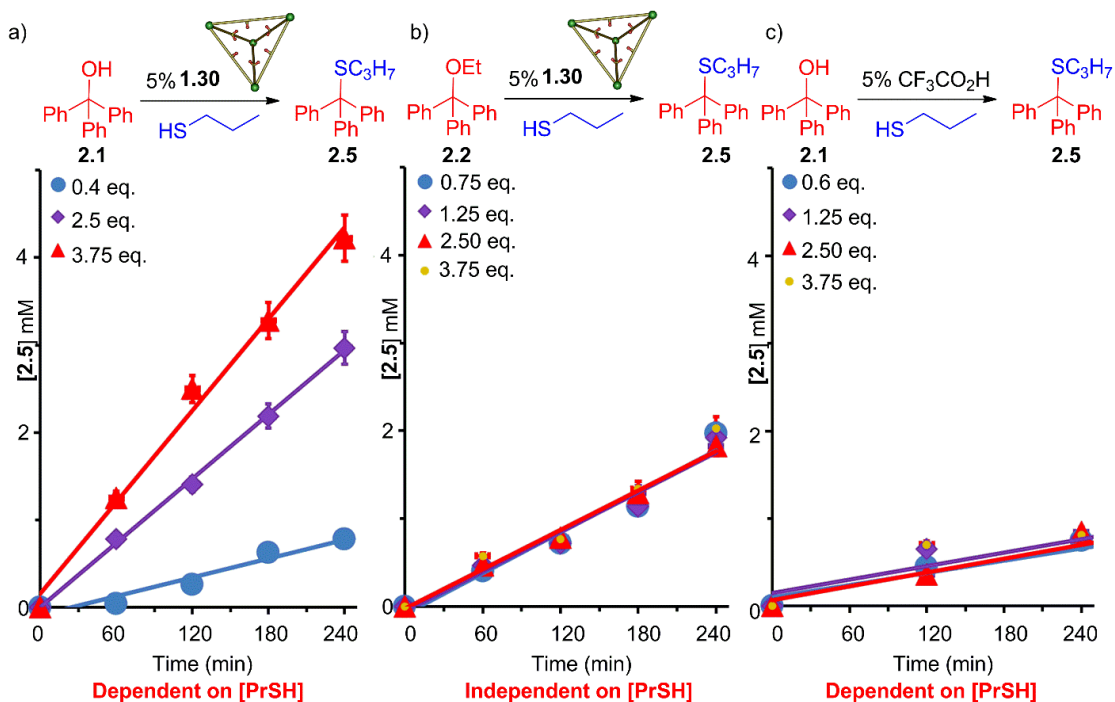


Figure 2.9. Initial rates with varying $[PrSH]$ a) **2.1** with 5 % **1.30**, 333 K; b) **2.2** with 5 % **1.30**, 333 K; c) **2.1** with 5 % CF_3CO_2H , 273 K. $[2.1] = 15.8$ mM, $[1.30]$ and $[CF_3CO_2H] = 0.8$ mM in CD_3CN ; concentrations were confirmed using dioxane as standard (7.9 mM).³

The rate observed can be significantly reduced by the addition of a large excess of **PrSH**. Compared to the binding affinities observed with either electrophile **2.1** or **2.2**,

PrSH has a significantly higher affinity for cage **1.30** and instead binds in a 1:2 manner. Saturation of the cavity can be observed with high [**PrSH**], preventing the binding and activation of the electrophile and inhibiting the substrate (Figure 2.10). Importantly, efficient turnover is observed in the cage-catalyzed process, and no product inhibition is observed with only 5% cage **1.30**. It is surprising that the cage complex can achieve such a high turnover in this bimolecular process. Due to entropy, the host favors binding a single large product rather than two smaller reactants. Reactions, therefore, tend to be stoichiometric rather than catalytic.²⁰⁻²¹ Most supramolecular hosts that are effective catalysts for bimolecular reactions, use water solubility effects to reduce the binding affinity of the product with respect to reactant(s), enabling turnover.²²⁻²³ However, cage **1.30** does not have a problem promoting the bimolecular reaction as **2.1** ($K_a = 15,800 \text{ M}^{-1}$), **2.2** ($K_a = 20,100 \text{ M}^{-1}$) and **PrSH** ($K_a = 114,000 \text{ M}^{-1}$) all display significantly higher affinities over product **2.5** ($K_a = 6,500 \text{ M}^{-1}$). While the binding affinities justify the reasoning for achieving high turnovers, it is still unclear why triphenylmethanol **2.1** and ethyl trityl ether **2.2** show variable rate profiles despite being so similar.

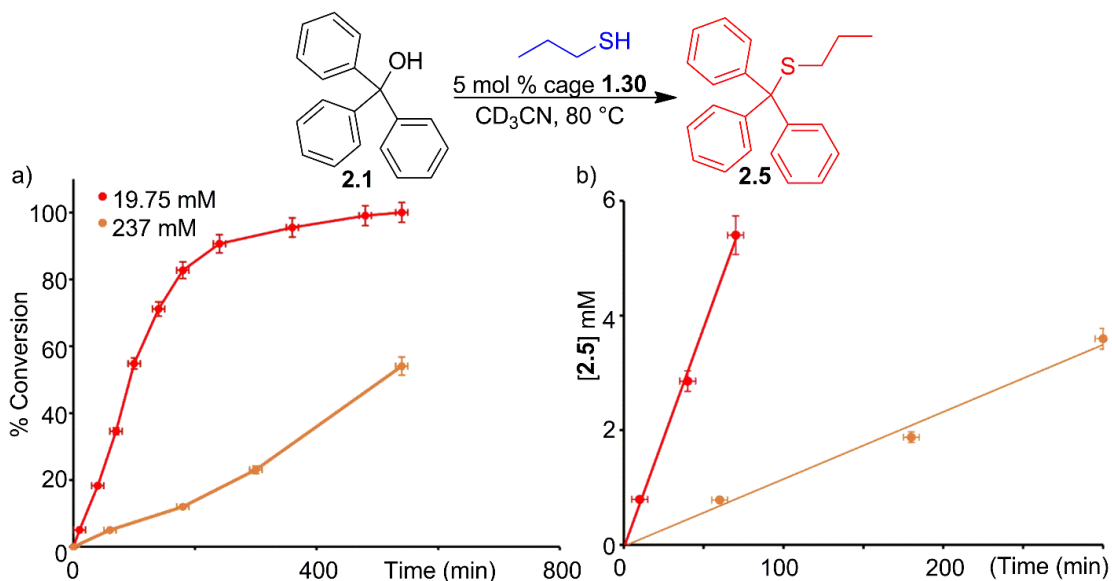


Figure 2.10. Substrate inhibition of **2.1** with **PrSH** in the presence of 5 % cage **1.30** in CD_3CN . a) Averaged percent conversion over time (min); b) initial rates, using 19.75 mM **PrSH** (red) and 237 mM **PrSH** (orange).³

In the reaction catalyzed by cage **1.30**, strong binding affinities for **1.30** and the formation of ternary complexes are observed. The variable binding affinities show several preequilibrium states that exist in the process. The cavity of **1.30** is large and can potentially form both homo- and hetero-ternary complexes. To reveal the formation of a ternary complex, a pre-formed complex with cage **1.30** and triphenylmethanol **2.1** was created and titrated with **PrSH**. Changes in the absorbance spectra were observed with each addition of **PrSH**. With the addition of a 1:1 mixture of **PrSH**:**2.1** to a solution of the cage in CH_3CN , a clear change in absorbance was observed in the spectra. These changes demonstrate the cavity is large enough to accommodate both triphenylmethanol **2.1** and **PrSH**. However, it is difficult to assess whether these changes result from formation of **1.30**•**2.1**•**PrSH** or simply a displacement of **2.1**, since the change in the cage absorbances is small.

2.7. Mechanistic Analysis

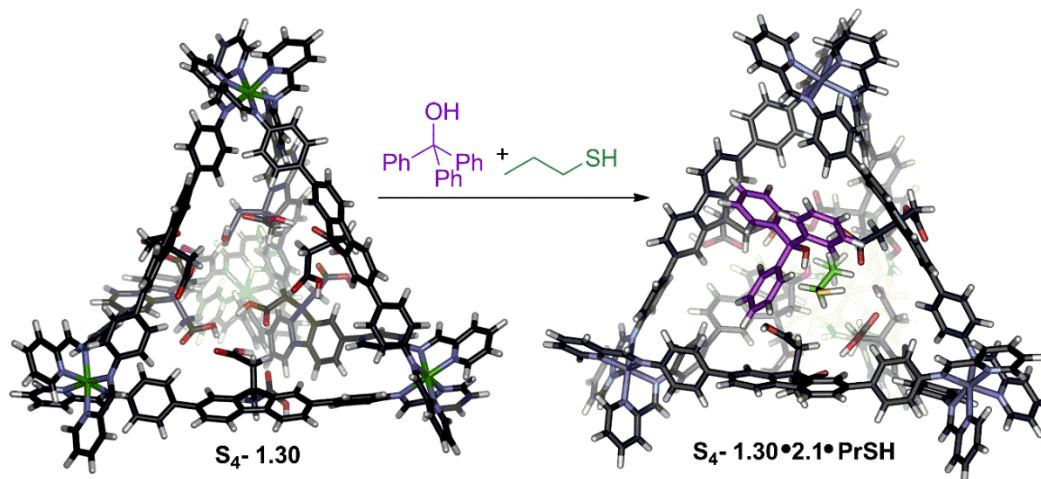


Figure 2.11. Model of heterocomplex **1.30•2.1a•PrSH** (Hartree-Fock, SPARTAN).³

The data and minimized structure of the host:guest complex support the possibility of the heterocomplex **1.30•2.1a•PrSH** being formed in solution (Figure 2.11). Since both electrophiles and nucleophiles exhibit a strong affinity for cage **1.30**, the reagents are likely to compete for binding inside the cavity. The following four possible pre-equilibria are represented: **1.30**, **1.30•(PrSH)**, **1.30•2.1a**, and the heterocomplex **1.30•2.1a•PrSH**.

Within the equilibria, two potential rate-determining steps can take place. The reaction may follow a unimolecular process identical to the classic S_N1 reaction. The S_N1 process consists of the electrophile being bound by cage **1.30** and then activated. Once activated, the trityl cation is released from the cavity and quickly reacts with **PrSH** outside of the complex. In this case, the nucleophile is not involved in the rate equation, and the rate is only dependent on the encapsulation of the electrophile. The reaction may also follow a bimolecular process. In this process, cage **1.30** encapsulates both electrophile and **PrSH** at the same time and forms the **1.30•2.1a•PrSH** ternary complex.²⁴ The following molecular

recognition event happens in the cavity, resulting in the activation of the electrophile and release of the product. A dependence on the concentration of nucleophile is observed, this time in the rate equation.

The study found that the mechanism depends on whether **2.1** or **2.2** was used as the electrophile. The unimolecular mechanism is dominant for **2.2**, where the reaction rate stays constant despite increasing $[\text{PrSH}]$. However, when **2.2** was used as the electrophile, a dependence on $[\text{PrSH}]$ was observed as the rate increased with increasing concentrations of nucleophile, implying that the mechanism partially proceeds through the **1.30**•**2.1**•**PrSH** ternary complex.

It is not fully apparent why the molecularity of the reaction differs with respect to **2.1** and **2.2**. While **2.2** is more basic than **2.1**, the initial rates using **PrSH** are identical. No competitive binding can take place, as the binding affinities of two electrophiles are identical. A high concentration of **PrSH** would saturate cage **1.30**, inhibiting encapsulation and activation of the electrophiles. The most practical explanation for this variable molecularity is due to the size of the molecules. Ether **2.2** limits the formation of a ternary complex with **PrSH** due to its larger size. The activation and release of the cationic intermediate to react with **PrSH** are more favorable than binding multiple guests (Figure 2.12a). In contrast, the formation of the ternary complex is observed when **2.1** was used with **PrSH**. The electrophile is small enough to bind simultaneously to **PrSH** in the cage (Figure 2.12b). With proper size matching and hydrogen bond interactions, the simple S_N1 process can be changed.

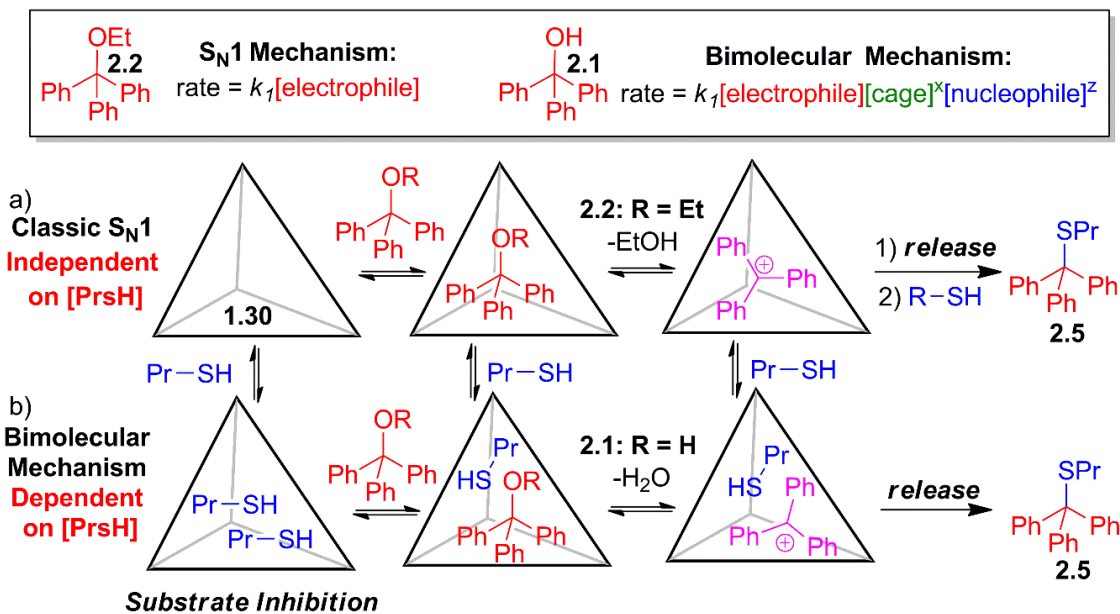


Figure 2.12. a) Classic S_N1 reaction observed with ethyl trityl ether **2.2** as the electrophile. b) Bimolecular process observed with triphenylmethanol **2.1** as the electrophile.³

This speculation is also related to the varying reaction rates observed with the four different nucleophiles. The binding affinities shown for each thiol in cage **1.30** show a preference for the equilibrium population of **1.30•2.1**. In some instances, **1.30•2.1•RSH** will modify the observed rate. Based on the proximity of the reactive species, the reaction between **2.1** and **PrSH** can occur through a concerted process, however, no real evidence of this phenomenon is seen. It is most likely that the loss of water occurs within the ternary complex. The bimolecular process occurs because of the selective substrate molecular recognition inside the active site of cage **1.30**. Overall, the cage is a significant part of the mechanism shown by the distinct reactivities with the various nucleophiles.

2.8. Catalytic Self-Destruction

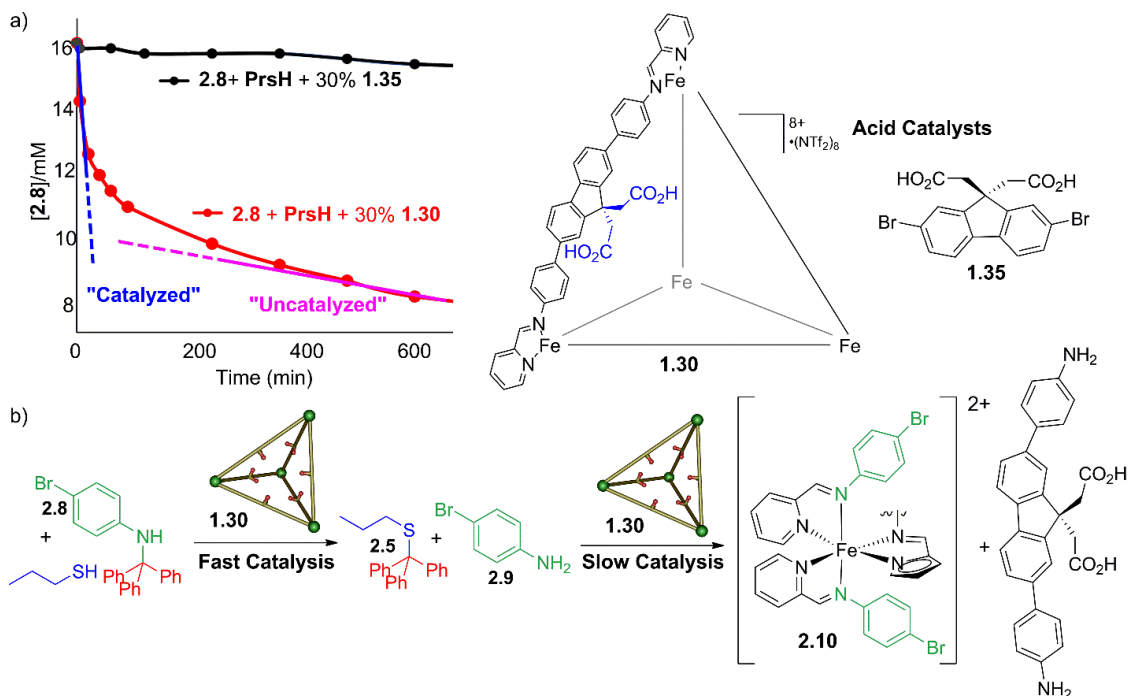


Figure 2.13. a) Detritylation that causes a negative feedback loop. b) The product is destroyed via transimination. $[2.8] = 15.8$ mM, $[PrSH] = 19.75$ mM, $[1.30] = 0.8$ mM in CD_3CN , 298 K; concentrations were confirmed using dioxane as standard (7.9 mM), rates monitored by 1H NMR.³

The self-assembled cage with 12 internal carboxylic acid functional groups has shown to be an effective catalyst. Large increases in initial rate are observed with respect to control experiments. Electrophiles containing alcohol groups were selected for this study due to their mild reactivity. However, the cage-catalyzed process is not limited to electrophiles such as these. Other electrophiles such as trityl anilines are considerably more basic than triphenylmethanol and should therefore be more reactive and allow for a faster substitution reaction. By using tritylaniline as the electrophile, the catalytic efficiency of cage **1.30** can be tested. Dr. Tabitha Miller showed that cage **1.30** is an effective catalyst for the reaction

between *N*-trityl-4-bromo-phenylaniline **2.8** and **PrSH**, forming the thioether product **2.9**, and resulting in amine **2.10**. The resulting amine **2.10** can then react with the cage by means of subcomponent exchange.²⁵ As the reaction progresses, however, the catalyst is destroyed in the process, which negatively affects the rate.

The cage-catalyzed substitution reaction between *N*-trityl-4-bromo-phenylaniline **2.8** and **PrSH** using 5% is exceedingly rapid. Product **2.5** is shown to appear within minutes at room temperature. The substitution reaction is a considerably faster when the reaction is ran using **2.8**, achieving ~25% conversion to product before the byproduct 4-bromoaniline **2.9** can react with cage **1.30**. Control experiments using diacid **1.35** as the catalyst show that the acid is still capable of activating **2.8**, although the reaction proceeds at a slower rate.

Figure 2.13 illustrates the substitution reactions with the various catalysts. Initial reaction with **2.1** is rapid until subcomponent exchange occurs, and the cage starts to decompose in the process. When the substitution process was repeated using diacid **1.35**, the reaction proceeds at a rate reflecting that of the post-destruction rate. This experiment shows that the acid groups are what enable the cage to catalyze this substitution reaction. Large rate accelerations are initially observed when the cage is intact. The reaction, however, becomes correspondingly slower once the cage starts decomposing. Therefore, by using tritylaniline **2.8** as the substrate, a “negative feedback loop” is created where the catalyst is inhibited by the subcomponent exchange that causes its self-destruction. In the process, ML₃ fragment **2.10** and diamine **1.31** are formed.

2.9. Conclusion

Acid cage **1.30** has been shown to catalyze reactions such as the solvolysis of aromatic acetals and thioetherification of trityl alcohols and ethers with >1000-fold rate enhancement with respect to the small molecule analogue **1.35**. The cage shows high binding affinities to each guest with affinities ranging from 3,200 – 199,000 M⁻¹. As a biomimetic catalyst, cage **1.3** displays reactivity patterns that are not possible using small molecules as catalysts. Due to its carboxylic acid groups, **1.30** can perform a cascade reaction involving the solvolysis of a pyridyl acetal followed by a cage-to-cage transformation via a subcomponent exchange process. When this reaction was performed with triflic acid, immediate decomposition of the initial cage was observed. In contrast to other reactions performed by supramolecular hosts, product inhibition is not a problem in both reaction processes.

Most importantly, the biomimetic reactor is capable of altering a *mechanism* of the reaction, not just accelerating it—a property usually only seen with enzymes. A bimolecular process is observed in the cage-catalyzed process, whereas the use of trifluoroacetic acid instead follows a normal, unimolecular S_N1 mechanism. The rate equation is affected by the electrophile used in the reaction. The smaller-sized substrate **2.1** follows a bimolecular process where both substrates are encapsulated in the cage. A change in mechanism is observed in the process in which the nucleophile is now involved in the rate equation. More so, a different molecularity is observed with small changes in the electrophile. When tritylethyl ether **2.2** was used as the electrophile, a classic S_N1 process was observed. Finally, the catalyst is capable of catalytic self-destruction in the presence

of tritylated amines. In this reaction sequence, the initial rate of the substitution reaction is fast, but is turned off by the decomposition of the catalyst by amine **2.10**, causing a negative feedback loop. The ability to bind multiple reactants in this nucleophilic substitution reaction requires strong molecular recognition events between cage **1.30** and the various substrates and intermediates. Overall, this study demonstrates the ability of cage hosts to be used as biomimetic nanoreactors in performing reactions that cannot be done using small-molecule catalysts.

2.10. References

1. Holloway, L. R.; Bogie, P. M.; Lyon, Y.; Ngai, C.; Miller, T. F.; Julian, R. R.; Hooley, R. J. Tandem reactivity of a self-assembled cage catalyst with endohedral acid groups. *J. Am. Chem. Soc.* **2018**, *140*, 8078–8081.
2. Ramsay, W. J.; Szczypiński, F. T.; Weissman, H.; Ronson, T. K.; Smulders, M. M. J.; Rybtchinski, B.; Nitschke, J. R. Designed enclosure enables guest binding within the 4200 Å³ cavity of a self-assembled cube. *Angew. Chem. Int. Ed.* **2015**, *54*, 5636–5640.
3. Bogie, P. M.; Holloway, L. R.; Ngai, C.; Miller, T. F.; Grewal, D.; Hooley, R. J. A self-assembled cage with endohedral acid groups both catalyzes substitution reactions and controls their molecularity. *Chem. Eur. J.* **2019**, *25*, 10232–10238.
4. Ma, S.; Smulders, M. M. J.; Hristova, Y.; Clegg, J. K.; Ronson, T. K.; Zarra, S.; Nitschke, J. R. Chain-reaction anion exchange between metal-organic cages. *J. Am. Chem. Soc.* **2013**, *135*, 5678–5684.
5. Zhao, C.; Toste, F. D.; Raymond, K. N.; Bergman, R. G. Nucleophilic substitution catalyzed by a supramolecular cavity proceeds with retention of absolute stereochemistry. *J. Am. Chem. Soc.* **2014**, *136*, 14409–14412.
6. Purse, B. W.; Ballester, P.; Rebek, J. Reactivity and molecular recognition: Amine methylation by an introverted ester. *J. Am. Chem. Soc.* **2003**, *125*, 14682–14683.
7. Murase, T.; Nishijima, Y.; Fujita, M. Cage-catalyzed Knoevenagel condensation under neutral conditions in water. *J. Am. Chem. Soc.* **2012**, *134*, 162–164.
8. Jiao, J.; Tan, C.; Li, Z.; Liu, Y.; Han, X.; Cui, Y. Design and assembly of chiral coordination cages for asymmetric sequential reactions. *J. Am. Chem. Soc.* **2018**, *140*, 2251–2259.
9. Jiao, J.; Li, Z.; Qiao, Z.; Li, X.; Liu, Y.; Dong, J.; Cui, Y. Design and self-assembly of hexahedral coordination cages for cascade reactions. *Nat. Commun.* **2018**, *9*, 1–8.
10. Chakrabarty, R.; Mukherjee, P. S.; Stang, P. J. Supramolecular coordination: self-assembly of finite two- and three-dimensional ensembles. *Chem. Rev.* **2011**, *111*, 6810–6918.

11. Manabe, K.; Iimura, S.; Sun, X. M.; Kobayashi, S. Dehydration reactions in water. Brønsted acid-surfactant-combined catalyst for ester, ether, thioether, and dithioacetal formation in water. *J. Am. Chem. Soc.* **2002**, *124*, 11971–11978.
12. Hong, C. M.; Bergman, R. G.; Raymond, K. N.; Toste, F. D. Self-assembled tetrahedral hosts as supramolecular catalysts. *Acc. Chem. Res.* **2018**, *51*, 2447–2455.
13. Fujita, M.; Umemoto, K.; Yoshizawa, M.; Fujita, N.; Kusukawa, T.; Biradha, K. Molecular paneling via coordination. *Chem. Commun.* **2001**, *6*, 509–518.
14. Holloway, L. R.; McGarraugh, H. H.; Young, M. C.; Sontising, W.; Beran, G. J.; Hooley, R. J. Structural switching in self-assembled metal–ligand helicate complexes via ligand-centered reactions. *Chem. Sci.* **2016**, *7*, 4423–4427.
15. Sharma, R. K.; Tam, J. P. Tandem thiol switch synthesis of peptide thioesters via N-S acyl shift on thiazolidine. *Org. Lett.* **2011**, *13*, 5176–5179.
16. Vishwanatha, T. M.; Bergamaschi, E.; Dömling, A. Sulfur-switch Ugi reaction for macrocyclic disulfide-bridged peptomimetics. *Org. Lett.* **2017**, *19*, 3195–3198.
17. Young, M. C.; Johnson, A. M.; Hooley, R. J. Self-promoted post-synthetic modification of metal–ligand M_2L_3 mesocates. *Chem. Commun.* **2014**, *50*, 1378–1380.
18. Association constants calculated using BindFit software, found at <http://supramolecular.org>.
19. Hibbert, D. B.; Thordarson, P. The death of the Job plot, transparency, open science and online tools, uncertainty estimation methods and other developments in supramolecular chemistry data analysis. *Chem. Commun.* **2016**, *52*, 12792–12805.
20. Kang, J.; Rebek, J. Entropically driven binding in a self-assembling molecular capsule. *Nature.* **1996**, *382*, 239–241.
21. Nishioka, Y.; Yamaguchi, T.; Yoshizawa, M.; Fujita, M. Unusual [2+4] and [22] cycloadditions of arenes in the confined cavity of self-assembled cages. *J. Am. Chem. Soc.* **2007**, *129*, 7000–7001.

22. Fiedler, D.; Leung, D. H.; Bergman, R. G.; Raymond, K. N. Selective molecular recognition, C-H bond activation, and catalysis in nanoscale reaction vessels. *Acc. Chem. Res.* **2005**, *38*, 349–358.
23. Kubitschke, J.; Javor, S.; Rebek, J. Deep cavitand vesicles–multicompartmental hosts. *Chem. Commun.* **2012**, *48*, 9251–9253.
24. E. V. Anslyn, D. Dougherty, in *Modern Physical Organic Chemistry*, *University Science Books*. **2004**.
25. Roberts, D. A.; Pilgrim, B. S.; Sirvinskaite, G.; Ronson, T. K.; Nitschke, J. R. Covalent post-assembly modification triggers multiple structural transformations of a tetrazine-edged Fe₄L₆ tetrahedron. *J. Am. Chem. Soc.* **2018**, *140*, 9616–9623.

Chapter 3 – Size and Shape-selective Cage-catalyzed Oxocarbenium Ion Catalysis

3.1. Introduction

Previous studies have shown that acid cage **1.30** is an effective promoter of both polar and tandem reactions, exhibiting high rate accelerations in the process.^{1,2} The ability for the host to catalyze these reactions is complicated by its sensitivity to strong nucleophiles, as they can destroy the metal-ligand bonds in the complex.³ Cage **1.30** was also capable of altering the molecularity of a reaction – a property usually only seen with enzymes.² These reactions show that the complex has unique properties. Not only can it bind multiple different guests inside its cavity, but rapid guest in/out exchange, high turnover, and limited product inhibition are observed during the reaction process. Furthermore, cage **1.30** also exhibits high binding affinities for all guests except for small hydrocarbons.^{1,2} High binding affinities are especially seen when using small molecules guests such as **PrSH** despite the existence of large gaps between the panels of **1.30**. These large gaps enable the rapid entry and departure of small guests from the cavity.^{2,4-6} The gaps between the panels¹ are 20 Å from Fe-Fe and are considered large, but not as large as other hosts found in literature.^{7,8}

So far, cage **1.30** has demonstrated the ability to catalyze both the hydrolysis of acetals and thioetherification of triphenylmethanol, exhibiting rate accelerations over a thousand-fold with respect to diacid **1.35** (Figure 3.1).^{1,2} Both cage **1.30** and diacid **1.35** possess dual carboxylic acid functional groups, albeit with different acidities, as the carboxylic acid groups in cage **1.30** are affected by the cationic nature of the complex. Stronger acids are therefore needed as controls for measuring the activity of cage **1.30**. Other factors such as affinity of the cage for each substrate, inhibition of both product and substrate, and

formation of ternary complexes also have a significant effect on the activity of **1.30** for certain substrates.² To explore more of the molecular recognition abilities of cage **1.30**, an investigation was performed on the factors that control the reactivity with the complex.⁹

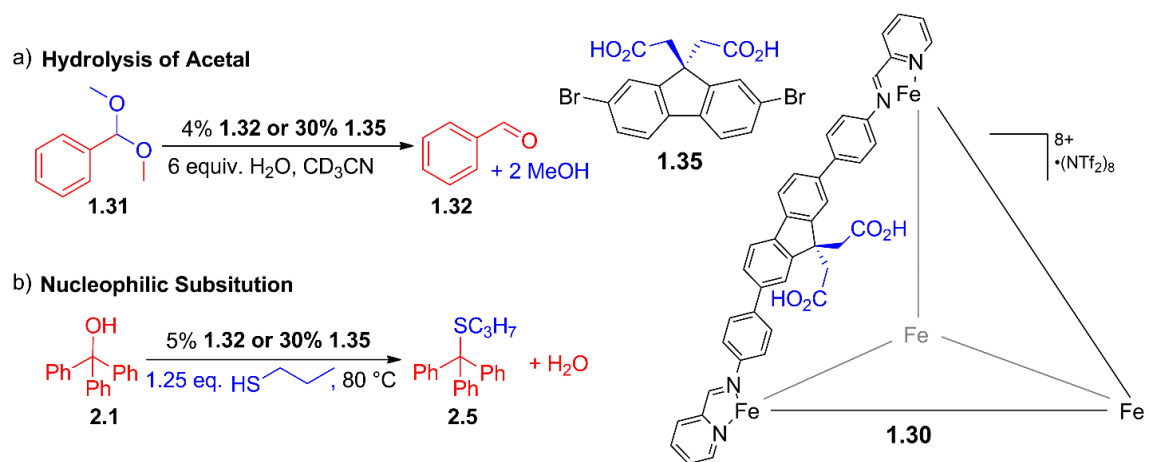


Figure 3.1. Reactions catalyzed by cage **1.30**. a) Hydrolysis of acetal.¹ b) Nucleophilic substitution of triphenylmethanol.²

3.2. Thioetherification of Vinyl Diphenylmethanol Derivatives

Since cage **1.30** is tolerant to both alcohols and thiol nucleophiles, this new study first focused on investigating the reactivity of cage **1.30** using **PrSH** as the nucleophile and various vinyl diphenylmethanol derivatives **3.1-3.4** as electrophiles. These electrophiles are of interest as they can react at multiple positions and form a variety of different substitution products. The reactions were performed in CD₃CN using 5% of the cage (with respect to electrophile) at 50 °C and monitored using ¹H NMR. Initially, two timepoints were taken, at 4 h and 24 h to minimize the effects of heating/cooling upon removing the sample from the heat to acquire NMRs throughout the process. Results show that the reaction with alcohol **3.1** as the electrophile only formed the conjugated, rearranged

product **3.5** with 36% conversion (Figure 3.2; Table 3.1). The thiol should be able to react at the quaternary center, but no trace of that reaction was observed in this process.

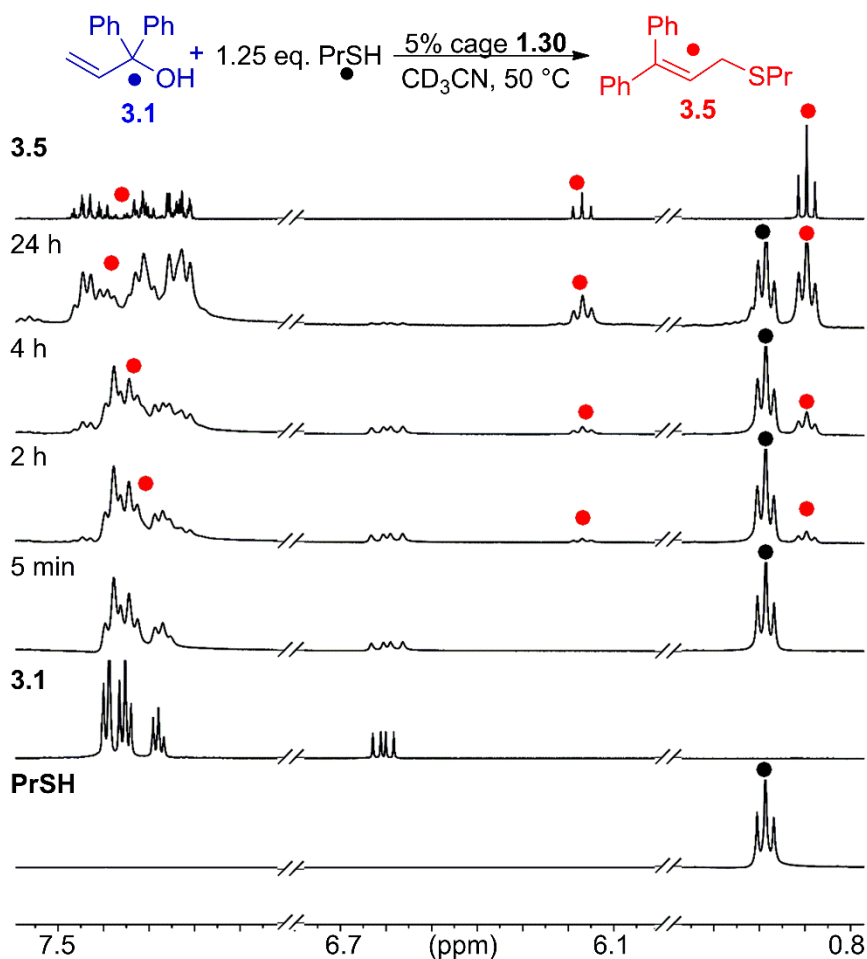


Figure 3.2. Expanded ^1H NMR spectra of the acid promoted reaction between **3.1** and **PrSH** in the presence of 5 mol % cage **1.30**.⁹

The thioetherification was tested under identical reaction conditions using the following small molecule acids as controls: camphorsulfonic acid (CSA) **3.6**, pivalic acid, trifluoroacetic acid (TFA), tartaric acid, and diacid **1.35** (Table 3.2). These acids have varying numbers and strengths of acid groups, and show corresponding differences in pKa. Out of the five acids, CSA **3.6** was found to be the most effective catalyst for the reaction,

showing a 37 % conversion into **3.5** after 4 h. When pivalic acid, trifluoroacetic acid, or tartaric acid was used as the catalyst, the reaction was considerably less effective, netting 1%, 6%, and 2%, conversion rates, respectively. Furthermore, diacid **1.35** was the least effective of all the catalysts tested, showing no reaction even after 24 h at 80 °C. Diacid **1.35**, interestingly, can be used as a cofactor inside cage **1.28** to catalyze the reaction with **3.1** or **3.3**. As we will see in chapter 5, using diacid **1.35** as a guest inside cage **1.28** can promote the thioetherification of triphenylmethanol.¹⁰ Using this host:guest pairing for the thioetherification reaction, a 9% conversion to product was seen after 24 h at 50 °C. When comparing the two reaction processes, a higher rate was observed when using cage **1.30** over the cofactor-mediated process. The reason for this slower reaction rate when using unfunctionalized cage **1.28** as the host and diacid **1.35** as the guest warrants further study (vide supra).

Table 3.1. Thioetherification of vinyl diphenylmethanol derivatives with acid catalysts.

3.1 R = OH
3.2 R = OCH₃
3.3 R = OMOM
3.4 R = OTHP

R	% Conversion Cage 1.30		% Conversion CSA 3.2	
	4 h	24 h	4 h	24 h
OH	36	88	37	82
OCH₃	35	75	45	>98
OMOM	19	47	64	>98

1.30

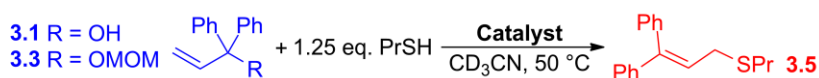
3.2

Reaction was performed at 323 K in CD₃CN; [3.1-3.4] = 15.8 mM, [PrSH] = 19.8 mM, [catalyst] = 0.8 mM. Concentrations were confirmed using dioxane as standard (7.9 mM).⁹

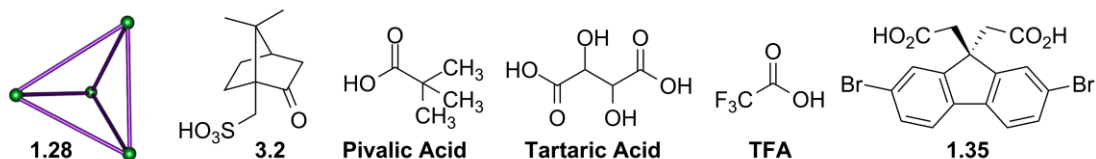
As CSA **3.6** was the most effective catalyst for the reaction, the small molecule acid was used as a control for comparison in the following experiments. In terms of pKa, CSA

has “comparable” acidity to the acid cage. The pKa of CSA is 1.2, whereas the diacid’s carboxylic acid has a pKa of ~3.5.^{11,12} Using CSA **3.6** as a control in the thioetherification of alcohol **3.1**, identical conversions were seen after 4 h with both catalysts, and complete conversion into the rearranged product was seen after 24 h (Table 3.1).

Table 3.2. Initial Rates and % conversion of thioetherification reaction using various controls.



Electrophile	Catalyst	% Conversion		Rate (x 10 ⁻⁴ mM/min)
		4 h	24 h	
3.1	5 mol % TFA	1	13	87
3.1	5 mol % Tartaric Acid	2	12	61
3.1	5 mol % Pivalic Acid	6	23	148
3.1	5 mol % cage 1.28 and 30 mol % diacid 1.35	2	9	59
3.3	5 mol % cage 1.28 and 30 mol % diacid 1.35	3	22	145



Reaction was performed at 323 K in CD₃CN; [**3.1** or **3.3**] = 15.8 mM, [PrSH] = 19.8 mM, [TFA, Tartaric Acid, Pivalic Acid, **1.28**] = 0.8 mM, [**1.35**] = 4.7 mM Concentrations were confirmed using dioxane as standard (7.9 mM).⁹

While identical conversion rates were observed with both catalysts when using alcohol **3.1**, small variations in the electrophile changed the effective conversion rate of the two catalysts. When the alcohol leaving group was changed to the methyl ether in **3.2**, a 45% conversion into **3.5** was observed after 4 h, and complete conversion was obtained after 24 h when using the small molecule acid **3.6**. This is likely due to the fact that ethers are more basic than alcohols.¹³ However, in the cage-catalyzed reaction, a slightly lower 35%

conversion to product was observed (Table 3.1). Despite the slower reaction, the cage was still stable throughout, showing no signs of decomposition throughout the process.

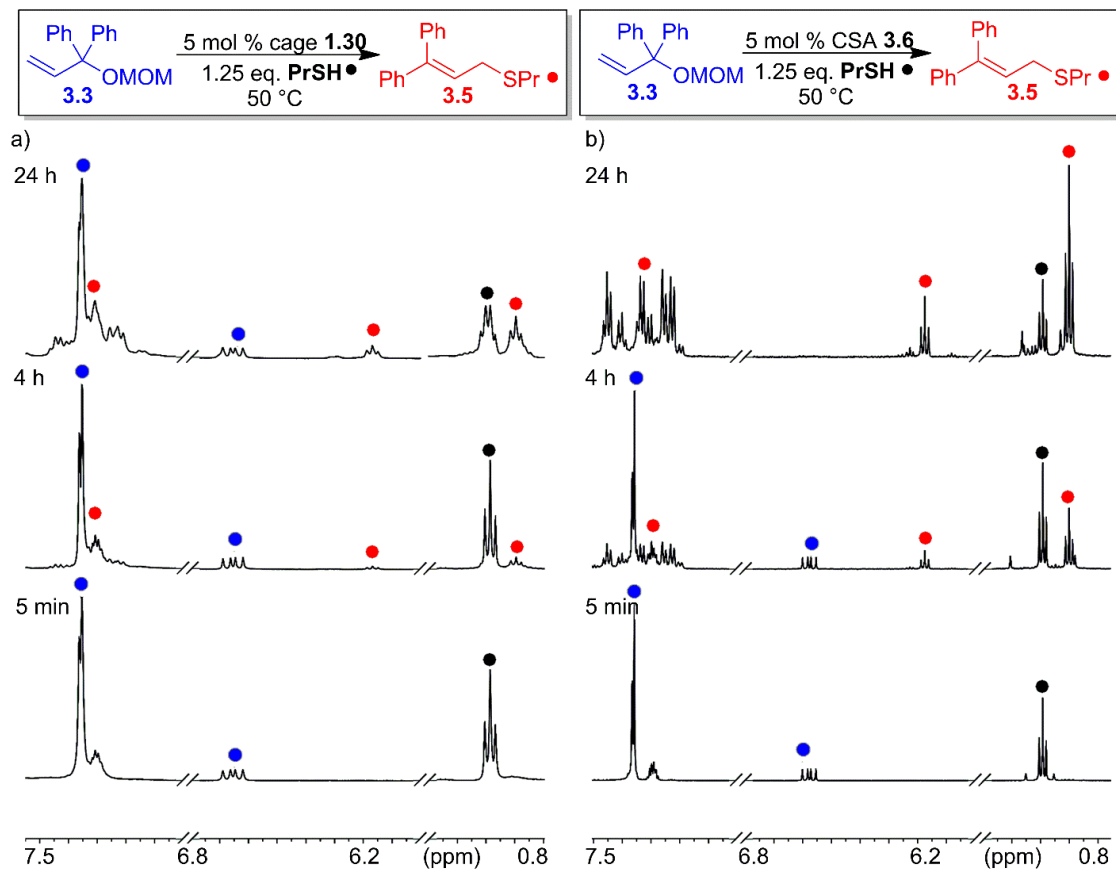


Figure 3.3. Expanded ¹H NMR spectra of the acid promoted reaction between **3.3** and **PrSH** in the presence of 5 mol % cage **1.30** or CSA **3.6**.⁹

Given that the size of the electrophile influences the reaction, electrophiles of larger sizes such as methoxymethyl (MOM) ether **3.3** were investigated. The relative reactivity of **3.3** is interesting to study due to having two reactive oxygen atoms that can be protonated. The reaction with **3.3** as the electrophile only formed the rearranged product **3.5**, with no evidence of oxocarbenium ion formation observed during the process with either cage **1.30** or CSA **3.6** (Figure 3.3). The two catalysts had different rates of reaction.

CSA **3.6** is a more effective catalyst than cage **1.30** when reacting with MOM ether **3.3**, as the former had 64% conversion after 4 h. Using cage **1.30** as the catalyst with **3.3** yielded a 19% conversion into **3.5** after 4 h, while only a 47% conversion into product was observed after 24 h (Table 3.1). These results so far illustrate that cage **1.30** and CSA **3.6** can show similar reactivity and conversion into product with certain substrates, as seen with alcohol **3.1**. However, simply changing the leaving group to methyl ether **3.2** or MOM ether **3.3** in the substrate can reduce the reactivity and overall conversion with cage **1.30** with respect to CSA **3.6**.

3.3. Thioetherification using THP Ether **3.4** and PrSH

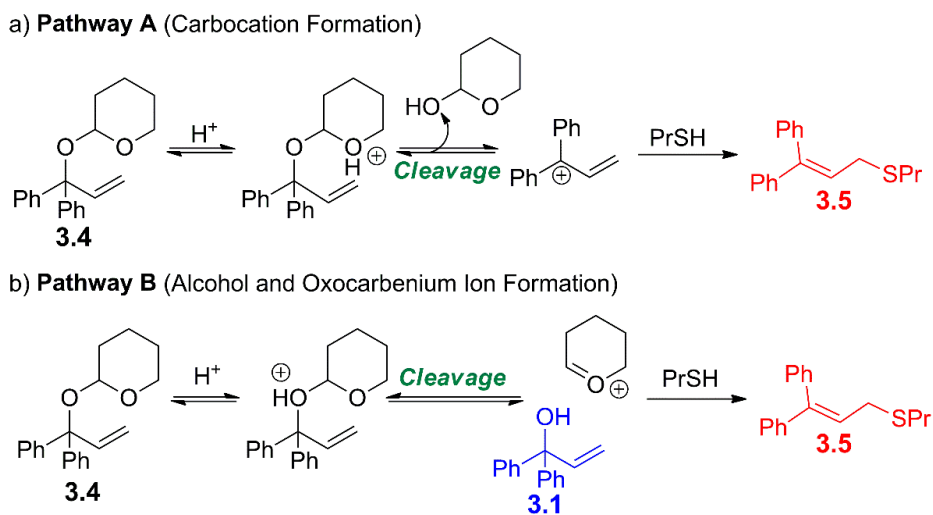


Figure 3.4. Two pathways in thioetherification of **3.4**. a) Pathway A shows carbocation formation. b) Pathway B shows oxocarbenium ion formation.⁹

Even with two reactive oxygens, only one product was formed with ether **3.3**. The MOM group in ether **3.3** is not easily removed and only forms **3.5**. To further this investigation, the reaction was repeated with tetrahydropyranyl (THP) ether **3.4**. The THP group in **3.4** is far easier to remove than the MOM in **3.3** and displays two reactive oxygens

as well that can be protonated by the acid catalysts. The protonation at either position can lead to cleavage at different bonds. The two pathways for this cleavage are displayed in Figure 3.4. If the oxygen is protonated in pathway A, cleavage leads to form the carbocation which then reacts with **PrSH** and rearranges into product **3.5**. This pathway was seen when **3.1-3.3** were used as electrophiles. In pathway B, the oxygen is protonated at the acetal center which leads to formation of alcohol **3.1** and an oxocarbenium ion intermediate. Further reaction with **PrSH** leads to formation of the same rearranged product **3.5** as found in pathway A.

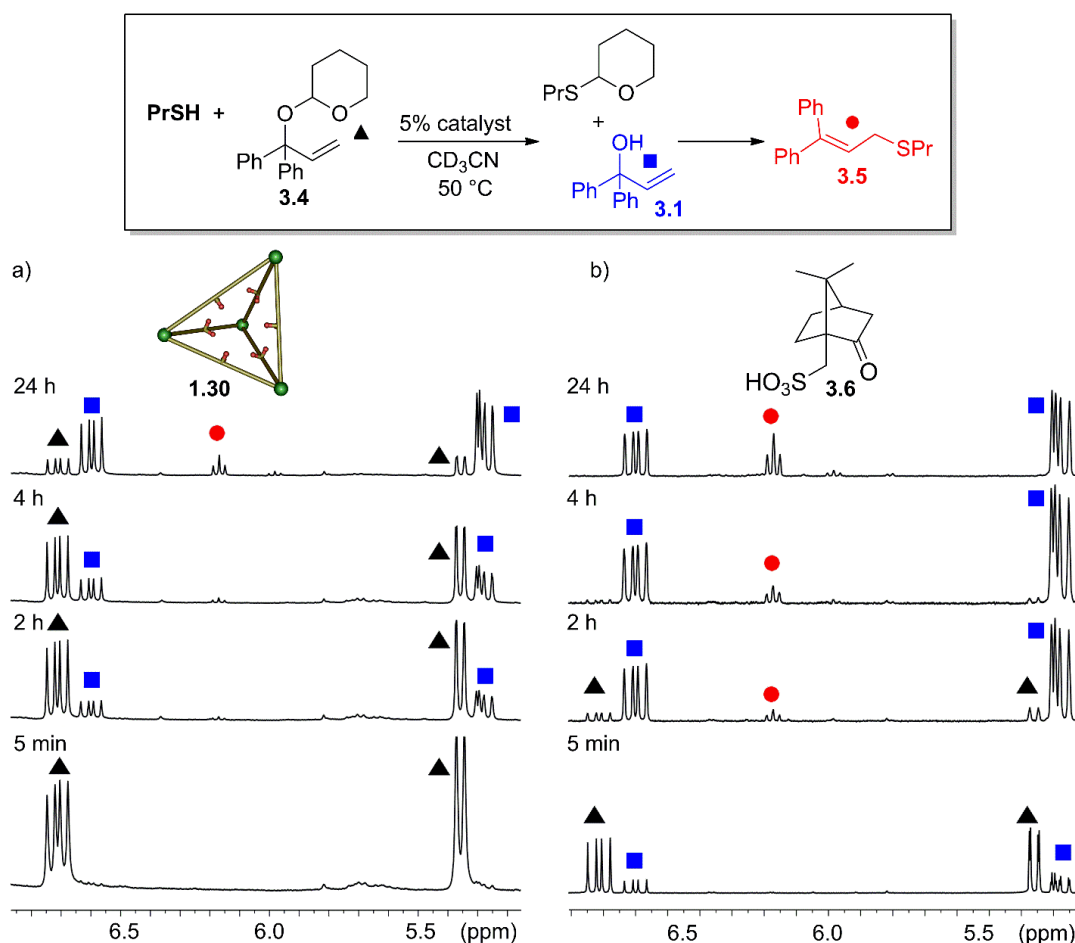


Figure 3.5. ^1H NMR spectra of the acid promoted reaction between **3.5** and **PrSH** in CD_3CN in the presence of: a) 5 mol % cage **1.30** b) 5 mol % CSA **3.6**.⁹

To find which pathway is favored, the reaction was performed at 23 °C with cage **1.30** and CSA **3.6**. When reacting with either catalyst, the THP group is removed, forming the alcohol and then rearranging into product **3.1**. However, when using CSA **3.6** as the catalyst, a significant difference in oxocarbenium ion reactivity is observed (Figure 3.5). The acid quickly removes the THP protecting group within 2 h at 23 °C, showing greater than a 90 % conversion (Table 3.3). In comparison to CSA **3.6**, cage **1.30** showed significantly less catalytic activity. The formation of an oxocarbenium ion was less favorable, and complete conversion into the rearranged product was not observed. These results show a difference in reactivity between electrophiles **3.1** and **3.6** when both cage **1.30** and CSA **3.6** were used as catalysts. The initial protonation step in the reaction is identical in the reaction with electrophiles **3.1** and **3.6**, but the rate of the reaction differs. When **3.1** was used as the electrophile, identical rates were obtained with both catalysts. However, when the formation of oxocarbeniums is involved, the reactivity differs significantly between the two catalysts.

Table 3.3. Oxocarbenium ion vs carbocation selectivity of acetal **4d**.

Time (h)	Cage 1.30			CSA 3.6		
	Overall conv. (%)			Overall conv. (%)		
2	27	18	9	100	69	31
4	44	27	17	100	47	53
10	73	39	34	100	27	73
21	95	30	66	100	5	95

Reaction was performed at 323 K in CD₃CN; [3.4] = 15.8 mM, [PrSH] = 19.8 mM, [catalyst] = 0.8 mM. Concentrations were confirmed using dioxane as standard (7.9 mM).⁹

To further determine the effect of the THP group on the reaction, the reaction was performed at the higher temperature of 50 °C. The reaction using CSA as the catalyst follows the same mechanistic pathway as the cage-catalyzed reaction in which the THP group is quickly removed to yield alcohol **3.1**. The alcohol is then rearranged into product **3.5** after reacting with the thiol nucleophile. While the oxocarbenium ion intermediate is clearly observed in the reaction, there are no signs of any carbocation intermediates forming in the process. In comparison to the reaction with CSA **3.6**, a significant difference in reactivity is observed with cage **1.30**. The THP group is removed more slowly in the cage-catalyzed process as only 66% conversion into **3.5** is observed after 24 h. This reactivity with **3.6** is interesting when compared to **3.1**. Even though only 66% conversion was observed with **3.4**, alcohol **3.1** showed complete conversion after 24 h. When comparing **3.4** to **3.1**, the THP group may be functioning as a protecting group, thereby slowing the reaction. Overall, the reaction with the THP ether **3.4** and **PrSH** shows no evidence of carbocation formation in the reaction using either cage **1.30** or CSA **3.6** as the catalyst. Both reactions follow pathway B in which the alcohol and oxocarbenium ion intermediate are formed before rearranging into product **3.5**. However, in the cage-catalyzed reaction, forming the oxocarbenium ion is a slower, less favorable process.

3.4. Thioetherification using Water as the Nucleophile

The reactivity with THP ether **3.4** can vary. This process was further investigated by changing the nucleophile from **PrSH** to H₂O. In the reactions performed with **PrSH**, THP ether **3.4** does not hydrolyze in the presence of small amounts of H₂O from the air and CD₃CN. To facilitate the reaction with H₂O, 6 mol. equiv. of the nucleophile was used.

The reaction was performed at either 23 °C or 50 °C and reacted with MOM ether **3.3** and THP ether **3.4** using 5% cage **1.30** or CSA **3.6** in CD₃CN.

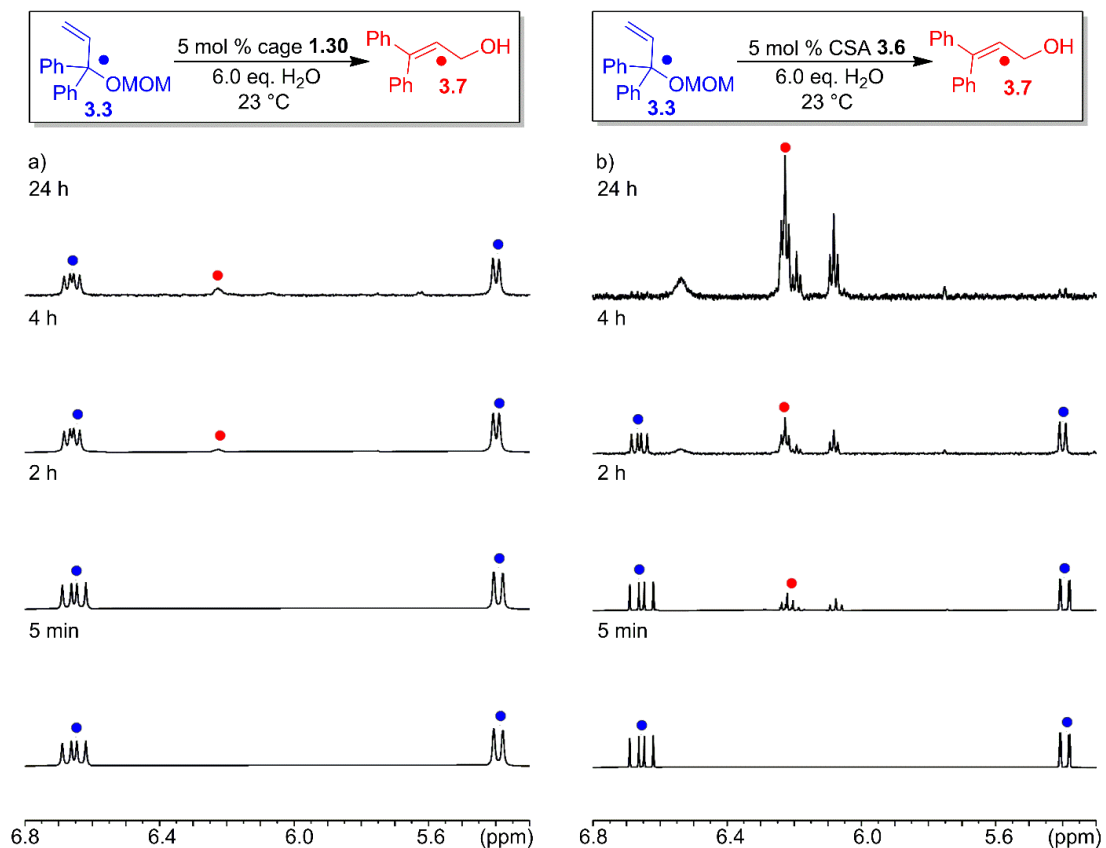


Figure 3.6. ¹H NMR spectra of the acid promoted reaction between **3.3** and H₂O in CD₃CN in the presence of: a) 5 mol % cage **1.30** b) 5 mol % CSA **3.6**.⁹

The reactivity of MOM ether **3.3** with H₂O as the nucleophile reflected that of PrSH as they both show lower conversions with cage **1.30**. The reaction was surprisingly unreactive in cage **1.30** compared to the other ethers, showing only a 19% conversion to rearranged alcohol **3.7** after 16 h at 50 °C. While increasing the temperature to 80 °C allowed for a higher conversion, cage **1.30** began to decompose during the process. In contrast with CSA **3.6**, complete conversion into **3.7** was observed after 16 h at 50 °C

(Figure 3.6). MOM ether **3.3** is once again observed to be far less reactive in cage **1.30** than expected.

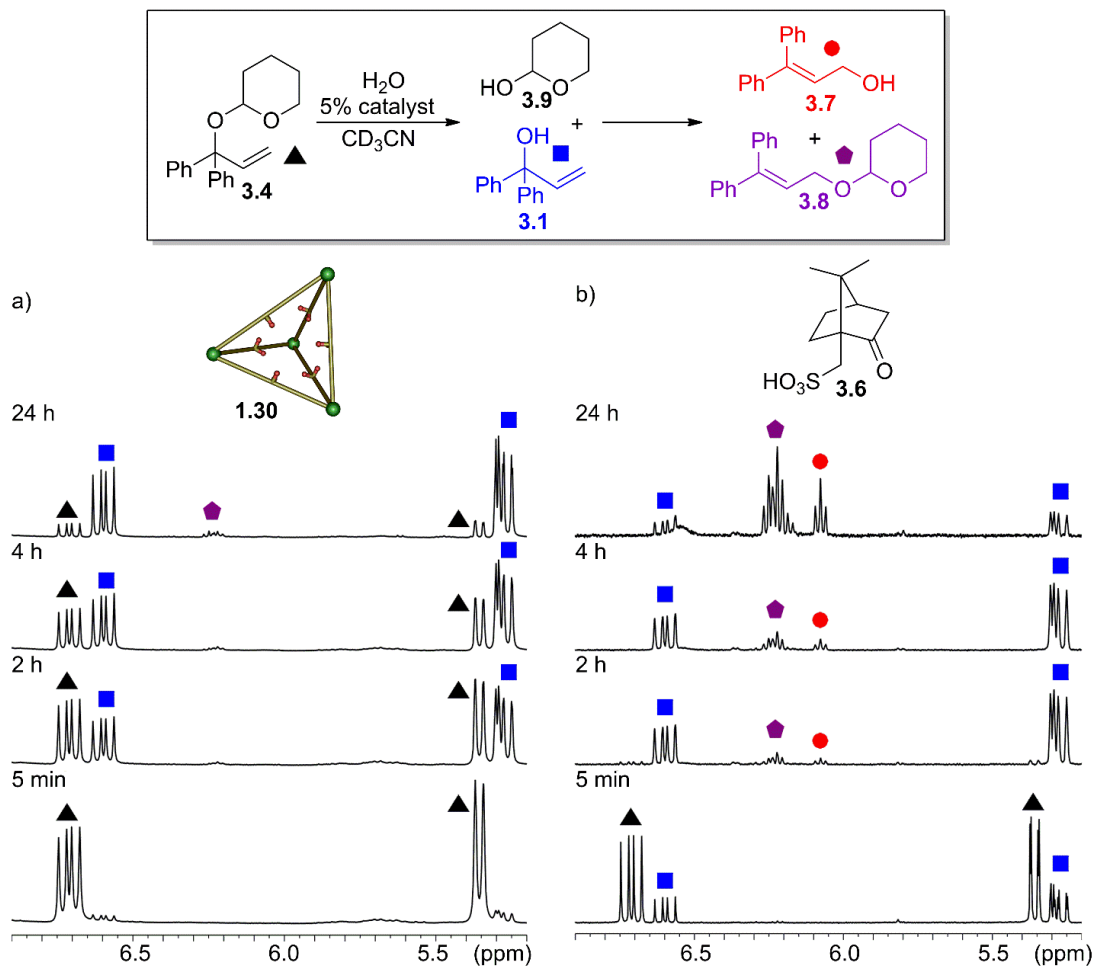


Figure 3.7. ¹H NMR spectra of the acid promoted reaction between **3.4** and H₂O in CD₃CN in the presence of: a) 5 mol % cage **1.30** b) 5 mol % CSA **3.6**.⁹

The reaction with the more reactive THP ether **3.4** was more revealing. The initial reaction with CSA **3.6** was rapid, and complete deprotection of the THP was observed after 10 minutes. Further reaction with the catalyst observed two products: the rearranged alcohol **3.7** and THP acetal **3.8**. THP acetal **3.8** was potentially formed by the acid catalyzed reaction of alcohol **3.1** and the cleaved byproduct **3.9**.

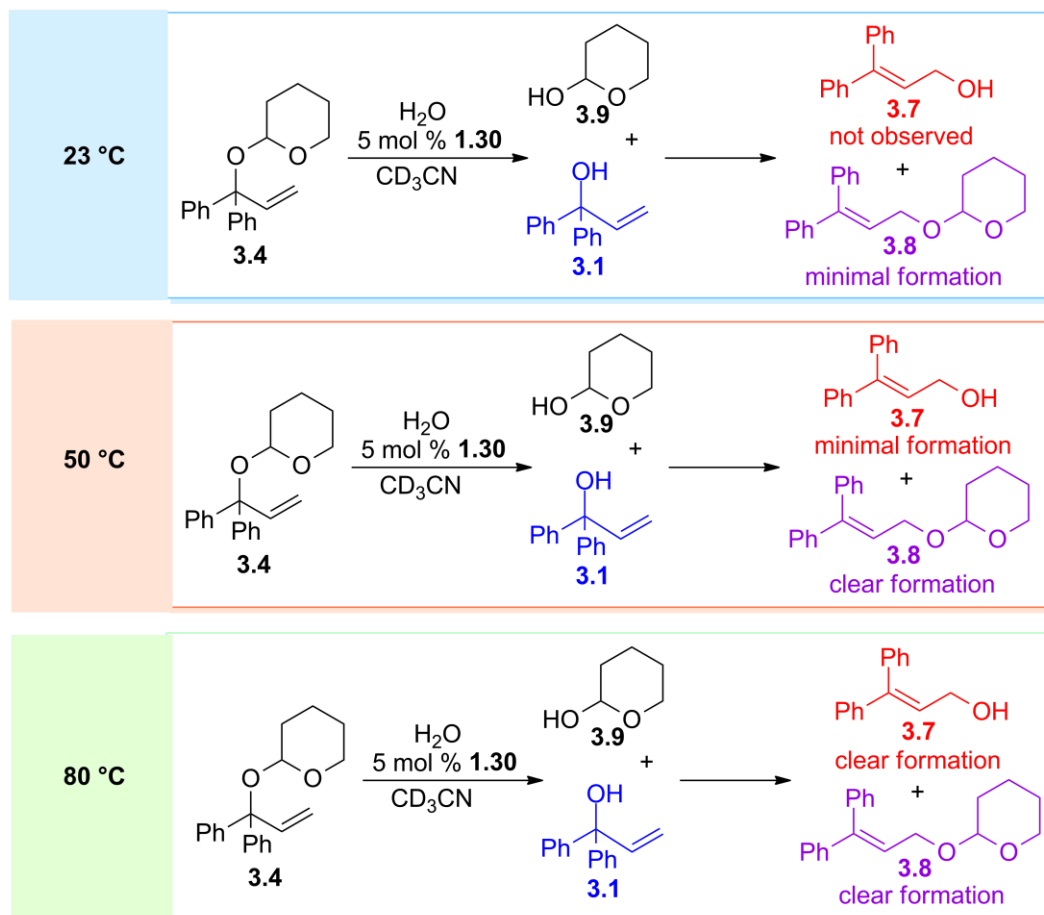


Figure 3.8. Reactions with tertiary alcohol derivative **3.4** and H_2O at different temperatures.⁷

Interestingly, cage **1.30** was able to remove the THP group and form the THP acetal **3.8** at 23 °C. However, minimal rearrangement to alcohol **3.8** was observed even after 24 h. Minimal rearrangement into alcohol **3.8** was also seen when the temperature was raised to 50 °C. At this temperature, clear formation of THP acetal **3.9** was noticed as well. When the temperature was raised higher to 80 °C, both products were formed and observed in the ^1H NMR. After reacting at such a high temperature, decomposition of the cage was observed (Figure 3.8). Our results show that the reactivity of cage **1.30** was altered when the size of the electrophile was changed. When THP ether **3.4** was used as the electrophile,

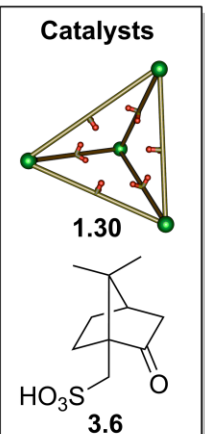
a reduction in reactivity was observed in comparison to alcohol **3.1**. This is potentially because the MOM and THP acetals act as a “protecting groups” for the reaction catalyzed by cage **1.30**.

3.5. Reactions with a Smaller Acetal Substrate

To analyze whether the cage was simply a poor choice for reactions with **3.4**, an investigation was performed with a smaller THP ether, namely 2-methoxytetrahydropyran **3.10**. While the larger guests of **3.1-3.4** show size-based selectivity, the reactivity changes with electrophile **3.10** due to its smaller size and the way coordinates inside the cavity. THP ether **3.10** was reacted with 5% cage **1.30** or CSA **3.6** with four different nucleophiles. These following nucleophiles vary in size: **PrSH**, *n*-octanethiol (*n*-**C₈SH**), *n*-dodecanethiol (*n*-**C₁₂SH**) and H₂O (Table 3.4).

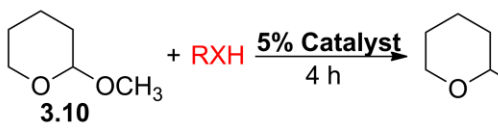
Table 3.4. Thioether/ether exchange with the small THP ether **3.10**.

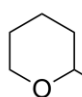
Catalysts



1.30

3.6



3.10 + RXH $\xrightarrow[4\text{ h}]{5\% \text{ Catalyst}}$ 

3.11: XR = SPr
3.12: XR = S(CH₂)₇CH₃
3.13: XR = (CH₂)₁₁CH₃
3.14: XR = OH

RXH	XR	% conversion, cage 1.30		% conversion, CSA 3.6	
		23 °C	50 °C	23 °C	50 °C
PrSH	SPr	14	62	72	80
<i>n</i>-C₈SH	S(CH₂)₇CH₃	8	63	68	82
<i>n</i>-C₁₂SH	S(CH₂)₁₁CH₃	12	60	63	82
H₂O	OH	28	30	28	26

Reaction was performed at 296 or 323 K in CD₃CN; [3.10] = 15.8 mM, [RXH] = 19.8 mM, [catalyst] = 0.8 mM. Concentrations were confirmed using dioxane as standard (7.9 mM).⁹

Initial results show that the cage-catalyzed reaction with the smaller THP ether **3.10** and **PrSH** reacts quicker in comparison to the larger THP ether **3.4**. After 4 h, a 62%

conversion into the thioacetal product **3.11** was observed for the smaller THP ether **3.4**, whereas a 27% conversion was obtained in the reaction with the larger THP ether **3.4**. Notably, **3.10** was never fully converted to product with either catalyst. Instead, the reaction formed an equilibrium between **3.10** and thioacetal product **3.11**, favoring the product in an 80:20 ratio. Similar rate differences were seen with the other nucleophiles. CSA **3.6** was considerably more effective in catalyzing the reaction between **3.10** and the thiol nucleophiles than cage **1.30** (Figure 3.9). While the reaction using cage **1.30** as the catalyst requires approximately 10 h to reach full equilibrium, the reaction with CSA **3.6** reaches equilibrium in 4 h at 50°C (Table 3.3).

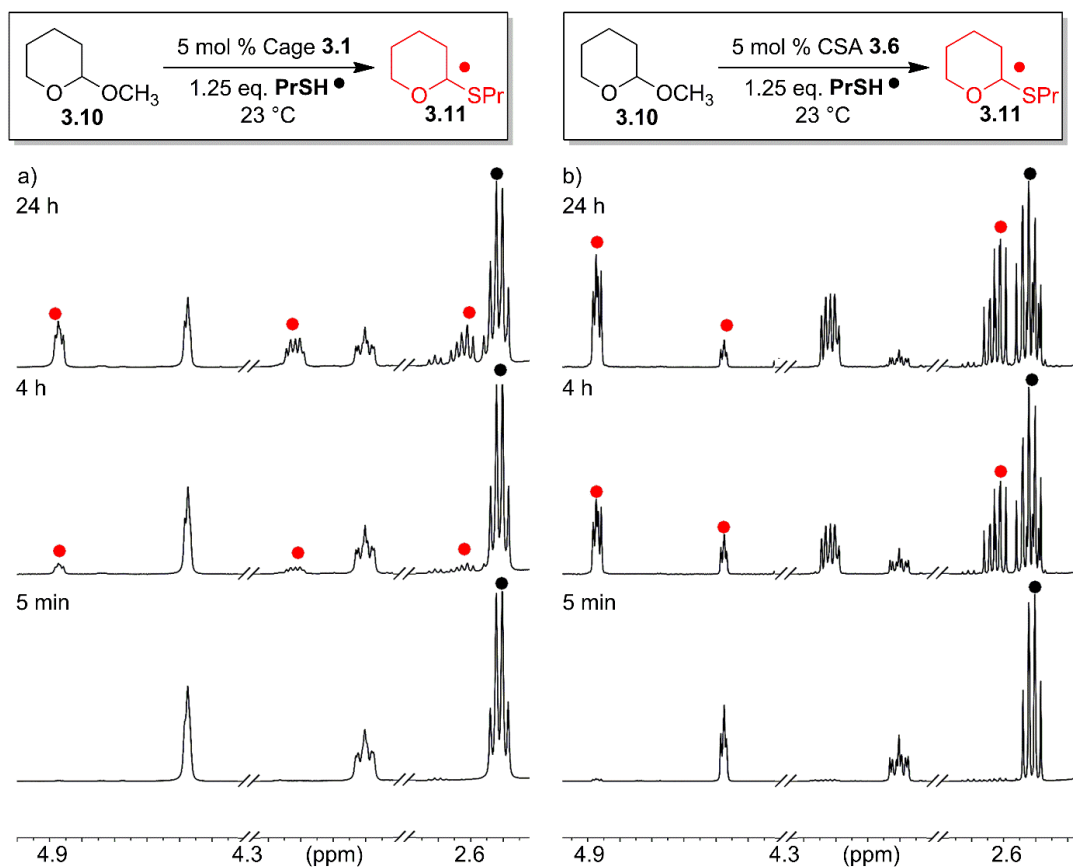


Figure 3.9. ¹H NMR spectra of the acid promoted reaction between **3.10** and **PrSH** in CD₃CN in the presence of: a) 5 mol % cage **1.30** b) 5 mol % CSA **3.6**.⁷

Further investigation shows that the reactivity can be altered when H₂O was used as the nucleophile in this reaction. When H₂O was used under the same conditions, the hydrolysis of acetal **3.10** formed the lactol **3.14** in a 30:70 ratio, favoring the starting material **3.10** over the product **3.12**. The reactivity does not seem to differ significantly between the two catalysts, and full equilibrium in this reaction can be achieved in 4 h at both 23 °C and 50 °C (Figure 3.10).

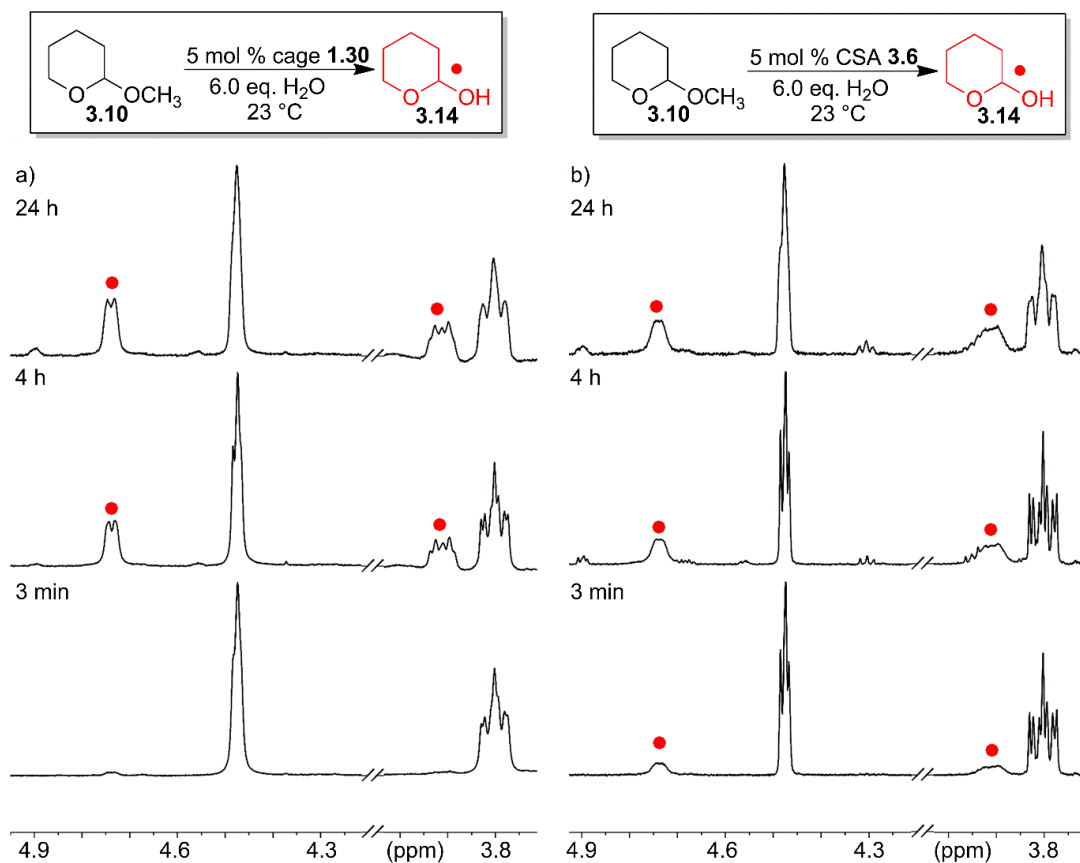


Figure 3.10. ¹H NMR spectra of the acid promoted reaction between **3.10** and H₂O in CD₃CN in the presence of: a) 5 mol % cage **1.30**; b) 5 mol % CSA **3.6**.⁹

3.6. Thioetherification of Isochromanyl Ethers

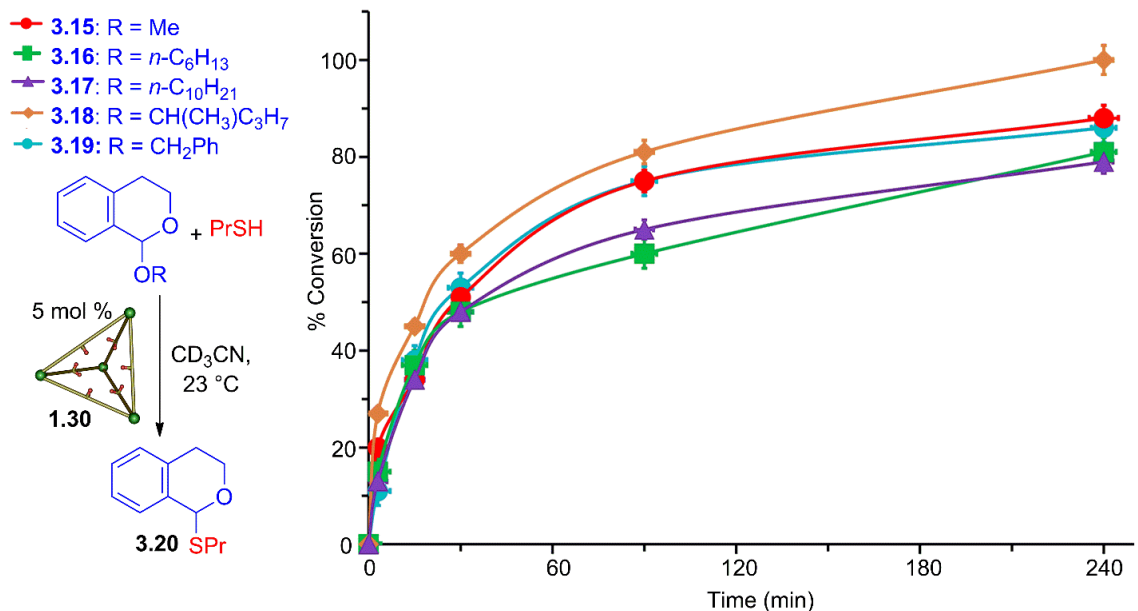


Figure 3.11. Reaction progress over time of the cage-catalyzed thioetherification of isochromanyl ethers.⁹

As a catalyst, cage **1.30** was shown to be size-selective in reactions using large electrophiles **3.1-3.4**, while reactions between smaller electrophiles and thiol nucleophiles showed decreases in relative reactivity. To further study why this occurs, a new set of electrophiles were synthesized by Connor Woods. These electrophiles consist of various isochromanyl ether derivatives **3.15-3.19** that have leaving groups of various sizes. The reaction was performed with these electrophiles at 23 °C using **PrSH** as the nucleophile (Figure 3.11). Out of all the derivatives, the reaction between secondary isoamyloxy isochroman **3.18** and **PrSH** catalyzes the reaction the fastest. Complete conversion into product **3.20** is obtained after 4-6 h at 23 °C, with the initial rates of all five of these substrates being comparable. While size-selectivity was observed with electrophiles **3.1-3.4** in the presence of 5% cage, size selectivity was not observed with isochromanyl ether

derivatives **3.15-3.19**. The cage-catalyzed reaction was also significantly slower than with the CSA **3.6** catalyst. A 2.7-fold acceleration was observed with methoxy isochroman **3.15** and **PrSH**. The initial rates of all five substrates differed significantly in reactivity in the process catalyzed by CSA **3.6**. For example, isoamyl **3.18** and benzyl **3.19** were 1.5 and 2-fold more reactive, respectively, than the more linear **3.15-3.17** (Figure 3.12).

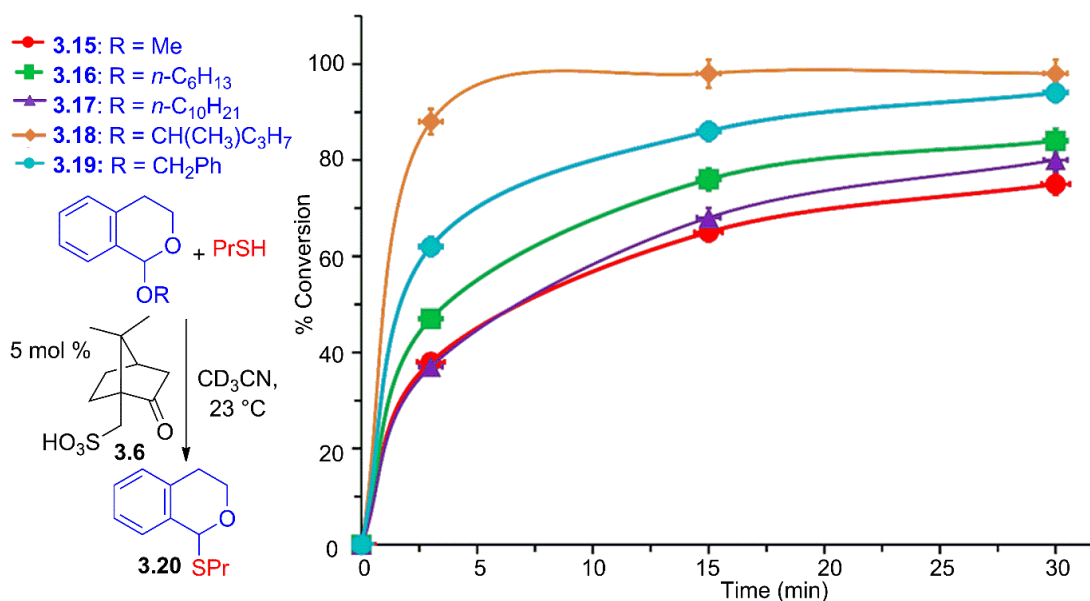


Figure 3.12. Reaction progress over time of the CSA-catalyzed thioetherification of isochromanyl ethers.⁹

These results indicate that minimal size and shape selectivity was observed using these isochromanyl ethers. To compare the results observed with CSA **3.6** and cage **1.30**, control experiments were performed with using diacid **1.35** as catalyst and using cage **1.30** with added diester **3.21** to block the cavity (Figure 3.13). Electrophile **3.15** is sufficiently reactive to allow some conversion to happen with diacid **1.35**. This reaction is incredibly slow, displaying only 3% conversion after 6 h. Despite having low reactivity, what we observed allows us to compare rates with cage **1.30**, which further illustrates the relatively

poor catalytic performance of the host with **3.15**. In comparison to the cage-catalyzed reaction of the thioetherification of triphenylmethanol **2.1**, where a greater than a 1000-fold rate enhancement was observed in respect to diacid **1.35**, only a 50-fold rate increase is observed in this case. This difference in rate illustrates the change in reactivity when using guests that are flat as opposed to other, more spherical guests.

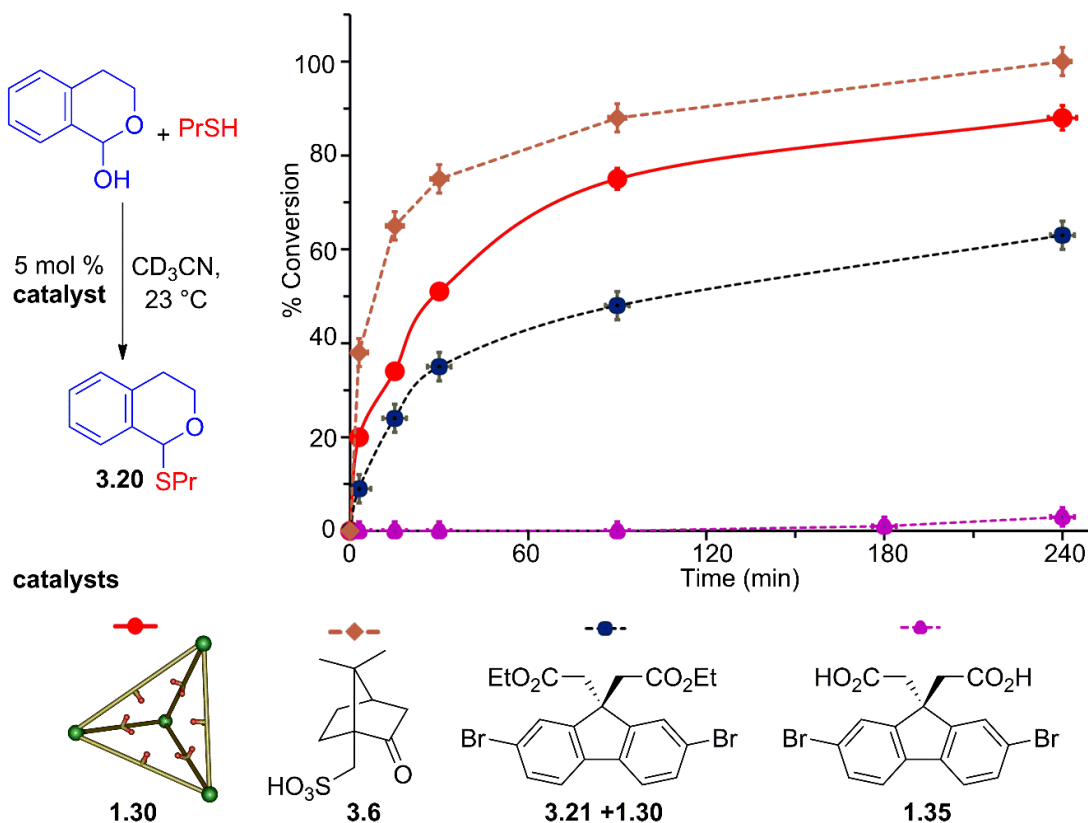


Figure 3.13. Reaction progress over time of the **3.15** using various control catalysts.⁹

To confirm the cavity of cage **1.30** can be blocked by a guest and, therefore, limit the binding of reactants, an equimolar amount of diester **3.21** was added. The guest shows a high binding affinity of $6.9 \pm 1.2 \times 10^3 \text{ M}^{-1}$ which is similar to that of methoxy isochroman **3.15** ($K_a = 5.7 \pm 0.5 \text{ M}^{-1}$). When the guest was added, the reaction was slowed down. This

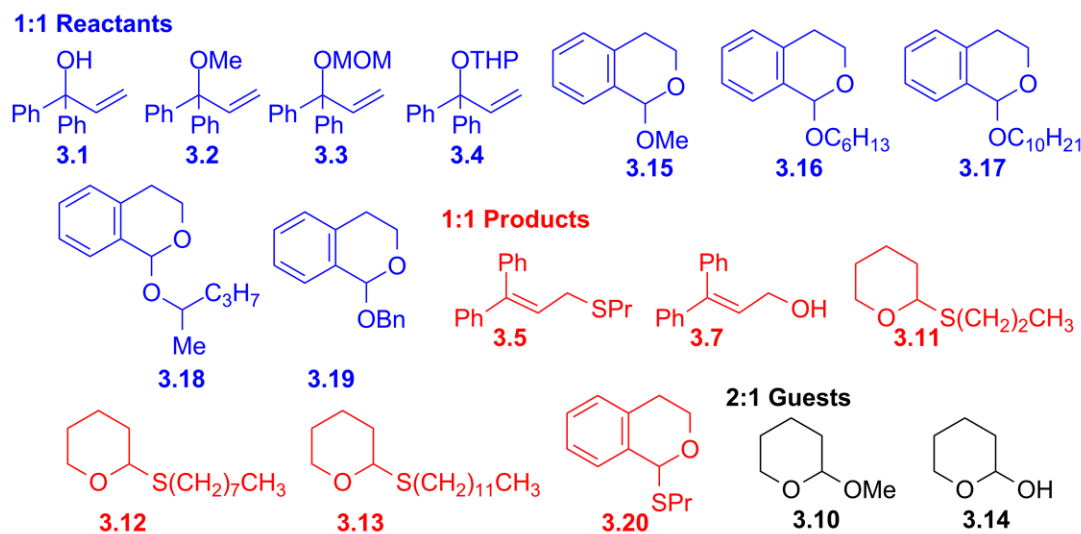
shows that the addition of guest can block the cavity which inhibits cage **1.30** from using its endohedral carboxylic acid groups to catalyze the reaction.

3.7. Binding to Various Guest Substrates

In experiments thus far, the overall relative reactivity of cage **1.30** is shown to be affected by both the size and shape of the substrates, and that the carboxylic acid groups in cage **1.30** are considerably more acidic than those found in diacid **1.35**. Despite the structural similarity between the substrates, the reactivity of cage **1.30** for these guests varies. While the cause of such variance in its relative reactivity with cage **1.30** is unclear, we do see that molecular recognition certainly plays an important effect in controlling this reactivity. The strength with which the substrate binds to the cage may be the cause and warrants further study.

To provide some explanation for the variable reactivity of substrates in cage **1.30**, studies were performed to observe how well each guest bound within cage **1.30**. Bryce da Camara titrated these guests into a 1.5 μM solution of cage **1.30** in CH_3CN , analyzed the changes in absorbance at both 330 and 370 nm, calculated the affinities of each guest, and fitted each guest for errors (Table 3.5).¹⁴⁻¹⁶ The larger electrophiles and products best fit the 1:1 binding model, whereas the smaller reactants and products best fit the 2:1 model. Alcohol **3.1** showed the greatest affinity for cage **1.30** with a K_a of 7400 M^{-1} . However, in when compared to the other derivatives, the difference in affinity is between 2.5-6-fold. The difference is so small that it cannot explain the decrease in reactivity for the thioetherification reaction with MOM ether **3.3** and THP ether **3.4**.

Table 3.5. Binding of various substrates and products in cage **1.30**.



1:1 Reactant	$K_a \times 10^3 \text{ M}^{-1}$	1:1 Reactant	$K_a \times 10^3 \text{ M}^{-1}$
3.1	7.4 ± 0.2	C₈SH	6.6 ± 0.2
3.2	1.3 ± 0.06	C₁₀SH	7.2 ± 0.4
3.3	2.9 ± 0.05		
3.4	1.5 ± 0.09		
3.15	5.7 ± 0.5		
3.16	4.4 ± 0.3		
3.17	5.6 ± 0.2		
3.18	3.6 ± 0.1		
3.19	5.0 ± 0.06		
		1:1 Product	$K_1 \times 10^3 \text{ M}^{-1}$
		3.5	4.8 ± 0.4
		3.7	5.1 ± 0.2
		3.11	4.7 ± 0.06
		3.12	15.9 ± 0.08
		3.13	6.1 ± 0.08
		3.20	2.8 ± 0.08
2:1 Guest	$K_{11} \times 10^3 \text{ M}^{-1}$	$K_{12} \times 10^3 \text{ M}^{-1}$	$\alpha (4K_{12}/K_{11})$
3.10	5.3 ± 0.7	0.009 ± 0.0001	0.004
3.14	6.6 ± 0.3	0.77 ± 0.05	0.46
PrSH	114 ± 15	0.75 ± 0.008	0.026

Titration were performed in CH₃CN, [**1.30**] = 3 μM , absorbance changes measured at 300 and 330 nm.^{9, 14-16}

Alcohol **3.1** showed the greatest affinity for cage **1.30**, while isoamyl isochroman **3.18** showed the weakest affinity. The low affinity explains why the reaction with **3.18** and **PrSH** has a slow rate when compared to CSA **3.6**. The differences in affinities between isochromanyl ether derivatives **3.15-3.19** are not very significant, however. In terms of

molecular volume, electrophiles **3.1-3.4** have volumes ranging from 168 to 235 Å³ while **3.15-3.19** have volumes from 126 to 249 Å³. Results show that the differences in size of the isochroman derivatives **3.15-3.19** do not play a significant factor in affecting the cage's affinity to the guest.

While guests thus far have exhibited 1:1 binding, the smaller THP ether **3.10** and **PrSH** bound in a 2:1 manner. Negatively cooperative binding is observed whenever the α values are less than 1. This means that the addition of the second guest is disfavored after the first guest binds. THP ether **3.10** displays a weaker affinity than **PrSH** and potentially plays a role in the lack of reactivity with cage **1.30** compared to CSA **3.6**.

3.8. Discussion of Results

In the thioetherification of various vinyl diphenyl methanol derivatives, cage **1.30** is an effective host for the reaction when compared to diacid **1.35**, effectively binding various substrates inside its cavity for acceleration. Size-shape selectivity is observed during the process with electrophiles **3.1-3.4** in which electrophile **3.1** shows a decrease in reactivity when compared to electrophiles **3.2-3.4**. To further explain the decrease in reactivity, models were made of cage **1.30** with electrophiles **3.1** and **3.4** bound within its cavity (Figure 3.14). Evidence shows that the tetrahydropyranyl group in THP ether **3.4** is positioned further away from the cage's carboxylic acid groups when bound than the alcohol group in **3.1**. Hence, electrophiles that have more bulk around the basic oxygen are activated less effectively due to its orientation. The -OR leaving group is further away from the carboxylic acid groups, leading to a decrease in reactivity. Furthermore, the THP group in **3.4** can function as a protecting group in an acid-catalyzed reaction, thereby lowering

the reactivity. This is surprising as the THP usually protects against basic reactions and is typically cleaved by acid. This phenomenon shows that the solvent or the dissociated acids must not be involved in the reaction. The carboxylic acid groups in the cage are likely the source of acidic protons in the reaction. For the reaction to occur effectively, cage **1.30** must be configured in a way that positions its carboxylic acid group right next to the -OR leaving group.

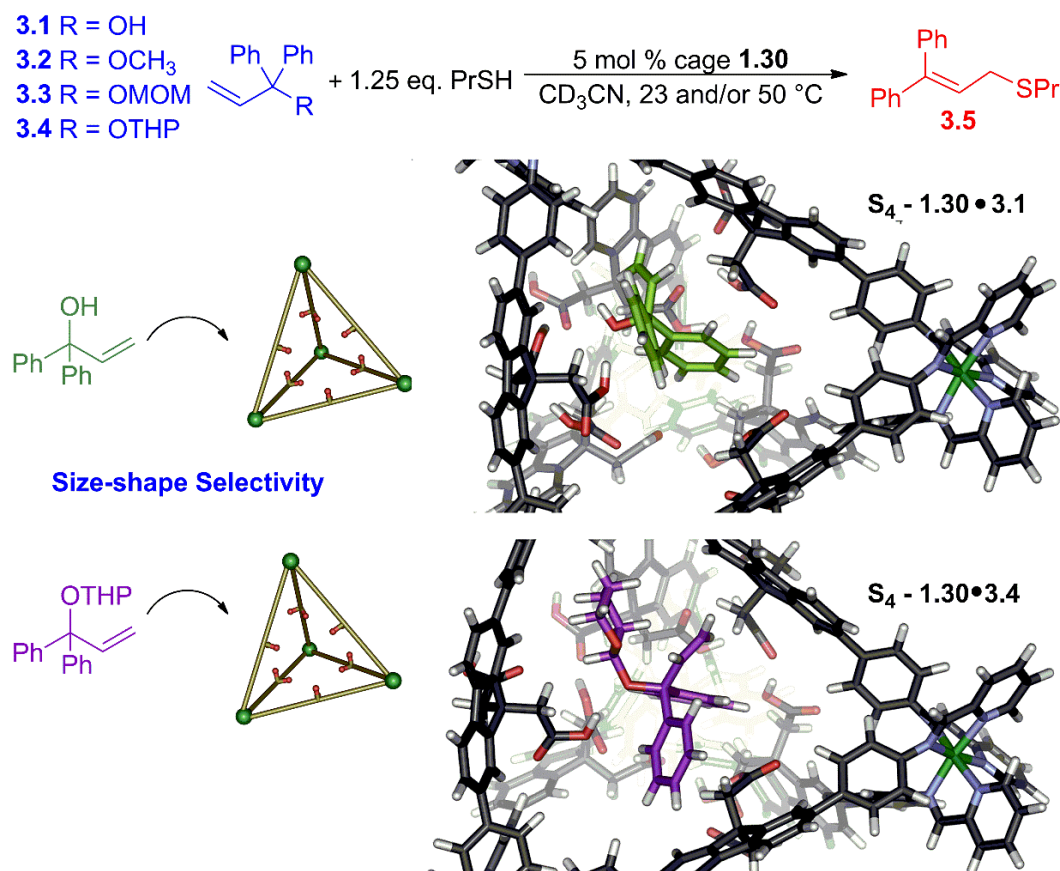


Figure 3.14. Models of substrates **3.1** and **3.4** inside cage **1.30**.⁹

In addition to the larger THP ether **3.4**, smaller THP ether **3.10** can also be bound and activated in the cage. However, limited selectivity is observed in the process. This effect can be attributed to substrate inhibition with **PrSH**. The nucleophile is small but displays

a stronger affinity to the cage complex than the **3.10**. Since **PrSH** binds the cage in a 2:1 manner and can fit two of the guest molecules inside the cavity of the cage, this can potentially affect the binding to electrophile **3.10** inside the cage. In the thioetherification reaction with **3.10**, the reactivity was reduced with cage **1.30** when compared to CSA **3.6**. However, in the hydrolysis reaction with H₂O as the nucleophile, the reaction was not slowed but instead happened at similar rates with both catalysts. The reason behind this decrease in reactivity could be due to substrate inhibition with **PrSH** and formation of unproductive ternary complexes during the process. The difference in rates observed in the other reactions catalyzed by cage **1.30** and CSA **3.6** shows that substrate inhibition plays a small factor in those reactions as well. While the concentrations of the nucleophile and electrophile are very similar, the inhibition process is somewhat limited.

Reactions catalyzed by cage **1.30** have shown to behave differently with differently structured guests. Larger guests have exhibited size-selectivity, while smaller THP ethers show limited size-selectivity. Previous studies have also shown that cage **1.30** has stronger selectivity for certain substrate shapes.^{1,2} While spherical guests are highly dependent on substitution, flat guests are shown to be unaffected by both size and shape differences. When the flat isochroman derivatives **3.15-3.19** of varying sizes and shapes were tested, a lack of selectivity was observed. To further explain this lack of selectivity, a model was made with electrophile **3.17** (Figure 3.15). Electrophile **3.17** has a volume of 249 Å³ which is over double the volume of **3.15**. The model shows that the panel gaps in the cage are so large that once the guest is bound the leaving group can easily extend out of the cavity.¹⁷ Therefore, changes in the leaving group and molecular volume of the guest can have a

minimal effect on selectivity. The positioning of the -OR group in **3.17** does not affect its ability to react with the carboxylic acid groups inside cage **1.30**. The cavity can also be blocked by addition of an equimolar amount of diester **3.21**, decreasing the rate and reducing the reactivity by 3-fold.

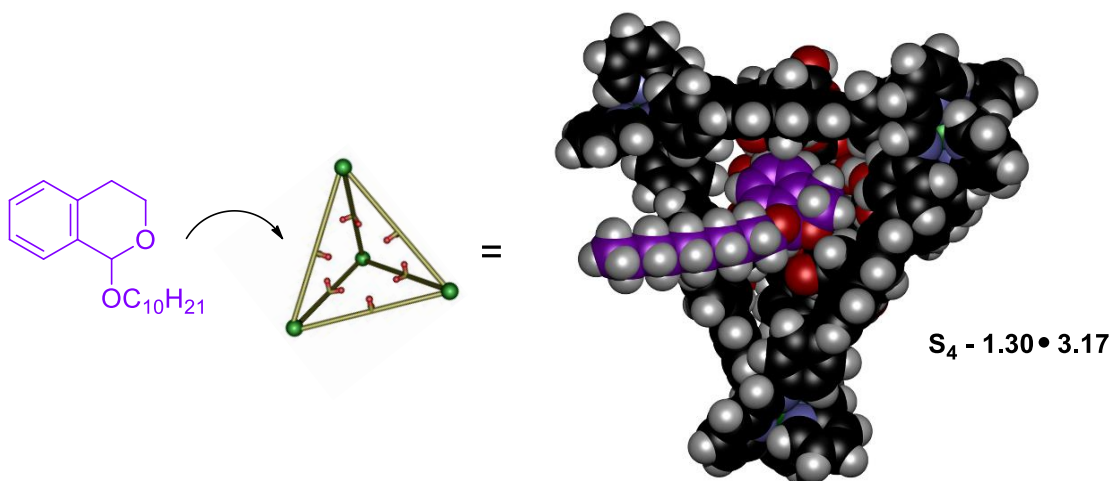


Figure 3.15. Models of substrates **3.17** inside cage **1.30**.⁹

Overall, the cage complex behaves differently than small molecule acids when acting as a catalyst, driven by its molecular recognition properties. The cavity has large gaps between the panels from which guests can freely enter and exit. It is for this reason that the interactions between the host and guests can take place at various locations. The binding affinity is affected by various CH- π , π - π , and hydrogen bonding interactions between the host and the guest. These interactions affect the binding of the small THP ether **3.10** and flat guests of **3.15-3.19**. These guests can be bound tightly and activated in the cavity. However, limited selectivity is observed in the process. These results show that the substrate does not have to fill the entire cavity, but that the electrophile must interact with the functional groups to promote an effective response. Due to its cationic nature, the cage

has reactivity similar to that of the strong acid CSA. These noncovalent interactions that assists in catalyzing reactions can be blocked by a large substrate, affecting both size and shape selectivity in the process.

3.9. Conclusion

In summary, a variety of oxocarbenium ion reactions can be catalyzed by cage **1.30**. Various pathways involving different intermediates can take place for these types of reactions. The reactivity is controlled through the manipulation of the size of both the nucleophile and electrophile. Furthermore, the reactivity is also affected by whether the leaving group of the electrophile can access the carboxylic acid groups in cage **1.30**. Overall, the study shows that cage **1.30** is an effective catalyst, showing high affinities for a variety of substrates and rapid turnover numbers. Factors such as product or substrate inhibition do not limit the reaction from occurring. Results show that smaller electrophiles inside cage **1.30** show minimal size-selectivity and react at a slower rate, and that guests that do not fill the cavity of the cage show a small effect on reactivity even when the size of the nucleophile or leaving group was altered. In addition, guests that are spherical can achieve up to a 1000-fold rate acceleration compared to diacid **1.35**. The host complex can be as active as the strong acid, CSA **3.6**. Cage **1.30**, overall, is reminiscent of enzymes in its ability to react rapidly with substrates of certain sizes and shapes, exhibiting strong rate accelerations during the reaction process.

3.10. References

1. Holloway, L. R.; Bogie, P. M.; Lyon, Y.; Ngai, C.; Miller, T. F.; Julian, R.R.; Hooley, R. J. Tandem reactivity of a self-assembled cage catalyst with endohedral acid groups. *J. Am. Chem. Soc.* **2018**, *140*, 8078–8081.
2. Bogie, P. M.; Holloway, L. R.; Ngai, C.; Miller, T. F.; Grewal, D. K.; Hooley, R. J. A self-assembled cage with endohedral acid groups both catalyzes substitution reactions and controls their molecularity. *Chem. Eur. J.* **2019**, *25*, 10232–10238.
3. Ma, S.; Smulders, M. M. J.; Hristova, Y.; Clegg, J. K.; Ronson, T. K.; Zarra, S.; Nitschke, J. R. Chain-reaction anion exchange between metal-organic cages. *J. Am. Chem. Soc.* **2013**, *135*, 5678–5684.
4. Manabe, K.; Iimura, S.; Sun, X. M.; Kobayashi, S. Dehydration reactions in water. Brønsted acid-surfactant-combined catalyst for ester, ether, thioether, and dithioacetal formation in water. *J. Am. Chem. Soc.* **2002**, *124*, 11971–11978.
5. Hong, C. M.; Bergman, R. G.; Raymond, K. N.; Toste, F. D. Self-assembled tetrahedral hosts as supramolecular catalysts. *Acc. Chem. Res.* **2018**, *51*, 2447–2455.
6. Fujita, M.; Umemoto, K.; Yoshizawa, M.; Fujita, N.; Kusukawa, T.; Biradha, K. Molecular paneling via coordination. *Chem. Commun.* **2001**, *6*, 509–518.
7. Harris, K.; Fujita, D.; Fujita, M. Giant hollow M_nL_{2n} spherical complexes: structure, functionalisation and applications. *Chem. Commun.* **2013**, *49*, 6703–6712.
8. Zhang, Q.; Catti, L.; Tiefenbacher, K. Catalysis inside the hexameric resorcinarene capsule. *Acc. Chem. Res.* **2018**, *51*, 2107–2114.
9. Ngai, C.; da Camara, B.; Woods, C. Z.; Hooley, R. J. Size and shape-selective oxocarbenium ion catalysis with a self-assembled cage host. *J. Org. Chem.* **2021**, *86*, 12862–12871.
10. Ngai, C.*; Bogie, P. M.*; Holloway, L. R.; Dietz, P. C.; Mueller, L. J.; Hooley, R. J. Cofactor-mediated nucleophilic substitution catalyzed by a self-assembled holoenzyme mimic. *J. Org. Chem.* **2019**, *84*, 12000–12008.

11. Brown, H.C. et al., in Braude, E.A. and F.C. Nachod *Determination of Organic Structures by Physical Methods*, Academic Press, New York, **1955**.
12. Dippy, J. F. J.; Hughes, S. R. C.; Rozanski, A. The dissociation constants of some symmetrically disubstituted succinic acids. *J. Chem. Soc.* **1959**, 2492–2498.
13. Deno, N. C.; Turner, J. O. The basicity of alcohols and ethers. *J. Org. Chem.* **1966**, *31*, 1969–1970.
14. Association constants calculated using BindFit software, found at <http://supramolecular.org>.
15. Hibbert, D. B.; Thordarson, P. The death of the Job plot, transparency, open science and online tools, uncertainty estimation methods and other developments in supramolecular chemistry data analysis. *Chem. Commun.* **2016**, *52*, 12792–12805.
16. Thordarson, P. Determining association constants from titration experiments in supramolecular chemistry. *Chem. Soc. Rev.* **2011**, *40*, 1305–1323.
17. Tiedemann, B. E. F.; Raymond, K. N. Dangling arms: a tetrahedral supramolecular host with partially encapsulated guests. *Angew. Chem., Int. Ed.* **2006**, *45*, 83–86.
18. Kirby, A. J. Enzyme mechanisms, models, and mimics. *Angew. Chem., Int. Ed.* **1996**, *35*, 707–724.

Chapter 4 – Supramolecular Cage-catalyzed oxa-Pictet Spengler Reaction

4.1. Introduction

While the acid cage **1.30** has proven to be an effective catalyst for both hydrolysis and thioetherification reactions with mild nucleophiles, these transformations are relatively simple.¹⁻³ Indeed, most reactions catalyzed by supramolecular hosts are generally uncomplicated and consists of only one or two steps such as cycloadditions or rearrangements.⁴⁻¹⁰ To catalyze more complex, multistep processes, supersized cavities that can fit multiple guests are usually required.¹¹⁻¹⁴ Smaller hosts can bind their guests tightly inside their cavities which can lead to various size-selective processes.¹⁵ While useful for binding smaller molecules, these smaller cavities are generally unable to accommodate larger, more complicated guests. This results in the inability to coencapsulate numerous guests inside which in turn makes the formation of product impossible. One notable exception to this is Raymond's Ga₄L₆ cage, in which organometallic reagents are used as cofactors to catalyze multistep reactions.¹⁶⁻²⁰

Despite all the advances that have been made in the field, enzymes are still more capable of catalyzing these multistep processes. Their active sites are decorated with functional groups that can bind multiple substrates inside the complex, leading to high specificity and selectivity. They can naturally tolerate both the presence and absence of large/small amounts of multiple different species. This is in contrast to traditional cages: small cages are overly size-selective and large cages, while able to effectively bind larger intermediates, weakly bind smaller guests. The general inability to bind smaller guests is due in part to the large cage's inability to tolerate empty space. The acid cage is an

exception to this generalization as the cavity can be filled with solvent. While supramolecular catalysts exhibit some of the features and traits displayed by enzymes, combining all these factors into one host is difficult.^{7,12,15,21-27} Cage **1.30**, with twelve internal carboxylic acid groups, has shown to be an effective host and serves as a good candidate to mimic enzymes in this way.¹ Experiments were performed with cage **1.30** to see if it can activate more complex, multistep reactions while retaining high rates of selectivity in the process. The choice of reaction is significant, as Fe-iminopyridine complexes²⁸ are not tolerant to strong nucleophiles, acids, or well-coordinating anions and are often insoluble in anything besides polar solvents.²⁹

4.2. Cage-catalyzed Oxa-Pictet Spengler Reaction

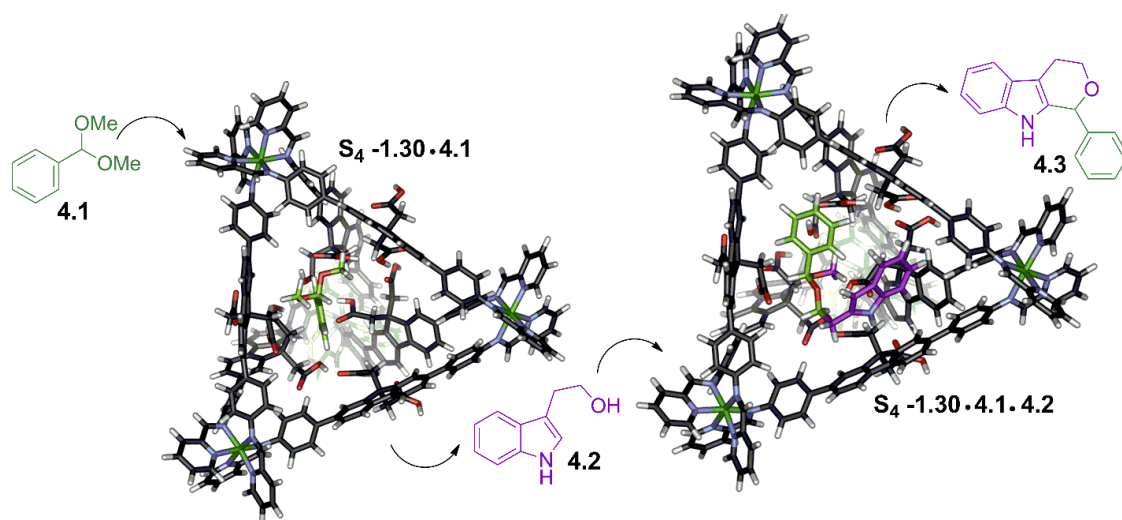


Figure 4.1. Cage-catalyzed oxa-Pictet Spengler reaction with acid cage **1.30** as the host.³⁰

Given that the cage **1.30** can accelerate reactions that proceed through benzylic cation and oxocarbenium ion intermediates, the multistep oxa-Pictet-Spengler cyclization was tested (Figure 4.1).³⁰ The oxa-Pictet Spengler reaction is the cyclization of tryptophan derivatives with an aldehyde and has been shown to be catalyzed by several strong Lewis

acids.^{31,32} Enantioselective outcomes are also feasible with the use of various organocatalysts.³³ Previous studies have shown that cage **1.30** can activate benzaldehyde dimethyl acetal **4.1** at 23 °C in CH₃CN.¹ Initial tests of the cage-catalyzed oxa-Pictet Spengler reactions were performed using **4.1** as the electrophile and tryptophol **4.2** as the nucleophile. Tryptophol **4.2** and 1.25 mol. eq. of acetal **4.1** and were mixed together in CD₃CN with 5% cage **1.30**, and the reaction was observed over time via ¹H NMR. Cage **1.30** was successfully able to perform the reaction, albeit with a low yield. This is likely because the hydrolysis of the acetal occurred faster than the cyclization when using undried deuterated acetonitrile, forming mainly the aldehyde byproduct rather than the cyclized product **4.3**. Cage **1.30** is not able to perform the cyclization between **4.1** and aldehydes.

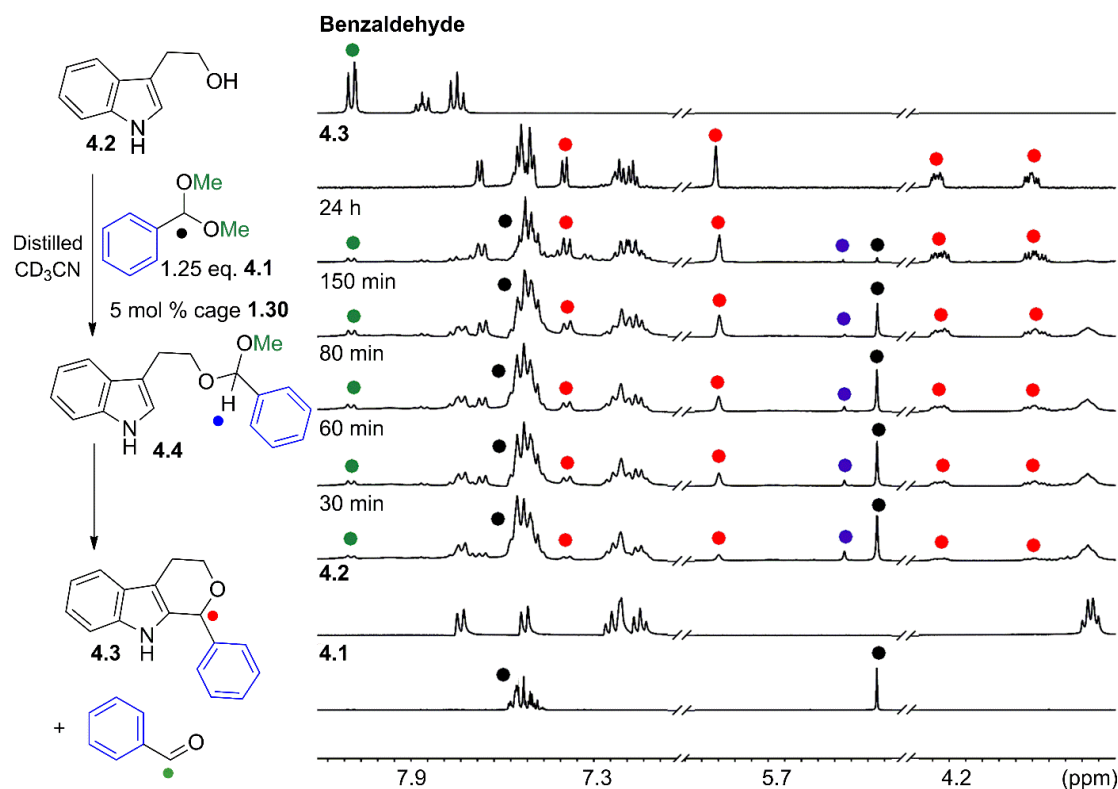


Figure 4.2. Expanded ¹H NMR spectra of the acid promoted reaction between **4.1** and **4.2** in the presence of 5 mol % cage **1.30**.³⁰

In an attempt to achieve cage-catalyzed cyclization using acetal **4.1**, the reaction was tested using distilled CD₃CN in air, minimizing the amount of water in the system enabling the reaction to succeed (Figure 4.2). In contrast to the previous reaction, large amounts of the cyclized product and small amounts of the aldehyde were observed. The presence of water (absorbed from the air) has some benefit as it enables us to analyze the mechanism. Using distilled CD₃CN in air is not only a simple solution but also gives us more insight into the reaction mechanism for different substrates by incorporating a competitive nucleophile (water) into the reaction. No cyclization was observed when using 5% of cage **1.28** or 30% of diacid **1.35** as control catalyst (Figure 4.3). The lack of cyclization is likely caused by the lack of reactive functional groups in cage **1.28**. Only when acidic functionality is introduced into the cavity of a host can we see the formation of the cyclization product. Twelve carboxylic acid functional groups, their acidity increased by the overall (positive) charge of the cage, are the facets that allow cage **1.30** to catalyze the cyclization reaction.

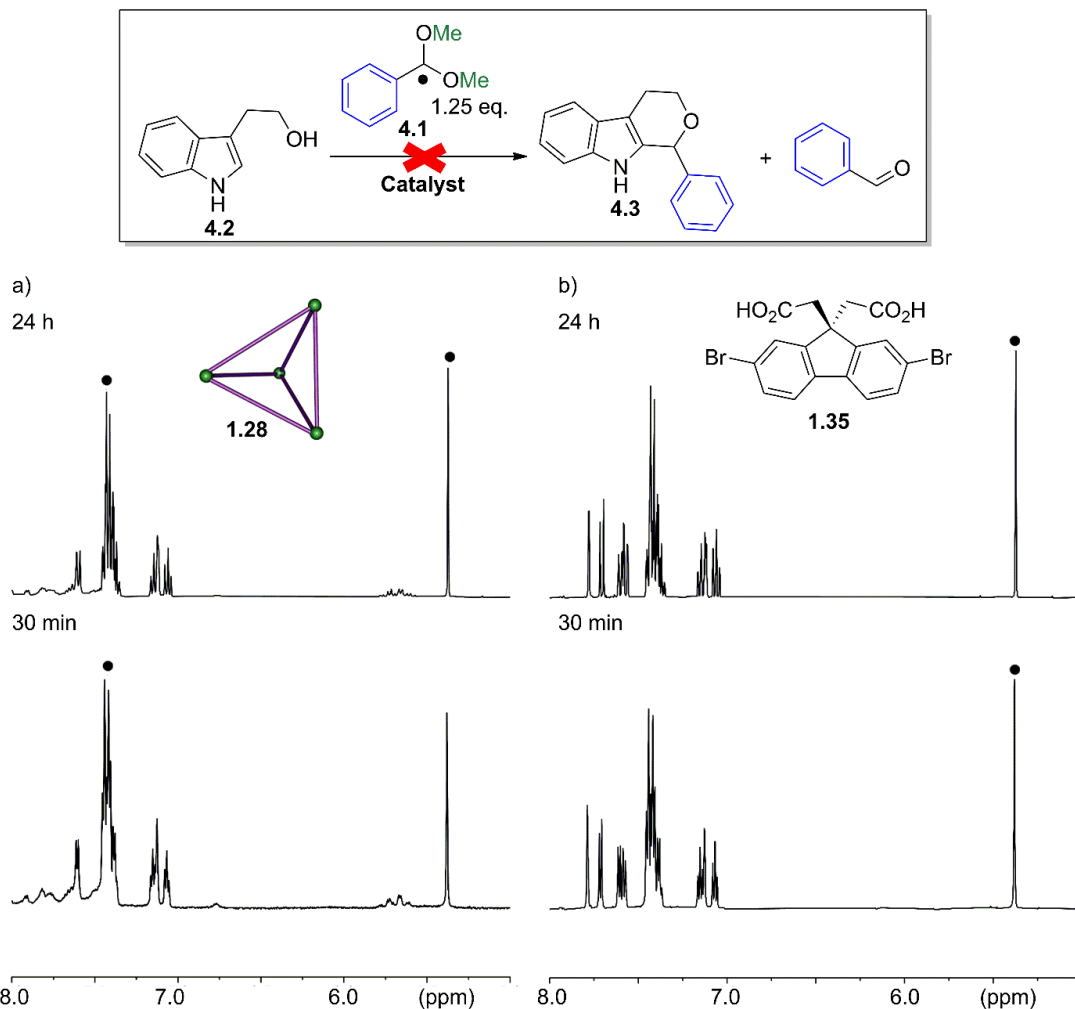


Figure 4.3. Control experiments with other cage hosts and acids for the oxa-Pictet Spengler reaction.³⁰

The oxa-Pictet Spengler is a challenging reaction for cage **1.30** to catalyze for two reasons. The first being that the reaction is usually performed in anhydrous, non-coordinating solvents. This is not a problem for small molecule Lewis acids that can coordinate freely to the different oxygen atoms that must be activated in the multistep mechanism. The second reason is that cage **1.30** must bind and activate both the acetal **4.1** and then activate the larger intermediate **4.4** for the indole and alcohol of **4.2** to attack the

carbonyl carbon of the electrophile. This is neither simple, nor a common feature for cages that are rigid and have inflexible cavities such as cage **1.30** (Figure 4.4).

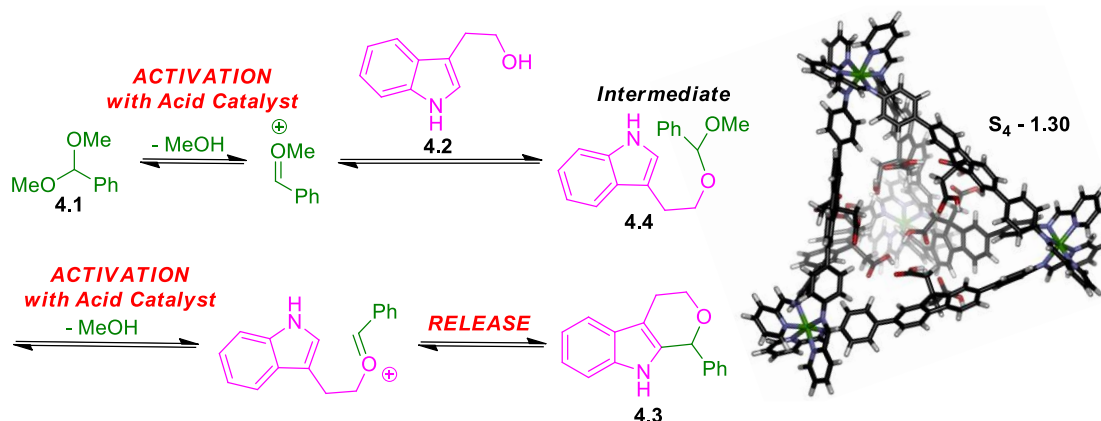


Figure 4.4. Reaction scheme of the oxa-Pictet Spengler reaction.³⁰

4.3. Reaction Scope

The scope of the oxa-Pictet Spengler reaction was extended to indoles and acetals of different sizes and reactivity using cage **1.30** as a catalyst (Figure 4.5; Table 4.1). The size of the acetal can be varied at the alcoholic R_2 (**4.1**, **4.7-4.8**) or R_3 position (**4.9-4.10**). Increasing the size of the R_2 leaving group from a dimethyl leaving group to a diethyl found in **4.7** or a dibutyl substituent found in **4.8** showed minimal effect when forming the cyclized product **4.4**. A yield of 80% was observed for both cases when using cage **1.30**.

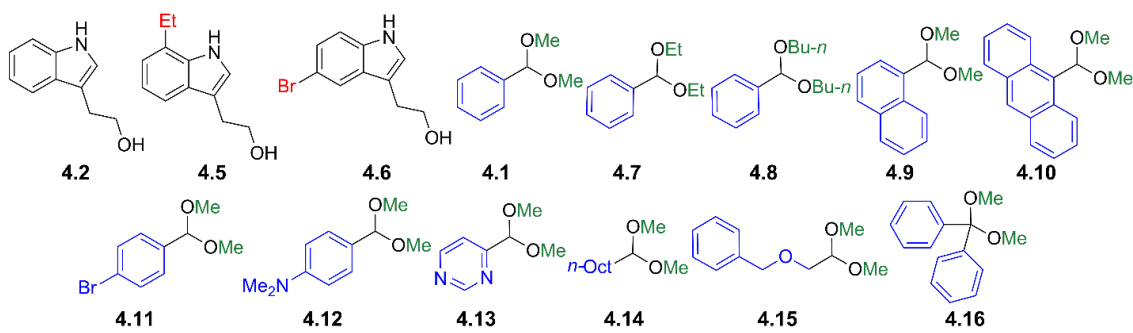
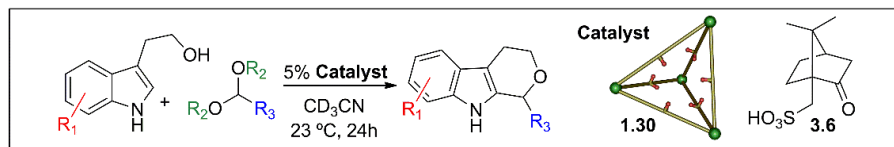


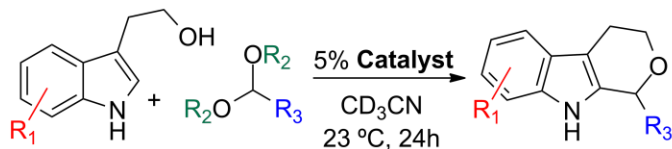
Figure 4.5. Indoles and acetals used in the oxa-Pictet Spengler reaction.³⁰

Increasing the size of the R₃ group in the acetal showed significant changes in reaction yield. The reaction yield lowered with each additional ring added to the acetal. The reaction with 1-naphthaldehyde *dimethyl acetal* **4.9** showed a 26% yield while the reaction with 9-(dimethoxymethyl)anthracene **4.10** yielded only 15% after 24 h. Interestingly, the hydrolysis varied, as 25% conversion to aldehyde was seen with **3.9** while 13% yield was observed when using **4.10**, as compared to only 7% obtained with benzaldehyde dimethyl acetal **4.1**.

In respect to **4.1**, aromatic dimethyl acetals with more electron poor rings (bromophenyl **4.11**, pyrimidine **4.13**) were, as anticipated, weak electrophiles for this reaction. Results showed no cyclization reaction or hydrolysis of the acetal observed with pyrimidine **4.13**, whereas a low yield of 17% into the cyclized product was seen with bromophenyl **4.11**. Alkyl acetals **4.14** and **4.15** and ketal **4.16** were also poor candidates for the reaction, resulting in no cyclization or low yields. Continuing the substrate scope, the most unexpected result observed was when 4-(dimethoxymethyl)-N,N-dimethylaniline

4.12 was utilized as the acetal. This acetal is more reactive with Brønsted acids but only showed a 56% product yield with cage **1.30** after 24 h.

Table 4.1. Yields for oxa-Pictet Spengler Cyclization promoted by cage **1.30** and CSA **3.6**.



Catalyst	Indole	Acetal/ Ketal	Cage 1.30 Product Yield %	Cage 1.30 Aldehyde Yield %	CSA 3.6 Product Yield %
		4.2	4.1	87	7
	4.5	4.1	39	19	62
	4.6	4.1	0	29	0
	4.2	4.7	80	11	84
	4.2	4.8	80	10	87
	4.2	4.9	26	25	62
	4.2	4.10	15	13	47
	4.2	4.11	17	9	53
	4.2	4.12	0	0	0
	4.2	4.13	12	14	52
	4.2	4.14	0	0	0
	4.2	4.15	56	22	15
	4.2	4.16	0	0	63

Reaction performed at 293 K in CH₃CN, [**4.2**, **4.5-4.6**] = 15.8 mM, [**4.1**, **4.7-4.16**] = 19.8 mM, [Catalyst] = 0.8 mM. Yield determined by integration against dioxane as standard (7.9 mM).³⁰

While the acetal was varied in size at two different locations, the indole was altered at one position. The larger 7-ethyl indole **4.5** was commercially available, while the 5-bromoindole **4.6** was synthesized in two steps.³⁴ These indoles were then reacted with acetal **4.1** and cage **1.30** using the same reaction conditions as before. In comparison with

4.2, the larger indoles **4.5** and **4.6** were not as effective with host **1.30**. Reaction between acetal **4.1** and tryptophol **4.5** lowered the yield, obtaining only 39% of the cyclized product, whereas the reaction with tryptophol **4.6** showed no oxa-Pictet Spengler with the host.

These results were then compared to the strong acid CSA **3.6** using similar reaction conditions. By reacting these substrates in a sealed flask using distilled CH₃CN, these conditions allowed for a comparison of the relative conversion between the two catalysts. In comparison with host **1.30**, the reactivity with CSA **3.6** showed less dependence on structure of the substrates. The most effective yields with CSA **3.6** were found again between the reaction with tryptophol **4.2** and acetals **4.1** and **4.7-4.8**, showing yields ranging from 84-90%. Furthermore, acetals **4.13** and **4.15**, which were unreactive with cage **1.30**, were also unreactive with CSA **3.6**, showing no conversion to product.

The most interesting results with CSA **3.6** were observed with the rest of the acetals. While factors such as substrates size and stabilizing groups significantly lowered the yields of the cyclized reaction with cage **1.30**, these acetals showed considerably greater yields between 47-63% with CSA **3.6**, regardless of these factors. For instance, the reactions between the larger acetals **4.9-4.11** and tryptophol **4.2** showed yields ranging from 47-62% compared to the low yields of 12-26% obtained with cage. In addition, alkyl acetal **4.14** was cyclized significantly slower in the cage-catalyzed reaction, showing a 12 % yield as opposed to a 52% yield obtained with CSA **3.6**.

The most surprising result of the study was when the cyclization reaction was performed with dimethylaminophenyl acetal **4.12** and CSA **3.6**. This acetal is very reactive, but only showed a 56% product yield with cage **1.30**. However, the cage-catalyzed reaction

was significantly faster than the reaction with CSA **3.6**, which gave only a 15% yield. Compared to CSA **3.6**, the cage is clearly selective for certain substrates. This selectivity is best observed when ketal **4.16** was used as the electrophile (Figure 4.6). The reaction with CSA **3.6** was able to form the cyclized product with a 63% yield after 24 h. However, no oxa-Pictet Spengler reaction was observed with cage **1.30** and only a small amount of hydrolysis into ketone **4.17** was seen.

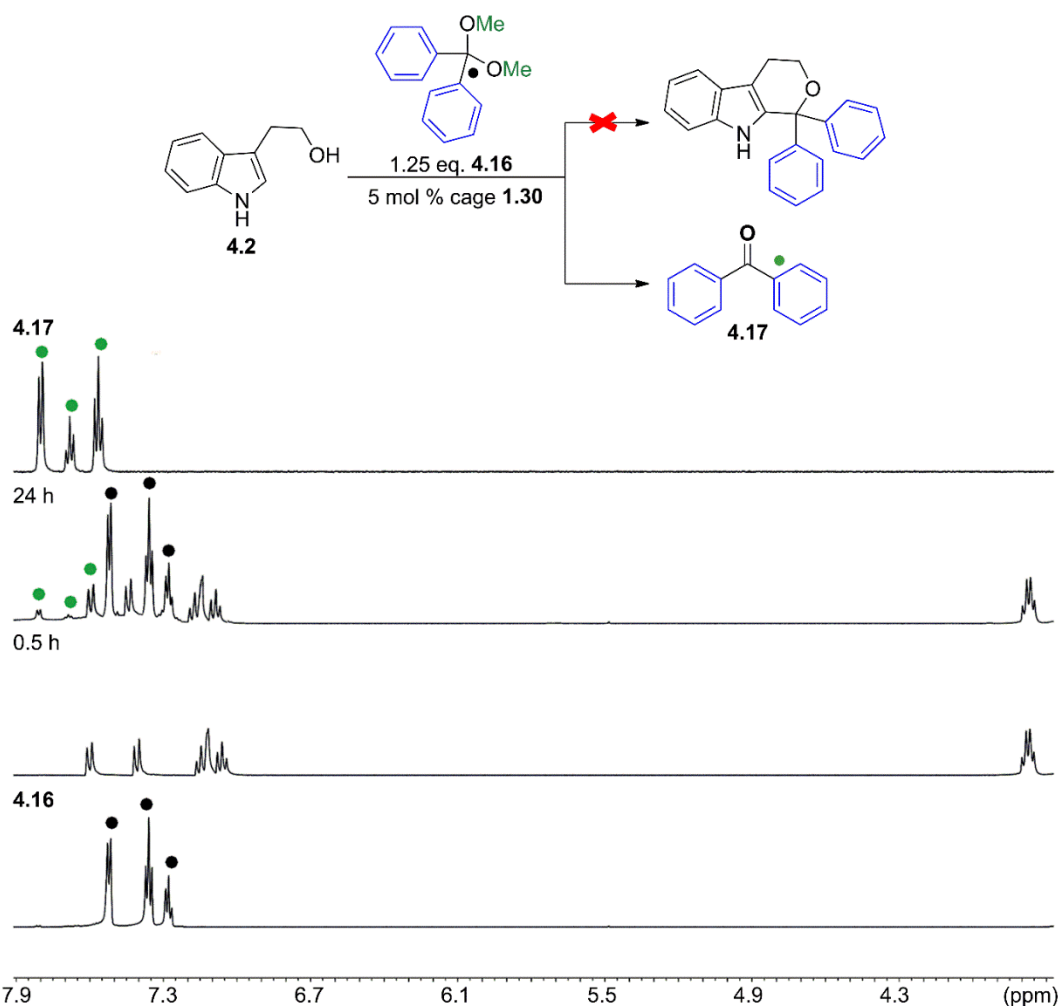


Figure 4.6. ¹H NMR spectra of the acid promoted reaction between **4.2** and **4.16** in the presence of 5 mol % cage **1.30**.³⁰

4.4. Host-Guest Binding Studies

These results reveal that the reaction with cage **1.30** is strongly influenced by both size and shape matching of the substrates in its internal cavity. To further investigate this selectivity, binding studies were performed to observe how cage **1.30** binds to the various substrates and products by UV/Vis absorbance titrations (Table 4.2). This method has shown to be effective in analyzing the binding of porous complexes such as cage **1.30**.^{1,2,35} Guests were titrated in a CH₃CN solution of cage **1.30**, and the absorbance changes of 300 and 330 nm were fitted using the Nelder-Mead method.³⁶⁻³⁸ Both 1:1 and 2:1 binding models were tested to determine the affinity and stoichiometry of each guest molecule, and the errors in each model were used to find out which model is most likely to occur.

Table 4.2. Binding affinities of various substrates and products.

1:2 Substrate	$K_1 \times 10^3 \text{ M}^{-1}$	$K_2 \times 10^3 \text{ M}^{-1}$	$\alpha (4K_2/K_1)$
4.1	8.6 ± 0.8	0.08 ± 0.002	0.04
4.7	20.0 ± 0.7	0.03 ± 0.001	0.06
4.8	34 ± 1.3	0.4 ± 0.01	0.05
4.9	4.7 ± 0.4	0.70 ± 0.04	0.60
1:1 Substrate	$K_1 \times 10^3 \text{ M}^{-1}$	1:1 Substrate	$K_1 \times 10^3 \text{ M}^{-1}$
4.2	3.9 ± 0.1	4.13	1.9 ± 0.04
4.5	4.1 ± 0.1	4.14	9.6 ± 0.4
4.6	7.4 ± 0.3	4.15	12 ± 1.0
4.10	4.0 ± 0.2	4.16	4.4 ± 0.5
4.11	12.0 ± 0.6	4.3	6.2 ± 0.3
4.12	8.3 ± 0.3	4.18	2.9 ± 0.1

Substrates

4.2: R₁ = H
 4.5: R₁ = Et
 4.6: R₁ = Br
 4.1: R₂ = Me
 4.7: R₂ = Et
 4.8: R₂ = *n*-Bu
 4.9: R₂ = C₁₀H₇
 4.10: R₂ = C₁₄H₉
 4.11: R₂ = C₆H₄Br
 4.12: R₂ = C₈H₁₀N
 4.13: R₂ = C₄H₃N₂
 4.14: R₂ = *n*-Oct
 4.15: R₂ = CH₂OBn
 4.16: R₂ = C₁₄H₁₃
 4.3: R₄ = Ph
 4.18: R₄ = C₁₄H₁₀

Reaction was performed at 296 K in CD₃CN, [**1.30**] = 3 μM, absorbance changes measured at 300/330nm.^{30,36-38}

Given the small size of most of these substrates, it is evident that binding to the host in a 2:1 manner is most likely to occur. However, results found that only the small acetals **4.1** and **4.7-4.9** favored the 2:1 model as opposed to the 1:1, while the larger substrates and products best fit the 1:1 binding model. Cages that form heteroternary complexes exhibit 2:1 binding also likely show some 1:1 binding character. As the reaction progresses, the substrates react forming intermediates that are comparable in size to the product, taking up more space in the cavity leading to binding in a 1:1 fashion. Products can be bound too tightly for them to easily leave the cavity, leading to product inhibition, and locking in some percentage of 1:1 binding. Other medium-sized substrates were more ambiguous when deciding upon binding models. Much like the heteroternary complexes formed using small substrates, these might bind in a 2:1 fashion to start the reaction and in a 1:1 fashion as the reaction proceeds. Large guests such as anthryl product **4.18** had high errors and undoubtedly only bound in a 1:1 fashion. Strong binding affinities of $>10^3 \text{ M}^{-1}$ were observed with all substrates. The 1:1 substrate varied in affinities between $2\text{-}12 \times 10^3 \text{ M}^{-1}$ while the 2:1 substrate showed a 7-fold variation in K_1 . In addition, guests that bound in a 2:1 manner all showed to exhibit negative cooperative binding.

Overall, all these guests showed relatively similar binding affinities due to their similar sizes and weak coordinating groups. Due to these guests having similar affinities, cage **1.30** can effectively catalyze the cyclization without one guest binding more effectively than the other substrates during the reaction. Cage **1.30** is not only capable of binding to each substrate but also has a cavity large enough to bind these products, intermediates, indoles, and acetals simultaneously.

4.5. Mechanistic Analysis

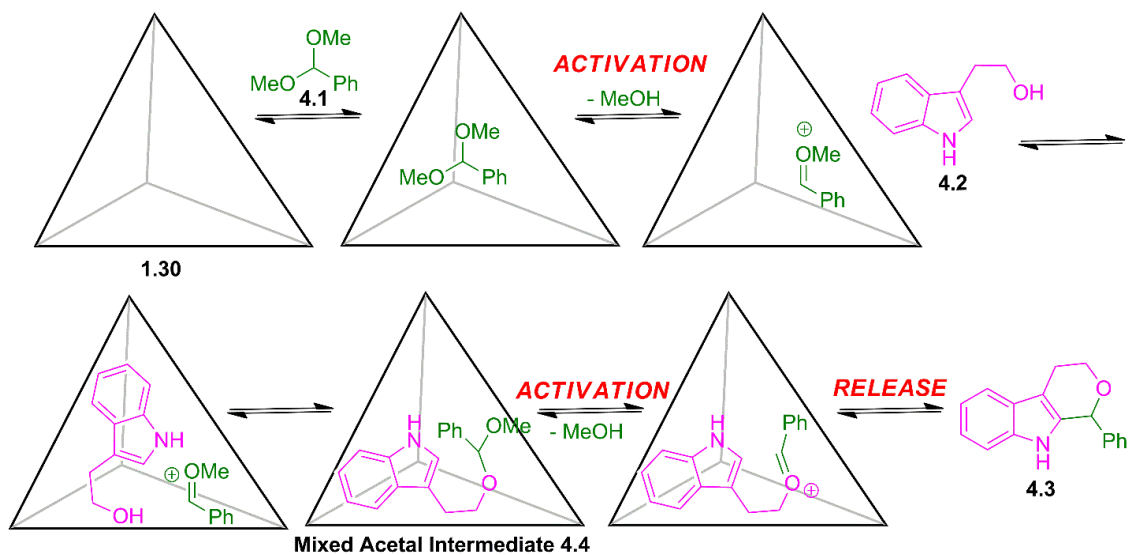


Figure 4.7. Mechanistic analysis of oxa-Pictet-Spengler with cage **1.30**.³⁰

This information on how the host binds to each substrate allows us to analyze the mechanism. The process first begins in binding acetal **4.1** inside the cavity of cage **1.30**. The acetal substrate is then protonated and activated by cage **1.30**. Methanol is lost in the process to afford the first oxocarbenium ion intermediate. While this step is feasible for all substrates, the next step is only practical if the acetal and the indole can be bound together inside the cavity to give the mixed acetal intermediate **4.4**. Smaller intermediates formed from smaller acetals can fit inside the cage more easily, increasing the rate of reaction. Conversely, larger intermediates from larger acetals are too large for the cage to retain, limiting formation of the desired product. Once the mixed acetal **4.4** is formed, the intermediate must be bound within cage **1.30** for the reaction to continue. As soon as the cage **1.30** binds the second intermediate, the acetal is protonated once more and activated for a second time to form a second oxocarbenium intermediate. The second intermediate is then cyclized to form product **4.3** and then released from the host (Figure 4.7).

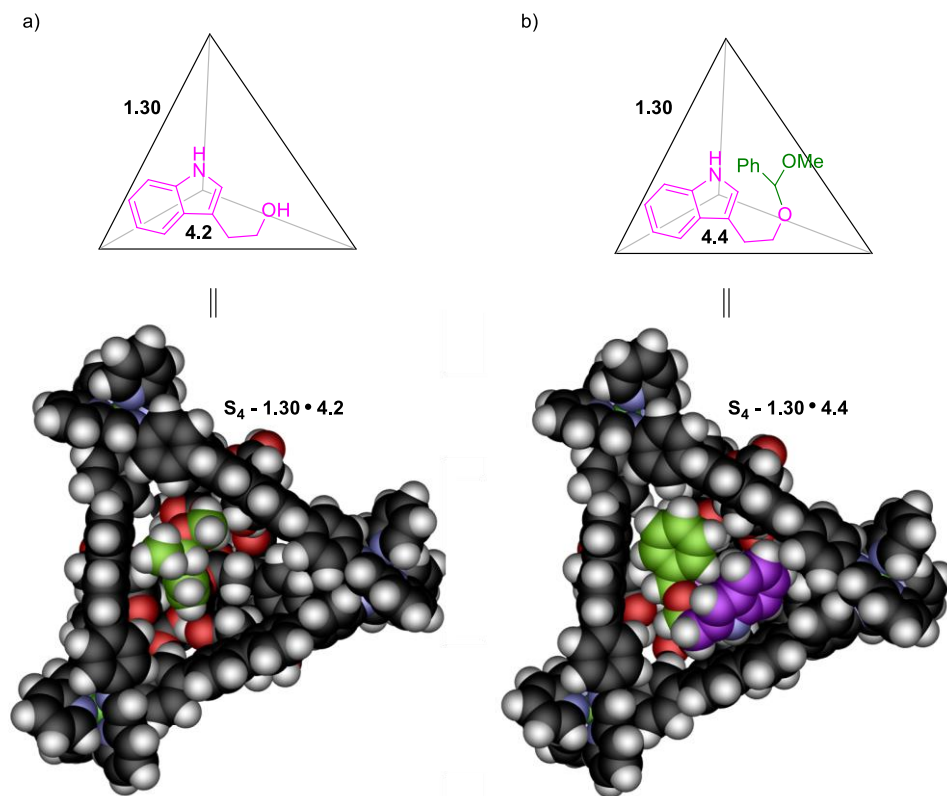


Figure 4.8. Model of cage **1.30** binding a) nucleophile **4.2**. b) intermediate **4.4**.³⁰

Cage **1.30** has a large cavity capable of accommodating these substrates and intermediates found in the mechanism. Models in which tryptophol **4.2** (Figure 4.8a) and intermediate **4.4** (Figure 4.8b) were bound separately inside cage **1.30** show that the cage can fit each guest inside and that **4.2** does not completely fill the host. In addition, intermediate **4.4** was observed in the reaction using ^1H NMR. Figure 4.9 shows that after 30 mins, two new peaks appear in the ^1H NMR. One of those peaks correspond to product **4.3** (red dot) being formed, whereas the other smaller peak is intermediate **4.4** (blue dot). Over time, acetal **4.1** is converted to product **4.3**, while the concentration of the mixed acetal decreases at a slow rate.

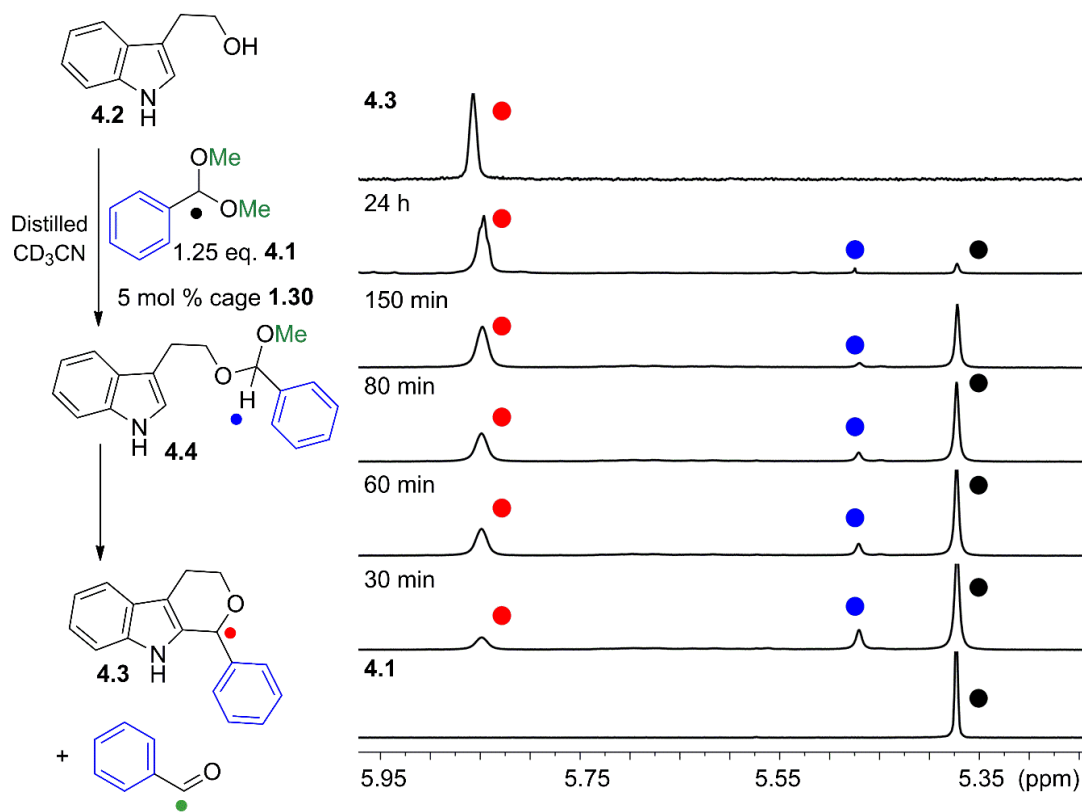


Figure 4.9. ^1H NMR of reaction showing disappearance of intermediate.³⁰

Lastly, the reaction was tested using a PF_6^- ion as a competitive guest. Cyclization into the product was observed using 5% of the cage and 50% of NaPF_6 (Figure 4.10). However, the reaction showed a 46% yield of **4.3** compared to 87% without the anion. This demonstrates that the competitive guest slows the reaction, but the anion does not completely block the cavity.

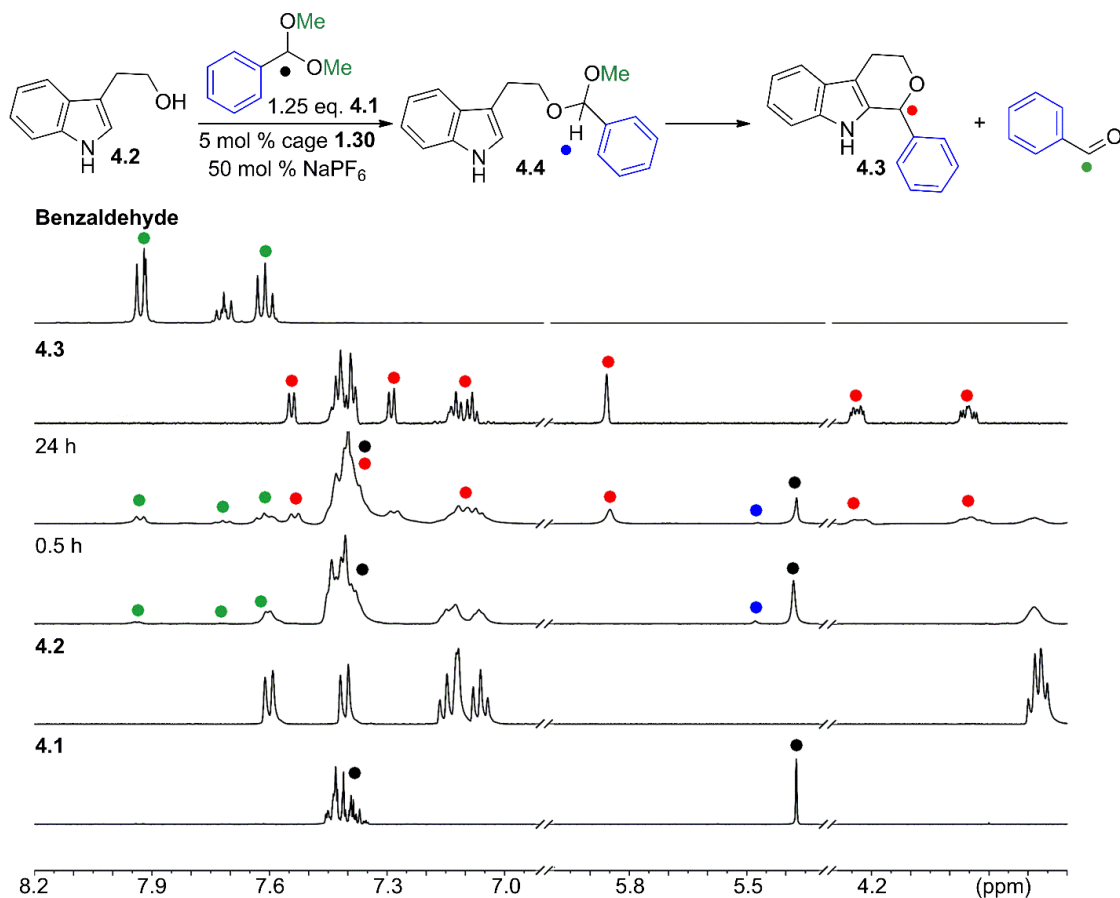


Figure 4.10. ^1H NMR spectra of the acid promoted substitution reaction between **4.1** and **4.2** in CD_3CN in the presence of 5 mol % cage **1.30** and 50 mol % of NaPF_6 .³⁰

4.6. Conclusion

Overall, this study reveals differences in reactivity based on the size and fitting of the intermediate molecule formed inside the cage. Fast in/out exchange of guests are observed which allows turnover and limits product or substrate inhibition. Large rate enhancements are observed in the cage-catalyzed reaction due to the internal carboxylic acid groups inside the cavity. Suitable size and shape matching between both reactants is critical for cyclization to occur. The cage-catalyzed reaction selectivity is unaffected by the length of the alcoholic leaving groups (R_2) on the acetals. However, an increase in size at the R_3

position on the acetal slows, or in the case of ketal **4.16**, completely stops the cyclization reaction. Size and fitting of the intermediate does not quite explain why **4.12** is more reactive in cage **1.30** than with CSA **3.6**. However, these results do show that the multistep reaction is impacted by more than just size and shape. This sensitivity to structure illustrates the unique, enzyme-like characteristics of the cage complex. The presence of an “active site” is essential for this reactivity profile, and this cage is the closest mimic of real enzymatic behavior in a synthetic system yet known.

4.7. References

1. Holloway, L. R.; Bogie, P. M.; Lyon, Y.; Ngai, C.; Miller, T. F.; Julian, R. R.; Hooley, R. J. Tandem reactivity of a self-assembled cage catalyst with endohedral acid groups. *J. Am. Chem. Soc.* **2018**, *140*, 8078–8081.
2. Bogie, P. M.; Holloway, L. R.; Ngai, C.; Miller, T. F.; Grewal, D.; Hooley, R. J. A self-assembled cage with endohedral acid groups both catalyzes substitution reactions and controls their molecularity. *Chem. Eur. J.* **2019**, *25*, 10232–10238.
3. Ngai, C.; da Camara, B.; Woods, C. Z.; Hooley, R. J. Size and shape-selective oxocarbenium ion catalysis with a self-assembled cage host. *J. Org. Chem.* **2021**, *86*, 12862–12871.
4. Martí-Centelles, V.; Lawrence, A. L.; Lusby, P. J. High activity and efficient turnover by a simple, self-assembled “artificial Diels–Alderase. *J. Am. Chem. Soc.* **2018**, *140*, 2862–2868.
5. Young, T. A.; Martí-Centelles, V.; Wang, J.; Lusby, P. J.; Duarte, F. Rationalizing the activity of an “artificial Diels–Alderase: establishing efficient and accurate protocols for calculating supramolecular catalysis. *J. Am. Chem. Soc.* **2019**, *142*, 1300–1310.
6. Jiao, J.; Li, Z.; Qiao, Z.; Li, X.; Liu, Y.; Dong, J.; Cui, Y. Design and self-assembly of hexahedral coordination cages for cascade reactions. *Nat. Commun.* **2018**, *9*, 1–8.
7. Hong, C. M.; Morimoto, M.; Kapustin, E. A.; Alzakhem, N.; Bergman, R. G.; Raymond, K. N.; Toste, F. D. Deconvoluting the role of charge in a supramolecular catalyst. *J. Am. Chem. Soc.* **2018**, *140*, 6591–6595.
8. Guo, J.; Fan, Y. Z.; Lu, Y. L.; Zheng, S. P.; Su, C. Y. Visible-light photocatalysis of asymmetric [2+ 2] cycloaddition in cage-confined nanospace merging chirality with triplet-state photosensitization. *Angew. Chem., Int. Ed.* **2020**, *59*, 8661–8669.
9. Roy, B.; Devaraj, A.; Saha, R.; Jharimune, S.; Chi, K. W.; Mukherjee, P. S. Catalytic intramolecular cycloaddition reactions by using a discrete molecular architecture. *Chem. Eur. J.* **2017**, *23*, 15704–15712.

10. Qiao, Y.; Zhang, L.; Li, J.; Lin, W.; Wang, Z. Switching on supramolecular catalysis via cavity mediation and electrostatic regulation. *Angew. Chem., Int. Ed.* **2016**, *128*, 12970–12974.
11. Ueda, Y.; Ito, H.; Fujita, D.; Fujita, M. Permeable self-assembled molecular containers for catalyst isolation enabling two-step cascade reactions. *J. Am. Chem. Soc.* **2017**, *139*, 6090–6093.
12. Yu, F.; Poole III, D.; Mathew, S.; Yan, N.; Hessels, J.; Orth, N.; Reek, J. N. Control over electrochemical water oxidation catalysis by preorganization of molecular ruthenium catalysts in self-assembled nanospheres. *Angew. Chem., Int. Ed.* **2018**, *130*, 11417–11421.
13. Wang, Q. Q.; Gonell, S.; Leenders, S. H.; Dürr, M.; Ivanović-Burmazović, I.; Reek, J. N. Self-assembled nanospheres with multiple endohedral binding sites pre-organize catalysts and substrates for highly efficient reactions. *Nat. Chem.* **2016**, *8*, 225–230.
14. Gramage-Doria, R.; Hessels, J.; Leenders, S. H.; Tröppner, O.; Dürr, M.; Ivanović-Burmazović, I.; Reek, J. N. Gold (I) catalysis at extreme concentrations inside self-assembled nanospheres. *Angew. Chem., Int. Ed.* **2014**, *126*, 13598–13602.
15. Brown, C. J.; Toste, F. D.; Bergman, R. G.; Raymond, K. N. Supramolecular catalysis in metal–ligand cluster hosts. *Chem. Rev.* **2015**, *115*, 3012–3035.
16. Hong, C. M.; Bergman, R. G.; Raymond, K. N.; Toste, F. D. Self-assembled tetrahedral hosts as supramolecular catalysts. *Acc. Chem. Res.* **2018**, *51*, 2447–2455.
17. Bender, T. A.; Bergman, R. G.; Raymond, K. N.; Toste, F. D. A supramolecular strategy for selective catalytic hydrogenation independent of remote chain length. *J. Am. Chem. Soc.* **2019**, *141*, 11806–11810.
18. Levin, M. D.; Kaphan, D. M.; Hong, C. M.; Bergman, R. G.; Raymond, K. N.; Toste, F. D. Scope and mechanism of cooperativity at the intersection of organometallic and supramolecular catalysis. *J. Am. Chem. Soc.* **2016**, *138*, 9682–9693.
19. Hart-Cooper, W. M.; Clary, K. N.; Toste, F. D.; Bergman, R. G.; Raymond, K. N. Selective monoterpene-like cyclization reactions achieved by water exclusion from reactive intermediates in a supramolecular catalyst. *J. Am. Chem. Soc.* **2012**, *134*, 17873–17876.

20. Bierschenk, S. M.; Bergman, R. G.; Raymond, K. N.; Toste, F. D. A nanovessel-catalyzed three-component aza-Darzens reaction. *J. Am. Chem. Soc.* **2020**, *142*, 733–737.
21. Sinha, I.; Mukherjee, P. S. Chemical transformations in confined space of coordination architectures. *Inorg. Chem.* **2018**, *57*, 4205–4221.
22. Zhang, Q.; Catti, L.; Tiefenbacher, K. Catalysis inside the hexameric resorcinarene capsule. *Acc. Chem. Res.* **2018**, *51*, 2107–2114.
23. Ward, M. D.; Hunter, C. A.; Williams, N. H. Coordination cages based on bis(pyrazolylpyridine) ligands: structures, dynamic behavior, guest binding, and catalysis. *Acc. Chem. Res.* **2018**, *51*, 2073–2082.
24. Suzuki, K.; Kawano, M.; Sato, S.; Fujita, M. Endohedral peptide lining of a self-assembled molecular sphere to generate chirality-confined hollows. *J. Am. Chem. Soc.* **2007**, *129*, 10652–10653.
25. Zhao, C.; Toste, F. D.; Raymond, K. N.; Bergman, R. G. Nucleophilic substitution catalyzed by a supramolecular cavity proceeds with retention of absolute stereochemistry. *J. Am. Chem. Soc.* **2014**, *136*, 14409–14412.
26. Pluth, M. D.; Bergman, R. G.; Raymond, K. N. Acid catalysis in basic solution: a supramolecular host promotes orthoformate hydrolysis. *Science*. **2007**, *316*, 85–88.
27. Fiedler, D.; Bergman, R. G.; Raymond, K. N. Supramolecular catalysis of a unimolecular transformation: Aza-Cope rearrangement within a self-assembled host. *Angew. Chem., Int. Ed.* **2004**, *116*, 6916–6919.
28. Mal, P.; Schultz, D.; Beyeh, K.; Rissanen, K.; Nitschke, J. R. An unlockable–relockable iron cage by subcomponent self-assembly. *Angew. Chem., Int. Ed.* **2008**, *47*, 8297–8301.
29. Percástegui, E. G.; Mosquera, J.; Ronson, T. K.; Plajer, A. J.; Kieffer, M.; Nitschke, J. R. Waterproof architectures through subcomponent self-assembly. *Chem. Sci.* **2019**, *10*, 2006–2018.

30. Ngai, C.; Sanchez-Marsetti, C. M.; Harman, W. H.; Hooley, R. J. Supramolecular catalysis of the oxa-Pictet–Spengler reaction with an endohedrally functionalized self-assembled cage complex. *Angew. Chem., Int. Ed.* **2020**, *59*, 23505–23509.
31. Cox, E. D.; Cook, J. M. The Pictet–Spengler condensation: a new direction for an old reaction. *Chem Rev.* **1995**, *95*, 1797–1842.
32. Stöckigt, J.; Antonchick, A. P.; Wu, F.; Waldmann, H. The Pictet–Spengler reaction in nature and in organic chemistry. *Angew. Chem., Int. Ed.* **2011**, *50*, 8538–8564.
33. Zhao, C.; Chen, S. B.; Seidel, D. Direct formation of oxocarbenium ions under weakly acidic conditions: catalytic enantioselective oxa-Pictet–Spengler reactions. *J. Am. Chem. Soc.* **2016**, *138*, 9053–9056.
34. Fu, L.; Davies, H. M. Scope of the reactions of indolyl- and pyrrolyl-tethered N-sulfonyl-1, 2, 3-triazoles: Rhodium (II)-catalyzed synthesis of indole- and pyrrole-fused polycyclic compounds. *Org. Lett.* **2017**, *19*, 1504–1507.
35. Ngai, C.; Bogie, P. M.; Holloway, L. R.; Dietz, P. C.; Mueller, L. J.; Hooley, R. J. **2019**. Cofactor-mediated nucleophilic substitution catalyzed by a self-assembled holoenzyme mimic. *J. Org. Chem.* **2019**, *84*, 12000–12008.
36. Association constants calculated using BindFit software, found at <http://supramolecular.org>.
37. Hibbert, D. B.; Thordarson, P. The death of the Job plot, transparency, open science and online tools, uncertainty estimation methods and other developments in supramolecular chemistry data analysis. *Chem. Commun.* **2016**, *52*, 12792–12805.
38. Thordarson, P. Determining association constants from titration experiments in supramolecular chemistry. *Chem. Soc. Rev.* **2011**, *40*, 1305–1323.

Chapter 5 – Biomimetic Catalysis via a Cofactor-Mediated Type Mechanism

5.1. Introduction

Another method to mimic enzymes, other than creating functionalized active sites, is through a cofactor-mediated process.¹ Apoenzymes are inactive by themselves but can form an active holoenzyme complex after binding with species such as flavins,² pyridoxal phosphate (PLP),³ or cobalamin.⁴ In doing so, these complexes become capable of binding with additional substrates and mediating their reactivity, thus enhancing both reaction rate and stereoselectivity. While the mechanism of cofactor-mediated catalysis has led to many prominent synthetic transformations throughout the years, mimics found in supramolecular chemistry are less common, and few examples exist.^{5–9} This is mainly because the binding, activating, and turning over multiple different species within a synthetic host is still inherently challenging.^{10–12} The examples of hosts that exist and can perform all these functions are usually very large Pd₁₂L₂₄ and Pd₂₄L₄₈ nanospheres¹³ or self-assembled resorcinarene hexamers¹⁴ with cavity volumes greater than 1375 Å³.^{15,16} These large nanospheres can bind multiple small molecules and catalyze various Bronsted acid^{17,18} or gold-catalyzed cyclization reactions,^{19,20} iminium-catalyzed conjugate additions,²¹ and carbonyl-olefin metatheses.²² However, due to their size, their binding affinities to these guests are relatively low. In contrast to these hosts, cages **1.28** and **1.30** (Figure 5.1) show high binding affinities for neutral molecules with affinities $\sim 10^5$ M⁻¹ in CH₃CN.²³

In this dissertation, it has been demonstrated that cage **1.30** is an effective biomimetic catalyst for both tandem and nucleophilic substitution reactions as well as various reactions that proceed through cations and oxocarbenium ions.^{23–26} As the substitution process with

cage **1.30** involves the formation of mixed ternary host-guest complexes, this suggests the potential for one of the two cage complexes to be used as a host for a cofactor-mediated process.²⁴ Since the thioetherification of triphenylmethanol **2.1** with **PrSH** described in Chapter 2 is well-suited for mechanistic analysis, initial tests were performed to see if unfunctionalized cage **1.28** could also catalyze the reaction in the presence of an appropriately sized acidic cofactor (Figure 5.1).^{24,27}

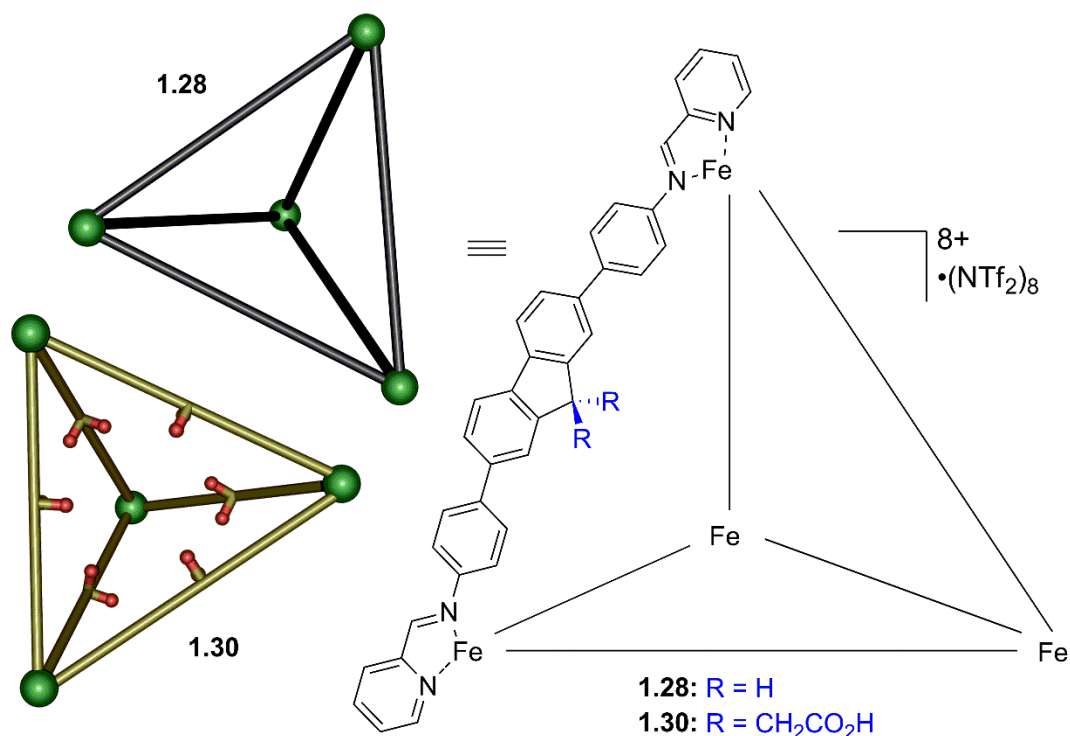


Figure 5.1. Structural and graphic models of unfunctionalized cage **1.28** and acid cage **1.30**.²⁷

5.2. Cofactor-mediated Catalysis

When triphenylmethanol **2.1** and **PrSH** were treated with cage **1.30**, a significant rate enhancement was observed over the course of various control processes.²⁴ To test the cooperative process, initial tests were performed with the fluorenyl-based diacid control

1.35 in the presence of cage **1.28**. Triphenylmethanol **2.1** was heated at 80 °C with 1.25 equiv. of **PrSH** in the presence of 5 mol % cage **1.28** and 30 mol % diacid **1.35** in CD₃CN. The initial rate of the reaction forming thioether **2.5** was monitored by ¹H NMR.

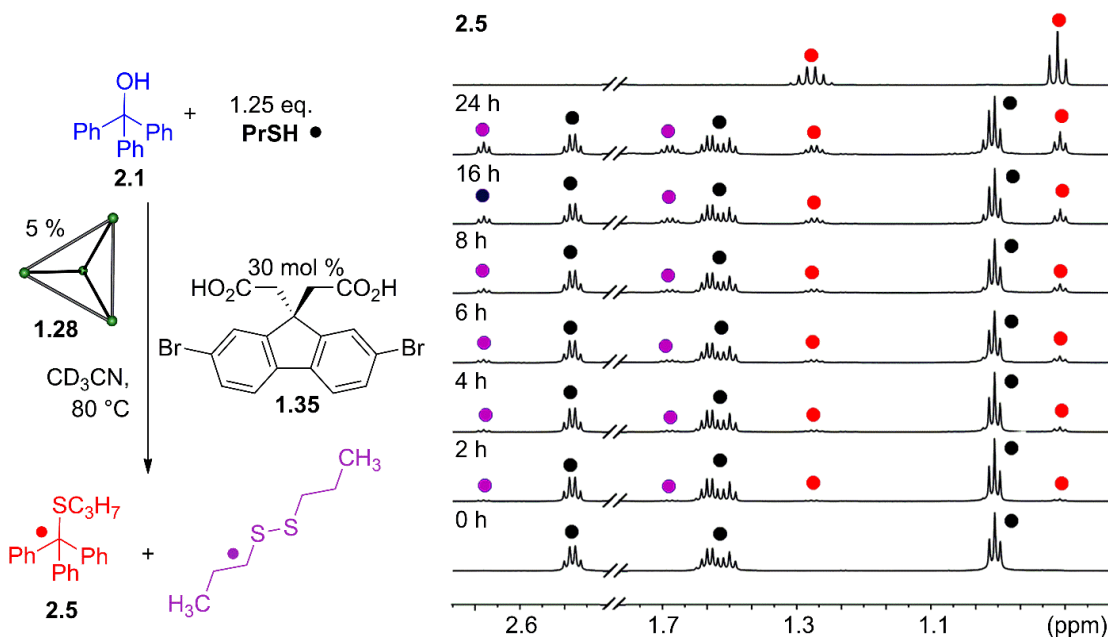


Figure 5.2. Expanded ¹H NMR spectra of the acid-promoted substitution reaction between **2.1** and **PrSH** in the presence of 5 mol % cage **1.30** and 30 mol % acid **1.35**.²⁷

The data in Figure 5.2 shows that the reaction was indeed catalyzed by the **1.28•1.35** combination, with some small amounts of disulfide detected, and no cage decomposition was observed over time, even after 12 h at reflux (Figure 5.2). The relative reaction rate was observed over time, even after 12 h at reflux (Figure 5.2). The relative reaction rate obtained was compared with the rates found when using only host **1.30** and diacid **1.35** in the process. The host-guest complex **1.28•1.35** is a considerably more effective catalyst for nucleophilic substitution than diacid **1.35** alone, showing more than a 50-fold increase in the initial rate compared to the reaction catalyzed by 30 mol % **1.35**.²⁷ Cage **1.28** alone was not capable of catalyzing the reaction by itself; the reaction was catalyzed using the combination of **1.28•1.35**. In comparing the cofactor-mediated process to the reaction

catalyzed by acid cage **1.30**, the reaction was found to be ~30 times slower than with acid cage **1.35**. While the reaction with **1.28**•**1.35** was considerably slower ($V = 39 \times 10^{-4}$ mM/min) than cage **1.30** ($V = 383 \times 10^{-4}$ mM/min), the experiment showed how effective the reaction is when cage **1.28** is combined with an acidic cofactor (Figure 5.3).²⁴ Diacid **1.35** is significantly enhanced in the presence of cage **1.28**, although **1.28** possesses no reactive functional groups. The results suggest that molecular recognition effects are involved in the cofactor-mediated process, and diacid **1.35** undeniably behaves as a cofactor and cage **1.28** as a holoenzyme mimic.

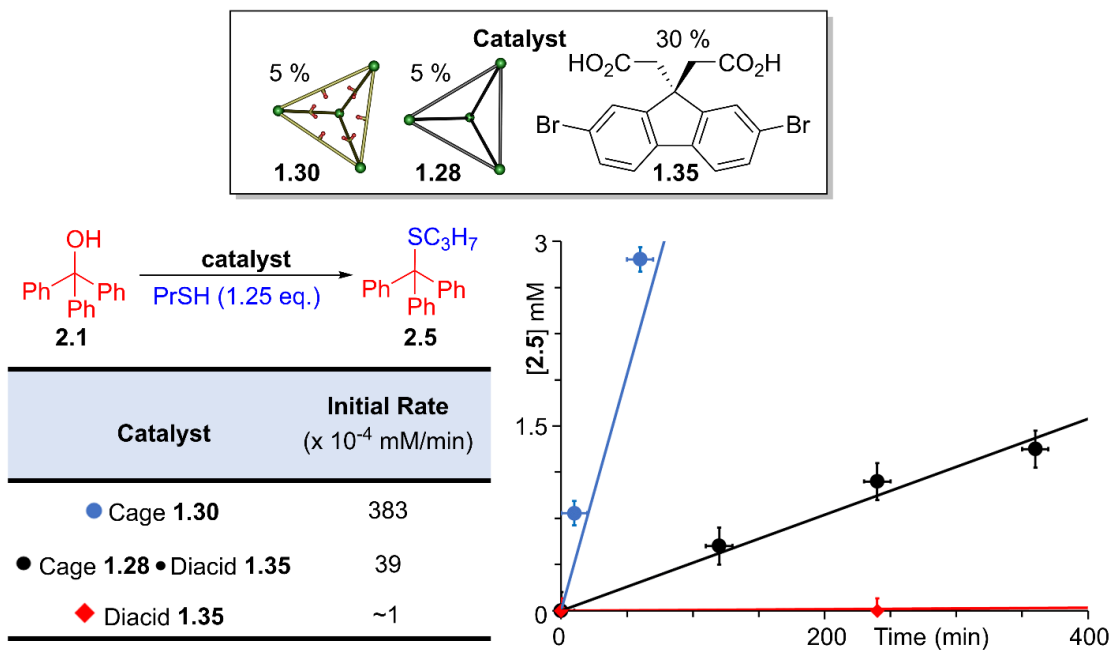


Figure 5.3. Comparison of initial rates to the cofactor-mediated reaction.^{24,27}

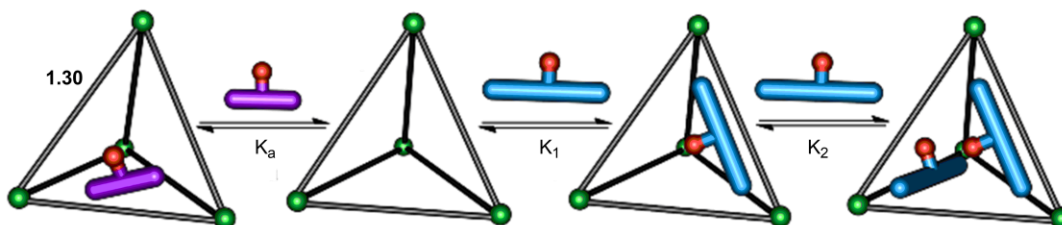
5.3. Binding of Various Substrates and Products

Host-guest binding studies were then used to determine if the cofactor-mediated reaction with cage **1.28** was due to molecular recognition. Although synthesized from a similar scaffold, there are several differences between cages **1.28** and **1.30** that need to be

considered when investigating the binding. The unfunctionalized cage **1.28** has a larger internal cavity than the acid cage **1.30**, cannot take advantage of the polar interactions between the carboxylic acid groups and guest in complex **1.30**, and has larger gaps between the panels due to a lack of functional groups in the cavity.²³ As a result, lower guest affinities should be observed in cage **1.28**, especially for small neutral molecules.

However, cage **1.28** has a complex structure and analyzing its binding to various guests is difficult. This is because cage **1.28** exists as three metal-centered isomers, and the ligand walls and cavity are large.²³ Methods such as the NMR time scale are not effective methods for investigation due to the fast in/out exchange rates of all guests, and only small changes in the chemical shifts of either guest or host are observed in the ¹H NMR.

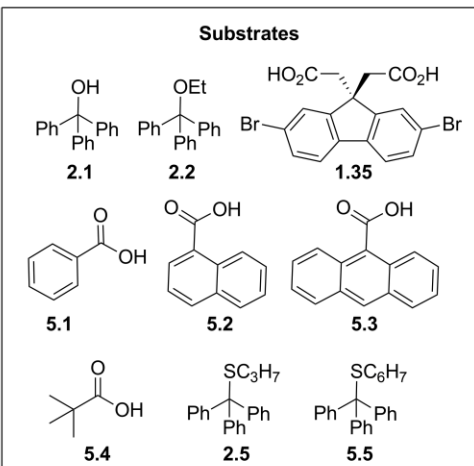
Table 5.1. Binding affinities to various substrates and products.



1:2 Substrate	$K_1 \times 10^3 \text{ M}^{-1}$	$K_2 \times 10^3 \text{ M}^{-1}$	$\alpha (4K_2/K_1)$
OctSH	174 ± 43	0.78 ± 0.53	0.018
2.2	47.1 ± 8.5	2.11 ± 0.38	0.18
1.35	19 ± 11	244 ± 89	51

1:1 Substrate	$K_1 \times 10^3 \text{ M}^{-1}$	1:1 Substrate	$K_1 \times 10^3 \text{ M}^{-1}$
PrSH	58.5 ± 47	5.4	2.4 ± 0.15
2.1	14.5 ± 0.77	2.5	24.8 ± 1.5
5.1	25.5 ± 1.0	5.5	91.7 ± 7.8
5.2	102.1 ± 5.2	(OctS) ₂	76.11 ± 3.8
5.3	95.4 ± 5.5		

Substrates



2.1: c1ccc(cc1)C(O)(c2ccccc2)c3ccccc3
 2.2: c1ccc(cc1)C(OCC)(c2ccccc2)c3ccccc3
 1.35: O=C(O)[C@H](c1ccc(Br)cc1)[C@@H](C(=O)O)c2ccc(Br)cc2
 5.1: c1ccc(cc1)C(=O)O
 5.2: O=C(O)c1ccc2ccccc2c1
 5.3: O=C(O)c1ccc2cc3ccccc3cc2c1
 5.4: CC(C)(C)C(=O)O
 2.5: c1ccc(cc1)C(SC3H7)(c2ccccc2)c3ccccc3
 5.5: c1ccc(cc1)C(SC3H7)(c2ccccc2)c3ccccc3

Titration were performed in CH₃CN, [**1.28**] = 1.5 μM, absorbance changes measured at 300/330 nm and 370 nm.^{27, 28–29}

While the NMR time scale method has its difficulties, UV-vis absorbance titrations are, fortunately, an effective method for measuring the binding of the supramolecular cages to various guests. High binding affinities and changes in the absorbance of cage **1.28** occur even at micromolar concentrations in CH₃CN. In this method, each guest was titrated into a 1.5 μM solution of cage **1.28** in CH₃CN, and changes in absorbance were noted at 330 and 370 nm. The affinities were initially fit to 1:1 and 1:2 binding models through Bindfit and then recalculated in greater detail by Dr. Len Mueller using the same mathematical model to determine the best fit for each compound.^{28,29} If cage **1.28** binds the guest in a 1:2 manner, it can exhibit either positive or negative cooperative binding. As discussed briefly in Chapter 3, negative cooperativity means that the addition of the second guest is disfavored by the first guest, whereas positive cooperativity means the first guest strengthens the binding of the second guest. Cooperativity is calculated by dividing $4K_2$ over K_1 to obtain an α constant. If $\alpha > 1$, the cooperativity is positive, and if $\alpha < 1$, the cooperativity is negative.²⁸

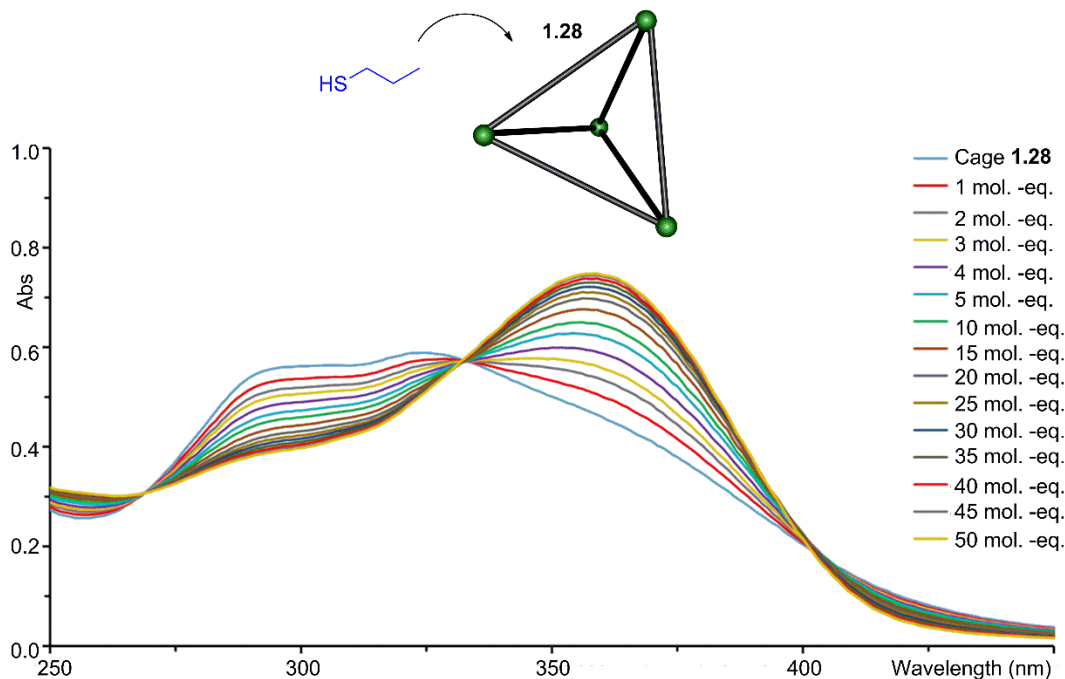


Figure 5.4. UV-Vis absorption titration of **PrSH** into a solution of **1.28** in CH_3CN .²⁷

To allow for a mechanistic investigation of the reaction, twelve different substrates were tested and analyzed (Table 5.1) by Dr. Paul Bogie. The substrates tested were the following: two trityl electrophiles (**2.1**, **2.2**), two differently sized nucleophiles (**PrSH**, **OctSH**), five acidic cofactors (**1.35**, **5.1**, **5.2**, **5.3**, **5.4**), two thioether products (**2.5**, **5.5**), and the dioctyl disulfide (**OctS**)₂. All substrates showed a strong affinity for cage **1.28**, even small guests such as **PrSH** (Figure 5.4). Pivalic acid **5.4** ($K_a = 2.4 \times 10^3$) was found to have the weakest affinity for cage **1.28**, while naphthoic acid **5.2** ($K_a = 102.1 \times 10^3$) was observed to have the strongest affinity. Although the larger guests exhibited greater affinities than the smaller guests, all the products were bound strongly, signifying that product inhibition can occur.

To determine the preference of each molecule for either the 1:1 or 1:2 binding model, the titration data were subjected to calculations using the same equations from Chapter 2 and confirmed through statistics by Dr. Len Mueller.^{24,28-29} From this analysis, it was found that many of these substrates bind in a 1:1 manner. However, there are several large guests that fit the 1:2 model best. The smallest guests, i.e. benzoic acid **5.1**, naphthoic acid **5.2**, pivalic acid **5.4**, and **PrSH**, can clearly bind in a 1:1 fashion. Slightly larger guests, such as anthroic acid **5.3** and triphenylmethanol **2.1**, are more ambiguous in affinity and could potentially bind in a 1:2 manner; however, the 1:1 binding model was statistically shown to be more probable. The guests that can clearly bind in a 1:2 manner are **OctSH**, ether **2.2**, and diacid **1.35**. The cooperativity for these guests, however, is not constant. **OctSH** and ether **2.2** exhibit negative cooperativity, while the diacid **1.35** displays strong positive cooperativity with $\alpha = 51$. The reason for this is unclear, but a potential explanation could be that such cooperativity is due to multiple H-bonds between the two diacids bonding inside the cavity.

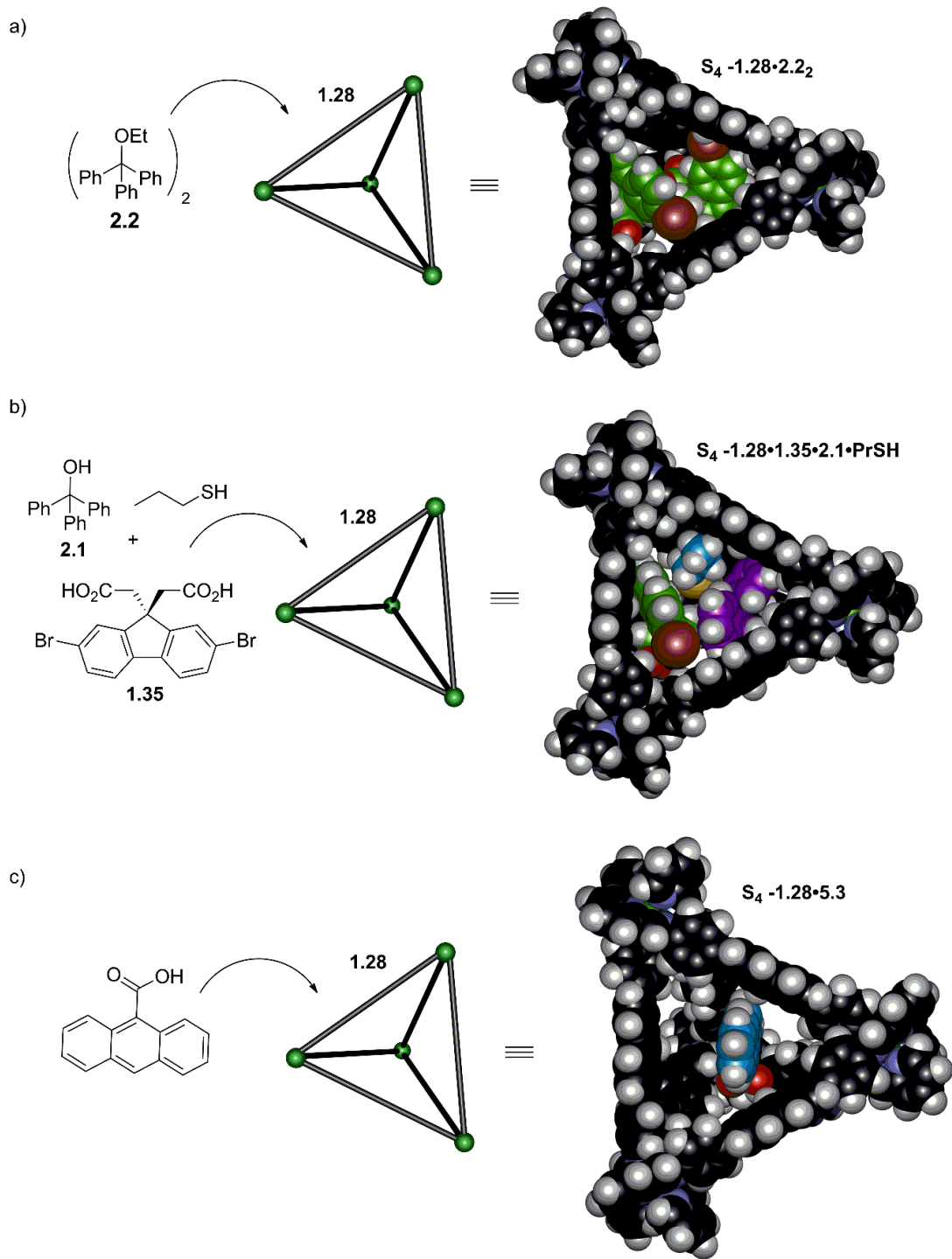


Figure 5.5. Minimized structures of guests encapsulated in cage **5.2** (SPARTAN).²⁷

Minimized structures were then made to illustrate the different binding modes of the cage complex in the reaction. Since the internal cavity of cage **1.28** is quite large, all the components in the reaction are small enough to possibly form ternary complexes or higher. The molecular minimization of the complex of **1.28•2.2₂** (Figure 5.5a), demonstrates the ease with which ternary complexes can be formed, even when larger substrates are used. Furthermore, it is shown that all three reactants in the thioetherification reaction **1.28•1.35•2.1•PrSH** (Figure 5.5b) can fit inside the cavity, leading to the formation of a quaternary complex, even though it is entropically unfavorable. This presents the question of why such high binding constants are observed, even in the cases of guests as small as **PrSH**. Large spaces in the cavity are observed upon binding only one guest in **1.28•5.3** (Figure 5.3c). The remainder of the cavity can be filled with solvent molecules, but the 55% occupancy rule shown by Rebek is not prevalent in this case.³⁰ The most reasonable suggestion is that the C-H/ π and π - π interactions between the small polar guests and the aromatic walls of cage **5.2** allow the transient formation of host-guest complexes.³¹⁻³³ Overall, the models provide possible representations of the host-guest interactions and complexes formed. The binding analysis provides evidence that the reaction is accelerated due to molecular recognition and occurs due to the host's ability to bind multiple species closely together within the cavity.

5.4. Varying the Size and Acidity of the Cofactor

To further this study, the kinetics of the reaction were investigated by varying one of the reaction's three components. Thus, the effect of varying the cofactor based on differences in size and pKa was analyzed.^{35,36} Five different cofactors were compared, and

all conditions and concentrations used for the reaction were maintained. The fluorenyl diacid **1.35** is the largest cofactor, with an estimated pKa of ~ 3.7 (based on comparison with 3,3-dimethylglutarate).^{35,36} The other cofactors, **5.1–5.4**, have only slight differences in pKa (**5.1** = 3.65, **5.2** = 3.69, **5.3** = 4.20, **5.4** = 5.03) but have significant differences in volume. Despite these small differences, the various cofactors showed substantial variation in catalytic activity, even in the absence of cage **1.28**. The initial rates for both the cage-mediated reaction and the reaction with the cofactor alone, in the absence of cage **5.2**, are shown in Figure 5.6 and Table 5.2.

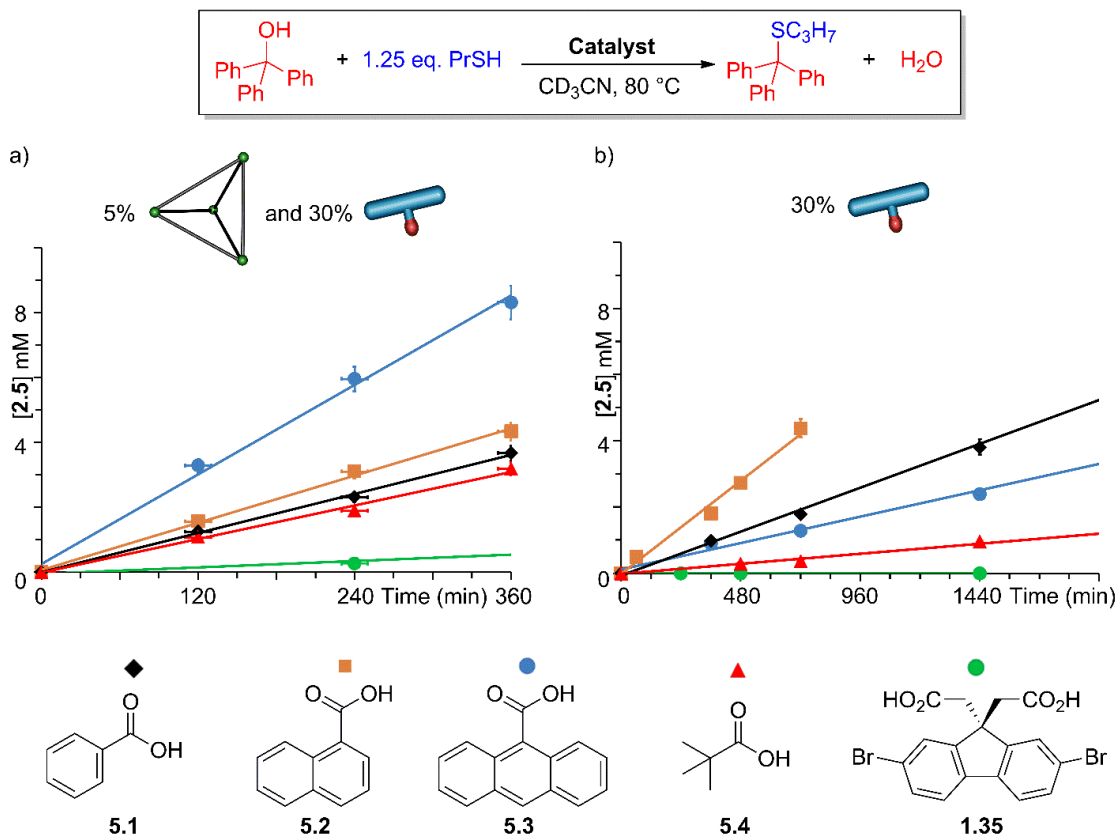
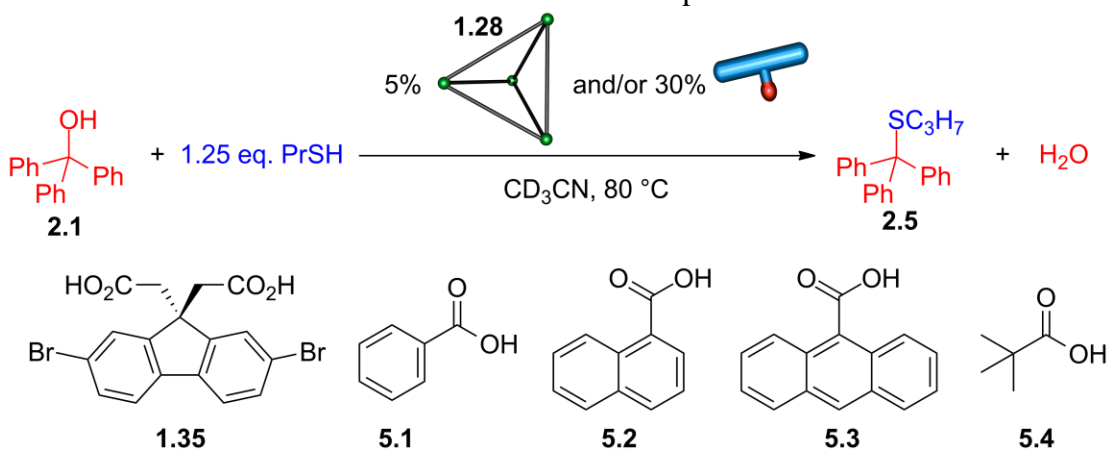


Figure 5.6. Reaction progress over time for thioetherification of electrophile **2.1** and **2.2** with PrSH. a) 5 mol % cage **1.28**/30 mol% cofactor **1.35**, **5.1–5.4** b) 30 mol % cofactor **1.35**, **5.1–5.4**.²⁷

When the reaction was catalyzed using 30 mol% of the cofactor alone, the initial rates varied to some extent and did not follow the trend of pKa. The best catalyst for this reaction was found to be 1-naphthoic acid **5.2**, while the diacid **1.35** promoted the reaction the least, despite having a similar pKa. The overall reaction rate order was **5.2** > **5.1** > **5.3** > **5.4** > **1.35**. The process was not effective when using the cofactor alone, with less than 30% conversion obtained after six hours at reflux (Figure 5.6b).

Table 5.2. Initial rates of thioetherification of electrophile **2.1** and **2.2** with **PrSH**.



Acid Cofactor	pKa	Cage Rate with Cofactor (x 10 ⁻⁴ mM/min)	Cofactor Rate (x 10 ⁻⁴ mM/min)	Acceleration
1.35	~3.70	39	0.7	56
5.1	3.65	229	19	12
5.2	3.69	126	67	1.9
5.3	4.20	109	33	3.3
5.4	5.03	92	8	12

[**2.1**] = 15.8 mM, [RSH] = 19.8 mM, reactions were performed at 80 °C in CD₃CN. Initial rates were determined using the first set of linear timepoints under 50% conversion by comparing $\Delta[\mathbf{2.5}]/t(\text{min})$.²⁷

When 5 mol% unfunctionalized cage **1.28** was added to the reaction, variations within the relative rates and their rate accelerations were found with different cofactors. The rate order changed to **1.28**•**5.3** > **1.28**•**5.2** > **1.28**•**5.1** > **1.28**•**5.4** > **1.28**•**1.35**. The addition of cage **1.28** had the greatest effect on the diacid **1.35**, 9-anthroic acid **5.3**, and pivalic acid **5.4**, showing a 10- to 50-fold rate enhancement. In contrast, only a small rate enhancement of ~2-fold was observed when 9-naphthoic acid **5.2** and benzoic acid **5.1** were used as the cofactor. The best cofactor for this cage-catalyzed reaction was 9-anthroic acid **5.4**, while the slowest was diacid **1.35** in the presence of the cage complex. Despite the two substrates having similar pK_as and the use of identical conditions, a 15-fold rate difference was observed. Pivalic acid **5.4**, which is smaller in size, had a higher initial rate than the larger diacid **1.35**.

In each ¹H NMR spectrum, no cage decomposition was observed, even under extended reaction times, but a small amount of disulfide was observed in the slower reactions with cage **1.28**. This was likely caused by small amounts of Fe^{II} that leached from cage **1.28** and atmospheric oxygen. Interestingly, cage **1.28** was unable to catalyze the nucleophilic substitution alone.

5.5. Varying the Cofactor Concentration

The next series of experiments were performed to see which components of the reaction are directly involved in the rate equation for this cofactor-mediated process. When using a small molecule acid as the catalyst, the mechanism followed an S_N1 process, where the rate-determining step is only dependent on the concentration of the electrophile. However, the mechanism as observed in acid cage **1.30** can change if added into the process. So, if

the cofactor, electrophile and/or nucleophile are bound by cage **1.28** before the rate-determining step, this would lead to dependence on the nucleophile concentration and, therefore, change the mechanism.

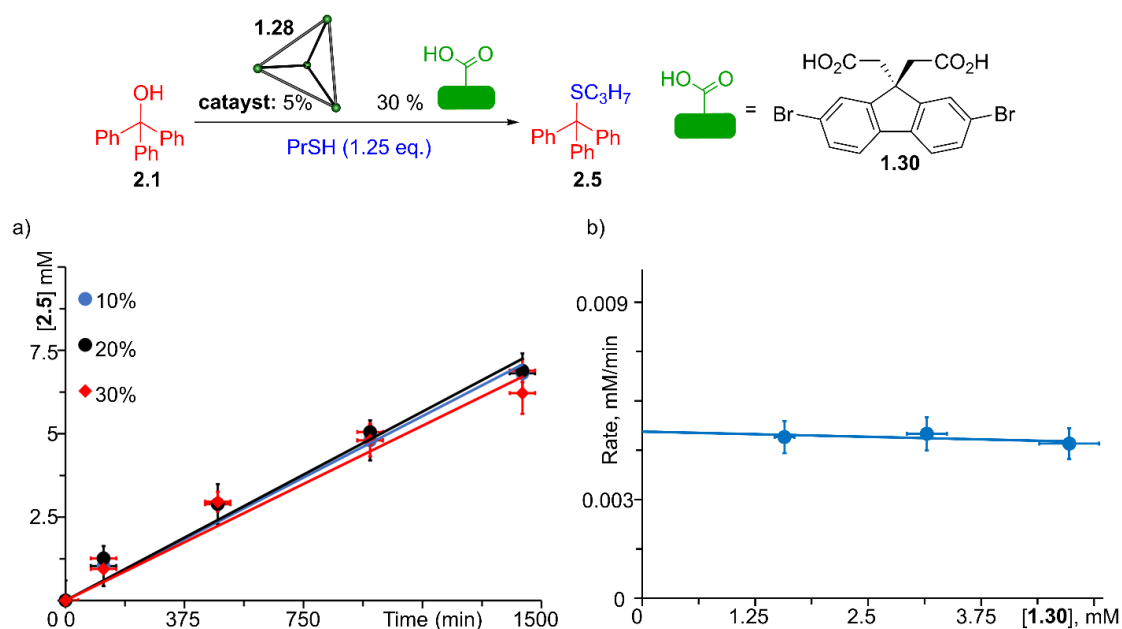


Figure 5.7. Varying concentration of diacid **1.30**. a) Reaction progress over time with varying concentrations [**1.30**]; b) reaction rate vs [**1.30**].²⁷

To further the investigation, the diacid **1.30** and 9-anthroic acid **5.3** were tested as cofactors, since both are strongly affected by the presence of the cage complex. One of the relevant questions in this study is whether the reaction rate is dependent on the cofactor concentration. Using the same reaction conditions, initial results displayed no increase in reaction rates when a greater concentration (from 10–30 mol %) of diacid **1.35** cofactor, in respect to electrophile, was used (Figures 5.7b and Figure 5.8). This is interesting as it means that the diacid **1.35** must be involved in the equation since the reaction cannot occur without the host. The reason for this is made clear by the way the complex binds to the molecule in a 1:2 fashion. Positive cooperative binding is observed ($\alpha = 51$), and so the

1.28•**1.30**₂ ternary complex, and not the binary complex **1.28**•**1.30** dominates the resting state, even at a 1:1 host-guest ratio. This means that cage **1.28** and the diacid **1.30** are dependent on each other. This cooperative binding increases the complex's affinity for more of the diacid **1.30**, as the rate is observed to be independent of the amount of cofactor used.

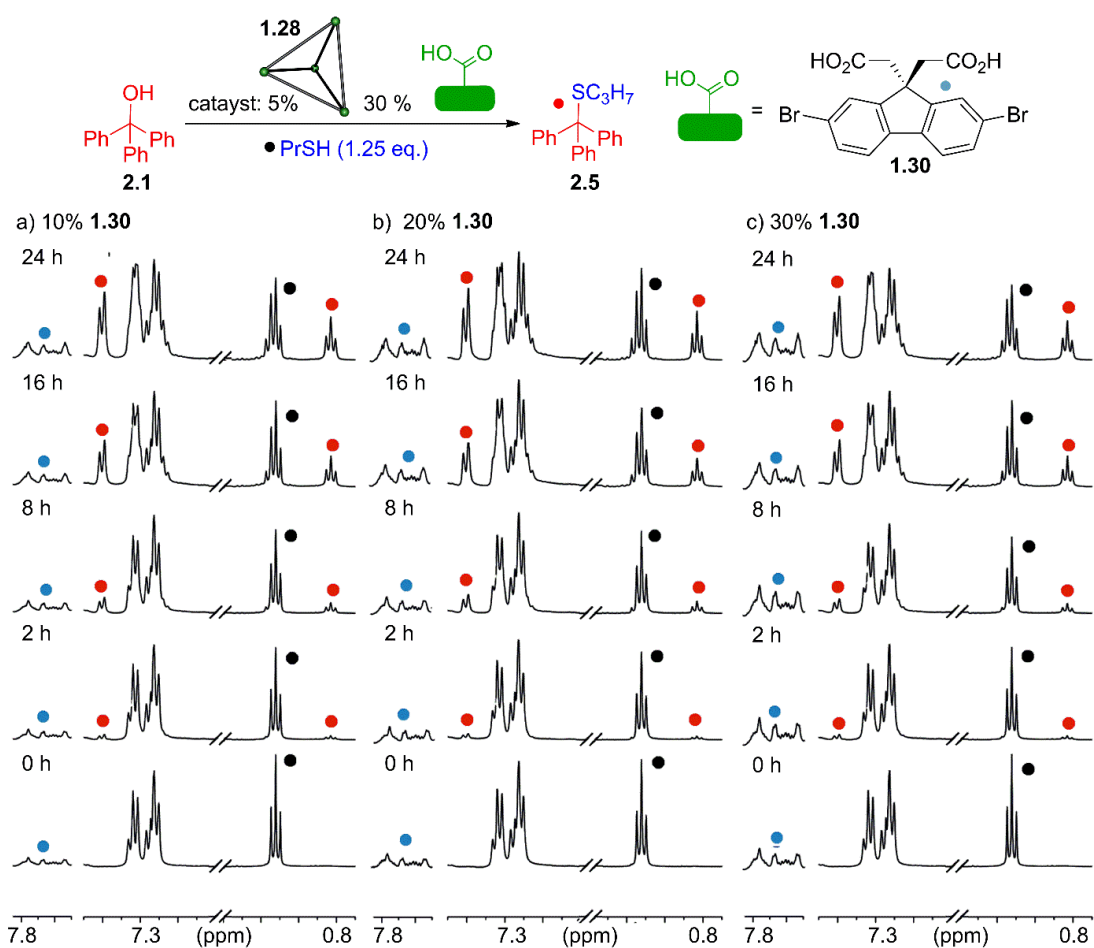


Figure 5.8. ¹H NMR spectra of the acid-promoted substitution reaction between **2.1** and **PrSH** in the presence of 5 mol % cage **1.28** and at varying concentrations of acid **1.30**, a) 1.58 mM, b) 3.15 mM, and c) 4.73 mM.²⁷

On the other hand, 9-anthroic acid **5.3** showed no increase in reaction rate when the concentration was increased. This can be attributed to the way the acid binds to the cage

complex in a 1:1 manner. Figure 5.9b shows that the reaction rate increases with greater concentration **5.3**. However, at high concentrations, the rate slows down. This is likely due to inhibition by saturation of cage **5.2** with excess amounts of the cofactor. Moreover, the titration of 9-anthroic acid **5.3** into cage **1.28** did not exhibit any positive cooperative binding, so the resting and active states of the complex with the cofactor are identical.

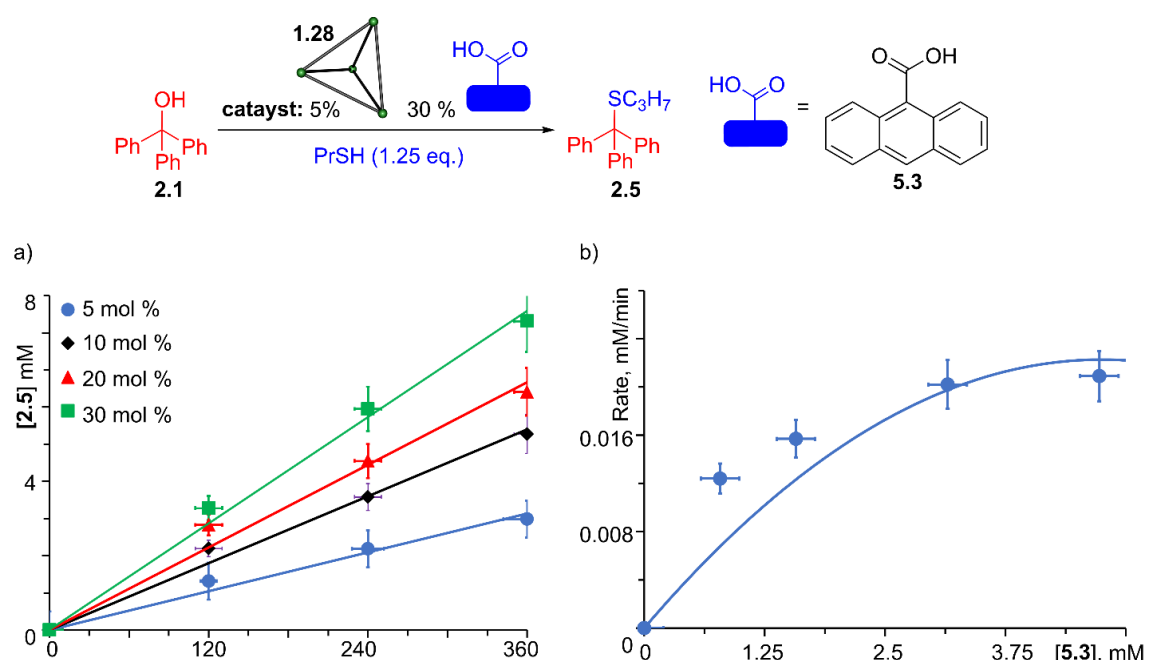


Figure 5.9. Varying concentration of acid **5.3**. a) Reaction progress over time with varying [5.3]; b) reaction rate vs [5.3].²⁷

5.6. Varying the Electrophile

One of the characteristics of the enzymatic catalysis of a reaction with 5 mol% acid cage **1.30** is the ability to change the molecularity of the reaction.²⁴ To determine whether this was generally true for cage-catalyzed reactions, the nucleophilic substitution reaction of **2.1** was repeated at varying [PrSH] with diacid **1.35** as the cofactor. As was the case for cage **1.30**, the reaction rate for the substitution catalyzed by **1.28**•**1.35** increased with

increasing $[\text{PrSH}]$, showing a dependence on the nucleophile concentration in the equation (Figure 5.10a). This differed from when the reaction was catalyzed by small molecule acids such as $\text{CF}_3\text{CO}_2\text{H}$, where no dependence on concentration of nucleophile was observed.²⁴ It is only when cage catalysts capable of molecular recognition are involved that this dependence is observed.²⁴ This data strongly indicates that the **1.28**•**1.35** complex was acting as a “holoenzyme” catalyst, with cage **1.28** as the “apoenzyme” and **1.35** as the cofactor.

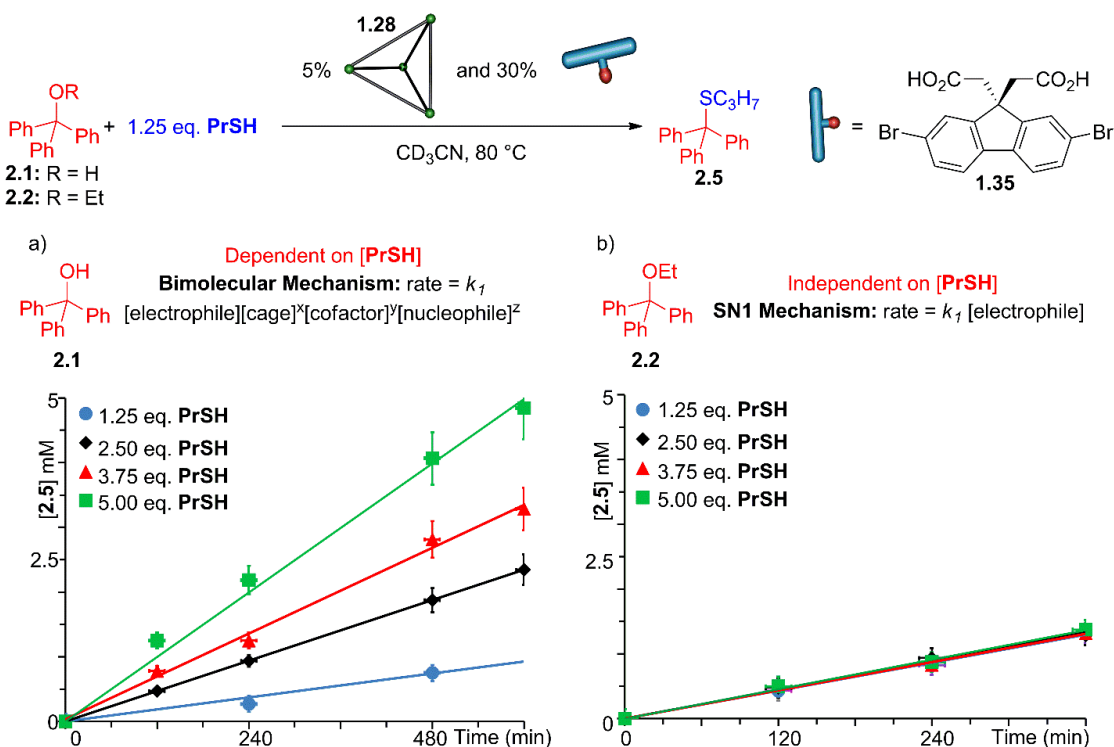


Figure 5.10. Variable rate dependency on changing the electrophile in the reaction with **1.35**. a) varying $[\text{PrSH}]$ with alcohol **2.1** b) varying $[\text{PrSH}]$ with ether **2.2**.²⁷

To further examine the similarities between the two catalysts, the study investigated the effects of changing the electrophile. In the reaction with cage **1.30**, the substitution of trityl ether **2.2** occurred at basically the same rate as alcohol **2.1** (Figure 5.10b). The only difference in this case was the lack of nucleophilic dependence in the substitution reaction.

The reaction with the **1.28**•**1.35** complex reflected the same outcome observed with acid cage **1.30**; even when the electrophiles are small and only differ slightly in pKa and size, the cation does not form in a similar S_N1 fashion. Therefore, it is clear that molecular recognition plays a significant role in changing the mechanism of the reaction for this cofactor-mediated process.

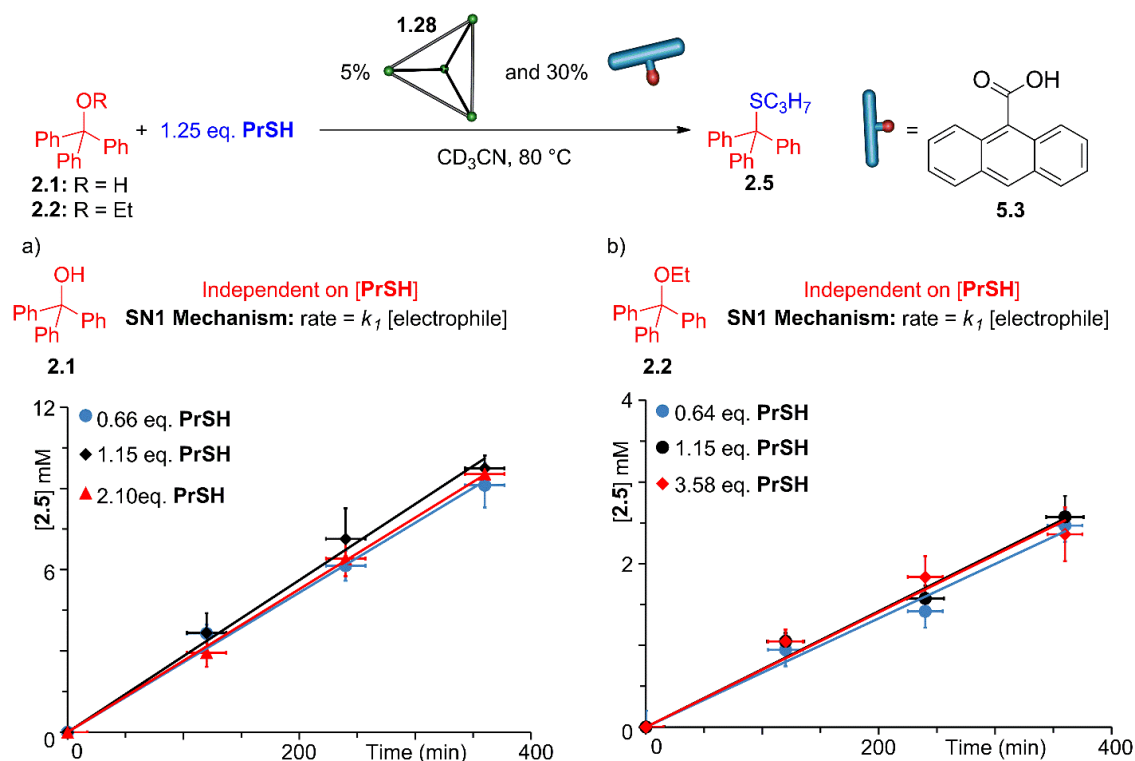


Figure 5.11. Variable rate dependency on changing the electrophile in the reaction with **5.3**. a) varying [PrSH] with alcohol **2.1** b) varying [PrSH] with ether **2.2**.²⁷

When 9-anthroic acid **5.3** was used as the cofactor with cage **1.28**, the kinetic properties of the reaction changed. The initial rate for substitution between alcohol **2.1** and PrSH was significantly faster with 9-anthroic acid **5.3** (260×10^{-4} mM/min) than with diacid **1.35** (39×10^{-4} mM/min), whereas the reaction rate with ether **2.2** had similar initial rates (**1.35**: 79×10^{-4} mM/min; **5.3**: 70×10^{-4} mM/min). The molecularity also differed somewhat with

5.3; both electrophiles **2.1** and **2.2** showed no dependence on **[PrSH]** (Figures 5.11 and 5.12).

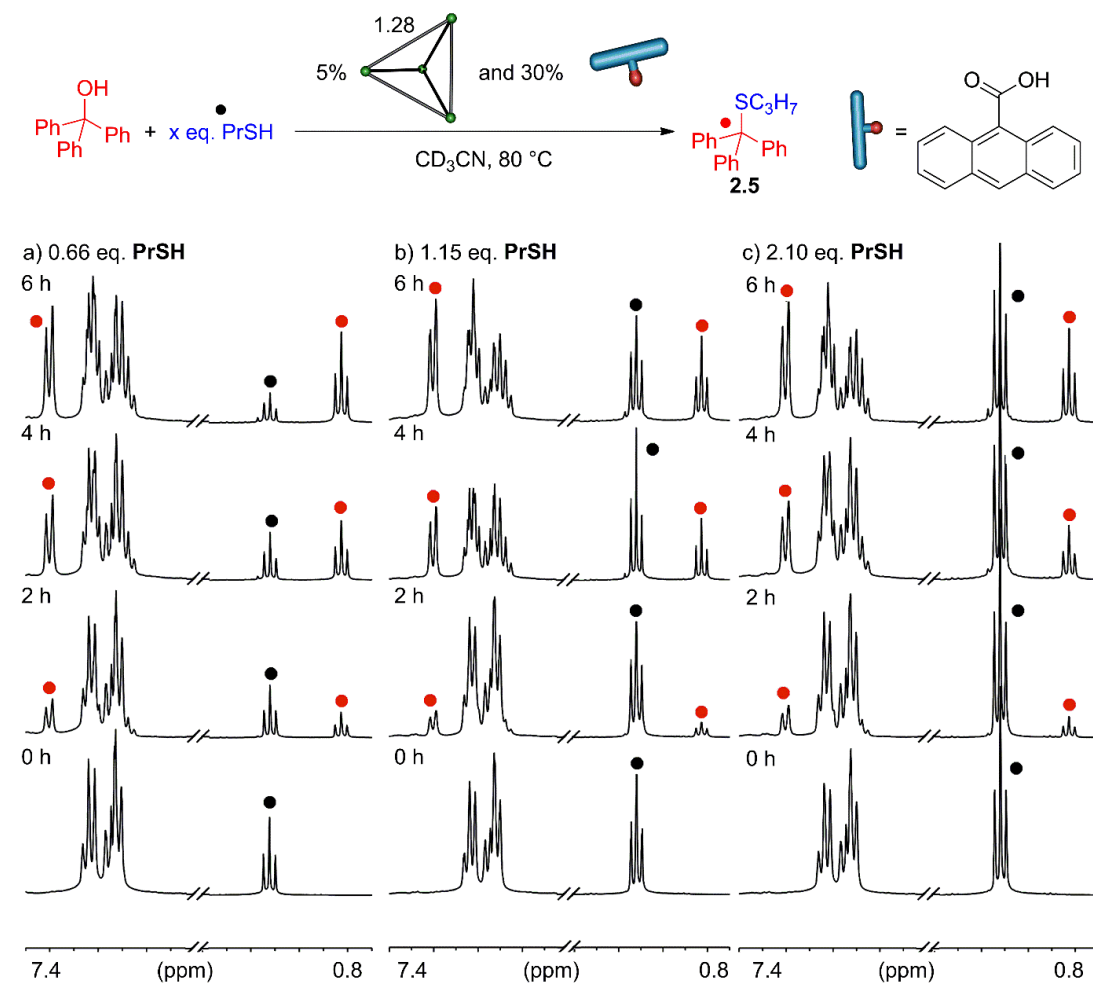


Figure 5.12. ^1H NMR spectra of the acid-promoted substitution reaction between **2.1** and **PrSH** in the presence of 5 mol% cage **1.28** and at varying concentrations of acid **5.3** a) 9.45 mM b) 18.11 mM, and c) 33.08 mM.²⁷

5.7. Varying the Nucleophile

By using *n*-octanethiol (**OctSH**) instead of **PrSH**, the size of the last component, the nucleophile, was varied. The initial rates for the substitution reaction between **OctSH** and both **2.1** (135×10^{-4} mM/min) and **2.2** (150×10^{-4} mM/min) were considerably faster than

those with **PrSH**. With varying concentrations of the different nucleophiles, the patterns observed were identical to those discussed above. Alcohol **2.1** exhibits a dependence on **[OctSH]** (Figure 5.12), whereas ether **2.2** exhibited no such dependence (Figure 5.13).

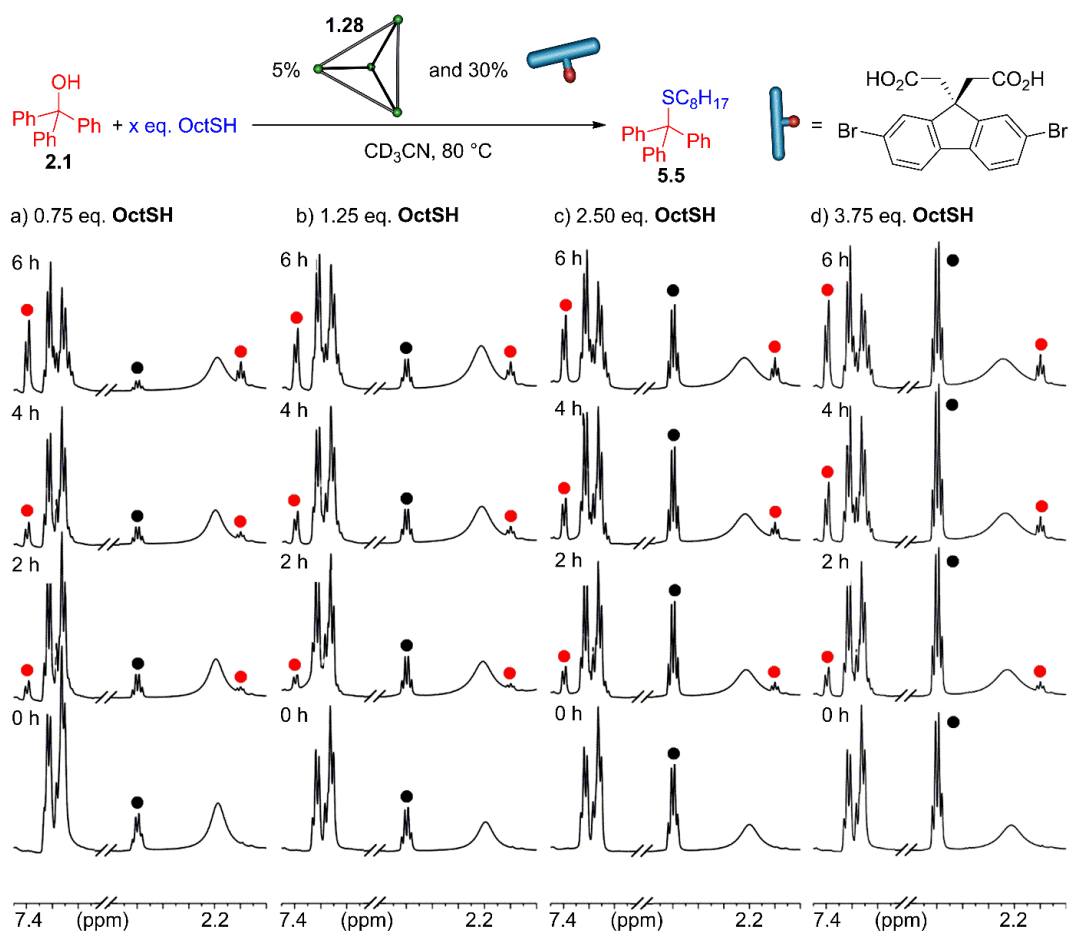


Figure 5.13. ^1H NMR spectra of the acid-promoted substitution reaction between **2.1** and **OctSH** in the presence of 5 mol % cage **1.28** and at varying concentrations of acid **1.30**, a) 11.88 mM, b) 21.26, c) 24.48 mM, and d) 62.37 mM.²⁷

In addition to the rate differences, the reaction with **OctSH** oxidatively dimerized into the disulfide faster than with **PrSH**. Fe(II)-iminopyridine cages have been observed to oxidize alkyl thiols slower than aryl thiols.²⁴ Even though **PrSH** and **OctSH** have similar oxidation potential, **OctSH** was oxidized at a rate 4-fold faster than **PrSH**. The accelerated

dimerization of **OctSH** can be explained by the nucleophile's bigger size and ability to colocalize two thiols inside the cavity of the cage complex. Due to its smaller size, **PrSH** does not form these 1:2 complexes favorably. Therefore, the nucleophile's dimerization rate is slower than that of **OctSH**.³⁶ With small changes in the structure of the reactants, large changes in both rate and dependence on nucleophile concentration were observed in this cofactor-mediated process.

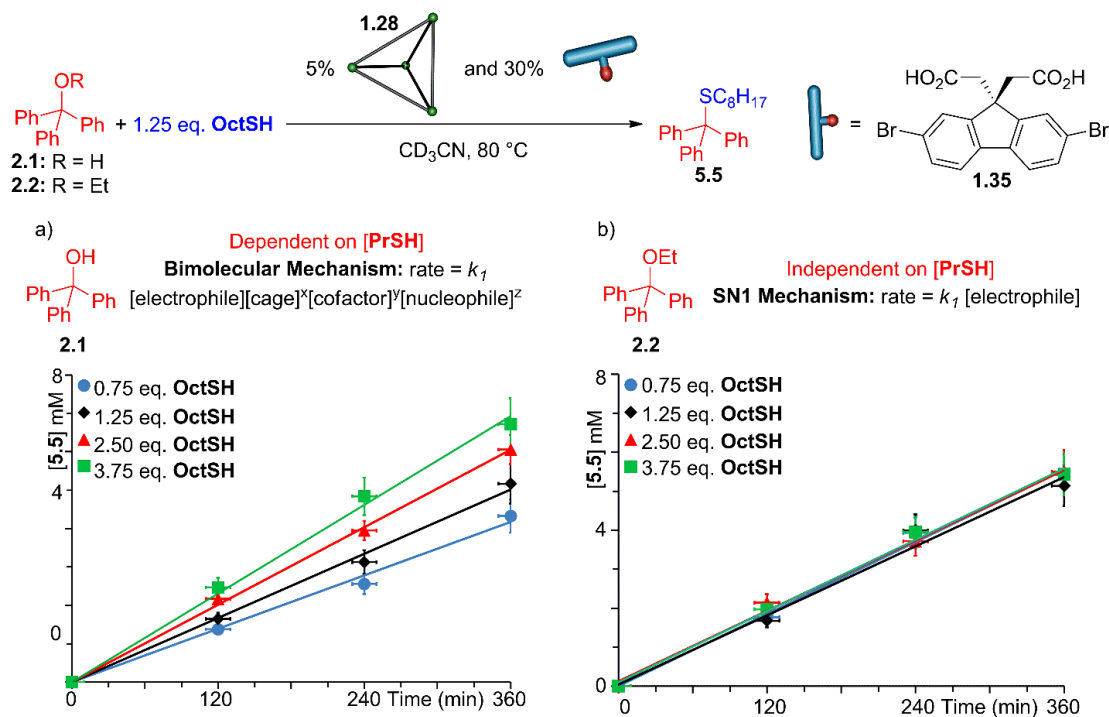


Figure 5.14. Variable rate dependency on changing the electrophile in the reaction with **1.35**. a) varying [**OctSH**] with alcohol **2.1** b) varying [**OctSH**] with ether **2.2**.²⁷

5.8. Mechanistic Analysis

The information found in both binding and kinetics show that in the presence of cage **1.28**, the mechanism experiences a range of effects. As there are as many as 4 components in the cage-catalyzed nucleophilic substitution, and since some of them can form 1:1 and 1:2 homo- and hetero-ternary complexes, not all equilibria will be shown. The cofactor-

mediated substitution was successful due to the strong affinities and the rapid in/out exchange rates of each substrate.

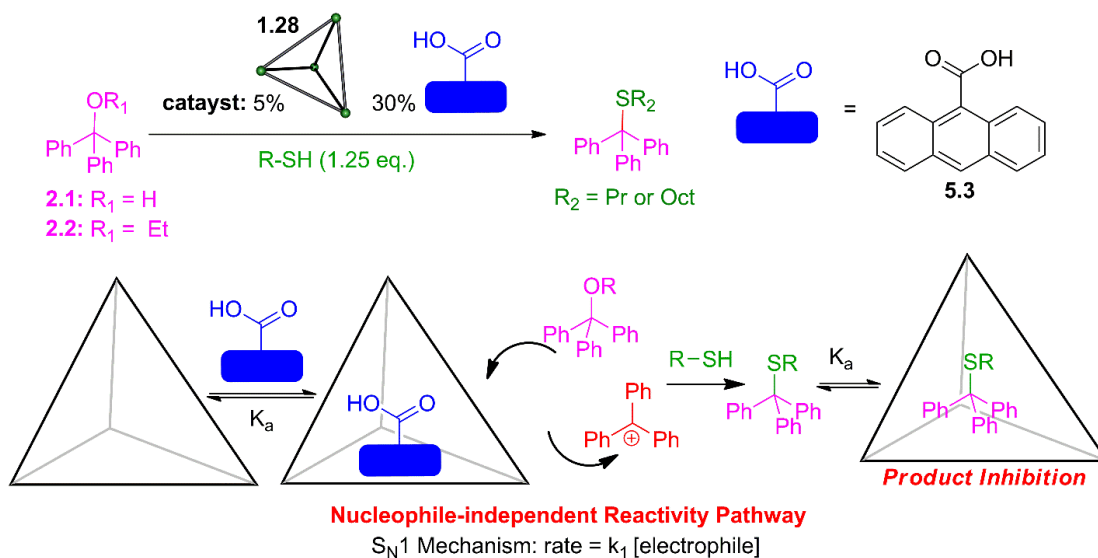


Figure 5.15. Nucleophile-independent pathway in cage-catalyzed cofactor reaction.²⁷

The classic $\text{S}_{\text{N}}1$ mechanism usually used to present a generalized version of the cofactor-mediated reaction is illustrated in Figure 5.14. As seen with 9-anthroic acid **5.3**, a nucleophile independence was observed with this cofactor, due to the binding of cage **1.28** to an acidic cofactor and electrophile first. The rate-determining step was the formation of the cation. The cation was then released from cage **1.28**, and was then subject to reaction with the nucleophile. Since products **2.5** and **5.5** had stronger affinities to cage **1.28** than the reactants, some product inhibition was observed at high conversions. This differed from what was observed in acid cage **1.30**, where the products had lower affinities than the reactants. The rate was controlled by the relative amounts of the combined components of acidic cofactor and electrophile in the solution and was not dependent on the affinity of individual components in the supramolecular cage. This revealed that the acceleration was

unclear why there was a dependence on the nucleophile concentration. After binding with the cofactor, cage **1.28** must bind both triphenylmethanol **2.1** and either **PrSH** or **OctSH** to form the quaternary complex needed for the process to occur and the desired product to be released. The model shows that this is possible, as all three components can fit inside the cavity (Figure 5.5b). Even though this is entropically unfavorable, the formation of the quaternary complex could be overcome by the expulsion of solvent molecules in the cavity. Furthermore, it is also unclear whether cage **1.28** with diacid **1.35** as the guest had a greater rate enhancement than the other cofactors, but it could potentially be attributed to the hydrogen bonding interaction between the two diacids present in the cavity.

5.9. Conclusion

This study has shown that cage **1.28** can be used as a host for a cofactor-mediated reaction. By encapsulating various acids as guests within its cavity, cage **1.28** can catalyze a nucleophilic substitution reaction. The process showed a nonlinear relationship to cofactor concentration in the reaction. Moreover, rate accelerations varied depending on the different sizes of the cofactors used. The study shows variable dependency on the nucleophile concentration in the equation. Overall, it was found that small changes in both the shape and size of the substrates greatly affect the mechanism. Molecular recognition plays an important part in the reaction, affecting both reaction rate and molecularity differently for differently sized substrates.

5.10. References

1. Richter, M. Functional diversity of organic molecule enzyme cofactors. *Nat. Prod. Rep.* **2013**, *30*, 1324–1345.
2. Fagan, R. L.; Palfey, B. A. Flavin-dependent enzymes. *Comprehensive Natural Products II - Chemistry and Biology.* **2010**, *7*, 37–113.
3. Eliot, A. C.; Kirsch, J. F. Pyridoxal phosphate enzymes: mechanistic, structural, and evolutionary considerations. *Annu. Rev. Biochem.* **2004**, *73*, 383–415.
4. Banerjee, R.; Ragsdale, S. W. The many faces of vitamin B12: catalysis by cobalamin-dependent enzymes. *Annu. Rev. Biochem.* **2003**, *72*, 209–247.
5. Kluger, R.; Tittman, K. Thiamin diphosphate catalysis: enzymic and nonenzymic covalent intermediates. *Chem. Rev.* **2008**, *108*, 1797–1833.
6. Breslow, R. On the mechanism of thiamine action. IV. Evidence from studies on model systems. *J. Am. Chem. Soc.* **1958**, *80*, 3719–3726.
7. Shinkai, S.; Ishikawa, Y.; Shinkai, H.; Tsuno, T.; Makishima, H.; Ueda, K.; Manabe, O. A crown ether flavin mimic: synthesis and properties of a flavin bearing a crown ring as a recognition site. *J. Am. Chem. Soc.* **1984**, *106*, 1801–1808.
8. Chevalier, Y.; Lock Toy Ki, Y.; le Nouen, D.; Mahy, J. P.; Goddard J. P.; Avenier, F. Aerobic Baeyer–Villiger oxidation catalyzed by a flavin-containing enzyme mimic in water. *Angew. Chem., Int. Ed.* **2018**, *57*, 16412–16415.
9. Dong, Z.; Luo, Q.; Liu, J. Artificial enzymes based on supramolecular scaffolds. *Chem. Soc. Rev.* **2012**, *41*, 7890–7908.
10. Rizzuto, F. J.; von Krbek, L. K. S.; Nitschke, J. R. Strategies for binding multiple guests in metal-organic cages. *Nat. Rev. Chem.* **2019**, *3*, 204–222
11. Hof, F.; Craig, S. L.; Nuckolls, C.; Rebek, J., Jr. Molecular encapsulation. *Angew. Chem., Int. Ed.* **2002**, *41*, 1488–1508.

12. Brown, C. J.; Toste, F. D.; Bergman, R. G.; Raymond, K. N. Supramolecular catalysis in metal-ligand cluster hosts. *Chem. Rev.* **2015**, *115*, 3012–3035.
13. Harris, K.; Fujita, D.; Fujita, M. Giant hollow M_nL_{2n} spherical complexes: structure, functionalisation and applications. *Chem. Commun.* **2013**, *49*, 6703–6712.
14. Zhang, Q.; Catti, L.; Tiefenbacher, K. Catalysis inside the hexameric resorcinarene capsule. *Acc. Chem. Res.* **2018**, *51*, 2107–2114.
15. MacGillivray, L. R.; Atwood, J. L. A chiral spherical molecular assembly held together by 60 hydrogen bonds. *Nature.* **1997**, *389*, 469–472.
16. Shivanyuk, A.; Rebek, J., Jr. Reversible encapsulation by self-assembling resorcinarene subunits. *Proc. Natl. Acad. Sci. U.S.A.* **2001**, *98*, 7662–7665.
17. Zhang, Q.; Tiefenbacher, K. Terpene cyclization catalyzed inside a self-assembled cavity. *Nat. Chem.* **2015**, *7*, 197–202.
18. Zhang, Q.; Catti, L.; Pleiss, J.; Tiefenbacher, K. Terpene cyclizations inside a supramolecular catalyst: Leaving-group-controlled product selectivity and mechanistic studies. *J. Am. Chem. Soc.* **2017**, *139*, 11482–11492.
19. Gramage-Doria, R.; Hessels, J.; Leenders, S. H. A. M.; Tröppner, O.; Dürr, M.; Ivanović-Burmazović, I.; Reek, J. N. H. Gold(I) catalysis at extreme concentrations inside self-assembled nanospheres *Angew. Chem., Int. Ed.* **2014**, *53*, 13380–13384.
20. Wang, Q.-Q.; Gonell, S.; Leenders, S. H. A. M.; Dürr, M.; Ivanović-Burmazović, I.; Reek, J. N. H. Self-assembled nanospheres with multiple endohedral binding sites pre-organize catalysts and substrates for highly efficient reactions. *Nat. Chem.* **2016**, *8*, 225–230.
21. Braüer, T. M.; Zhang, Q.; Tiefenbacher, K. Iminium catalysis inside a self-assembled supramolecular capsule: Modulation of enantiomeric excess. *Angew. Chem., Int. Ed.* **2016**, *55*, 7698–7701.
22. Catti, L.; Tiefenbacher, K. Brønsted acid-catalyzed carbonyl-olefin metathesis inside a self-assembled supramolecular host. *Angew. Chem., Int. Ed.* **2018**, *57*, 14589–14592

23. Holloway, L. R.; Bogie, P. M.; Lyon, Y.; Ngai, C.; Miller, T. F.; Julian, R. R.; Hooley, R. J. Tandem reactivity of a self-assembled cage catalyst with endohedral acid groups. *J. Am. Chem. Soc.* **2018**, *140*, 8078–8081.
24. Bogie, P. M.; Holloway, L. R.; Ngai, C.; Miller, T. F.; Grewal, D.; Hooley, R. J. A self-assembled cage with endohedral acid groups both catalyzes substitution reactions and controls their molecularity. *Chem. Eur. J.* **2019**, *25*, 10232–10238.
25. Ngai, C.; da Camara, B.; Woods, C. Z.; Hooley, R. J. Size and shape-selective oxocarbenium ion catalysis with a self-assembled cage host. *J. Org. Chem.* **2021**, *86*, 12862–12871.
26. Ngai, C.; Sanchez-Marsetti, C. M.; Harman, W. H.; Hooley, R. J. Supramolecular catalysis of the oxa-Pictet–Spengler reaction with an endohedrally functionalized self-assembled cage complex. *Angew. Chem., Int. Ed.* **2020**, *59*, 23505–23509.
27. Ngai, C.*; Bogie, P. M.*; Holloway, L. R.; Dietz, P. C.; Mueller, L. J.; Hooley, R. J. Cofactor-mediated nucleophilic substitution catalyzed by a self-assembled holoenzyme mimic. *J. Org. Chem.* **2019**, *84*, 12000–12008.
28. Hibbert, D. B.; Thordarson, P. The death of the Job plot, transparency, open science and online tools, uncertainty estimation methods and other developments in supramolecular chemistry data analysis. *Chem. Commun.* **2016**, *52*, 12792–12805.
29. Thordarson, P. Determining association constants from titration experiments in supramolecular chemistry. *Chem. Soc. Rev.* **2011**, *40*, 1305–1323.
30. Mecozzi, S.; Rebek, J., Jr. The 55% solution: a formula for molecular recognition in the liquid state. *Chem. Eur. J.* **1998**, *4*, 1016–1022.
31. Rizzuto, F. J.; Carpenter, J. P.; Nitschke, J. R. Multisite binding of drugs and natural products in an entropically favorable, heteroleptic receptor. *J. Am. Chem. Soc.* **2019**, *141*, 9087–9095.
32. Meng, W.; Breiner, B.; Rissanen, K.; Thoburn, J. D.; Clegg, J. K.; Nitschke, J. R. A self-assembled M₈L₆ cubic cage that selectively encapsulates large aromatic guests. *Angew. Chem., Int. Ed.* **2011**, *50*, 3479–3483.

33. Ramsay, W. J.; Szczypiński, F. T.; Weissman, H.; Ronson, T. K.; Smulders, M. M. J.; Rybtchinski, B.; Nitschke, J. R. Designed enclosure enables guest binding within the 4200 Å³ cavity of a self-assembled cube. *Angew. Chem., Int. Ed.* **2015**, *54*, 5636–5640.
34. Brown, H. C.; Braude, E. A.; Nachod, F.C. et al. Determination of Organic Structures by Physical Methods; Academic Press: New York, **1955**.
35. Dippy, J. F. J.; Hughes, S. R. C.; Rozanski, A. The dissociation constants of some symmetrically disubstituted succinic acids. *J. Chem. Soc.* **1959**, 2492–2498.
36. da Camara, B.; Dietz, P. C.; Chalek, K. R.; Mueller, L. J.; Hooley, R. J. Selective, cofactor-mediated catalytic oxidation of alkanethiols in a self-assembled cage host. *Chem. Commun.* **2020**, *56*, 14263-14266.

Chapter 6 – Synthesis of a Cage Complex with Endohedral Amine Groups

6.1. Introduction

The functional groups in an enzyme's active site can act as various acids, bases, nucleophiles, or even electrophiles, and show different properties in free solution.¹⁻⁴ For instance, the β -lysine-87 residue in the enzyme tryptophan synthase displays different protonation states during catalysis.⁴ These enzymes accept protons from solvents and donate them to substrates at close to neutral pH, modulating the pKa values of key side chains during catalysis. This moderation of side-chain acidity and basicity is controlled by forces in the structure, such as hydrogen bonds, and affects the enzyme's mechanism.³

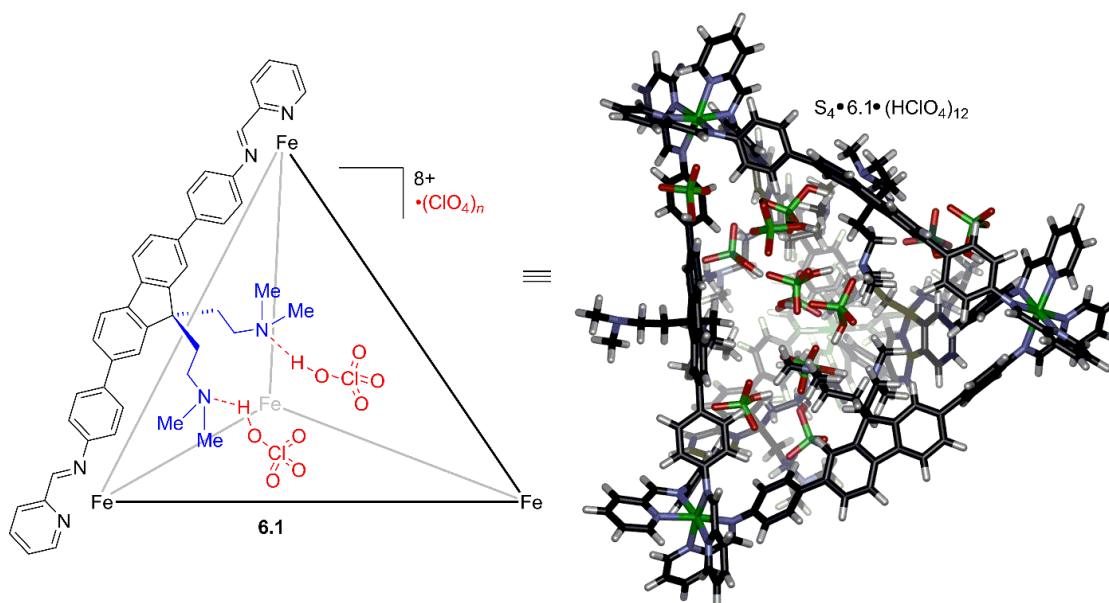


Figure 6.1. New cage complex with 12 internal alkylamine groups.³⁰

Developing the ability to mimic an enzyme's active site by incorporating reactive functional groups in supramolecular cages is an ongoing challenge. Metal-mediated self-assembly has been used to synthesize various nanoscale polyhedral with internal functionality.⁵⁻¹⁰ Functional groups such as oligopeptides,¹¹ guanidinium ions,^{12,13}

polyols,^{8,14} and ureas¹⁵ have been incorporated inside various hosts and investigated for their ability to selectively recognize anions⁷⁻¹⁰ and catalyze various acid-base reactions.¹⁵

Previously, this dissertation focused on investigating the molecular recognition and catalytic abilities of cage **1.30** with 12 internal carboxylic acid groups.¹⁶⁻¹⁹ However, cage **1.30** is highly reactive and unstable, so it is difficult to study. To promote new reactivity and further understand the mechanisms carried out by enzymes, new cage complexes with functional groups must be synthesized. These complexes are frequently charged, and this charge is significant in both molecular recognition and catalysis. Comprehensive studies have been conducted on the effects of the cage's structure on recognition and catalysis for unfunctionalized charged cages in water.²⁰⁻²⁹ However, there are few examples of the effect of charged cage complexes on internally functionalized groups. To investigate the effect of the charged superstructure on the internal groups, cage **6.1** with 12 internal alkylamine groups was synthesized (Figure 6.1).³⁰

6.2. Synthesis of Ligand with Internal Amines

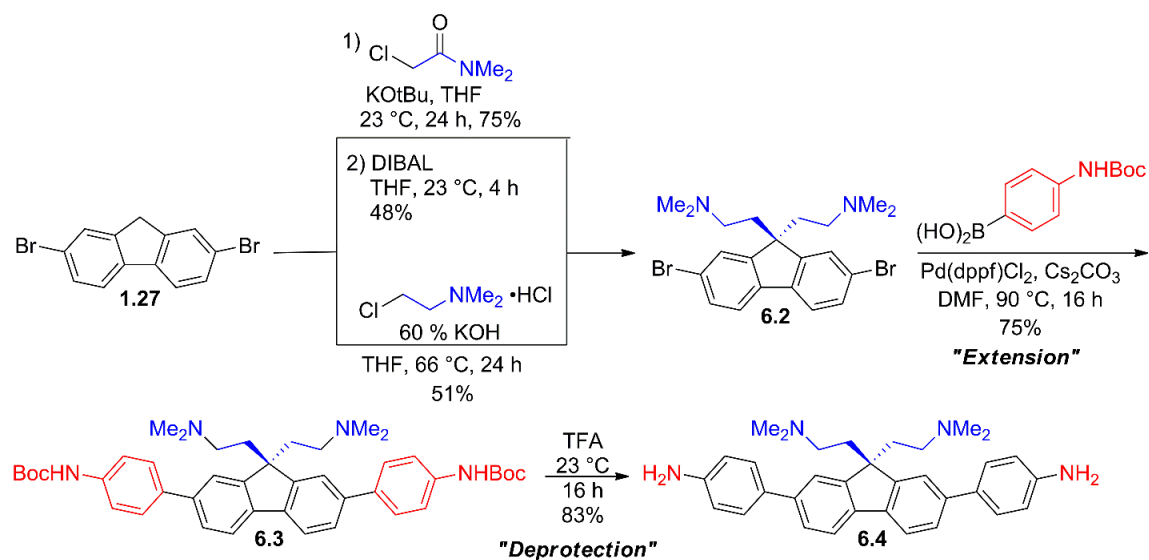


Figure 6.2. Synthesis of new amine ligand **6.4**.³⁰

Ligand **6.4** was carefully chosen for self-assembly into cage **6.1**. The functional groups in the ligand should not compete with formation of the iminopyridine complex and disrupt the assembly process. Ligand **6.4** can be synthesized in four or five steps, starting from the same 2,7- dibromofluorene scaffold seen in the synthesis of cages **1.28** and **1.30** (Figure 6.2).¹⁶

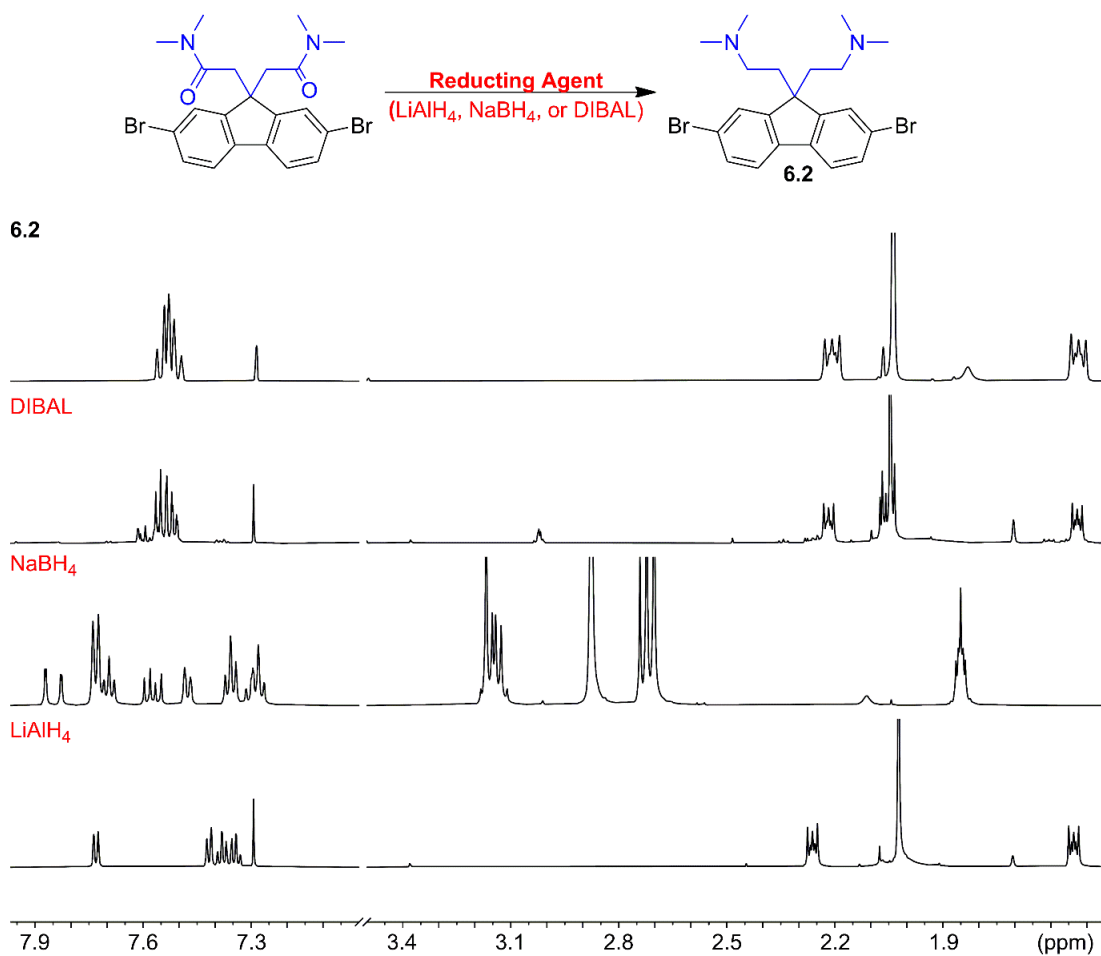


Figure 6.3. Attempts at converting amides to amines using various reducing agents.³⁰

The first step is the addition of two dimethylamine groups. The dimethylamine precursor **6.2** can be synthesized in two ways. The longer route comprises a nucleophilic substitution to incorporate two amide functional groups on 2,7-dibromofluorene **1.27** using

2-chloro-N,N-dimethylacetamide with potassium tert-butoxide. When trying to reduce the amides to amines, attempts were made with lithium aluminum hydride (LiAlH_4), sodium borohydride NaBH_4 , and diisobutylaluminum hydride (DIBAL) as the reducing agent. LiAlH_4 as the reducing agent was able to perform the reduction but also removed the bromine groups in the process, whereas the reduction with NaBH_4 did not form the desired product. Even though LiAlH_4 and NaBH_4 were not effective reduction agents, DIBAL was successfully able to perform the reduction (Figure 6.3).

Another way the two functional groups can be incorporated is to perform the reaction directly onto 2,7-dibromofluorene using 2-dimethylaminoethyl chloride•HCl. The reaction was tested with potassium tert-butoxide, 50% NaOH, and 50% KOH in either THF or toluene as the solvent. It was found that THF dissolved the reagents better than toluene, and the addition of the two dimethyl amine groups in THF worked best when 50% KOH was used as the base, yielding 51% of **6.2**. When attempting to repeat the process, it was discovered that the reaction must be performed under air-free conditions to prevent oxidization into 2,7-dibromofluorenone.

Once the functional groups were added, the process became similar to that of the synthesis of cage **1.30**.¹⁶ Amine **6.2** was extended with aromatic rings through a Suzuki coupling. The BOC groups in **6.3** were then deprotected using TFA. With the dimethyl amine ligand **6.4** in hand, attempts were made to assemble a cage complex.

6.3. Assembly of the Cage Complex

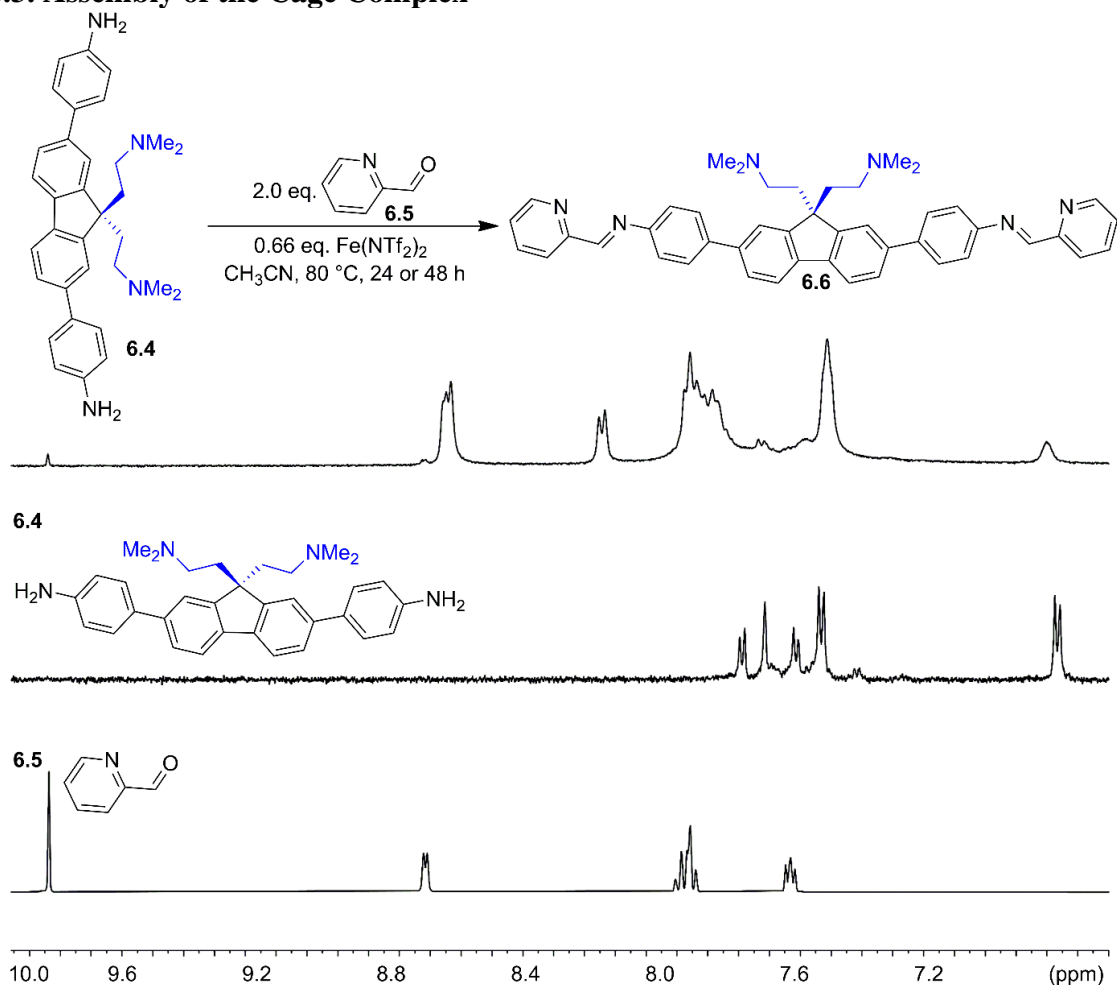


Figure 6.4. First attempt at forming a self-assembled complex.³⁰

Assembling a cage with basic amine groups can be challenging, however, and there are few examples of such complexes. This is because the iminopyridines can be transaminated by primary amines,^{31,32} whereas secondary and tertiary amines can competitively coordinate with the metals.^{33,34} In the first attempt to synthesize the cage, the same conditions and procedures used to synthesize the acid cage were followed:¹⁶ the ligand was heated at 80 °C with 1.32 eq. of aldehyde **6.5** and 0.66 eq. of iron triflimide (Fe(NTf₂)₂) in

CH₃CN for 24 h and 48 h. Mainly the bis-imine ligand was observed after the reaction (Figure 6.4).

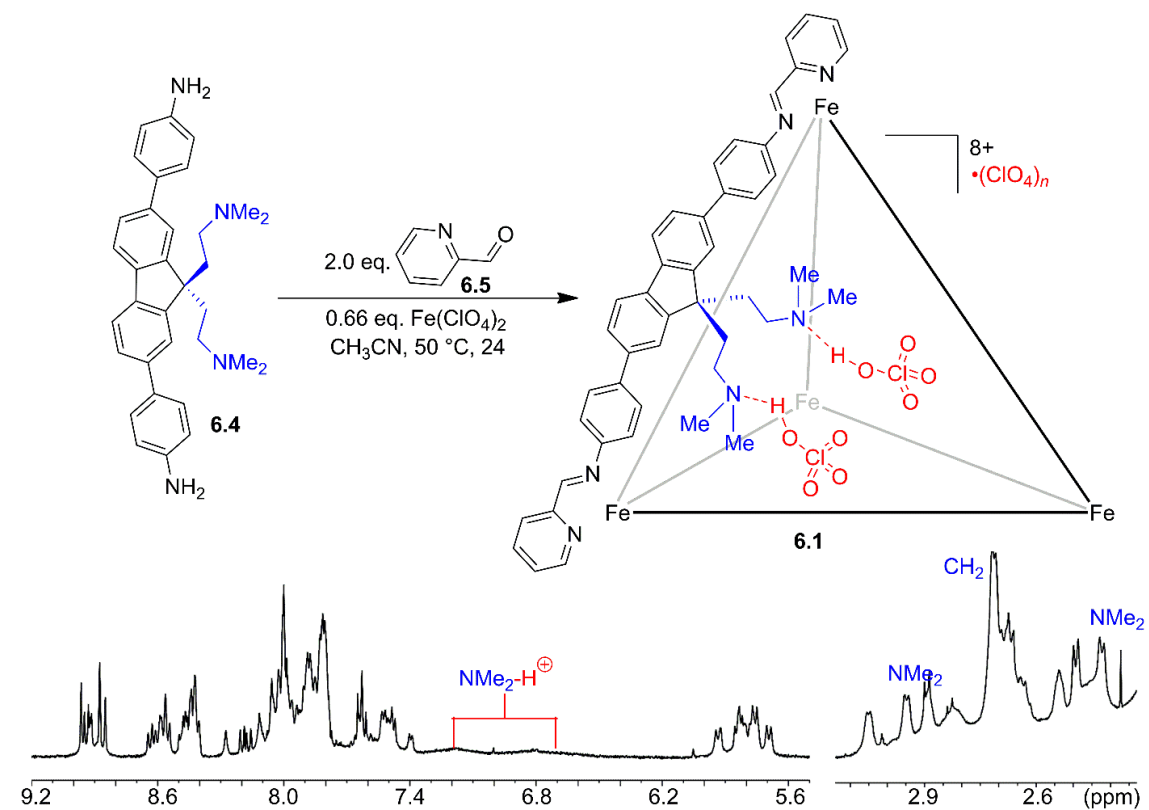


Figure 6.5. ¹H NMR of cage **6.1**, formed with ligand **6.4** and aldehyde **6.5**.³⁰

Since these conditions were ineffective, the reaction conditions for self-assembly were varied. In a third attempt to form the complex, the anion in the metal was changed from triflimide to perchlorate. This mainly formed the bis-imine ligand again; however, some evidence of assembly was observed in the process. It became apparent that by lowering the temperature to 50 °C and using excess Fe(ClO₄)₂, the M₄L₆ tetrahedral cage was formed in 48% yield (Figure 6.5). The ¹H NMR of cage **6.1** is similar to that of cages **1.28** and **1.30**.¹⁶ The imine region shows 8 different peaks, corresponding to all three isomers with T, C₃, and S₄ symmetry^{16,35-36} with an isomeric ratio of 10:45:45, respectively (Figure 6.6). This

ratio is similar to that of the unfunctionalized cage **1.28**, which has a ratio of 28:33:39 (T:C₃:S₄).¹⁶

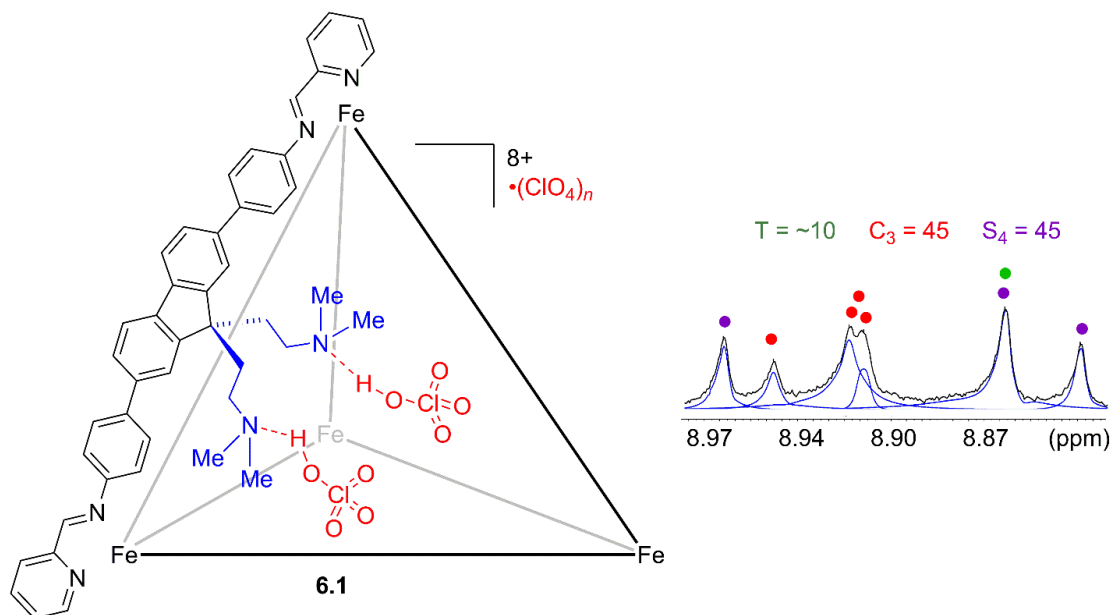


Figure 6.6. Three isomers observed in the imine region of ¹H NMR of cage **6.1**.³⁰

6.4. Characterization of the Cage Complex

Various 2D NMRs (DOSY, COSY, TOCSY, NOESY, ROESY, DEPT-HSQC, and HMBC) were taken to further characterize the cage complex. The 2D DOSY showed that all the signals in the ¹H NMR were involved in the structure of the cage, with each peak displaying a diffusion constant of $4.04 \times 10^{-10} \text{ m}^2/\text{s}$ (Figure 6.7a).

Looking closely at all the NMRs, the ¹H NMR, 2D COSY, and 2D ROESY showed that the internal amines might be protonated. This was first illustrated by a broad mound at $\delta \sim 6.8\text{--}7.2$ ppm in the ¹H NMR (Figure 6.5). The 2D ROESY, 2D COSY, and 2D NOESY reinforced the potential of a bound protic guest due to unclear crosspeaks, scalar coupling, and NOE crosspeaks, respectively in the spectrum between the dimethyl amine (NMe₂) groups ($\delta \sim 2.4\text{--}3.1$ ppm) and the broad mound (Figure 6.7bc). The peaks for NMe₂ were

split into doublets due to coupling to internal perchloric acids instead of the splitting observed due to cage isomerism.

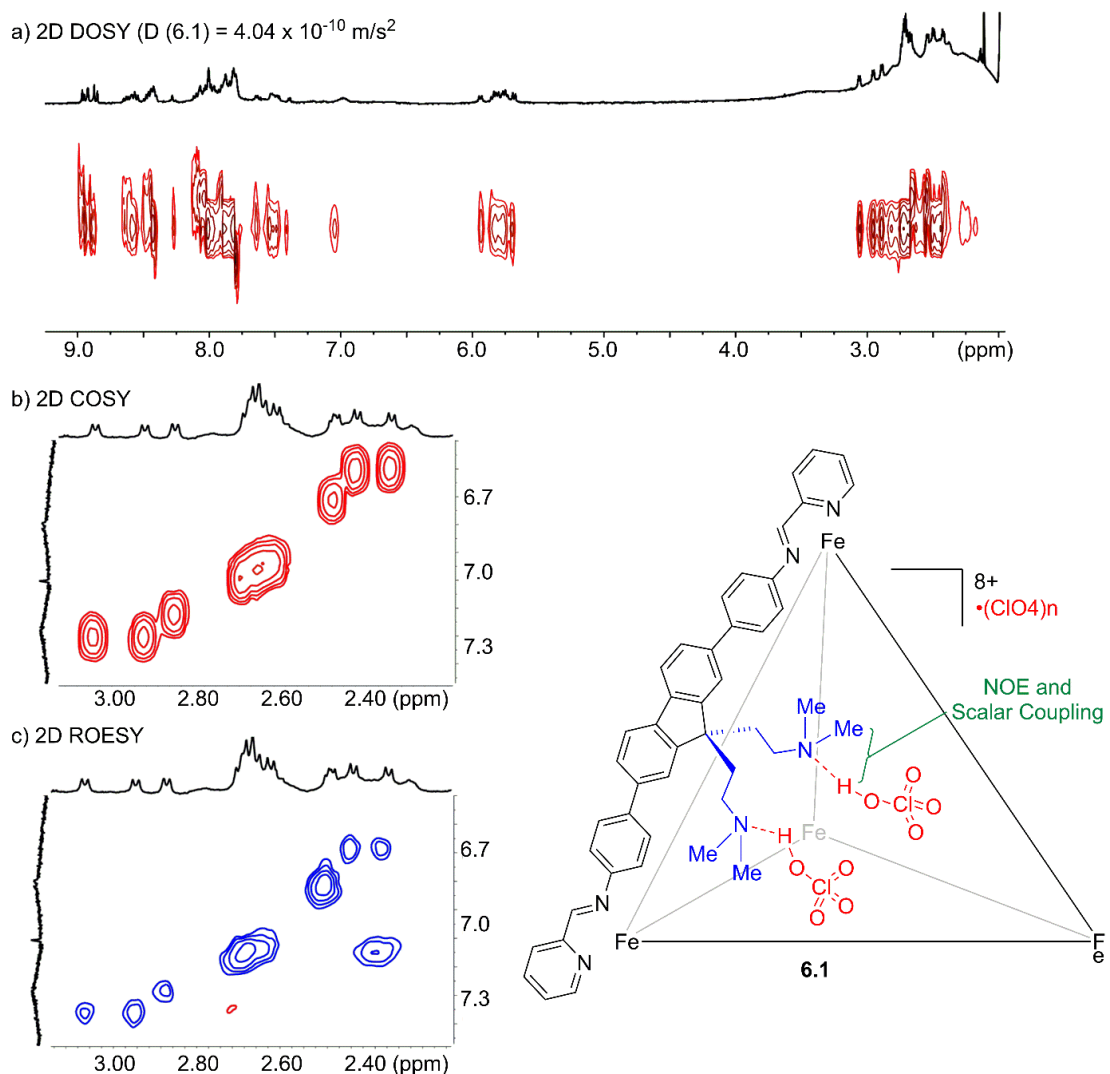
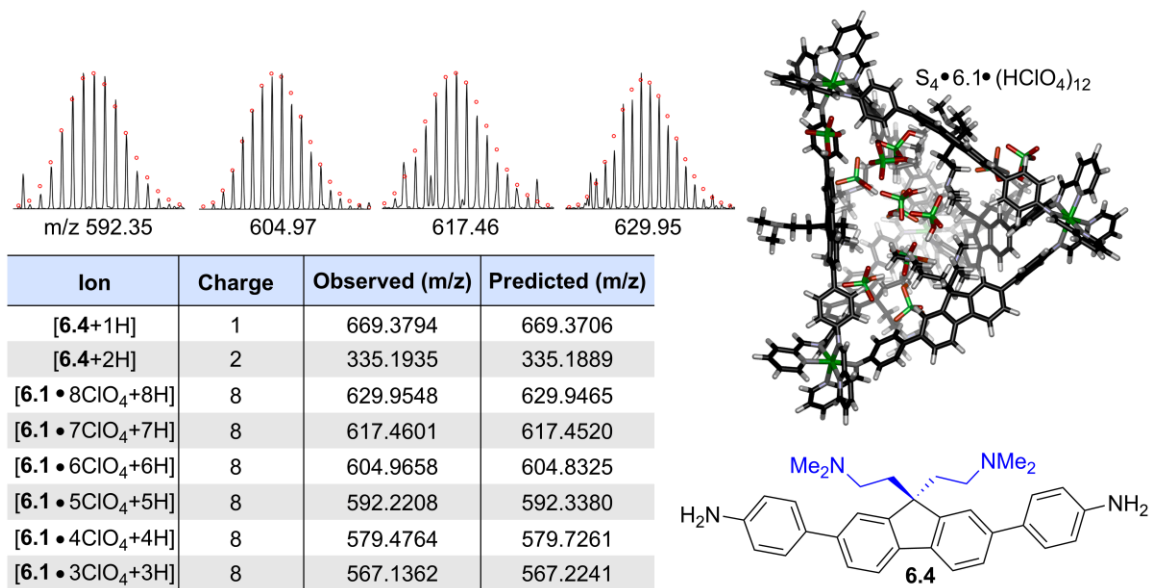


Figure 6.7. Characterization data of cage **6.1**. a) 2D DOSY spectrum. b) 2D COSY spectrum. c) 2D ROESY spectrum.³⁰

Due to the sensitivity of the amine groups and the presence of three different isomers, the crystal of cage **6.1** could not be grown. However, evidence of amine protonation was found in the mass spectrum of the $[\text{Fe}_4\text{L}_6]^{8+}$ assembly by Hoi-Ting Wu and used to help determine the structure. The spectrum showed multiple 8+ ions from 3 to 8 perchlorate

species observed for the cage complex. In addition, the mass data also displayed two +1 and +2 ions from 1 to 2 perchlorate species associated with the ligand. Therefore, this data confirmed that the bound guest was present and the internal NMe₂ groups were protonated by perchlorates in solution.

Table 6.1. Assigned ions for experimentally observed peaks.



ESI-MS analysis, using an instrument with a nanoESI source and an orbitrap mass analyzer.³⁰

The exact number of perchlorate anions is still unclear. The model shows that 12 perchlorate anions can fit inside the cavity of the cage complex (Figure 6.1). Further experimentation shows that the cavity is blocked by these perchlorate anions. No binding was observed when neutral diester **3.21** was titrated into the cage, whereas the acid cage showed a strong affinity with the guest with a $K_a = 6.9 \pm 1.2 \times 10^3 \text{ M}^{-1}$ (Figure 6.8).¹⁸

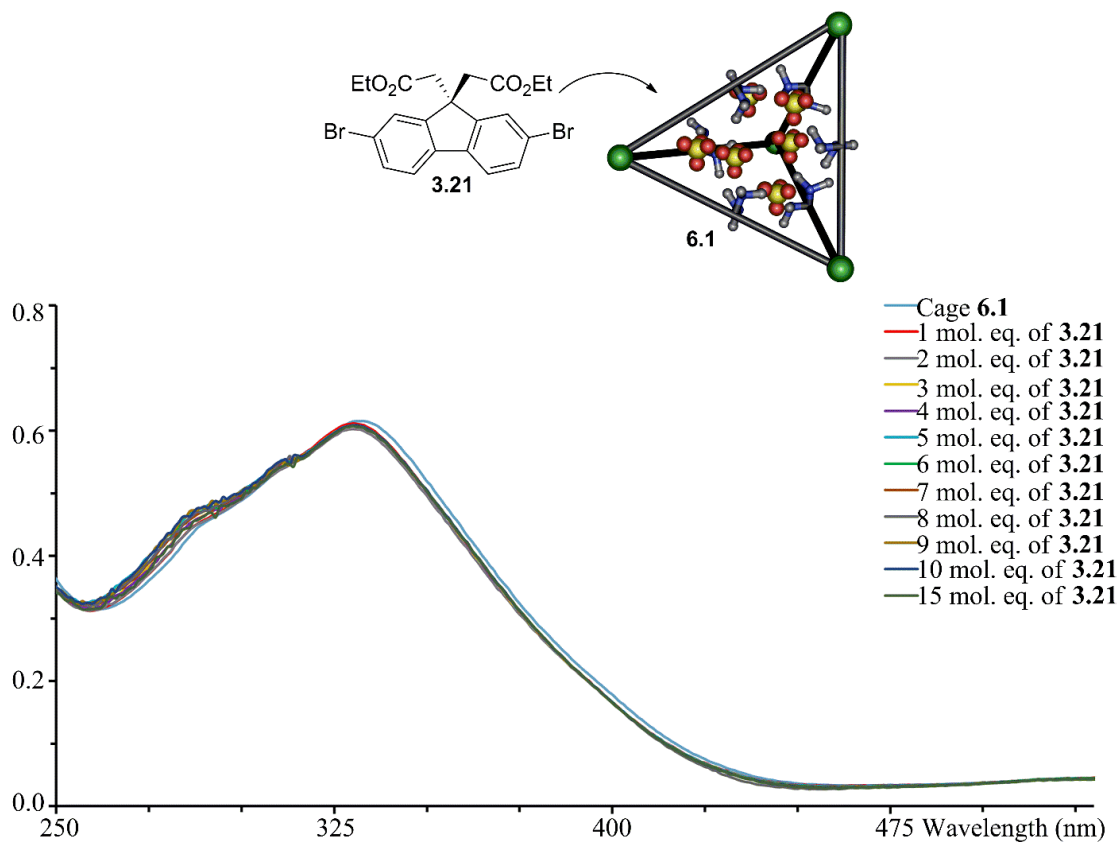


Figure 6.8. UV-Vis absorption spectrum of the titration of neutral guest **3.21** into a 1.5 μM solution of cage **6.1** in CH_3CN . Neutral guest **3.21** was added in 1 μL aliquots from a 4.5 mM stock solution in CH_3CN .³⁰

6.5. Titrations of Basic Guests into the Complex

Experiments were then performed to determine the number of acids present, on average, in a cage solution. Initial experiments show that when cage **6.1** was treated with D_2O , the protons close to the dimethyl amine groups were exchanged with the solvent (Figure 6.9). Since these protons are exchangeable, titrations were performed using different bases of varying pK_a to remove the protons.³⁷

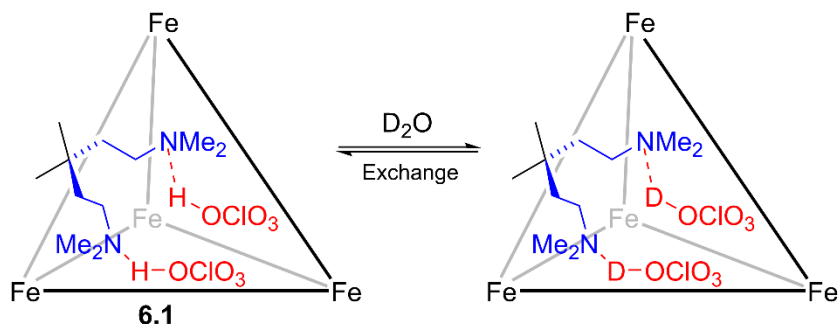


Figure 6.9. Proton exchange between cage **6.1** and D_2O .³⁰

Triethylenediamine (DABCO) **6.7** (pK_a in $CH_3CN = 18.3$) was titrated first as it has an identical pK_a to the Me_2EtN (pK_a in $CH_3CN = 18.3$)³⁷ group in cage **6.1**. The titration first shows that DABCO **6.7** is highly tolerant inside cage **6.1**, and the complex is stable even after 40 mol. eq. of **6.7**. Initially, the perchlorate salt of DABCO **6.8** was observed after about 2 mol. eq. of the base. After 10 eq. of **6.7**, the salt was still observed, indicating that **6.8** is a stronger base than the amines in cage **6.1**, and there are at least 10 protons present in the complex. Although the peaks in the 1H NMR shifted, all three isomers were still present and remained generally constant in ratio.

The changes in chemical shift were analyzed by Christopher Williams and Dr. Leonard Mueller who determined the most likely number of protons in the internal cavity of the complex using a reservoir model. Since the perchlorate salt of DABCO **6.8** is not affected up to 11 mol. eq., the data suggests that the amines are fully protonated in the beginning, and the first 11 protons act as strong acids in comparison to DABCO **6.7**. With addition of more guest, the acids continued to be removed following a 1:1 deprotonation equilibrium, and the pK_a moved closer to that of **6.7**. When all the protons were removed by the base, the pK_a of the cage complex become equivalent to that of DABCO **6.7** (Figure 6.10ab).

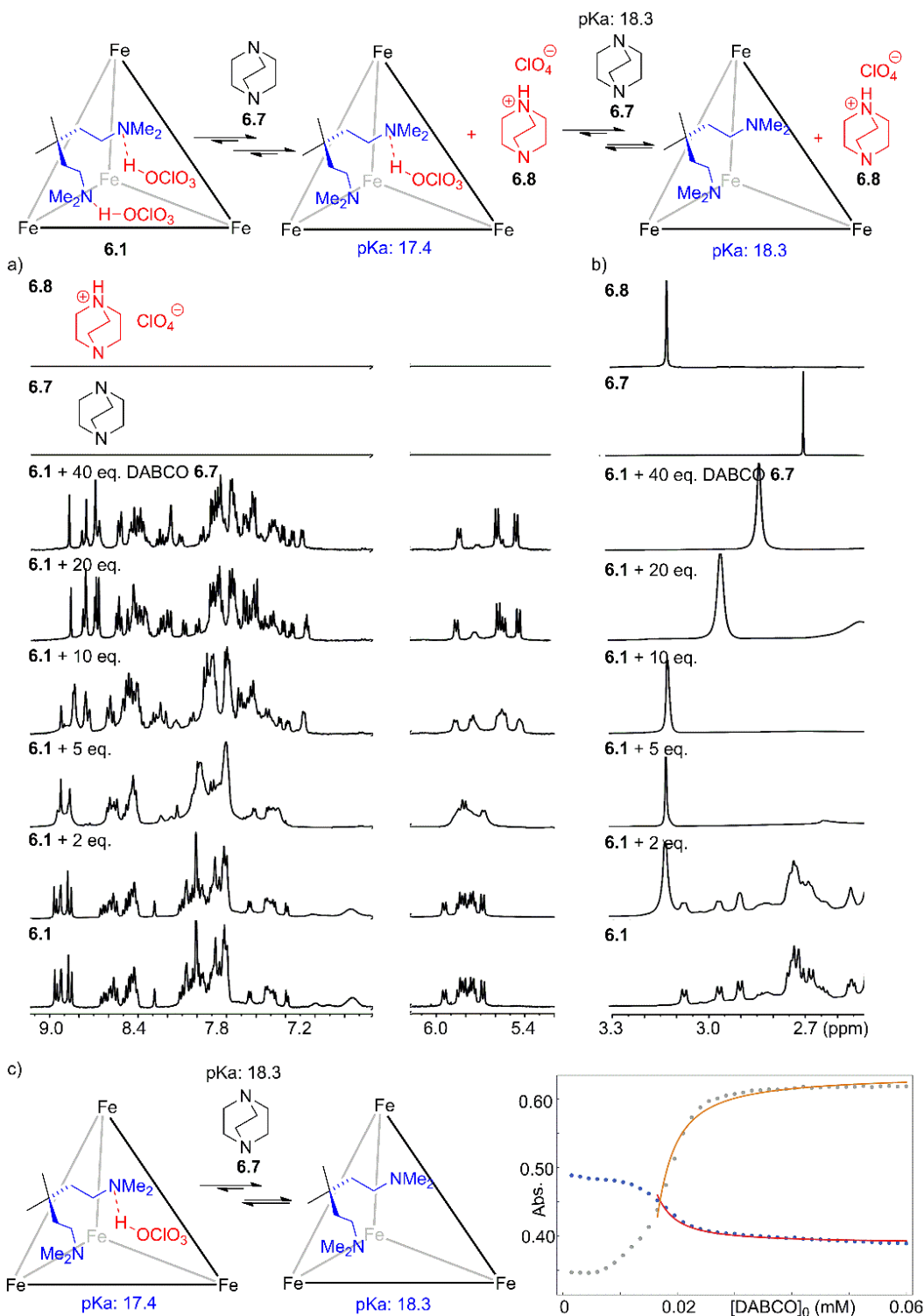
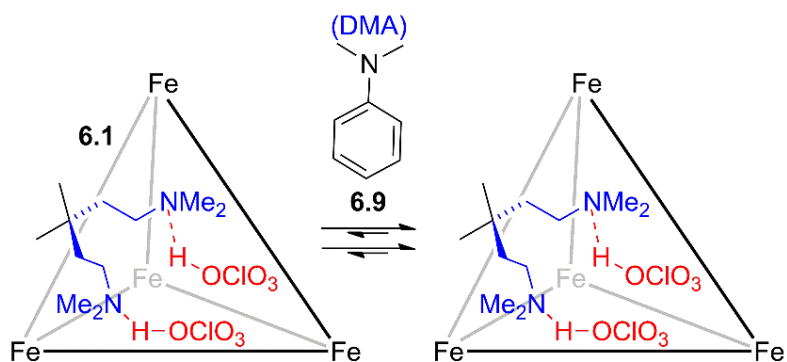


Figure 6.10. a) ^1H NMR spectra of the titration of DABCO **6.7** into 5 mol % cage **6.1** showing cage stability b) and deuterium and hydrogen exchange. c) Dataplot of the UV absorbance changes of cage **6.1** upon titration of DABCO **6.7** in CH_3CN .³⁰

To afford a more complete representation of these results, a titration up to 40 mol. eq. of **6.7** into cage **6.1** was performed using UV absorbance spectroscopy, and the absorbance changes were measured at 320 and 370 nm. The results supported the findings from the ^1H NMR, in which the first set of protons in cage **6.1** behaved like strong acids, and the final protons were closer to the pKa of DABCO **6.7**. Fitting 12 separate equilibria is unrealistic. For a more practical fit, it was initially assumed that the first 11 protons in cage **6.1** were strong acids compared to DABCO **6.7**. Fitting the datapoints after 11 equivalents of base brought focus on the final set of protons. The change in pKa for the final deprotonation reaction was calculated to be 0.85 ± 0.08 , making the pKa of the complex with 6 internal acids equal to 17.4 ± 1 (Figure 6.10c).

a) **Weak Base** - minimal protonation of DMA **6.9**



b) **Strong Bases** - cage **6.1** decomposes after 3 eq. of base

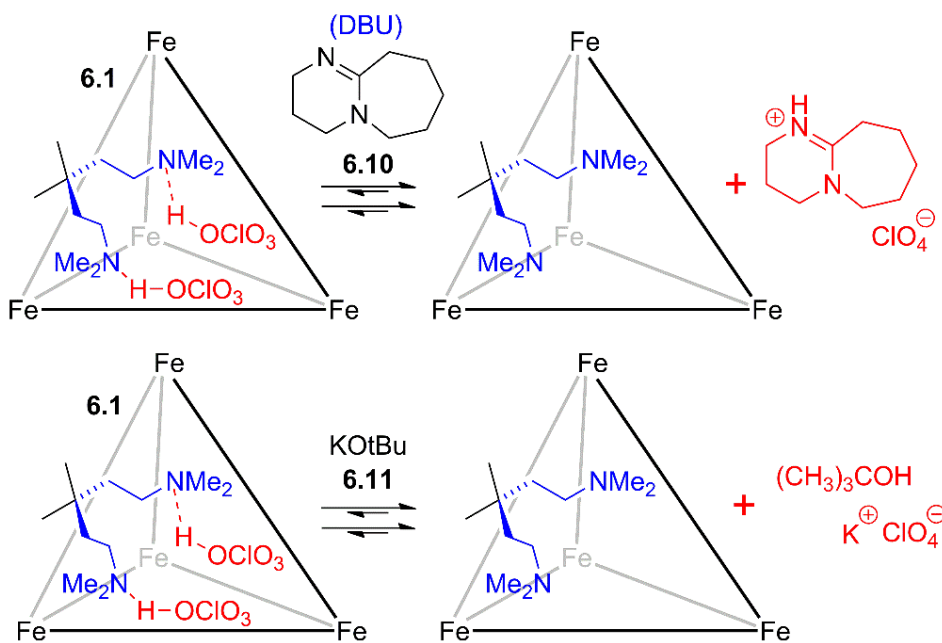


Figure 6.11. Titration of bases into cage **6.1**. a) weak base DMA. b) strong bases DBU and KOtBu.³⁰

Further experiments show that the cage is more acidic and contains more than 12 perchlorates. Titration of a weaker base *N,N*-dimethylaniline (DMA) **6.9** (pK_a in CH_3CN) = 11.4) showed minimal protonation of the amines. However, the addition of the more basic 1,8-diazabicyclo[5.4.0]undec-7-ene (DBU) **6.10** (pK_a in CH_3CN 24.3) and potassium tert-butoxide (KOtBu) **6.11** (pK_a in CH_3CN ³⁷) formed a perchlorate salt similar to that observed in the titration with DABCO. However, the cage was not tolerant to stronger

bases. The addition of above 3 mol. eq. of the guest resulted in decomposition of the cage due to the metal center sequestering iron (Figure 6.11).

6.6. Investigating Ability to Promote or Inhibit Chemical Reactions

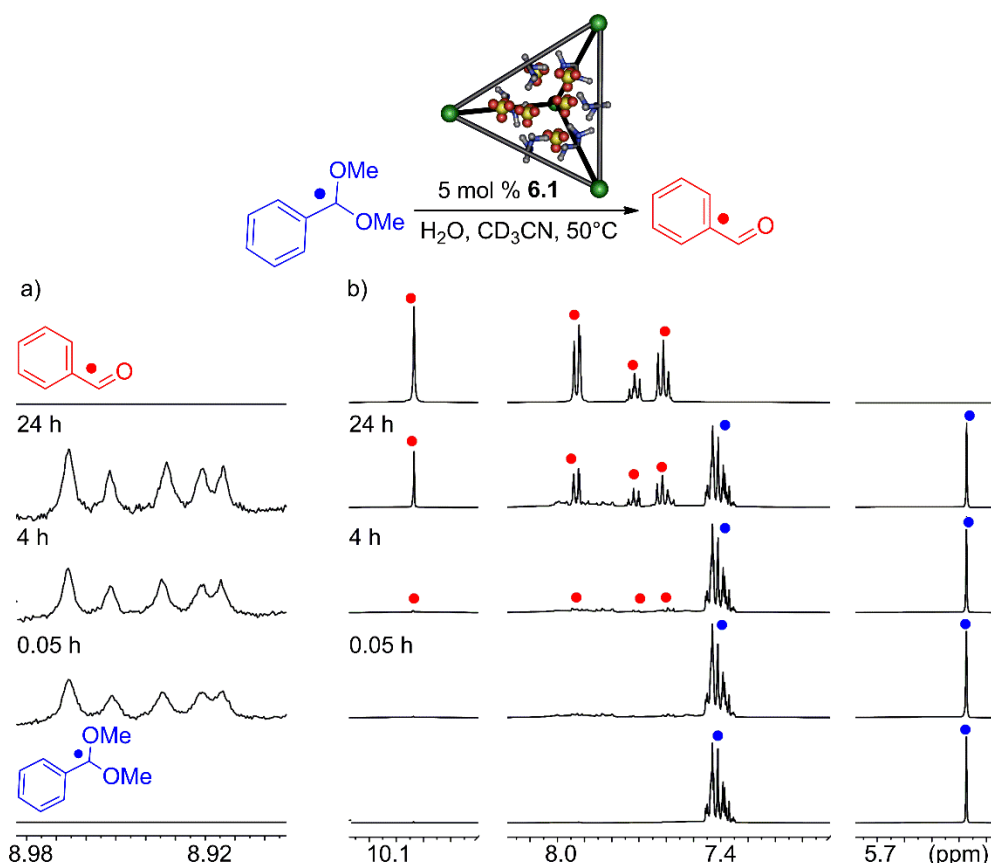


Figure 6.12. ¹H NMR spectra of the reaction between benzaldehyde dimethyl acetal and H₂O in the presence of 5 mol % cage **6.1** showing: a) cage stability b) product formation.³⁰

These results indicate that the amine cage is acidic and can catalyze acidic reactions. Hence, the hydrolysis of the acetal was tested to confirm this fact using 5% cage **6.1** and 6 eq. of H₂O at 50 °C (Figure 6.12). The cage-catalyzed reaction resulted in an initial rate of 41×10^4 mM/min that was slower than the acid cage at 23 °C (2410×10^4 mM/min).¹⁶ In addition to being able to promote acidic reactions, cage **6.1** was observed to inhibit base-catalyzed processes such as the Knoevenagel condensation between benzaldehyde and

malononitrile. No reaction resulted with both 5% cage **6.1** and 5% DABCO **6.7** together. However, in the absence of a cage, DABCO **6.7** alone was able to catalyze the reaction, resulting in a 75% conversion (Figure 6.13).

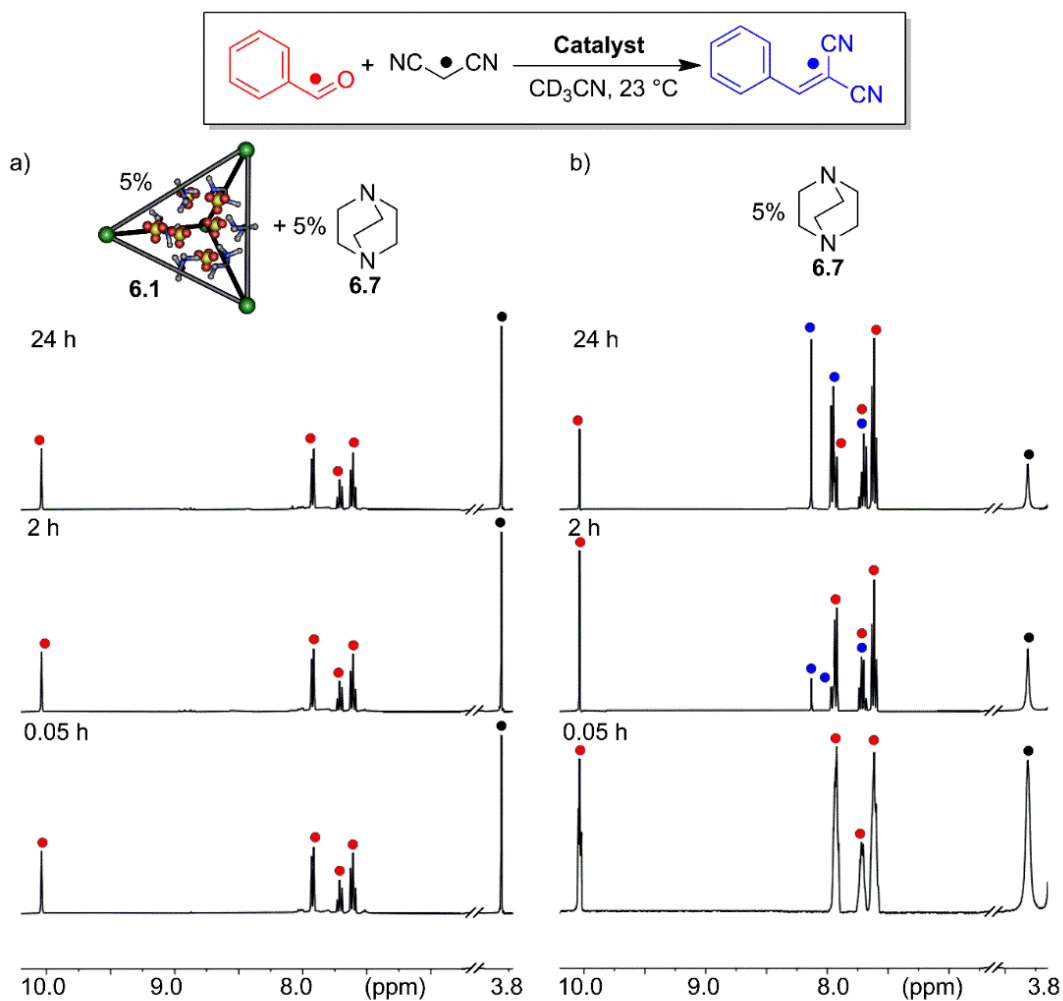


Figure 6.13. ^1H NMR spectra of the reaction between benzaldehyde and malononitrile in the presence of a) 5 mol % cage **6.1** and 5% DABCO **6.7**. b) 5 % DABCO **6.7**.³⁰

6.7. Amine Detritylation Reactions

Finally, the relative acidity of the 12 protonated amines was tested using these three tritylated amines. With tritylated isoquinoline **6.12**, the products formed were the ammonium salt **6.13** and triphenylmethanol **2.1** (Figure 6.14a; Figure 6.15). No cage

decomposition was seen even after this strongly basic amine was formed. The initial reaction to form the ammonium salt happened quickly, with 20% conversion in approximately 3 minutes. After the first 3–4 protons were removed from the cage, the overall charge lessened, and the cage became an increasingly weaker acid. Figure 7.4 shows that the reaction slowed down rapidly, reaching 40% conversion after 4 h and 45% conversion after 24 h. When 6 protons were removed, the cage was no longer acidic enough for the reaction to continue (Figure 6.15).

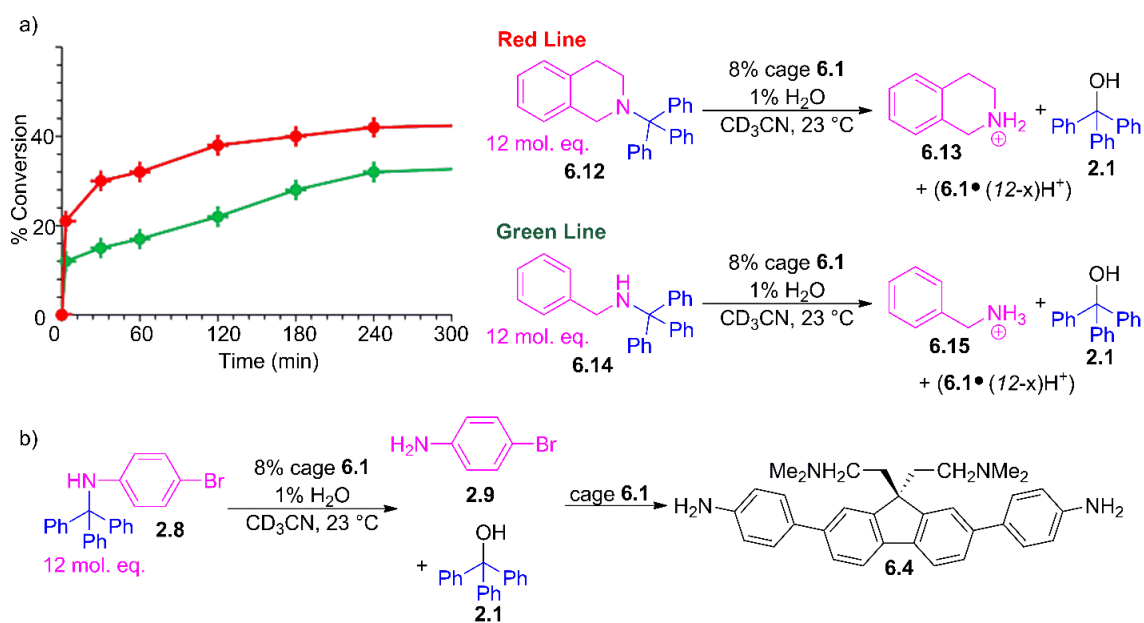


Figure 6.14. a) Reaction progress over time monitored by ¹H NMR with tritylated isoquinoline **6.12** (red) and N-tritylbenzylamine **6.14** (green). b) Cage **6.1** is transiminated and destroyed using N-trityl-4-bromoaniline **2.8**.³⁰

N-tritylbenzylamine **6.14** as the electrophile followed the same reaction pathway shown in the green line in Figure 6.14b. No cage decomposition was observed, and the benzylamine salt **6.15** was formed. However, if N-trityl-4-bromoaniline **2.8** is used, the neutral aniline **2.9** is formed over the protonated product. The cage is then transiminated

and destroyed. As a result, the cage cannot protect itself against weakly basic amines, only strong amines.

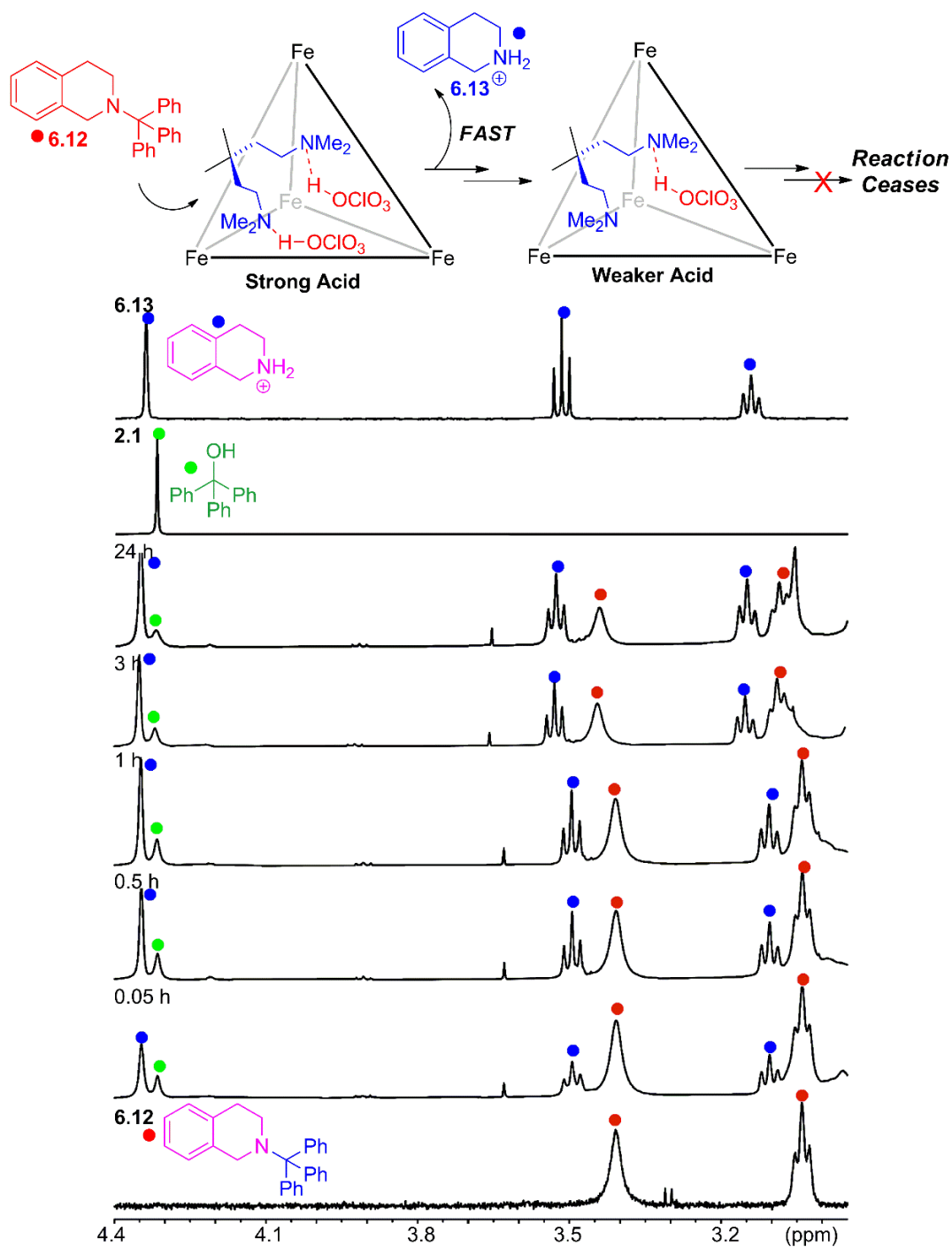


Figure 6.15. ¹H NMR spectra of the reaction between **6.12** and **6.13** in the presence of 5 mol % cage **6.1**.³⁰

6.8. Conclusion

Assembling cage complexes with amine groups can be quite difficult. Even in anhydrous, air-free conditions, the synthesis can only be accomplished using excess $\text{Fe}(\text{ClO}_4)_2$. Even though the cage's formation is discrete, the amine functional groups are protonated due to the water created after the formation of iminopyridine during self-assembly. The excess iron becomes essential for this reason as the "hydroxide" formed is removed from iron oxide salts. Attempts were made to remove water using activated molecular sieves; however, cage **6.1** was especially effective in capturing water. Even with activated molecular sieves removing the water in the reaction, the internal amines were still protonated in complex **6.1**. However, the reaction with molecular sieves was observed to be less effective than in the absence of sieves.

Other experiments were performed to see if the assembly of cage **6.1** could be accomplished in an alternative way. The first alternative method investigated whether the assembly could occur using an equimolar amount of $\text{Fe}(\text{ClO}_4)_2$ and HClO_4 . Only the bis-imine ligand was observed in the reaction, and no cage was formed in the process. This implies that addition of a strong acid is not effective, and that slight changes can disrupt the assembly process. The second alternative method explored whether other Fe^{II} salts could enable assembly of the cage complex. The metal salts $\text{Fe}(\text{NTf}_2)_2$, $\text{Fe}(\text{OTf})_2$, FeSO_4 , and $\text{Fe}(\text{BF}_4)_2 \cdot 6\text{H}_2\text{O}$ were tested. No assembly occurred with the Fe^{II} salts of $\text{Fe}(\text{NTf}_2)_2$ and FeSO_4 , whereas $\text{Fe}(\text{OTf})_2$ caused an unstable formation. However, it was found that cage **6.1** was capable of forming with $\text{Fe}(\text{BF}_4)_2 \cdot 6\text{H}_2\text{O}$. This resulted in a cage complex with a similar NMR spectra to the assembly with $\text{Fe}(\text{ClO}_4)_2$ (Figure 6.16).³⁸ Other evidence from

previous studies confirms this effect, in which iminopyridine complexes can be directed and formed by the presence of hydrogen-bonding groups.

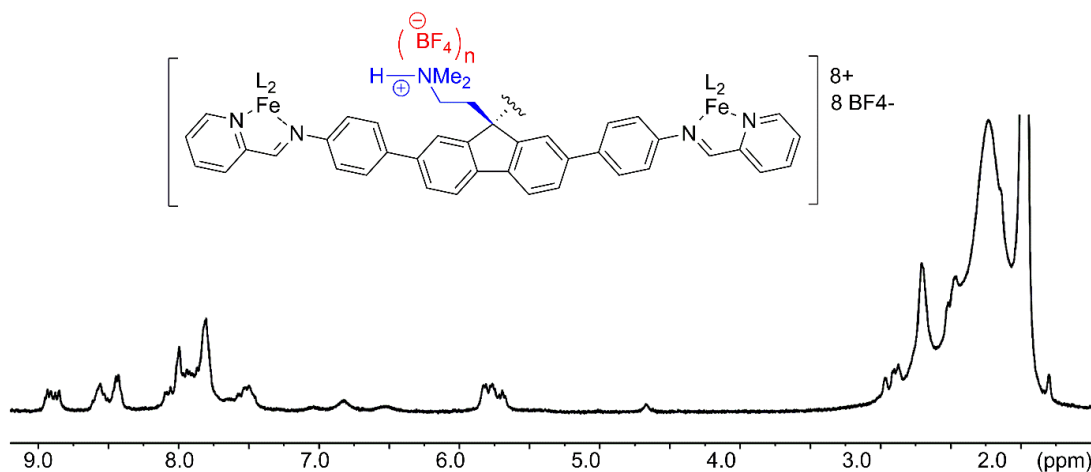


Figure 6.16. ^1H NMR spectrum of the BF_4 salt of cage **6.1**.³⁰

Characterization using various 1D and 2D NMRs of the complex showed that all 12 internal amines were protonated and carried an overall charge of 20^+ . The perchlorates were observed to be interacting with the internal amines in the 2D COSY. Not only was scalar coupling observed, but this implied that the positive charge from the perchlorates must be located on the nitrogen centers. The perchlorates are essential in forming cage **6.1**. Entrapping the perchloric acids, however, causes the internal amines to be less basic than normal in comparison to a molecule in free solution.

Removal of the acids by bases of varying pKa showed that the removal of the first acid is easily done with the base N,N'-dimethylaniline **6.9** (pKa = 11.4). However, the protons became more difficult to remove as the overall charge decreased from 20^+ towards 8^+ . The final proton displayed one full pKa value less than the expected value of 18.3. The amines, therefore, are less basic in free solution than expected. This is reminiscent of enzymes,

whose functional groups can adopt different protonation states in solution when catalyzing a reaction. Similar to an enzyme's ability to control the acidity and basicity of its side-chain in its active sites, cage **6.1** was shown to exhibit the same control using its internal amines. Further studies will attempt to remove the protons on the amine, to explore its ability to catalyze reactions as a base.

6.9. References

1. C. Walsh, *Enzymatic Reaction Mechanisms*; W. H. Freeman, **1979**.
2. A. Fersht, *Structure and mechanism in protein science: a guide to enzyme catalysis and protein folding*; Macmillan, **1999**.
3. W. P. Jencks, *Catalysis in Chemistry and Enzymology*; McGraw-Hill, **1969**.
4. Caulkins, B. G.; Bastin, B.; Yang, C.; Neubauer, T. J.; Young, R. P.; Hilario, E.; Mueller, L. J. Protonation states of the tryptophan synthase internal aldimine active site from solid-state NMR spectroscopy: direct observation of the protonated Schiff base linkage to pyridoxal-5'-phosphate. *J. Am. Chem. Soc.* **2014**, *136*, 12824–12827.
5. Bogie, P. M.; Miller, T. F.; Hooley, R. J. Synthesis and applications of endohedrally functionalized metal-ligand cage complexes. *Isr. J. Chem.* **2019**, *59*, 130–139.
6. Suzuki, K.; Iida, J.; Sato, S.; Kawano, M.; Fujita, M. Discrete and well-defined hydrophobic phases confined in self-assembled spherical complexes. *Angew. Chem., Int. Ed.* **2008**, *47*, 5780–5782.
7. Mal, P.; Schultz, D.; Beyeh, K.; Rissanen, K.; Nitschke, J. R. An unlockable–relockable iron cage by subcomponent self-assembly. *Angew. Chem., Int. Ed.* **2008**, *47*, 8297–8301.
8. Riddell, I. A.; Smulders, M. M.; Clegg, J. K.; Nitschke, J. R. Encapsulation, storage and controlled release of sulfur hexafluoride from a metal–organic capsule. *Chem. Commun.* **2011**, *47*, 457–459.
9. Zhang, D.; Ronson, T. K.; Mosquera, J.; Martinez, A.; Guy, L.; Nitschke, J. R. Anion binding in water drives structural adaptation in an azaphosphatrane-functionalized $\text{Fe}^{\text{II}}_4\text{L}_4$ tetrahedron. *J. Am. Chem. Soc.* **2017**, *139*, 6574–6577.
10. Zhang, D.; Ronson, T. K.; Mosquera, J.; Martinez, A.; Nitschke, J. R. Selective anion extraction and recovery using a $\text{Fe}^{\text{II}}_4\text{L}_4$ cage. *Angew. Chem., Int. Ed.* **2018**, *130*, 3779–3783.

11. Suzuki, K.; Kawano, M.; Sato, S.; Fujita, M. Endohedral peptide lining of a self-assembled molecular sphere to generate chirality-confined hollows. *J. Am. Chem. Soc.* **2007**, *129*, 10652–10653.
12. Wang, Q. Q.; Gonell, S.; Leenders, S. H.; Dürr, M.; Ivanović-Burmazović, I.; Reek, J. N. Self-assembled nanospheres with multiple endohedral binding sites pre-organize catalysts and substrates for highly efficient reactions. *Nat. Chem.* **2016**, *8*, 225–230.
13. Gramage-Doria, R.; Hessels, J.; Leenders, S. H.; Tröppner, O.; Dürr, M.; Ivanović-Burmazović, I.; Reek, J. N. Gold (I) catalysis at extreme concentrations inside self-assembled nanospheres. *Angew. Chem., Int. Ed.* **2014**, *126*, 13598–13602.
14. Bolliger, J. L.; Belenguer, A. M.; Nitschke, J. R. Enantiopure water-soluble [Fe₄L₆] cages: host–guest chemistry and catalytic activity. *Angew. Chem., Int. Ed.* **2013**, *52*, 7958–7962.
15. Custelcean, R.; Bonnesen, P. V.; Duncan, N. C.; Zhang, X.; Watson, L. A.; Van Berkel, G.; Hay, B. P. Urea-functionalized M₄L₆ cage receptors: anion-templated self-assembly and selective guest exchange in aqueous solutions. *J. Am. Chem. Soc.* **2012**, *134*, 8525–8534.
16. Holloway, L. R.; Bogie, P. M.; Lyon, Y.; Ngai, C.; Miller, T. F.; Julian, R. R.; Hooley, R. J. Tandem reactivity of a self-assembled cage catalyst with endohedral acid groups. *J. Am. Chem. Soc.* **2018**, *140*, 8078–8081.
17. Bogie, P. M.; Holloway, L. R.; Ngai, C.; Miller, T. F.; Grewal, D.; Hooley, R. J. A self-assembled cage with endohedral acid groups both catalyzes substitution reactions and controls their molecularity. *Chem. Eur. J.* **2019**, *25*, 10232–10238.
18. Ngai, C.; da Camara, B.; Woods, C. Z.; Hooley, R. J. Size and shape-selective oxocarbenium ion catalysis with a self-assembled cage host. *J. Org. Chem.* **2021**, *86*, 12862–12871.
19. Ngai, C.; Sanchez-Marsetti, C. M.; Harman, W. H.; Hooley, R. J. Supramolecular catalysis of the oxa-Pictet–Spengler reaction with an endohedrally functionalized self-assembled cage complex. *Angew. Chem., Int. Ed.* **2020**, *59*, 23505–23509.

20. Hong, C. M.; Bergman, R. G.; Raymond, K. N.; Toste, F. D. Self-assembled tetrahedral hosts as supramolecular catalysts. *Acc. Chem. Res.* **2018**, *51*, 2447–2455.
21. Fiedler, D., Bergman, R. G.; Raymond, K. N. Supramolecular catalysis of a unimolecular transformation: Aza-Cope rearrangement within a self-assembled host. *Angew. Chem., Int. Ed.* **2004**, *116*, 6916–6919.
22. Pluth, M. D.; Bergman, R. G.; Raymond, K. N. Acid catalysis in basic solution: a supramolecular host promotes orthoformate hydrolysis. *Science*. **2007**, *316*, 85–88.
23. Hastings, C. J.; Pluth, M. D.; Bergman, R. G.; Raymond, K. N. Enzymelike catalysis of the Nazarov cyclization by supramolecular encapsulation. *J. Am. Chem. Soc.* **2010**, *132*, 6938–6940.
24. Zhao, C.; Toste, F. D.; Raymond, K. N.; Bergman, R. G. Nucleophilic substitution catalyzed by a supramolecular cavity proceeds with retention of absolute stereochemistry. *J. Am. Chem. Soc.* **2014**, *136*, 14409–14412.
25. Yoshizawa, M.; Tamura, M.; Fujita, M. Diels-Alder in aqueous molecular hosts: unusual regioselectivity and efficient catalysis. *Science*. **2006**, *312*, 251–254.
26. Murase, T.; Nishijima, Y.; Fujita, M. Cage-catalyzed Knoevenagel condensation under neutral conditions in water. *J. Am. Chem. Soc.* **2012**, *134*, 162–164.
27. Takezawa, H.; Shitozawa, K.; Fujita, M. Enhanced reactivity of twisted amides inside a molecular cage. *Nat. Chem.* **2020**, *12*, 574–578.
28. Cullen, W.; Misuraca, M. C.; Hunter, C. A.; Williams, N. H.; Ward, M. D. Highly efficient catalysis of the Kemp elimination in the cavity of a cubic coordination cage. *Nat. Chem.* **2016**, *8*, 231–236.
29. Cullen, W.; Metherell, A. J.; Wragg, A. B.; Taylor, C. G.; Williams, N. H.; Ward, M. D. Catalysis in a cationic coordination cage using a cavity-bound guest and surface-bound anions: inhibition, activation, and autocatalysis. *J. Am. Chem. Soc.* **2018**, *140*, 2821–2828.
30. Ngai, C.; Wu, H.T.; da Camara B.; Williams, C. G.; Mueller, L.J.; Julian R. R.; Hooley, R. J. Moderated basicity of endohedral amine groups in an octa-cationic self-assembled cage. *Angew. Chem. Int. Ed.* **2022**, e202117011.

31. Jiménez, A.; Bilbeisi, R. A.; Ronson, T. K.; Zarra, S.; Woodhead, C.; Nitschke, J. R. Selective Encapsulation and Sequential Release of Guests Within a Self-Sorting Mixture of Three Tetrahedral Cages. *Angew. Chem., Int. Ed.* **2014**, *53*, 4556–4560.
32. Ueda, Y.; Ito, H.; Fujita, D.; Fujita, M. Permeable self-assembled molecular containers for catalyst isolation enabling two-step cascade reactions. *J. Am. Chem. Soc.*, **2017**, *139*, 6090–6093.
33. Dai, F. R.; Wang, Z. Modular assembly of metal–organic supercontainers incorporating sulfonylcalixarenes. *J. Am. Chem. Soc.* **2012** *134*, 8002–8005.
34. Qiao, Y.; Zhang, L.; Li, J.; Lin, W.; Wang, Z. Switching on supramolecular catalysis via cavity mediation and electrostatic regulation. *Angew. Chem., Int. Ed.* **2016**, *128*, 12970–12974.
35. Meng, W.; Clegg, J. K.; Thoburn, J. D.; Nitschke, J. R. Controlling the transmission of stereochemical information through space in terphenyl-edged Fe₄L₆ cages. *J. Am. Chem. Soc.*, **2011**, *133*, 13652–13660.
36. Ronson, T. K., Meng, W., & Nitschke, J. R. Design principles for the optimization of guest binding in aromatic-paneled Fe^{II}₄L₆ cages. *J. Am. Chem. Soc.* **2017**, *139*, 9698–9707.
37. Tshepelevitsh, S.; Kütt, A.; Lõkov, M.; Kaljurand, I.; Saame, J.; Heering, A.; Leito, I. On the basicity of organic bases in different media. *Eur. J. Org. Chem.* **2019**, 6735–6748.
38. Young, M. C.; Holloway, L. R.; Johnson, A. M.; Hooley, R. J. A supramolecular sorting hat: Stereocontrol in metal–ligand self-assembly by complementary hydrogen bonding. *Angew. Chem., Int. Ed.* **2014**, *126*, 9990–9994.

Chapter 7 - Experimental

7.1. General Information

^1H NMR and ^{13}C NMR spectra were recorded on Bruker Avance NEO 400 MHz and 600 MHz NMR spectrometer. The spectrometers were automatically tuned and matched to the correct operating frequencies. Proton (^1H) and carbon (^{13}C) chemical shifts are reported in parts per million (δ) with respect to tetramethylsilane (TMS, $\delta = 0$), and referenced internally with respect to the protio solvent impurity for CD_3CN (^1H : 1.94 ppm, ^{13}C : 118.3 ppm). Deuterated NMR solvents were obtained from Cambridge Isotope Laboratories, Inc., Andover, MA, and used without purification, except for cage characterization, whereby the deuterated NMR solvent (CD_3CN) was distilled over calcium hydride. The distilled CD_3CN was transferred under nitrogen into a nitrogen-filled glovebox with standard techniques. Spectra were digitally processed (phase and baseline corrections, integration, peak analysis) using Bruker Topspin 1.3 and MestreNova. All other materials were obtained from Aldrich Chemical Company (St. Louis, MO), or Fisher Scientific (Fairlawn, NJ), and were used as received. Solvents were dried through a commercial solvent purification system (Pure Process Technologies, Inc.). UV/Vis spectroscopy was performed on a Cary 60 Photospectrometer using the Varian Scans program to collect data. Infrared spectra were recorded on a Bruker IFS HR-FTIR spectrometer, and wavenumbers are reported in cm^{-1} . In chapter 6, the mass spectrometric sample of cage **6.1** was prepared in 100% CH_3CN and infused into a Thermo Orbitrap Velos Pro mass spectrometer (Thermo Fisher Scientific, San Jose, CA, USA) with a homebuilt nanoESI source. The spray voltage, capillary temperature, and the S-lens RF

level were set to 1.7 kV, 160 °C, and 45% respectively. Full mass spectra were acquired with a resolution of $r = 30\,000$. Thermo Xcalibur was used to analyze MS data and prepare the predicted isotope patterns. For all other molecules, high resolution accurate mass spectral data were obtained from the Analytical Chemistry Instrumentation Facility at the University of California, Riverside, on an Agilent 6545 QTOF LC/MS instrument.

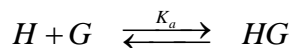
7.2. General Binding Calculations

For chapters 2-5, the binding constants for 1:1 and 1:2 host-guest complex models were determined by UV/Vis titration experiments and binding constants extracted following the general approach outlined by Thordarson,¹⁻³ modified as described below. In brief, UV/Vis absorptions at 300 and 370 nm were monitored as a function of added guest and simultaneously fit using a non-linear least-squares (maximum likelihood) approach written within the Mathematica programming environment.⁴ For the 1:1 equilibrium model, the binding constant (K_a) and molar absorptivities (at both wavelengths) for the pure host (H) and host-guest (HG) complex were determined. For the 1:2 equilibrium model, both the first (K_1) and second (K_2) binding constants were determined, along with molar absorptivities for the host, host-guest (HG), and host-dual-guest (HG_2) complexes. The precise equilibria and corresponding equations are detailed below. Error bars for each of the fit parameters were determined by a numerical calculation of the covariance matrix and are reported above as \pm standard error.⁵ The error analysis assumes normally distributed, random error that is independent of data point; in such a case, the sum of the squared-residuals follows the chi-squared distribution for $N-k$ degrees of freedom,⁶ where N is the number of measured data points and k the number of fit parameters (5 and 8 for the 1:1 and

1:2 models, respectively). The significance of the 1:2 model was judged based on the inverse ratio of the squared residuals compared to the 1:1 model. Again, if the errors are normally distributed, this ratio follows the F-distribution for N-5 (numerator) and N-8 (denominator) degrees of freedom. To be considered statistically “better,” the 1:2 model must improve the residuals beyond what normal statistical fluctuations would be expected to sample with the observed noise and finite number of measured points. This is quantified via the p-value, which gives the probability that the observed improvement in residuals for the 1:2 complex model can be explained as statistical “luck.” A small value indicates that the model truly is better – that is, that more of the underlying data trends are reproduced so that the residuals are actually smaller. To be considered significant in this context, we take p-values below 0.001.

Equilibrium Models:¹⁻³

The 1:1 host-guest binding



has an association constant

$$K_a = \frac{[HG]}{[H][G]}$$

from which the concentration of the host, guest, and complex can be related back to initial (or total added) concentrations, H_0 and G_0 , of each

$$[H] = \frac{1}{2} \left(H_0 - G_0 - \frac{1}{K_a} \right) + \frac{1}{2} \sqrt{\left(G_0 - H_0 - \frac{1}{K_a} \right)^2 + 4 \frac{G_0}{K_a}}$$

$$[G] = \frac{1}{2} \left(G_0 - H_0 - \frac{1}{K_a} \right) + \frac{1}{2} \sqrt{\left(G_0 - H_0 - \frac{1}{K_a} \right)^2 + 4 \frac{G_0}{K_a}}$$

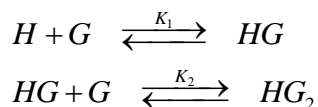
$$[HG] = \frac{1}{2} \left(G_0 + H_0 + \frac{1}{K_a} \right) - \frac{1}{2} \sqrt{\left(G_0 - H_0 - \frac{1}{K_a} \right)^2 + 4 \frac{G_0}{K_a}}$$

The absorbance at a given wavelength λ can then be written as

$$\begin{aligned} A^\lambda &= \varepsilon_H^\lambda [H] + \varepsilon_{HG}^\lambda [HG] \\ &= \varepsilon_H^\lambda \left\{ \frac{1}{2} \left(H_0 - G_0 - \frac{1}{K_a} \right) + \frac{1}{2} \sqrt{\left(G_0 - H_0 - \frac{1}{K_a} \right)^2 + 4 \frac{G_0}{K_a}} \right\} + \\ &\quad \varepsilon_{HG}^\lambda \left\{ \frac{1}{2} \left(G_0 + H_0 + \frac{1}{K_a} \right) - \frac{1}{2} \sqrt{\left(G_0 - H_0 - \frac{1}{K_a} \right)^2 + 4 \frac{G_0}{K_a}} \right\} \end{aligned}$$

where it is assumed that the guest on its own does not absorb. This is the expression that is used to simultaneously fit the experimental absorption data at 300 and 370 nm, A^{300} and A^{370} , as a function of added guest, G_0 , to determine K_a and ε_H^{300} , ε_{HG}^{300} , ε_H^{370} , and ε_{HG}^{370} .

The 1:2 host-guest binding is assumed to be a non-cooperative, sequential two-step process



which is characterized by two binding constants

$$\begin{aligned} K_1 &= \frac{[HG]}{[H][G]} \\ K_2 &= \frac{[HG_2]}{[HG][G]} \end{aligned}$$

We analyze this for the case in which the approximation $[G] \approx G_0$ is valid, which corresponds to the limit in which $K_1[H] \ll 1$ or when G_0 is in large excess. This condition can be relaxed, but appears valid in our situation. With these caveats,

$$[H] = \frac{H_0}{1 + K_1 G_0 + K_1 K_2 G_0^2}$$

$$[G] \approx G_0$$

$$[HG] = \frac{K_1 H_0 G_0}{1 + K_1 G_0 + K_1 K_2 G_0^2}$$

$$[HG_2] = \frac{K_1 K_2 H_0 G_0^2}{1 + K_1 G_0 + K_1 K_2 G_0^2}$$

and the absorbance can be written

$$\begin{aligned} A^\lambda &= \varepsilon_H^\lambda [H] + \varepsilon_{HG}^\lambda [HG] + \varepsilon_{HG_2}^\lambda [HG_2] \\ &= \varepsilon_H^\lambda \frac{H_0}{1 + K_1 G_0 + K_1 K_2 G_0^2} + \varepsilon_{HG}^\lambda \frac{K_1 H_0 G_0}{1 + K_1 G_0 + K_1 K_2 G_0^2} + \varepsilon_{HG_2}^\lambda \frac{K_1 K_2 H_0 G_0^2}{1 + K_1 G_0 + K_1 K_2 G_0^2} . \end{aligned}$$

This expression is used to simultaneously fit the experimental absorption data at 300 and

370 nm, A^{300} and A^{370} , as a function of added guest, G_0 , to determine K_1 , K_2 , ε_H^{300} , ε_{HG}^{300} , $\varepsilon_{HG_2}^{300}$,

ε_H^{370} , ε_{HG}^{370} , and $\varepsilon_{HG_2}^{370}$.

7.3. Experimental for Chapter 2

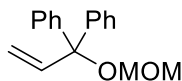
See the following publications for full synthesis/characterization:

- Bogie, P. M.; Holloway, L. R.; Ngai, C.; Miller, T. F.; Grewal, D.; Hooley, R. J. A self-assembled cage with endohedral acid groups both catalyzes substitution reactions and controls their molecularity. *Chem. Eur. J.* **2019**, *25*, 10232–10238.
- Bogie, P. M. Designing functional cages: From luminescent sensors to artificial enzymes. **2019**. (Doctoral dissertation, UC Riverside).

General Method for Acid-Promoted Substitution Reactions:

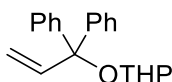
Trityl substrate (6.3 μmol , 1 mol. -eq.) was placed in an NMR tube followed by 5 mol % acid cage **1.30** (0.31 μmol , 2 mg) or 30 mol % control acid **1.35** (1.86 mmol, 0.95 mg). The nucleophile (1.25 mol. -eq., 7.9 μmol , 3.9 μL of 2 M solution in CD_3CN) was then added followed by 1,4-Dioxane as the internal standard (0.5 mol. -eq. 3.2 μmol , 1.6 μL of 2 M solution in CD_3CN). 400 μL of CD_3CN was added, and the tube was capped and quickly shaken to dissolve all solids. Control trials use 30 mol % of diacid **1.35** to maintain the same concentration of COOH groups present in 5 mol % of the M_4L_6 cage **2.6**. An initial ^1H NMR spectrum of the reaction mixture was obtained to verify the correct amounts of reagents. The sample was then heated at the specified temperature and the reaction progress monitored over time. Rate calculation trials were performed in triplicate. The percent conversion values were obtained via integration of the product and substrate peaks against the internal standard and the calculated values of duplicate trials were averaged.

7.4. Experimental for Chapter 3



Synthesis of 1-(methoxymethyl)prop-2-ene-1,1-diyl)dibenzene (3.3):

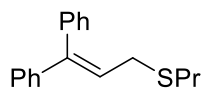
Sodium hydride (60% dispersion in mineral oil, 30 mg, 1.24 mmol, 2 equiv.), was placed in a Schlenk flask with a stir bar and purged with N₂. Tetrahydrofuran (1.0 mL) was then syringed into the flask. The mixture was then stirred at room temperature for 10 minutes before 1,1-diphenylprop-2-en-1-ol (130 mg, 0.620 mmol, 1 equiv.) and bromo(methoxy)methane (85 mg, 0.682 mmol, 1.1 equiv.) was added. After 2 h, the solution was filtered to remove the NaH, the solvent was removed. The product was purified by silica column chromatography (10% *EtOAc*/hexane) to obtain a colorless liquid (yield: 122.9 mg, 78%). IR (CHCl₃): ν_{\max} (cm⁻¹) 3059, 2883, 1599, 1027, 924, and 772. ¹H NMR (600 MHz, CDCl₃) δ 7.39 – 7.26 (m, 10H), 6.63 (dd, *J* = 17.2, 10.7 Hz, 1H), 5.39 (dd, *J* = 10.7, 1.2 Hz, 1H), 4.98 (dd, *J* = 17.2, 1.2 Hz, 1H), 4.76 (s, 2H), 3.42 (s, 3H); ¹³C {¹H} NMR (151 MHz, CDCl₃) δ 143.9, 141.1, 128.0, 127.9, 127.3, 117.4, 114.9, 92.4, 55.7. HRMS (ESI-TOF) *m/z* calc^d for C₁₇H₁₈NaO₂ ([M+Na]⁺): 277.1199; found 277.1179.



Synthesis of 2-((1,1-diphenylallyl)oxy)tetrahydro-2H-pyran (3.4):

p-Toluenesulfonic acid (0.53 g, 0.0031 mol, 5 mol %) was placed in a Schlenk flask with a stir bar and purged with N₂. Tetrahydrofuran (500 ml) and 1,1-diphenylprop-2-en-1-ol (13 g, 0.062 mol, 1 equiv.) was then syringed into the flask. To this solution, 4-dihydro-2H-pyran (7.8 g, 0.093 mol, 1.5 equiv.) was added, and the mixture was stirred at room

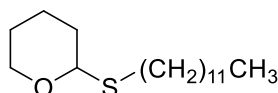
temperature. After 16 h, the solution was diluted with EtOAc and washed with sat. NaHCO₃ and brine. The organic phase was then dried with MgSO₄ and concentrated in vacuo. The product was purified by silica column chromatography (10% EtOAc/hexane) to obtain a colorless liquid (yield: 15.5 g, 85%). IR (CHCl₃): ν_{\max} (cm⁻¹) 3025, 2942, 1608, 1075, 988, 772. ¹H NMR (600 MHz, CDCl₃) δ 7.43 (dd, J = 8.3, 1.3 Hz, 2H), 7.39 – 7.20 (m, 8H), 6.72 (dd, J = 17.3, 10.7 Hz, 1H), 5.37 (dd, J = 10.7, 1.4 Hz, 1H), 4.85 (d, J = 1.4 Hz, 1H), 4.83 – 4.75 (m, 1H), 4.00 (ddd, J = 11.5, 6.9, 4.9 Hz, 1H), 3.57 – 3.22 (m, 1H), 2.00 (ddt, J = 11.8, 8.8, 5.0 Hz, 1H), 1.91 – 1.60 (m, 2H), 1.73 – 1.37 (m, 3H). ¹³C{¹H} NMR (151 MHz, CDCl₃) δ 144.5, 144.1, 141.7, 128.1, 127.9, 127.4, 117.5, 85.3, 62.4, 31.7, 25.5, 19.8. HRMS (ESI-TOF) m/z calc^d for C₂₀H₂₂O₂Na ([M+Na]⁺): 317.1512; found 317.1501.



Synthesis of (3,3-diphenylallyl)(propyl)sulfane (3.5):

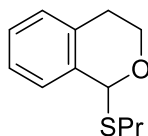
Substrate **2.1** (130 mg, 0.620 mmol, 1 equiv.) and CSA (43.2 mg, 186 μ mol, 30 mol %), were placed in a Schlenk flask with a stir bar and purged with N₂. The substrate was then dissolved in dry CH₃CN (1.0 mL). Propanethiol (1.0 mL) was added to the flask, and the reaction was stirred at room temperature in a sand bath for 16 h. The solvent was removed and the product dried *in vacuo*. The products were purified by silica gel chromatography eluting with 0-30% EtOAc/hexane and afforded a colorless liquid (yield: 148.1 mg, 89%): IR (CH₃CN): ν_{\max} (cm⁻¹) 3005, 2943, 1631, 1375, 1038, 918, 748. ¹H NMR (400 MHz, CD₃CN) δ 7.48 – 7.37 (m, 3H), 7.36 – 7.28 (m, 3H), 7.27 – 7.19 (m, 4H), 6.17 (t, J = 7.9

Hz, 1H), 3.22 (d, $J = 7.9$ Hz, 2H), 2.47 – 2.42 (m, 2H), 1.42 (dt, $J = 14.6, 7.3$ Hz, 2H), 0.90 (t, $J = 7.3$ Hz, 3H). $^{13}\text{C}\{^1\text{H}\}$ NMR (151 MHz, CD_3CN) δ 129.8, 128.3, 128.2, 127.2, 125.7, 117.0, 32.7, 30.0, 22.7, 12.6. HRMS (ESI-TOF) m/z calc^d for $\text{C}_{18}\text{H}_{19}\text{S}$ ($[\text{M}-\text{H}]^-$): 267.1213; found 267.1212.



Synthesis of 2-(dodecylthio)tetrahydro-2H-pyran (3.13):

Substrate **3.10** (102 mg, 0.620 mmol, 1 equiv.) and CSA **3.6** (43.2 mg, 186 μmol , 30 mol %), were placed in a Schlenk flask with a stir bar and purged with N_2 . The substrate was then dissolved in dry CH_3CN (1.0 mL). Propanethiol (1.0 mL) was added to the flask, and the reaction was stirred at room temperature in a sand bath for 16 h. The solvent was removed and the product dried *in vacuo*. The products were purified by silica gel chromatography eluting with 0-30% EtOAc/hexane and afforded a colorless liquid (yield: 154.5 mg, 87%): IR (CH_3CN): ν_{max} (cm^{-1}) 2998, 2943, 1443, 1375, 1038, 918, 832, 751, 655. ^1H NMR (400 MHz, CD_3CN) δ 4.87 (dd, $J = 6.3, 3.8$ Hz, 1H), 4.01 (dt, $J = 10.7, 5.3$ Hz, 1H), 3.48 (dt, $J = 11.1, 5.2$ Hz, 1H), 2.68 – 2.50 (m, 2H), 1.88 (dtd, $J = 13.7, 7.2, 6.4, 2.9$ Hz, 1H), 1.78 (tdq, $J = 11.0, 7.2, 4.5, 3.7$ Hz, 1H), 1.66 – 1.50 (m, 6H), 1.38 (dd, $J = 13.2, 6.9$ Hz, 2H), 1.31 (s, 16H), 0.91 (t, $J = 6.8$ Hz, 3H). $^{13}\text{C}\{^1\text{H}\}$ NMR (100 MHz, CD_3CN) δ 81.9, 64.0, 31.6, 31.6, 31.4, 29.9, 29.9, 29.7, 29.2, 29.0, 28.9, 28.7, 28.6, 25.5, 22.4, 21.5, 13.4. HRMS (ESI-TOF) m/z calc^d for $\text{C}_{17}\text{H}_{35}\text{OS}$ ($[\text{M}+\text{H}]^+$): 287.2403; found 287.2410.



Synthesis of 1-(propylthio)isochromane (3.20):

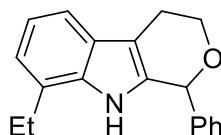
Substrate **3.15** (102 mg, 0.620 mmol, 1 equiv.) and CSA **3.6** (43.2 mg, 186 μmol , 30 mol %), were placed in a Schlenk flask with a stir bar and purged with N_2 . The substrate was then dissolved in dry CH_3CN (1.0 mL). Propanethiol (1.0 mL) was added to the flask, and the reaction was stirred at room temperature in a sand bath for 16 h. The solvent was removed and the product dried *in vacuo*. The products were purified by silica gel chromatography eluting with 0-30% EtOAc/hexane and afforded a colorless liquid (yield: 105.9 mg, 82%): IR (CH_3CN): ν_{max} (cm^{-1}) 3005, 2944, 1418, 1375, 1038, 918, 749. ^1H NMR (400 MHz, CD_3CN) δ 7.24 – 7.13 (m, 4H), 6.25 (s, 1H), 4.43 – 4.33 (m, 1H), 3.88 (ddd, $J = 11.4, 6.4, 1.4$ Hz, 1H), 3.08 – 2.96 (m, 1H), 2.81 (ddd, $J = 13.0, 7.7, 6.6$ Hz, 1H), 2.73 – 2.58 (m, 2H), 1.80 – 1.68 (m, 2H), 1.04 (t, $J = 7.3$ Hz, 3H). $^{13}\text{C}\{^1\text{H}\}$ NMR (100 MHz, CD_3CN) δ 134.9, 133.7, 128.1, 126.5, 126.4, 124.9, 82.7, 58.7, 23.0, 21.7, 13.4, 12.1. HRMS (ESI-TOF) m/z calc^d for $\text{C}_{12}\text{H}_{15}\text{OS}$ ($[\text{M}-\text{H}]$): 207.0849; found 207.0842.

General Method for Acid-Promoted Substitution Reactions:

The electrophile (1 mol.-eq., 6.3 μmol , 10 μL of 0.63 M solution in CD_3CN) was placed in an NMR tube followed by 5 mol % cage **1.30** (0.31 μmol , 2 mg), 5 mol % CSA **3.6** (0.315 μmol , 10 μL of 0.0315 M solution in CD_3CN), 30 mol % control **1.35** (1.86 mmol, 5 μL of 0.372 M solution in CD_3CN) or 1 mol.-eq. cavity filling guest **3.21** (6.3 μmol , 10 μL of 0.63 M solution in CD_3CN). The nucleophile (1.25 mol.-eq., 7.9 μmol , 10 μL of 0.79 M solution in CD_3CN) was then added followed by 1,4-dioxane as the internal standard

(0.5 mol.-eq., 3.2 μmol , 10 μL of 0.32 M solution in CD_3CN). A combined total volume of 400 μL of CD_3CN was added, and the tube was capped and sealed around with parafilm. The sample was quickly shaken. The reaction progress was monitored over time. An initial ^1H NMR spectrum of the reaction mixture was obtained to verify the stoichiometry of the sample. The percent conversion values were obtained via integration of the product and substrate peaks against the internal standard. Experiments were performed in triplicates.

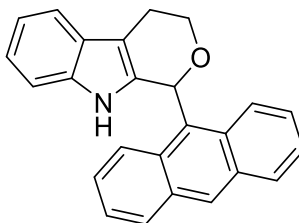
7.5. Experimental for Chapter 4



Synthesis of 8-ethyl-1-phenyl-1,3,4,9-tetrahydropyrano[3,4-b]indole (4.19):

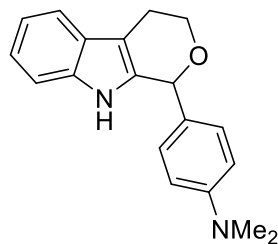
Tryptophol **4.5** (100 mg, 0.620 mmol, 1 equiv.), CSA **3.6** (43.2 mg, 186 mmol, 30 mol %), were placed in a Schlenk flask with a stir bar and purged with N_2 . The substrate was then dissolved in dry CHCl_3 (1.0 mL). Acetal **4.1** (.775 mmol, 1.25 equiv.) was added to the flask, and the reaction was stirred at room temperature in a sand bath for 16 h. The solvent was removed and the product dried *in vacuo*. The indole product was purified by aluminum oxide column chromatography eluting with 0-30% *EtOAc*/hexane to afford a white solid (yield: 77%): IR (CH_3CN): ν_{max} 3164, 3000, 2944, 1630, 1440, 1375, 1038, 918, 705, and 538 cm^{-1} ; ^1H NMR (600 MHz, CD_3CN) δ 8.76 (s, 1H), 7.47 – 7.31 (m, 6H), 7.04 (t, J = 7.5 Hz, 1H), 6.99 (s, 1H), 5.87 (s, J = 1.8 Hz, 1H), 4.15 (dt, J = 11.2, 4.8 Hz, 1H), 3.93 (ddd, J = 11.2, 8.1, 4.3 Hz, 1H), 2.98 (dddd, J = 15.1, 8.1, 5.0, 1.8 Hz, 1H), 2.83 (dtd, J = 15.5, 4.4, 1.8 Hz, 1H), 2.76 (q, J = 7.5 Hz, 2H), 1.22 (t, J = 7.6 Hz, 3H); ^{13}C NMR (600 MHz, CD_3CN) δ 140.55, 134.97, 133.62, 128.78, 128.43, 128.36, 126.99, 126.76, 120.37,

119.47, 115.67, 108.68, 75.4, 63.23, 23.85, 22.11, 13.70; HRMS (ESI-TOF) m/z calc^d for C₁₉H₁₉NO: 277.1471, found 278.1544 ([M+H]⁺).



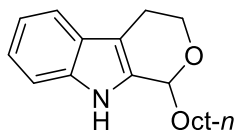
Synthesis of 1-(anthracen-9-yl)-1,3,4,9-tetrahydropyrano[3,4-b]indole (4.18):

Tryptophol **4.2** (100 mg, 0.620 mmol, 1 equiv.), CSA **3.6** (43.2 mg, 186 mmol, 30 mol %), were placed in a Schlenk flask with a stir bar and purged with N₂. The substrate was then dissolved in dry CHCl₃ (1.0 mL). Acetal **4.10** (.775 mmol, 1.25 equiv.) was added to the flask, and the reaction was stirred at room temperature in a sand bath for 16 h. The solvent was removed and the product dried *in vacuo*. The indole product was purified by recrystallization with methanol to afford a yellow solid (yield: 60%): IR (CH₃CN): ν_{\max} 3164, 3002, 2944, 1620, 1443, 1370, 1038, 918, 749, and 536 cm⁻¹; ¹H NMR (600 MHz, CD₃CN) δ 8.68 (s, 1H), 8.65 (d, $J = 9.3$ Hz, 1H), 8.47 (s, 1H), 8.42 (d, $J = 11.6$ Hz, 1H), 8.20 (d, $J = 10.2$ Hz, 1H), 8.11 – 8.04 (m, 1H), 7.72 – 7.65 (m, 1H), 7.61 (d, $J = 10.5$ Hz, 2H), 7.44 – 7.36 (m, 2H), 7.27 – 7.19 (m, 1H), 7.12 – 7.05 (m, 1H), 7.03 (d, $J = 3.7$ Hz, 2H), δ 4.65 – 4.59 (m, 1H), 4.32 (td, $J = 11.6, 3.7$ Hz, 1H), 3.45 (dddd, $J = 15.7, 11.8, 6.0, 2.5$ Hz, 1H), 3.09 – 2.94 (m, 1H); ¹³C NMR (600 MHz, CD₃CN) 136.32, 136.18, 129.32, 128.68, 127.04, 126.87, 126.41, 125.82, 125.18, 125.06, 123.09, 121.31, 119.18, 117.96, 110.88, 106.58, 71.51, 66.94, 22.13; HRMS (ESI-TOF) m/z calc^d for C₂₅H₁₉NO: 349.1548, found 350.1519 ([M+H]⁺).



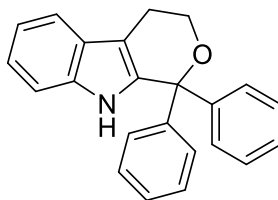
Synthesis of N,N-dimethyl-4-(1,3,4,9-tetrahydropyrano[3,4-b]indol-1-yl)aniline (4.20):

Tryptophol **4.2** (100 mg, 0.620 mmol, 1 equiv.), CSA **3.6** (43.2 mg, 186 mmol, 30 mol %), were placed in a Schlenk flask with a stir bar and purged with N₂. The substrate was then dissolved in dry CHCl₃ (1.0 mL). Acetal **4.12** (.775 mmol, 1.25 equiv.) was added to the flask, and the reaction was stirred at room temperature in a sand bath for 16 h. The solvent was removed and the product dried *in vacuo*. The indole product was purified by aluminum oxide column chromatography eluting with 0-30% *EtOAc*/hexane to afford a white solid (yield: 85%): IR (CH₃CN): ν_{\max} 3163, 3004, 2944, 1630, 1443, 1375, 1038, 918, 748, and 536 cm⁻¹; ¹H NMR (600 MHz, CD₃CN) δ 8.70 (s, 1H), 7.53 (d, J = 7.7 Hz, 1H), 7.28 (d, J = 7.9 Hz, 1H), 7.17 (d, J = 8.7 Hz, 2H), 7.09 (dt, J = 23.7, 7.1 Hz, 2H), 6.76 (d, J = 8.7 Hz, 2H), 5.74 (s, 1H), 4.19 (dt, J = 11.1, 4.7 Hz, 1H), 3.91 (ddt, J = 11.3, 8.9, 4.2 Hz, 1H), 3.01 – 2.97 (m, 1H), 2.96 (s, 6H), 2.83 – 2.77 (m, 1H); ¹³C NMR (600 MHz, CD₃CN) δ 141.08, 136.30, 134.87, 129.39, 126.37, 123.18, 121.25, 118.97, 117.87, 112.06, 110.94, 107.84, 75.28, 63.52, 39.70, 22.08; HRMS (ESI-TOF) m/z calc^d for C₁₉H₂₀N₂O: 292.1576, found 293.1665 ([M+H]⁺).



Synthesis of 1-(1,3,4,9-tetrahydropyrano[3,4-b]indol-1-yl)octan-1-one (4.21):

Tryptophol 4.2 (100 mg, 0.620 mmol, 1 equiv.), CSA 3.6 (43.2 mg, 186 mmol, 30 mol %), were placed in a Schlenk flask with a stir bar and purged with N₂. The substrate was then dissolved in dry CHCl₃ (1.0 mL). Acetal 4.14 (.775 mmol, 1.25 equiv.) was added to the flask, and the reaction was stirred at room temperature in a sand bath for 16 h. The solvent was removed and the product dried *in vacuo*. The indole product was purified by aluminum oxide column chromatography eluting with 0-30% EtOAc/hexane to afford a white solid (yield: 70%): IR (CH₃CN): ν_{\max} 3160, 3002, 2943, 1630, 1442, 1375, 1084, 918, 748, 535 cm⁻¹; ¹H NMR (600 MHz, CD₃CN) δ 9.00 (s, 1H), 7.47 (d, *J* = 7.7 Hz, 1H), 7.37 (d, *J* = 8.1 Hz, 1H), 7.12 (t, *J* = 7.5 Hz, 1H), 7.06 (t, *J* = 7.4 Hz, 1H), 4.82 (d, *J* = 7.7 Hz, 1H), 4.24 – 4.17 (m, 1H), 3.78 (td, *J* = 10.6, 3.9 Hz, 1H), 2.85 (ddd, *J* = 14.7, 9.2, 5.6 Hz, 1H), 2.68 (d, *J* = 15.4 Hz, 1H), 1.54 – 1.42 (m, 2H), 1.42 – 1.26 (m, 10H), 0.92 (t, *J* = 6.8 Hz, 3H); ¹³C NMR (600 MHz, CD₃CN) δ 136.11, 135.66, 127.10, 121.07, 118.94, 117.06, 110.93, 107.11, 72.68, 63.95, 34.03, 31.62, 29.32, 29.00, 24.91, 22.41, 22.08, 13.41; HRMS (ESI-TOF) *m/z* calc^d for C₁₈H₂₅NO: 271.1936, found 272.2020 ([M+H]⁺).



Synthesis of 1,1-diphenyl-1,3,4,9-tetrahydropyrano[3,4-b]indole (4.22):

Tryptophol **4.2** (100 mg, 0.620 mmol, 1 equiv.), CSA **3.6** (43.2 mg, 186 μ mol, 30 mol %), were placed in a Schlenk flask with a stir bar and purged with N₂. The substrate was then dissolved in dry CHCl₃ (1.0 mL). Acetal **4.16** (.775 mmol, 1.25 equiv.) was added to the flask, and the reaction was stirred at room temperature in a sand bath for 16 h. The solvent was removed and the product dried *in vacuo*. The indole product was purified by aluminum oxide column chromatography eluting with 0-30% EtOAc/hexane to afford a white solid (yield: 75%): IR (CHCl₃): ν_{\max} 3230.3, 3030.2, 2959.7, 1621.0, 1453.7, 1096.2, 912.9, 742.8 cm⁻¹; ¹H NMR (600 MHz, CDCl₃) δ 7.87 – 7.81 (m, 1H), 7.63 (t, *J* = 7.4 Hz, 1H), 7.59 (d, *J* = 7.6 Hz, 1H), 7.56 – 7.48 (m, 2H), 7.34 (dd, *J* = 8.0, 2.9 Hz, 5H), 7.30 (d, *J* = 5.7 Hz, 2H), 7.23 – 7.18 (m, 1H), 7.18 – 7.14 (m, 1H), 4.01 (t, *J* = 5.7 Hz, 2H), 3.00 (t, *J* = 5.7 Hz, 2H); ¹³C NMR (600 MHz, CDCl₃) δ 144.19, 136.13, 135.77, 132.40, 130.06, 128.28, 128.16, 127.87, 122.09, 119.69, 118.65, 111.05, 108.47, 60.92, 22.21.; HRMS (ESI-TOF) *m/z* calc^d for C₂₃H₁₉NO: 325.1501, found 326.1531 ([M+H]⁺).

General procedure for cage-catalyzed Pictet-Spengler reactions:

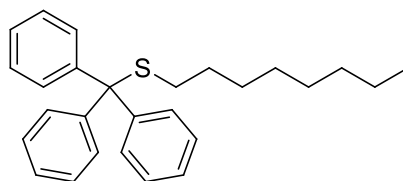
In a glove box, tryptophol **4.2** or **4.5-4.6** (1 mol.-eq., 6.3 μ mol, 10 μ L of 0.63 M solution in CD₃CN) was placed in an NMR tube followed by 5 mol % cage **1.28** or cage **1.30** (0.31 μ mol, 2 mg) or 30 mol % diacid **1.35** (1.86 mmol, 5 μ L of 0.372 M solution in CD₃CN) alone. The electrophile (1.25 mol.-eq., 7.9 μ mol, 3.9 μ L of 2 M solution in CD₃CN) was then added followed by 1,4-dioxane as the internal standard (0.5 mol. -eq., 3.2 μ mol, 1.6 μ L of 2 M solution in CD₃CN). A combined total volume of 400 μ L of distilled CD₃CN was added, and the tube was capped and sealed around with electrical tape. The sample

was taken out of the glovebox and quickly shaken to dissolve all solids. The reaction progress monitored over time. An initial ^1H NMR spectrum of the reaction mixture was obtained to verify the stoichiometry of the sample. The percent conversion values were obtained via integration of the product and substrate peaks against the internal standard.

General procedure for control Pictet-Spengler reactions:

In a sealed, oven dried flask, tryptophol **4.2** or **4.5-4.6** (1 mol.-eq, 6.3 μmol , 10 μL of 0.63 M solution in CH_3CN) was added followed by 5 mol % CSA **3.6** (0.31 μmol , 10 μL of 0.031 M solution in CH_3CN). The electrophile (1.25 mol.-eq, 7.9 μmol , 3.9 μL of 2 M solution in CH_3CN) was then included followed by 1,4-dioxane as the internal standard (0.5 mol. -eq., 3.2 μmol , 1.6 μL of 2 M solution in CH_3CN). A combined total volume of 400 μL of distilled CH_3CN was added. The sealed flask was wrapped around with parafilm and quickly shaken. After 24 h, the solution was evaporated, dried, and an ^1H NMR spectrum in CDCl_3 was taken. Experiments were performed in triplicates. The yields were obtained via integration of the product and substrate peaks against the internal standard.

7.6. Experimental for Chapter 5



Synthesis of octyl trityl sulfide (5.5):

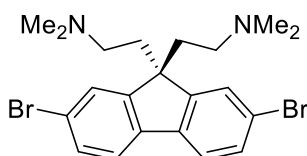
Trityl chloride (100 mg, 0.36 mmol) was placed in a Schlenk flask with a stir bar and purged with N_2 . *n*-Octanethiol (OctSH) (0.12 ml, 1.8 mmol) was added to the flask, and the reaction was stirred at 80 $^\circ\text{C}$ in a heating mantle for 12 h. The solvent was removed,

and the product dried *in vacuo* to yield pure product as a white crystalline solid (105.6 mg, 76 %). ^1H NMR (400 MHz, CD_3CN) δ 7.43 (dd, $J = 5.6, 3.7$ Hz, 6H), 7.35 – 7.31 (m, 6H), 7.28 – 7.24 (m, 3H), 2.3 (t, $J = 7.4$ Hz, 2H), 1.4-1.13 (m, 12H), 0.89 (t, $J = 7.4$ Hz, 3H). ^{13}C $\{^1\text{H}\}$ NMR (101 MHz, CD_3CN) δ 145.1, 129.4, 127.8, 126.6, 66.1, 31.5, 28.8, 28.7, 28.6, 28.2, 22.3, 13.4. HRMS (ESI-TOF) m/z calc^d for $\text{C}_{27}\text{H}_{32}\text{S}$: 388.2225, found 387.2141 ($[\text{M}-\text{H}]^-$).

General procedure for substitution reactions:

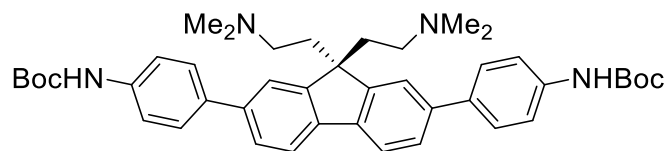
Electrophile **2.1** or **2.2** (1 mol.-eq., 6.3 μmol , 10 μL of 0.63 M solution) was placed in an NMR tube followed by 5 mol % cage **1.30** (0.31 μmol , 2 mg) and 30 mol % acid **1.35** (1.86 mmol, 5 μL of 0.372 M solution in CD_3CN) or 30% acid **1.35** alone. The nucleophile (1.25 mol.-eq., 7.9 μmol , 3.9 μL of 2 M solution in CD_3CN) was then added followed by 1,4-dioxane as the internal standard (0.5 mol. -eq., 3.2 μmol , 1.6 μL of 2 M solution in CD_3CN). A combined total volume of 400 μL of CD_3CN was added, and the tube was capped and quickly shaken to dissolve all solids. An initial ^1H NMR spectrum of the reaction mixture was obtained to verify the stoichiometry of the sample. The sample was then heated at 80 $^\circ\text{C}$ and the reaction progress monitored over time. Rate calculation trials were performed in triplicate. The percent conversion values were obtained via integration of the product and substrate peaks against the internal standard and the calculated values of repeated trials were averaged.

7.7. Experimental for Chapter 6



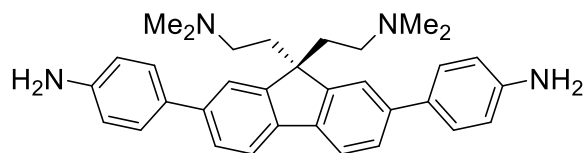
Synthesis of 2,2'-(2,7-dibromo-9H-fluorene-9,9-diyl)bis(N,N-dimethylethanamine) (6.2):

2,7-Dibromo-9H-fluorene **1.27** (2.0 g, 6.2 mmol, 1.0 eq.) and 2-dimethylaminoethyl chloride hydrochloride (3.6 g, 24.7 mmol, 4.0 eq.) were placed in a 250 mL two-neck flask under nitrogen atmosphere. Then, a KOH aqueous solution (30 mL, 60%, wt) and THF (30 mL) were injected. The reaction mixture was stirred at reflux for 24 h. After cooling to room temperature, water was poured into the mixture to dissolve the salt and extracted with dichloromethane. The organic extraction was washed using saturated sodium bicarbonate and brine (3 x 20 mL each) and dried over anhydrous sodium sulfate. The organic solvent was removed in vacuo, and the residue was dissolved in hexanes and filtered. The crude product was purified by column chromatography on basic alumina using 0-100% EtOAc/hexane to yield a light-yellow solid (1.5 g, 51%). IR (CHCl₃): ν_{\max} (cm⁻¹) 2944, 2856, 2815, 2763, 1448, 1250, 1035, 805, 642. ¹H NMR 400 MHz, (CDCl₃) δ 7.59 – 7.45 (m, 6.15H), 2.24 – 2.17 (m, 4H), 2.04 (s, 11.95H), 1.57 – 1.47 (m, 4H). ¹³C{¹H} NMR (151 MHz, CDCl₃) δ 151.0, 138.8, 130.7, 126.2, 121.9, 121.3, 53.8, 52.9, 45.4, 38.8. HRMS (ESI-TOF) m/z calc^d for C₂₁H₂₇Br₂N₂ ([M+H]⁺): 465.0463; found 465.0530.



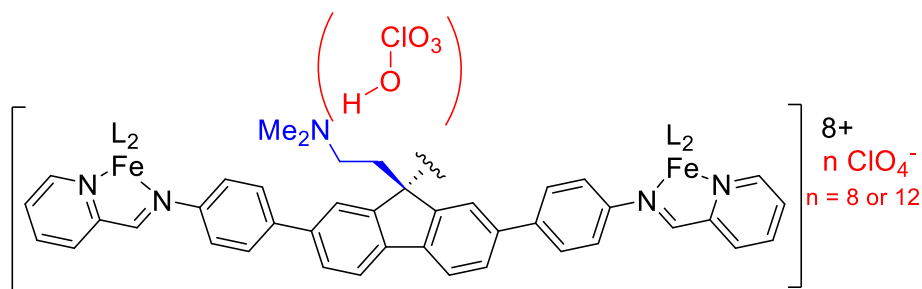
Synthesis of Di-tert-butyl((9,9-bis(2-(dimethylamino)ethyl)-9H-fluorene-2,7-diyl)bis(4,1phenylene))dicarbamate (6.3):

To a Schlenk flask was added **6.2** (700 mg, 1.5 mmol, 1.0 eq.), 4-BOCaminophenylboronic acid (888 mg, 3.75 mmol, 1.8 eq.), cesium carbonate (2.9 g, 4.8 mmol, 3.2 eq.), and Pd(dppf)Cl₂ (110 mg, 0.08 mmol, 15 mol %). The flask was then purged with N₂, 6 mL of DMF was added and the flask quickly purged a second time. The mixture was stirred at 90 °C for 16 h, then the reaction was cooled to room temperature and diluted with 100 mL of water. The product was extracted with diethyl ether (4 x 60 mL) and the organic layer washed with a solution of 1 M NaCO₃ and 1 M sorbitol in water (30 mL) followed by washings with saturated sodium bicarbonate and brine (3 x 20 mL each). The cloudy organic layer was dried with magnesium sulfate, filtered through a celite plug and the solvent removed in vacuo. The product was sonicated in hexanes and then filtered once more to give the product as a tan solid (777 mg, 75 %). IR (CH₃CN): ν_{\max} (cm⁻¹) 3163, 3005, 2944, 2292, 2252, 2114, 1443, 1421, 1375, 1038, 749. ¹H NMR 400 MHz, (CDCl₃) δ 7.77 (d, *J* = 7.9 Hz, 2H), 7.68 – 7.61 (m, 7H), 7.50 (d, *J* = 8.0 Hz, 4H), 6.58 (s, 2H), 2.52 (m, 4H), 2.24 (s, 12H), 1.88 (m, 4H), 1.57 (s, 18H). ¹³C{¹H} NMR (151 MHz, CD₃CN) δ 152.7, 149.8, 139.9, 139.4, 137.7, 136.0, 127.6, 126.2, 120.8, 120.2, 118.9, 80.6, 53.9, 52.4, 45.1, 38.0, 28.4. HRMS (ESI-TOF) *m/z* calc^d for C₄₃H₅₅N₄O₄ ([M+H]⁺): 691.4165; found 691.4239.



Synthesis of 4,4'-(9,9-bis(2-(dimethylamino)ethyl)-9H-fluorene-2,7-diyl)dianiline (6.4):

6.3 (250 mg, 0.362 mmol, 1 eq.) was placed in a round-bottomed flask with a stir bar. Trifluoroacetic acid (5 mL, neat) was added to the flask and the mixture was stirred for 16 h at room temperature. The mixture was slowly added to a beaker containing 100 mL of ice water. The solution was brought to pH 12 using 2 M NaOH, and the precipitate filtered. The amine was purified by aluminum oxide chromatography eluting first with EtOAc and then methanol. This yielded a tan powder (147 mg, 83 %). IR (CH₃CN): ν_{max} (cm⁻¹) 3496, 3361, 3164, 3002, 2944, 2833, 2261, 1631, 1193, 1037, 764, 594. ¹H NMR 400 MHz, (DMSO-*d*₆) δ 7.74 (d, *J* = 7.9 Hz, 2H), 7.68 (s, 2H), 7.52 (d, *J* = 8.1 Hz, 2H), 7.45 (d, *J* = 8.2 Hz, 4H), 6.68 (d, *J* = 8.1 Hz, 4H), 5.24 (s, 4H), 2.32 – 2.22 (m, 4H), 1.89 (s, 12H), 1.53 – 1.39 (m, 4H). ¹³C{¹H} NMR (151 MHz, CD₃CN) δ 149.8, 147.7, 140.4, 138.7, 131.0, 128.4, 127.7, 120.4, 119.9, 114.7, 69.4, 53.6, 48.9, 43.8. HRMS (ESI-TOF) *m/z* calc^d for C₃₃H₃₉N₄ ([M+H]⁺): 491.3096; found 491.3166.



Synthesis of Cage 6.1:

6.4 (10 mg, 0.02 mmol, 1.0 eq.) was placed in a round bottomed flask with a stir bar and acetonitrile (4.3 mL) was added to the flask followed by 2-formylpyridine (4.0 μ L, 0.04 mmol, 2.0 eq.). Iron (II) perchlorate hydrate (13 mg, 0.025 mmol, 1.25 eq.) was added, and the solution stirred at 50 $^{\circ}$ C for 24 hours. The solution was allowed to cool and was filtered to remove any undissolved solids. The acetonitrile was removed in vacuo. A small amount of acetonitrile (0.5 mL) was then added to the flask followed by ether. The solid was filtered and washed with additional ether to yield a dark purple solid (48 mg, 48 %). See figures 7.136–7.149, and 7.152 and Table 7.1 for full NMR and MS characterization.

General procedure for titrations:

Cage **6.1** (5 mol %, 0.31 μ mol, 1.6 mg) was placed in an NMR tube. A volume of 400 μ L of CD₃CN was added, the tube was capped, and the sample was quickly shaken. A ¹H NMR spectrum was taken. To the NMR tube, various bases (10 μ L of 0.0315 M solution in CD₃CN) or D₂O (1-100 μ L) were titrated into Cage **6.1**. A ¹H NMR spectrum was taken each time.

General procedure for hydrolysis of acetal reaction:

Benzaldehyde dimethyl acetal (1 mol.-eq., 6.3 μ mol, 10 μ L of 0.63 M solution in CD₃CN) was placed in an NMR tube followed by 5 mol % cage **6.1** (0.31 μ mol, 1.6 mg).

Water (6.0 mol.-eq., 37.8 μmol , 10 μL of 3.78 M solution in CD_3CN) was then added followed by 1,4-dioxane as the internal standard (0.5 mol.-eq., 3.2 μmol , 10 μL of 0.32 M solution in CD_3CN). A combined total volume of 400 μL of CD_3CN was added, and the tube was capped and sealed around with parafilm. The sample was quickly shaken. The reaction progress was monitored over time. An initial ^1H NMR spectrum of the reaction mixture was obtained to verify the stoichiometry of the sample. The percent conversion values were obtained via integration of the product and substrate peaks against the internal standard.

General procedure for Knoevenagel condensation reaction:

Benzaldehyde (1 mol.-eq., 6.3 μmol , 10 μL of 0.63 M solution in CD_3CN) was placed in an NMR tube followed by 5 mol % cage **6.1** (0.31 μmol , 1.6 mg). Malononitrile (1.25 mol.-eq., 7.9 μmol , 10 μL of 0.79 M solution in CD_3CN) was then added followed by 1,4-dioxane as the internal standard (0.5 mol.-eq., 3.2 μmol , 10 μL of 0.32 M solution in CD_3CN). A combined total volume of 400 μL of CD_3CN was added, and the tube was capped and sealed around with parafilm. The sample was quickly shaken. The reaction progress was monitored over time. An initial ^1H NMR spectrum of the reaction mixture was obtained to verify the stoichiometry of the sample. The percent conversion values were obtained via integration of the product and substrate peaks against the internal standard.

General procedure for detritylation reactions:

Trityl amine **6.12**, **6.14**, or **2.8** (12 mol.-eq., 6.0 μmol , 10 μL of 0.6 M solution in CD_3CN) was placed in an NMR tube followed by cage **1** (8 mol %, 0.5 μmol , 2.6 mg or 32 mol %, 2.0 μmol , 10 mg). A volume of 390 μL of CD_3CN was added, and the tube was

capped and sealed around with parafilm. The sample was quickly shaken. The reaction progress was monitored over time. An initial ^1H NMR spectrum of the reaction mixture was obtained to verify the stoichiometry of the sample. The percent conversion values were obtained via integration of the product and substrate peaks.

Base Titration Fitting and pKa Determination:

NMR Titration

Figure 7.154 shows the ^1H chemical shift of DABCO **6.7** as a function of concentration relative to cage **6.1**. Upon initial addition of DABCO **6.7**, the observed chemical shift is that of DABCO- H^+ **6.8**. At concentrations > 10 equivalents, the chemical shift asymptotically approaches that for the unprotonated species. The response is consistent with a simple reservoir model in which cage 1 holds n abstractable protons that are removed stoichiometrically upon addition of DABCO **6.7** to give the protonated species, DABCO- H^+ **6.8**. After all available protons have been released, adding excess DABCO **6.7** leads to a simple fast-exchange average of protonated and unprotonated DABCO species in solution. Although finer detail might reveal a sigmoidal transition between these 2 regimes, the chemical shift data can be well fit to a simple model

$$\langle \nu(m) \rangle = \begin{cases} \nu_{BH^+} & m \leq n \\ \frac{n}{m} \nu_{BH^+} + \frac{(m-n)}{m} \nu_B & m > n \end{cases} \quad (1)$$

as shown in Figure 7.168. Here, the changes in chemical shift were fit using a non-linear least-squares (maximum likelihood) approach written within the Mathematica programming environment⁷ to determine the number of abstractable protons, $n = 11 (\pm 1)$. This is consistent with the amines in cage 6.1 being fully protonated ($n = 12$).

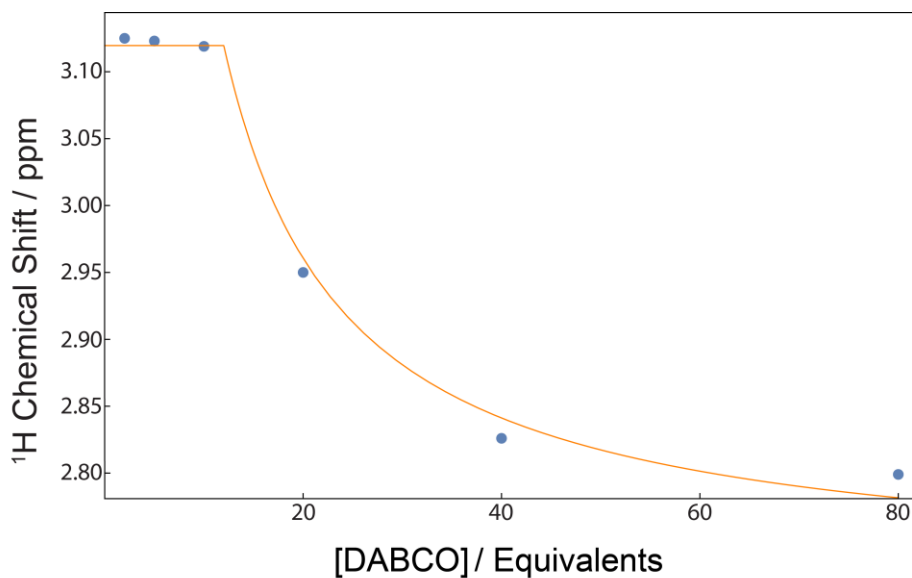
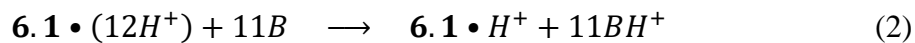


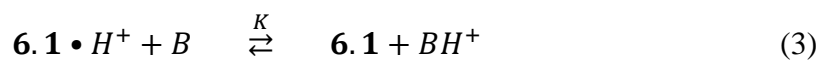
Figure 7.1. Dataplot of the change in chemical shift of DABCO- H^+ when added to cage **6.1**.

UV/Vis Titration

UV/Vis titration data were fit to a model in which the first 11 equivalents of base were assumed to react stoichiometrically ($K \gg 1$) with the fully protonated compound **6.1** • ($12H^+$),



while the final equivalent established an equilibrium



The equilibrium constant for this reaction can be related back to the K_a for $\mathbf{6.1} \cdot H^+$ and BH^+

$$K = \frac{[\mathbf{1}][BH^+]}{[\mathbf{1} \cdot H^+][B]} = \frac{K_{a,\mathbf{1} \cdot H^+}}{K_{a,BH^+}}. \quad (4)$$

After the addition of 11 equivalents of base, mass balance gives

$$[\mathbf{6.1}]_0 = [\mathbf{6.1} \cdot H^+] + [\mathbf{6.1}] \quad (5)$$

$$[B]_0 = [B \cdot H^+] + [B] \quad (6)$$

and

$$\begin{aligned} [B \cdot H^+] &= 11[\mathbf{6.1}]_0 + [\mathbf{6.1}] \\ &= 11[\mathbf{6.1} \cdot H^+] + 12[\mathbf{6.1}] \end{aligned} \quad (7)$$

Equations (4)-(7) can be solved simultaneously to give $[\mathbf{6.1}]$, $[\mathbf{6.1} \cdot H^+]$, $[B]$, and $[B \cdot H^+]$ as function of K and $[\mathbf{6.1}]_0$ and $[B]_0$, the total amounts of compound $\mathbf{1}$ and base added.

$$\begin{aligned} [\mathbf{6.1}] &= \frac{1}{2(K-1)} \left([\mathbf{6.1}]_0(2K - (K-1)n - 1) + [B]_0K \right. \\ &\quad \left. - \sqrt{4[\mathbf{6.1}]_0^2(K-1)n + ([B]_0K - [\mathbf{6.1}]_0((K-1)n - 1))^2} \right) \\ [\mathbf{6.1} \cdot H^+] &= \frac{1}{2(K-1)} \left([\mathbf{6.1}]_0((K-1)n - 1) - [B]_0K \right. \\ &\quad \left. + \sqrt{4[\mathbf{6.1}]_0^2(K-1)n + ([B]_0K - [\mathbf{6.1}]_0((K-1)n - 1))^2} \right) \end{aligned}$$

$$\begin{aligned}
[B] &= \frac{1}{2(K-1)} \left([\mathbf{6.1}]_0 (-(K-1)n - 1) + [B]_0 (K-2) \right. \\
&\quad \left. + \sqrt{4[\mathbf{6.1}]_0^2 (K-1)n + ([B]_0 K - [\mathbf{6.1}]_0 ((K-1)n - 1))^2} \right) \\
[B \cdot H^+] &= \frac{1}{2(K-1)} \left([\mathbf{6.1}]_0 ((K-1)n + 1) + [B]_0 K \right. \\
&\quad \left. - \sqrt{4[\mathbf{1}]_0^2 (K-1)n + ([B]_0 K - [\mathbf{6.1}]_0 ((K-1)n - 1))^2} \right)
\end{aligned}
\tag{8}$$

where in this case $n = 12$. The absorbance at a given wavelength λ can then be written as

$$A^\lambda = \varepsilon_1^\lambda [\mathbf{6.1}] + \varepsilon_{\mathbf{1}\cdot H^+}^\lambda [\mathbf{6.1} \cdot H^+] \tag{9}$$

where it is assumed that the base on its own does not absorb.

Equation (9) was used to simultaneously fit the experimental absorption data at 320 and 370 nm, A^{320} and A^{370} , as a function of added base (DABCO **6.7**; B_0) using a non-linear least-squares (maximum likelihood) approach written within the Mathematica programming environment.⁵ The best fit is shown in Figure 7.1 and gives $K = 7.12 \pm 0.6$, or taking the $-\log_{10}$ of both sides of equation 4, $\text{pKa}(\mathbf{6.1}\cdot H^+) - \text{pKa}(\text{DABCO } \mathbf{6.7}) = -0.85 \pm 0.08$.

7.8. Selected Spectra for Chapter 2

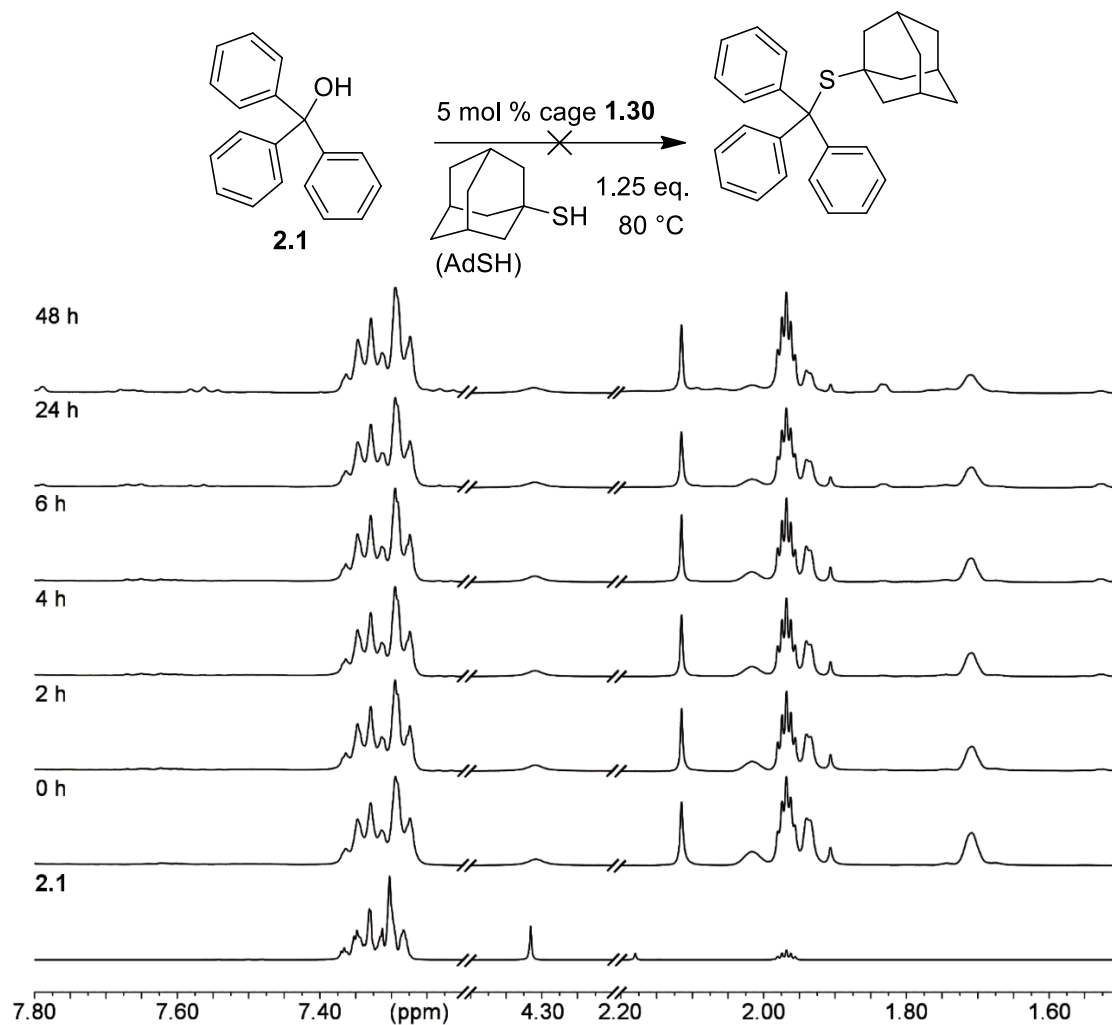


Figure 7.2. ¹H NMR spectra (7.80-7.20 ppm, 4.40-4.20 ppm, 2.20-1.50 ppm) of the acid promoted substitution reaction between **2.1** and adamantane thiol in the presence of 5 mol % cage **1.30**. The reaction was performed at 80 °C and monitored over time (400 MHz, 298K, CD₃CN).

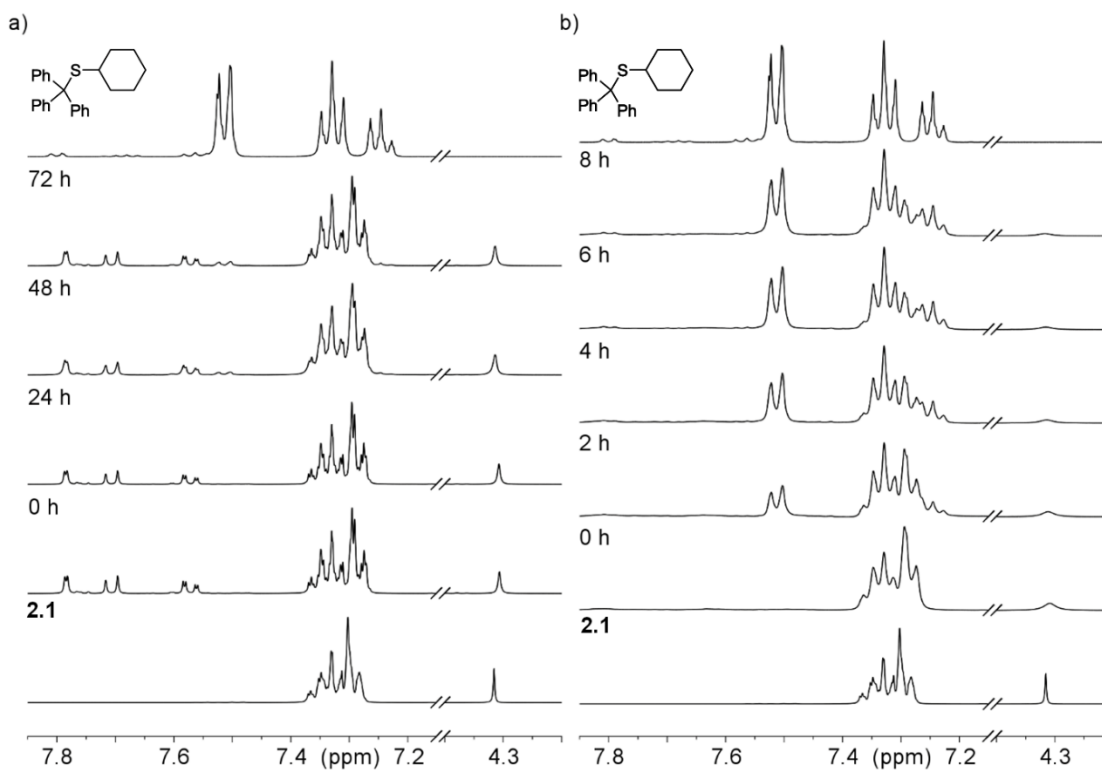
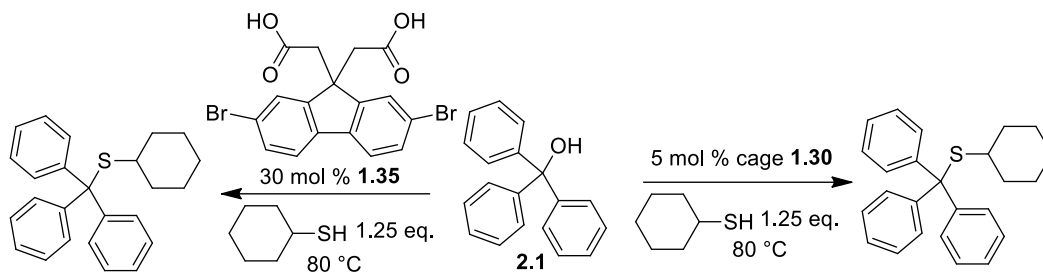


Figure 7.3. ^1H NMR spectra (7.80-7.20 ppm, 4.40-4.20 ppm) of the acid promoted substitution reaction between **2.1** and cyclohexyl thiol in $400\ \mu\text{L}$ CD_3CN in the presence of: a) 30 mol % control acid **1.35** b) 5 mol % cage **1.30**. Both reactions were performed at 80 °C and monitored over time (400 MHz, 298 K, CD_3CN).

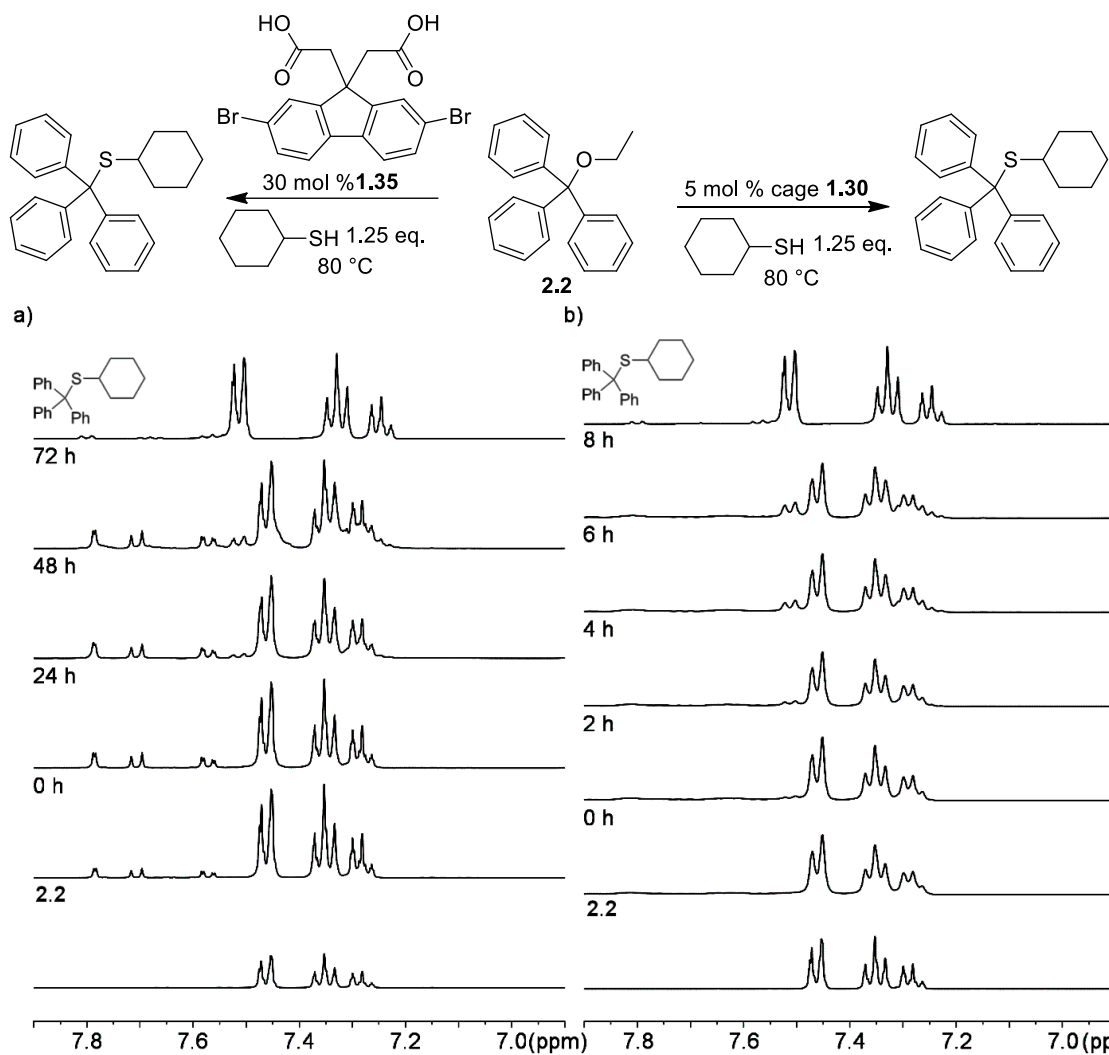


Figure 7.4. ^1H NMR spectra (7.90–6.90 ppm) of the acid promoted S_N1 reaction between **2.2** and cyclohexyl thiol in the presence of: a) 30 mol % control acid **1.35** or b) 5 mol % cage **1.30**. The reaction was performed at 80 °C and monitored over time (400 MHz, 298K, CD_3CN).

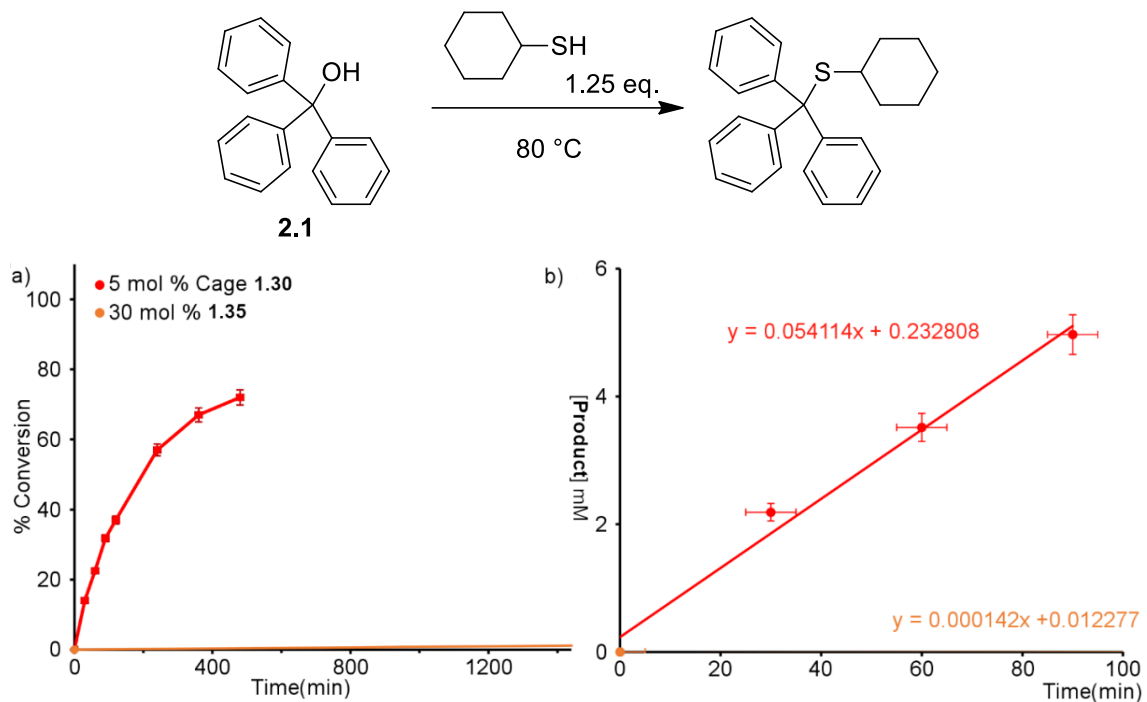


Figure 7.5. Graphed results of the acid promoted substitution reaction between **2.1** and cyclohexyl thiol in the presence of: 5 mol % cage **1.30** (red), 30 mol % control acid **1.35** (orange). a) Averaged percent conversion values are plotted against time in minutes. b) Calculation of initial rate based on change in concentration of [product] over time in minutes.

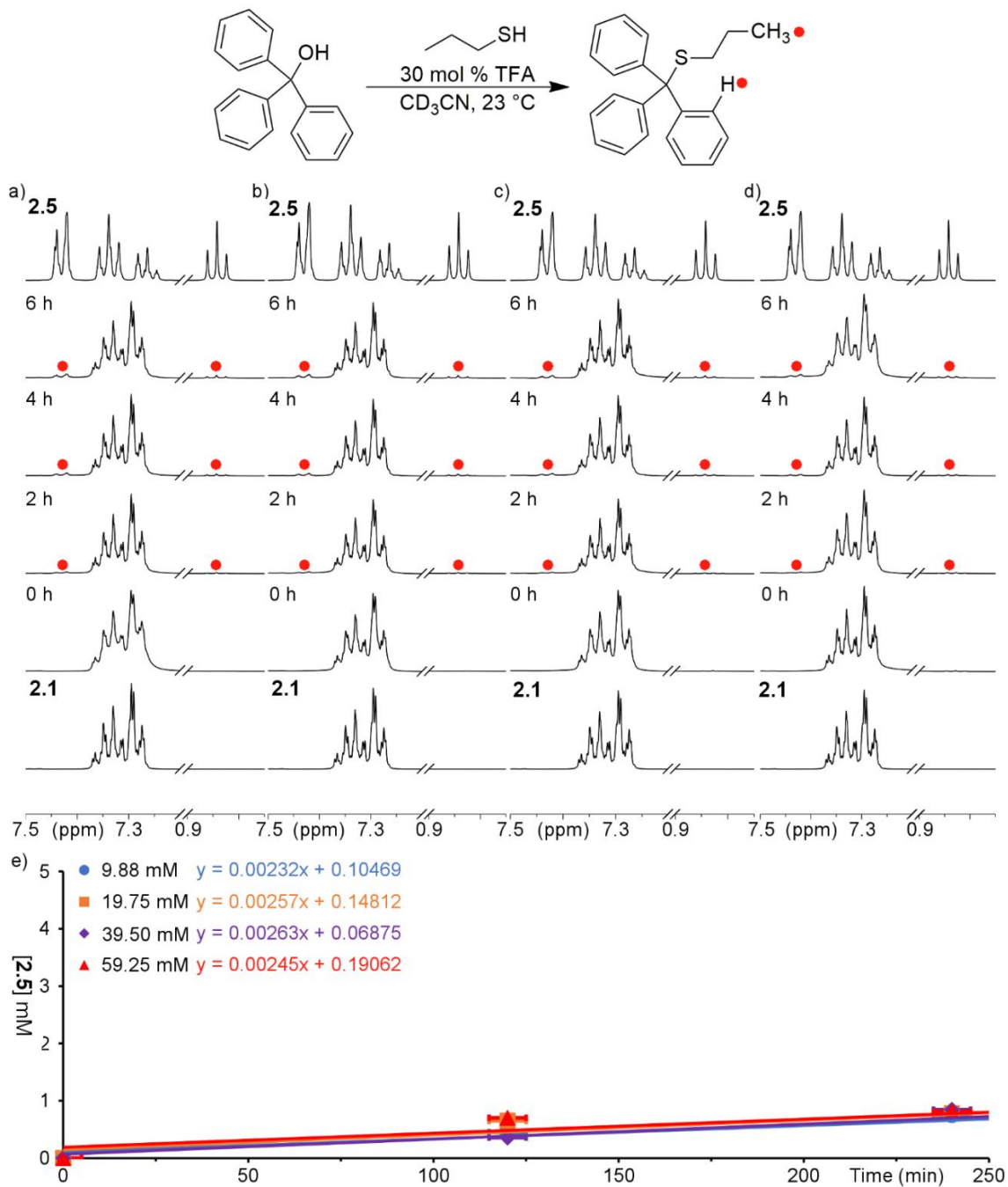


Figure 7.6. ¹H NMR spectra of the acid promoted substitution reaction between **2.1** and **PrSH** in the presence of 30 mol % TFA, at varying concentrations of **PrSH** a) 9.88 mM, b) 19.75, c) 39.5 mM, and d) 59.25 mM, performed at 23 °C and monitored over time (400 MHz, 298K, CD₃CN). d) Graphed results of reaction order study represented in change in [2.5] over time in minutes. The slope of the line was taken to equal the initial rate of the reaction and the order was obtained as an average over several trials to be 0 order in nucleophile (**PrSH**).

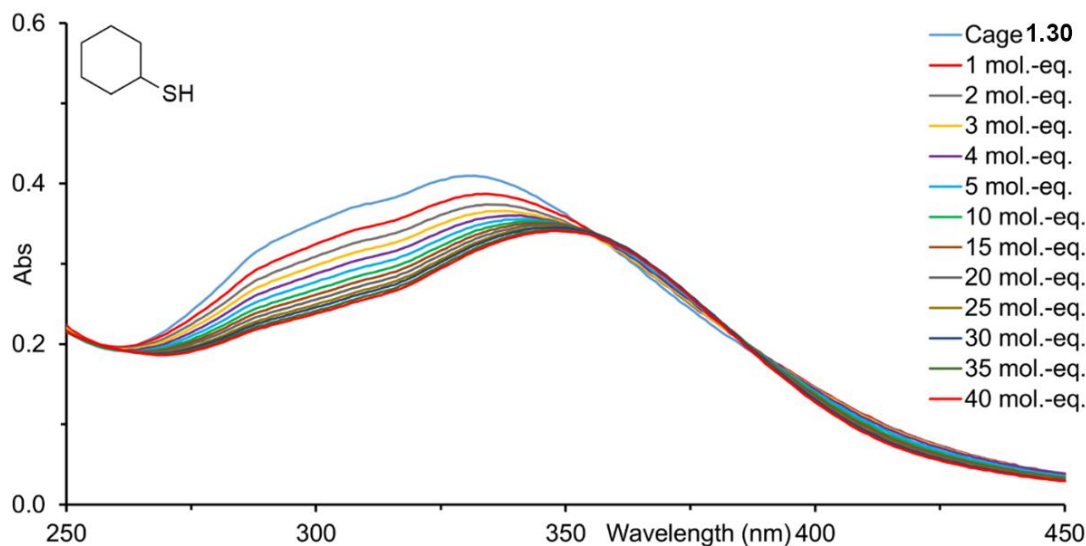


Figure 7.7. UV-Vis absorption spectrum of the titration of **CySH** into a 3 μM solution of cage **1.30** in CH_3CN . **CySH** was added in 1-5 μL aliquots from a 9 mM stock solution in CD_3CN .

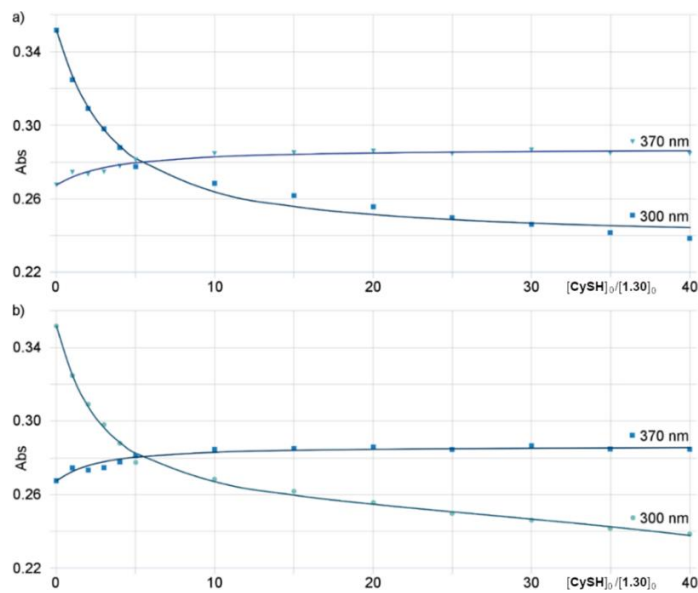


Figure 7.8. a) 1:1 binding fit model for guest **CySH** calculated via linear regression analysis using the Nelder-Mead method from the change in absorbance at two points (300 nm and 370 nm) using supramolecular.org ($K_a = 113.9 \pm 15.0 \times 10^3 \text{ M}^{-1}$). b) 1:2 binding fit model calculated via linear regression analysis using the Nelder-Mead method from the change in absorbance at two points (300 nm and 370 nm) using supramolecular.org¹⁻³ ($K_{11} = 156.1 \pm 11.2 \times 10^3 \text{ M}^{-1}$, $K_{12} = 4.0 \pm 0.4 \times 10^3 \text{ M}^{-1}$).

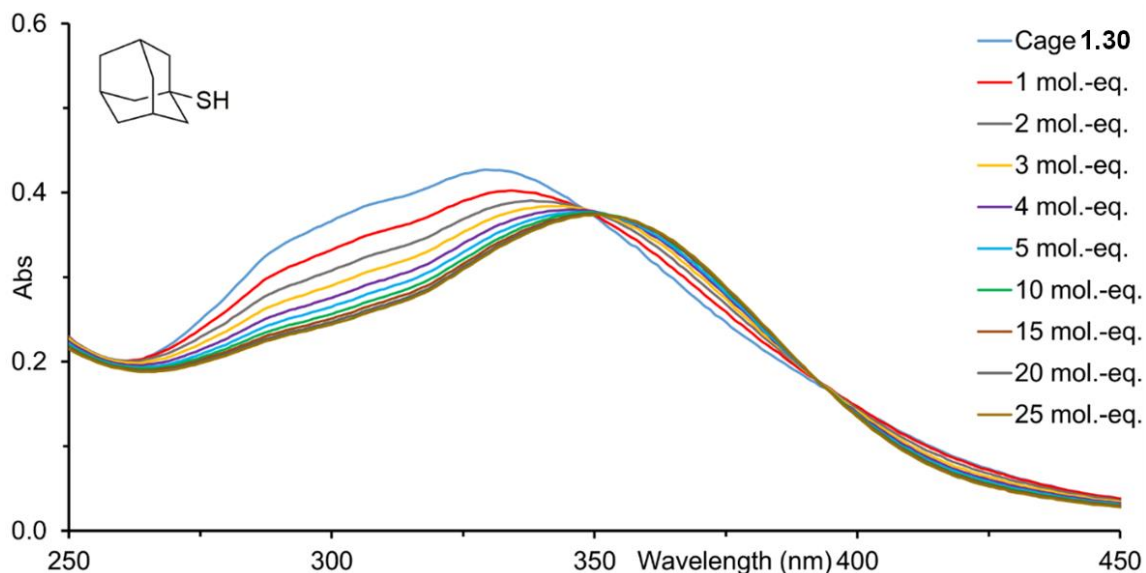


Figure 7.9. UV-Vis absorption spectrum of the titration of **AdSH** into a 3 μM solution of cage **1.30** in CH_3CN . **AdSH** was added in 1-5 μL aliquots from a 9 mM stock solution in CD_3CN .

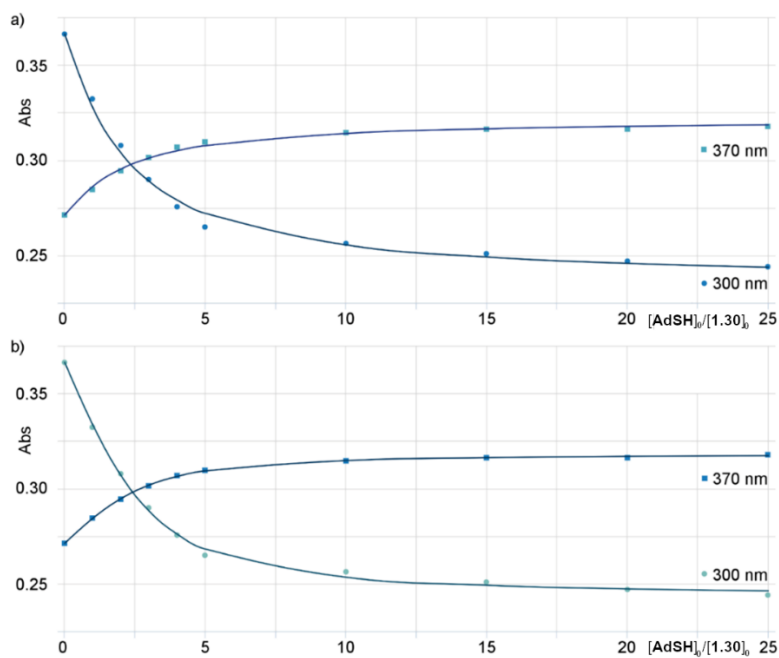


Figure 7.10. a) 1:1 binding fit model for guest **AdSH** calculated via linear regression analysis using the Nelder-Mead method from the change in absorbance at two points (300 nm and 370 nm) using supramolecular.org ($K_a = 199.4 \pm 17.0 \times 10^3 \text{ M}^{-1}$).¹⁻³ b) 1:2 binding fit model calculated for guest **AdSH** via linear regression analysis using the Nelder-Mead method from the change in absorbance at two points (300 nm and 370 nm) using supramolecular.org ($K_{11} = 362.7 \pm 100.1 \times 10^3 \text{ M}^{-1}$, $K_{12} = 220.8 \pm 45.3 \times 10^3 \text{ M}^{-1}$).¹⁻³

7.9. Selected Spectra for Chapter 3

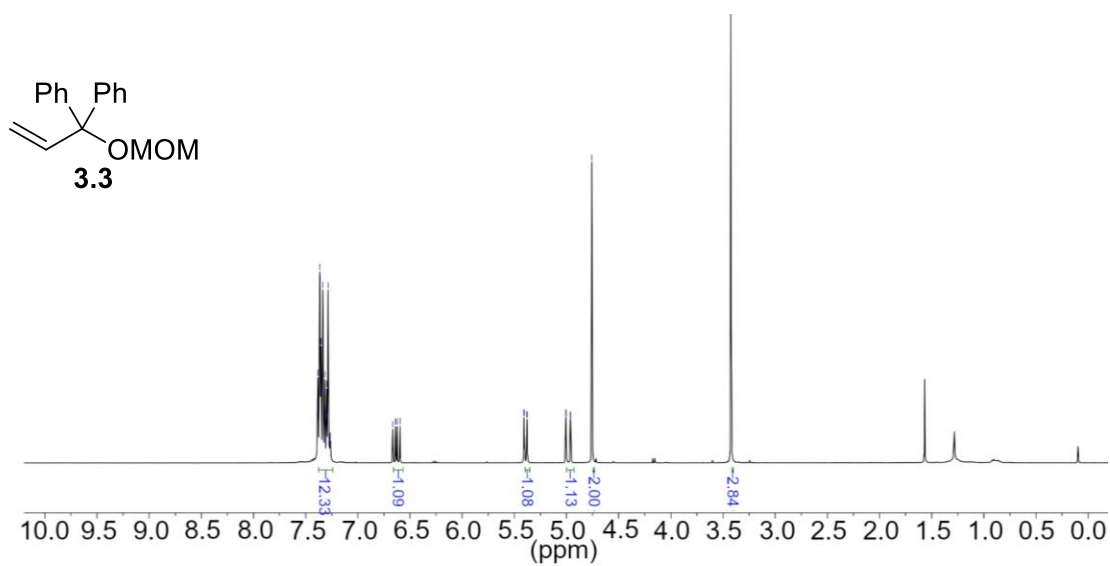


Figure 7.11. ¹H NMR spectrum of **3.3** (600 MHz, 298K, CDCl₃).

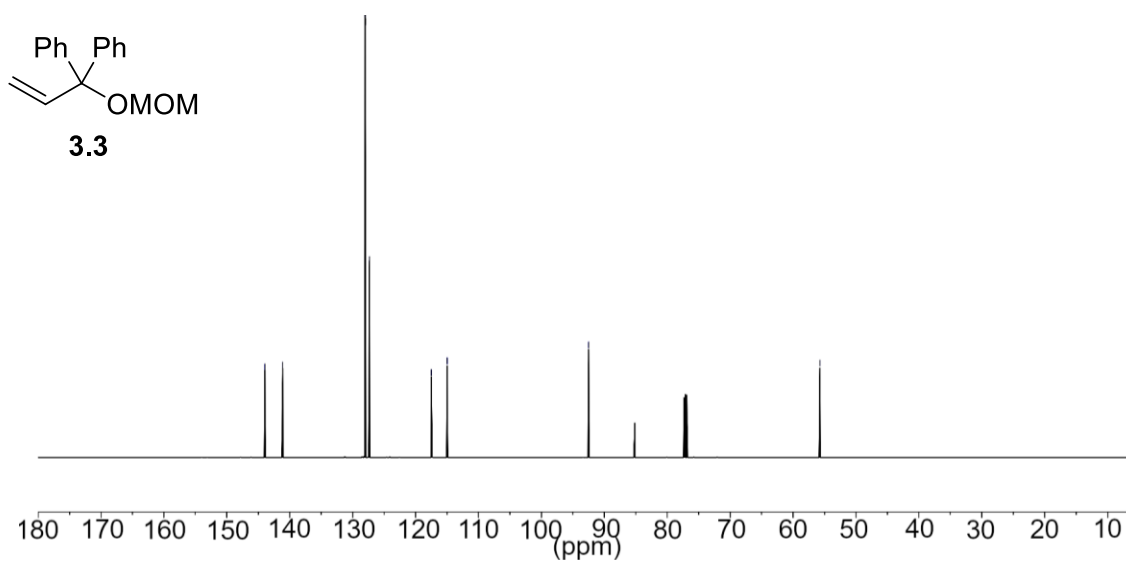


Figure 7.12. ¹³C{¹H} NMR spectrum of **3.3** (151 MHz, 298K, CDCl₃).

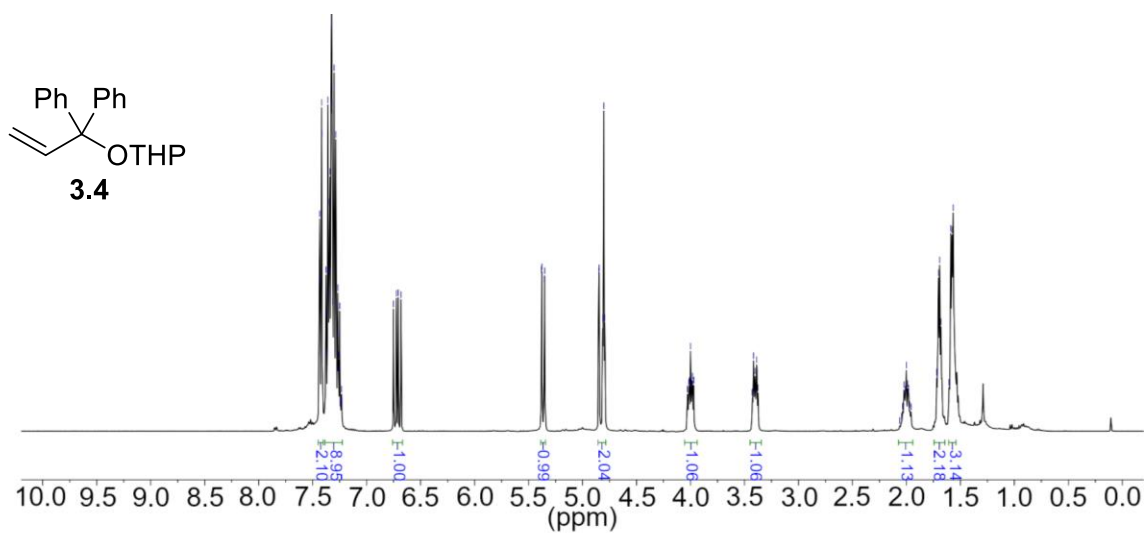


Figure 7.13. ^1H NMR spectrum of **3.4** (600 MHz, 298K, CDCl_3).

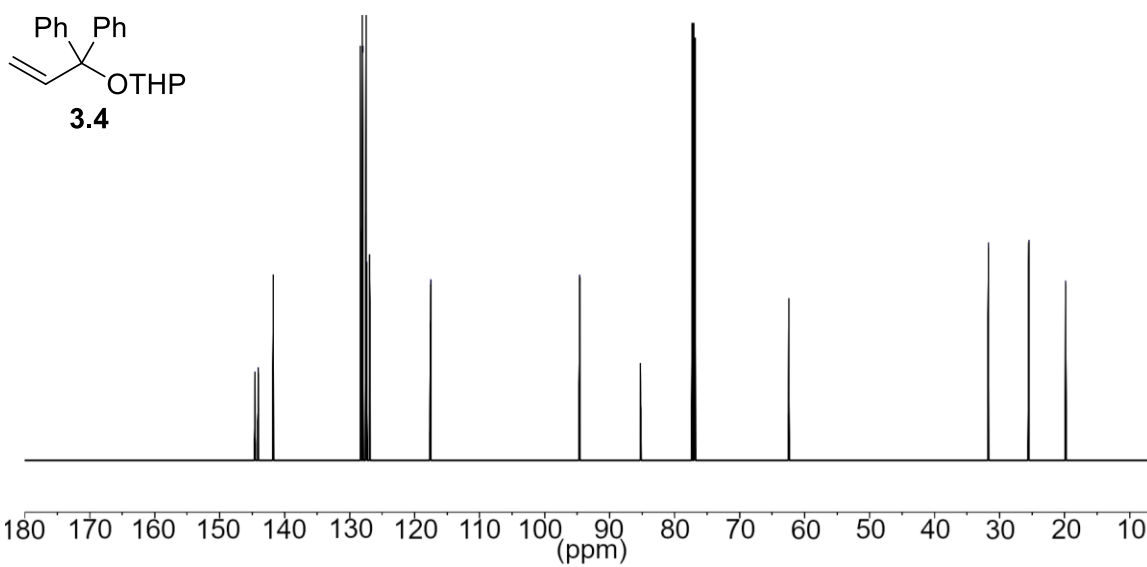


Figure 7.14. $^{13}\text{C}\{^1\text{H}\}$ NMR spectrum of **3.14** (151 MHz, 298K, CDCl_3).

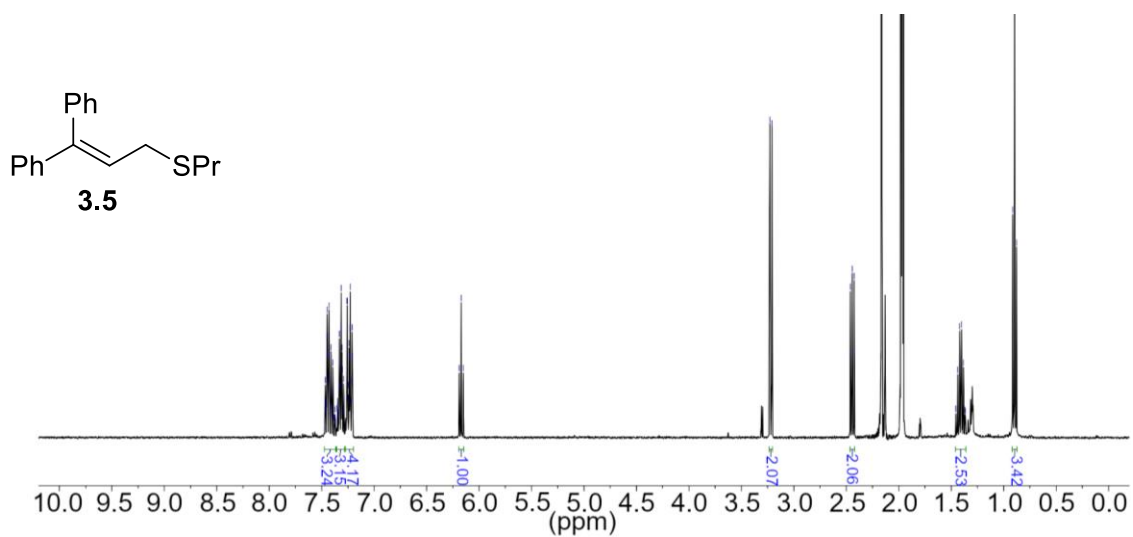


Figure 7.15 ^1H NMR spectrum of **3.5** (600 MHz, 298K, CD_3CN).

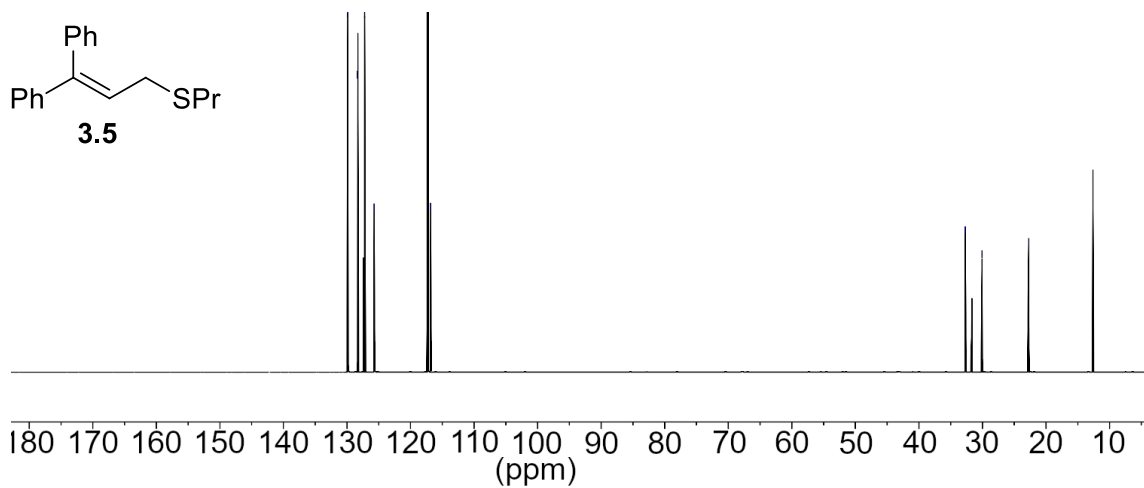
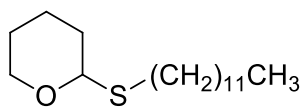


Figure 7.16. $^{13}\text{C}\{^1\text{H}\}$ NMR spectrum of **3.5** (151 MHz, 298K, CD_3CN).



3.13

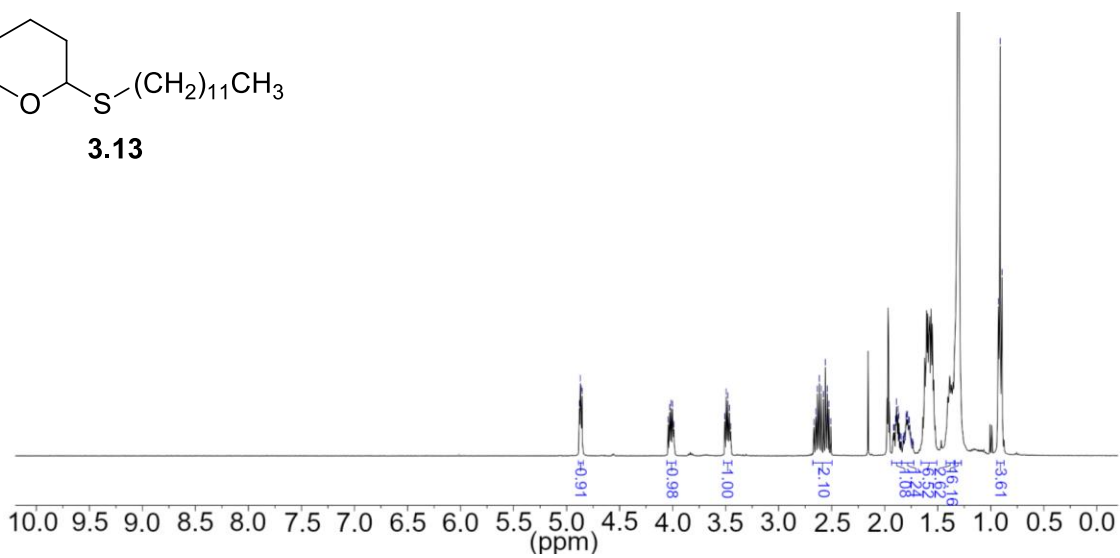
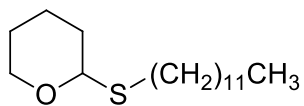


Figure 7.17. ¹H NMR spectrum of **3.13** (400 MHz, 298K, CD₃CN).



3.13

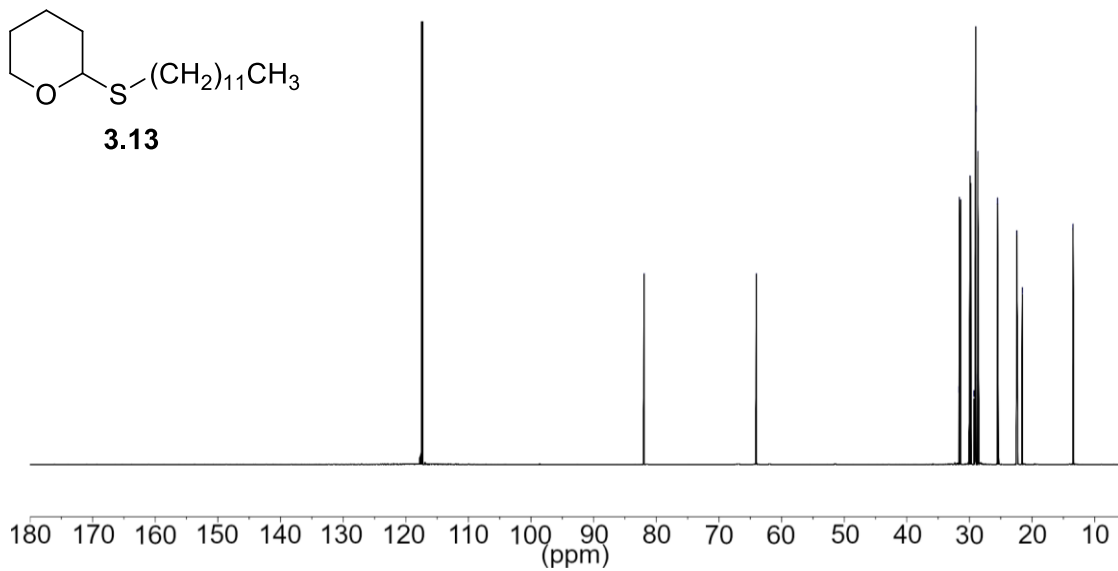


Figure 7.18. ¹³C{¹H} NMR spectrum of **3.13** (100 MHz, 298K, CD₃CN)

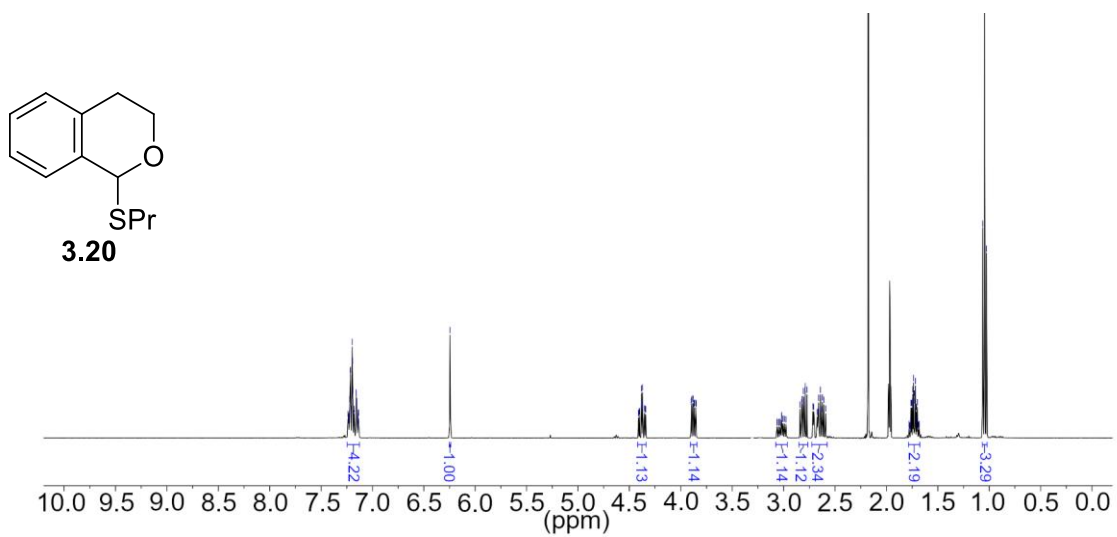


Figure 7.19. ^1H NMR spectrum of **3.20** (400 MHz, 298K, CD_3CN).

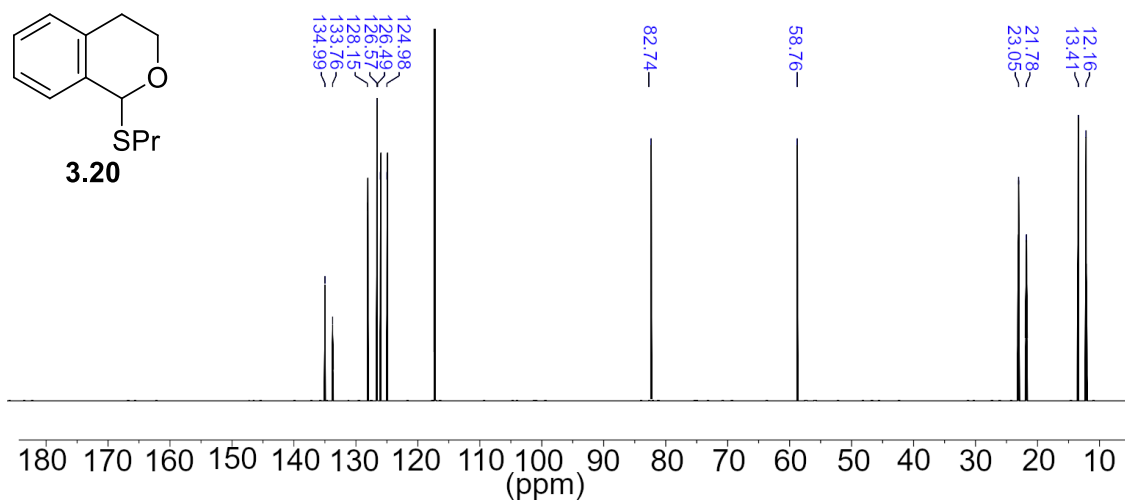


Figure 7.20. $^{13}\text{C}\{^1\text{H}\}$ NMR spectrum of **3.20** (100 MHz, 298K, CD_3CN)

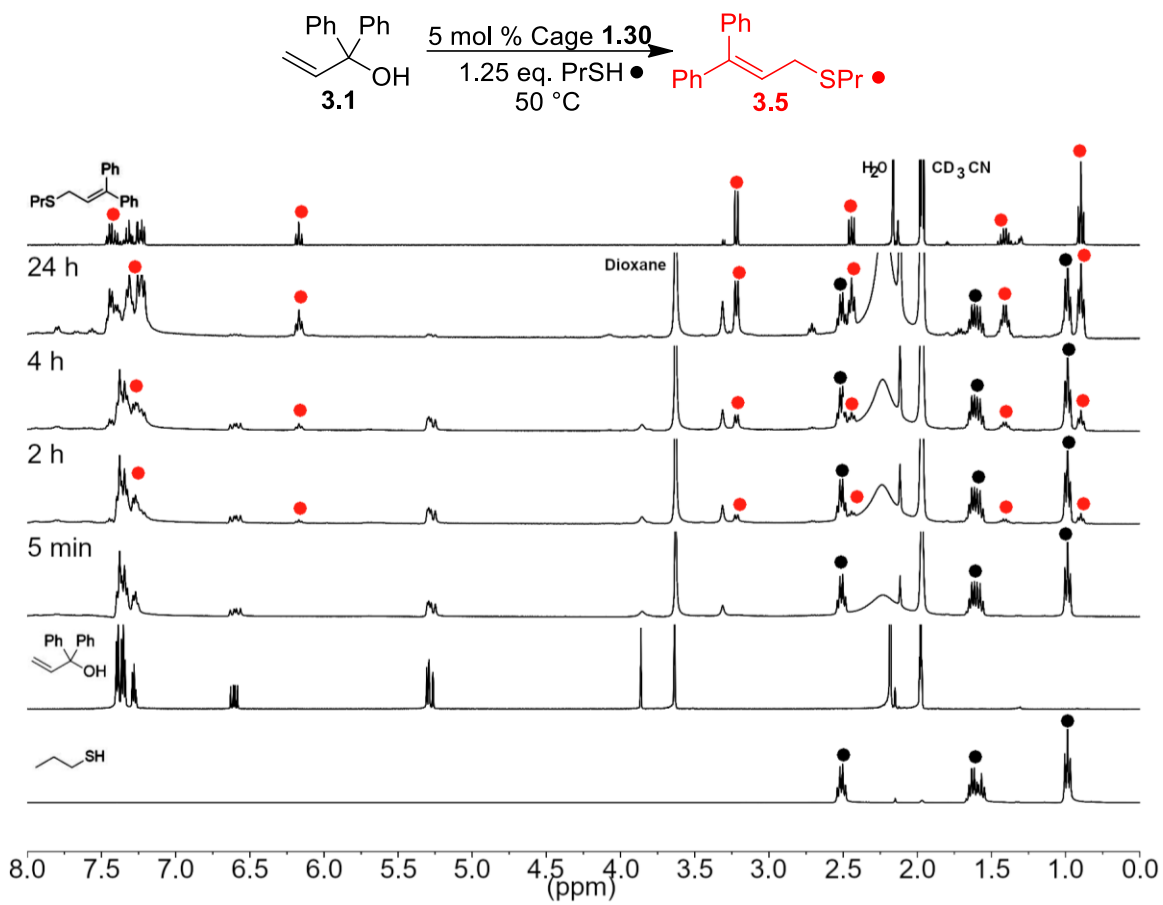


Figure 7.21. Full ^1H NMR spectra of the acid promoted reaction between **3.1** and *n*-propyl thiol in the presence of 5 mol % cage **1.30**. [**3.1**] = 15.8 mM, [**PrSH**] = 19.8 mM, [**1.30**] = 0.8 mM, the reaction was performed at 50 °C in CD_3CN and monitored over time (400 MHz, 323 K, CD_3CN).

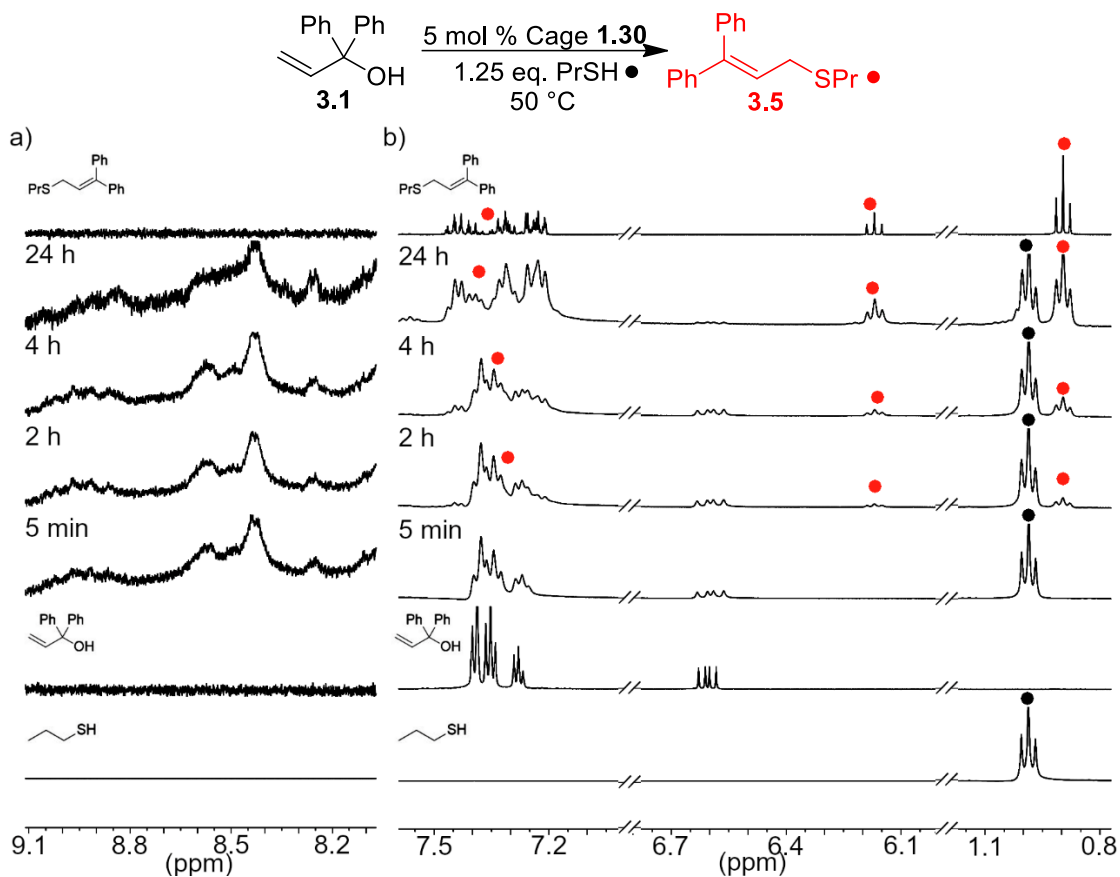


Figure 7.22. Expanded ^1H NMR spectra of the acid promoted reaction between **3.1** and *n*-propyl thiol in the presence of 5 mol % cage **1.30** showing: a) Cage stability (9.1-8.1 ppm) b) Product formation (7.6-7.0 ppm, 6.8-6.0 ppm, and 1.2-0.8 ppm). [**3.1**] = 15.8 mM, [**PrSH**] = 19.8 mM, [**1.30**] = 0.8 mM, the reaction was performed at 50 °C in CD_3CN and monitored over time (400 MHz, 323 K, CD_3CN).

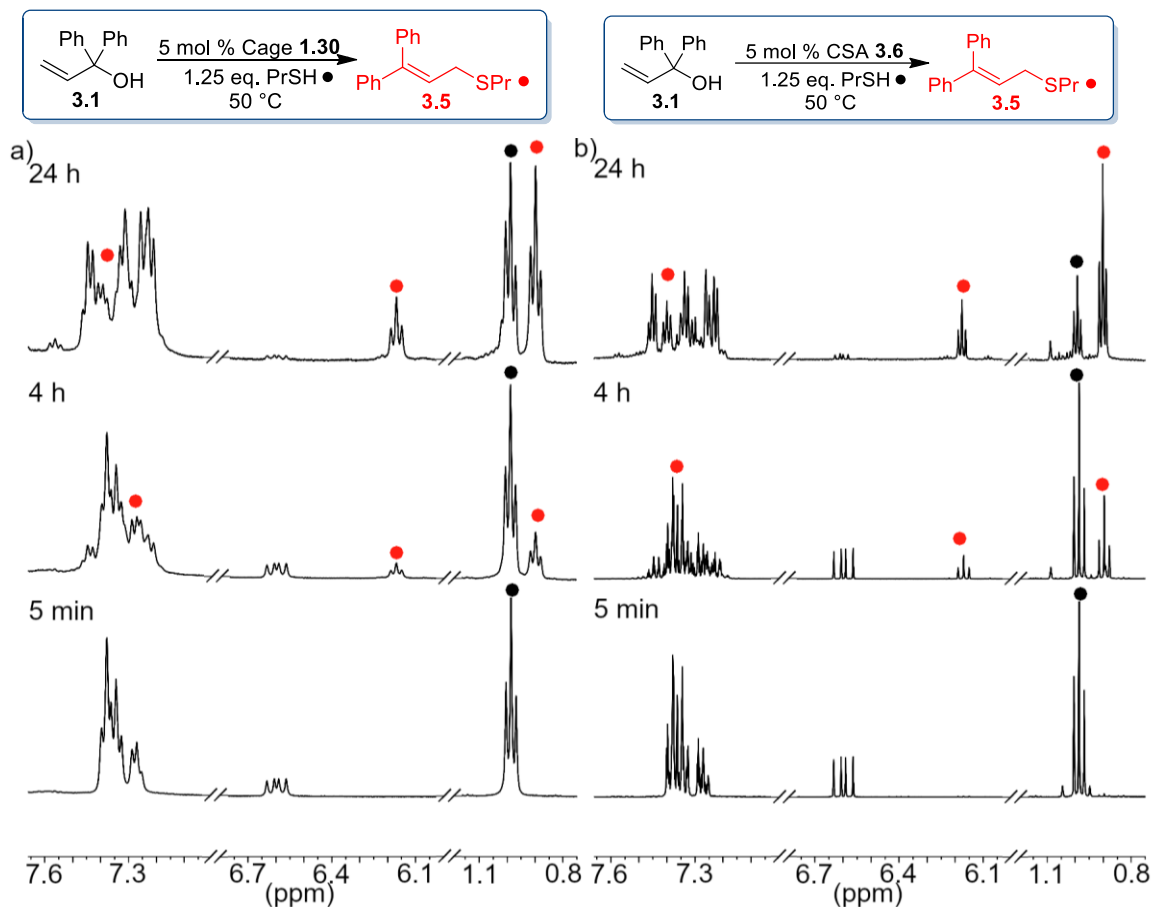


Figure 7.23. ^1H NMR spectra (7.65–7.10 ppm, 6.8–6.0 ppm, and 1.2–0.8 ppm) of the acid promoted reaction between **3.1** and *n*-propyl thiol in 400 μL CD_3CN in the presence of: a) 5 mol % cage **1.30** b) 5 mol % CSA **3.6**. $[\mathbf{3.1}] = 15.8 \text{ mM}$, $[\text{PrSH}] = 19.8 \text{ mM}$, $[\mathbf{1.30}] = 0.8 \text{ mM}$, $[\mathbf{3.6}] = 0.8 \text{ mM}$, reactions were performed at 50 °C in CD_3CN and monitored over time (400 MHz, 323 K, CD_3CN).

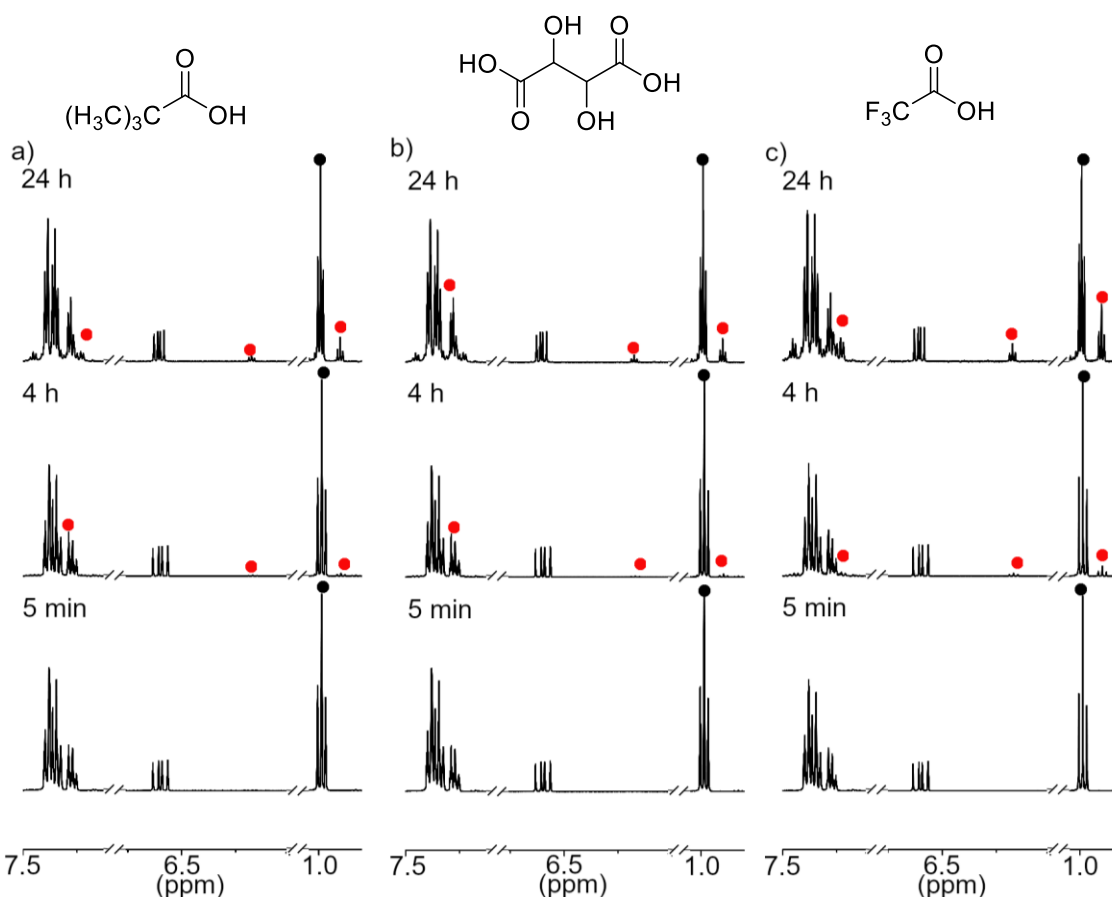
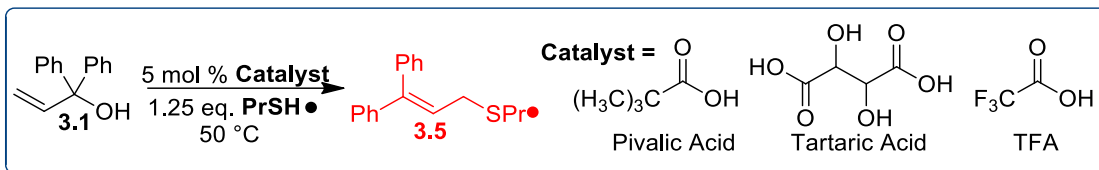


Figure 7.24. ^1H NMR spectra (7.5-7.1 ppm, 6.8-6.0 ppm, and 1.1-0.8 ppm) of the acid promoted reaction between **3.1** and n-propyl thiol in 400 μL CD_3CN in the presence of: a) 5 mol % pivalic acid b) 5 mol % tartaric acid c) 5 mol % trifluoroacetic acid. $[\mathbf{3.1}] = 15.8$ mM, $[\text{PrSH}] = 19.8$ mM, $[\text{Catalyst}] = 0.8$ mM reactions were performed at 50 $^\circ\text{C}$ in CD_3CN and monitored over time (400 MHz, 323 K, CD_3CN).

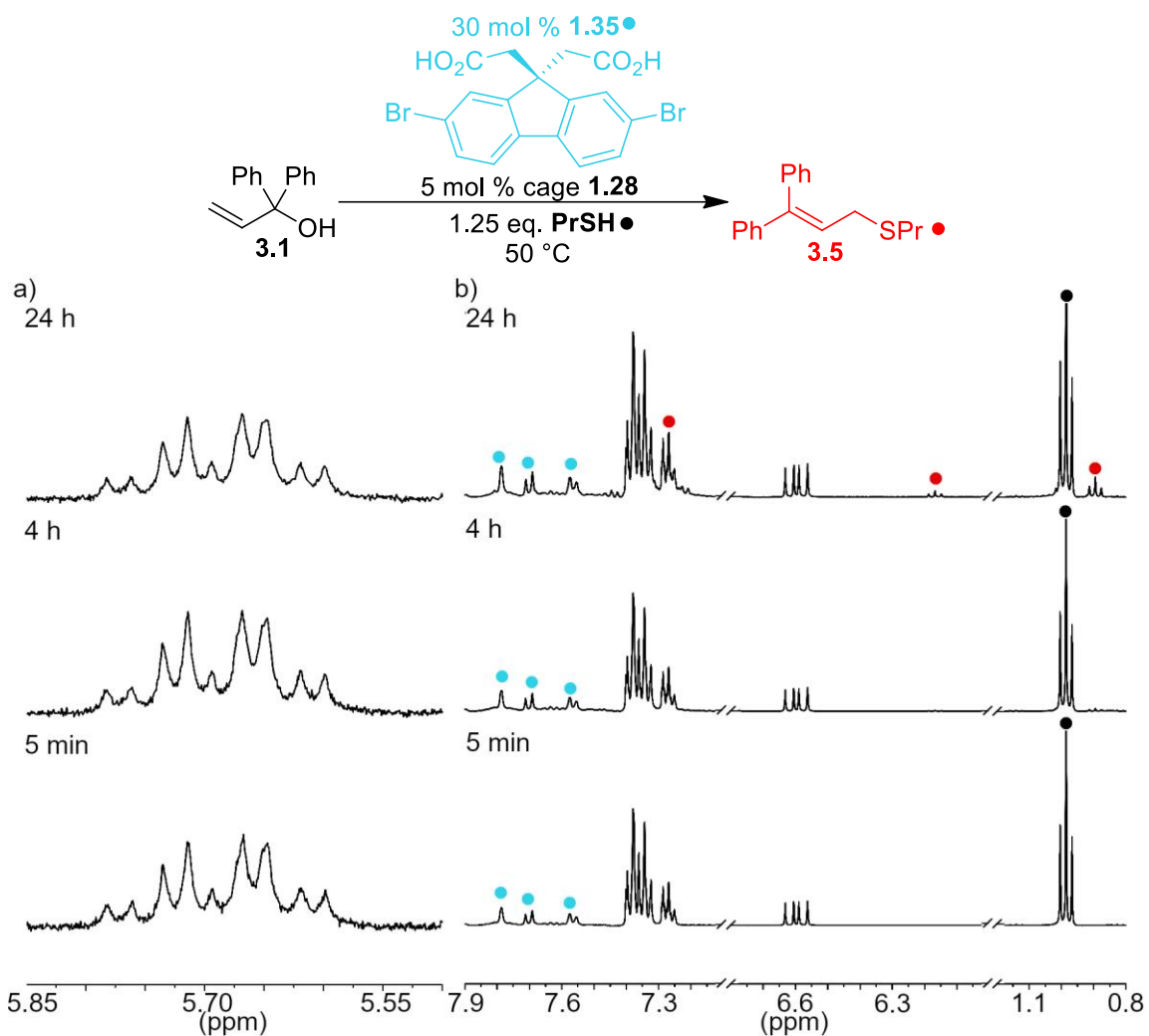


Figure 7.25. Expanded ^1H NMR spectra of the acid promoted reaction between **3.1** and n-propyl thiol in the presence of 5 mol % **1.28** showing: a) Cage stability (5.85-5.55 ppm) b) Product formation (7.9-7.1 ppm, 6.8-6.0 ppm, and 1.2-0.8 ppm). [**3.1**] = 15.8 mM, [**PrSH**] = 19.8 mM, [**1.28**] = 0.8 mM, [**1.35**] = 4.7 mM, the reaction was performed at 50 °C in CD_3CN and monitored over time (400 MHz, 323 K, CD_3CN).

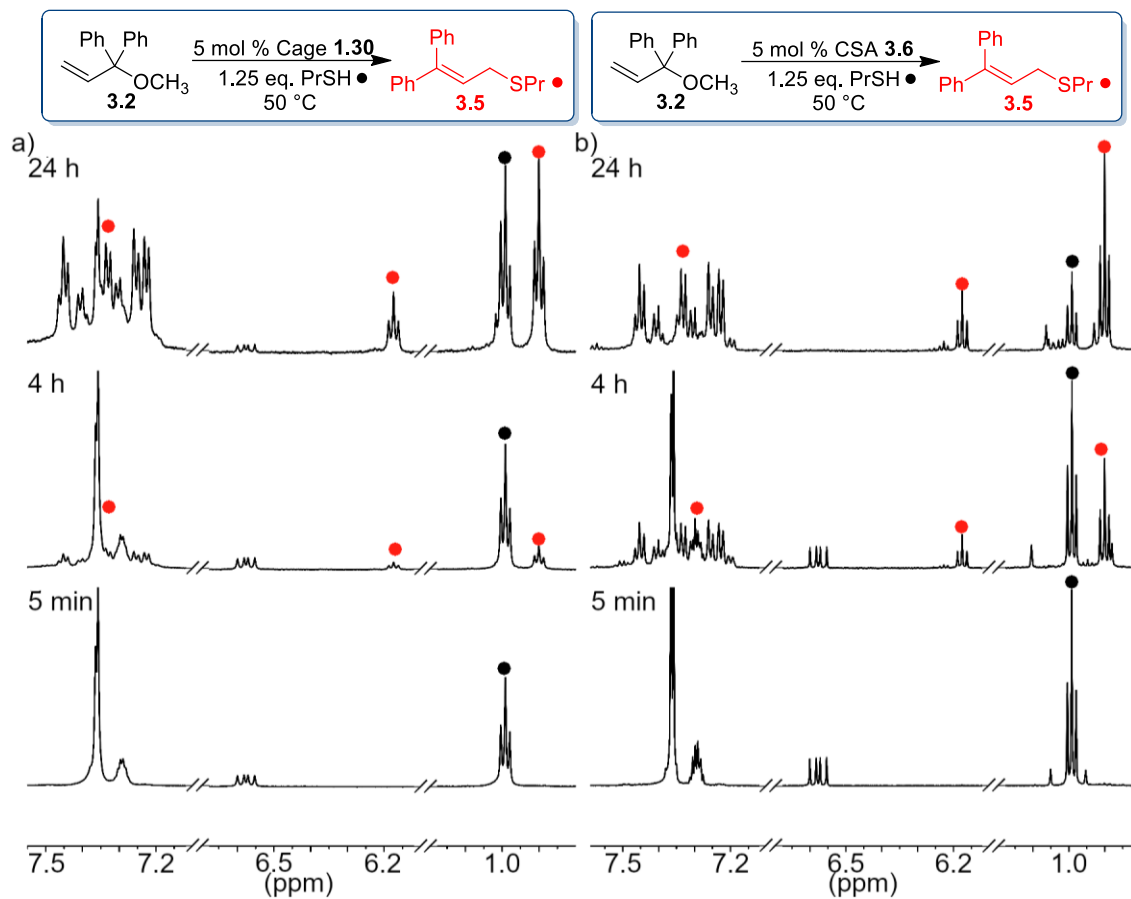


Figure 7.26. ^1H NMR spectra (7.65-7.10 ppm, 6.8-6.1 ppm, and 1.2-0.8 ppm) of the acid promoted reaction between **3.2** and *n*-propyl thiol in 400 μL CD_3CN in the presence of: a) 5 mol % cage **1.30** b) 5 mol % CSA **3.6**. [**3.2**] = 15.8 mM, [**PrSH**] = 19.8 mM, [**1**] = 0.8 mM, [**3.6**] = 0.8 mM, reactions were performed at 50 $^\circ\text{C}$ in CD_3CN and monitored over time (400 MHz, 323 K, CD_3CN).

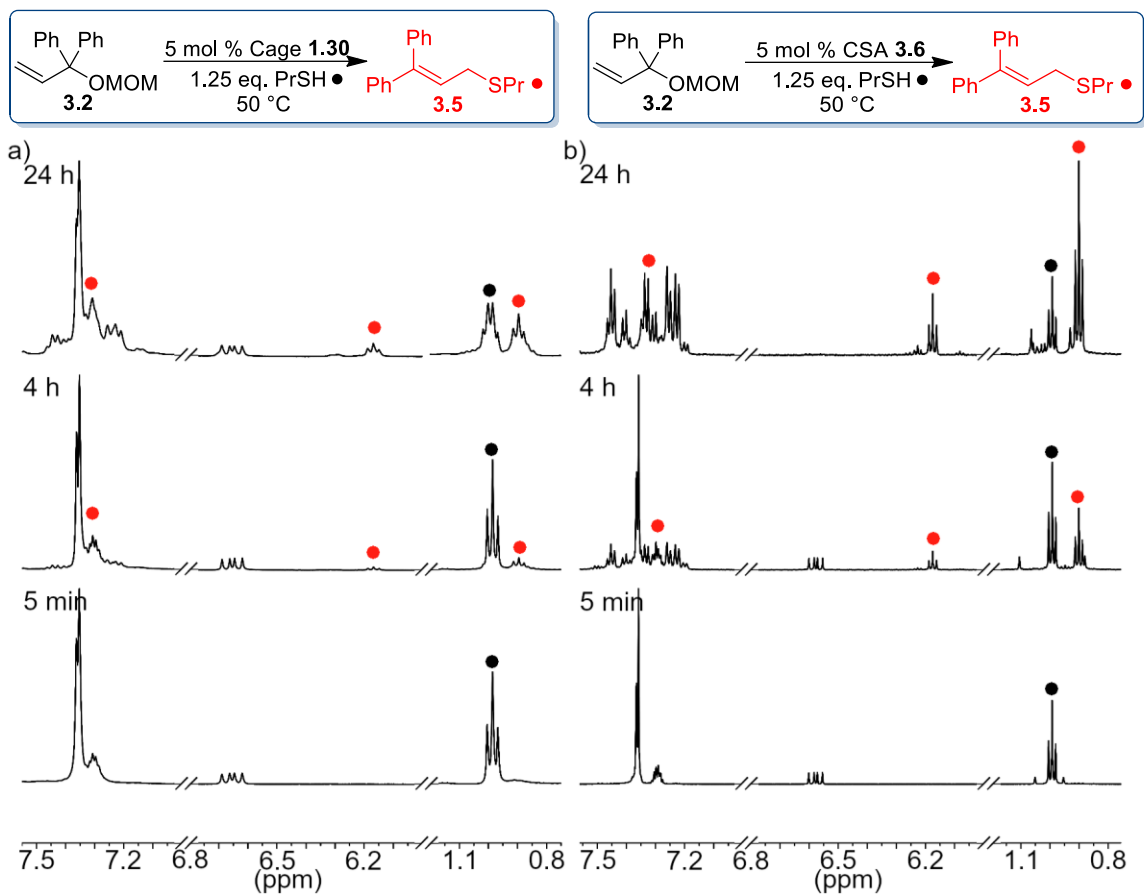


Figure 7.27. ^1H NMR spectra (7.55-7.0 ppm, 6.8-6.0 ppm, and 1.2-0.8 ppm) of the acid promoted reaction between **3.3** and *n*-propyl thiol in 400 μL CD_3CN in the presence of: a) 5 mol % cage **1.30** b) 5 mol % CSA **3.6**. [**3.3**] = 15.8 mM, [**PrSH**] = 19.8 mM, [**1.30**] = 0.8 mM, [**3.6**] = 0.8 mM, reactions were performed at 50 $^\circ\text{C}$ in CD_3CN and monitored over time (400 MHz, 323 K, CD_3CN).

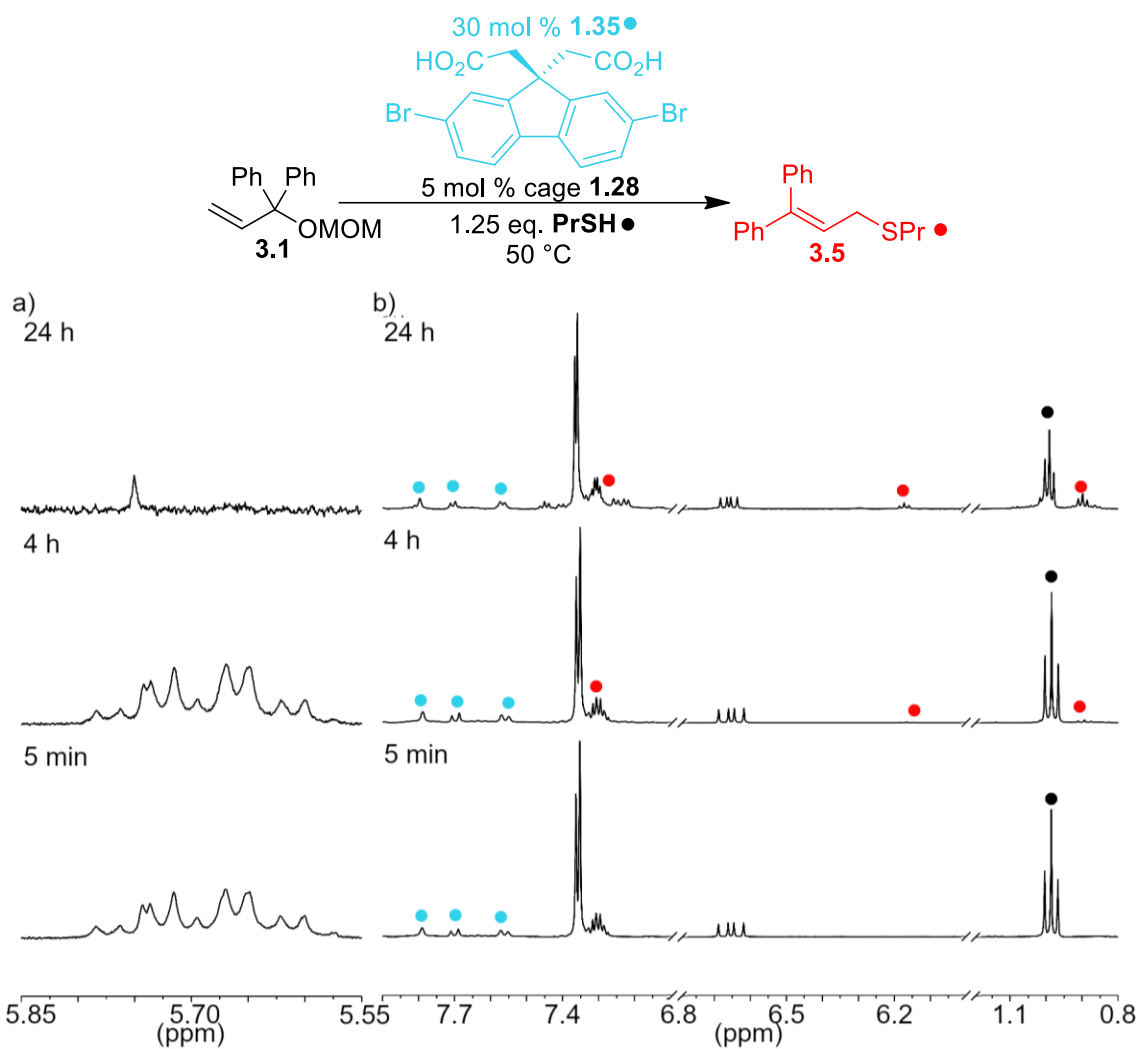
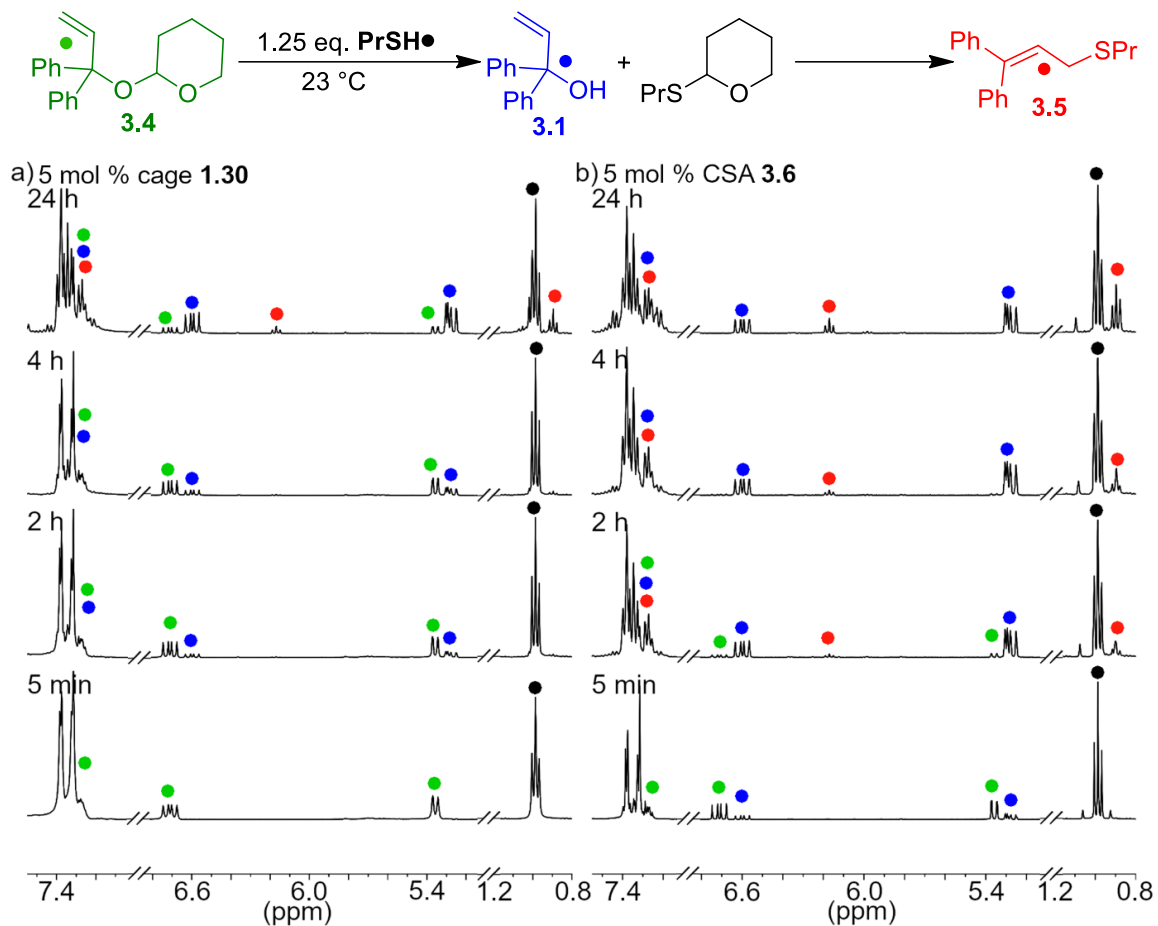


Figure 7.28. Expanded ¹H NMR spectra of the acid promoted reaction between **3.3** and *n*-propyl thiol in the presence of 5 mol % **1.28** showing: a) Cage stability (5.85-5.55 ppm) b) Product formation (7.9-7.1 ppm, 6.8-6.0 ppm, and 1.2-0.8 ppm). [**3.3**] = 15.8 mM, [**PrSH**] = 19.8 mM, [**1.28**] = 0.8 mM, [**1.35**] = 4.7 mM, the reaction was performed at 50 °C in CD₃CN and monitored over time (400 MHz, 323 K, CD₃CN).



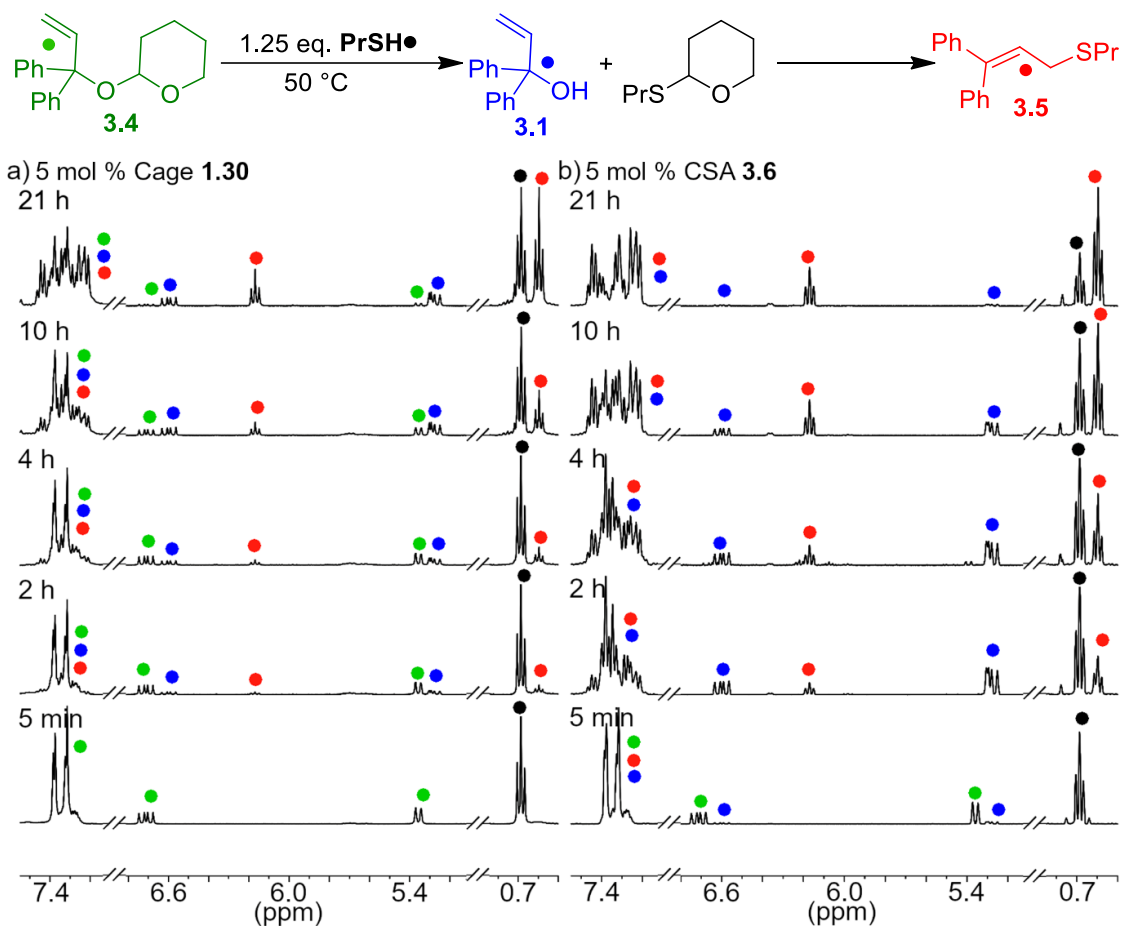


Figure 7.30. ^1H NMR spectra (7.5-7.1 ppm, 6.8-6.0 ppm, and 1.2-0.8 ppm) of the acid promoted reaction between **3.4** and *n*-propyl thiol in 400 μL CD_3CN in the presence of: a) 5 mol % cage **1.30** b) 5 mol % CSA **3.6**. [**3.4**] = 15.8 mM, [PrSH] = 19.8 mM, [**1.30**] = 0.8 mM, [**3.6**] = 0.8 mM, reactions were performed at $50\text{ }^\circ\text{C}$ in CD_3CN and monitored over time (400 MHz, 323 K, CD_3CN).

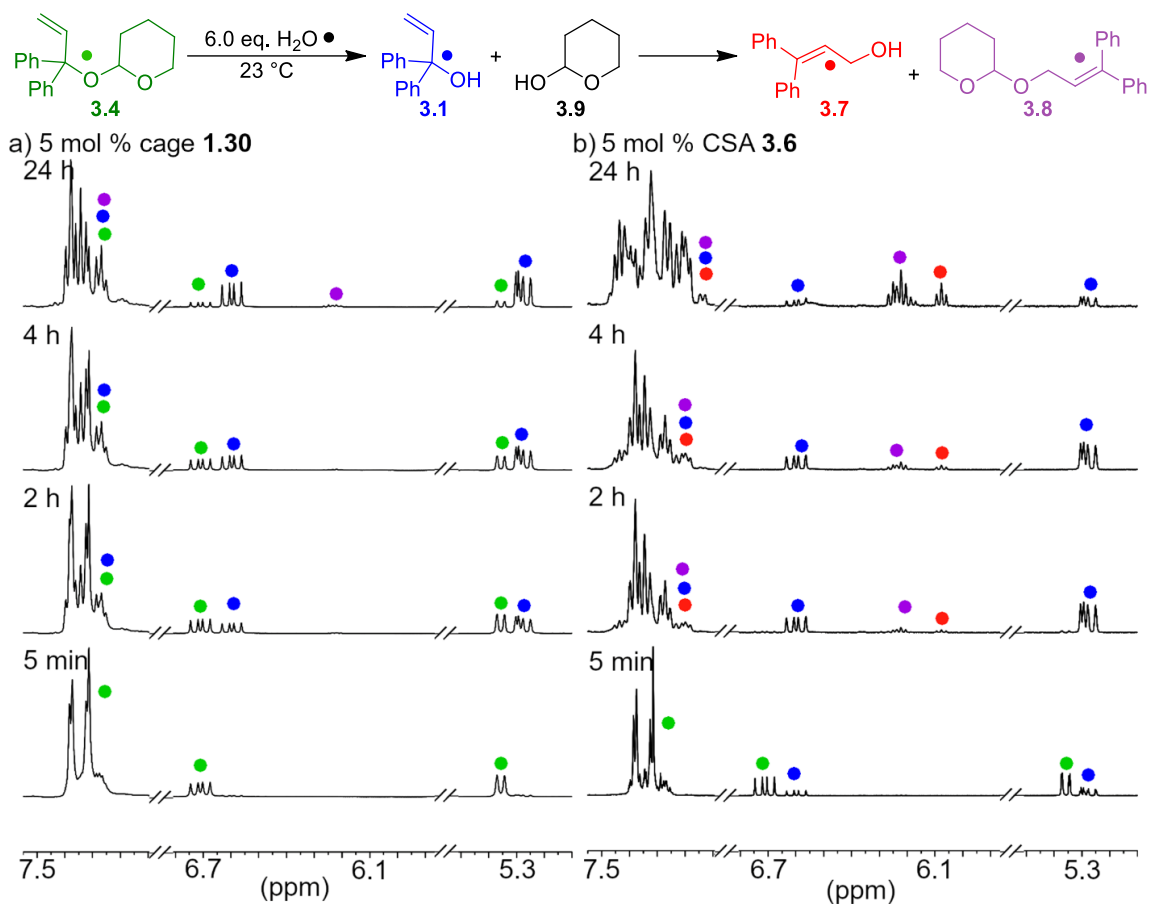


Figure 7.31. ¹H NMR spectra (7.51-7.0 ppm and 6.8-5.8 ppm) of the acid promoted reaction between **3.4** and H₂O in 400 μL CD₃CN in the presence of: a) 5 mol % cage **1.30** b) 5 mol % CSA **3.6**. [**3.4**] = 15.8 mM, [H₂O] = 94.5 mM, [**1.30**] = 0.8 mM, [**3.6**] = 0.8 mM, reactions were performed at 23 °C in CD₃CN and monitored over time (400 MHz, 298 K, CD₃CN).

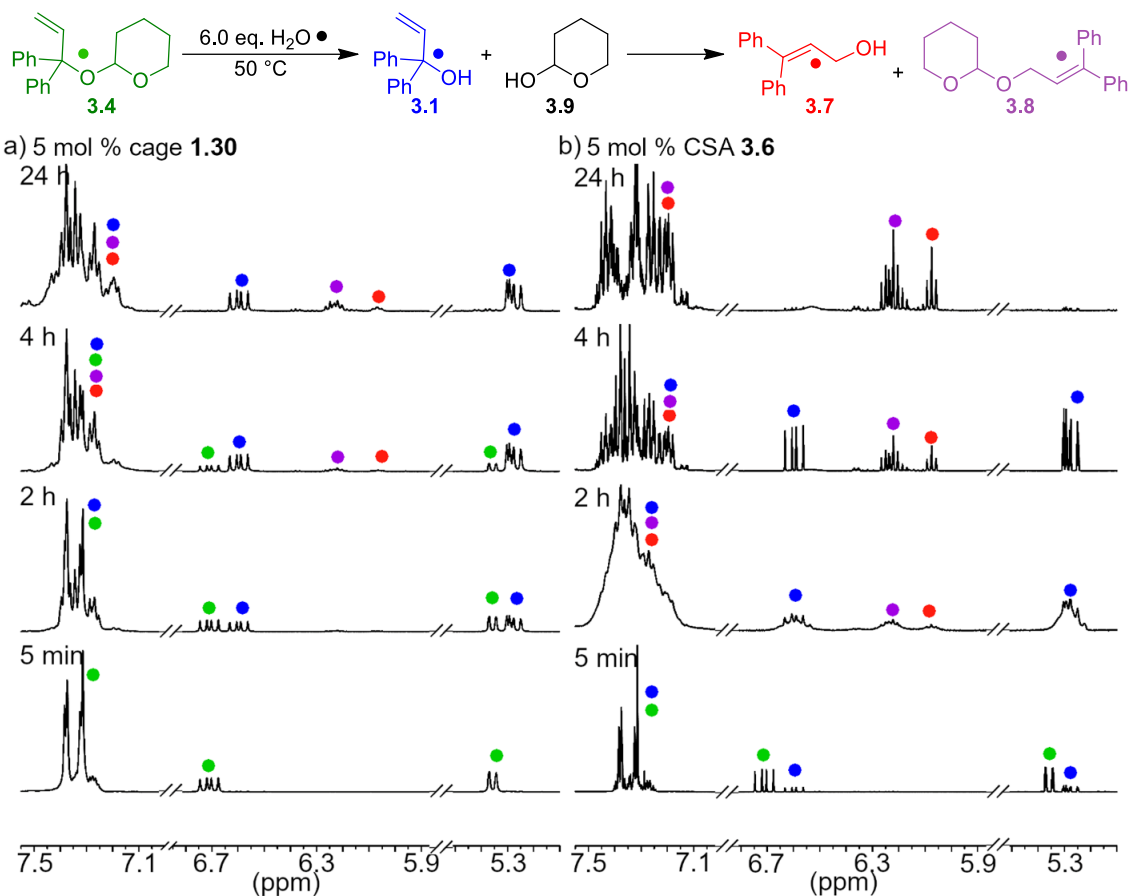


Figure 7.32. ¹H NMR spectra (7.51-7.0 ppm and 6.8-5.8 ppm) of the acid promoted reaction between **3.4** and H₂O in 400 μL CD₃CN in the presence of: a) 5 mol % cage **1.30** b) 5 mol % CSA **3.6**. [**3.4**] = 15.8 mM, [H₂O] = 94.5 mM, [**1.30**] = 0.8 mM, [**3.6**] = 0.8 mM, reactions were performed at 50 °C in CD₃CN and monitored over time (400 MHz, 323 K, CD₃CN).

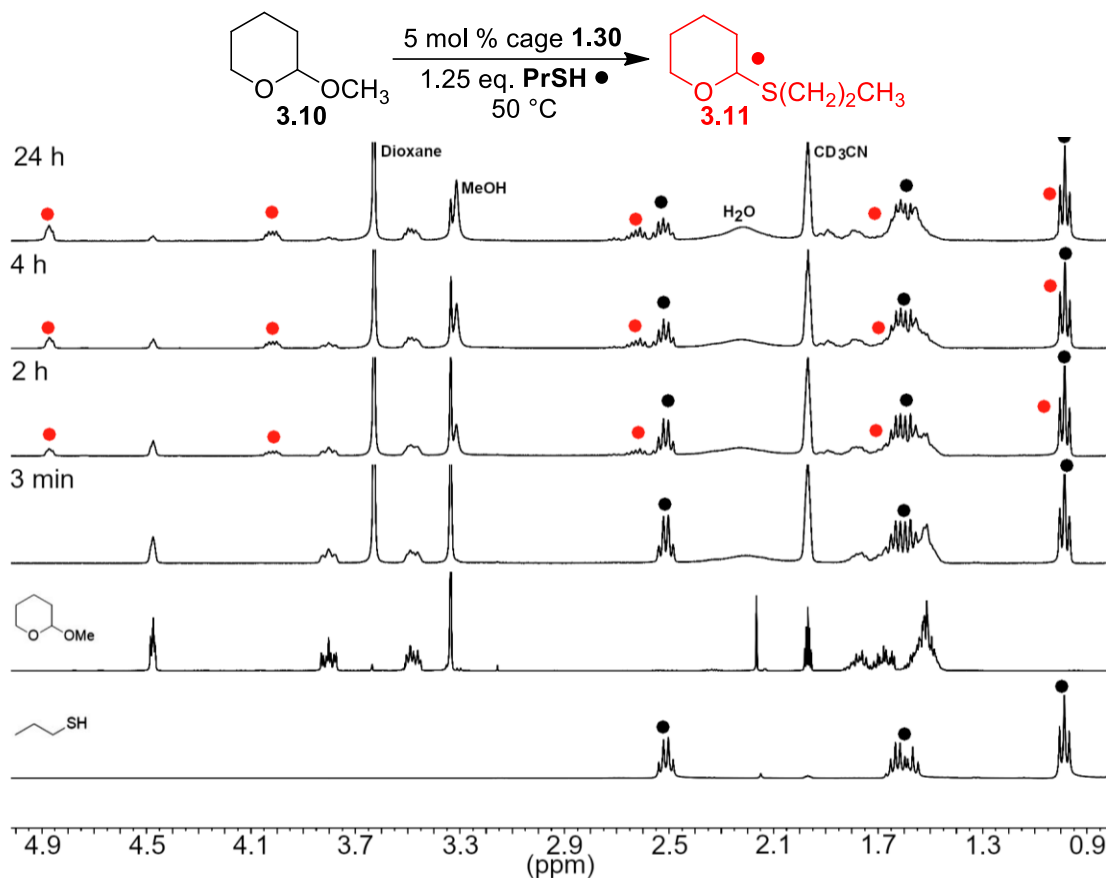


Figure 7.33. Full ^1H NMR spectra of the acid promoted reaction between **3.10** and *n*-propyl thiol in the presence of 5 mol % cage **1.30**. $[\mathbf{3.10}] = 15.8\text{ mM}$, $[\text{PrSH}] = 19.8\text{ mM}$, $[\mathbf{1.30}] = 0.8\text{ mM}$, the reaction was performed at $50\text{ }^\circ\text{C}$ in CD_3CN and monitored over time (400 MHz, 323 K, CD_3CN).

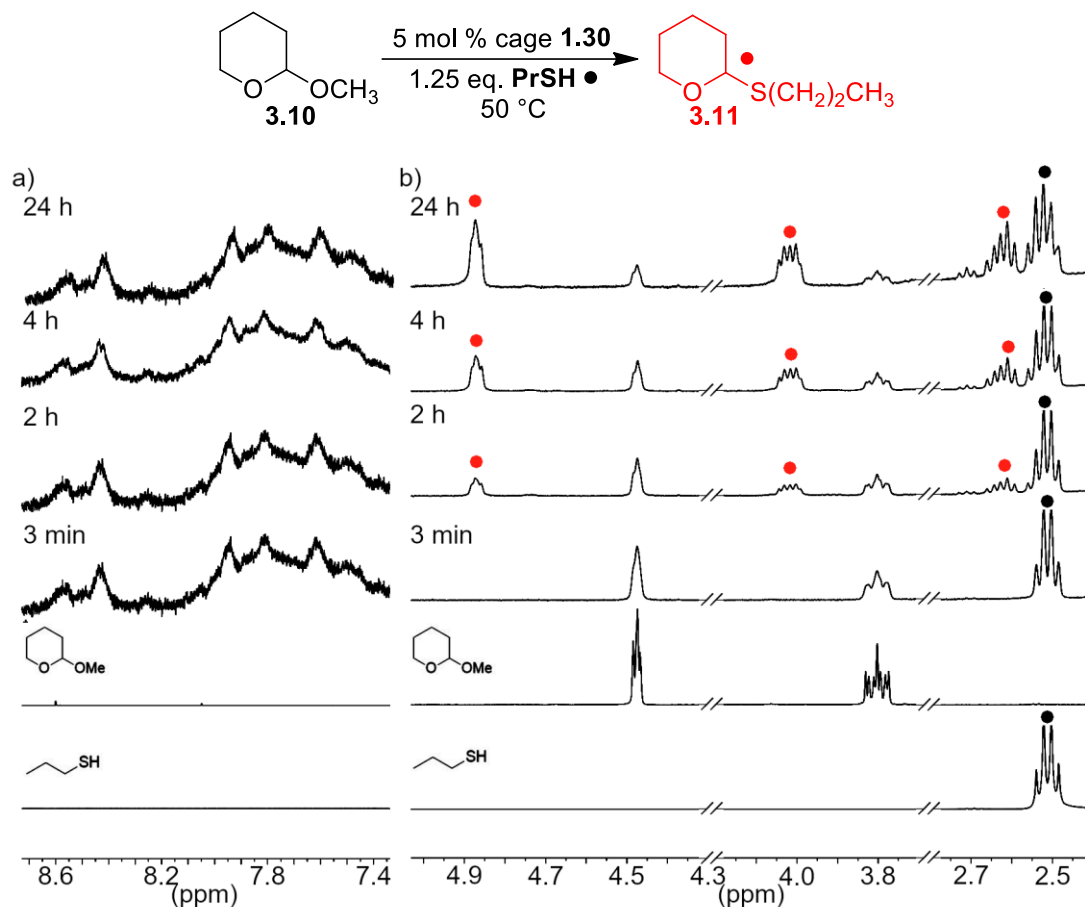


Figure 7.34. Expanded ¹H NMR spectra of the acid promoted reaction between **3.10** and *n*-propyl thiol in the presence of 5 mol % cage **1.30** showing: a) Cage stability (8.7-7.3 ppm) b) Product formation (5.1 – 4.3 ppm, 4.2 -3.7 ppm, and 2.7 -2.3 ppm). [**3.10**] = 15.8 mM, [PrSH] = 19.8 mM, [**1.30**] = 0.8 mM, the reaction was performed at 50 °C in CD₃CN and monitored over time (400 MHz, 323 K, CD₃CN).

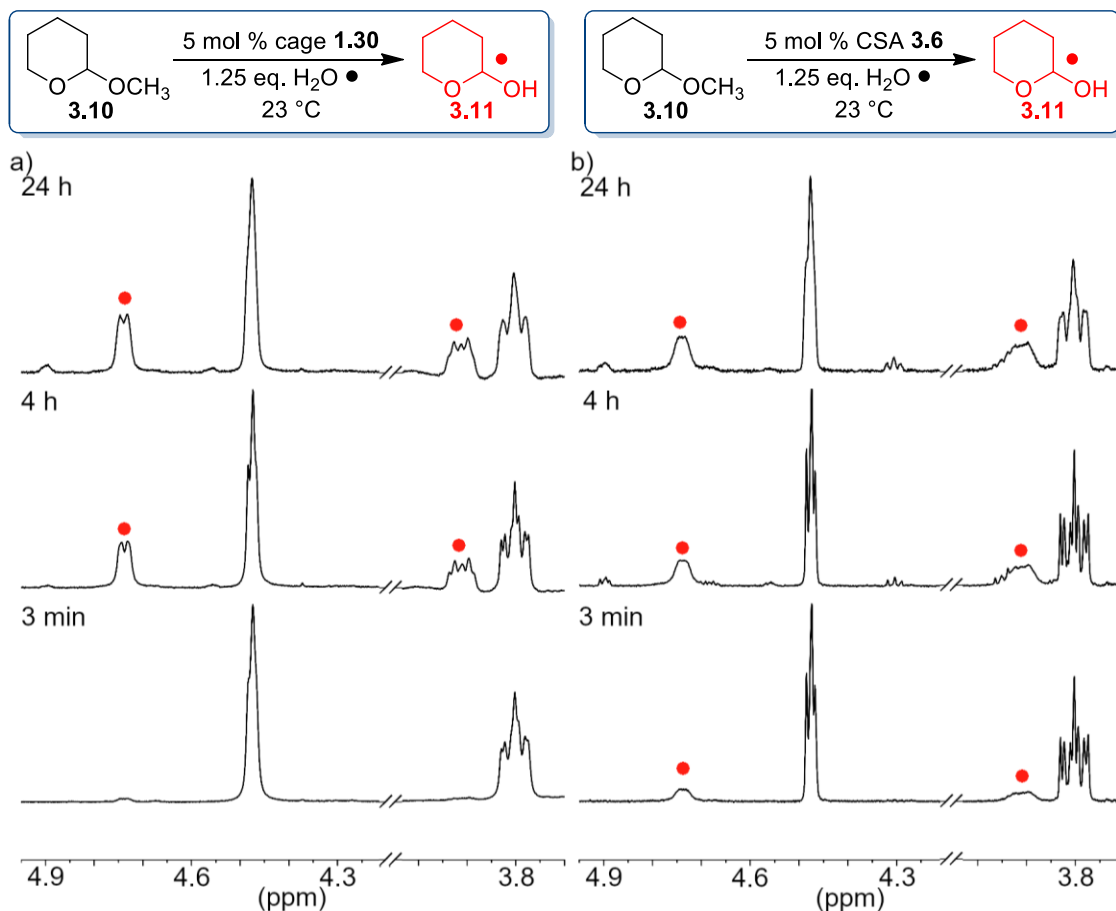


Figure 7.35. ^1H NMR spectra (4.9-4.2 ppm and 4.0-3.7 ppm) of the acid promoted reaction between **3.10** and H_2O in 400 μL CD_3CN in the presence of: a) 5 mol % cage **1.30** b) 5 mol % CSA **3.6**. $[\mathbf{3.10}] = 15.8\text{ mM}$, $[\text{H}_2\text{O}] = 94.5\text{ mM}$, $[\mathbf{1.30}] = 0.8\text{ mM}$, $[\mathbf{3.6}] = 0.8\text{ mM}$, reactions were performed at 23 $^\circ\text{C}$ in CD_3CN and monitored over time (400 MHz, 296 K, CD_3CN).

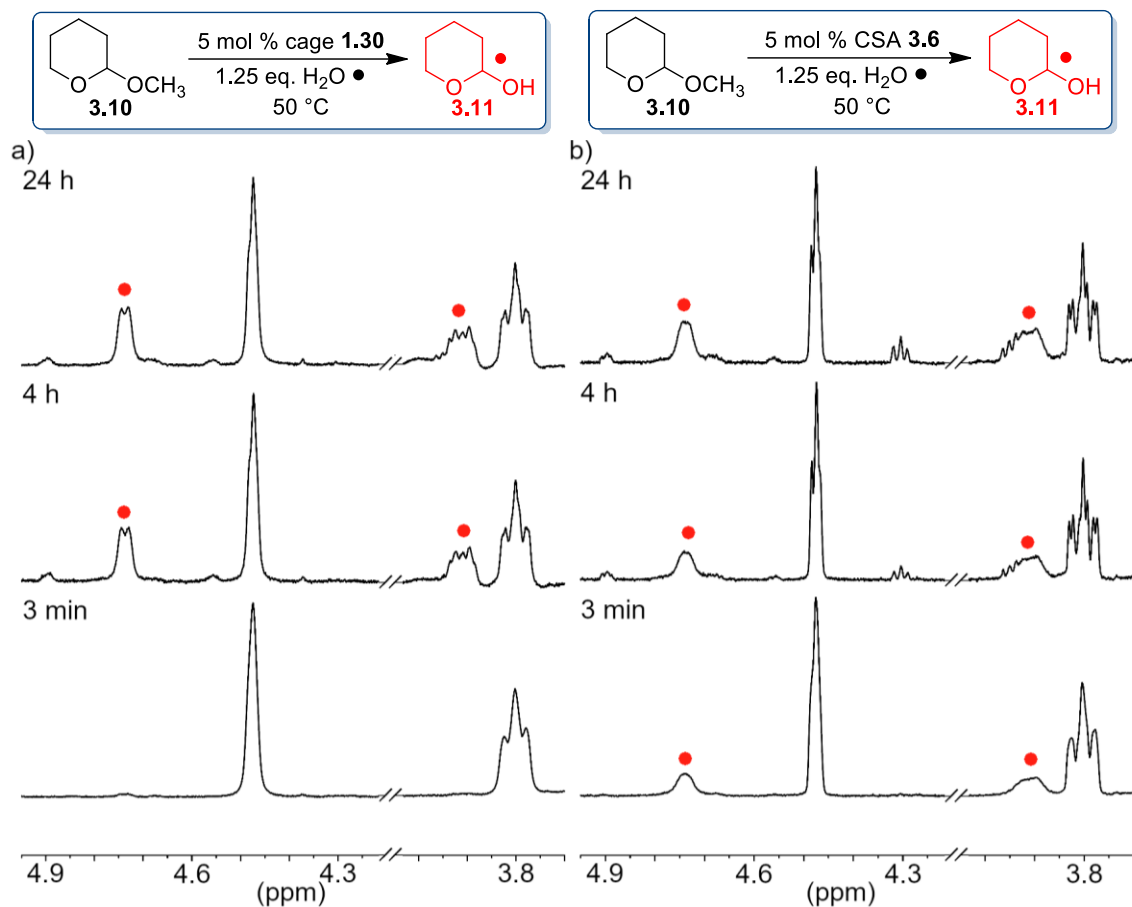


Figure 7.36. ^1H NMR spectra (4.9–4.2 ppm and 4.0–3.7 ppm) of the acid promoted reaction between **3.10** and H_2O in $400\ \mu\text{L}$ CD_3CN in the presence of: a) 5 mol % cage **1.30** b) 5 mol % CSA **3.6**. $[\mathbf{3.10}] = 15.8\ \text{mM}$, $[\text{H}_2\text{O}] = 94.5\ \text{mM}$, $[\mathbf{1.30}] = 0.8\ \text{mM}$, $[\mathbf{3.6}] = 0.8\ \text{mM}$, reactions were performed at $50\ ^\circ\text{C}$ in CD_3CN and monitored over time (400 MHz, 323 K, CD_3CN).

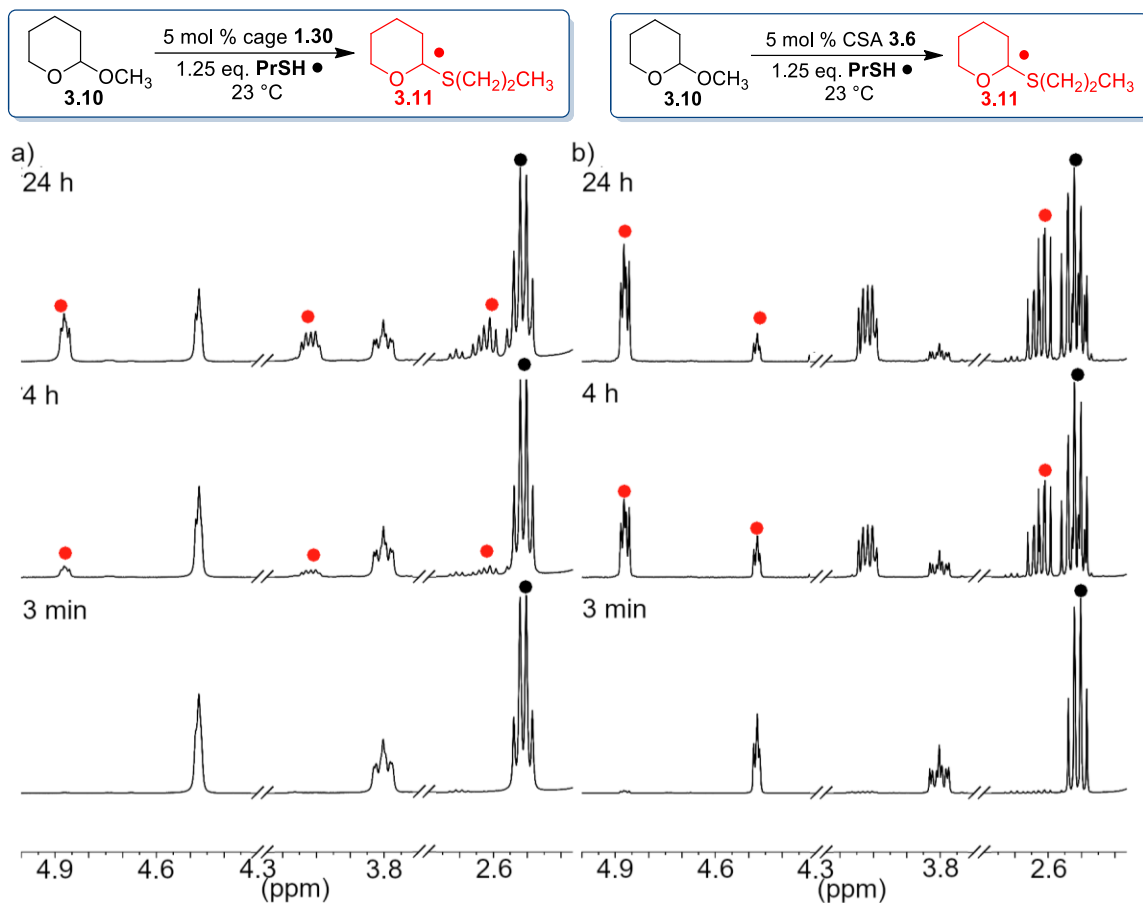


Figure 7.37. ^1H NMR spectra (4.9–4.2 ppm and 2.7–2.3 ppm) of the acid promoted reaction between **3.10** and **PrSH** in 400 μL CD_3CN in the presence of: a) 5 mol % cage **1.30** b) 5 mol % CSA **3.6**. $[\mathbf{3.10}] = 15.8 \text{ mM}$, $[\text{PrSH}] = 19.8 \text{ mM}$, $[\mathbf{1.30}] = 0.8 \text{ mM}$, $[\mathbf{3.6}] = 0.8 \text{ mM}$, reactions were performed at 23 $^\circ\text{C}$ in CD_3CN and monitored over time (400 MHz, 296 K, CD_3CN).

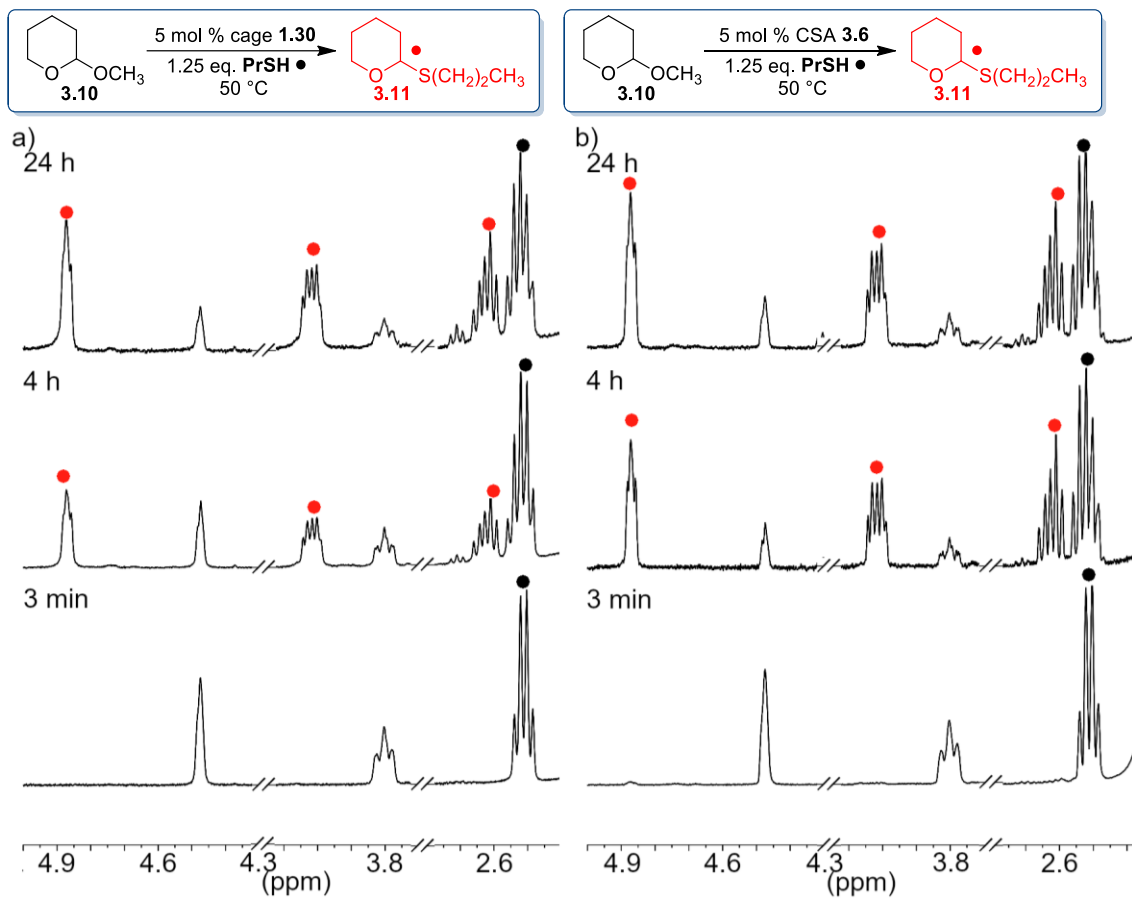


Figure 7.38. ^1H NMR spectra (4.9–4.2 ppm and 2.7–2.3 ppm) of the acid promoted reaction between **3.10** and **PrSH** in 400 μL CD_3CN in the presence of: a-b) 5 mol % cage **1.30** c-d) 5 mol % CSA **3.6**. [**3.10**] = 15.8 mM, [**PrSH**] = 19.8 mM, [**1.30**] = 0.8 mM, [**3.6**] = 0.8 mM, reactions were performed at 50 $^\circ\text{C}$ in CD_3CN and monitored over time (400 MHz, 323 K, CD_3CN).

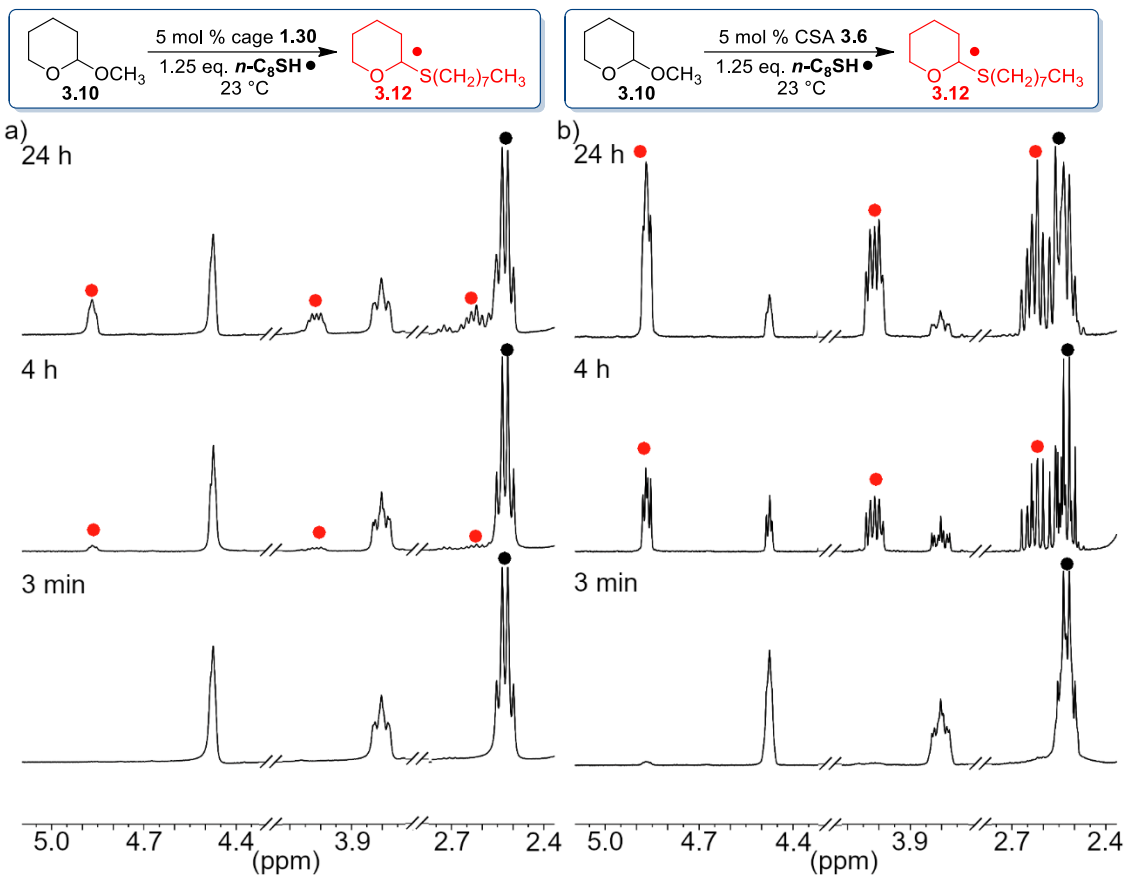


Figure 7.39. ¹H NMR spectra (5.1-4.3 ppm, 4.15-3.7 ppm, and 2.8-2.4 ppm) of the acid promoted reaction between **3.10** and *n*-octyl thiol in 400 μ L CD₃CN in the presence of: a) 5 mol % cage **1.30** b) 5 mol % CSA **3.6**. [**3.10**] = 15.8 mM, [*n*-C₈SH] = 19.8 mM, [**1.30**] = 0.8 mM, [**3.6**] = 0.8 mM, reactions were performed at 23 °C in CD₃CN and monitored over time (400 MHz, 296 K, CD₃CN).

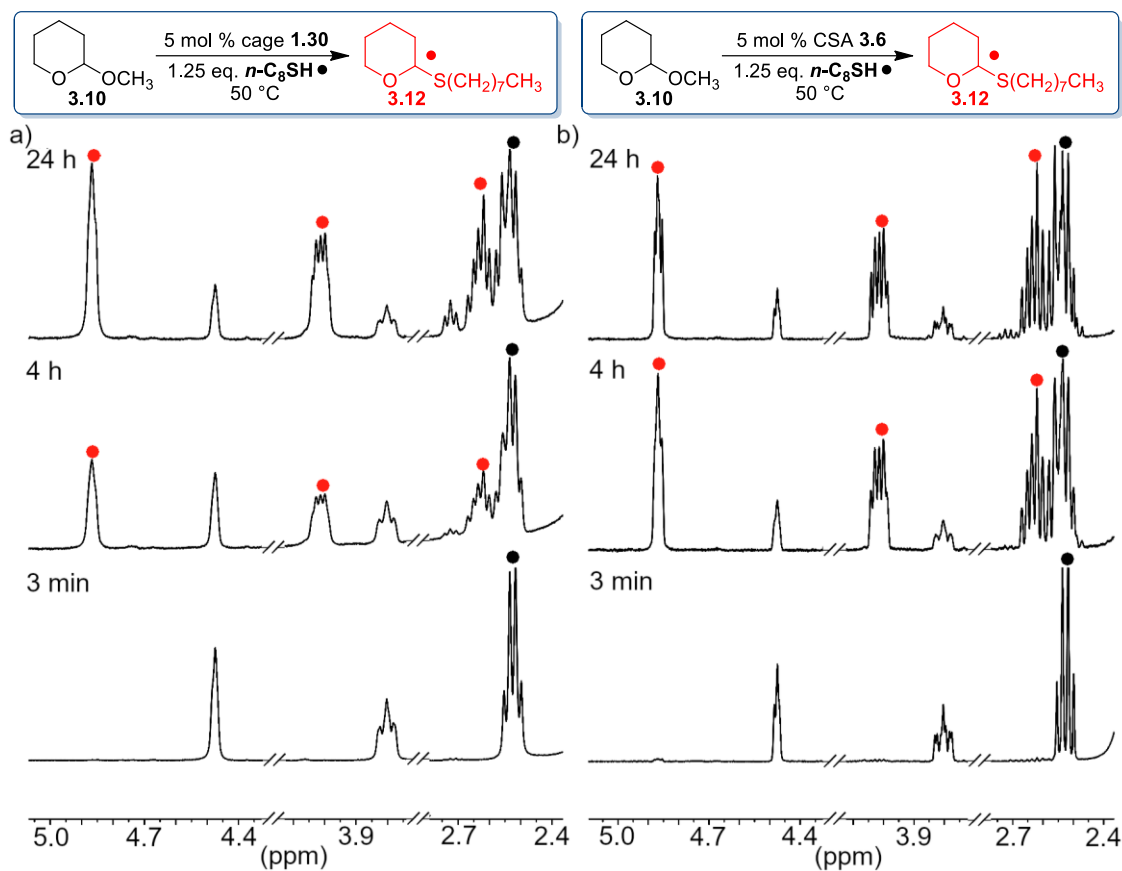


Figure 7.40. ^1H NMR spectra (5.1-4.3 ppm, 4.15-3.7 ppm, and 2.8-2.4 ppm) of the acid promoted reaction between **3.10** and *n*-octyl thiol in 400 μL CD_3CN in the presence of: a) 5 mol % cage **1.30** b) 5 mol % CSA **3.6**. [**3.10**] = 15.8 mM, [$n\text{-C}_8\text{SH}$] = 19.8 mM, [**1.30**] = 0.8 mM, [**3.6**] = 0.8 mM, reactions were performed at 50 °C in CD_3CN and monitored over time (400 MHz, 323 K, CD_3CN).

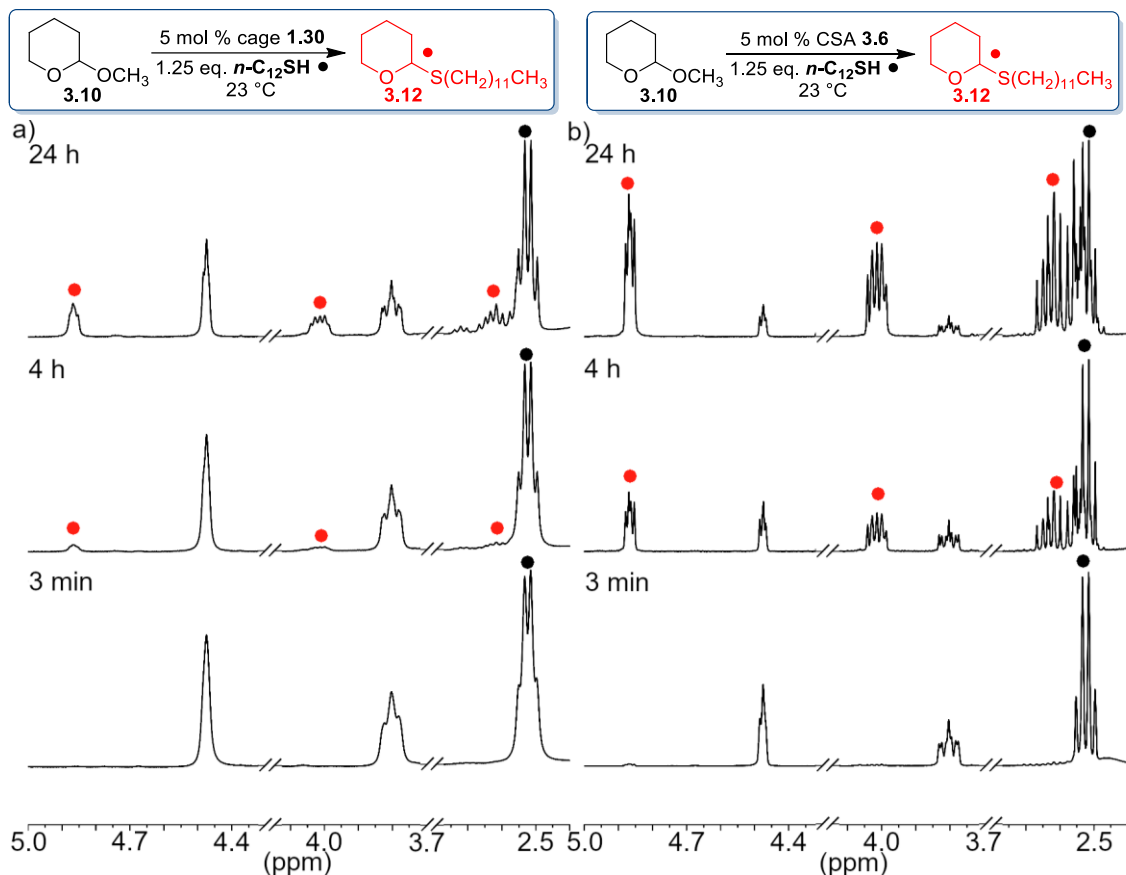


Figure 7.41. ^1H NMR spectra (5.0-4.3 ppm, 4.15-3.7 ppm, and 2.8-2.4 ppm) of the acid promoted reaction between **3.10** and *n*-dodecyl thiol in $400\ \mu\text{L}$ CD_3CN in the presence of: a) 5 mol % cage **1.30** b) 5 mol % CSA **3.6**. [**3.10**] = 15.8 mM, [*n*- C_{12}SH] = 19.8 mM, [**1.30**] = 0.8 mM, [**3.6**] = 0.8 mM, reactions were performed at 23°C in CD_3CN and monitored over time (400 MHz, 296 K, CD_3CN).

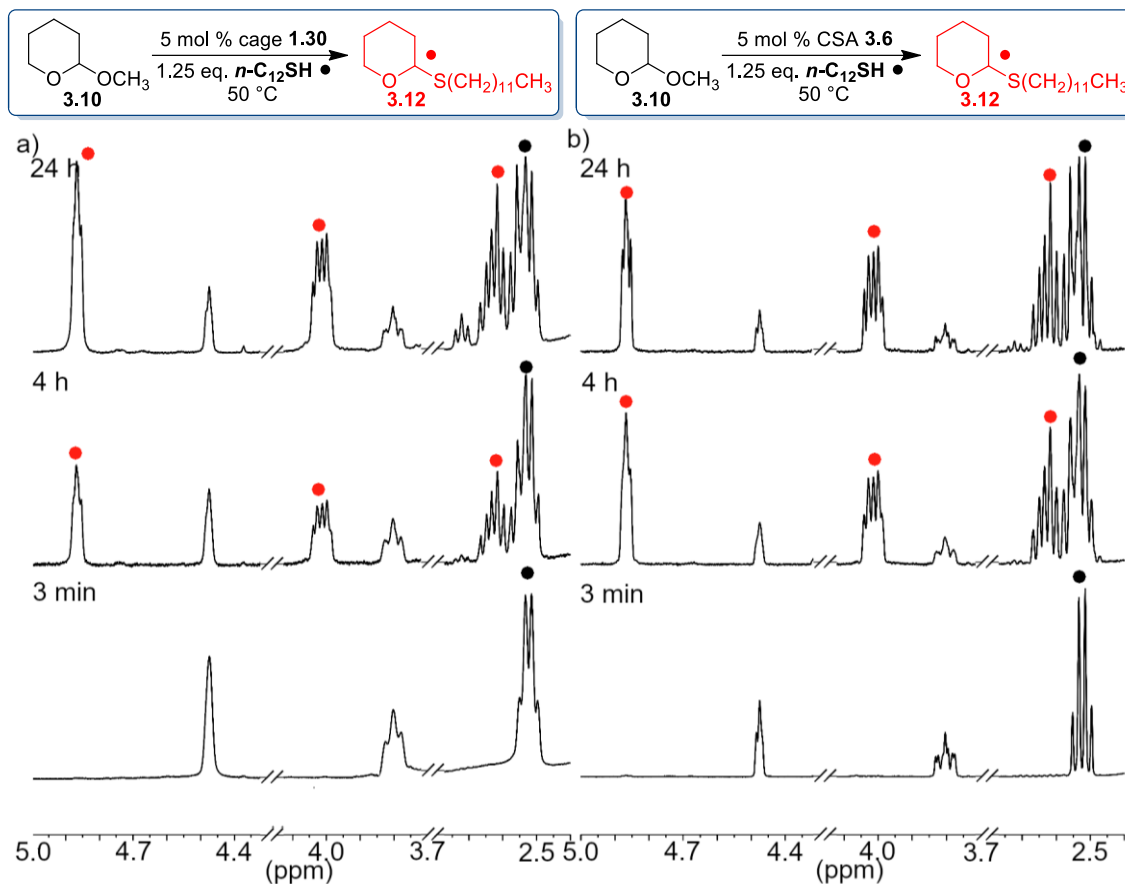


Figure 7.42. ^1H NMR spectra (5.0-4.3 ppm, 4.15-3.7 ppm, and 2.8-2.4 ppm) of the acid promoted reaction between **3.10** and *n*-dodecyl thiol in 400 μL CD₃CN in the presence of: a) 5 mol % cage **1.30** b) 5 mol % CSA **3.6**. [**3.10**] = 15.8 mM, [*n*-C₁₂SH] = 19.8 mM, [**1.30**] = 0.8 mM, [**3.6**] = 0.8 mM, reactions were performed at 50 °C in CD₃CN and monitored over time (400 MHz, 323 K, CD₃CN).

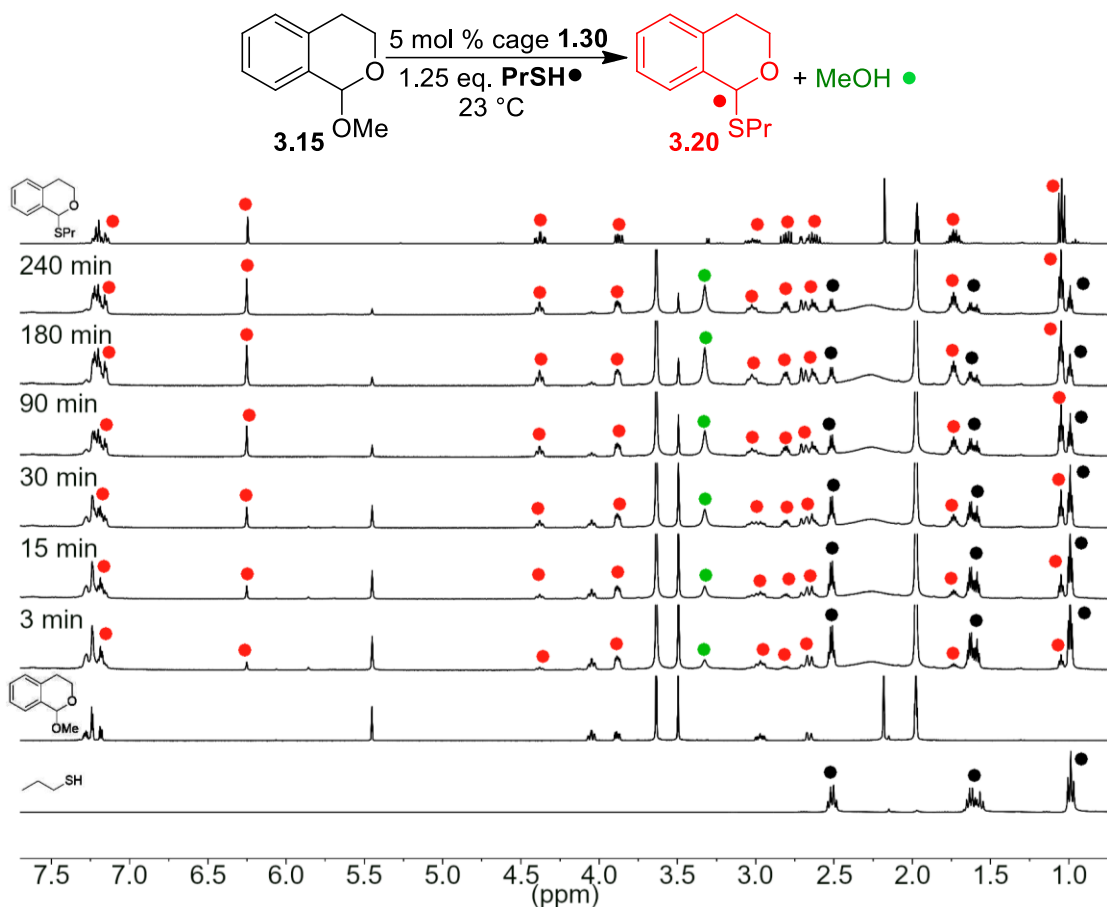


Figure 7.43. Full ^1H NMR spectra of the acid promoted reaction between **3.15** and *n*-propyl thiol in the presence of 5 mol % cage **1.30**. [**3.15**] = 15.8 mM, [PrSH] = 19.8 mM, [**1.35**] = 0.8 mM, the reaction was performed at 23 °C in CD_3CN and monitored over time (400 MHz, 296 K, CD_3CN).

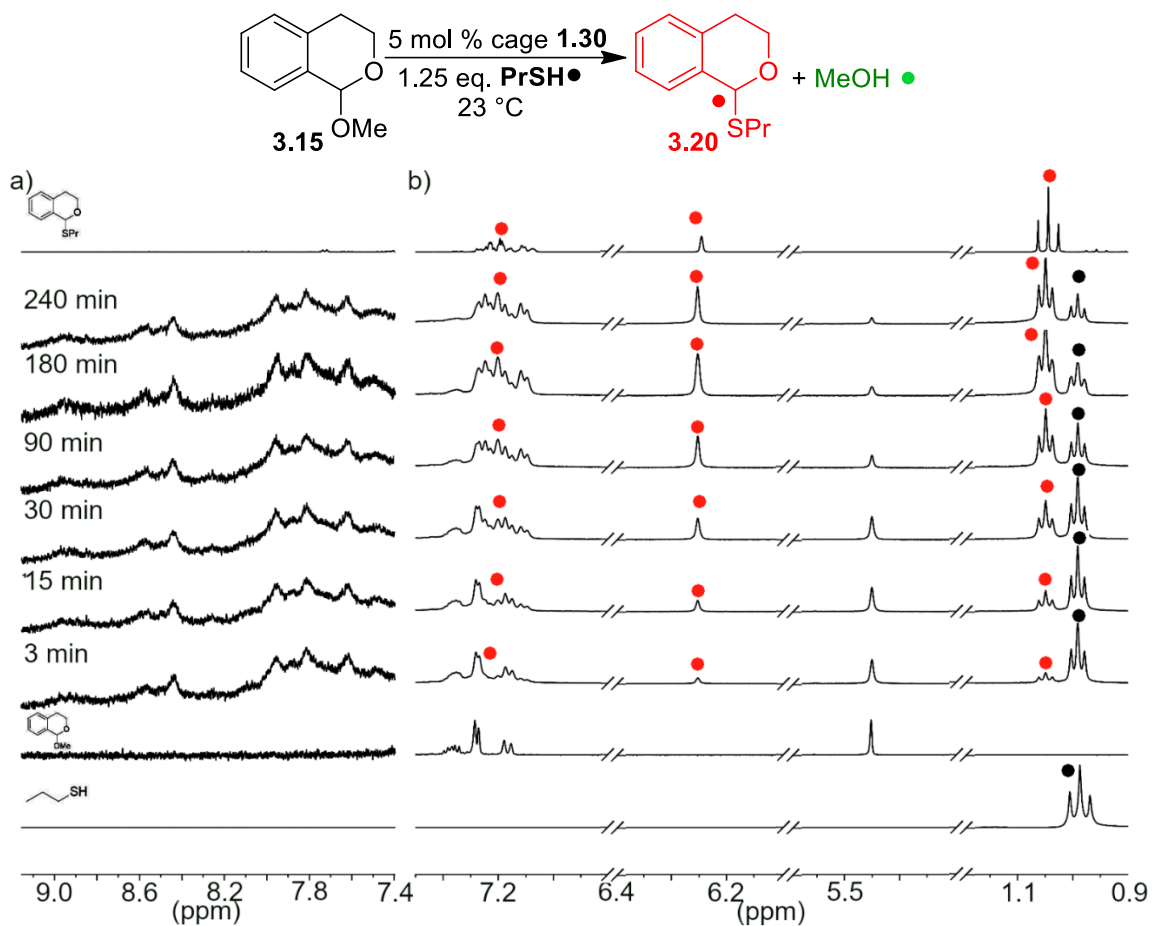


Figure 7.44. Expanded ^1H NMR spectra of the acid promoted reaction between **3.15** and *n*-propyl thiol in the presence of 5 mol % cage **1.30** showing: a) Cage stability (9.1-7.4 ppm) b) Product formation (7.5-6.8 ppm, 6.4-6.0 ppm, 5.7-5.1 ppm, and 1.3-0.9 ppm). $[\mathbf{3.15}] = 15.8\text{ mM}$, $[\text{PrSH}] = 19.8\text{ mM}$, $[\mathbf{1.30}] = 0.8\text{ mM}$, the reaction was performed at 23 $^\circ\text{C}$ in CD_3CN and monitored over time (400 MHz, 296 K, CD_3CN).

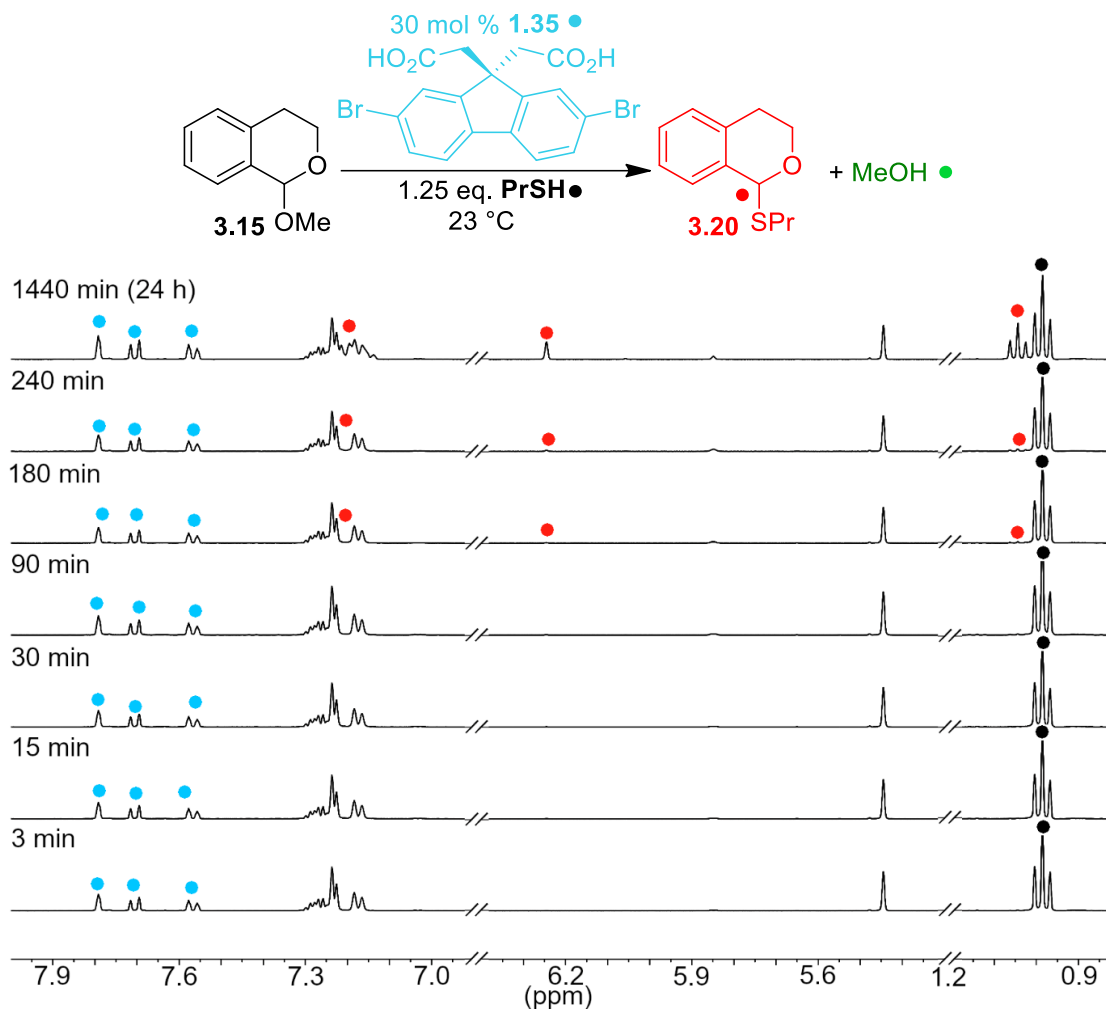


Figure 7.45. ^1H NMR spectra (8.0–6.9 ppm, 6.4–5.3 ppm, and 1.2–0.8 ppm) of the acid promoted reaction between **3.15** and *n*-propyl thiol in 400 μL CD_3CN in the presence of 30 mol % weak acid control **1.35**. [**3.15**] = 15.8 mM, [**PrSH**] = 19.8 mM, [**1.35**] = 4.7 mM, reactions were performed at 23 $^\circ\text{C}$ in CD_3CN and monitored over time (400 MHz, 296 K, CD_3CN).

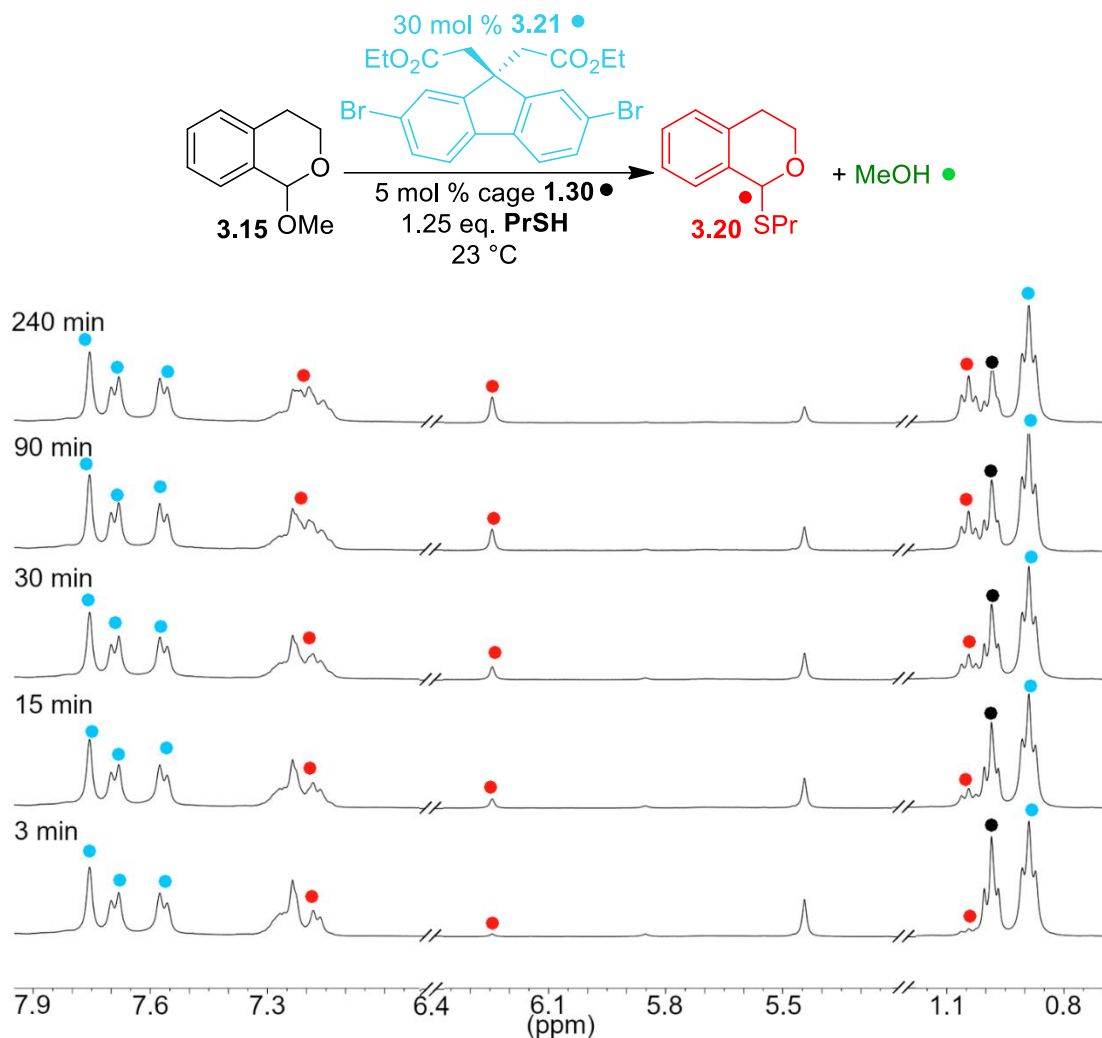


Figure 7.46. ¹H NMR spectra (7.95–6.9 ppm, 6.4–5.2 ppm, and 1.2–0.65 ppm) of the acid promoted reaction between **3.15** and n-propyl thiol in 400 μL CD₃CN in the presence of 5 mol % cage **1.30** and 1 equivalent of cavity-filling guest **3.21**. [**3.15**] = 15.8 mM, [**PrSH**] = 19.8 mM, [**1.30**] = 0.8 mM, [**3.21**] = 15.8 mM, reactions were performed at 23 °C in CD₃CN and monitored over time (400 MHz, 296 K, CD₃CN).

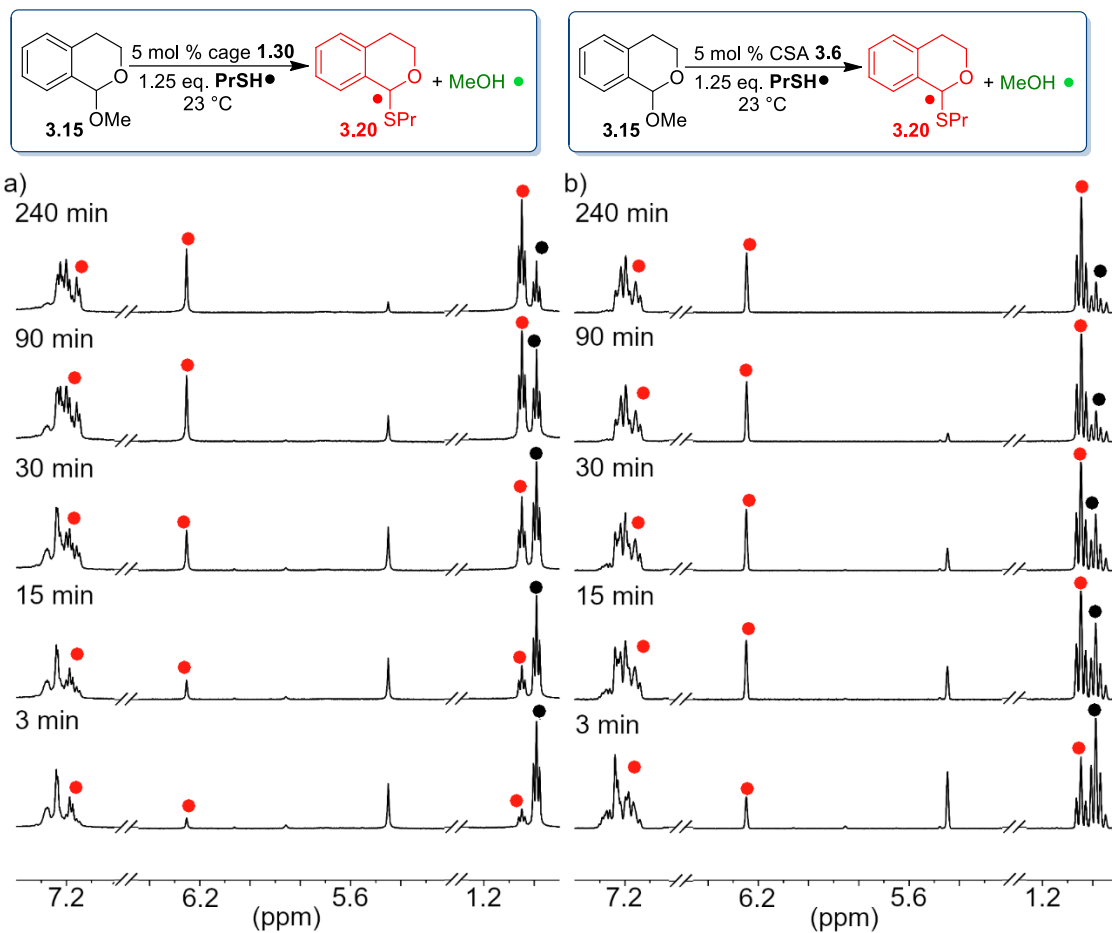
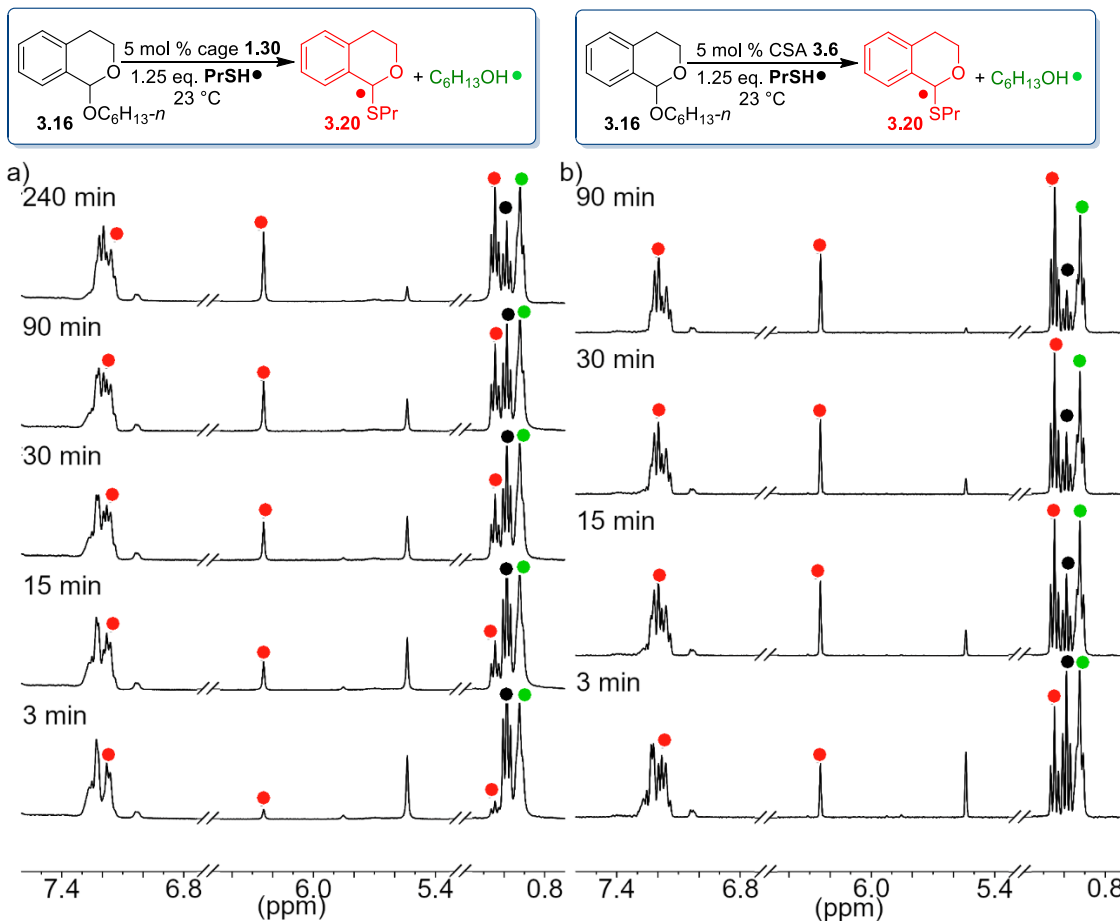


Figure 7.47. ^1H NMR spectra (7.4–7.0 ppm, 6.5–5.2 ppm, and 1.3–0.9 ppm) of the acid promoted reaction between **3.15** and *n*-propyl thiol in 400 μL CD_3CN in the presence of: a) 5 mol % cage **1.30** b) 5 mol % CSA **3.6**. [**3.15**] = 15.8 mM, [**PrSH**] = 19.8 mM, [**1.30**] = 0.8 mM, [**3.6**] = 0.8 mM, reactions were performed at 23 $^\circ\text{C}$ in CD_3CN and monitored over time (400 MHz, 296 K, CD_3CN).



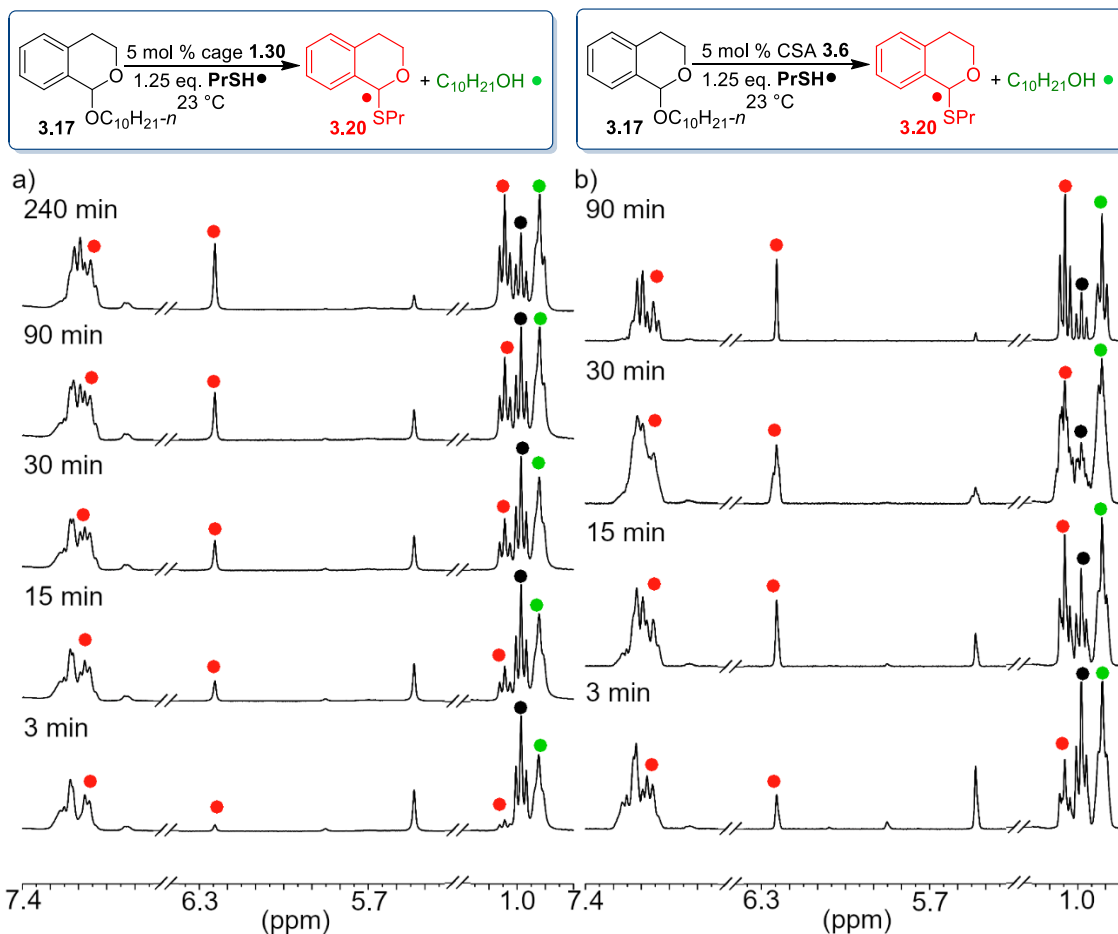


Figure 7.49. ^1H NMR spectra (7.4-6.9 ppm, 6.4-5.4 ppm, and 1.2-0.8 ppm) of the acid promoted reaction between **3.17** and *n*-propyl thiol in $400\ \mu\text{L}$ CD_3CN in the presence of: a) $5\ \text{mol}\ \%$ cage **1.30** b) $5\ \text{mol}\ \%$ CSA **3.6**. [**3.17**] = $15.8\ \text{mM}$, [**PrSH**] = $19.8\ \text{mM}$, [**1.30**] = $0.8\ \text{mM}$, [**3.6**] = $0.8\ \text{mM}$, reactions were performed at $23\ ^\circ\text{C}$ in CD_3CN and monitored over time ($400\ \text{MHz}$, $296\ \text{K}$, CD_3CN).

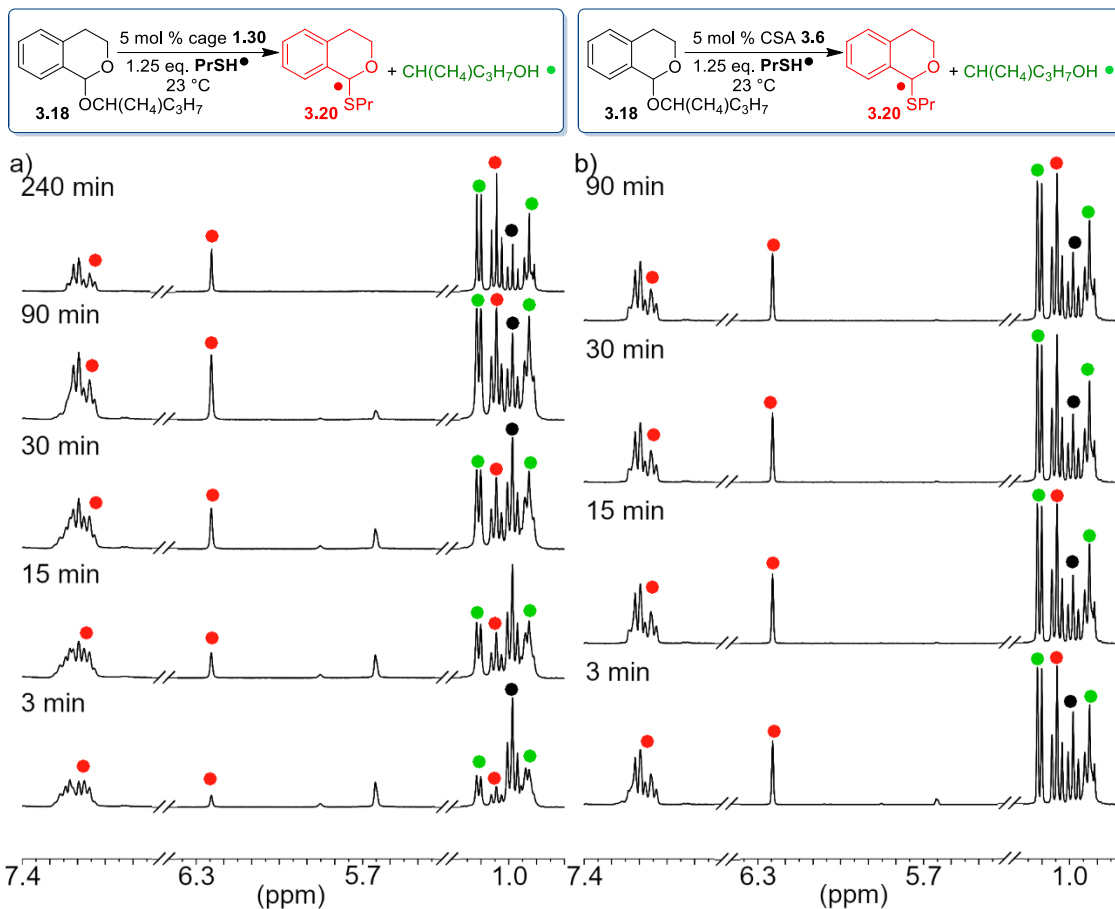


Figure 7.50. ^1H NMR spectra (7.4-6.9 ppm, 6.4-5.4 ppm, and 1.2-0.8 ppm) of the acid promoted reaction between **3.18** and *n*-propyl thiol in 400 μL CD_3CN in the presence of: a) 5 mol % cage **1.30** b) 5 mol % CSA **3.6**. [**3.18**] = 15.8 mM, [**PrSH**] = 19.8 mM, [**1.30**] = 0.8 mM, [**3.6**] = 0.8 mM, reactions were performed at 23 $^\circ\text{C}$ in CD_3CN and monitored over time (400 MHz, 296 K, CD_3CN).

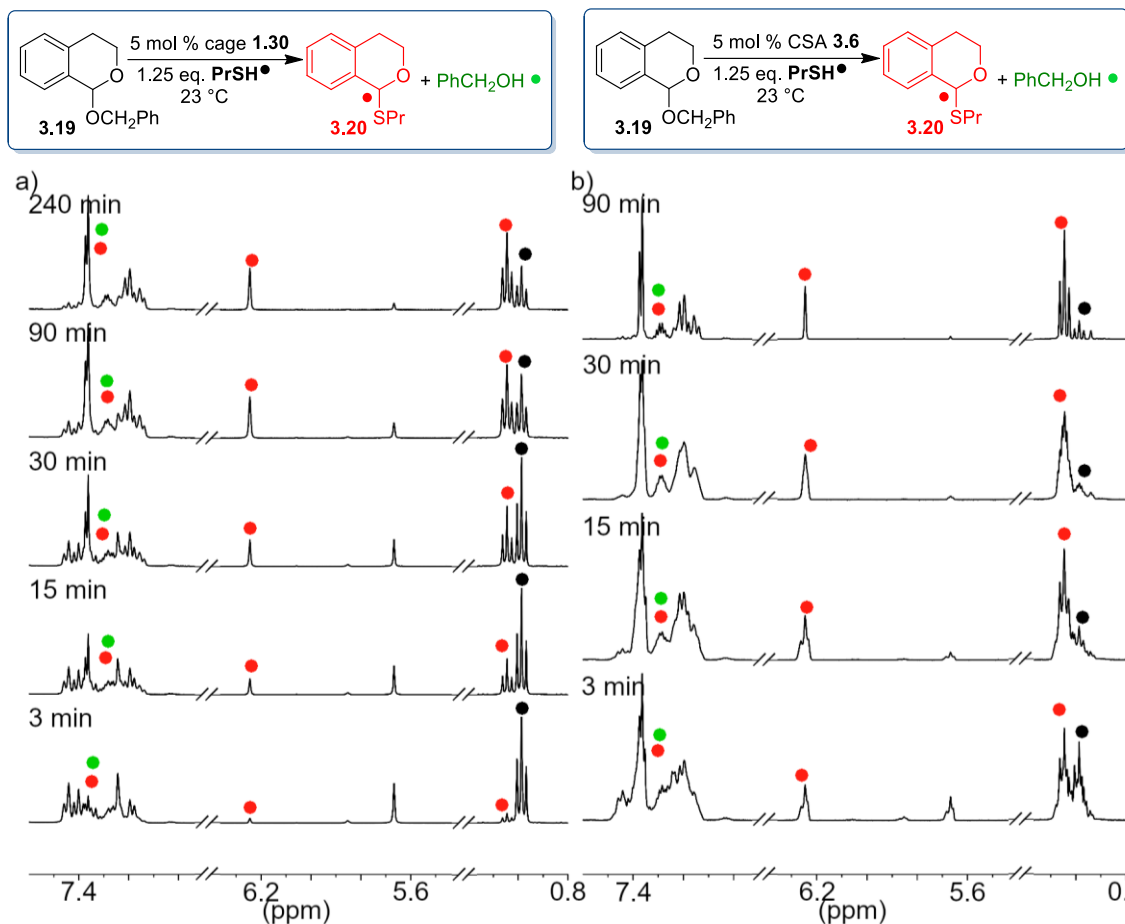


Figure 7.51. ^1H NMR spectra (7.4-6.9 ppm, 6.4-5.4 ppm, and 1.2-0.8 ppm) of the acid promoted reaction between **3.19** and *n*-propyl thiol in 400 μL CD_3CN in the presence of: a) 5 mol % cage **1.30** b) 5 mol % CSA **3.6**. [**3.19**] = 15.8 mM, [**PrSH**] = 19.8 mM, [**1.30**] = 0.8 mM, [**3.6**] = 0.8 mM, reactions were performed at 23 $^\circ\text{C}$ in CD_3CN and monitored over time (400 MHz, 296 K, CD_3CN).

7.10. Selected Spectra for Chapter 4

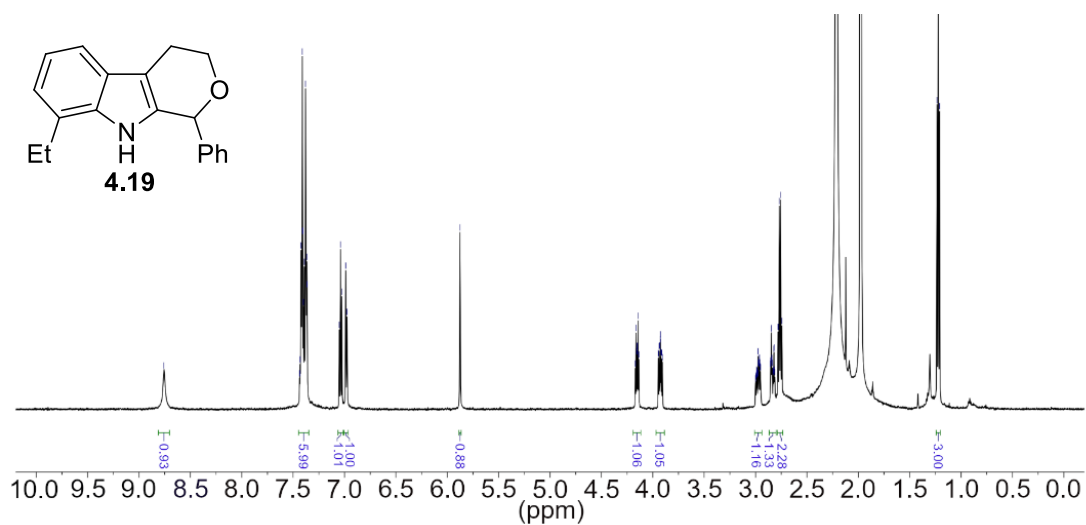


Figure 7.52. ^1H NMR spectrum of **4.19** (600 MHz, 298K, CD_3CN).

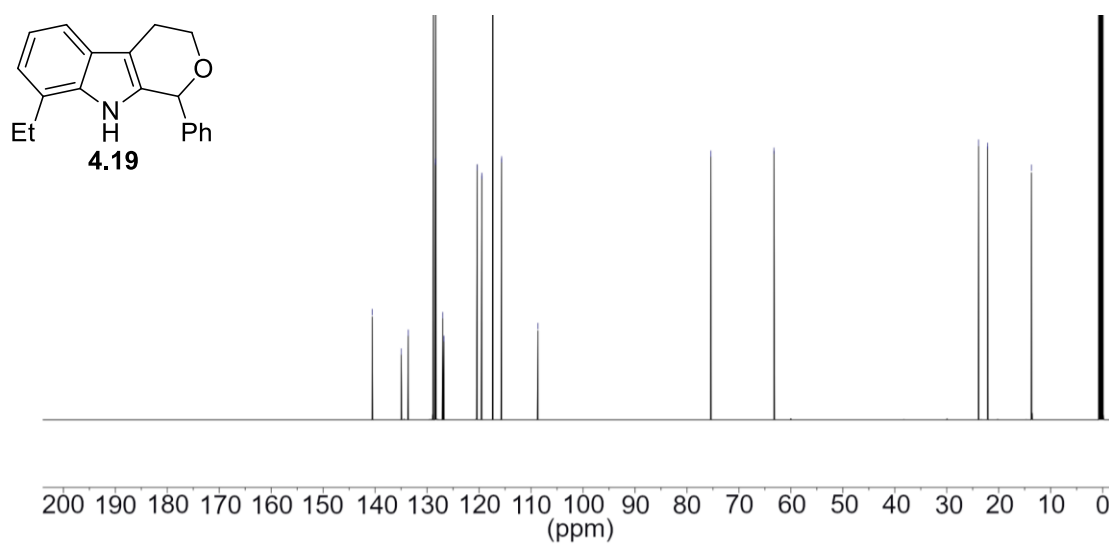


Figure 7.53. ^{13}C NMR spectrum of **4.19** (600 MHz, 298K, CD_3CN).

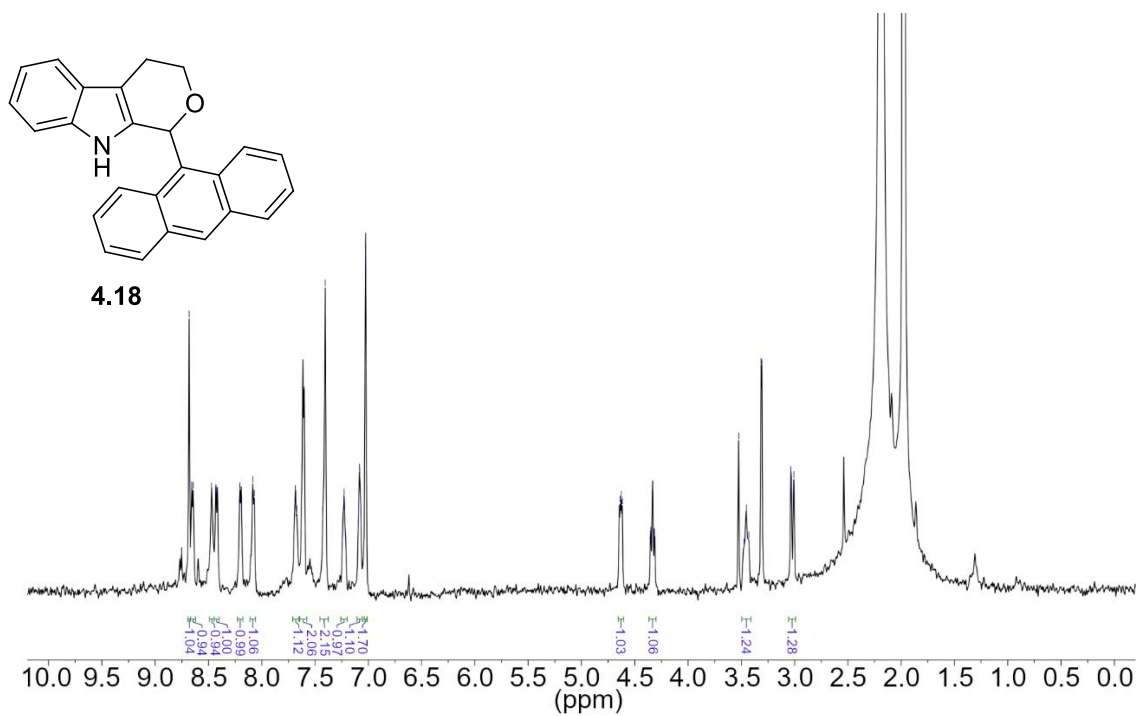


Figure 7.54. ^1H NMR spectrum of **4.18** (600 MHz, 298K, CD_3CN).

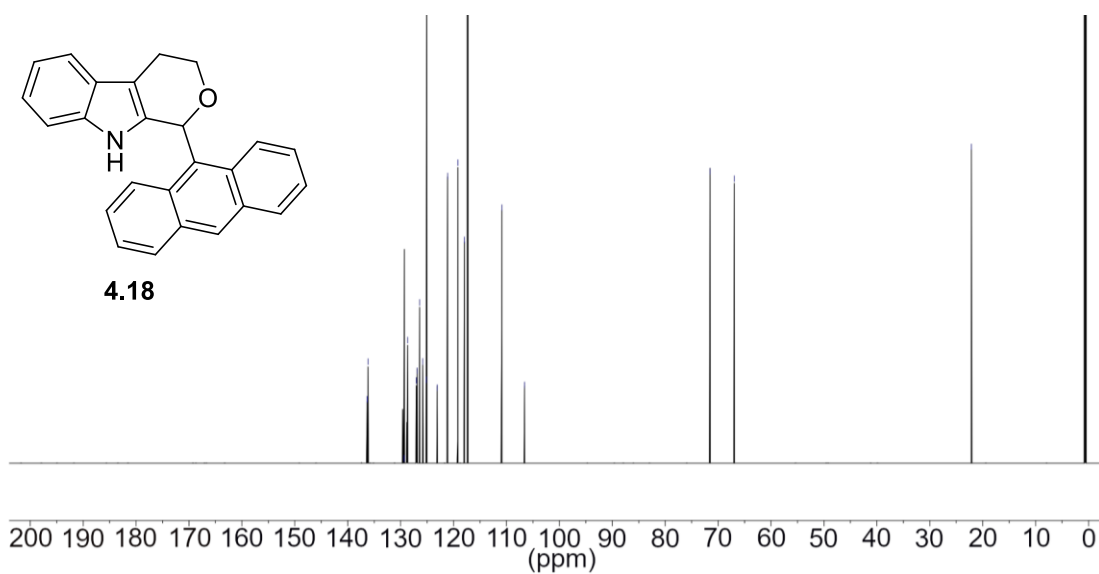


Figure 7.55. ^{13}C NMR spectrum of **4.18** (600 MHz, 298K, CD_3CN).

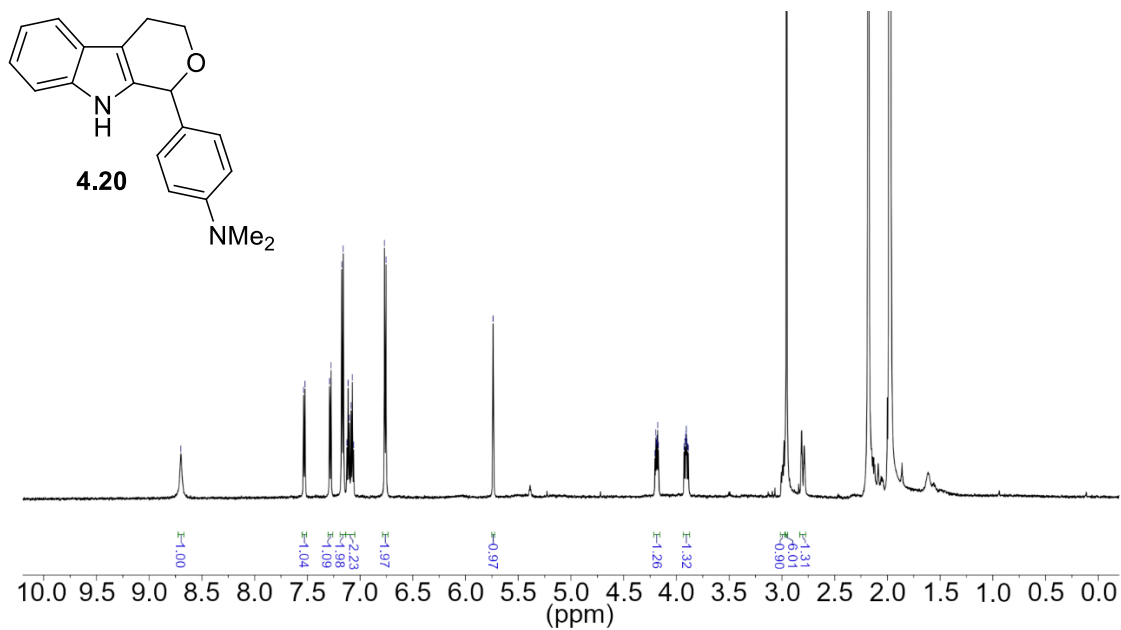


Figure 7.56. ¹H NMR spectrum of **4.20** (600 MHz, 298K, CD₃CN).

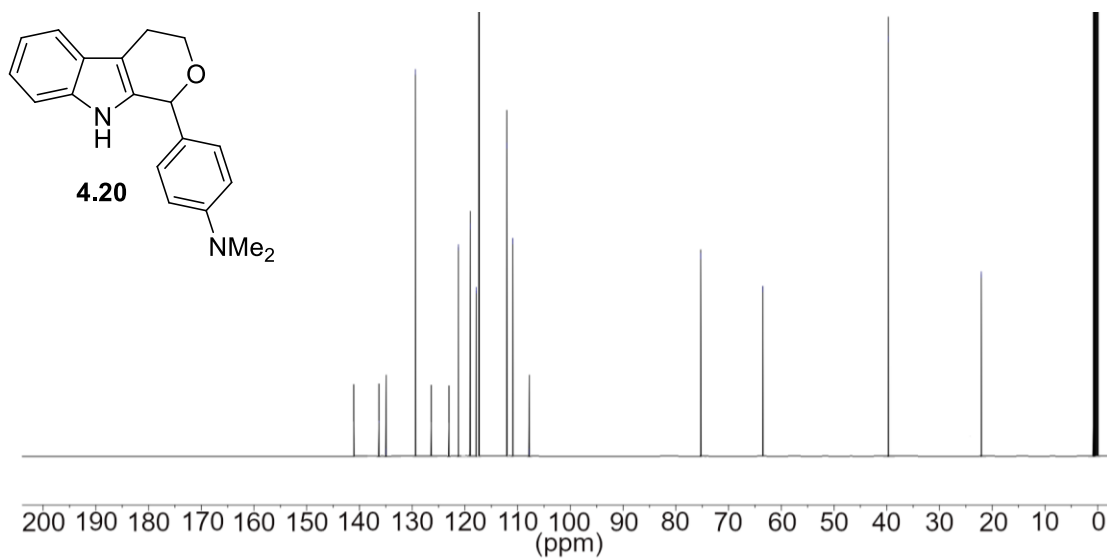
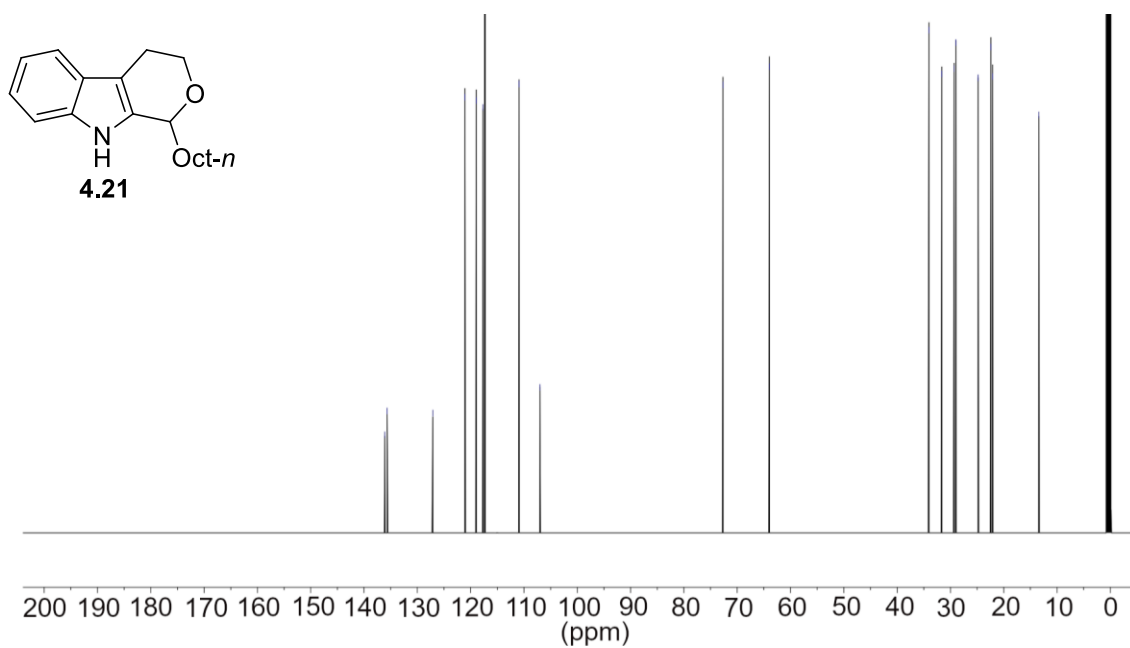
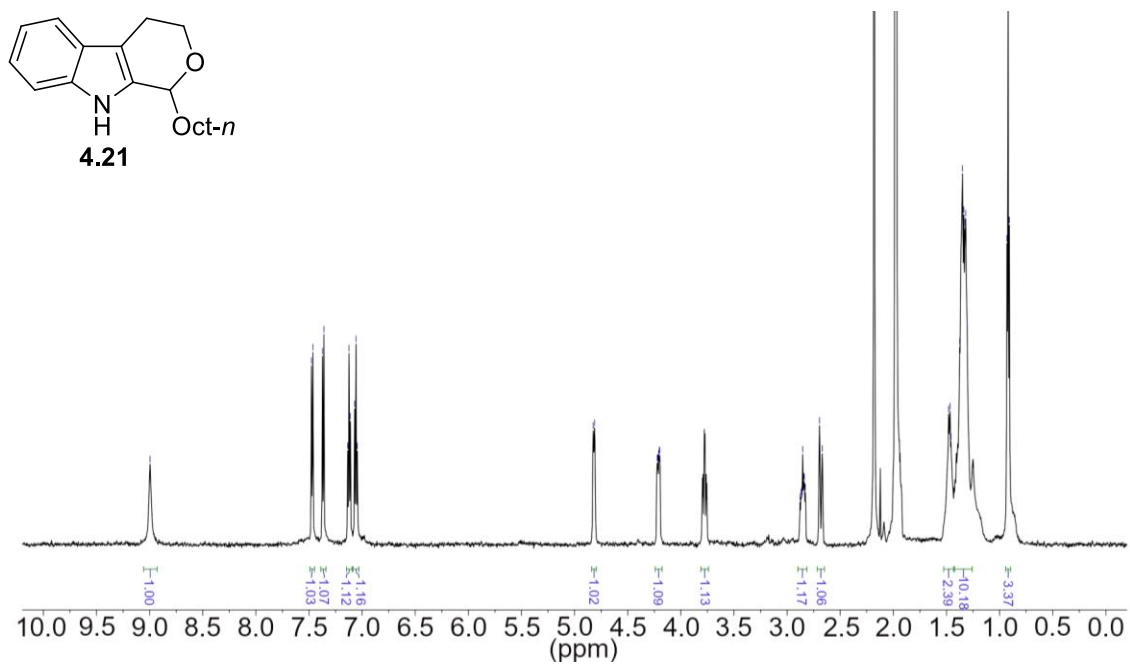


Figure 7.57. ¹³C NMR spectrum of **4.20** (600 MHz, 298K, CD₃CN).



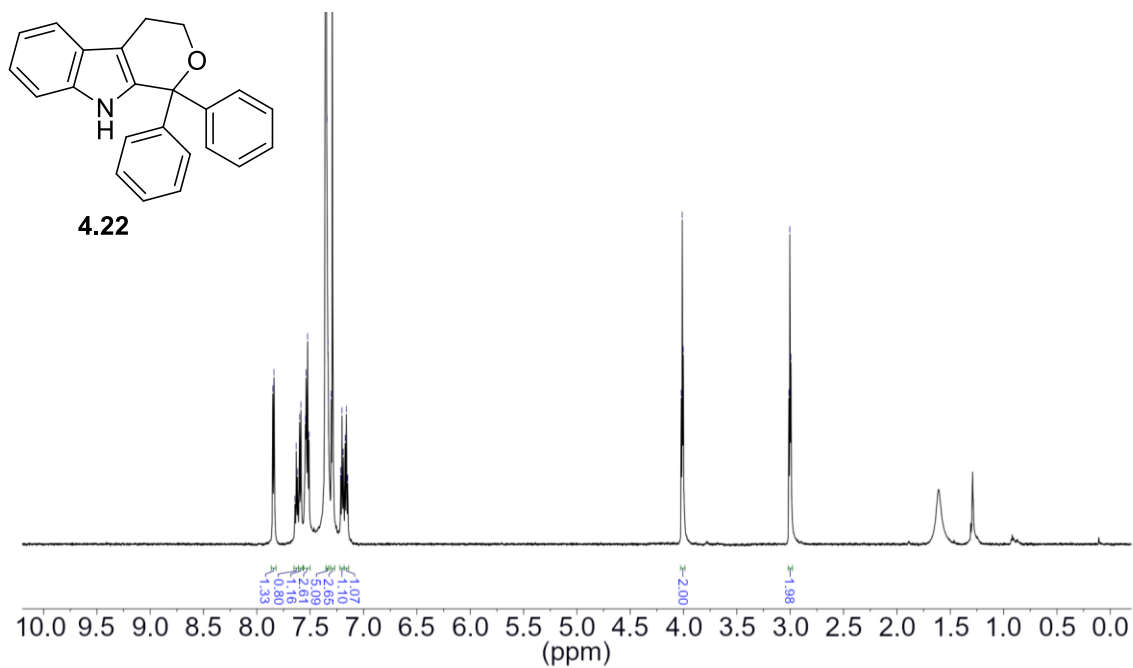


Figure 7.60. ¹H NMR spectrum of **4.22** (600 MHz, 298K, CDCl₃).

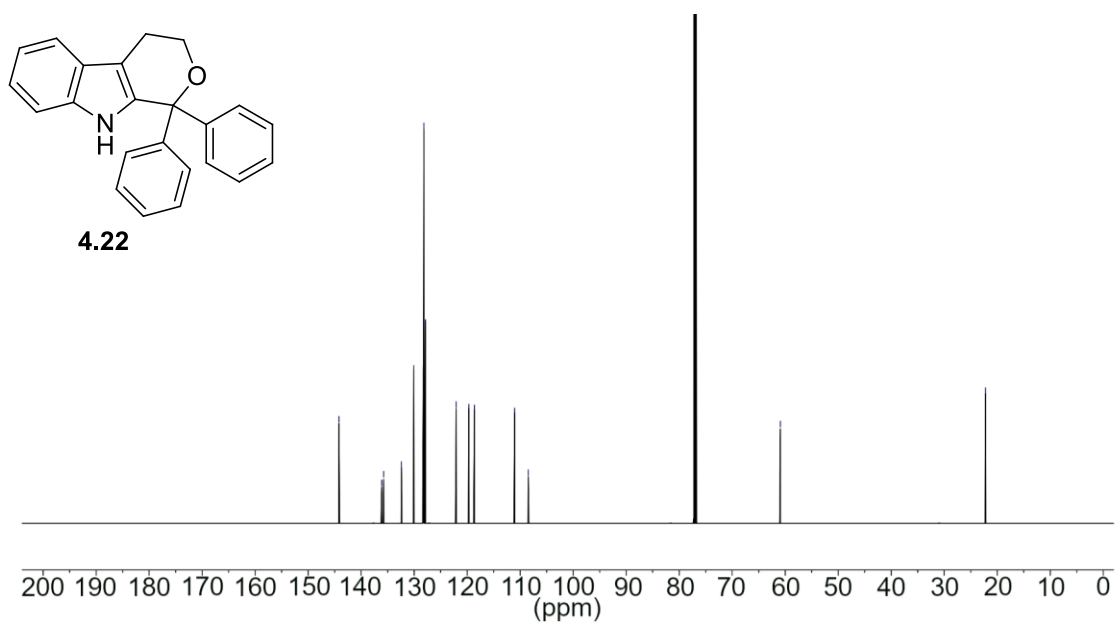


Figure 7.61. ¹³C NMR spectrum of **4.22** (600 MHz, 298K, CDCl₃).

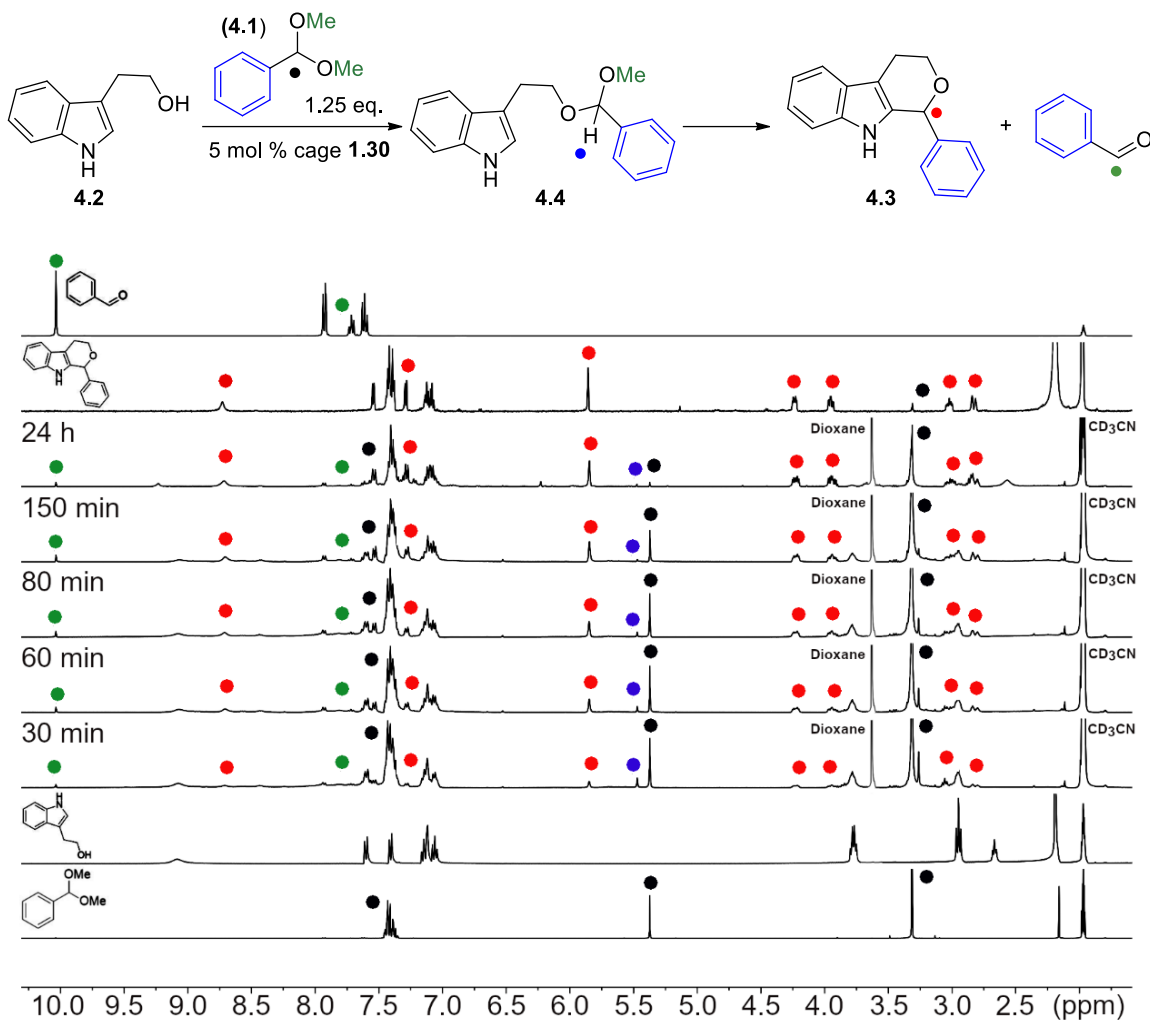


Figure 7.62. Full ¹H NMR spectra of the acid promoted reaction between **4.1** and **4.2** in the presence of 5 mol % cage **1.30**. [**4.2**] = 15.8 mM, [**4.1**] = 19.8 mM, [**1.30**] = 0.8 mM, the reaction was performed at room temperature in CD₃CN and monitored over time (400 MHz, 298 K, CD₃CN).

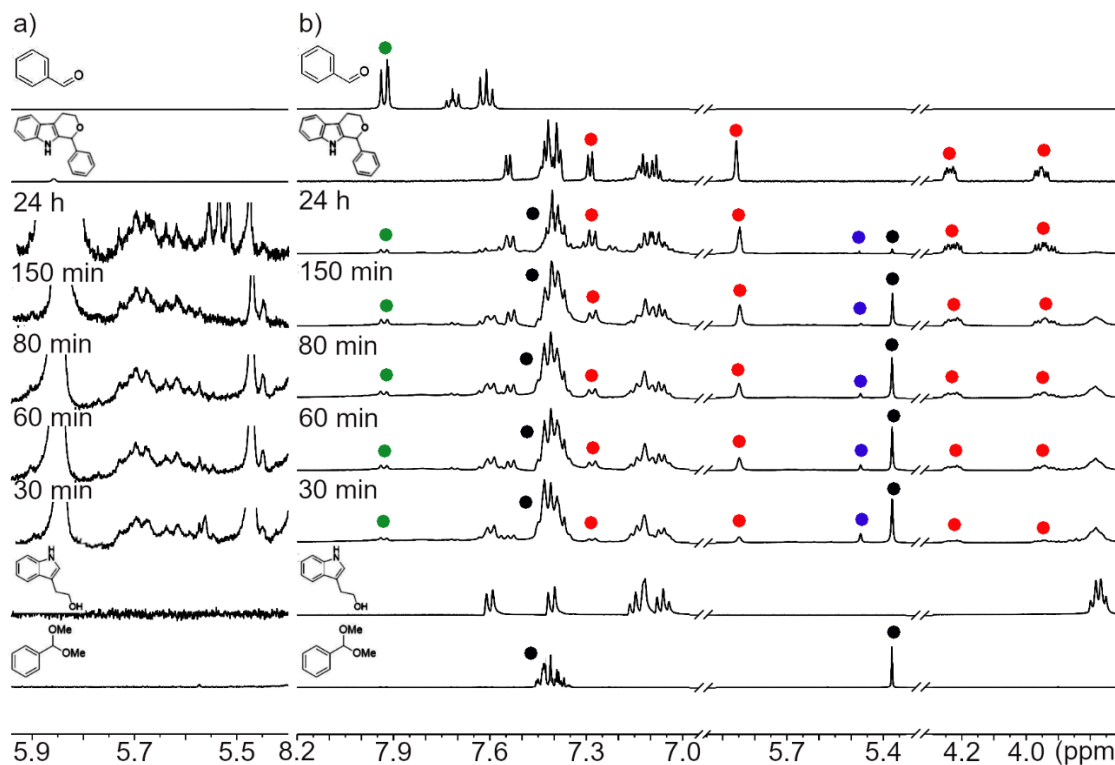
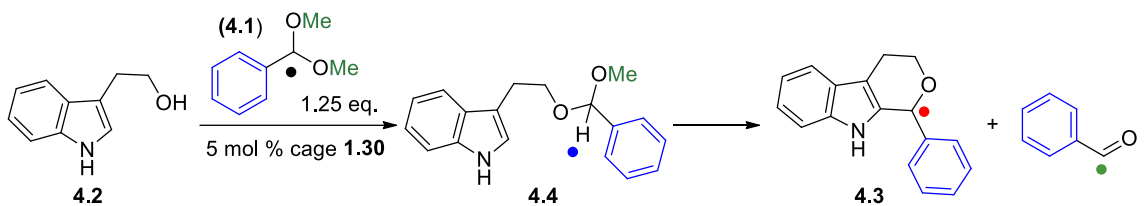


Figure 7.63. Expanded ^1H NMR spectra of the acid promoted substitution reaction between **4.1** and **4.2** in the presence of 5 mol % cage **1.30** showing: a) Cage stability (5.95-5.4 ppm) b) Product formation (8.2-6.9 ppm, 6.0-5.3 ppm, 4.3-3.7 ppm). [**4.2**] = 15.8 mM, [**4.1**] = 19.8 mM, [**1.30**] = 0.8 mM, the reaction was performed at room temperature in CD_3CN and monitored over time (400 MHz, 298 K, CD_3CN).

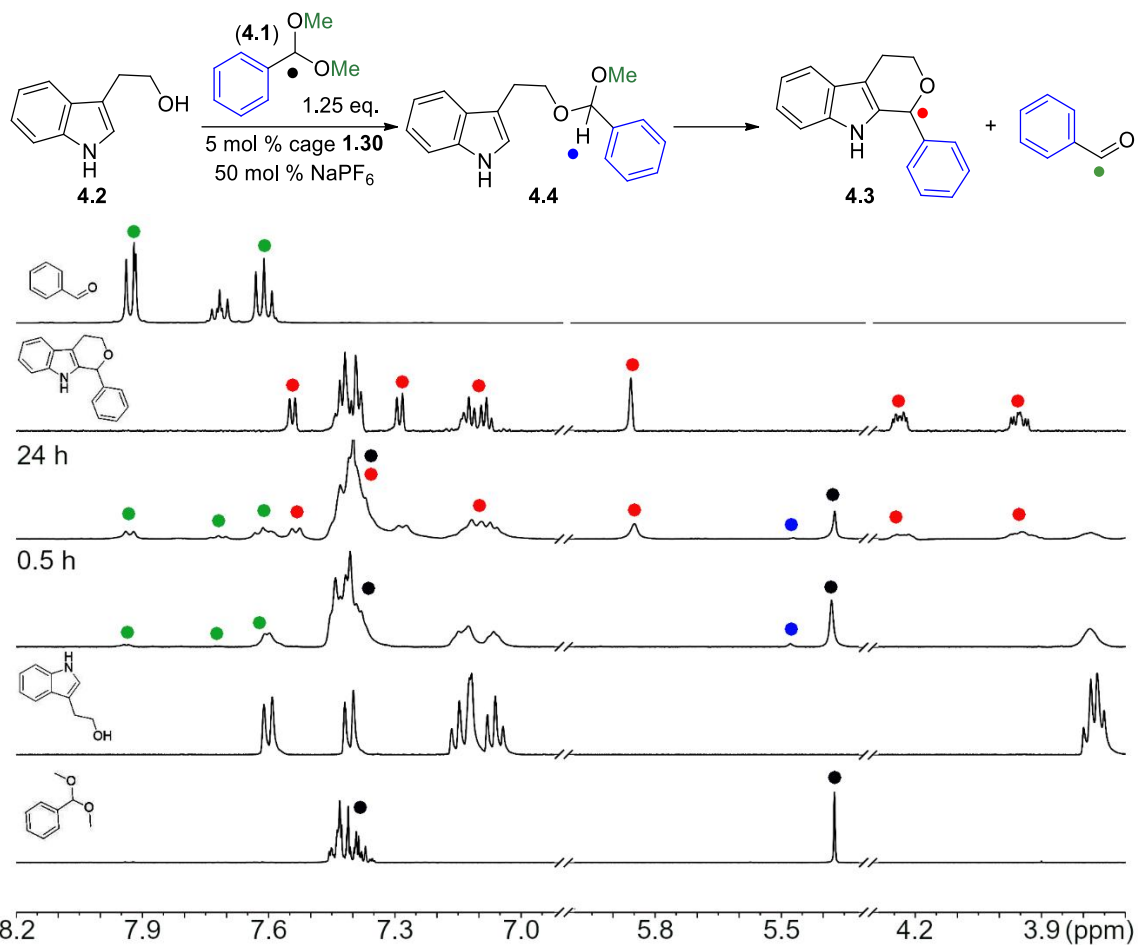


Figure 7.64. ^1H NMR spectra (8.2-6.9 ppm, 6.0-5.3 ppm, 4.3-3.7 ppm) of the acid promoted substitution reaction between **4.1** and **4.2** in 400 μL CD_3CN in the presence of 5 mol % cage **1.30** and 50 mol % of NaPF_6 . [**4.2**] = 15.8 mM, [**4.1**] = 19.8 mM, [**1.30**] = 0.8 mM, [NaPF_6] = 7.9 mM the reaction was performed at room temperature in CD_3CN and monitored over time (600 MHz, 298 K, CD_3CN).

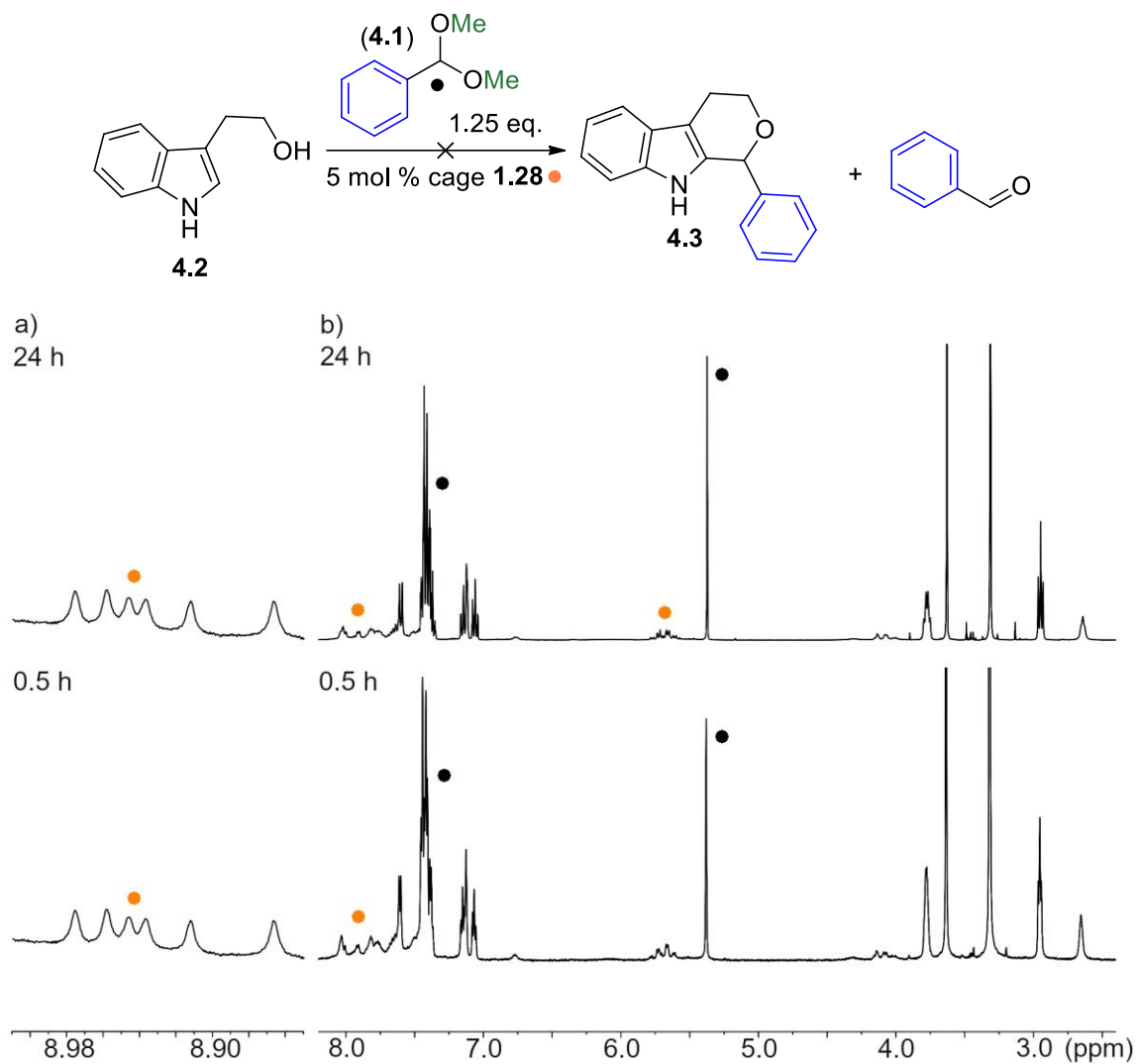


Figure 7.65. Expanded ¹H NMR spectra of the acid promoted substitution reaction between **4.1** and **4.2** in the presence of 5 mol % cage **1.28** showing: a) Cage stability (9.01-8.85 ppm) b) Product formation (8.2-2.4 ppm) in CD₃CN. [**4.2**] = 15.8 mM, [**4.1**] = 19.8 mM, [**1.28**] = 0.8 mM, the reaction was performed at room temperature in CD₃CN and monitored over time (600 MHz, 298 K, CD₃CN).

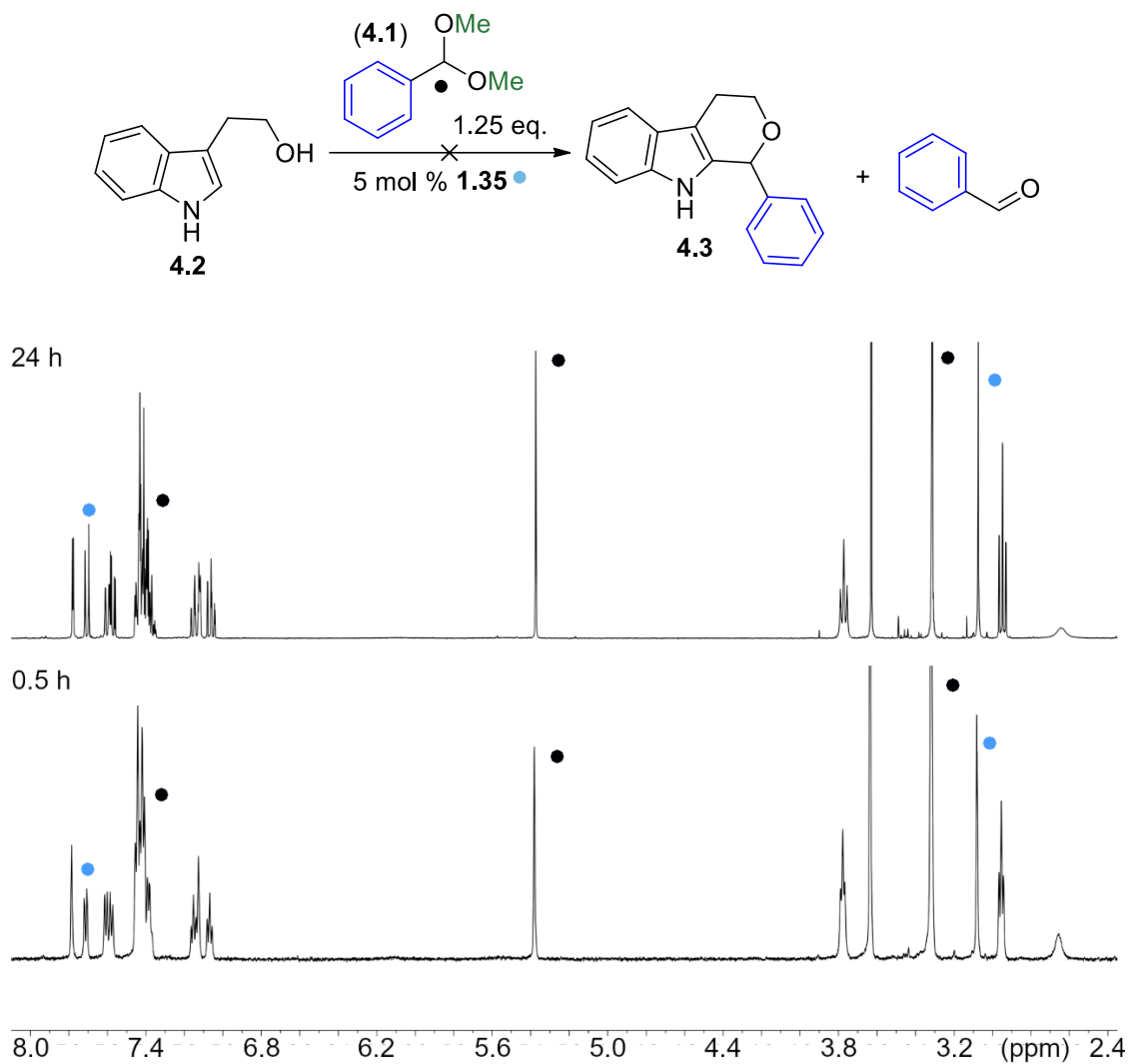


Figure 7.66. ^1H NMR spectra (8.05–2.35 ppm) of the acid promoted substitution reaction between **4.1** and **4.2** in 400 μL CD_3CN in the presence of 30 mol % diacid **1.35**. [**4.2**] = 15.8 mM, [**4.1**] = 19.8 mM, [**1.35**] = 4.74 mM, the reaction was performed at room temperature in CD_3CN and monitored over time (600 MHz, 298 K, CD_3CN).

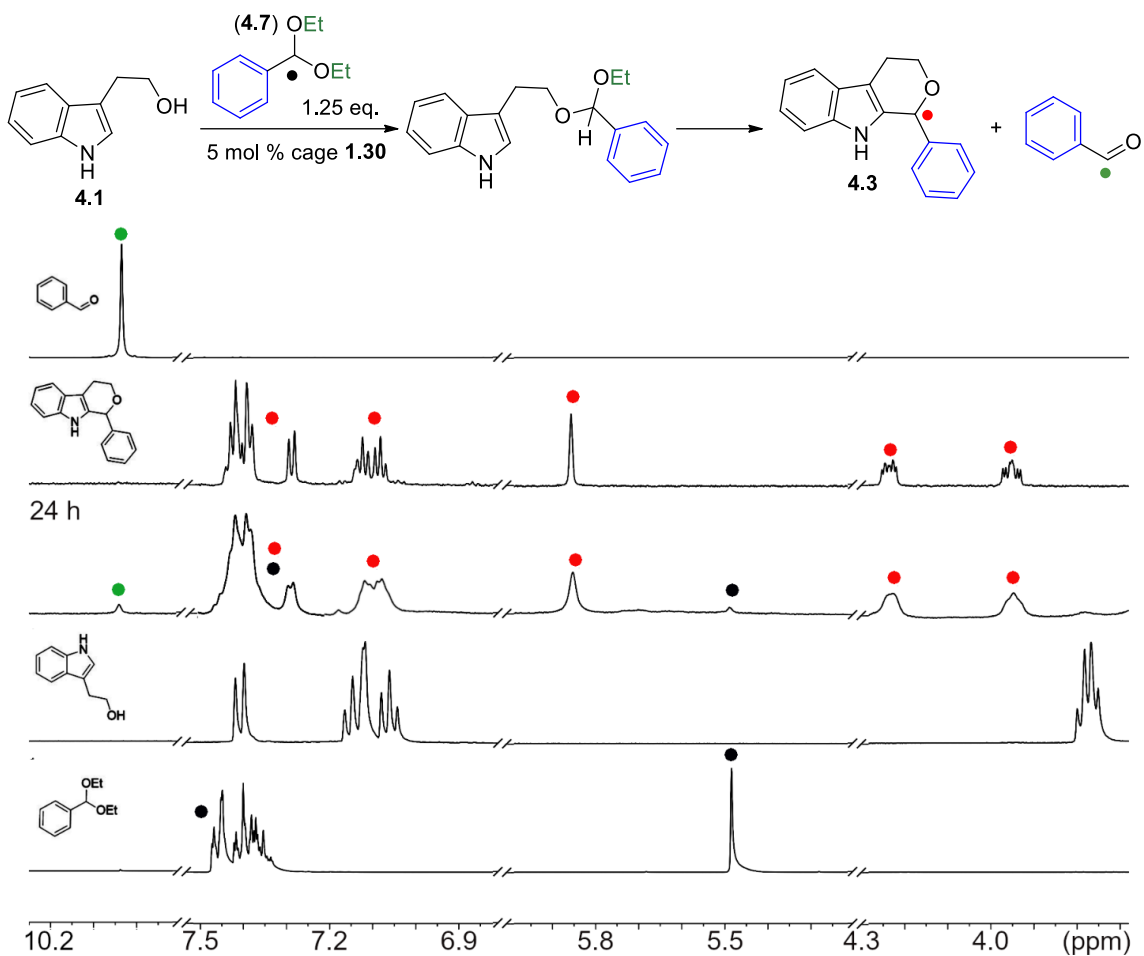


Figure 7.67. ¹H NMR spectra (10.35-9.8 ppm, 7.6-6.8 ppm, 6.0-5.2 ppm, 4.3-3.68 ppm) of the acid promoted substitution reaction between **4.2** and **4.7** in 400 μ L CD₃CN in the presence of 5 mol % cage **1.30**. [**4.1**] = 15.8 mM, [**4.7**] = 19.8 mM, [**1.30**] = 0.8 mM, the reaction was performed at room temperature in CD₃CN and monitored over time (600 MHz, 298 K, CD₃CN).

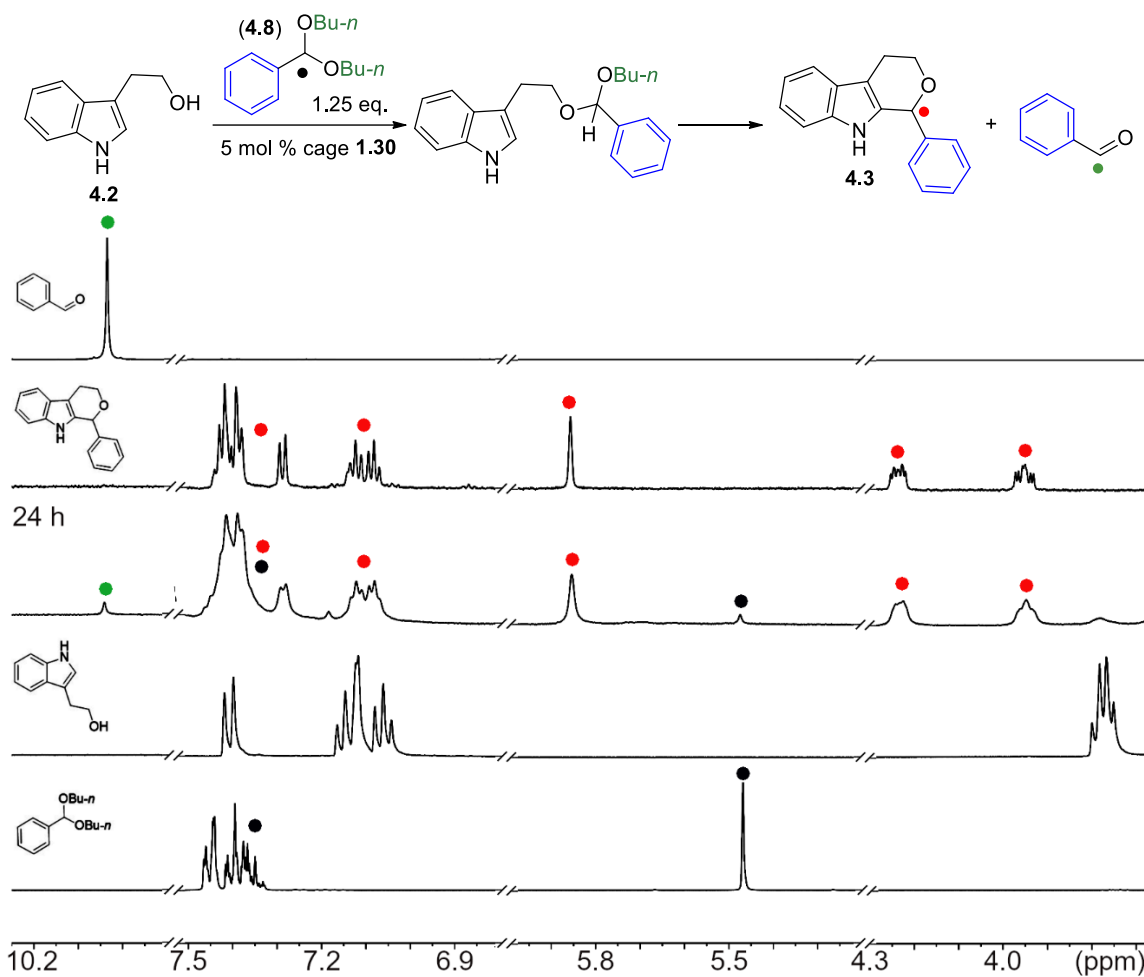


Figure 7.68. ¹H NMR spectra (10.35-9.8 ppm, 7.6-6.8 ppm, 6.0-5.2 ppm, 4.3-3.68 ppm) of the acid promoted substitution reaction between **4.2** and **4.8** in 400 μL CD₃CN in the presence of 5 mol % cage **1.30**. [**4.2**] = 15.8 mM, [**4.8**] = 19.8 mM, [**1.30**] = 0.8 mM, the reaction was performed at room temperature in CD₃CN and monitored over time (600 MHz, 298 K, CD₃CN).

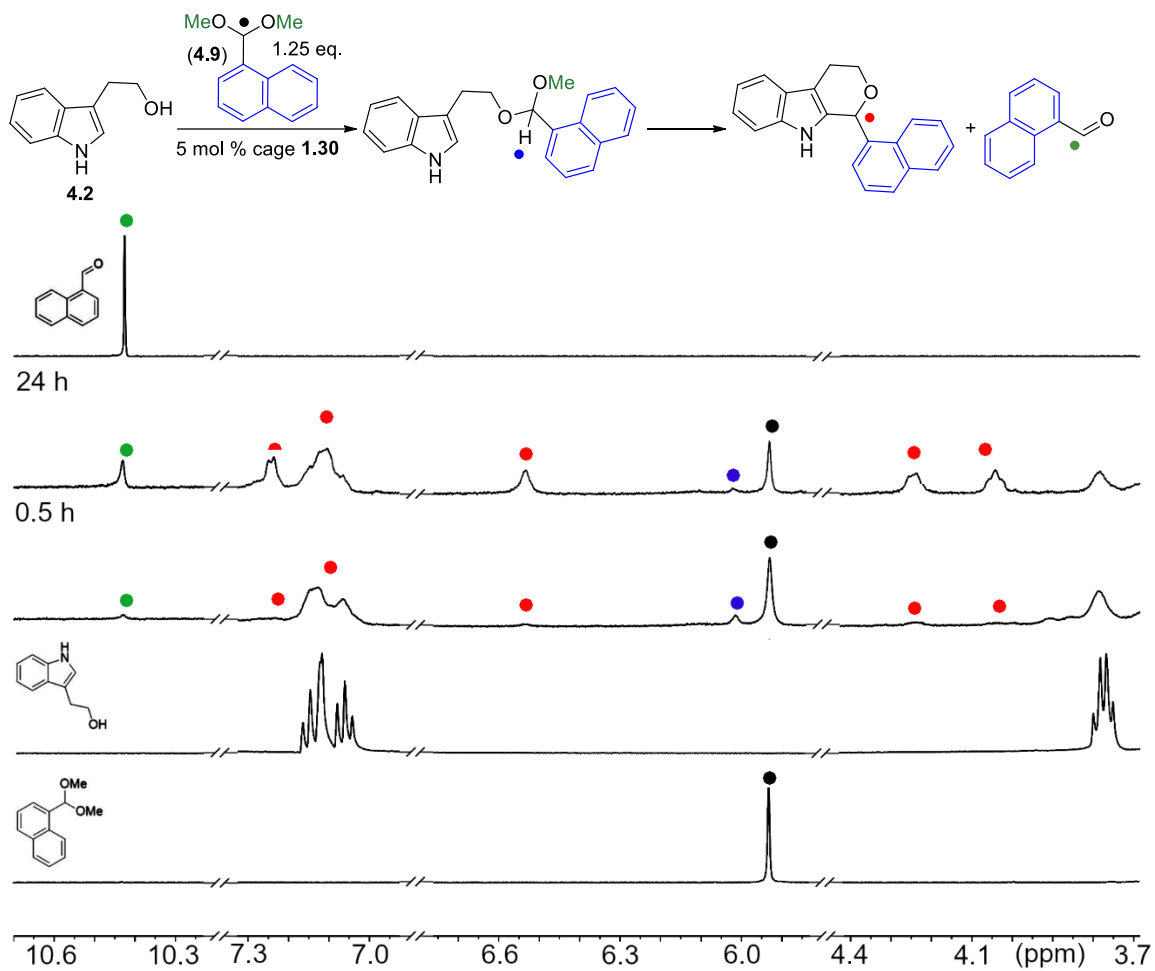


Figure 7.69. ¹H NMR spectra (10.7-10.2 ppm, 7.35-6.9 ppm, 6.8-5.8 ppm, 4.45-3.68 ppm) of the acid promoted substitution reaction between **4.2** and **4.9** in 400 μ L CD₃CN in the presence of 5 mol % cage **1.30**. [**4.2**] = 15.8 mM, [**4.9**] = 19.8 mM, [**1.30**] = 0.8 mM, the reaction was performed at room temperature in CD₃CN and monitored over time (600 MHz, 298 K, CD₃CN).

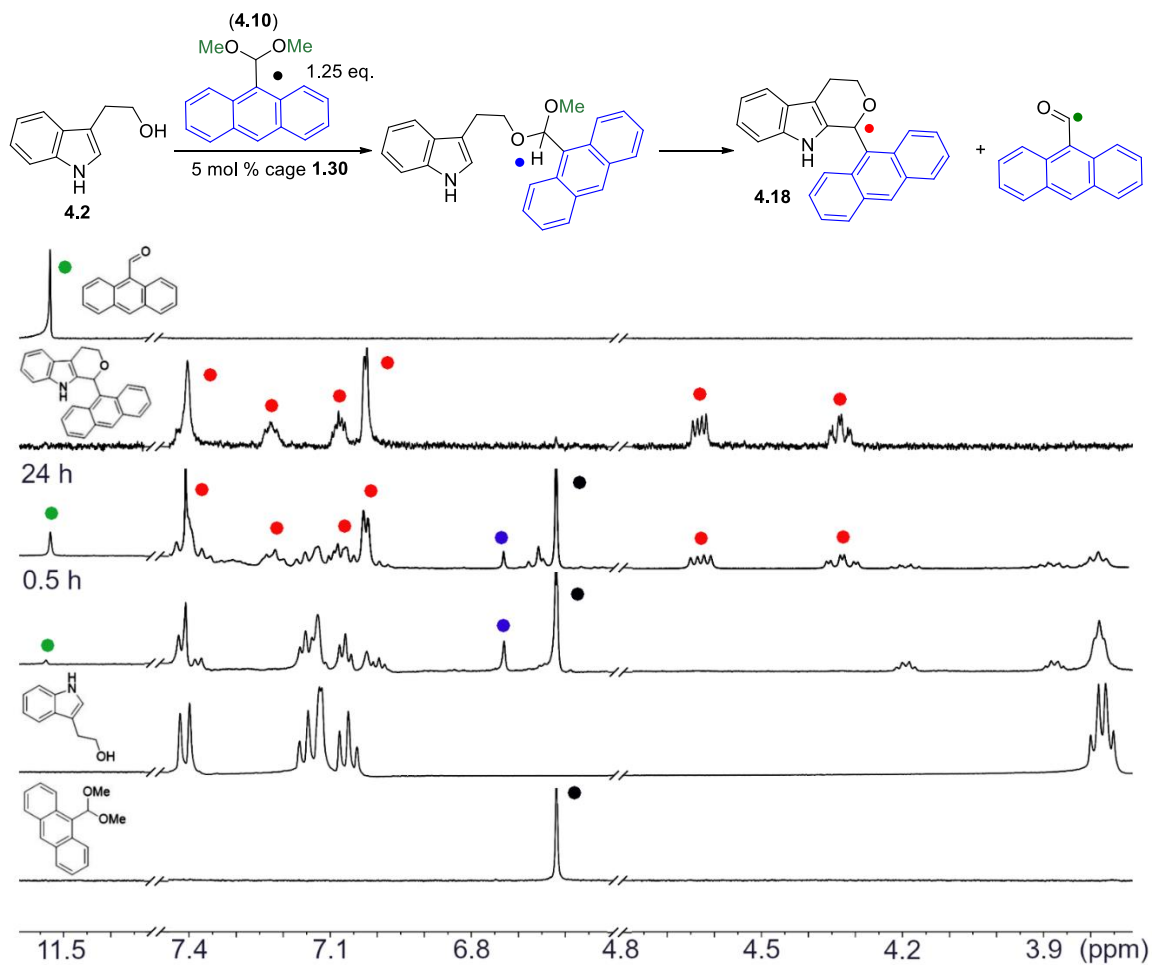


Figure 7.70. ^1H NMR spectra (11.6-11.3 ppm, 7.45-6.5 ppm, 4.8-3.7 ppm) of the acid promoted substitution reaction between **4.2** and **4.10** in 400 μL CD_3CN in the presence of 5 mol % cage **1.30**. [**4.2**] = 15.8 mM, [**4.10**] = 19.8 mM, [**1.30**] = 0.8 mM, the reaction was performed at room temperature in CD_3CN and monitored over time (600 MHz, 298 K, CD_3CN).

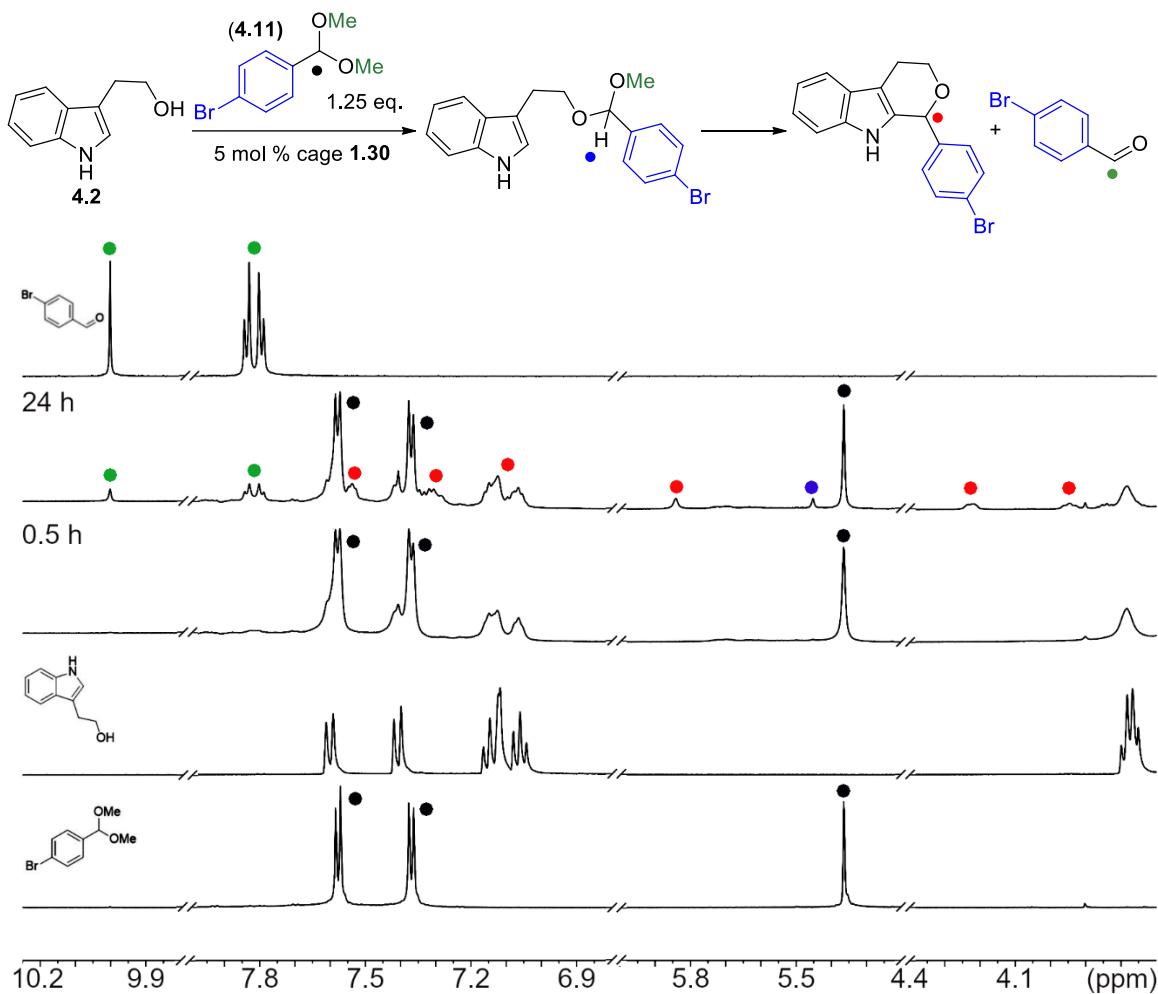


Figure 7.71. ¹H NMR spectra (10.25-9.8 ppm, 8.0-6.8 ppm, 6.0-5.2 ppm, 4.4-3.7 ppm) of the acid promoted substitution reaction between **4.2** and **4.11** in 400 μ L CD₃CN in the presence of 5 mol % cage **1.30**. [**4.2**] = 15.8 mM, [**4.11**] = 19.8 mM, [**1.30**] = 0.8 mM, the reaction was performed at room temperature in CD₃CN and monitored over time (600 MHz, 298 K, CD₃CN).

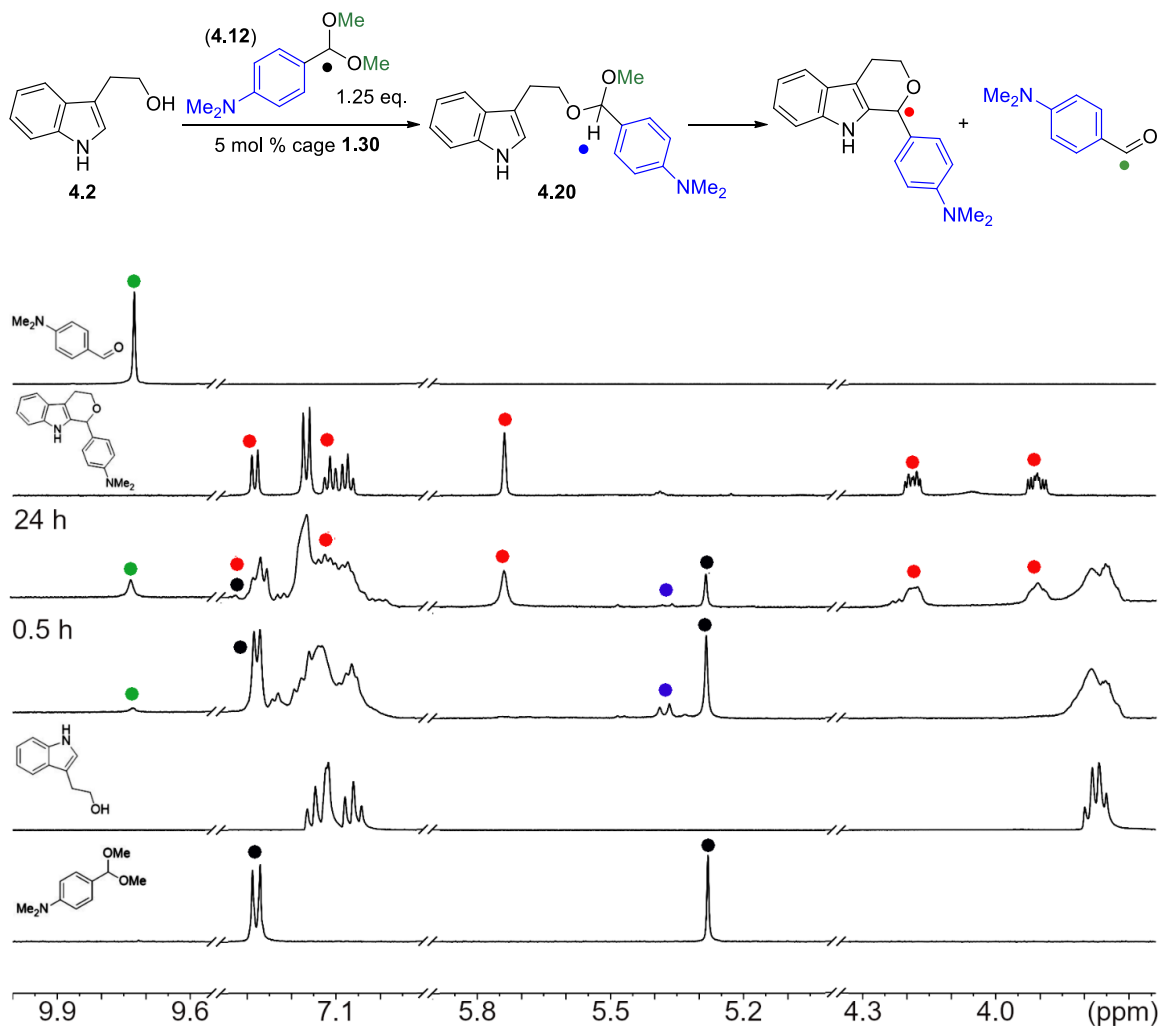


Figure 7.72. ¹H NMR spectra (10.0-9.55 ppm, 7.36-6.9 ppm, 5.9-5.0 ppm, 4.35-3.3.64 ppm) of the acid promoted substitution reaction between **4.2** and **4.12** in 400 μL CD₃CN in the presence of 5 mol % cage **1.30**. [**4.2**] = 15.8 mM, [**4.12**] = 19.8 mM, [**1.30**] = 0.8 mM, the reaction was performed at room temperature in CD₃CN and monitored over time (600 MHz, 298 K, CD₃CN).

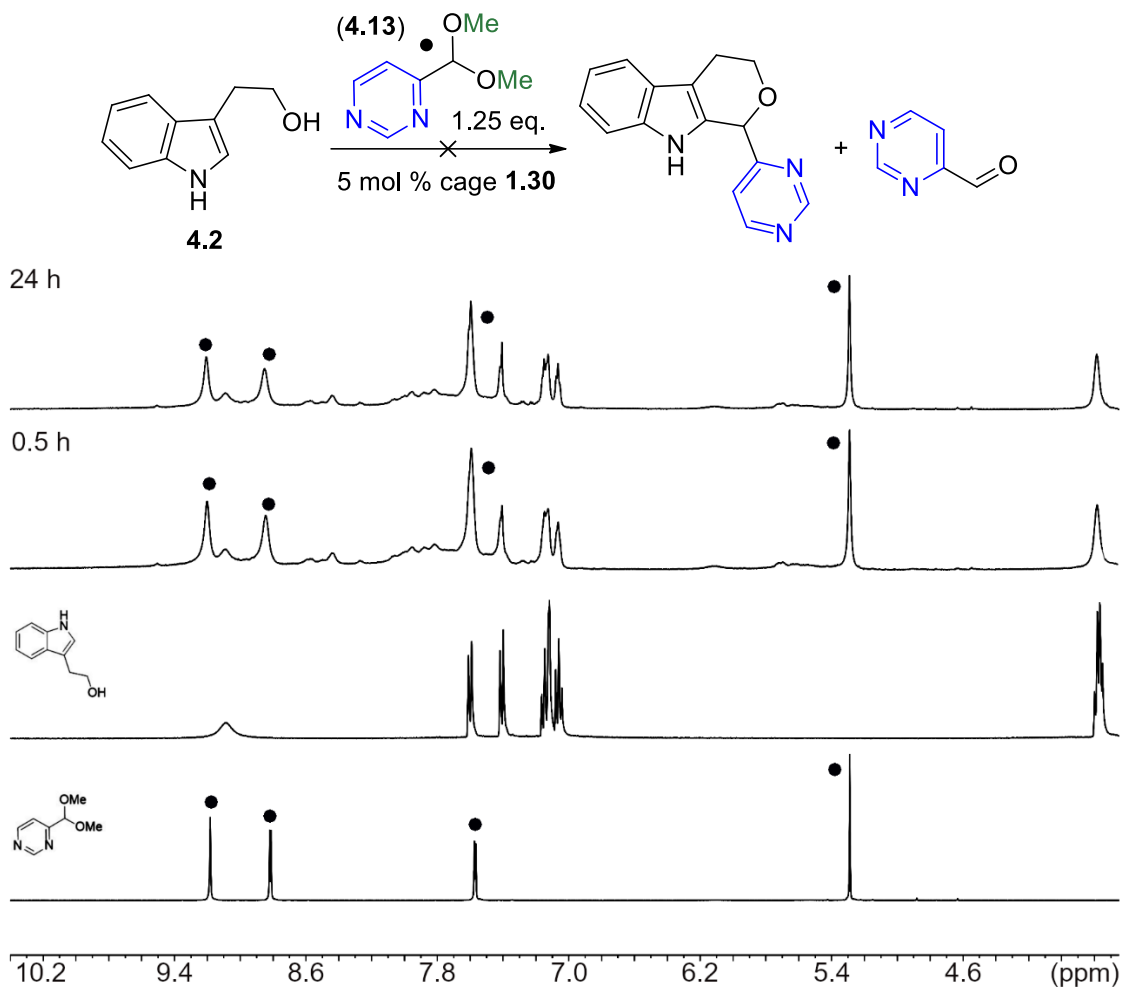


Figure 7.73. ^1H NMR spectra (10.4–3.65 ppm) of the acid promoted substitution reaction between **4.2** and **4.13** in 400 μL CD_3CN in the presence of 5 mol % cage **1.30**. [**4.2**] = 15.8 mM, [**4.13**] = 19.8 mM, [**1.30**] = 0.8 mM, the reaction was performed at room temperature in CD_3CN and monitored over time (600 MHz, 298 K, CD_3CN).

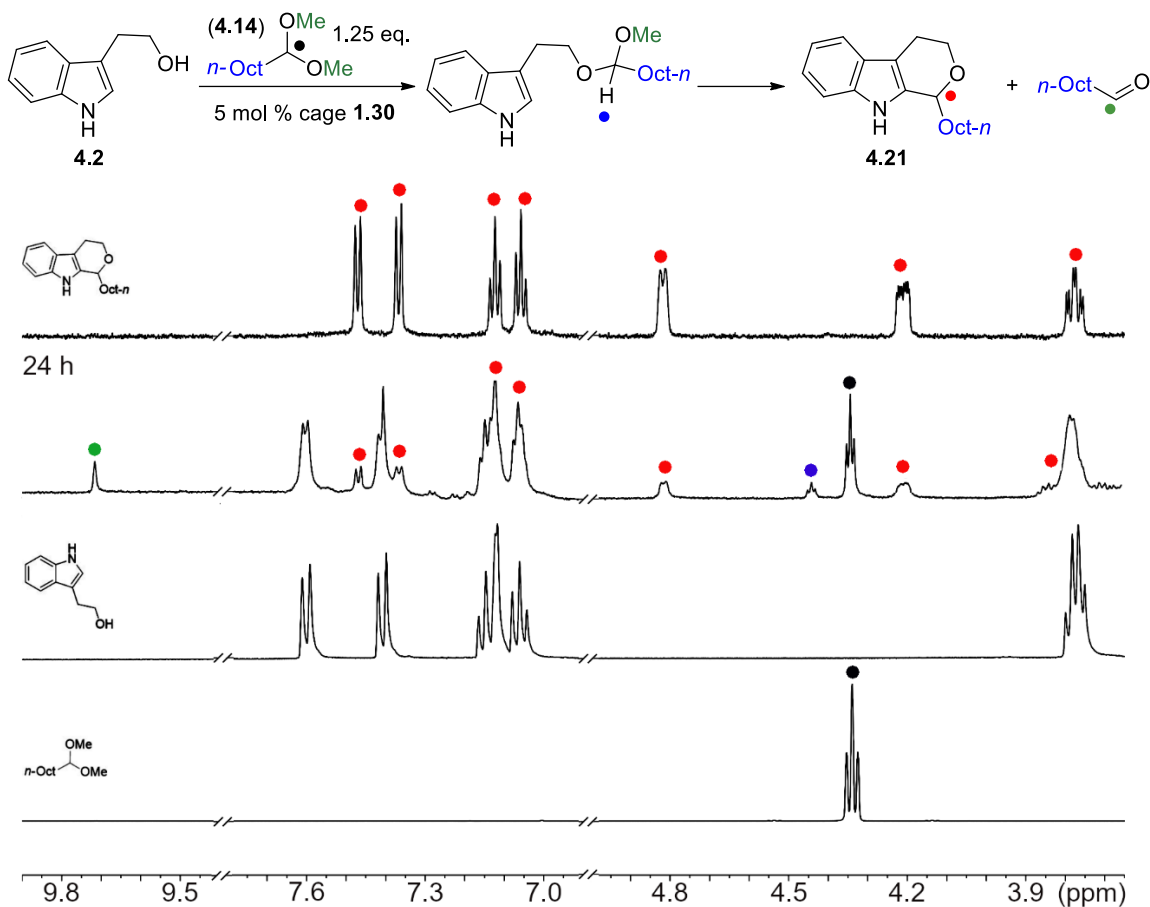


Figure 7.74. ¹H NMR spectra (9.9-9.55 ppm, 7.8-6.9 ppm, 5.0-3.65 ppm) of the acid promoted substitution reaction between **4.2** and **4.14** in 400 μ L CD₃CN in the presence of 5 mol % cage **1.30**. [**4.2**] = 15.8 mM, [**4.14**] = 19.8 mM, [**1.30**] = 0.8 mM, the reaction was performed at room temperature in CD₃CN and monitored over time (600 MHz, 298 K, CD₃CN).

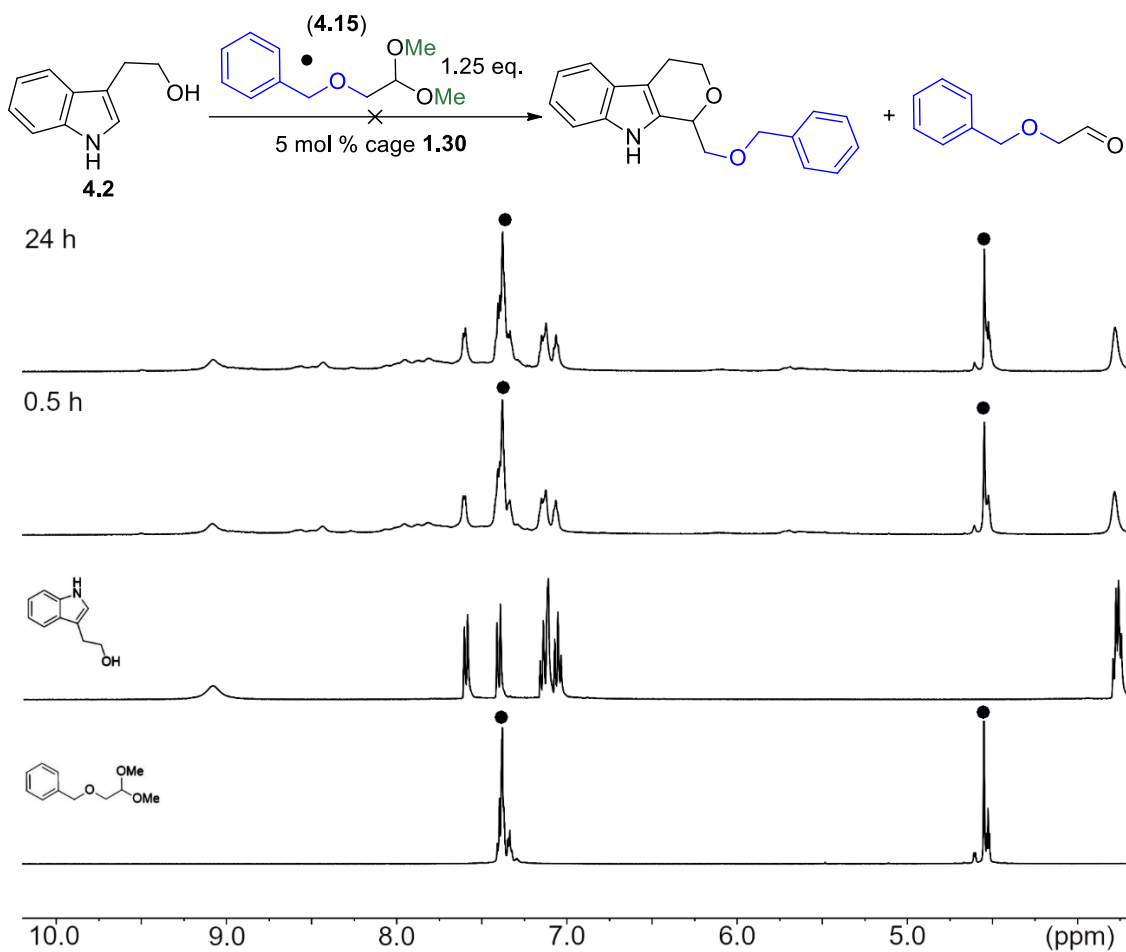


Figure 7.75. ^1H NMR spectra (10.1–3.70 ppm) of the acid promoted substitution reaction between **4.2** and **4.15** in 400 μL CD_3CN in the presence of 5 mol % cage **1.30**. [**4.2**] = 15.8 mM, [**4.15**] = 19.8 mM, [**1.30**] = 0.8 mM, the reaction was performed at room temperature in CD_3CN and monitored over time (600 MHz, 298 K, CD_3CN).

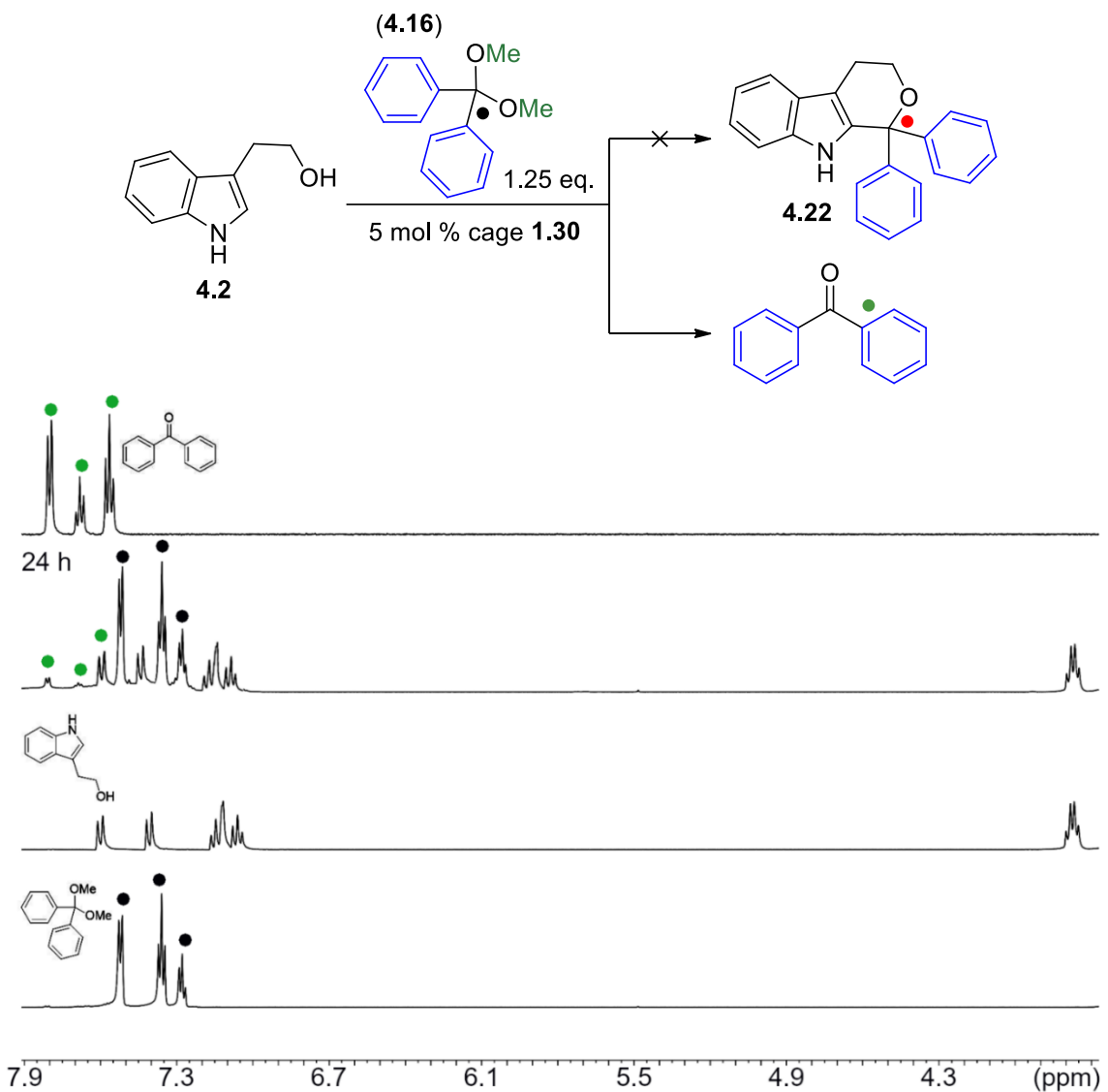


Figure 7.76. ^1H NMR spectra (7.9 – 3.67 ppm) of the acid promoted substitution reaction between **4.2** and **4.16** in 400 μL CD_3CN in the presence of 5 mol % cage **1.30**. $[\mathbf{4.2}] = 15.8$ mM, $[\mathbf{4.16}] = 19.8$ mM, $[\mathbf{1.30}] = 0.8$ mM, the reaction was performed at room temperature in CD_3CN and monitored over time (600 MHz, 298 K, CD_3CN).

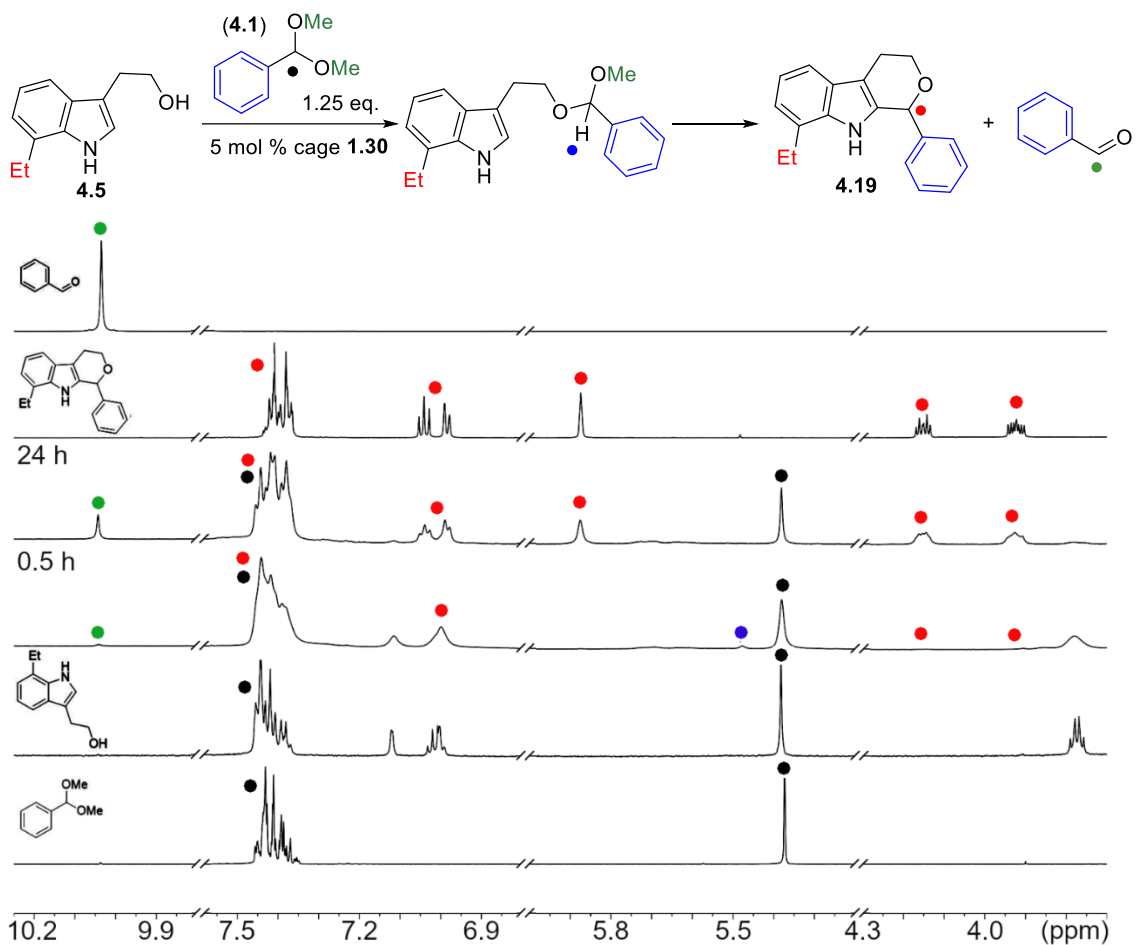


Figure 7.77. ¹H NMR spectra (10.25-9.8 ppm, 7.58-6.8 ppm, 6.2-5.2 ppm, 4.3-3.7 ppm) of the acid promoted substitution reaction between **4.1** and **4.5** in 400 μ L CD₃CN in the presence of 5 mol % cage **1.30**. [**4.5**] = 15.8 mM, [**4.1**] = 19.8 mM, [**1.30**] = 0.8 mM, the reaction was performed at room temperature in CD₃CN and monitored over time (600 MHz, 298 K, CD₃CN).

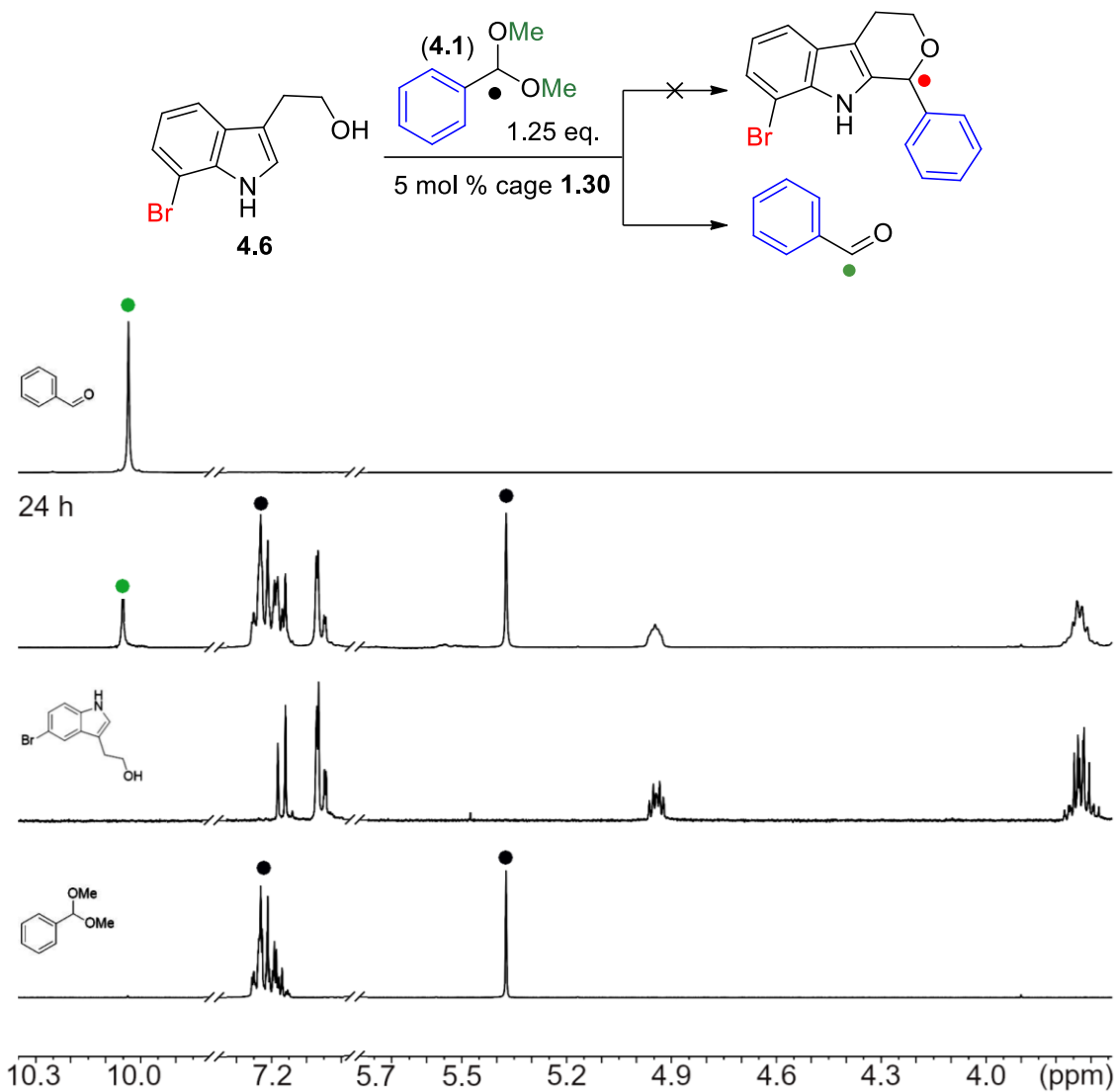


Figure 7.78. ¹H NMR spectra (10.35–3.65 ppm) of the acid promoted substitution reaction between **4.6** and **4.1** in 400 μ L CD₃CN in the presence of 5 mol % cage **1.30**. [**4.6**] = 15.8 mM, [**4.1**] = 19.8 mM, [**1.30**] = 0.8 mM, the reaction was performed at room temperature in CD₃CN and monitored over time (600 MHz, 298 K, CD₃CN).

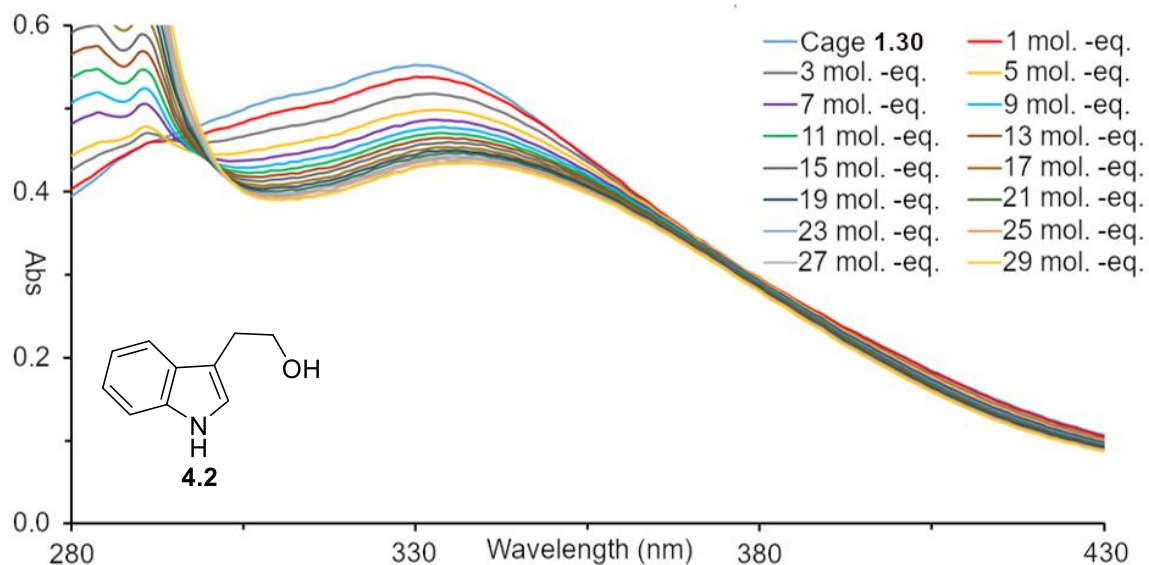


Figure 7.79. UV-Vis absorption spectrum of the titration of **4.2** into a 3 μM solution of cage **1.30** in CH_3CN . **4.2** was added in 1-2 μL aliquots from a 9 mM stock solution in CD_3CN .

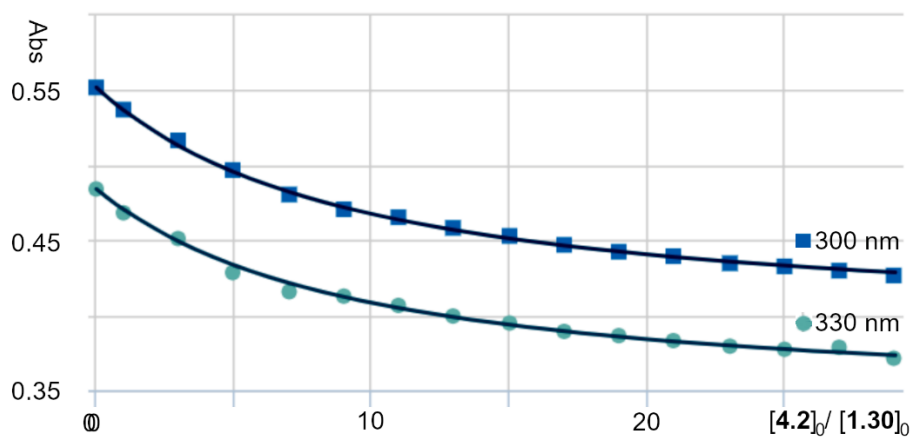


Figure 7.80. 1:1 binding fit model for guest **4.2** calculated via linear regression analysis using the Nelder-Mead method from the change in absorbance at two points (300 nm and 330 nm) using supramolecular.org.¹⁻³ ($K_a = 3.9 \pm 0.1 \times 10^3 \text{ M}^{-1}$).

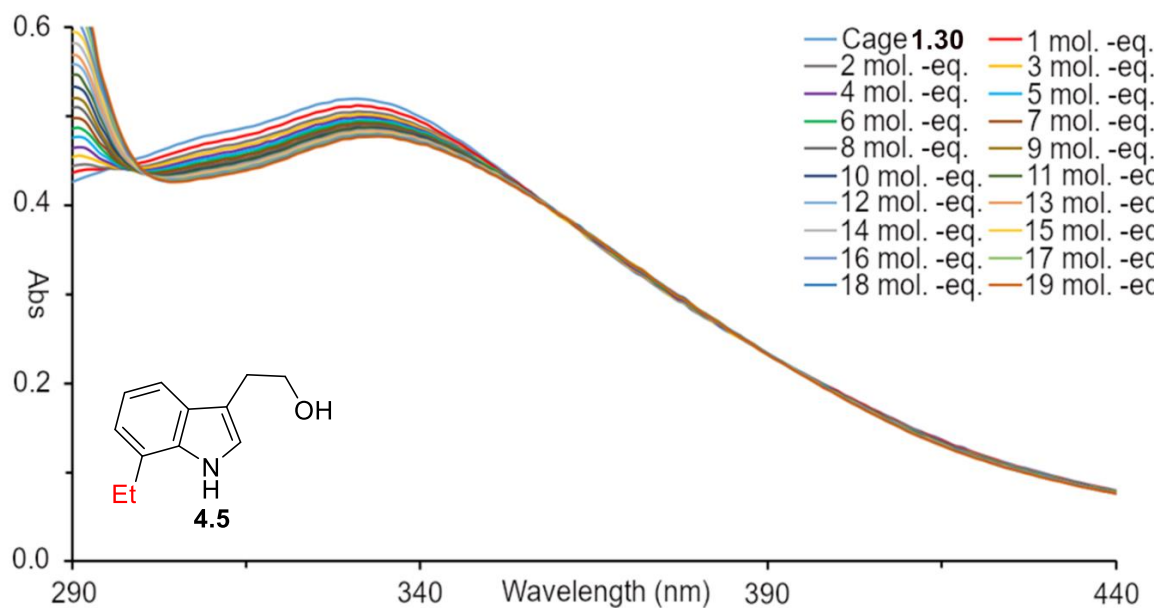


Figure 7.81. UV-Vis absorption spectrum of the titration of **4.5** into a 3 μM solution of cage **1.30** in CH_3CN . **4.5** was added in 1 μL aliquots from a 9 mM stock solution in CD_3CN .

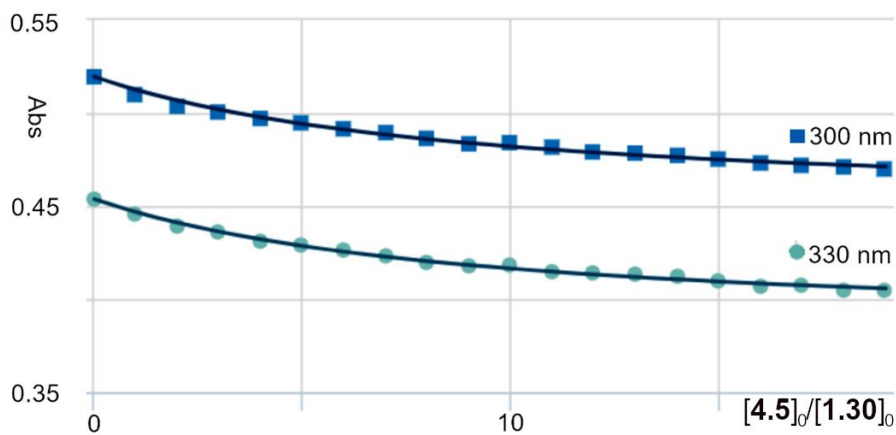


Figure 7.82. 1:1 binding fit model for guest **4.5** calculated via linear regression analysis using the Nelder-Mead method from the change in absorbance at two points (300 nm and 330 nm) using supramolecular.org.¹⁻³ ($K_a = 4.1 \pm 0.1 \times 10^3 \text{ M}^{-1}$).

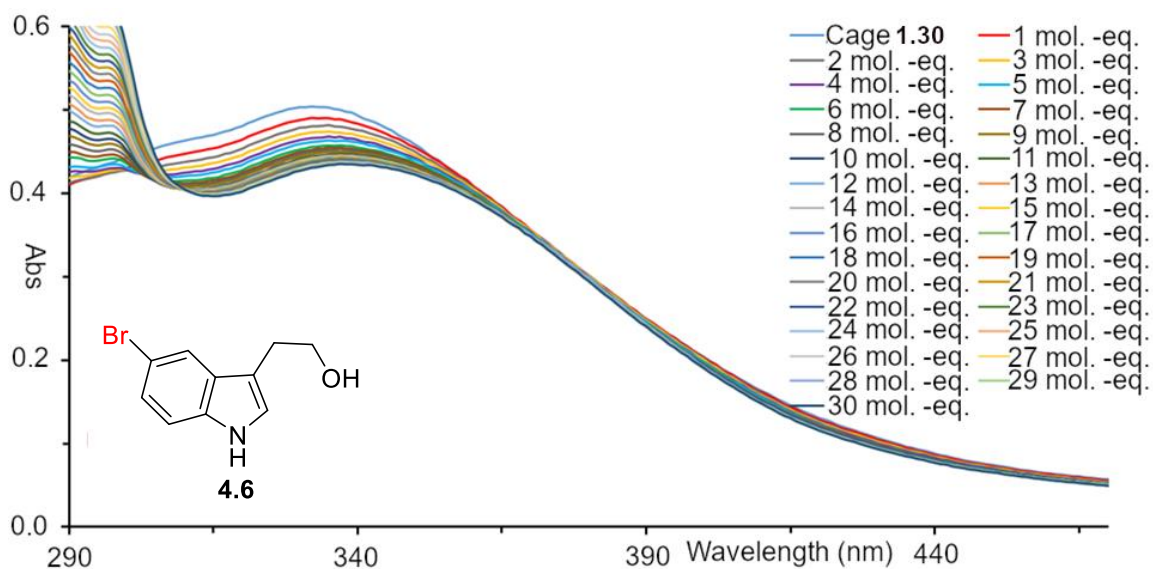


Figure 7.83. UV-Vis absorption spectrum of the titration of **4.6** into a 3 μM solution of cage **1.30** in CH_3CN . **4.6** was added in 1 μL aliquots from a 9 mM stock solution in CD_3CN .

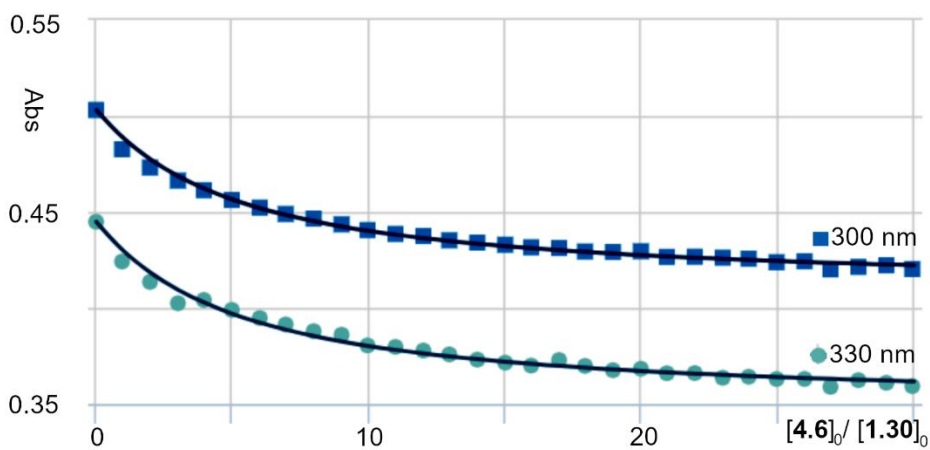


Figure 7.84. 1:1 binding fit model for guest **4.6** calculated via linear regression analysis using the Nelder-Mead method from the change in absorbance at two points (300 nm and 330 nm) using supramolecular.org.¹⁻³ ($K_a = 7.4 \pm 0.3 \times 10^3 \text{ M}^{-1}$).

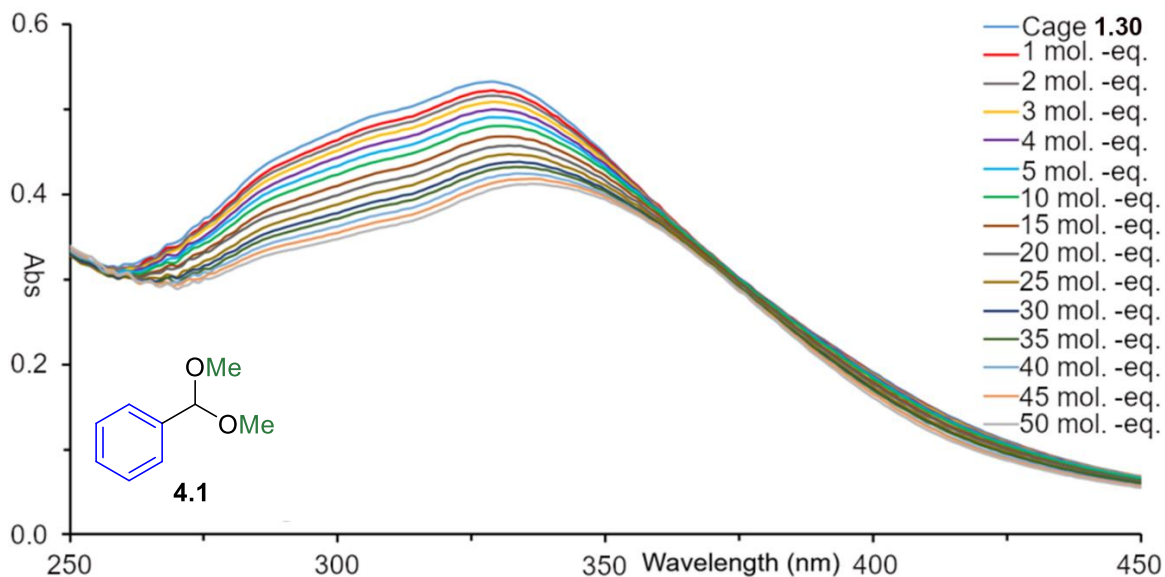


Figure 7.85. UV-Vis absorption spectrum of the titration of **4.1** into a 3 μM solution of cage **1.30** in CH_3CN . **4.1** was added in 1-5 μL aliquots from a 9 mM stock solution in CD_3CN .

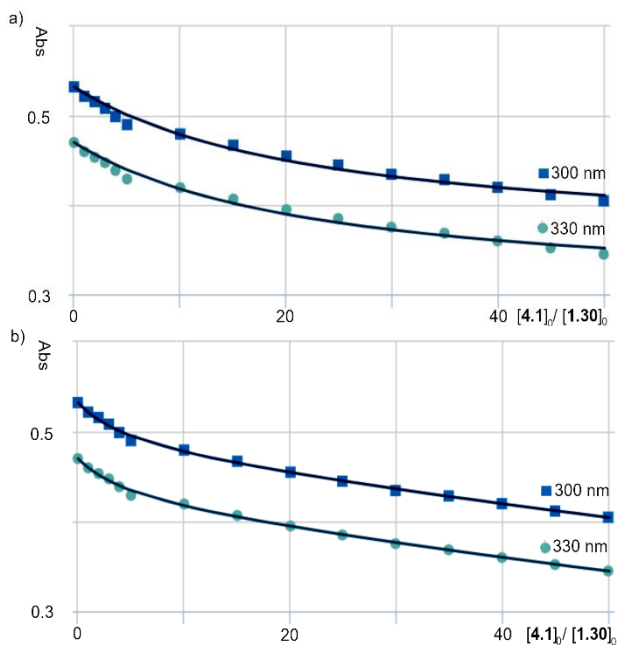


Figure 7.86. a) 1:1 binding fit model for guest **4.1** calculated via linear regression analysis using the Nelder-Mead method from the change in absorbance at two points (300 nm and 330 nm) using supramolecular.org.¹⁻³ ($K_a = 1.5 \pm .09 \times 10^3 \text{ M}^{-1}$). b) 1:2 binding fit model calculated via linear regression analysis using the Nelder-Mead method from the change in absorbance at two points (300 nm and 330 nm) using supramolecular.org.¹⁻³ ($K_1 = 8.6 \pm 0.8 \times 10^3 \text{ M}^{-1}$, $K_2 = 0.08 \pm 0.002 \times 10^3 \text{ M}^{-1}$).

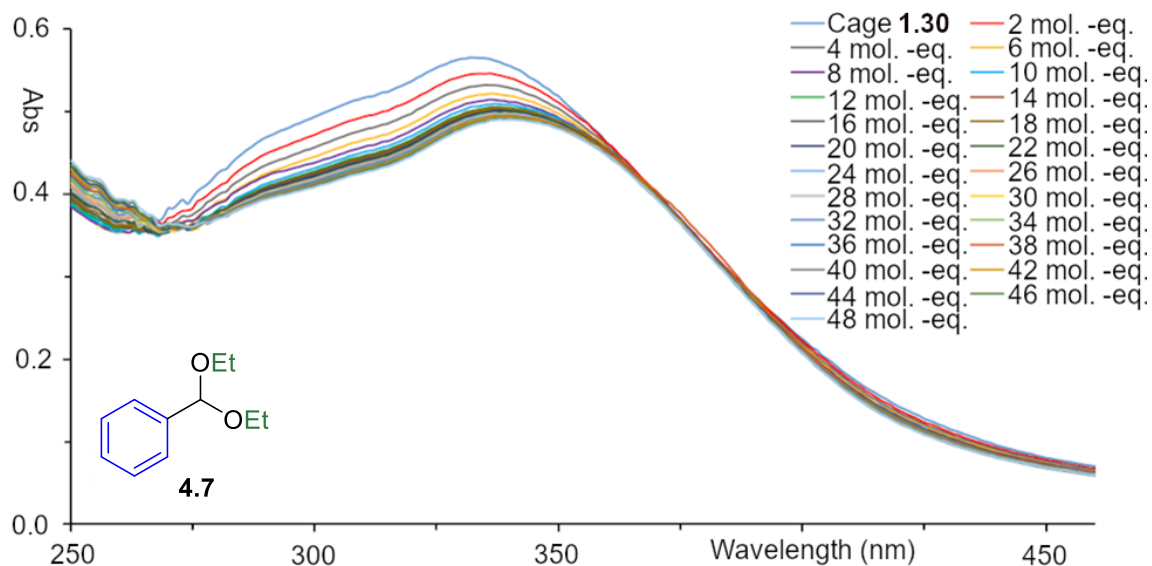


Figure 7.87. UV-Vis absorption spectrum of the titration of **4.7** into a 3 μM solution of cage **1.30** in CH_3CN . **4.7** was added in 2 μL aliquots from a 9 mM stock solution in CD_3CN .

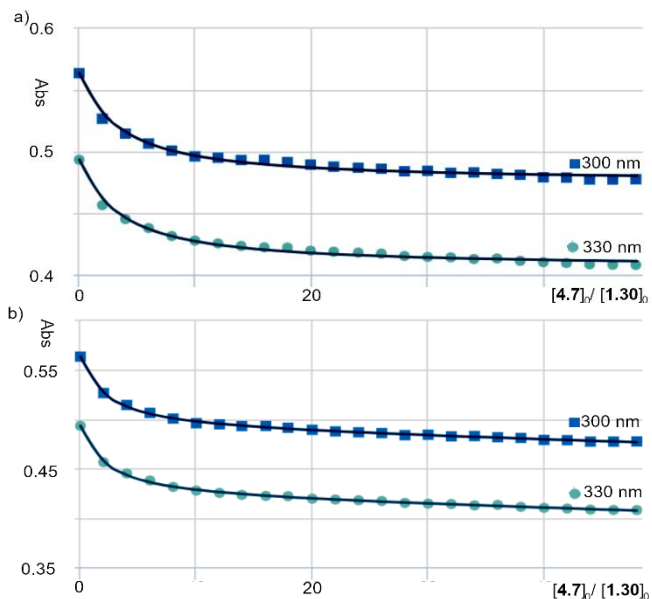


Figure 7.88. a) 1:1 binding fit model for guest **4.7** calculated via linear regression analysis using the Nelder-Mead method from the change in absorbance at two points (300 nm and 330 nm) using supramolecular.org.¹⁻³ ($K_a = 11 \pm 0.63 \times 10^3 \text{ M}^{-1}$). b) 1:2 binding fit model calculated via linear regression analysis using the Nelder-Mead method from the change in absorbance at two points (300 nm and 330 nm) using supramolecular.org.^{[8],[9]} ($K_1 = 20.0 \pm 0.7 \times 10^3 \text{ M}^{-1}$, $K_2 = 0.03 \pm 0.001 \times 10^3 \text{ M}^{-1}$).

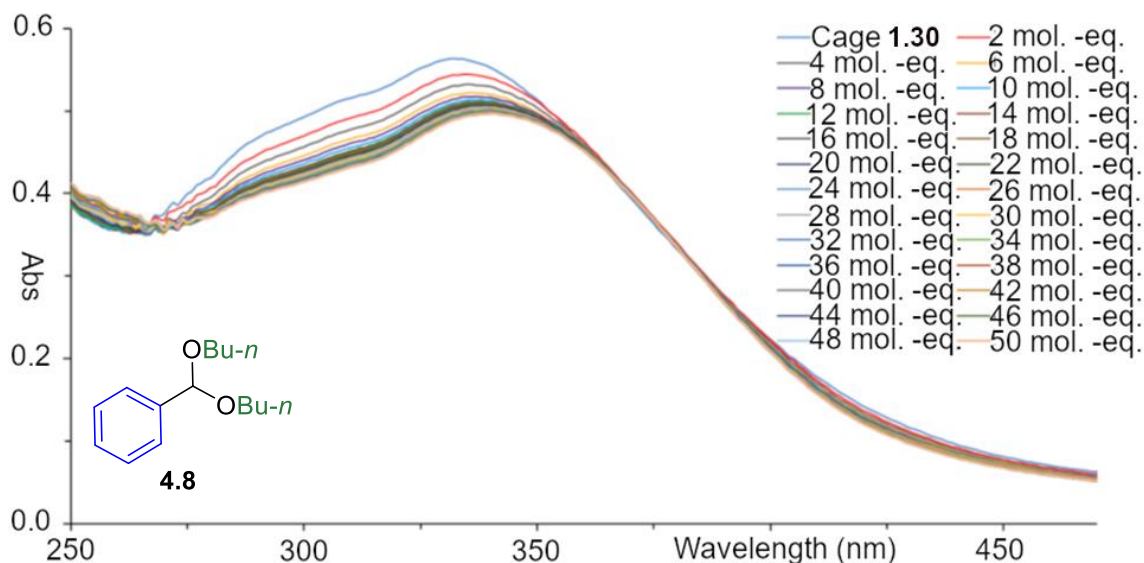


Figure 7.89. UV-Vis absorption spectrum of the titration of **4.8** into a 3 μM solution of cage **1.30** in CH_3CN . **4.8** was added in 2 μL aliquots from a 9 mM stock solution in CD_3CN .

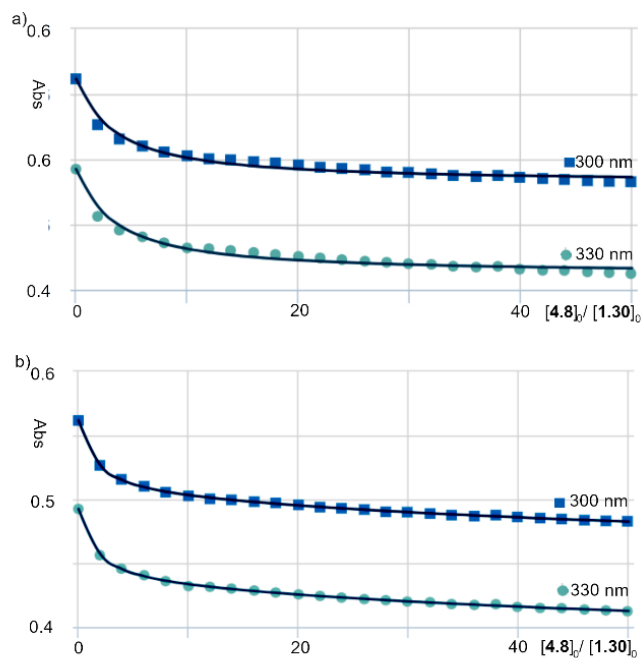


Figure 7.90. a) 1:1 binding fit model for guest **4.8** calculated via linear regression analysis using the Nelder-Mead method from the change in absorbance at two points (300 nm and 330 nm) using supramolecular.org.¹⁻³ ($K_a = 11 \pm .84 \times 10^3 \text{ M}^{-1}$). b) 1:2 binding fit model calculated via linear regression analysis using the Nelder-Mead method from the change in absorbance at two points (300 nm and 330 nm) using supramolecular.org.¹⁻³ ($K_1 = 34.0 \pm 1.3 \times 10^3 \text{ M}^{-1}$, $K_2 = 0.40 \pm 0.01 \times 10^3 \text{ M}^{-1}$).

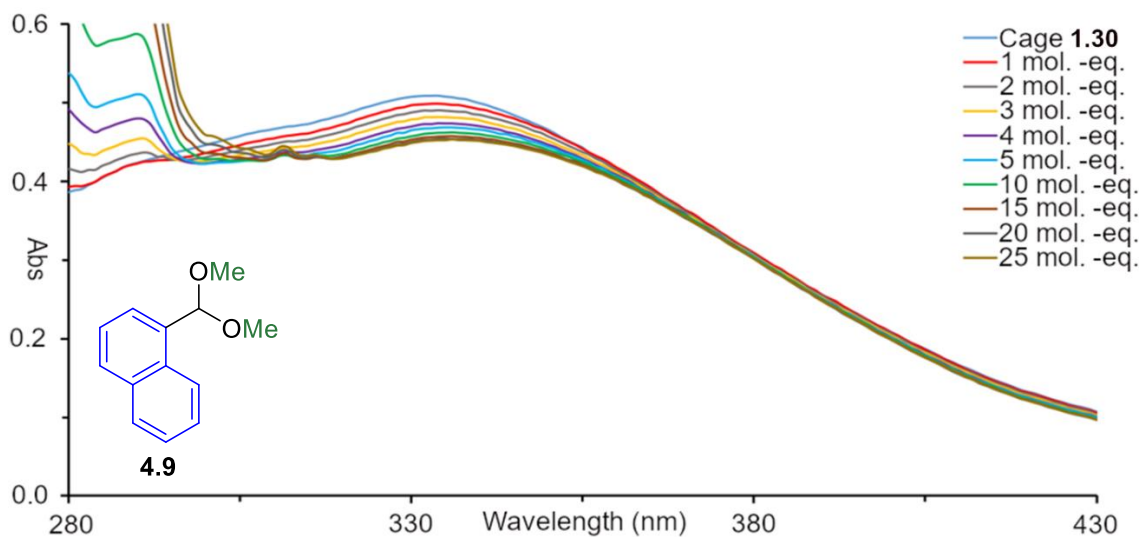


Figure 7.91. UV-Vis absorption spectrum of the titration of **4.9** into a 3 μM solution of cage **1.30** in CH_3CN . **4.9** was added in 1-5 μL aliquots from a 9 mM stock solution in CD_3CN .

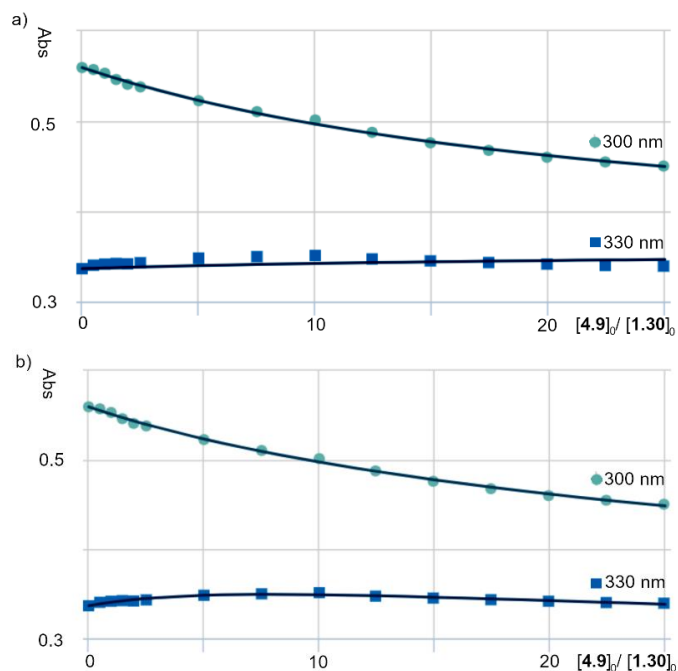


Figure 7.92. a) 1:1 binding fit model for guest **4.9** calculated via linear regression analysis using the Nelder-Mead method from the change in absorbance at two points (300 nm and 330 nm) using supramolecular.org.¹⁻³ ($K_a = 1.4 \pm 0.09 \times 10^3 \text{ M}^{-1}$). b) 1:2 binding fit model calculated via linear regression analysis using the Nelder-Mead method from the change in absorbance at two points (300 nm and 330 nm) using supramolecular.org.¹⁻³ ($K_1 = 4.7 \pm 0.4 \times 10^3 \text{ M}^{-1}$, $K_2 = 0.70 \pm 0.04 \times 10^3 \text{ M}^{-1}$).

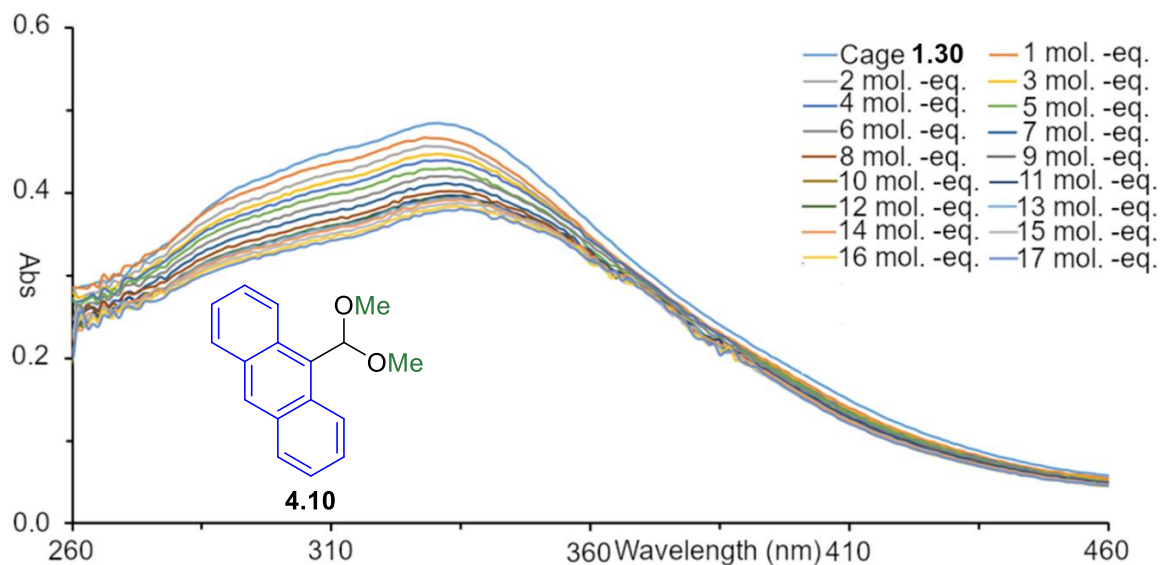


Figure 7.93. UV-Vis absorption spectrum of the titration of **4.10** into a 3 μM solution of cage **1.30** in CH₃CN. **4.10** was added in 1 μL aliquots from a 9 mM stock solution in CD₃CN.

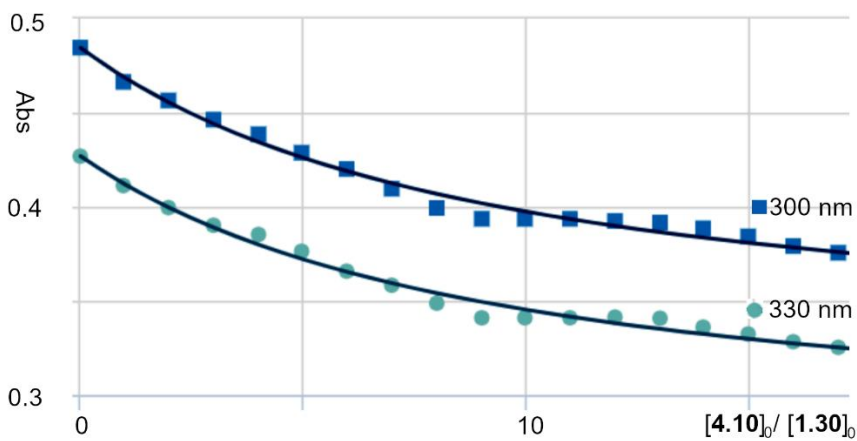


Figure 7.94. 1:1 binding fit model for guest **4.10** calculated via linear regression analysis using the Nelder-Mead method from the change in absorbance at two points (300 nm and 330 nm) using supramolecular.org.¹⁻³ ($K_a = 4.0 \pm 0.2 \times 10^3 \text{ M}^{-1}$).

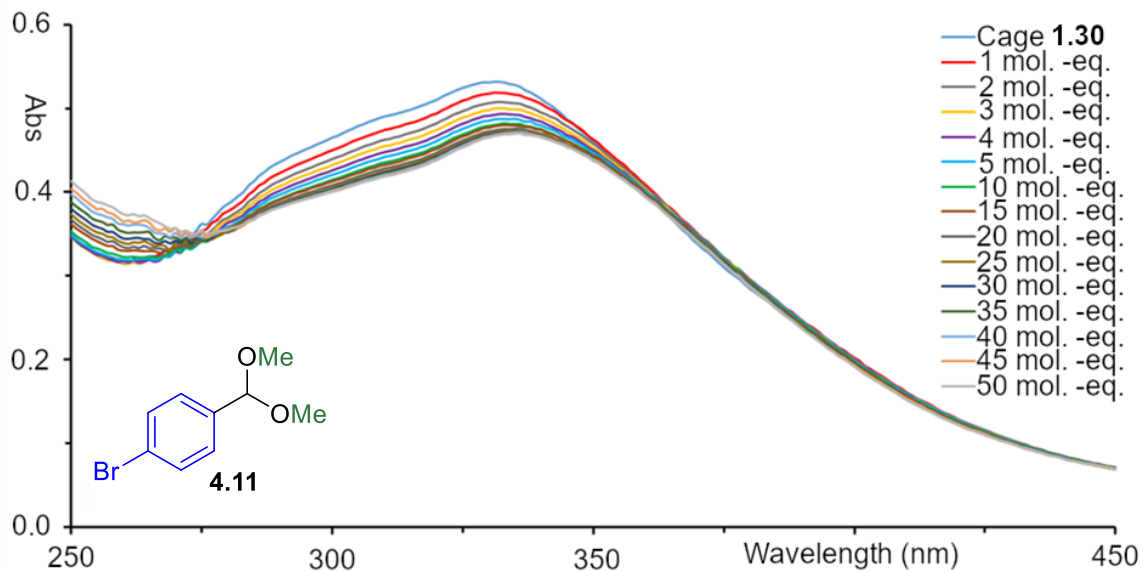


Figure 7.95. UV-Vis absorption spectrum of the titration of **4.11** into a 3 μM solution of cage **1.30** in CH_3CN . **4.11** was added in 1-5 μL aliquots from a 9 mM stock solution in CD_3CN .

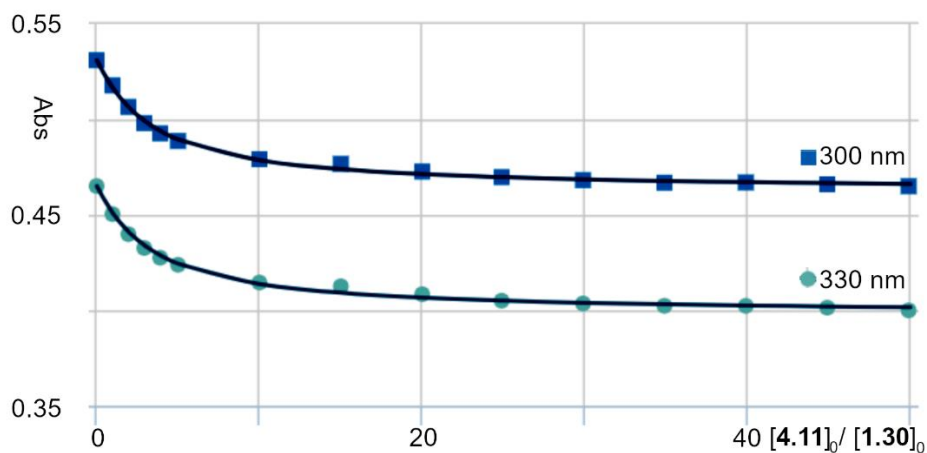


Figure 7.96. 1:1 binding fit model for guest **4.11** calculated via linear regression analysis using the Nelder-Mead method from the change in absorbance at two points (300 nm and 330 nm) using supramolecular.org.¹⁻³ ($K_a = 12.0 \pm 0.6 \times 10^3 \text{ M}^{-1}$).

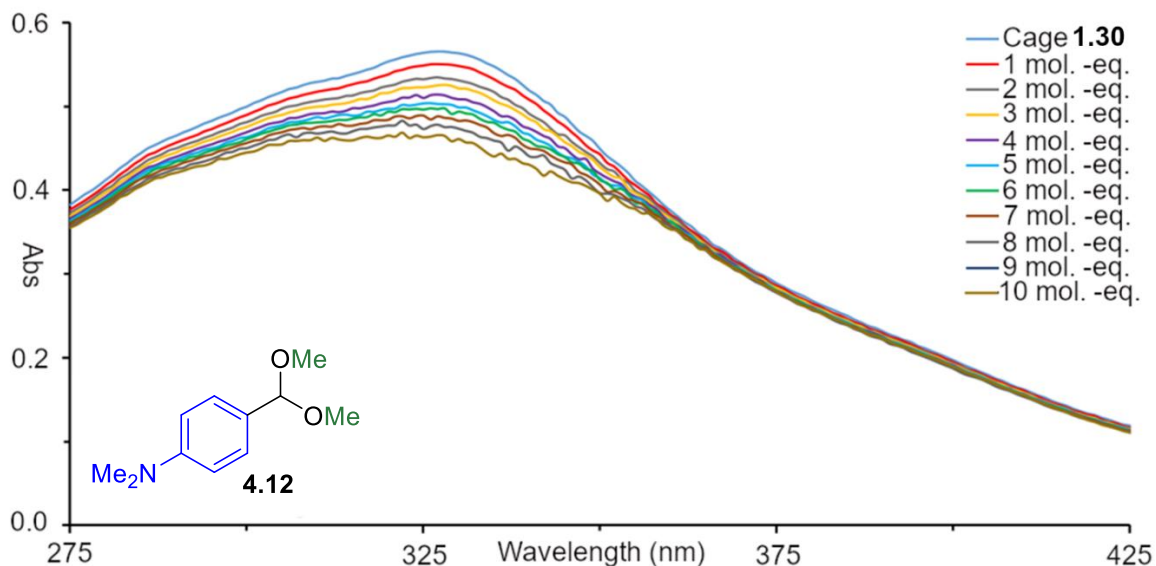


Figure 7.97. UV-Vis absorption spectrum of the titration of **4.12** into a 3 μM solution of cage **1.30** in CH_3CN . **4.12** was added in 1 μL aliquots from a 9 mM stock solution in CD_3CN .

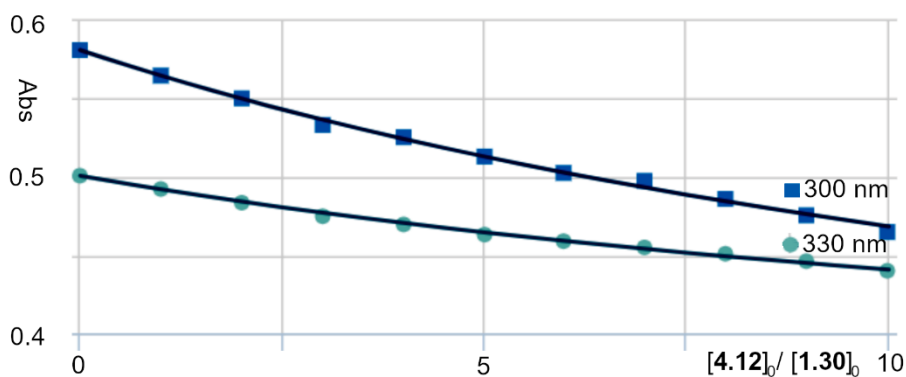


Figure 7.98. 1:1 binding fit model for guest **4.12** calculated via linear regression analysis using the Nelder-Mead method from the change in absorbance at two points (300 nm and 330 nm) using supramolecular.org.¹⁻³ ($K_a = 12.0 \pm 0.6 \times 10^3 \text{ M}^{-1}$).

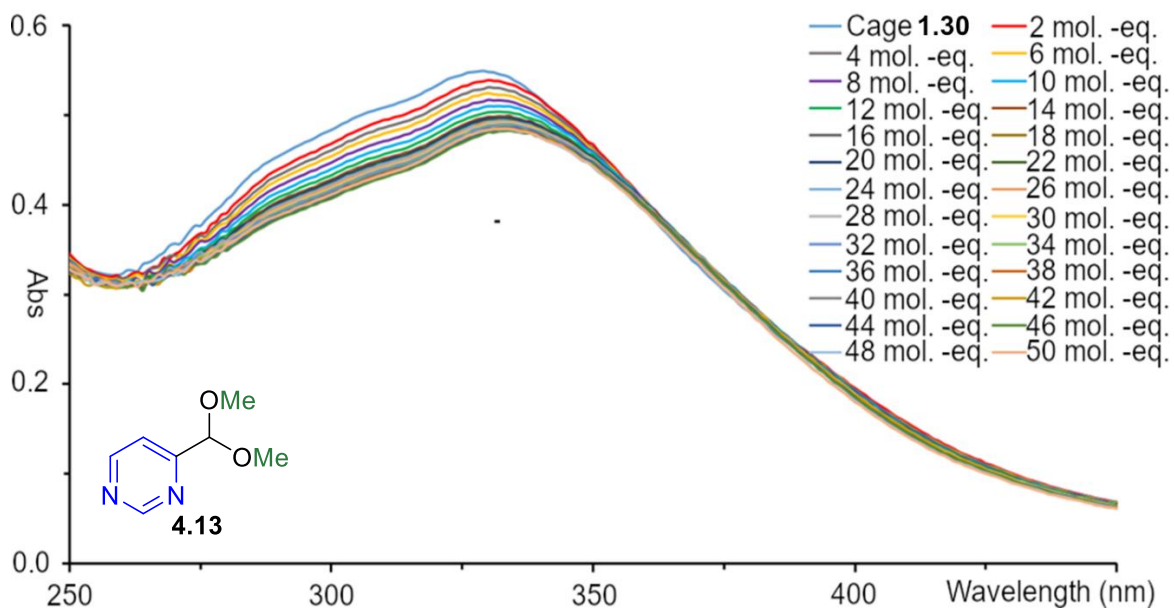


Figure 7.99. UV-Vis absorption spectrum of the titration of **4.13** into a 3 μM solution of cage **1.30** in CH_3CN . **4.13** was added in 2 μL aliquots from a 9 mM stock solution in CD_3CN .

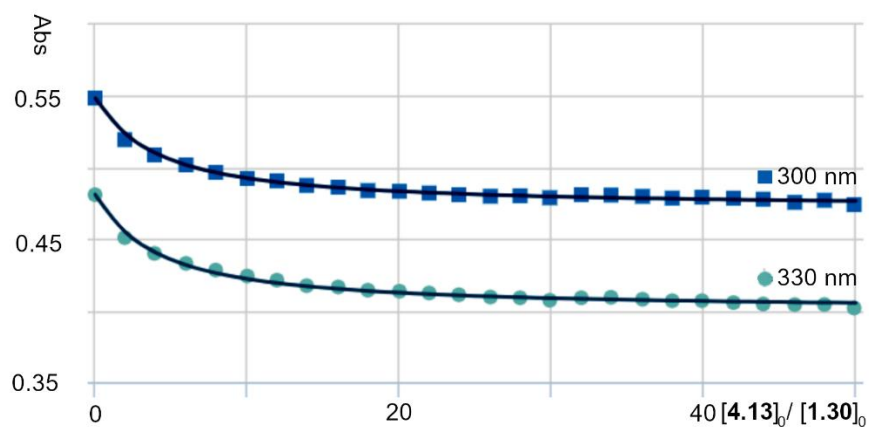


Figure 7.100. 1:1 binding fit model for guest **4.13** calculated via linear regression analysis using the Nelder-Mead method from the change in absorbance at two points (300 nm and 330 nm) using supramolecular.org.¹⁻³ ($K_a = 9.6 \pm 0.4 \times 10^3 \text{ M}^{-1}$).

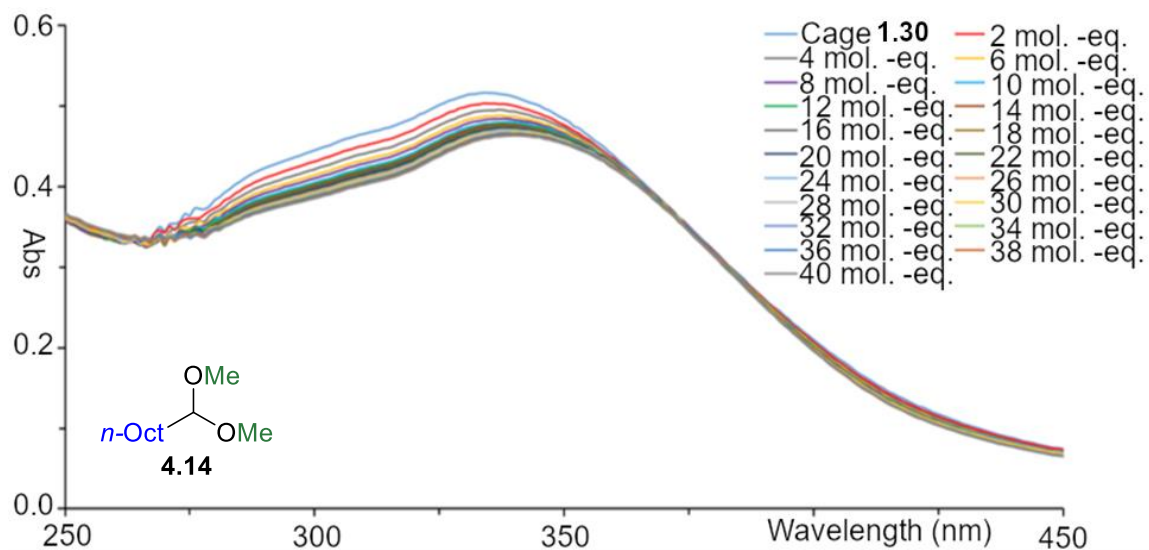


Figure 7.101. UV-Vis absorption spectrum of the titration of **4.14** into a 3 μM solution of cage **1.30** in CH_3CN . **4.14** was added in 2 μL aliquots from a 9 mM stock solution in CD_3CN .

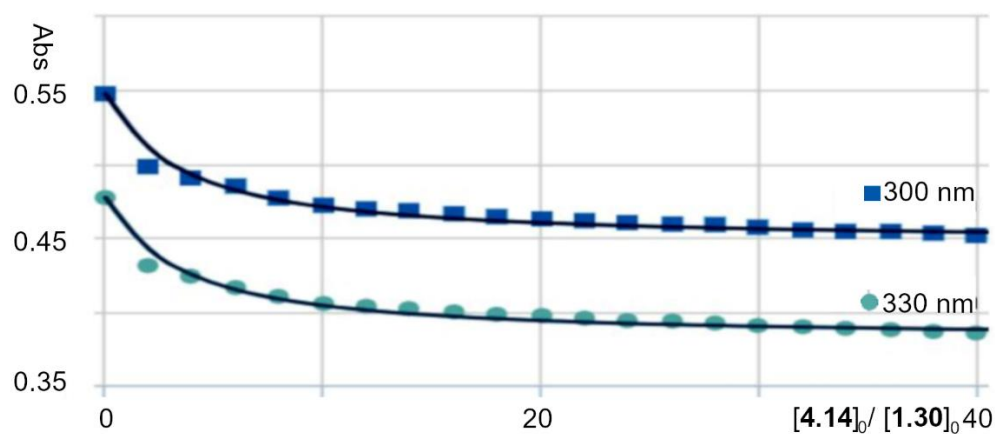


Figure 7.102. 1:1 binding fit model for guest **4.14** calculated via linear regression analysis using the Nelder-Mead method from the change in absorbance at two points (300 nm and 330 nm) using supramolecular.org.¹⁻³ ($K_a = 12.0 \pm 1.0 \times 10^3 \text{ M}^{-1}$).

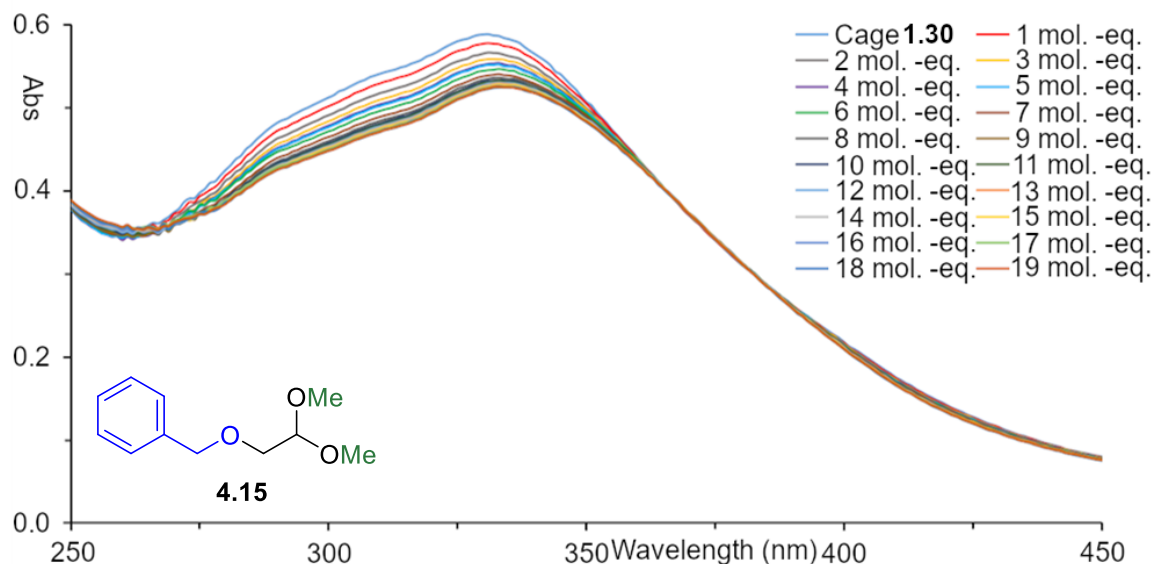


Figure 7.103. UV-Vis absorption spectrum of the titration of **4.15** into a 3 μM solution of cage **1.30** in CH_3CN . **4.15** was added in 1 μL aliquots from a 9 mM stock solution in CD_3CN .

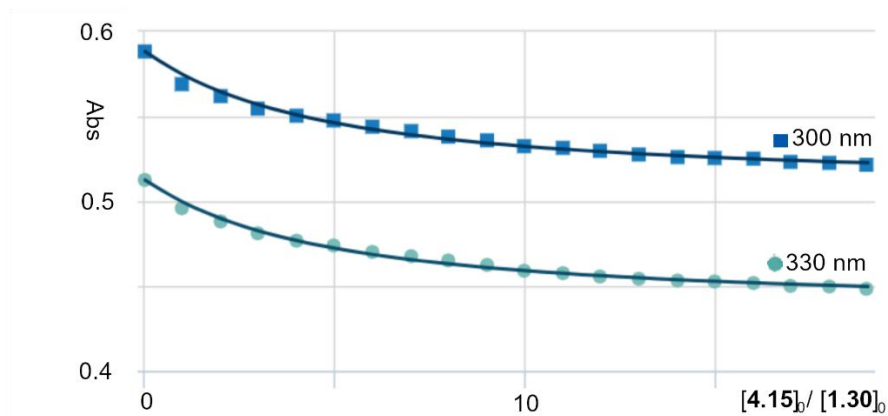


Figure 7.104. 1:1 binding fit model for guest **4.15** calculated via linear regression analysis using the Nelder-Mead method from the change in absorbance at two points (300 nm and 330 nm) using supramolecular.org.¹⁻³ ($K_a = 8.3 \pm 0.3 \times 10^3 \text{ M}^{-1}$).

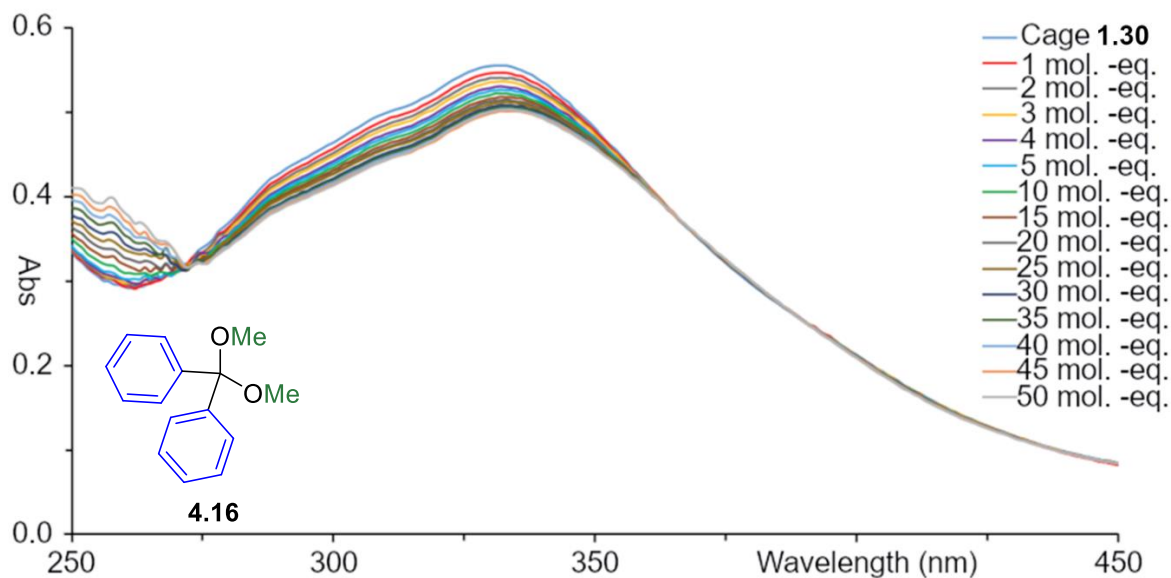


Figure 7.105. UV-Vis absorption spectrum of the titration of **4.16** into a 3 μM solution of cage **1.30** in CH_3CN . **4.16** was added in 1-5 μL aliquots from a 9 mM stock solution in CD_3CN .

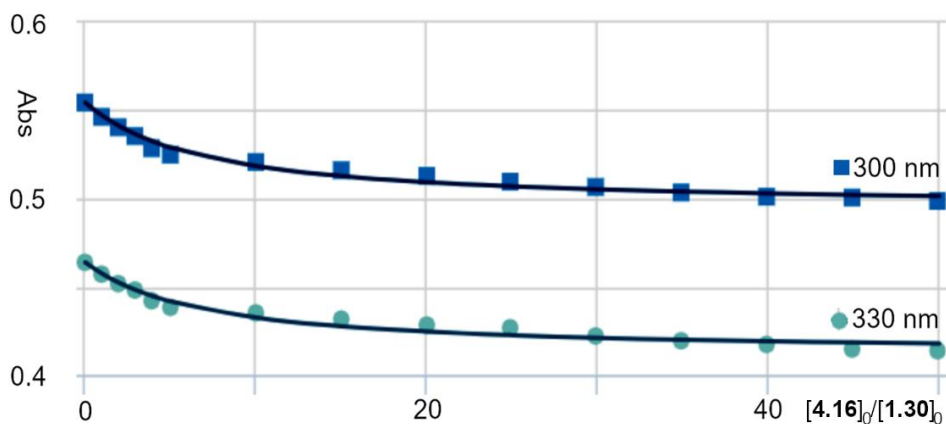


Figure 7.106. 1:1 binding fit model for guest **4.16** calculated via linear regression analysis using the Nelder-Mead method from the change in absorbance at two points (300 nm and 330 nm) using supramolecular.org.¹⁻³ ($K_a = 4.4 \pm 0.53 \times 10^3 \text{ M}^{-1}$).

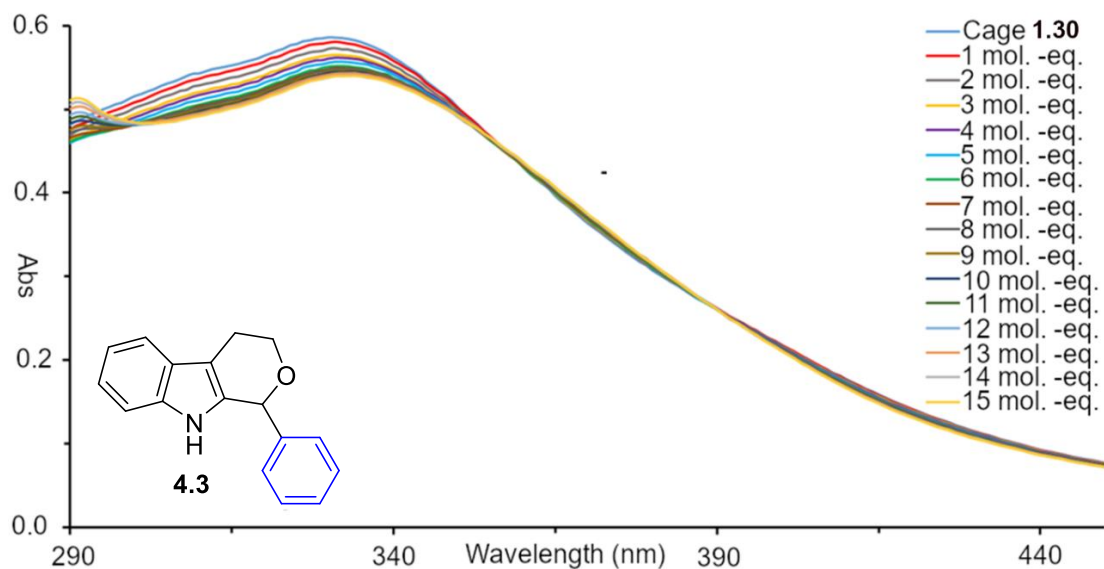


Figure 7.107. UV-Vis absorption spectrum of the titration of **4.3** into a 3 μM solution of cage **1.30** in CH_3CN . **4.3** was added in 1 μL aliquots from a 9 mM stock solution in CD_3CN .

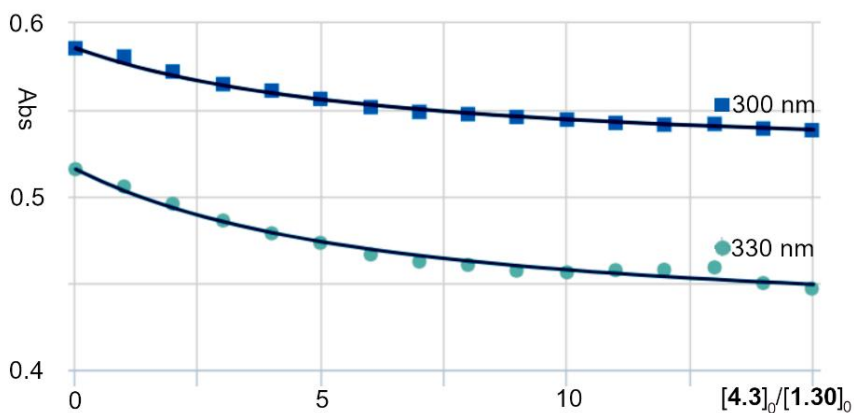


Figure 7.108. 1:1 binding fit model for guest **4.3** calculated via linear regression analysis using the Nelder-Mead method from the change in absorbance at two points (300 nm and 330 nm) using supramolecular.org.¹⁻³ ($K_a = 6.2 \pm 0.3 \times 10^3 \text{ M}^{-1}$).

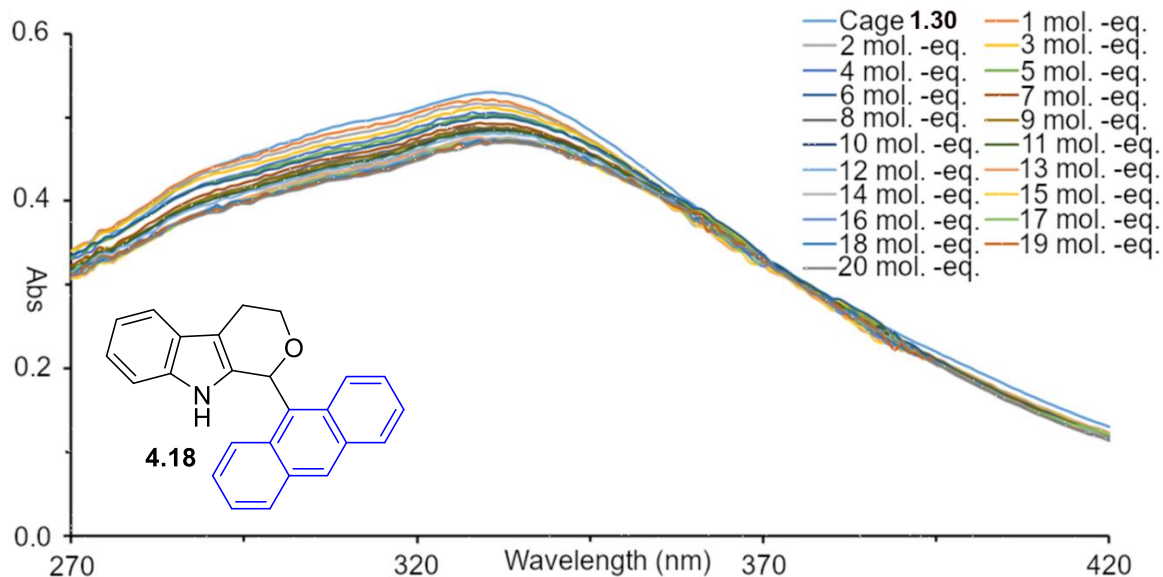


Figure 7.109. UV-Vis absorption spectrum of the titration of **4.18** into a 3 μM solution of cage **1.30** in CH_3CN . **4.18** was added in 1 μL aliquots from a 9 mM stock solution in CD_3CN .

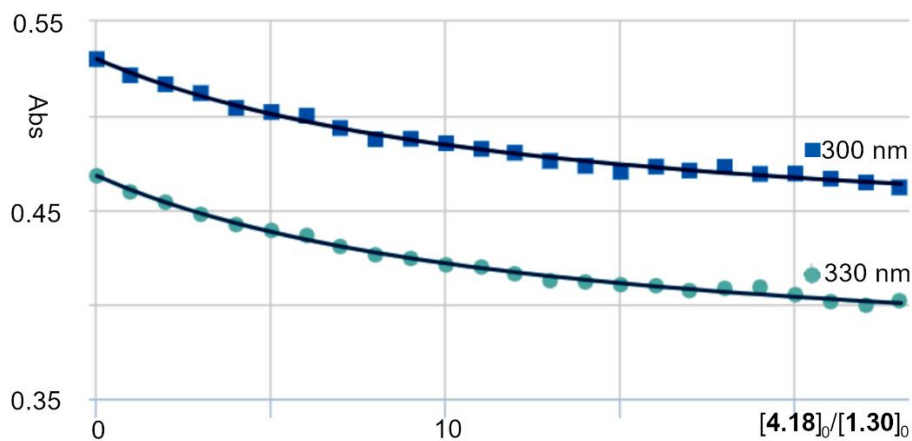


Figure 7.110. 1:1 binding fit model for guest **4.18** calculated via linear regression analysis using the Nelder-Mead method from the change in absorbance at two points (300 nm and 330 nm) using supramolecular.org.¹⁻³ ($K_a = 2.9 \pm 0.1 \times 10^3 \text{ M}^{-1}$).

7.11. Selected Spectra for Chapter 5

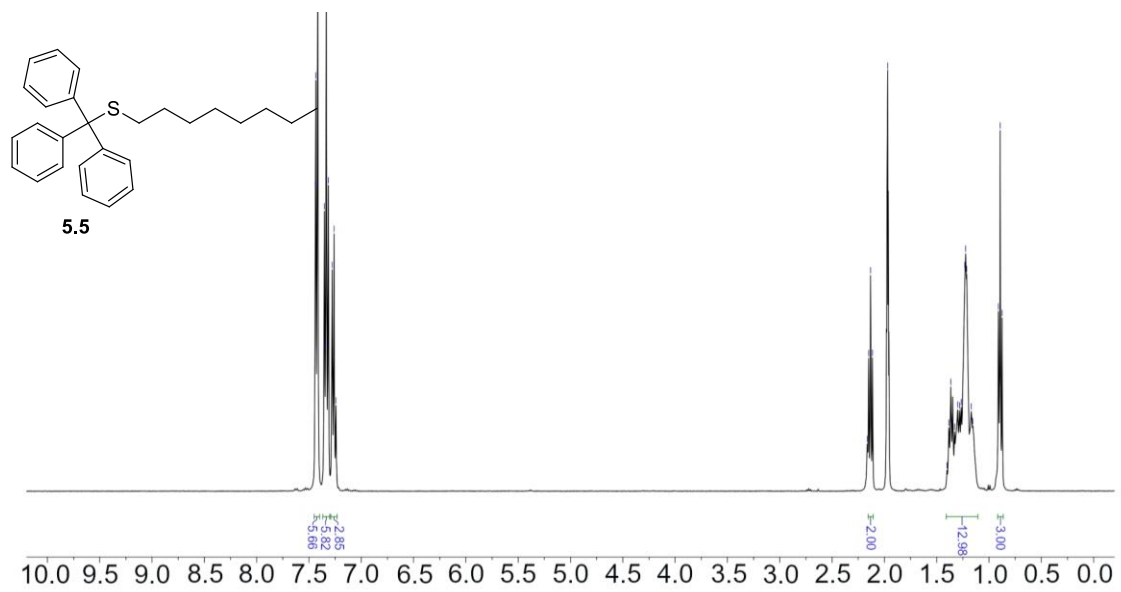


Figure 7.111. ¹H NMR spectrum of **5.5** (400 MHz, 298K, CD₃CN).

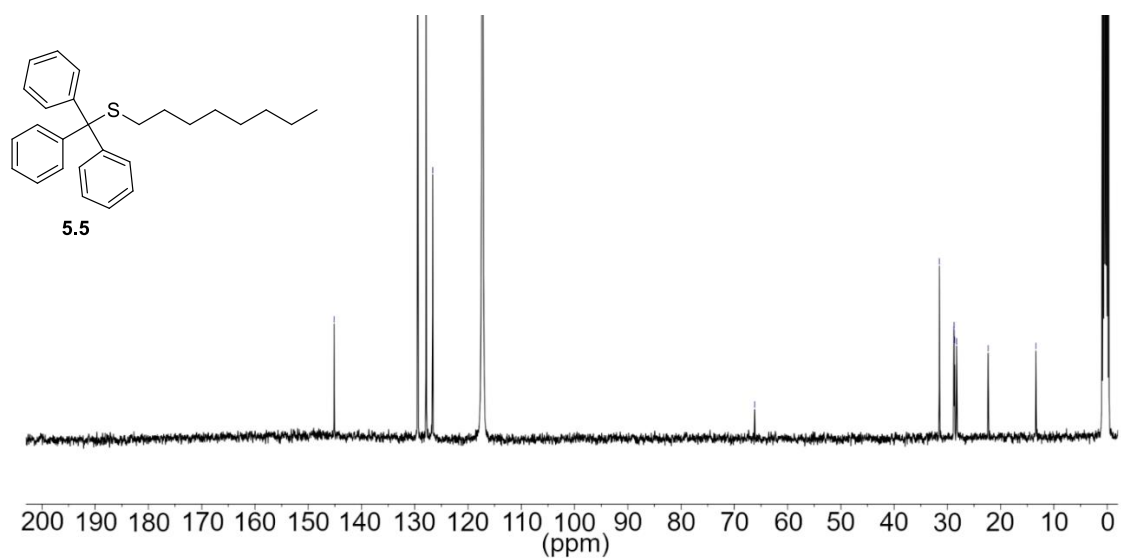


Figure 7.112. ¹³C NMR spectrum of **5.5** (100 MHz, 298K, CD₃CN).

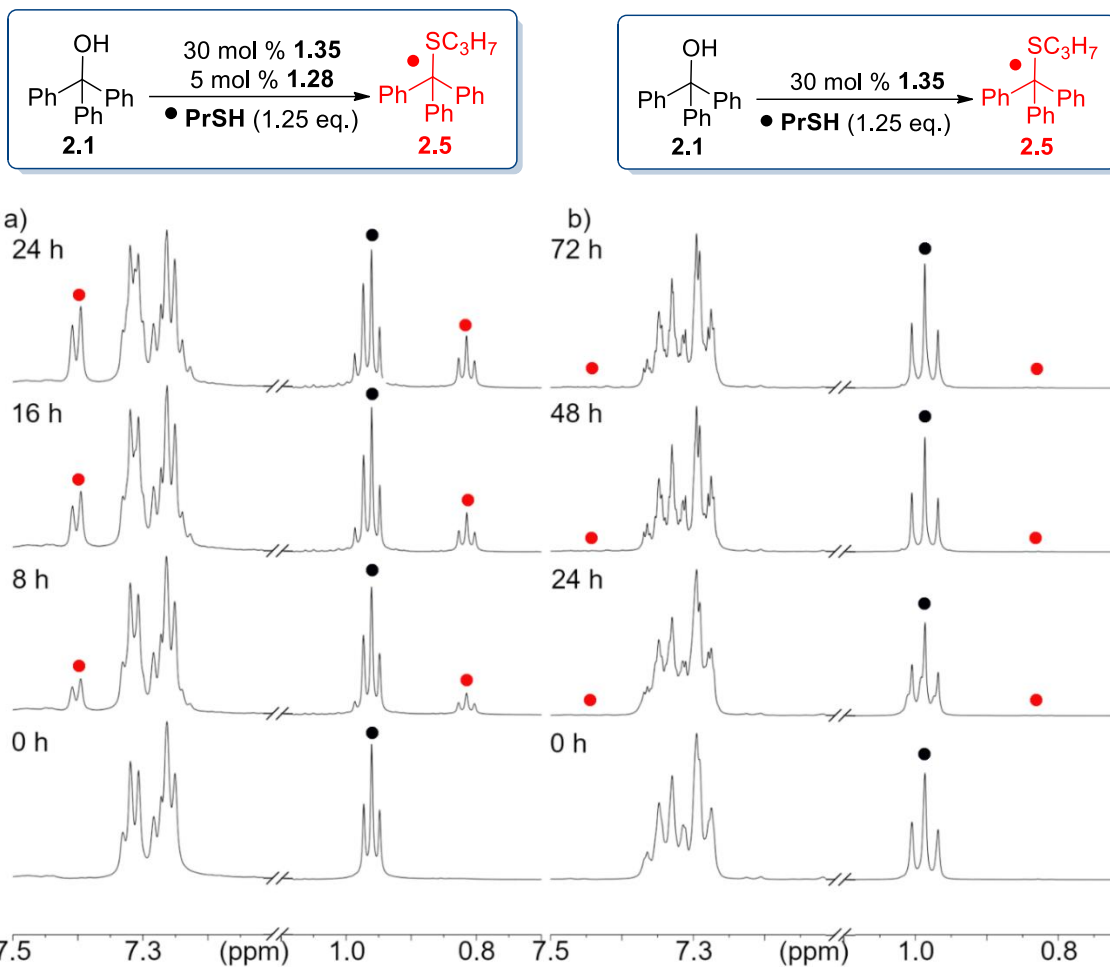


Figure 7.113. ^1H NMR spectra (7.50-7.10 ppm, 1.10-0.70 ppm) of the acid promoted substitution reaction between **2.1** and *n*-propyl thiol in 400 μL CD_3CN in the presence of: a) 5 mol % cage **1.28** and 30 mol % acid **1.35** b) 30 mol % acid **1.35**. [**2.1**] = 15.8 mM, [**PrSH**] = 19.8 mM, [**1.28**] = 0.8 mM, [**1.35**] = 4.74 mM, reactions were performed at 80 $^\circ\text{C}$ in CD_3CN and monitored over time (400 MHz, 298 K, CD_3CN).

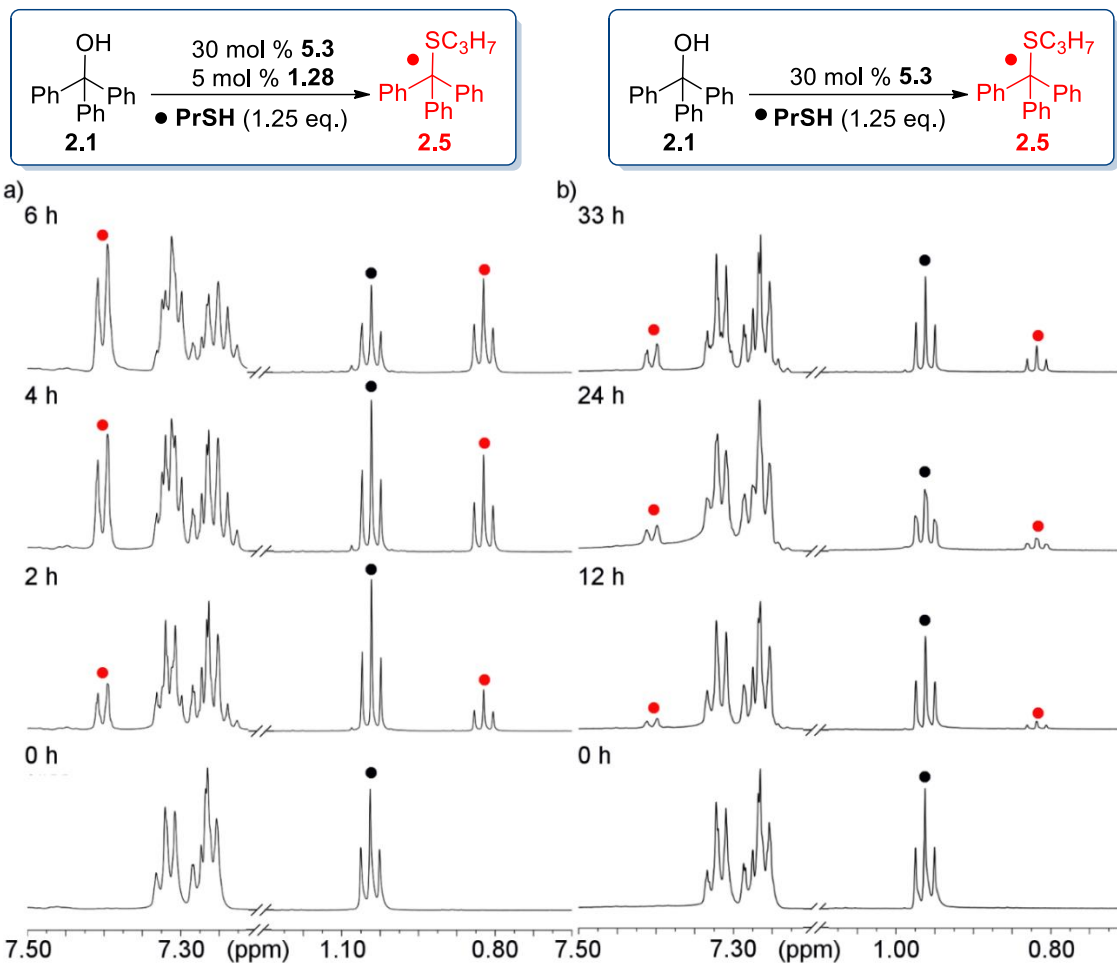


Figure 7.114. ^1H NMR spectra (7.50-7.10 ppm, 1.30-0.60 ppm) of the acid promoted substitution reaction between **2.1** and *n*-propyl thiol in 400 μL CD_3CN in the presence of: a) 5 mol % cage **1.28** and 30 mol % acid **5.3** b) 30 mol % acid **3b**. [**5.3**] = 15.8 mM, [**PrSH**] = 19.8 mM, [**1.28**] = 0.8 mM, [**5.3**] = 4.74 mM, reactions were performed at 80 $^\circ\text{C}$ in CD_3CN and monitored over time (600 MHz, 298 K, CD_3CN).

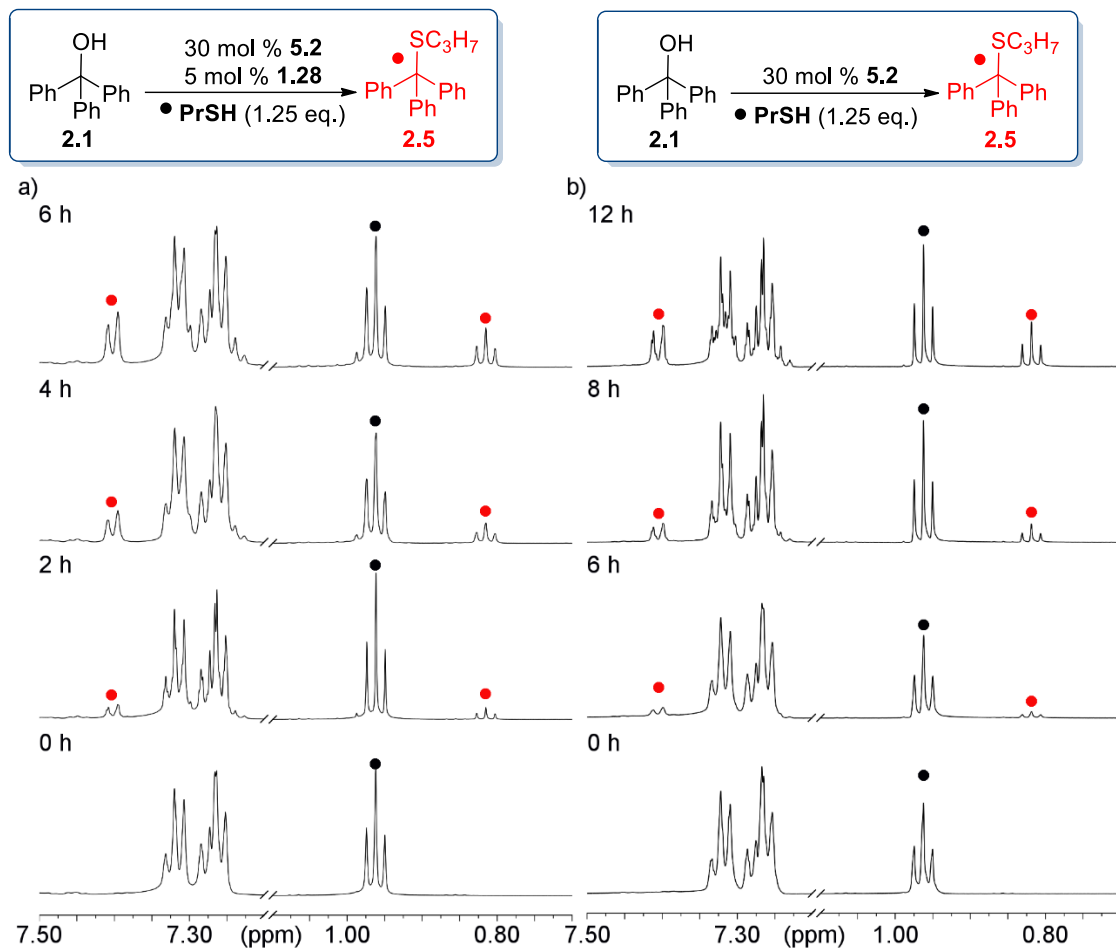


Figure 7.115. ^1H NMR spectra (7.5–7.10 ppm, 1.3–0.60 ppm) of the acid promoted substitution reaction between **2.1** and *n*-propyl thiol in 400 μL CD_3CN in the presence of: a) 5 mol % cage **1.28** and 30 mol % acid **5.2** b) 30 mol % acid **5.2**. [**2.1**] = 15.8 mM, [**PrSH**] = 19.8 mM, [**1.28**] = 0.8 mM, [**5.2**] = 4.74 mM, were performed at 80 $^\circ\text{C}$ in CD_3CN and monitored over time (600 MHz, 298 K, CD_3CN).

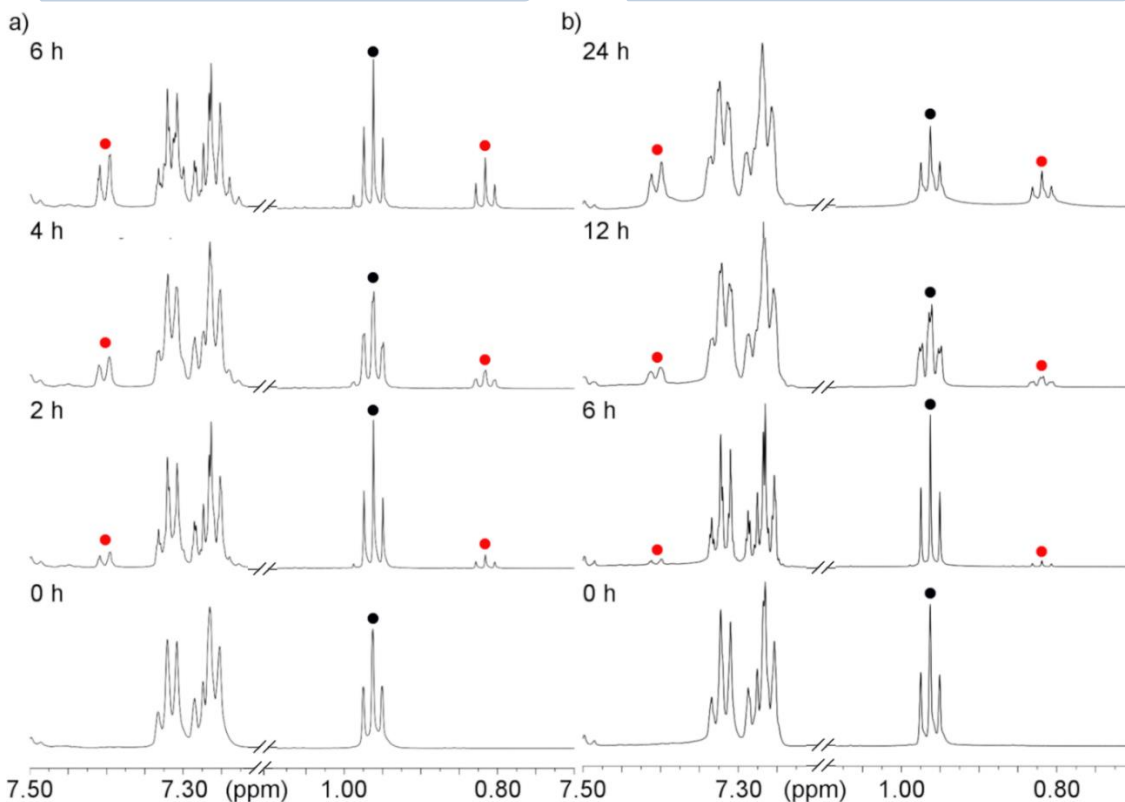
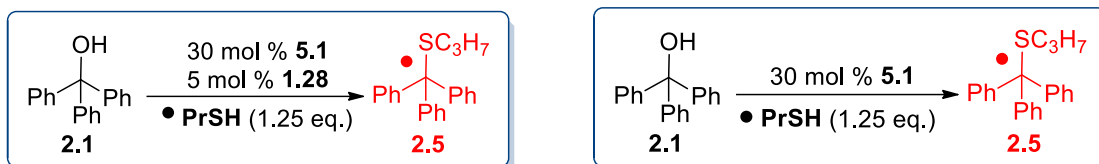


Figure 7.116. ^1H NMR spectra (7.5-7.10 ppm, 1.3-0.60 ppm) of the acid promoted substitution reaction between **2.1** and *n*-propyl thiol in 400 μL CD_3CN in the presence of: a) 5 mol % cage **1.28** and 30 mol % acid **5.1** b) 30 mol % acid **5.1**. [**2.1**] = 15.8 mM, [**PrSH**] = 19.8 mM, [**1.28**] = 0.8 mM, [**5.1**] = 4.74 mM, reactions were performed at 80 $^\circ\text{C}$ in CD_3CN and monitored over time (600 MHz, 298 K, CD_3CN).

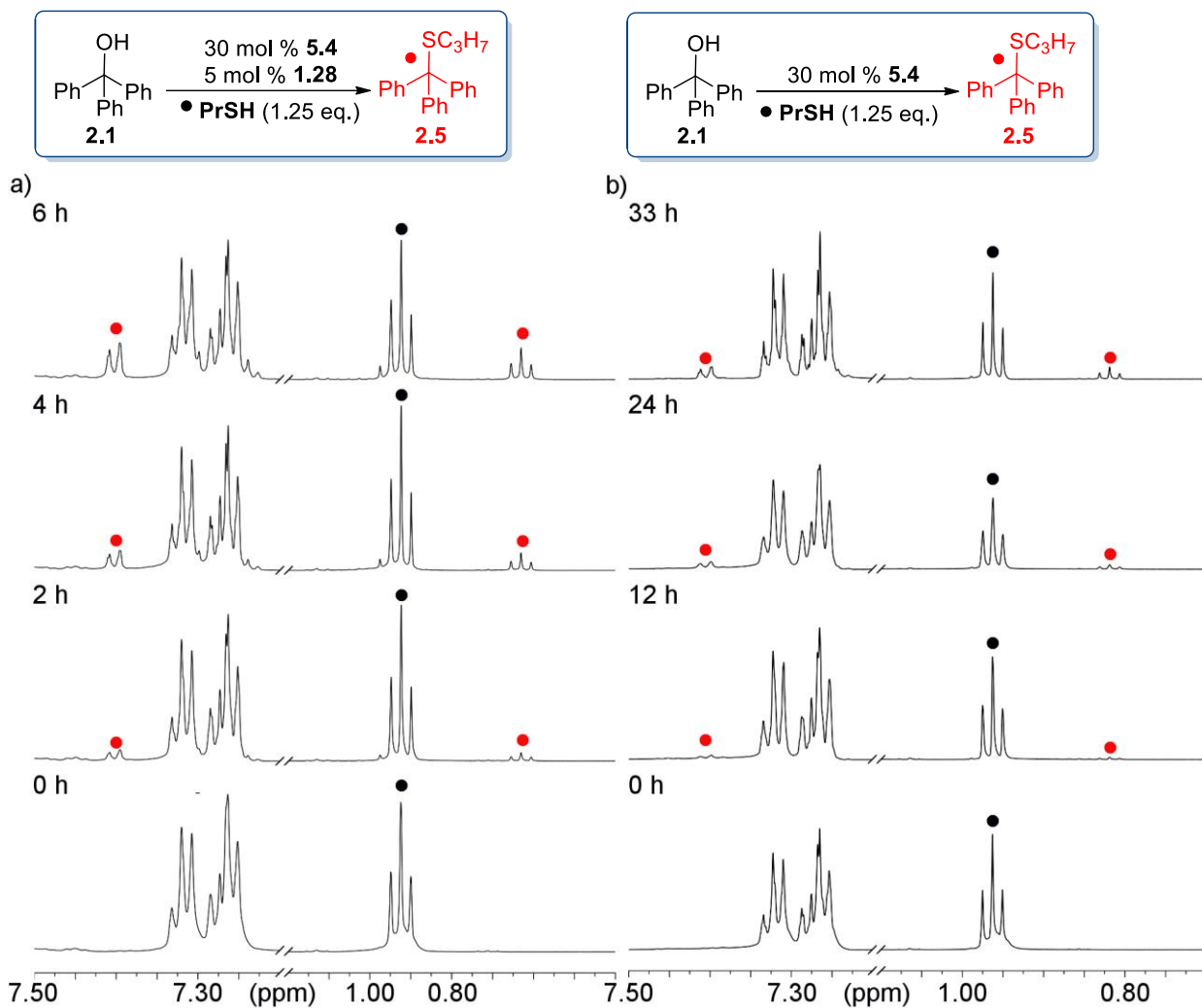


Figure 7.117. ^1H NMR spectra (7.5-7.10 ppm, 1.30-0.70 ppm) of the acid promoted substitution reaction between **2.1** and *n*-propyl thiol in 400 μL CD_3CN in the presence of: a) 5 mol % cage **1.28** and 30 mol % acid **5.4** b) 30 mol % acid **5.4**. $[\mathbf{2.1}] = 15.8 \text{ mM}$, $[\text{PrSH}] = 19.8 \text{ mM}$, $[\mathbf{1.28}] = 0.8 \text{ mM}$, $[\mathbf{5.4}] = 4.74 \text{ mM}$, reactions were performed at 80 $^\circ\text{C}$ in CD_3CN and monitored over time (600 MHz, 298 K, CD_3CN).

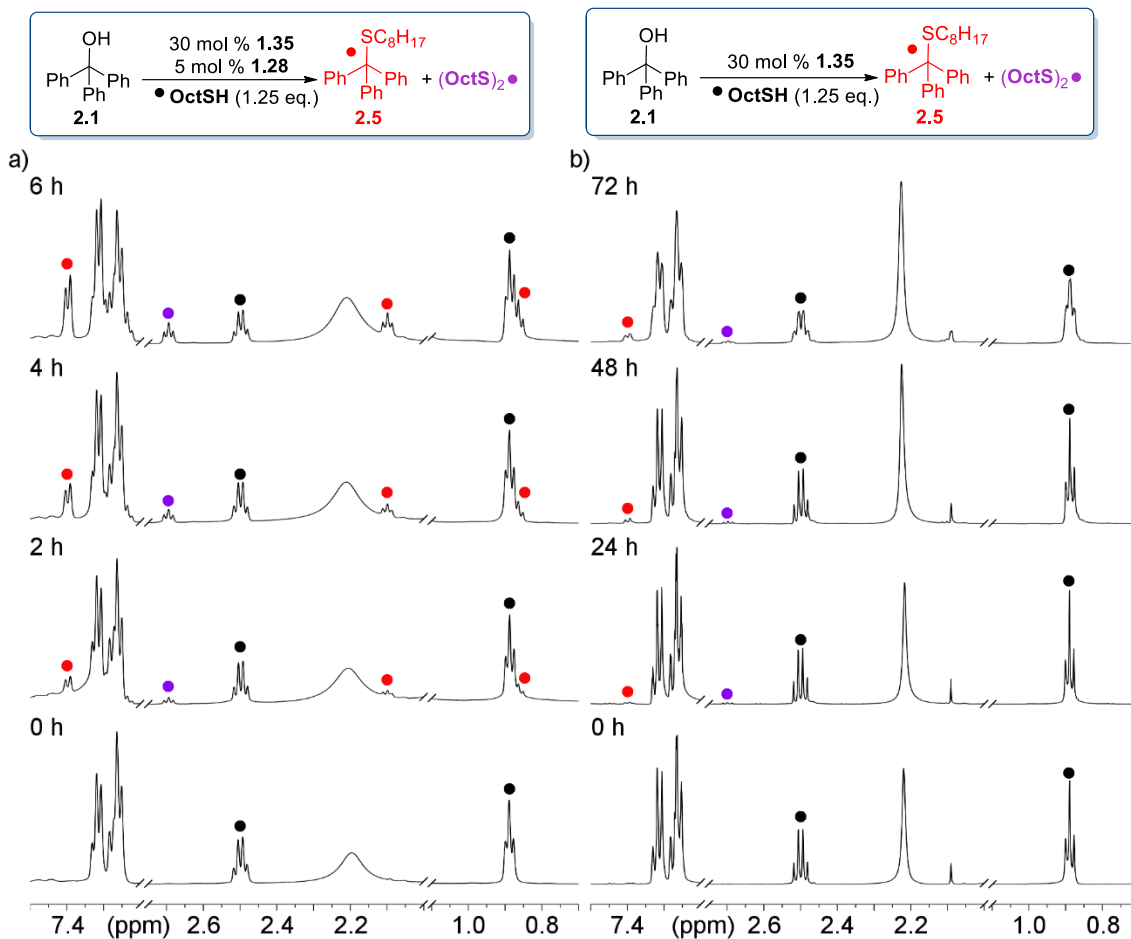


Figure 7.118. ^1H NMR spectra (7.50-7.20 ppm, 2.75-2.00 ppm, 1.10-0.70 ppm) of the acid promoted substitution reaction between **2.1** and *n*-octyl mercaptan in 400 μL CD_3CN in the presence of: a) 5 mol % cage **1.28** and 30 mol % acid **1.35** b) 30 mol % acid **1.35**. [**2.1**] = 15.8 mM, [**OctSH**] = 19.8 mM, [**1.28**] = 0.8 mM, [**1.35**] = 4.74 mM, reactions were performed at 80 $^\circ\text{C}$ in CD_3CN and monitored over time (600 MHz, 298 K, CD_3CN).

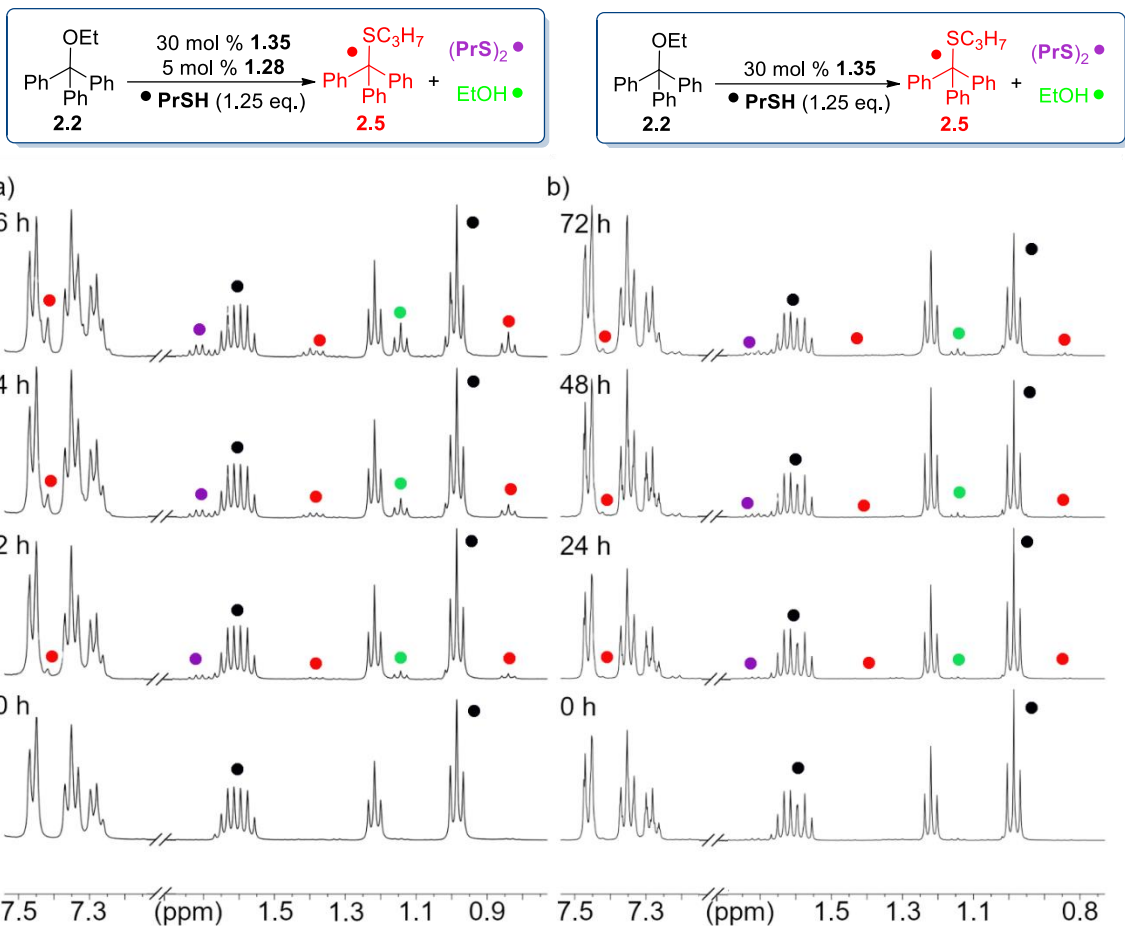


Figure 7.119. ^1H NMR spectra (7.55-7.10 ppm, 1.80-0.70 ppm) of the acid promoted substitution reaction between **2.2** and *n*-propyl thiol in 400 μL CD_3CN in the presence of: a) 5 mol % cage **1.28** and 30 mol % acid **1.35** b) 30 mol % acid **1.35**. $[\mathbf{2.2}] = 15.8$ mM, $[\text{PrSH}] = 19.8$ mM, $[\mathbf{1.28}] = 0.8$ mM, $[\mathbf{1.35}] = 4.74$ mM, reactions were performed at 80 $^\circ\text{C}$ in CD_3CN and monitored over time (600 MHz, 298 K, CD_3CN).

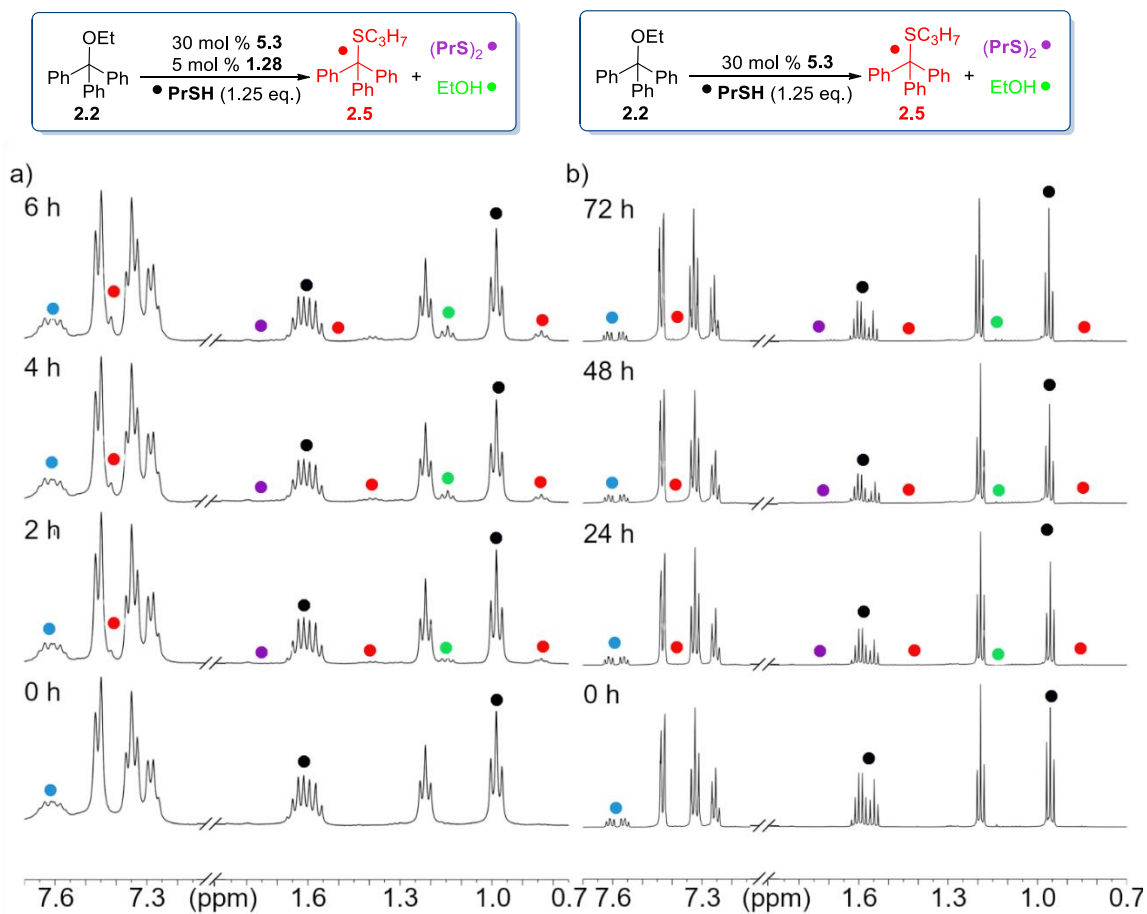


Figure 7.120. ^1H NMR spectra (7.70-7.10 ppm, 1.90-0.70 ppm) of the acid promoted substitution reaction between **4b** and *n*-propyl thiol in 400 μL CD_3CN in the presence of: a) 5 mol % cage **1.28** and 30 mol % acid **3b** b) 30 mol % acid **3b**. [**4b**] = 15.8 mM, [**PrSH**] = 19.8 mM, [**1**] = 0.8 mM, [**3b**] = 4.74 mM, reactions were performed at 80 $^\circ\text{C}$ in CD_3CN and monitored over time (600 MHz, 298 K, CD_3CN).

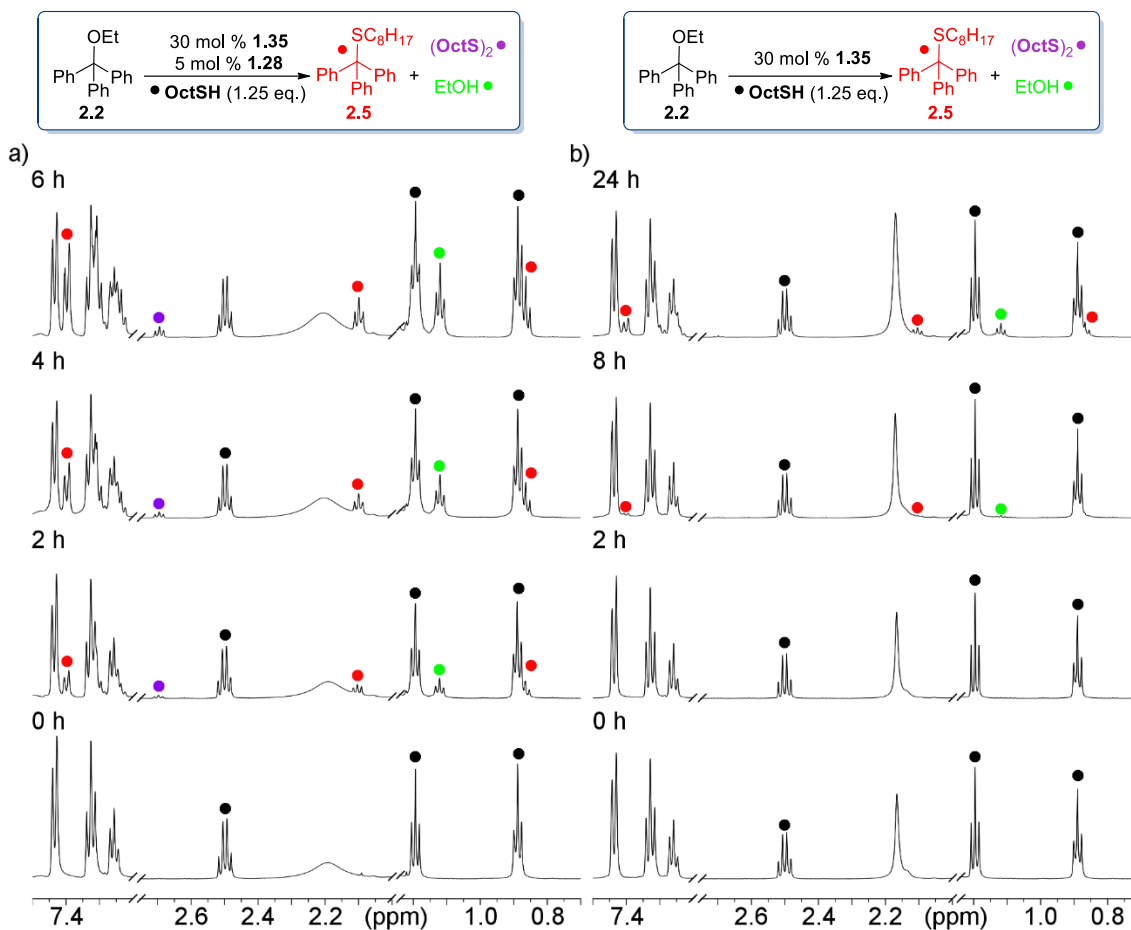


Figure 7.121. ^1H NMR spectra (7.50-7.20 ppm, 2.75-2.00 ppm, 1.14-0.70 ppm) of the acid promoted substitution reaction between **2.2** and *n*-octyl mercaptan in 400 μL CD_3CN in the presence of: a) 5 mol % cage **1.28** and 30 mol % acid **1.35** b) 30 mol % acid **1.35**. $[\mathbf{2.2}] = 15.8 \text{ mM}$, $[\text{OctSH}] = 19.8 \text{ mM}$, $[\mathbf{1.28}] = 0.8 \text{ mM}$; $[\mathbf{1.35}] = 4.74 \text{ mM}$, reactions were performed at 80 $^\circ\text{C}$ in CD_3CN and monitored over time (600 MHz, 298 K, CD_3CN).

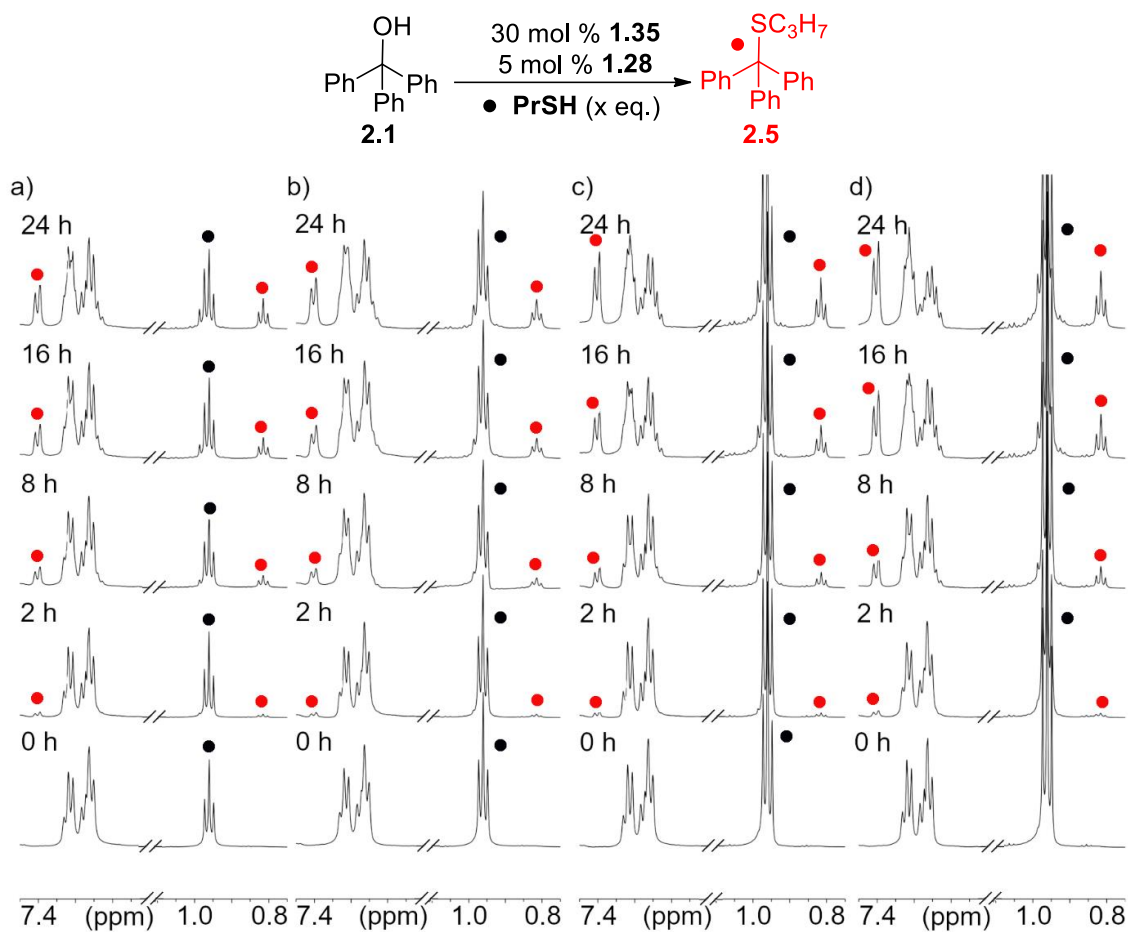


Figure 7.122. ^1H NMR spectra of the acid promoted substitution reaction between **2.1** and *n*-propyl thiol in the presence of 5 mol % cage **1.28** and 30 mol % acid **1.35**, at varying concentrations of PrSH a) 19.75 mM b) 37.3 mM c) 59.25 mM and d) 76.07 mM. $[\mathbf{2.1}] = 15.8$ mM, $[\mathbf{1.28}] = 0.8$ mM; $[\mathbf{1.35}] = 4.74$ mM, reactions were performed at 80 °C in CD_3CN and monitored over time (400 MHz, 298K, CD_3CN).

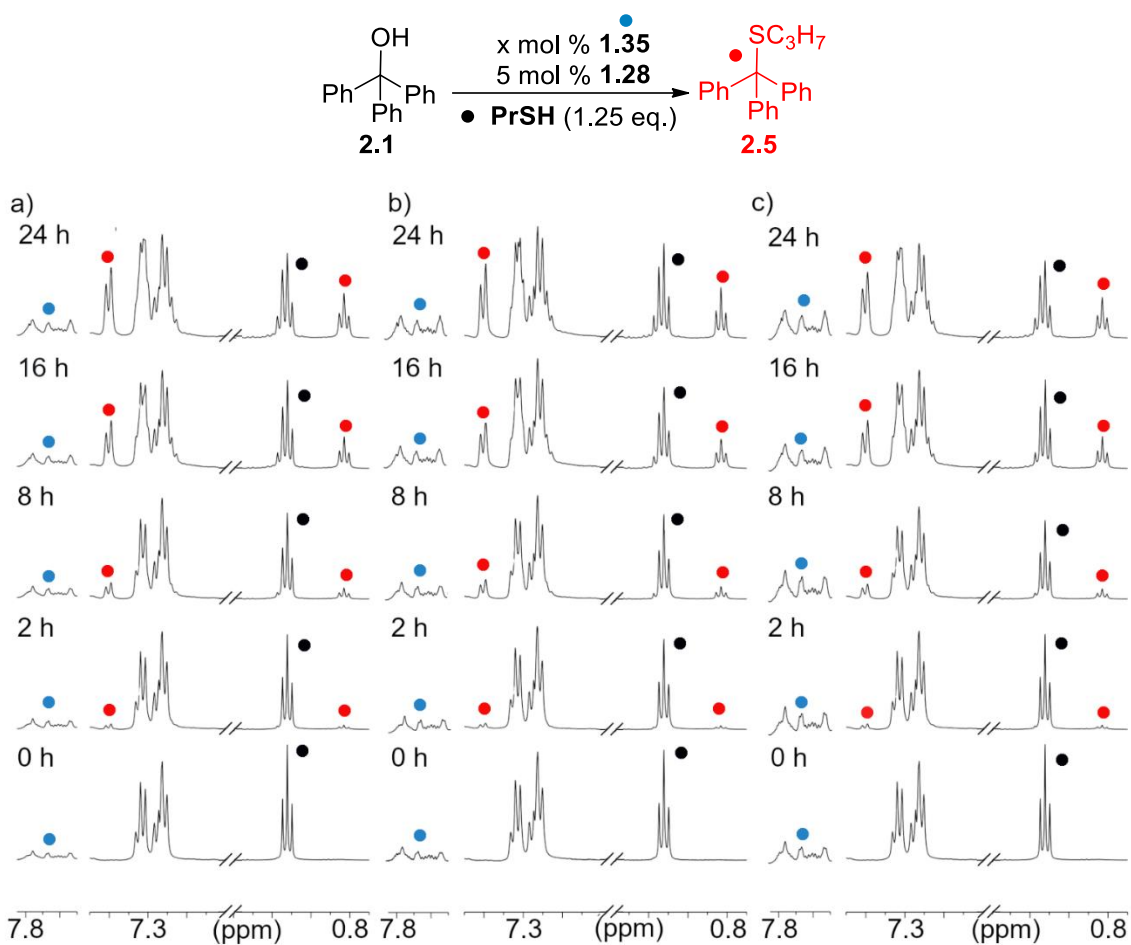


Figure 7.123. ^1H NMR spectra of the acid promoted substitution reaction between **2.1** and *n*-propyl thiol in the presence of 5 mol % cage **1.28** and at varying concentrations of acid **1.35**, a) 1.58 mM, b) 3.15 mM and c) 4.73 mM. $[\mathbf{2.1}] = 15.8$ mM, $[\text{PrSH}] = 19.8$ mM, $[\mathbf{1.28}] = 0.8$ mM, reactions were performed at 80 °C in CD_3CN and monitored over time (600 MHz, 298K, CD_3CN).

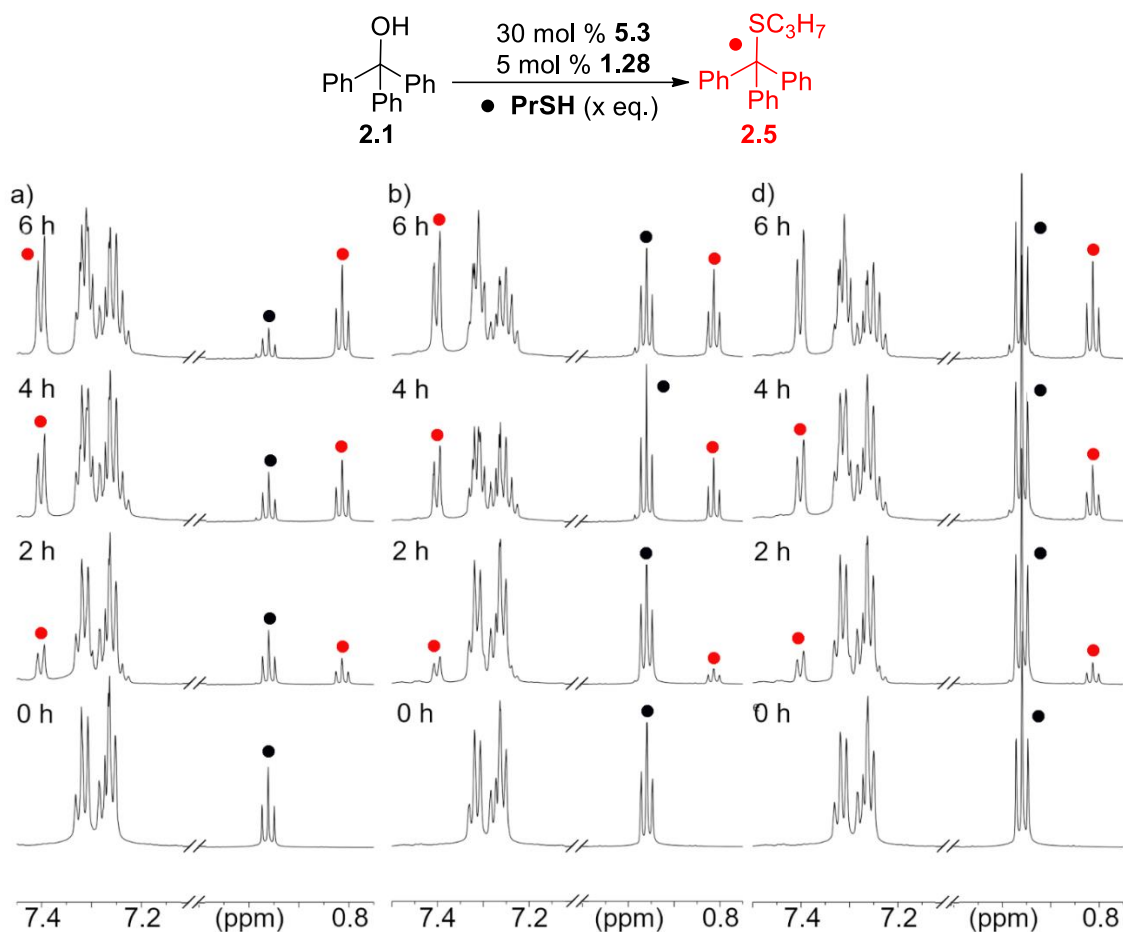


Figure 7.124. ^1H NMR spectra of the acid promoted substitution reaction between **2.1** and *n*-propyl thiol in the presence of 5 mol % cage **1.28** and 30 mol % acid **5.3**, at varying concentrations of **PrSH** a) 9.45 mM b) 18.11 mM and c) 33.08 mM. [**2.1**] = 15.8 mM, [**1.28**] = 0.8 mM, [**5.3**] = 4.74 mM, reactions were performed at 80 °C in CD_3CN and monitored over time (400 MHz, 298K, CD_3CN).

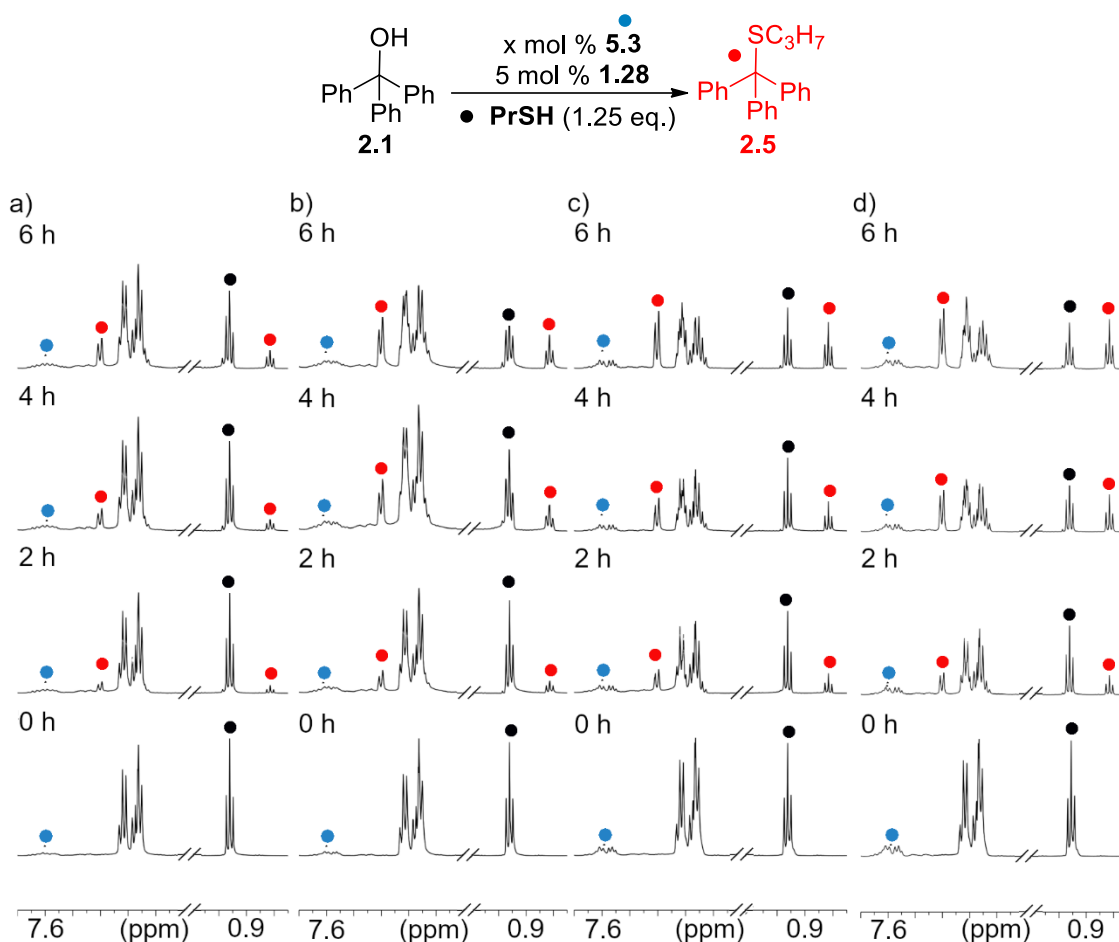


Figure 7.125. ^1H NMR spectra of the acid promoted substitution reaction between 2.1 and *n*-propyl thiol in the presence of 5 mol % cage 1.28 and at varying concentrations of acid 5.3, a) 0.79 mM, b) 1.58 mM, c) 3.15 mM and d) 4.73 mM. [2.1] = 15.8 mM, [PrSH] = 19.8 mM, [1.28] = 0.8 mM, reactions were performed at 80 °C in CD_3CN and monitored over time (600 MHz, 298K, CD_3CN).

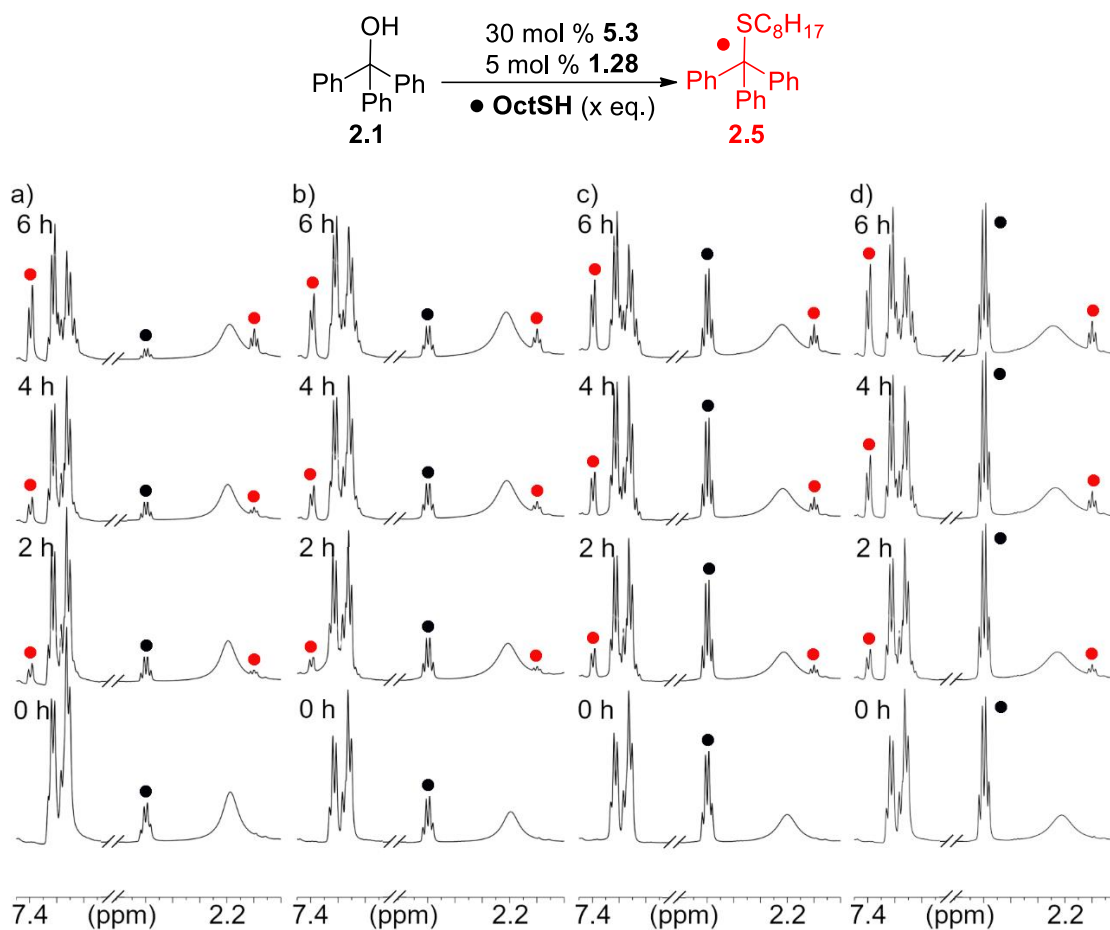


Figure 7.126. ^1H NMR spectra of the acid promoted substitution reaction between **2.1** and *n*-octyl mercaptan in the presence of 5 mol % cage **1.28** and 30 mol % acid **1.35**, at varying concentrations of **OctSH** a) 11.88 mM, b) 21.26 mM, c) 24.48 mM, and d) 62.37 mM. $[\mathbf{2.1}] = 15.8$ mM, $[\mathbf{1.28}] = 0.8$ mM, $[\mathbf{1.35}] = 4.74$ mM, reactions were performed at 80 °C in CD_3CN and monitored over time (600 MHz, 298K, CD_3CN).

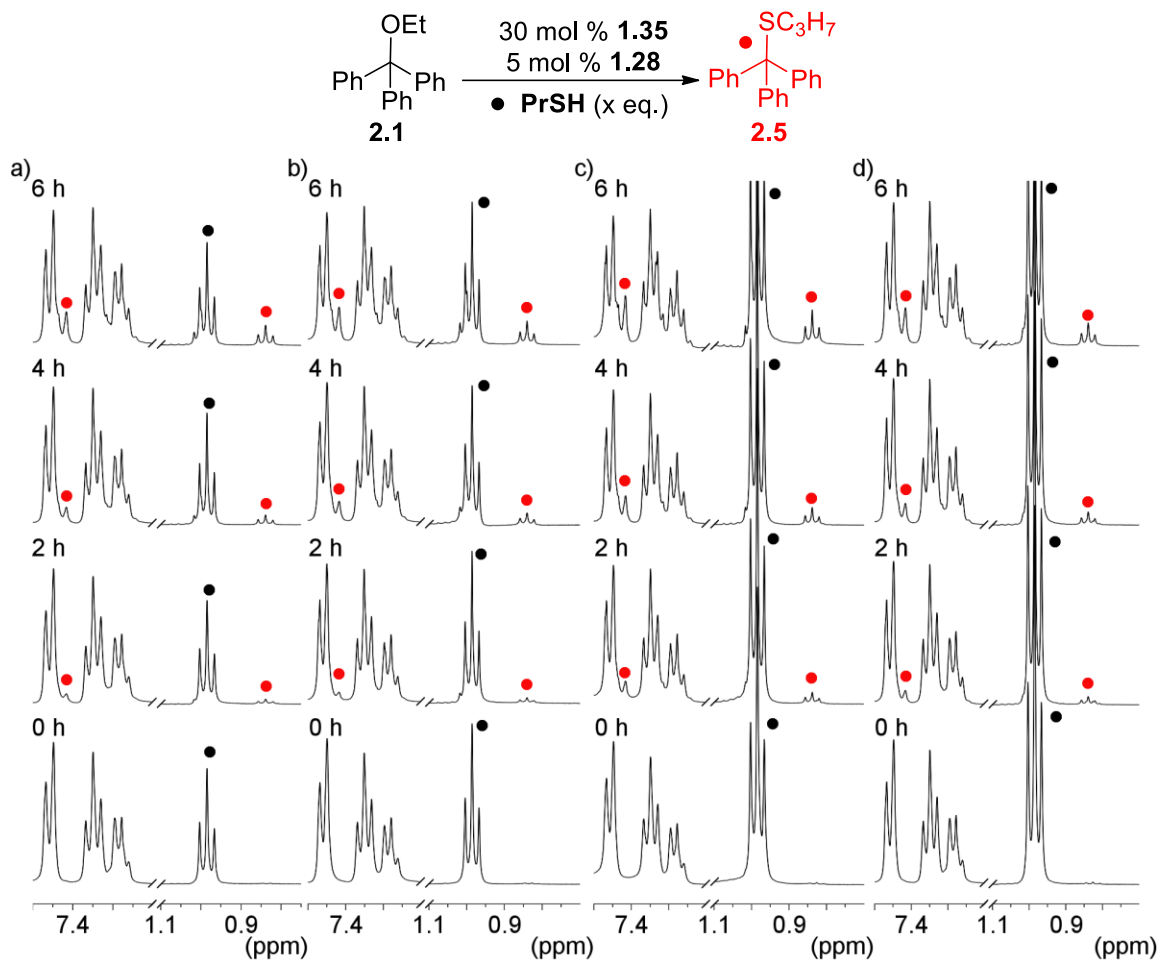


Figure 7.127. ^1H NMR spectra of the acid promoted substitution reaction between **2.2** and *n*-propyl thiol in the presence of 5 mol % cage **1.28** and 30 mol % acid **1.35**, at varying concentrations of **PrSH** a) 14.96 mM, b) 23.63, c) 39.5 mM, and d) 54.96 mM. $[\mathbf{2.2}] = 15.8$ mM, $[\mathbf{1.28}] = 0.8$ mM, $[\mathbf{1.35}] = 4.74$ mM, reactions were performed at 80 °C in CD_3CN and monitored over time (400 MHz, 298K, CD_3CN).

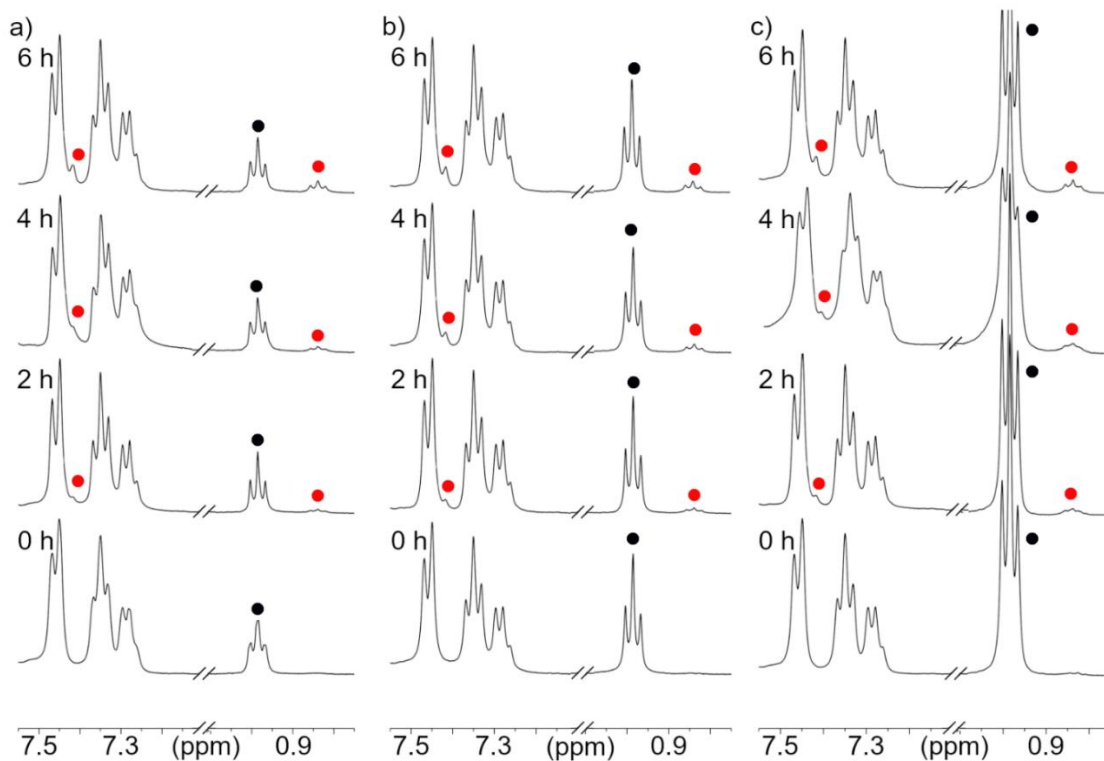
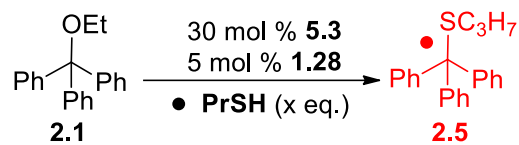


Figure 7.128. ^1H NMR spectra of the acid promoted substitution reaction between **2.2** and *n*-propyl thiol in the presence of 5 mol % cage **1.28** and 30 mol % acid **5.3**, at varying concentrations of **PrSH** a) 10.08 mM, b) 18.11, and c) 56.3 mM. [**2.2**] = 15.8 mM, [**1.28**] = 0.8 mM, [**5.3**] = 4.74 mM, reactions were performed at 80 °C in CD_3CN and monitored over time (400 MHz, 298K, CD_3CN).

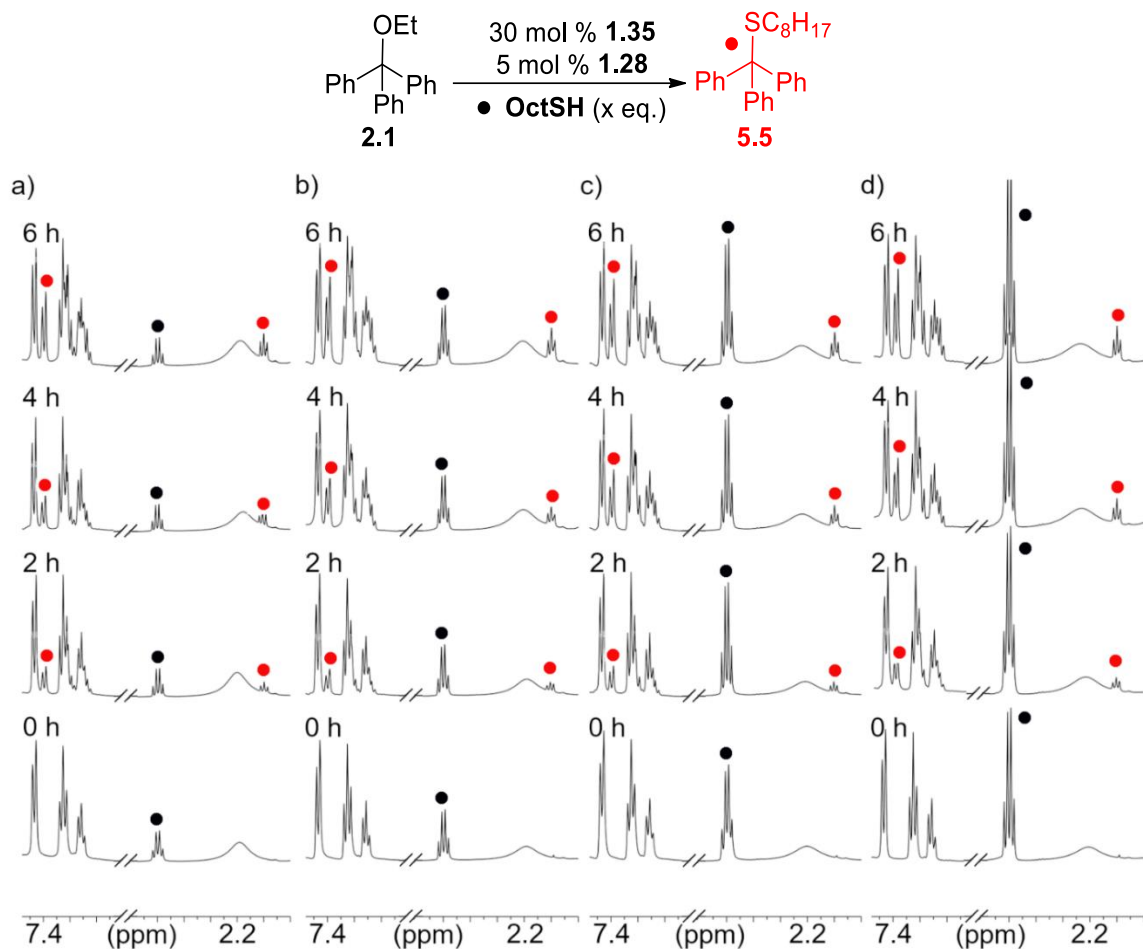


Figure 7.129. ^1H NMR spectra of the acid promoted substitution reaction between **2.2** and *n*-octyl mercaptan in the presence of 5 mol % cage **1.28** and 30 mol % acid **1.35**, at varying concentrations of **OctSH** a) 12.28 mM, b) 20.94 mM, c) 39.37 mM, and d) 57.65 mM. $[\mathbf{2.2}] = 15.8 \text{ mM}$, $[\mathbf{1.28}] = 0.8 \text{ mM}$, $[\mathbf{1.35}] = 4.74 \text{ mM}$, reactions were performed at $80 \text{ }^\circ\text{C}$ in CD_3CN and monitored over time (600 MHz, 298K, CD_3CN).

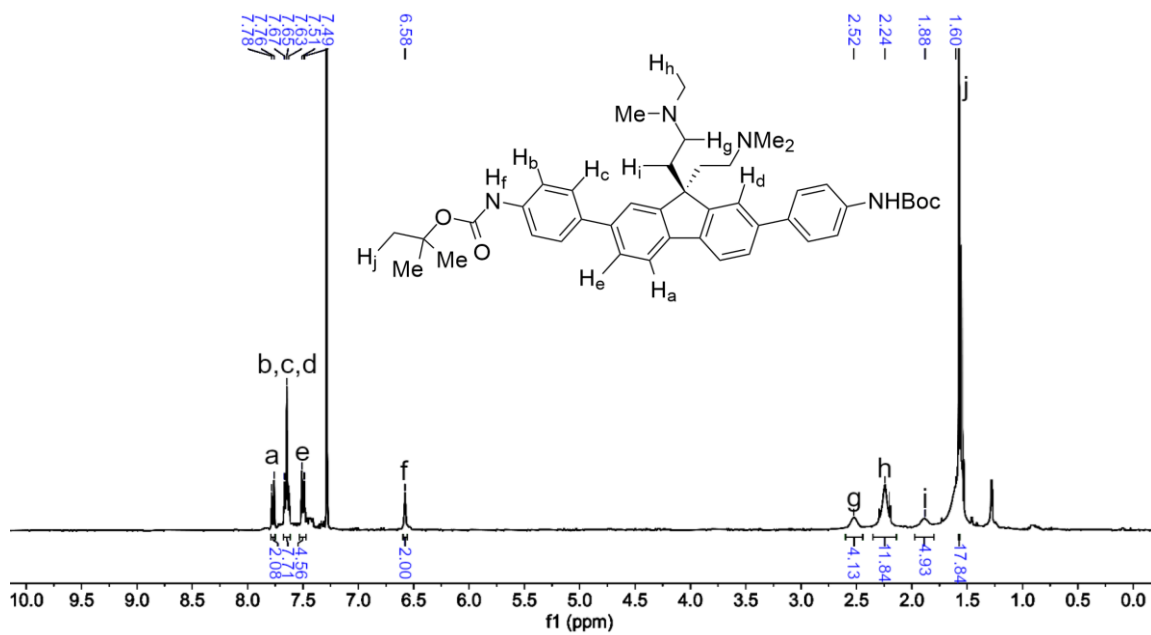


Figure 7.132. ^1H NMR spectrum of **6.3** (CD_3CN , 400 MHz, 298 K).

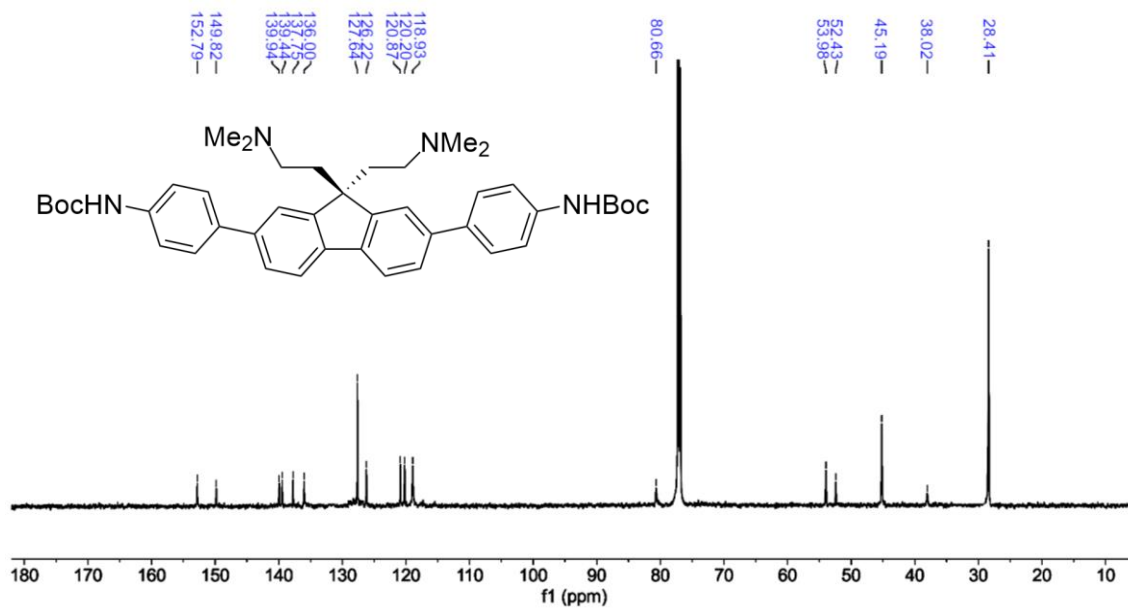


Figure 7.133. $^{13}\text{C}\{^1\text{H}\}$ NMR spectrum of **6.3** (CDCl_3 , 100 MHz, 298 K).

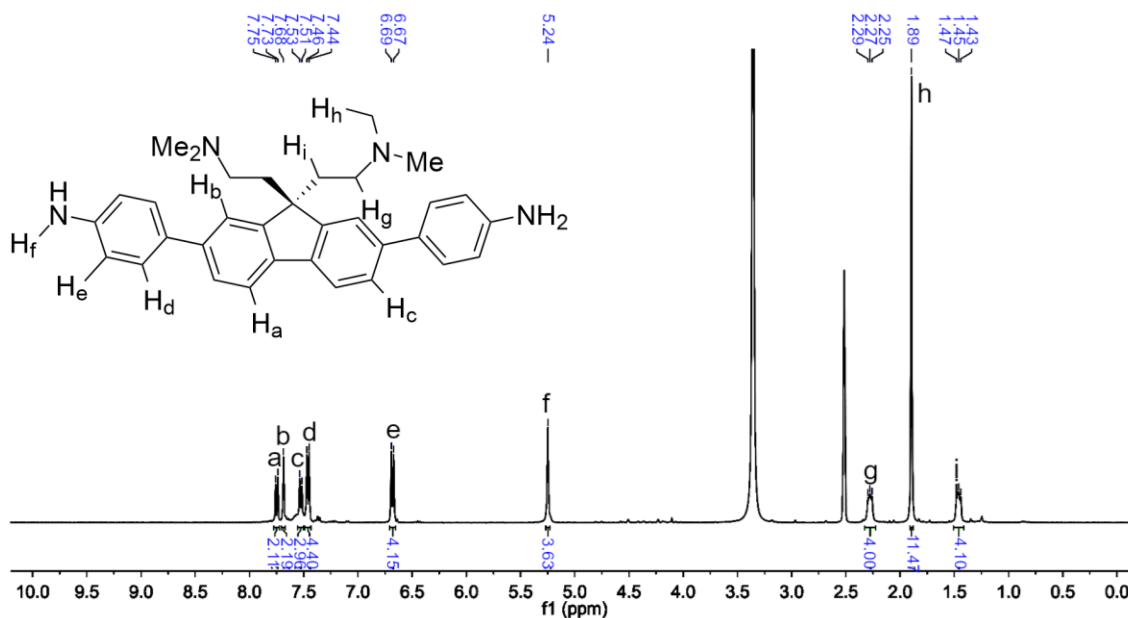


Figure 7.134. ^1H NMR spectrum of **6.4** (DMSO- d_6 , 400 MHz, 298 K).

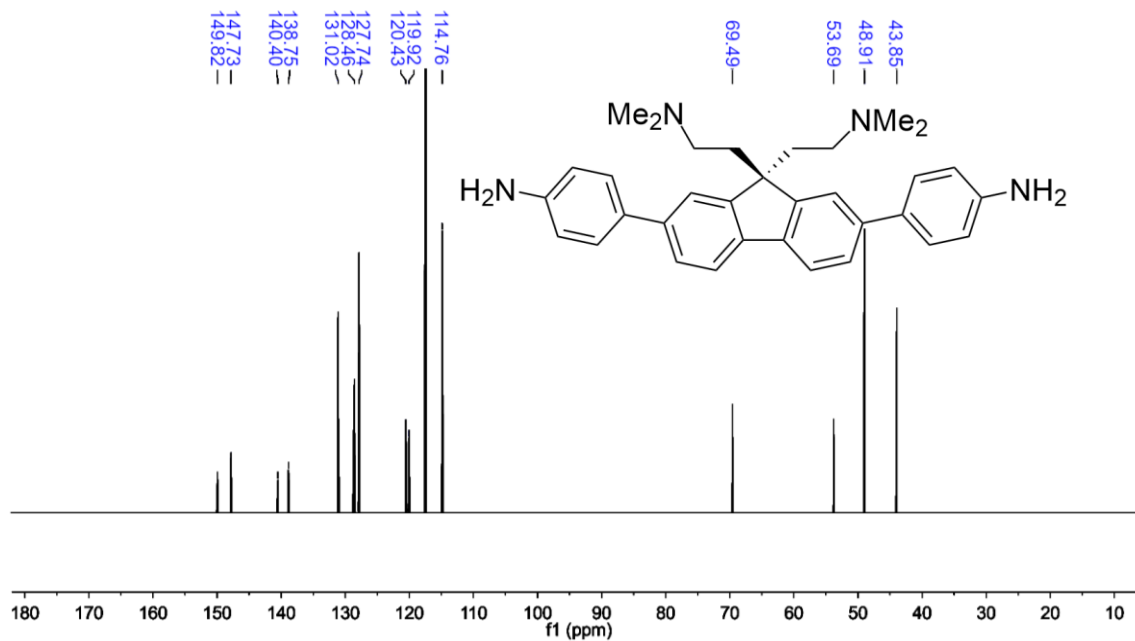


Figure 7.135. $^{13}\text{C}\{^1\text{H}\}$ NMR spectrum of **6.4** (DMSO- d_6 , 100 MHz, 298 K).

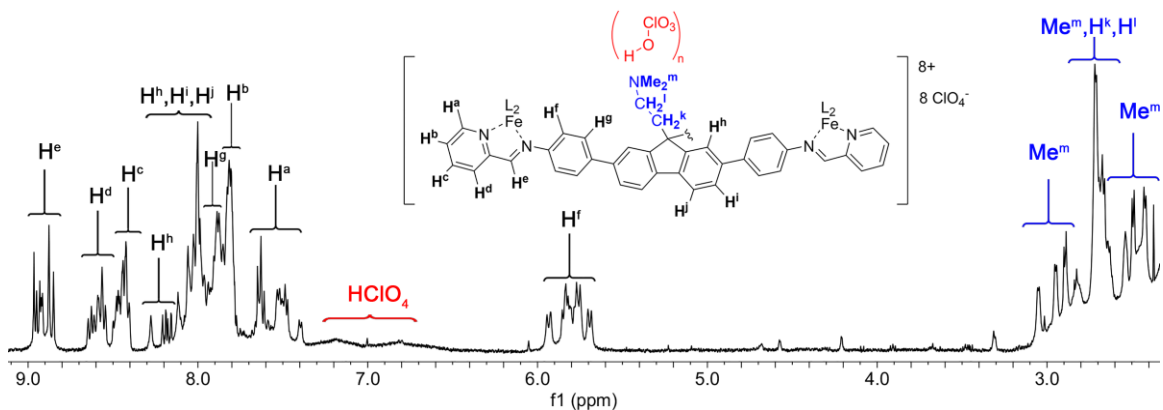


Figure 7.136. ^1H NMR spectrum of cage **6.1** (CD_3CN , 400 MHz, 298 K).

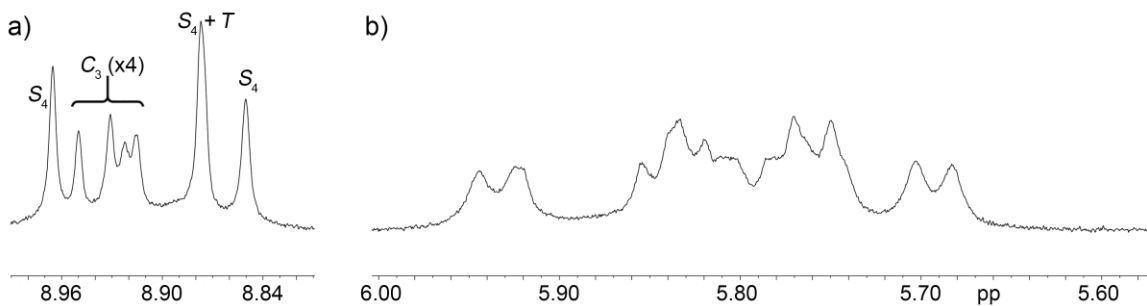


Figure 7.137. Expansions of the ^1H NMR spectrum of cage **6.1** (CD_3CN , 400 MHz, 298 K): a) imine region (H^e); b) aniline region (H^f), indicating isomer distribution.

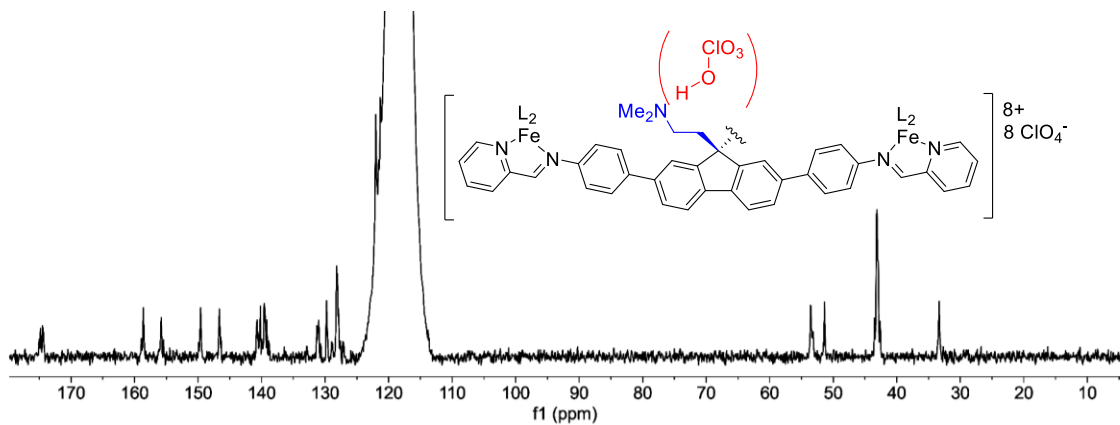


Figure 7.138. $^{13}\text{C}\{^1\text{H}\}$ NMR spectrum of cage **6.1** (CD_3CN , 100 MHz, 298 K).

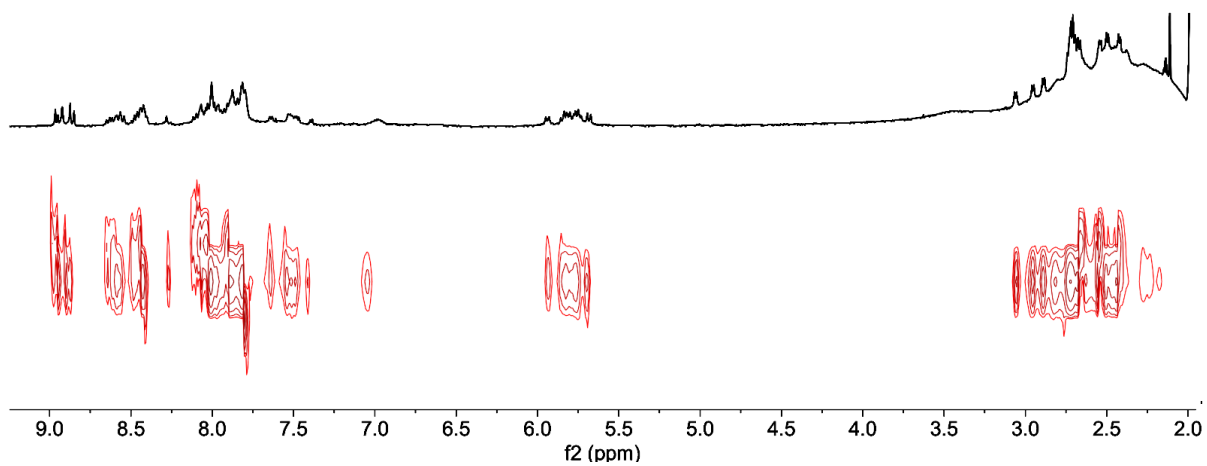


Figure 7.139. 2D-DOSY NMR spectrum of cage **6.1** (CD_3CN , 600 MHz, 298 K, $D(\mathbf{6.1}) = 4.04 \times 10^{-10} \text{ m}^2/\text{s}^2$).

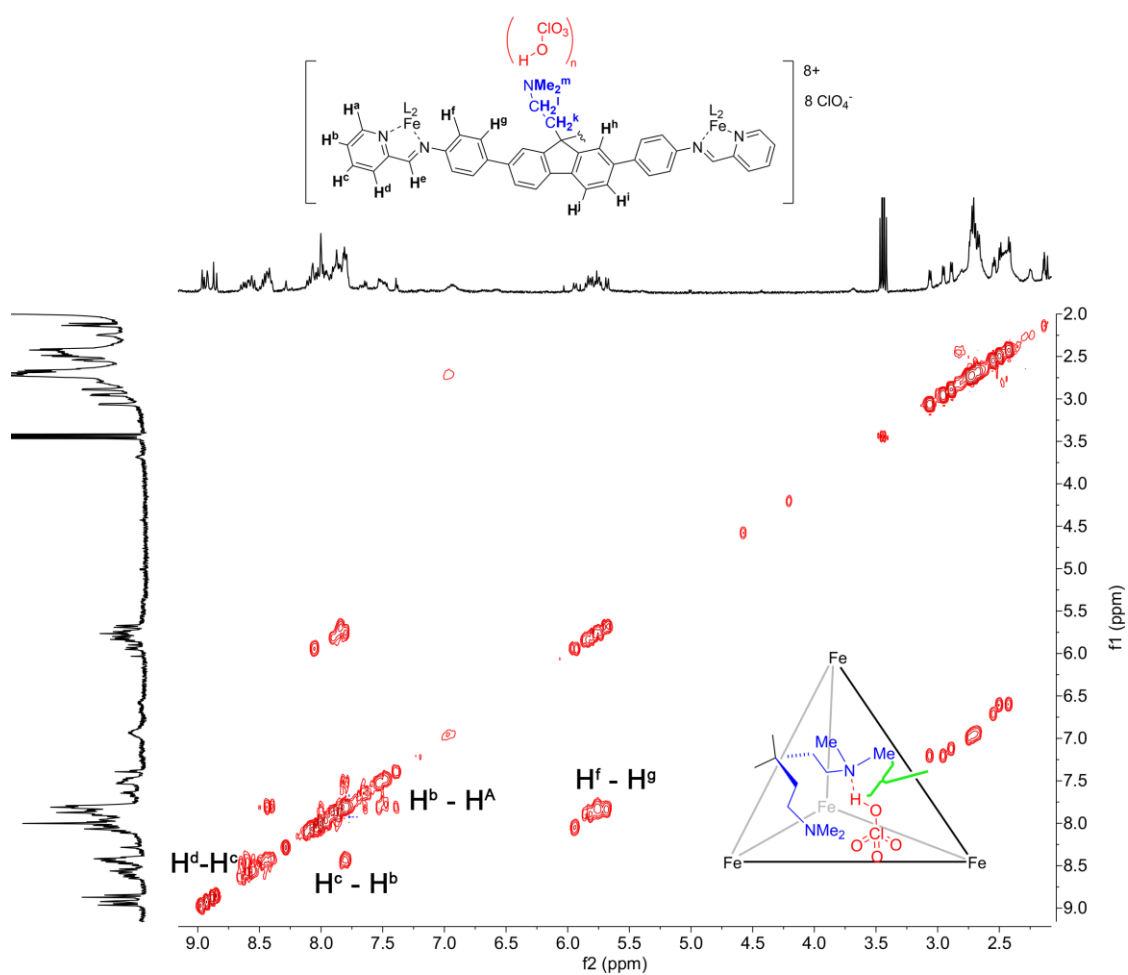


Figure 7.140. gCOSY NMR spectrum of cage **6.1** (CD_3CN , 400 MHz, 298 K).

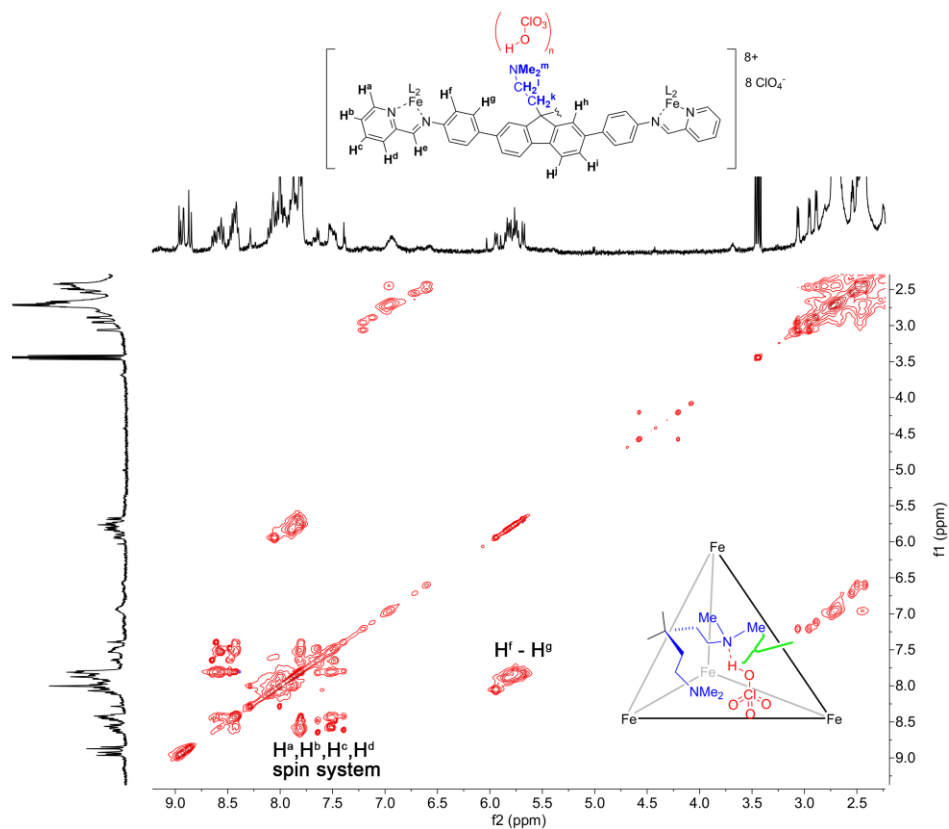


Figure 7.141. TOCSY NMR spectrum of cage **6.1** (CD_3CN , 600 MHz, 298 K, mixing time = 80 ms).

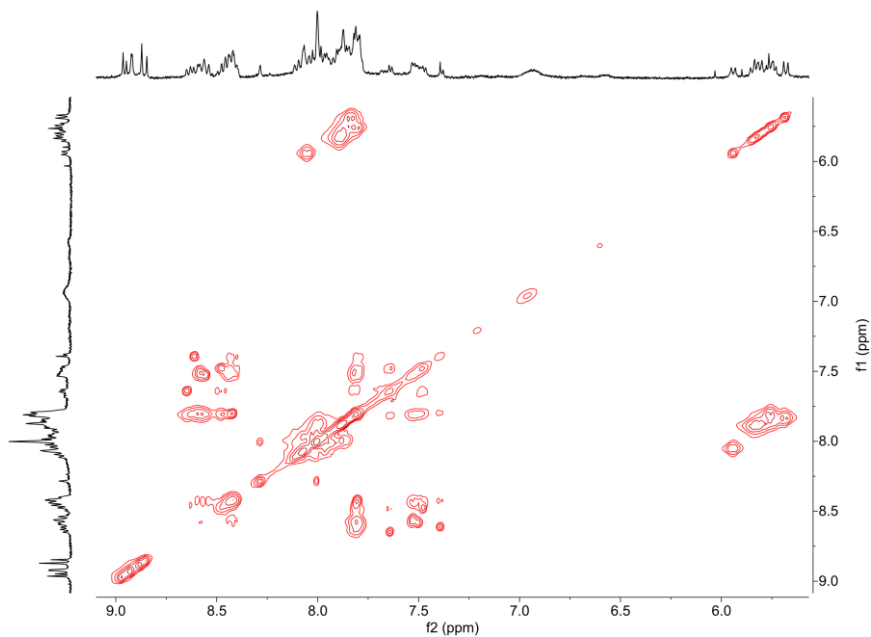


Figure 7.142. Expansion of the aromatic region of the TOCSY NMR spectrum of cage **6.1** (CD_3CN , 600 MHz, 298 K, mixing time = 80 ms).

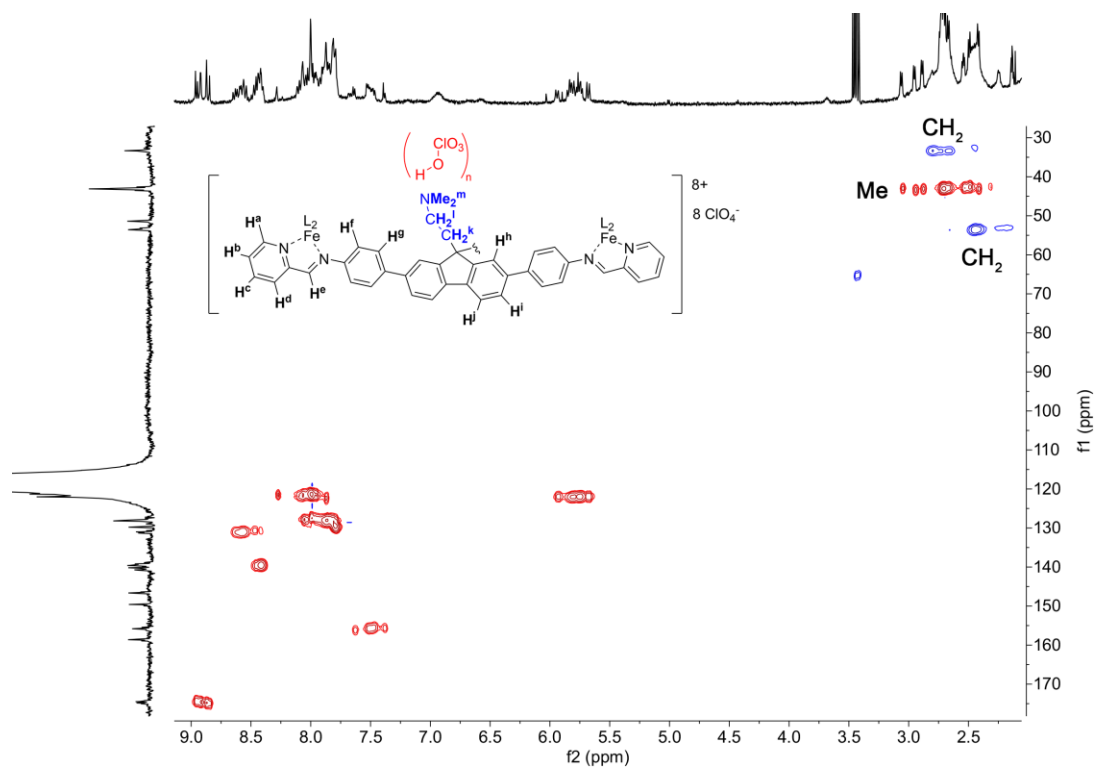


Figure 7.143. DEPT-HSQC NMR spectrum of cage **6.1** (CD_3CN , 400 MHz, 298 K).

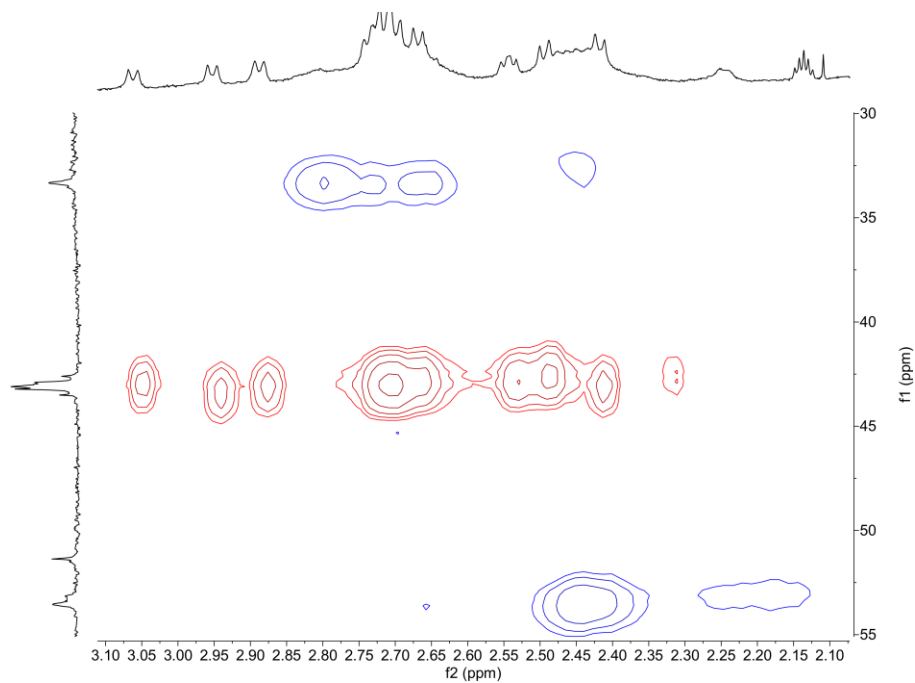


Figure 7.144. Expansion of the aliphatic region of the DEPT-HSQC NMR spectrum of cage **6.1** indicating the CH_2 (blue) and NMe_2 groups (red) in the spectrum (CD_3CN , 400 MHz, 298 K).

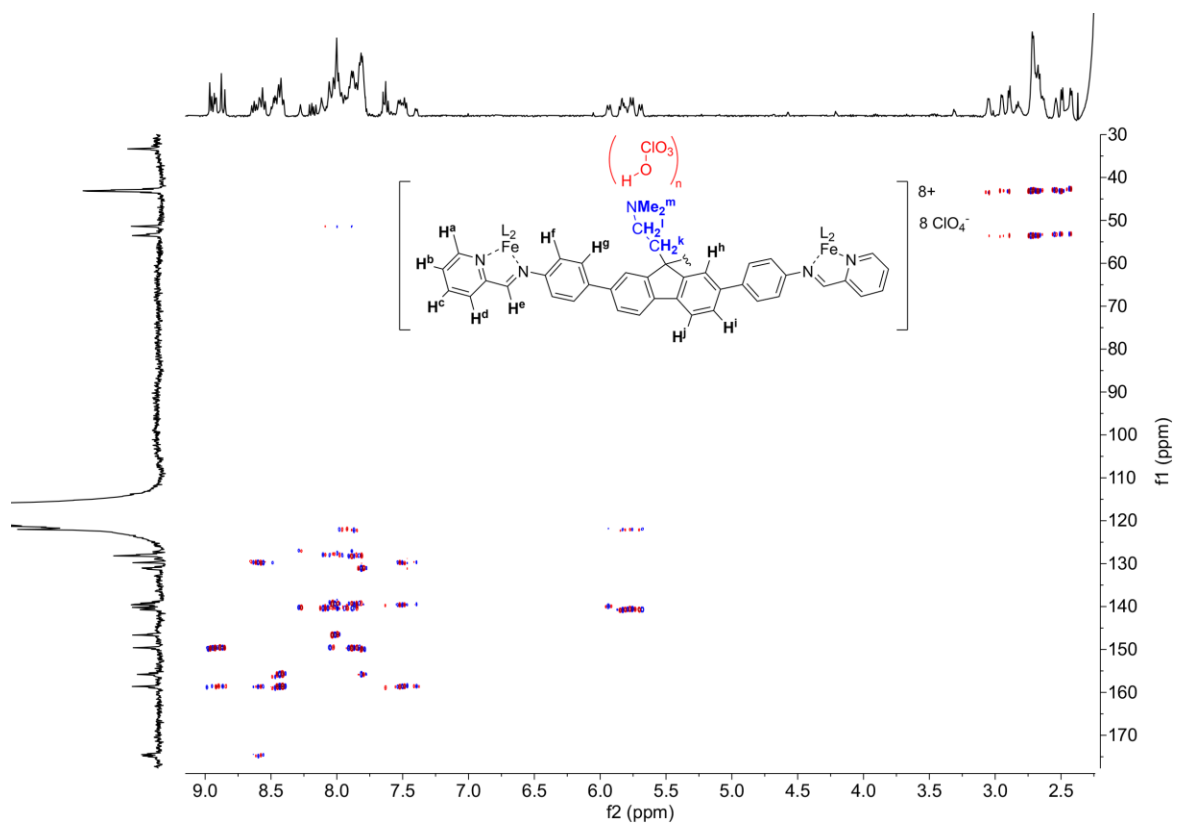


Figure 7.145. HMBC NMR spectrum of cage **6.1** (CD₃CN, 400 MHz, 298 K).

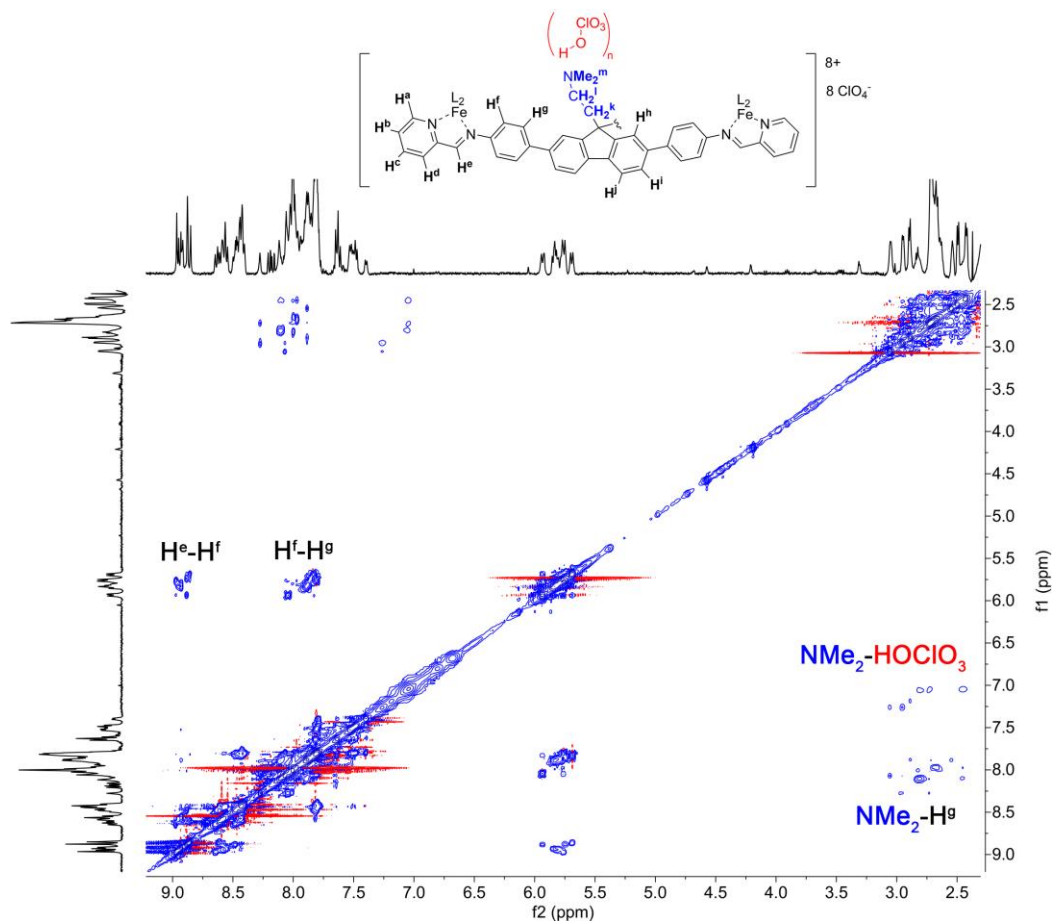


Figure 7.146. gNOESY NMR spectrum of cage **6.1** (CD₃CN, 600 MHz, 298 K, mixing time = 300 ms).

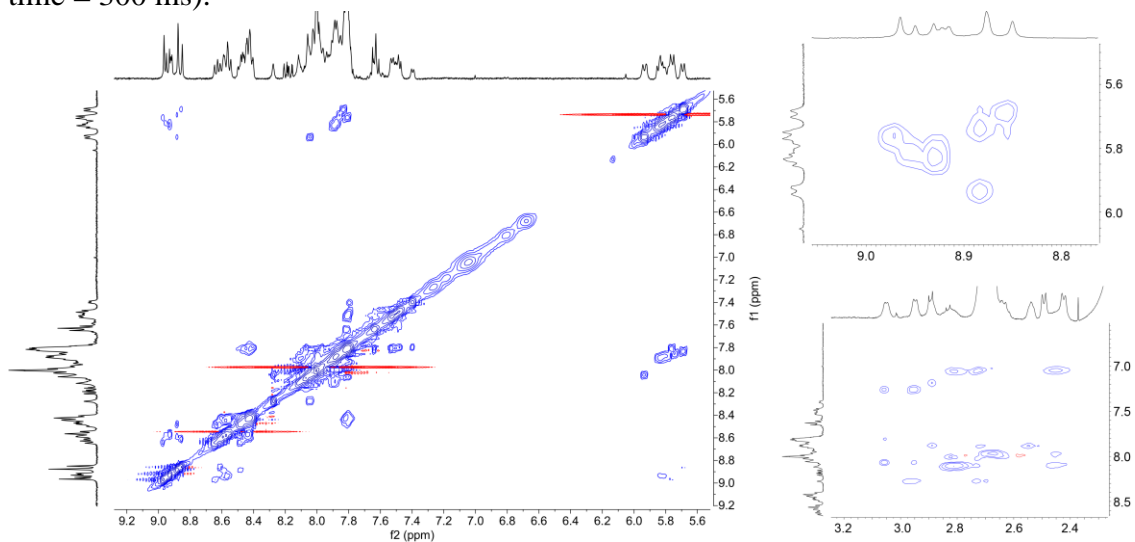


Figure 7.147. Expansions of the gNOESY NMR spectrum of cage **6.1** (CD₃CN, 600 MHz, 298 K, mixing time = 300 ms).

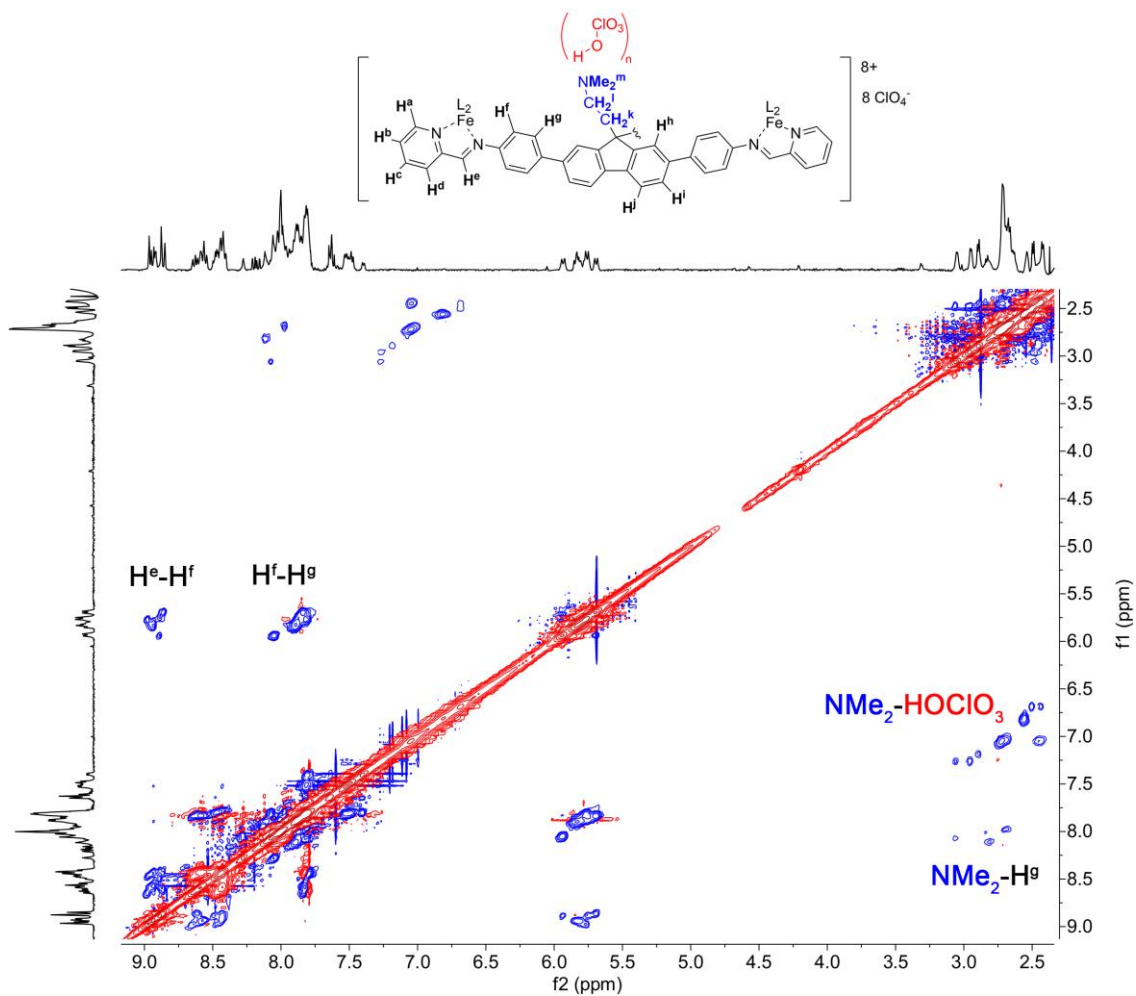


Figure 7.148. gROESY NMR spectrum of cage **6.1** (CD₃CN, 600 MHz, 298 K, mixing time = 300 ms).

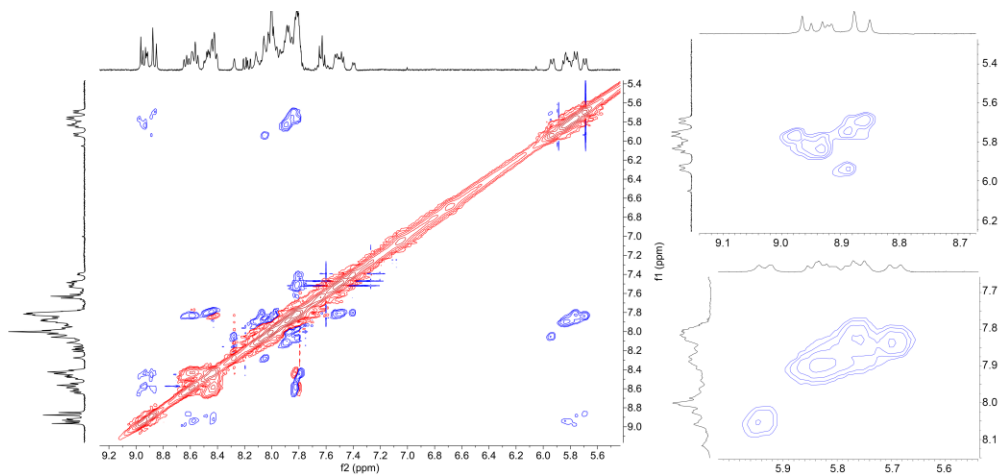


Figure 7.149. Expansions of the gROESY NMR spectrum of cage **6.1** (CD₃CN, 600 MHz, 298 K, mixing time = 300 ms).

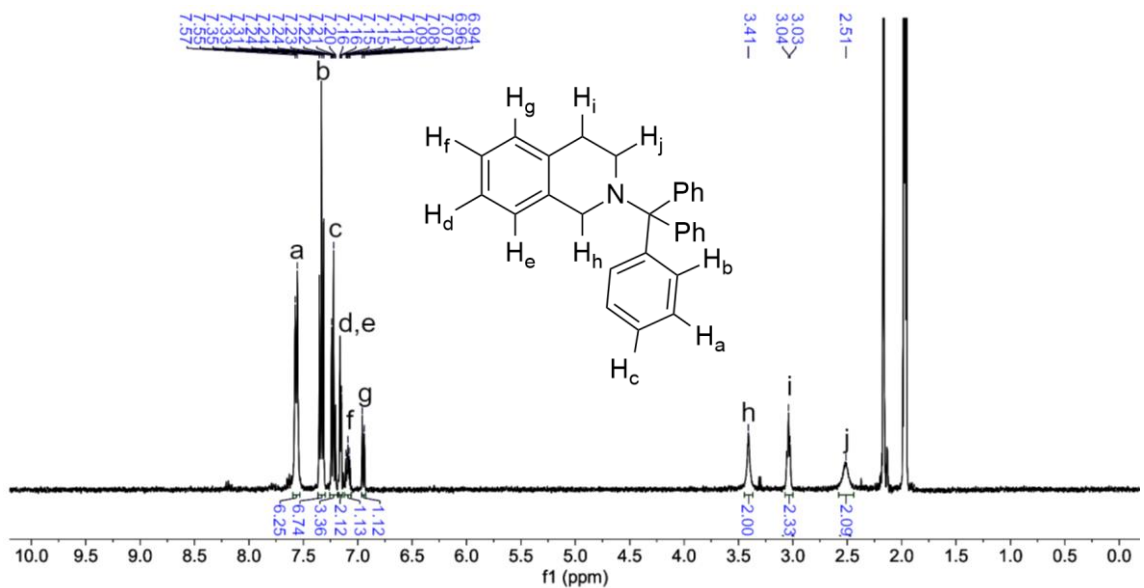


Figure 7.150. ^1H NMR spectrum of **6.12** (CD_3CN , 400 MHz, 298 K).

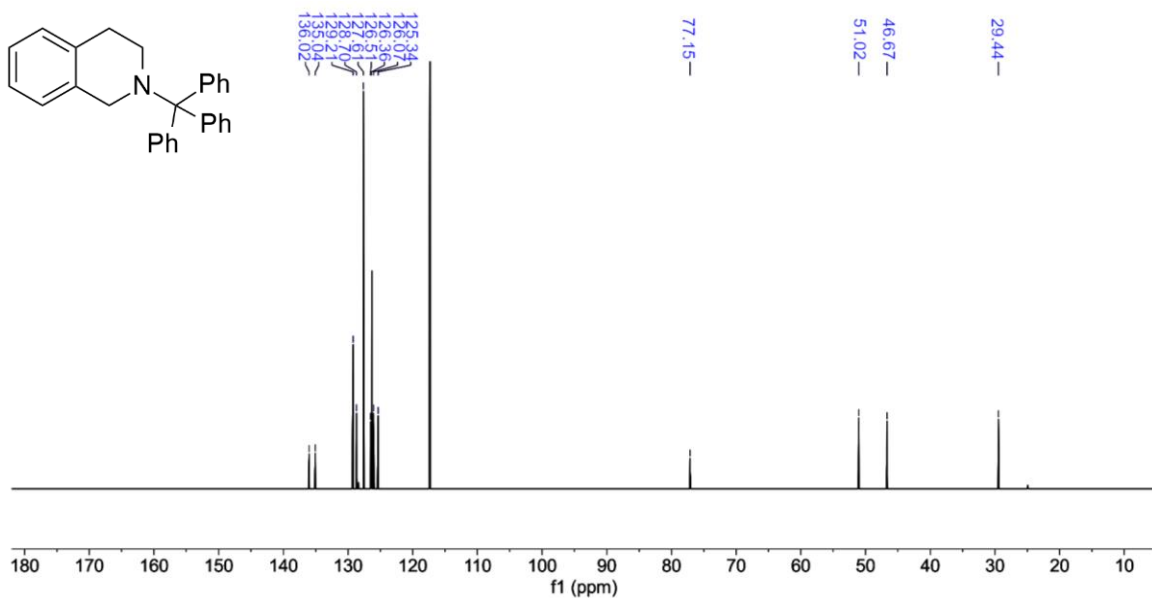


Figure 7.151. $^{13}\text{C}\{^1\text{H}\}$ NMR spectrum of **6.12** (CDCl_3 , 100 MHz, 298 K).

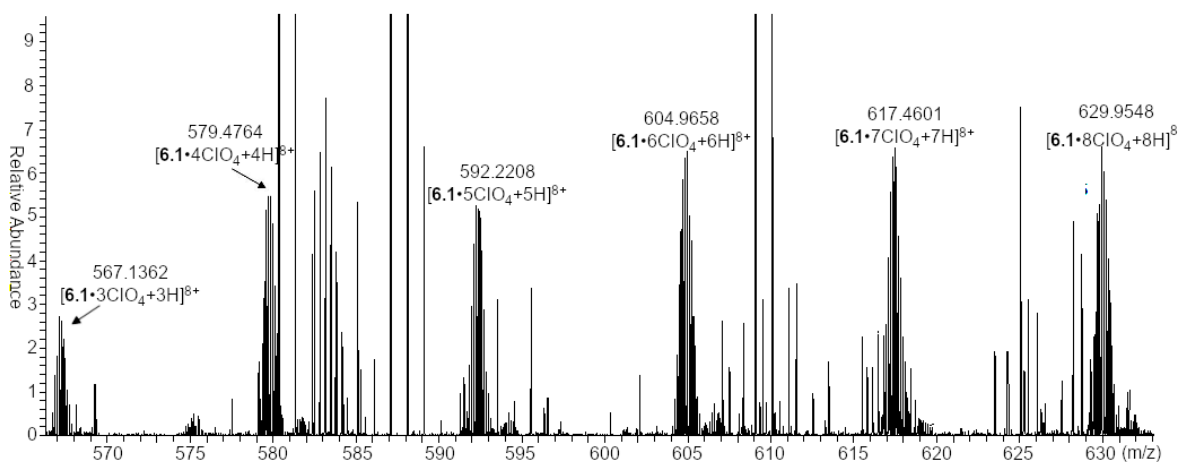


Figure 7.152. Expanded region from 567-633 m/z of ESI-mass spectrum of cage **6.1** in 100 % CH₃CN.

Table 7.1. Assigned ions for experimentally observed peaks.

Ion	Charge	Observed (m/z)	Predicted (m/z)
[6.4 +1H]	1	669.3794	669.3706
[6.4 +2H]	2	335.1935	335.1889
[6.1 •8ClO ₄ +8H]	8	629.9548	629.9465
[6.1 •7ClO ₄ +7H]	8	617.4601	617.4520
[6.1 •6ClO ₄ +6H]	8	604.9658	604.8325
[6.1 •5ClO ₄ +5H]	8	592.2208	592.3380
[6.1 •4ClO ₄ +4H]	8	579.4764	579.7261
[6.1 •3ClO ₄ +3H]	8	567.1362	567.2241

ESI-MS analysis, using an instrument with a nanoESI source and an orbitrap mass analyzer.

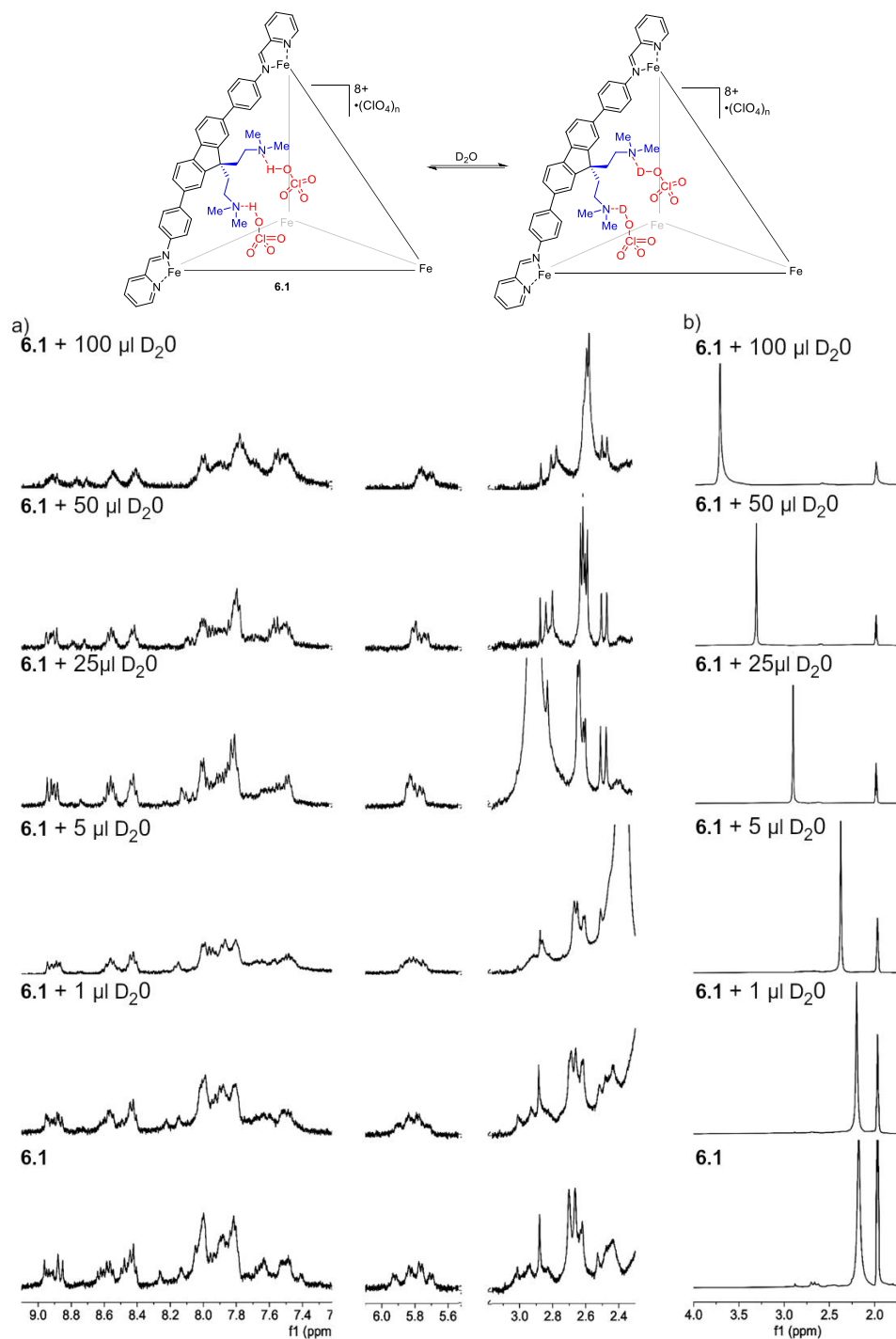


Figure 7.153. ^1H NMR spectra of the titration of D_2O into 5 mol % cage **6.1** showing: a) Cage stability (9.1 – 7.2 ppm, 6.2 – 5.5 ppm, and 3.2 – 2.3 ppm) b) Deuterium and hydrogen exchange (4.0 – 1.7 ppm). [**6.1**] = 0.8 – 0.63 mM, the reaction was performed at 23 °C in CD_3CN and monitored over time (400 MHz, 296 K, CD_3CN).

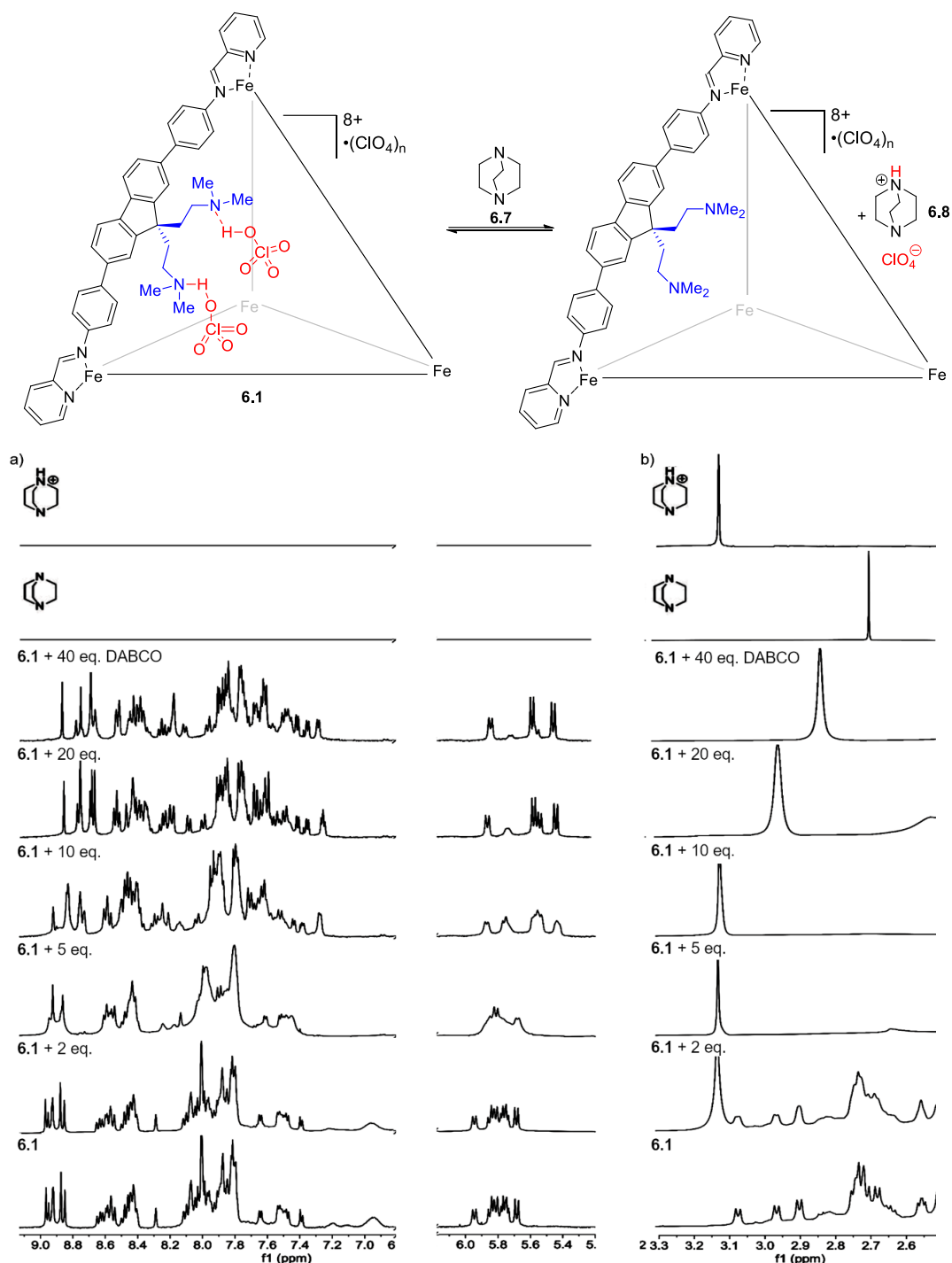


Figure 7.154. ^1H NMR spectra of the titration of DABCO **6.7** into 5 mol % cage **6.1** showing: a) Cage stability (9.2 – 6.8 ppm and 6.2 – 5.2 ppm) b) Formation of ammonium salt (3.3 – 2.5 ppm). $[\text{DABCO } \mathbf{6.7}] = 1.5 - 15.75 \text{ mM}$, $[\mathbf{6.1}] = 0.8 - 0.39 \text{ mM}$, the reaction was performed at 23°C in CD_3CN and monitored over time (400 MHz, 296 K, CD_3CN).

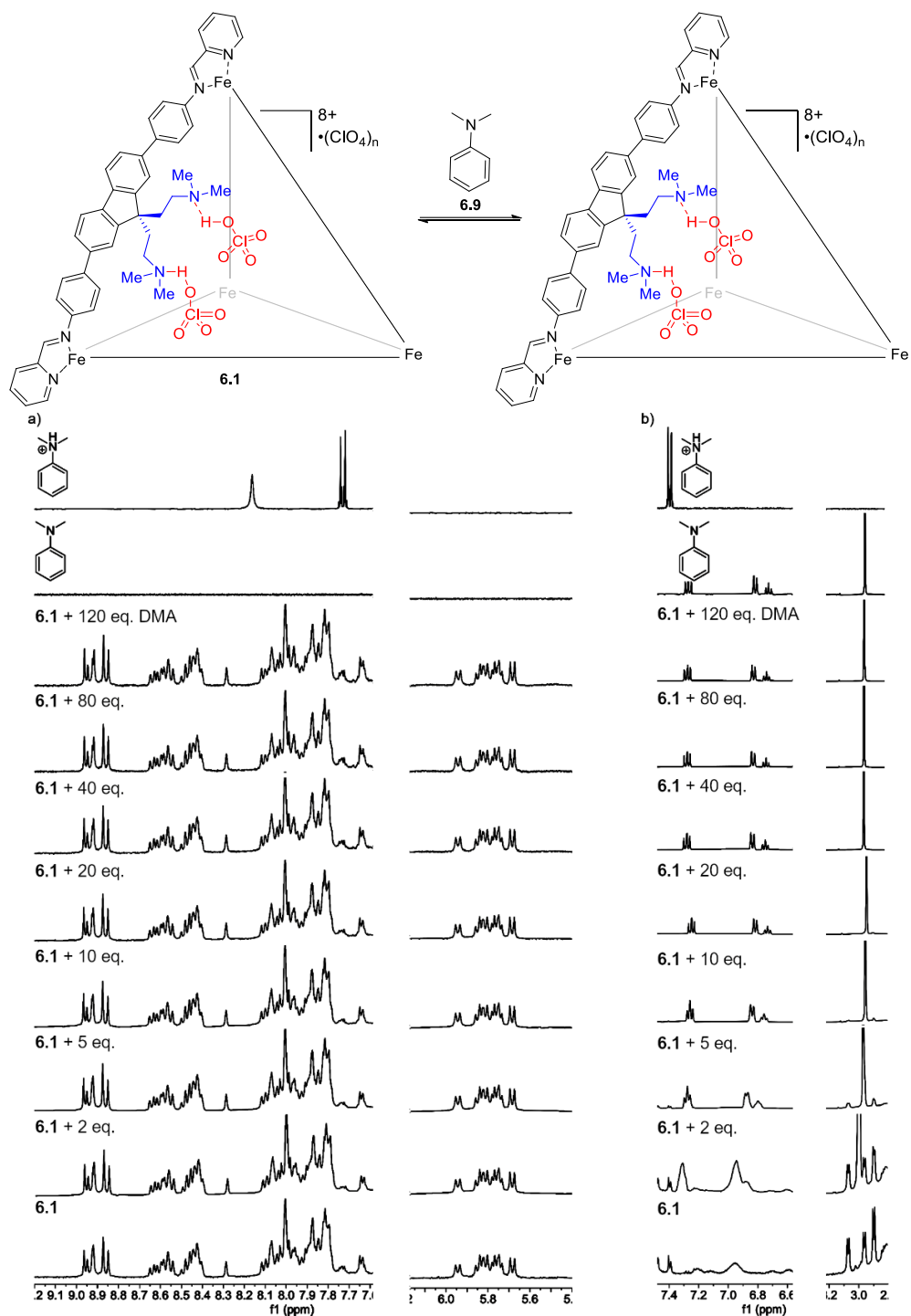


Figure 7.155. ^1H NMR spectra of the titration of DMA **6.9** into 5 mol % cage **6.1** showing: a) Cage stability (9.15 – 7.55 ppm and 6.2 – 5.45 ppm) b) Formation of ammonium salt (7.35 – 7.40 ppm and 3.3 – 2.85 ppm). [DMA **6.9**] = 1.5 – 23.6 mM, [**6.1**] = 0.8 – 0.2 mM, the reaction was performed at 23 °C in CD_3CN and monitored over time (400 MHz, 296 K, CD_3CN).

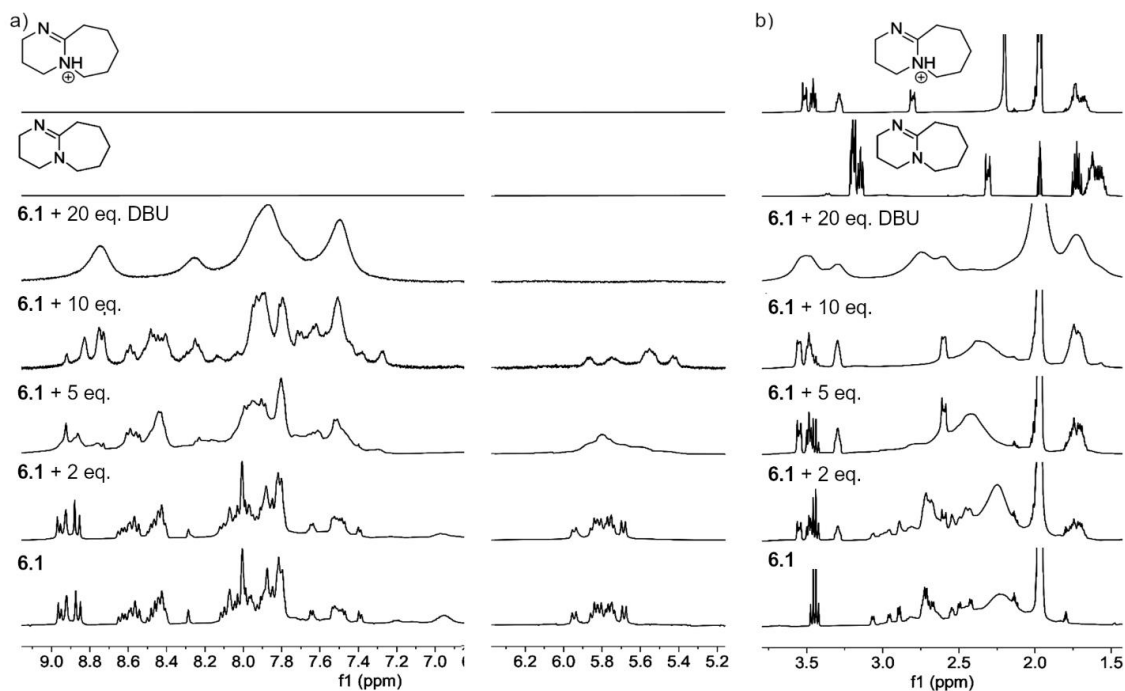
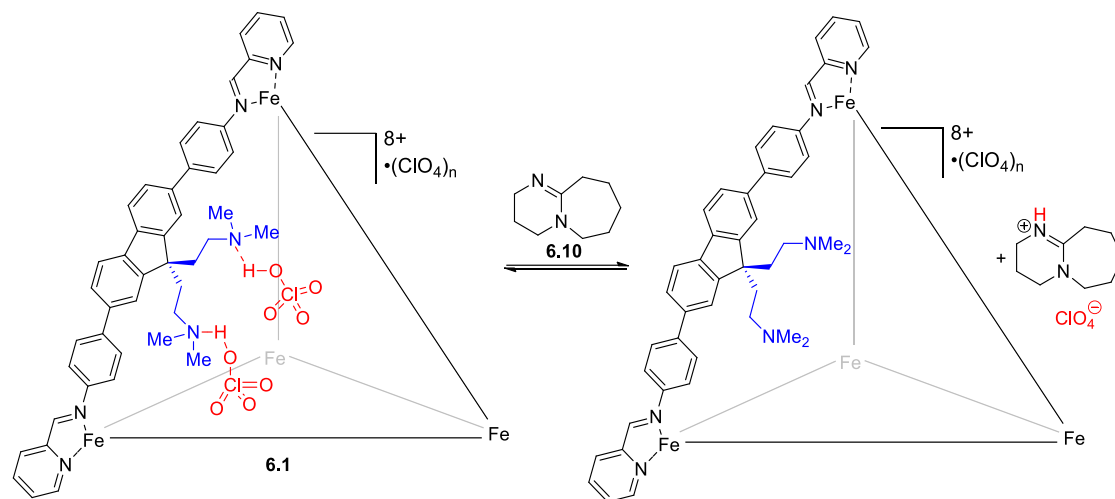


Figure 7.156. ¹H NMR spectra of the titration of DBU into 5 mol % cage **6.1** showing: a) Cage stability (9.2 – 6.8 ppm and 6.4 – 5.1 ppm) b) Formation of ammonium salt (3.8 – 1.45 ppm). [DBU] = 1.5 – 10.5 mM, [**6.1**] = 0.8 – 0.53 mM, the reaction was performed at 23 °C in CD₃CN and monitored over time (400 MHz, 296 K, CD₃CN).

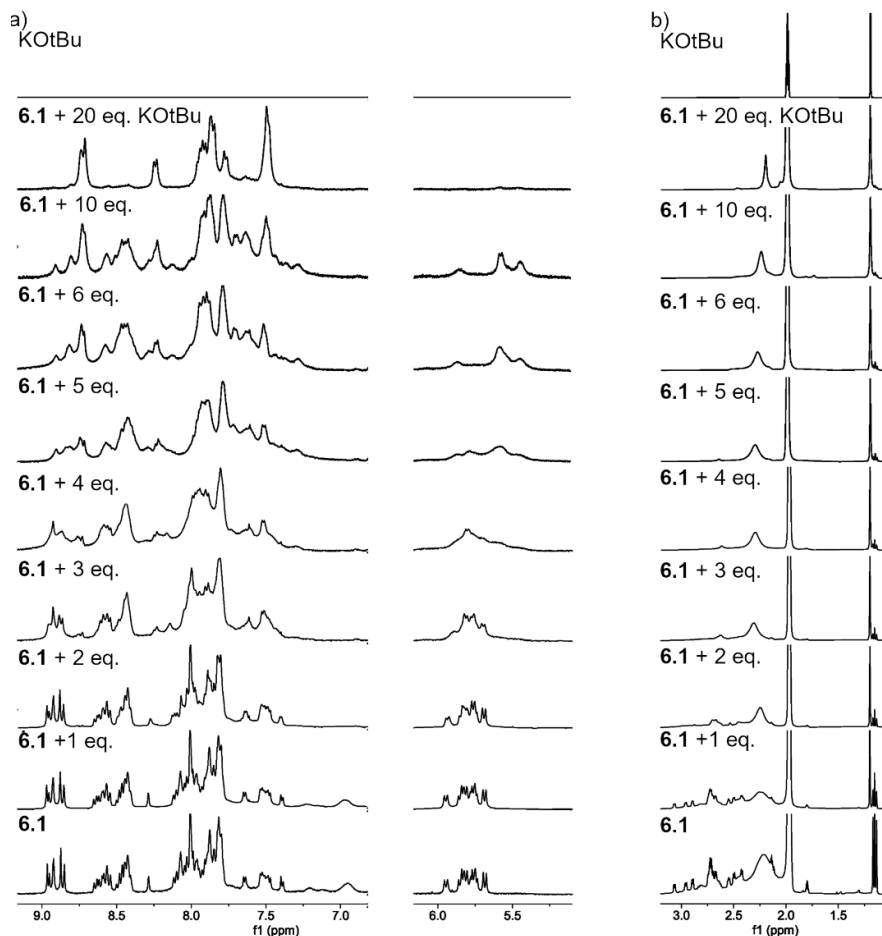
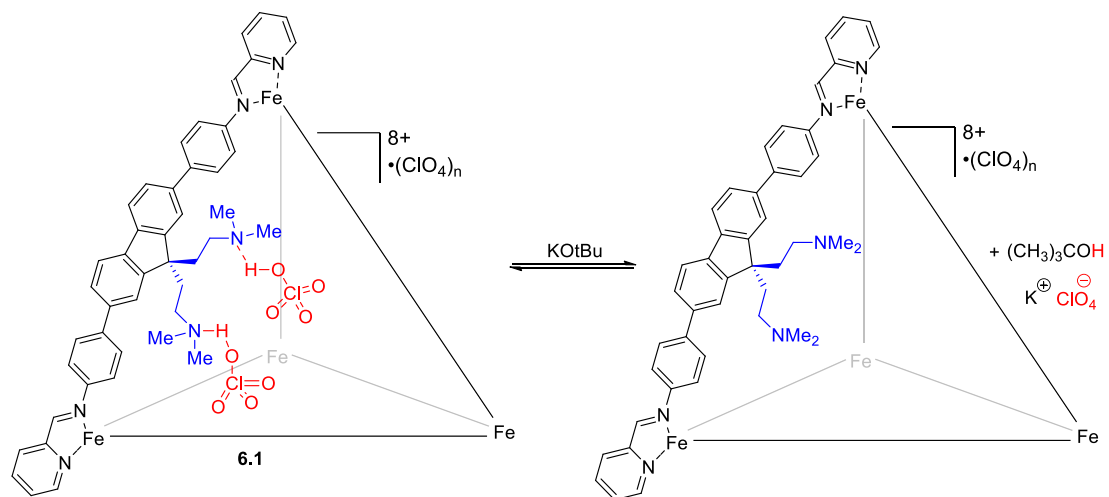


Figure 7.157. ^1H NMR spectra of the titration of KO^tBu into 5 mol % cage **6.1** showing: a) Cage stability (9.2 – 6.8 ppm and 6.2 – 5.1 ppm) b) Formation of ammonium salt (3.2 – 1.0 ppm). $[\text{KO}^t\text{Bu}] = 0.77\text{--}10.5$ mM, $[\mathbf{6.1}] = 0.8\text{--}0.53$ mM, the reaction was performed at 23 °C in CD_3CN and monitored over time (400 MHz, 296 K, CD_3CN).

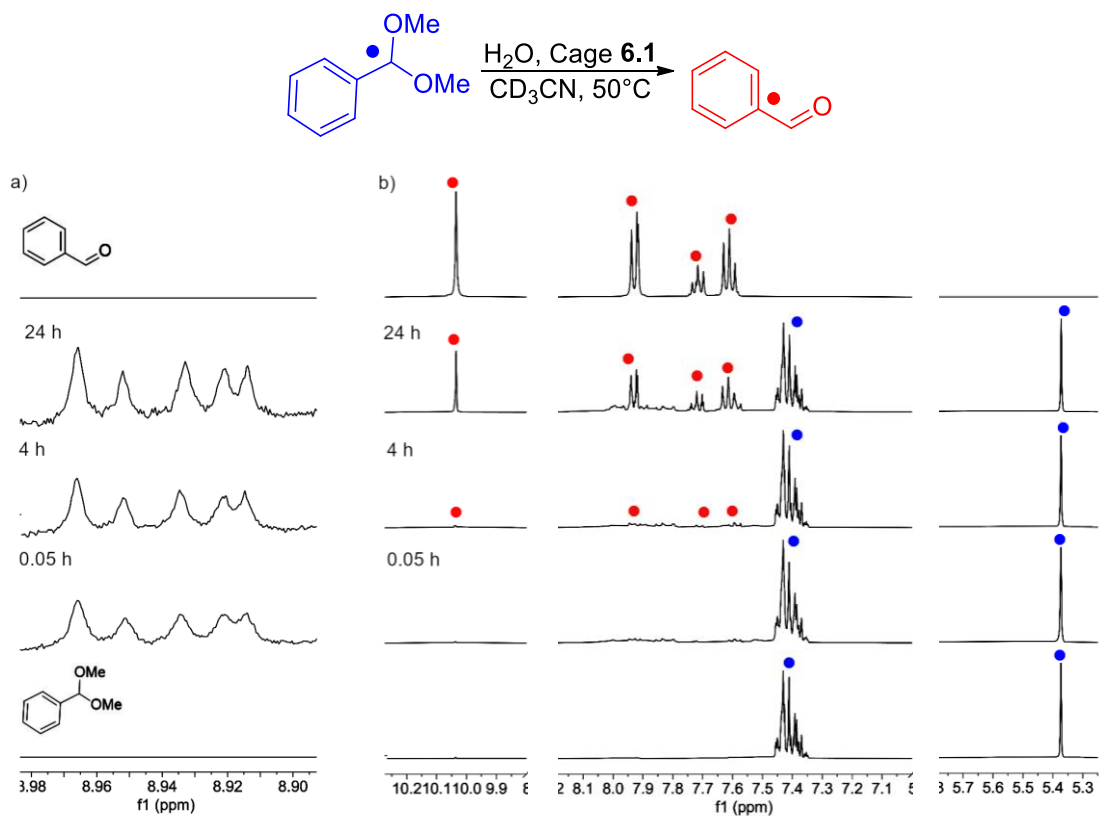


Figure 7.158. ^1H NMR spectra of the reaction between benzaldehyde dimethyl acetal (BDA) and H_2O in the presence of 5 mol % cage **6.1** showing: a) Cage stability (8.99 – 8.89 ppm) b) Product formation (10.3 – 9.8 ppm, 8.2 – 7.0 ppm, and 5.8 – 5.2 ppm). **[BDA]** = 15.75 mM **[H₂O]** = 94.5 mM, **[6.1]** = 0.8 mM, reaction was performed at 50 °C in CD_3CN and monitored over time (400 MHz, 323 K, CD_3CN).

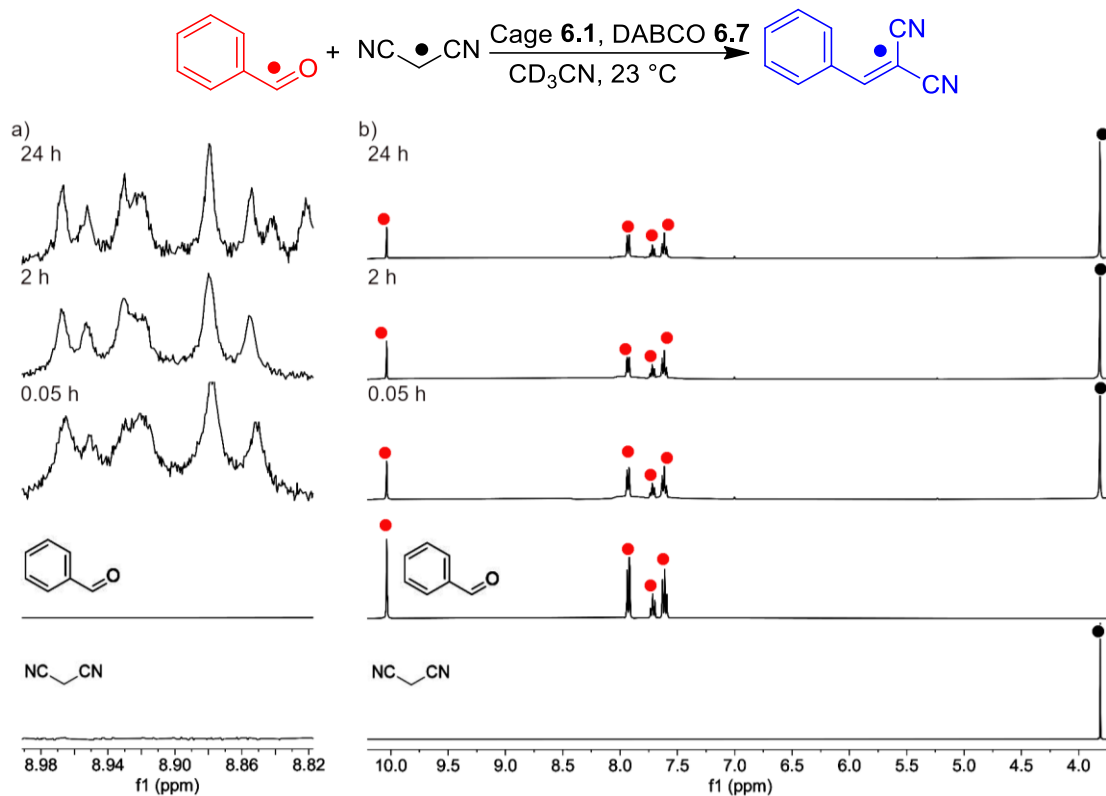


Figure 7.159. ¹H NMR spectra of the reaction between benzaldehyde and malonitrile in the presence of 5 mol % cage **1** and 5 mol % DABCO showing: a) Cage stability (8.99 – 8.82 ppm) b) No product formation (10.1 – 3.5). [Benzaldehyde] = 15.75 mM [Malonitrile] = 19.6 mM, [**6.1**] = 0.8 mM, [DABCO] = 0.8 mM, reaction was performed at 23 °C in CD₃CN and monitored over time (400 MHz, 296 K, CD₃CN).

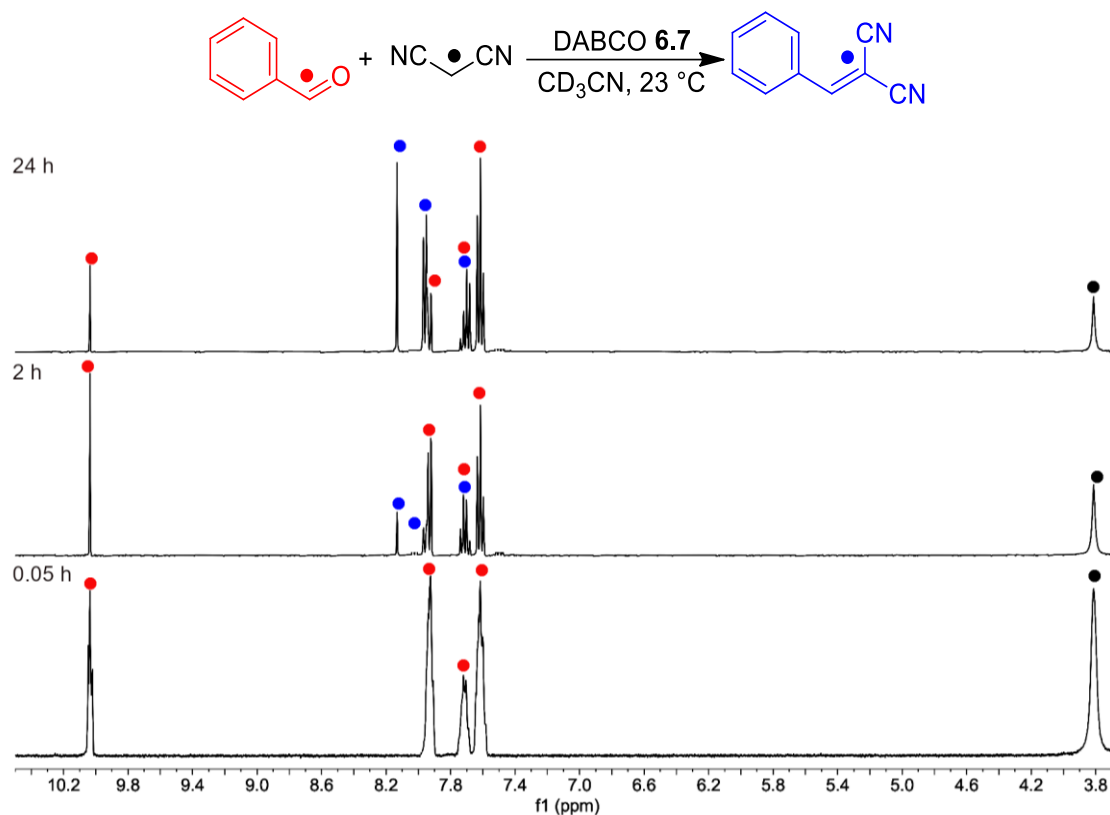


Figure 7.160. ^1H NMR spectra of the reaction between benzaldehyde and malononitrile in the presence of 5 mol % DABCO **6.7** showing product formation (10.1 – 3.5). $[\text{Benzaldehyde}] = 15.75 \text{ mM}$ $[\text{Malononitrile}] = 19.6 \text{ mM}$, $[\text{DABCO } \mathbf{6.7}] = 0.8 \text{ mM}$, reaction was performed at $23 \text{ }^\circ\text{C}$ in CD_3CN and monitored over time (400 MHz, 296 K, CD_3CN).

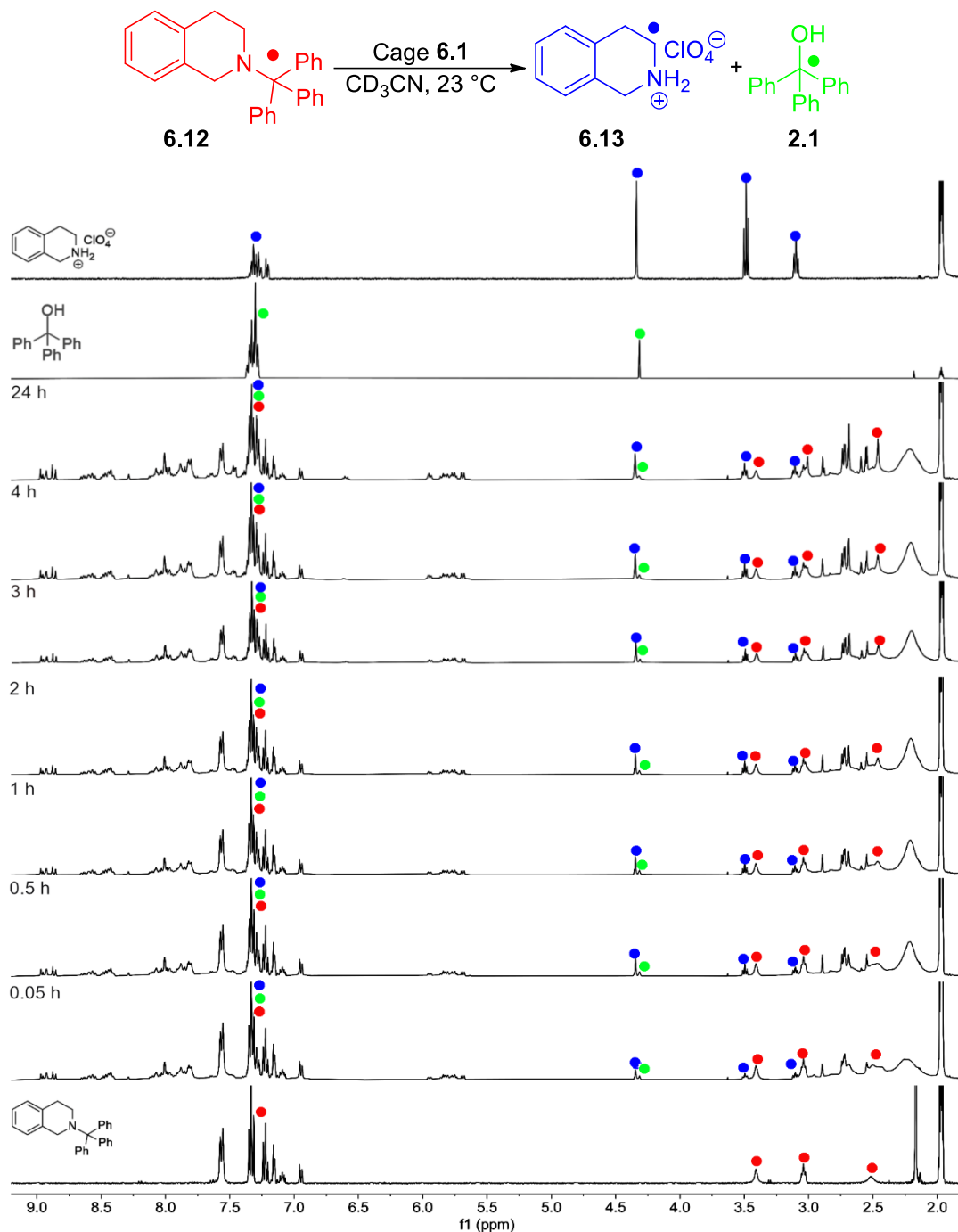


Figure 7.161. Full ^1H NMR spectra of the reaction of **6.12** in the presence of 5 mol % cage **6.1**. [**6.12**] = 15 mM, [**6.1**] = 1.25 mM, the reaction was performed at 23 °C in CD_3CN and monitored over time (400 MHz, 296 K, CD_3CN).

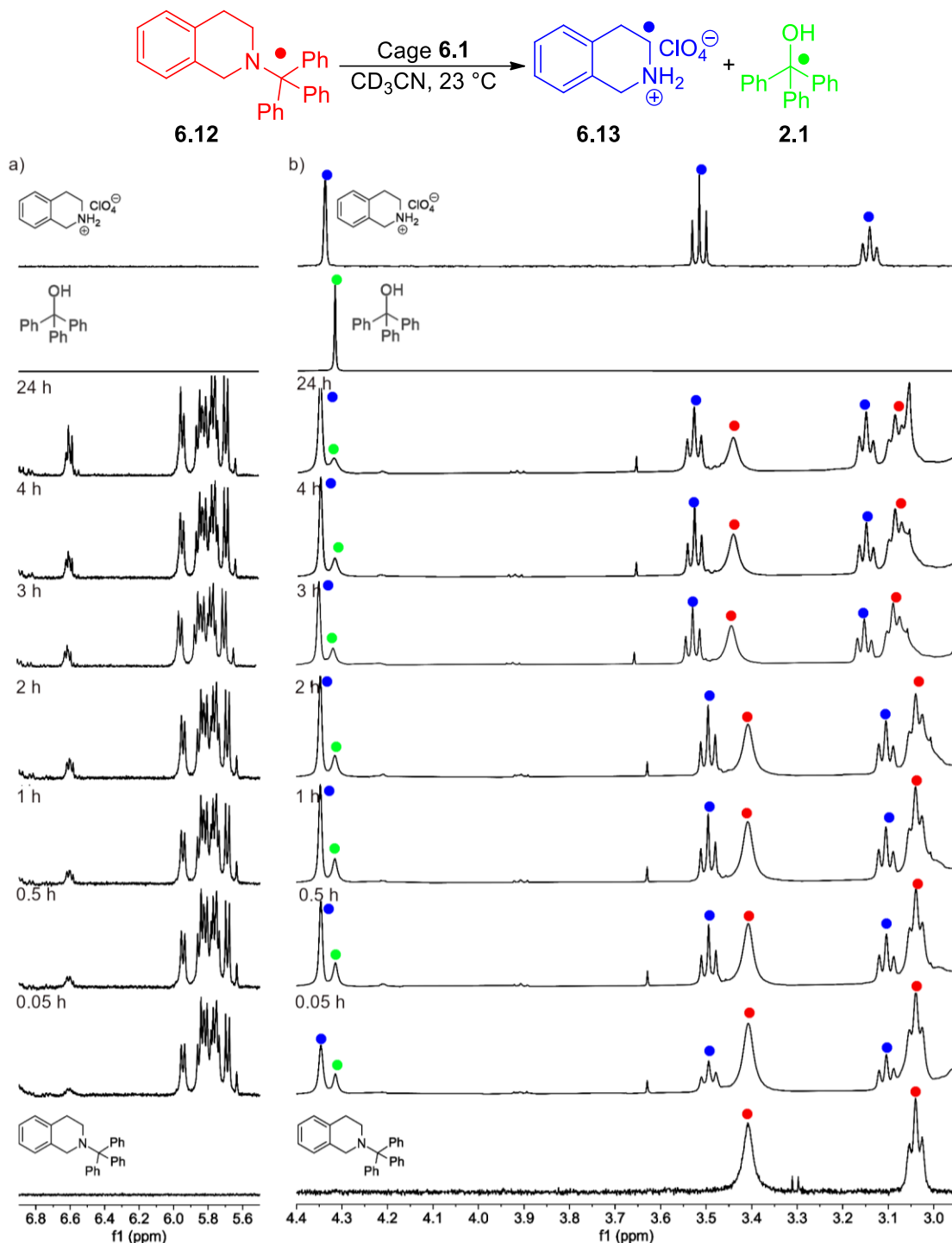


Figure 7.162. Expanded ^1H NMR spectra of the reaction of **6.12** in the presence of 5 mol % cage **6.1** showing: a) Cage stability (6.9 – 5.5 ppm) b) Product formation (4.4 – 2.9). $[\mathbf{6.12}] = 15 \text{ mM}$, $[\mathbf{6.1}] = 1.25 \text{ mM}$, the reaction was performed at $23 \text{ }^\circ\text{C}$ in CD_3CN and monitored over time (400 MHz, 296 K, CD_3CN).

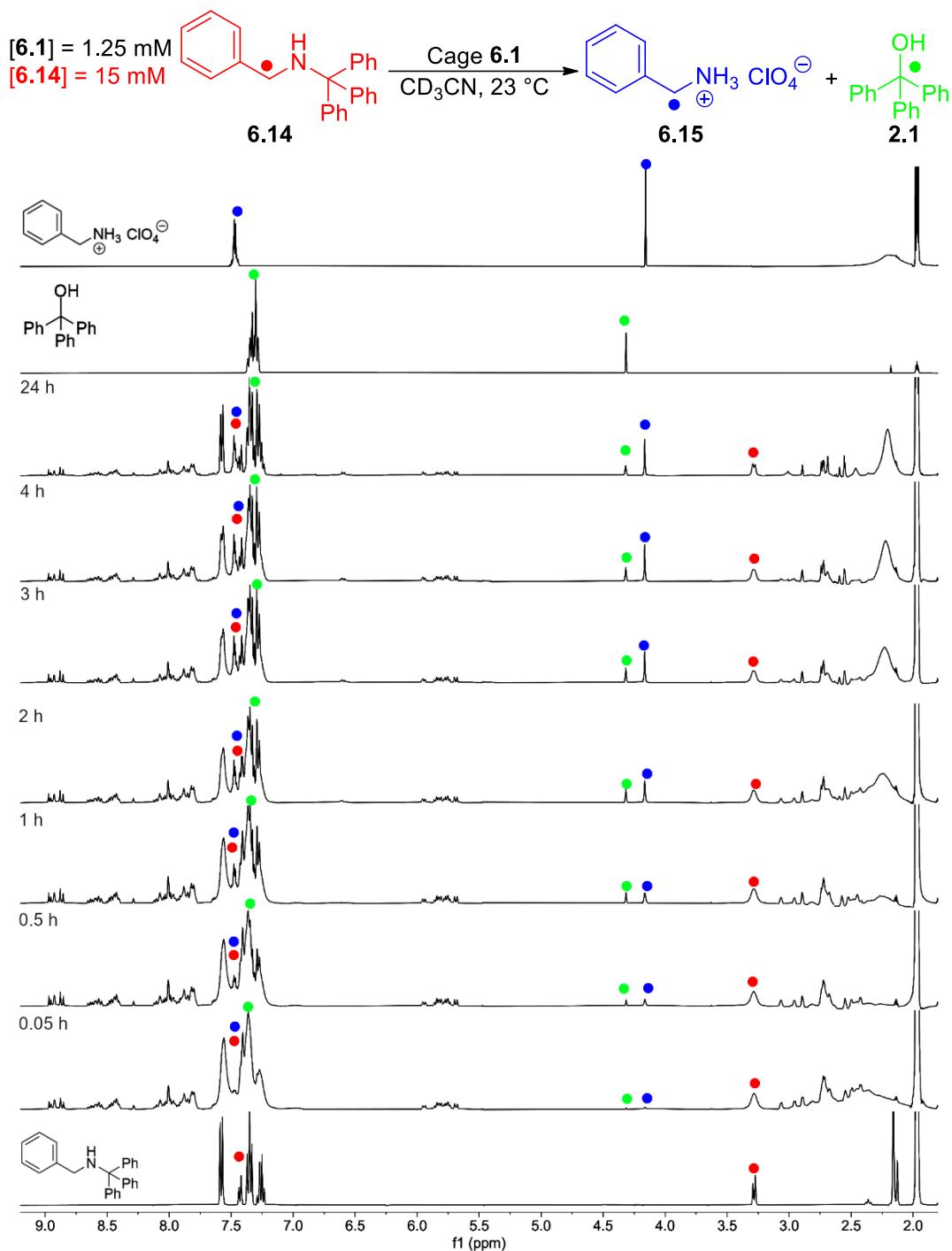


Figure 7.163. Full ^1H NMR spectra of the reaction of N-tritylbenzylamine **6.14** in the presence of 8 mol % cage **6.1**. $[6.14] = 15 \text{ mM}$, $[6.1] = 1.25 \text{ mM}$, the reaction was performed at $23 \text{ }^\circ\text{C}$ in CD_3CN and monitored over time (400 MHz, 296 K, CD_3CN).

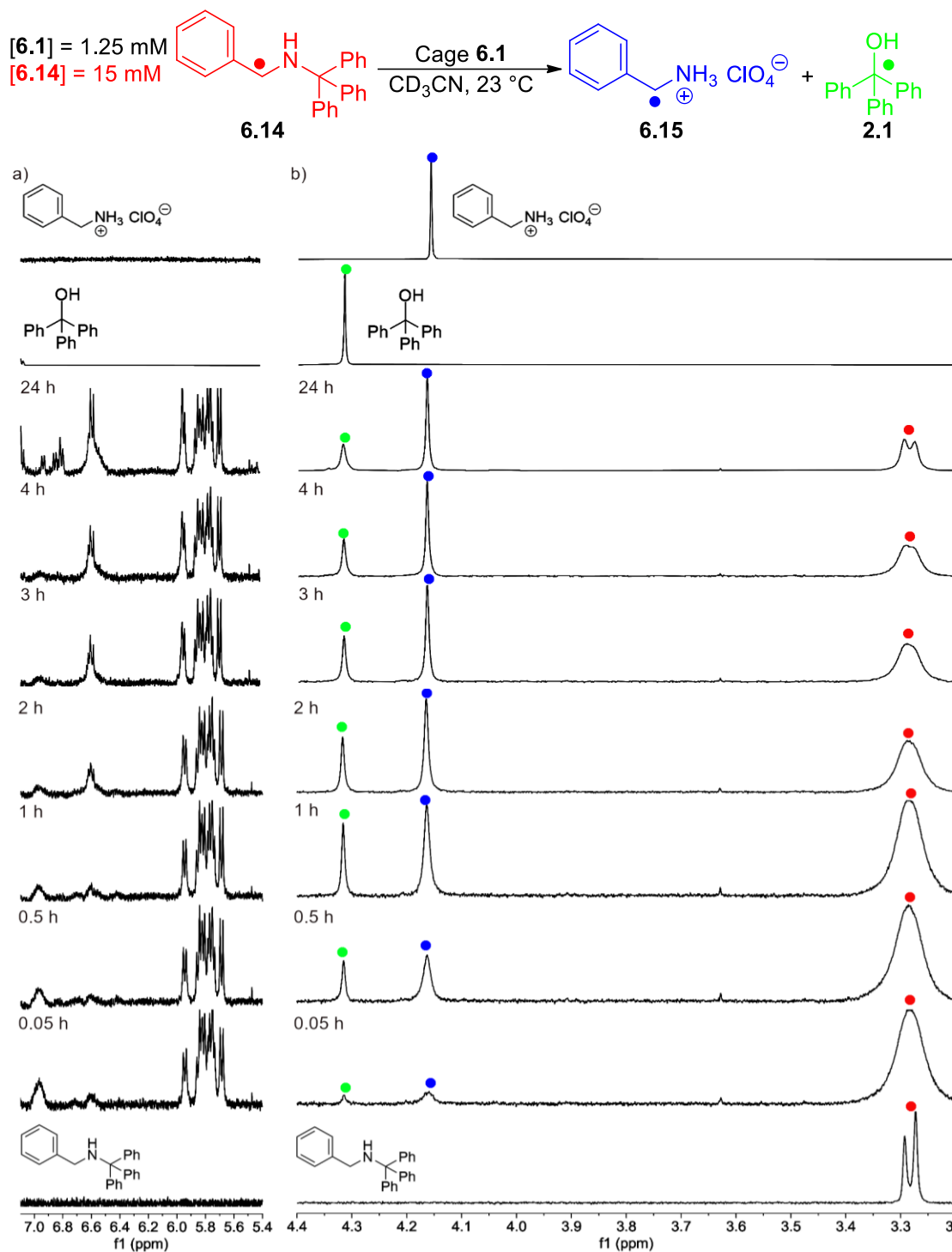


Figure 7.164. Expanded ^1H NMR spectra of the reaction of N-tritylbenzylamine **6.14** in the presence of 8 mol % cage **6.1** showing: a) Cage stability (7.1 – 5.4 ppm) b) Product formation (4.4 – 3.2). $[6.14] = 15 \text{ mM}$, $[6.1] = 1.25 \text{ mM}$, the reaction was performed at 23°C in CD_3CN and monitored over time (400 MHz, 296 K, CD_3CN).

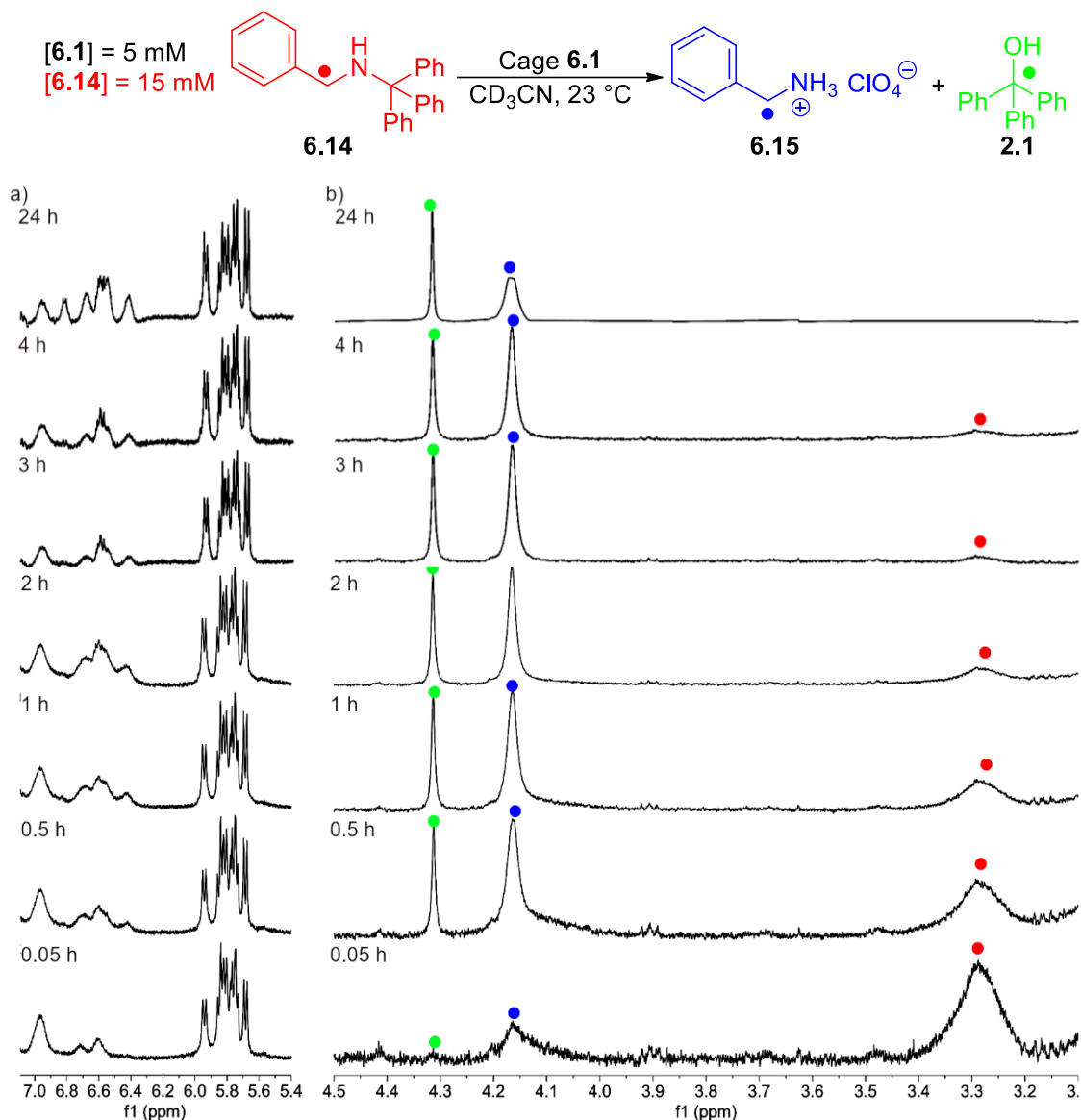


Figure 7.165. Expanded ^1H NMR spectra of the reaction of N-tritylbenzylamine **6.14** in the presence of 32 mol % cage **6.1** showing: a) Cage stability (7.1 – 5.4 ppm) b) Product formation (4.5 – 3.1). $[6.14] = 15 \text{ mM}$, $[6.1] = 5 \text{ mM}$, the reaction was performed at $23 \text{ }^\circ\text{C}$ in CD_3CN and monitored over time (400 MHz, 296 K, CD_3CN).

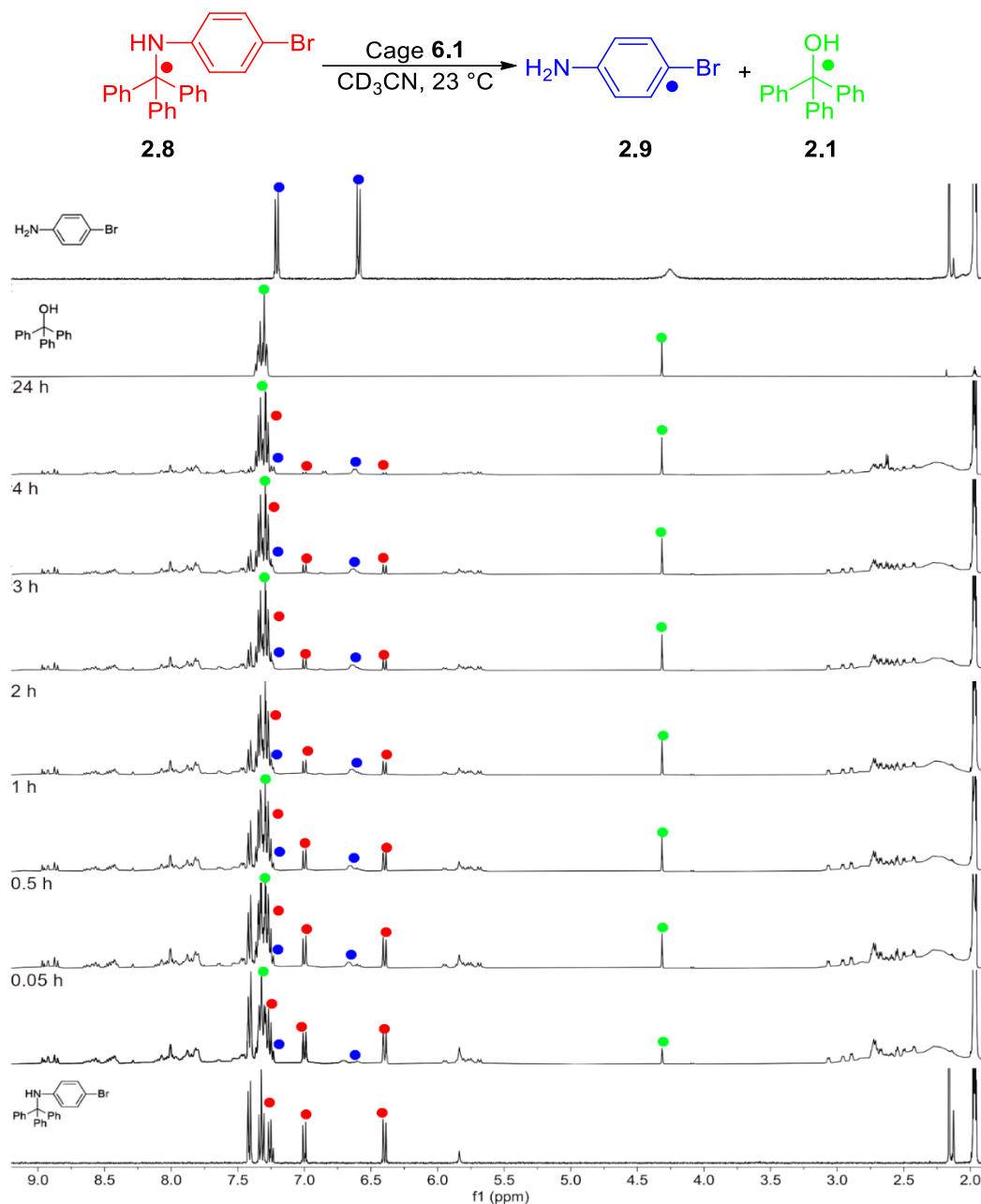


Figure 7.166. Full ^1H NMR spectra of the reaction of N-trityl-4-bromoaniline in the presence of 8 mol % cage **6.1**. $[\mathbf{2.8}] = 15$ mM, $[\mathbf{6.1}] = 1.25$ mM, the reaction was performed at 23 $^\circ\text{C}$ in CD_3CN and monitored over time (400 MHz, 296 K, CD_3CN).

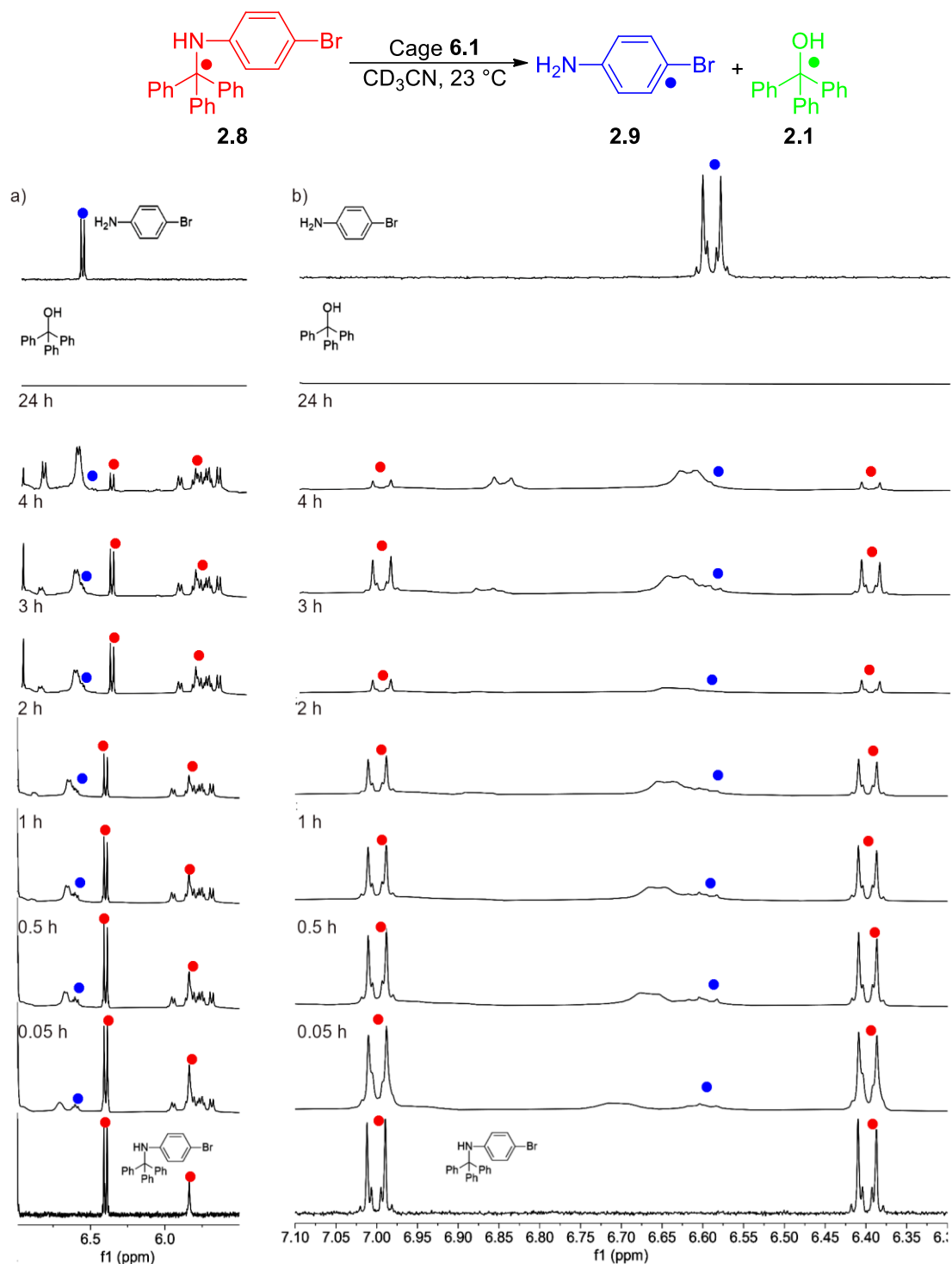


Figure 7.167. Expanded ^1H NMR spectra of the reaction of N-trityl-4-bromoaniline **2.8** in the presence of 32 mol % cage **6.1** showing: a) Cage stability (7.1 – 5.4 ppm) b) Product formation (4.5 – 3.1). [**2.8**] = 15 mM, [**6.1**] = 5 mM, the reaction was performed at 23 °C in CD_3CN and monitored over time (400 MHz, 296 K, CD_3CN).

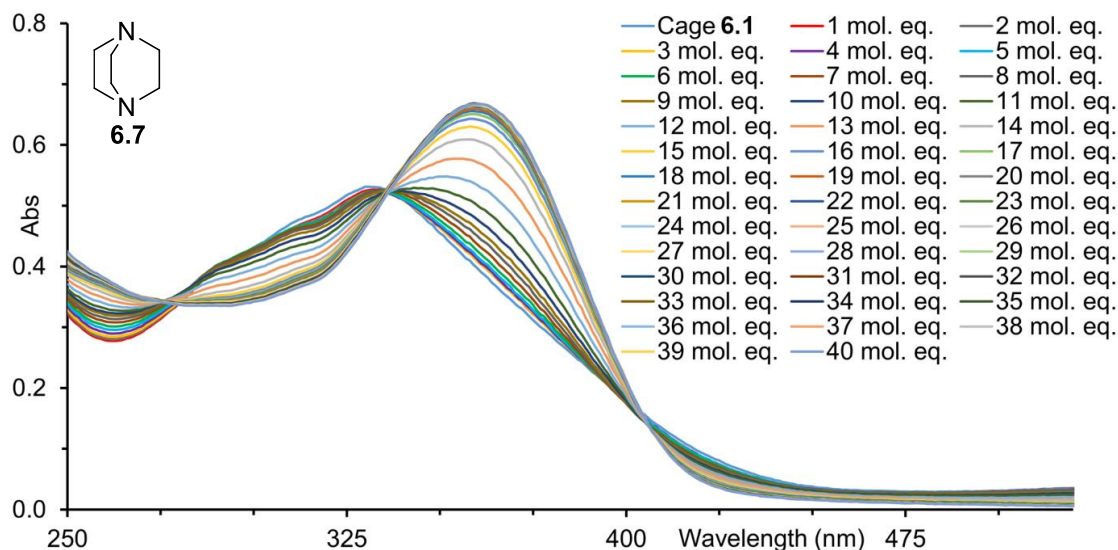


Figure 7.168. UV-Vis absorption spectrum of the titration of DABCO **6.7** into a 1.5 μM solution of cage **6.1** in CH_3CN . DABCO **6.7** was added in 1 μL aliquots from a 4.5 mM stock solution in CH_3CN .

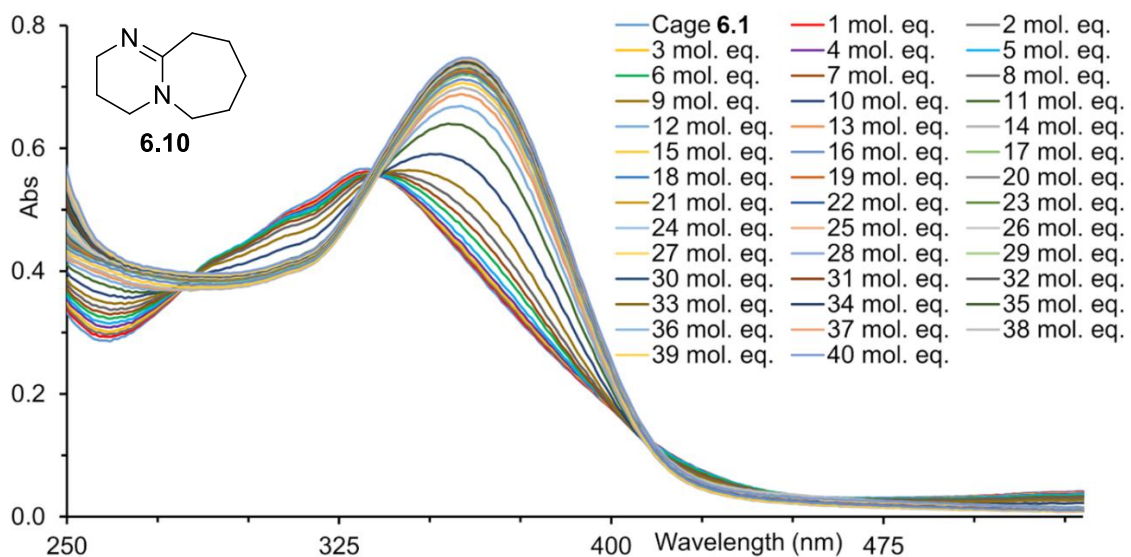


Figure 7.169. UV-Vis absorption spectrum of the titration of DBU **6.10** into a 1.5 μM solution of cage **6.1** in CH_3CN . DBU **6.10** was added in 1 μL aliquots from a 4.5 mM stock solution in CH_3CN .

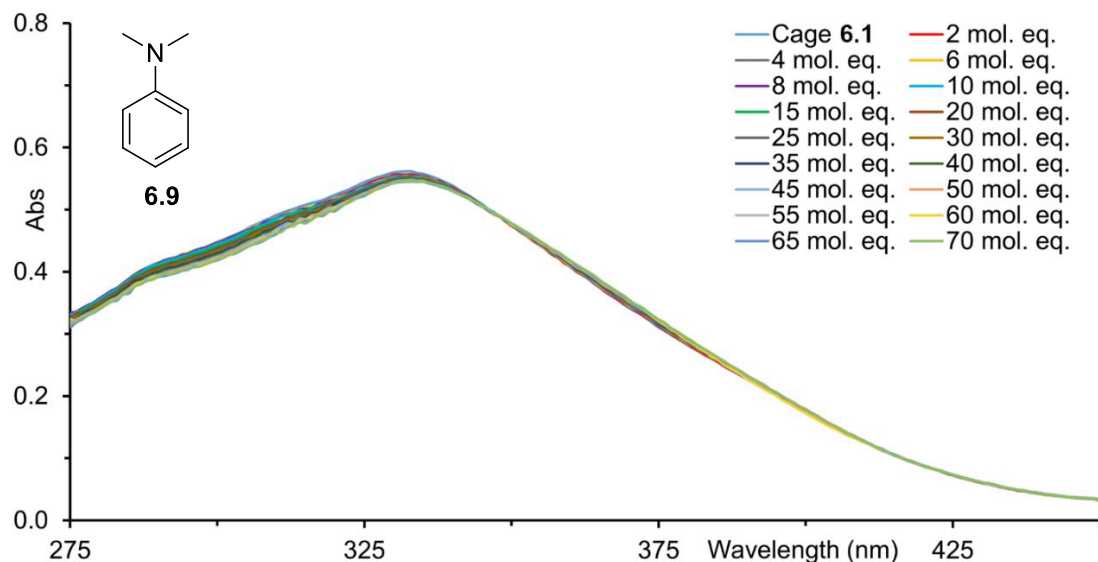


Figure 7.170. UV-Vis absorption spectrum of the titration of DMA **6.9** into a 1.5 μM solution of cage **6.1** in CH_3CN . DMA **6.9** was added in 2-5 μL aliquots from a 4.5 mM stock solution in CH_3CN .

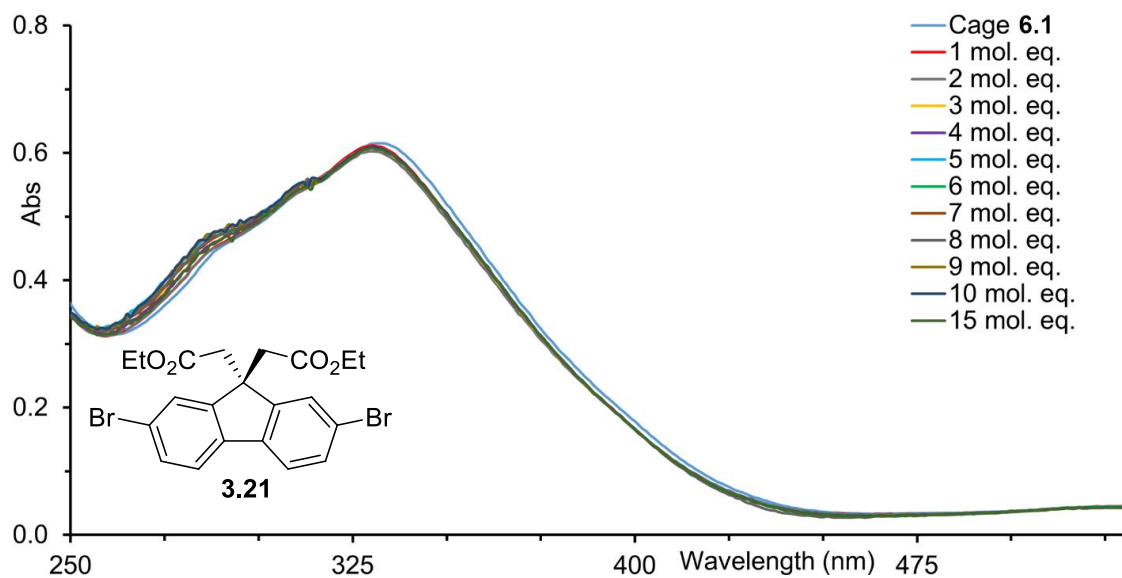


Figure 7.171. UV-Vis absorption spectrum of the titration of neutral guest **3.21** into a 1.5 μM solution of cage **6.1** in CH_3CN . **3.21** was added in 1 μL aliquots from a 4.5 mM stock solution in CH_3CN .

7.13. References

1. Association constants calculated using BindFit software, found at <http://supramolecular.org>.
2. Hibbert, D. B.; Thordarson, P. The death of the Job plot, transparency, open science and online tools, uncertainty estimation methods and other developments in supramolecular chemistry data analysis. *Chem. Commun.* **2016**, *52*, 12792–12805.
3. Thordarson, P. Determining association constants from titration experiments in supramolecular chemistry. *Chem. Soc. Rev.* **2011**, *40*, 1305–1323.
4. Mathematica. 11.2, Wolfram Research, Inc., Champaign, Illinois 2017.
5. Press, W.H.; Teukolsky, S.A.; Vetterling, W.T.; Flannery, B.P. Numerical Recipes in C, 2nd ed. Cambridge University Press, Cambridge, 1992.
6. Garland, C. W.; Nibler, J. W.; Shoemaker, D. P. Experiments in Physical Chemistry, 8th ed.; McGraw-Hill Higher Education, Boston, MA, 2009.
7. Wolfram Research Inc, Mathematica. 11.2, Wolfram Research, Inc., Champaign, Illinois 2017.